Electron and Scanning Probe Microscopies

2010 Contractors' Meeting

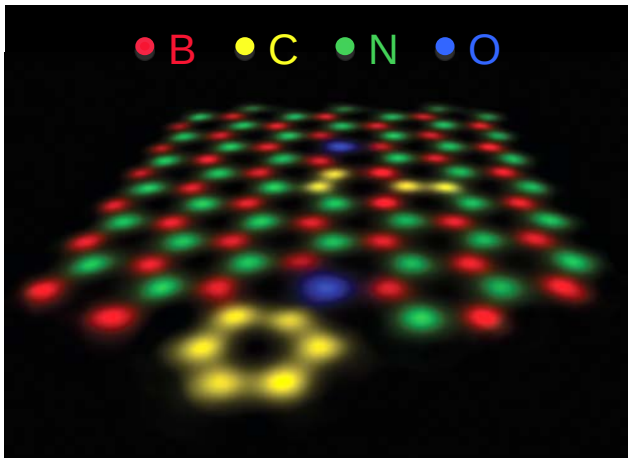

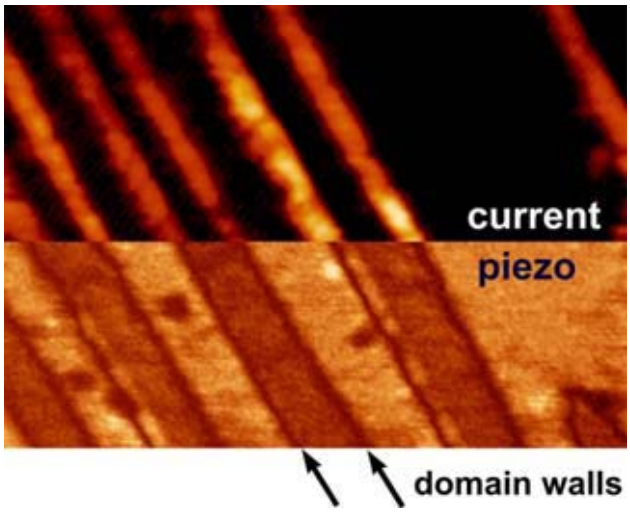

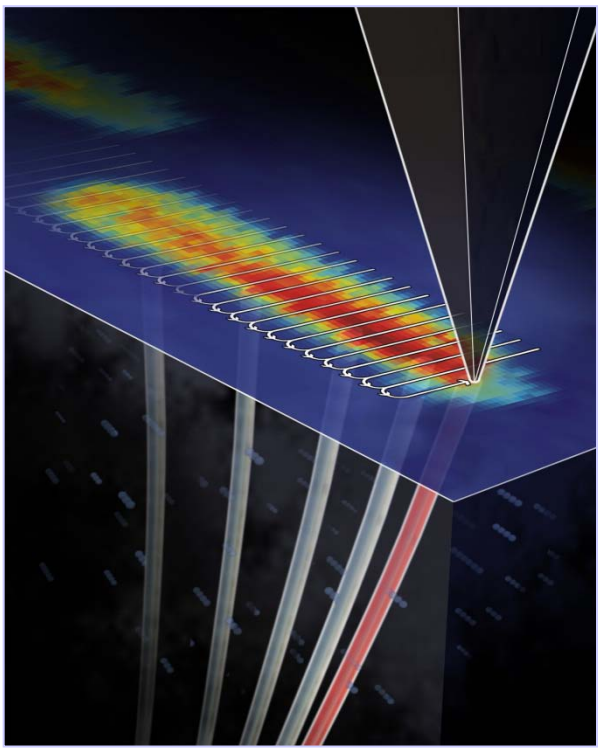

Airlie Conference Center
Warrenton, Virginia
October 3 - 6, 2010

U.S. DEPARTMENT OF ENERGY

Office of Basic Energy Sciences
Division of Materials Sciences and Engineering

On the Cover

Upper left: *Atom by atom imaging and identification of impurities in monolayer boron nitride.* Annular dark-field imaging in an aberration-corrected scanning transmission electron microscope optimized for low voltage operation can resolve and identify the chemical type of every atom in monolayer hexagonal boron nitride that contains substitutional defects. The results demonstrate that atom-by-atom structural and chemical analysis of all radiation-damage-resistant atoms present in, and on top of, ultra-thin sheets has now become possible. Cover story published in *Nature* **464**, 571–574 (2010).
Courtesy: S. Pennycook, Oak Ridge National Laboratory

Right: *Nanomanipulation of quantum vortices in the high-temperature superconductor YBCO*. A magnetic force microscope tip pulls a single vortex through a crystal. The vortex acts like a one-dimensional elastic string moving through a three-dimensional pinning landscape. Quantitative measurements of the force required to pull the vortex under various conditions reveal the structure of the vortex-defect interaction. Work published in *Nature Physics* **5**, 35–39 (2009).
Courtesy: K. Moler, Stanford Institute for Materials & Energy Sciences/SLAC

Lower left: *Nanoscale conducting domain walls in multiferroic $BiFeO_3$.* Local current and piezoresponse at conducting domain 109^o domain walls in a 100 nm thick La-doped $BiFeO_3$ film shows the direct measurement of polarization-controlled electron transport through thin ferroelectric films. Work published in *Nature Materials* **8**, 229 (2009).
Courtesy: S. Kalinin et al., Oak Ridge National Laboratory

This document was produced under contract number DE-AC05-06OR23100 between the U.S. Department of Energy and Oak Ridge Associated Universities.

The research grants and contracts described in this document are supported by the U.S. DOE Office of Science, Office of Basic Energy Sciences, Materials Sciences and Engineering Division.

Foreword

This volume comprises the scientific content of the 2010 Contractors' Meeting on Electron and Scanning Probe Microscopies (ESPM) sponsored by the Division of Materials Sciences and Engineering (DMS&E) in the Office of Basic Energy Sciences (BES) of the U. S. Department of Energy (DOE). The meeting, held on October 3-6, 2010 at the Airlie Conference Center, Warrenton, VA, is the third contractors' meeting in this area and is one among a series of research theme-based contractors' meetings conducted by DMS&E. The meeting highlights materials research using advanced electron and scanning probe microscopy and spectroscopy techniques, and it also features research that cuts across other BES program areas where appropriate and relevant.

The Electron and Scanning Probe Microscopies Core Research Activity supports basic research in materials sciences using advanced electron and scanning probe microscopy and spectroscopy techniques to understand the atomic, electronic, and magnetic structures and properties of materials. To address forefront scientific challenges, new state-of-the-art microscopy and spectroscopy, as well as the associated theoretical tools to maximize understanding of the experiments, are essential and showcased at the meeting. Topical areas using ESPM highlighted in this year's meeting include ferroelectrics, superconductivity, magnetism, nanomaterials and nanoscale phenomena, and materials for clean energy.

The purpose of this contractors' meeting is to bring together researchers funded by BES in the ESPM area on a periodic basis (biennially at present), to facilitate the exchange of new results and research highlights, to foster new ideas and collaborations among the participants, and to identify needs of the research community. The meeting will also help DMS&E in assessing the state of the program, identifying new research directions and programmatic needs.

It is a great pleasure to express my sincere thanks to all the meeting participants for their investment of time and for their willingness to share their ideas and latest research results. The advice and help of Meeting Chairs, Kam Moler and John Spence, in organizing this meeting are deeply appreciated. Thanks also go to Teresa Crockett from DMS&E and to Joreé O'Neal and Lee-Ann Talley from the Oak Ridge Institute for Science and Education for their outstanding work in taking care of all the logistical aspects of the meeting.

Jane G. Zhu
Program Manager, Electron and Scanning Probe Microscopies
Division of Materials Sciences and Engineering
Office of Basic Energy Sciences
U. S. Department of Energy

U. S. Dept of Energy
Office of Basic Energy Sciences

Electron and Scanning Probe Microscopies Contractors' Meeting

Airlie Conference Center, Warrenton, VA
October 3-6, 2010

SUNDAY, OCTOBER 3

3:00 – 6:00 pm	Arrival and Registration
5:00 – 6:00 pm	Reception (No Host)
6:00 – 7:00 pm	***** Dinner *****
7:00 – 7:40 pm	*Welcome* *Division and Program Updates* Linda Horton Director, Division of Materials Sciences and Engineering Jane Zhu Program Manager, Electron and Scanning Probe Microscopies **Invited Talk and Workshop Update** Chairs: John Spence and Kam Moler
7:40 – 8:10 pm	Gary Rubloff, NEES, University of Maryland (Invited) *Nanostructures for Energy Storage: What Can We Learn from Imaging and Spectroscopy?*
8:10 – 8:40 pm	Dawn Bonnell, University of Pennsylvania *DMSE Council Workshop on Frontiers of Atomic-Scale Functionality Imaging*
8:40 – 9:10 pm	Ian Robertson, University of Illinois *DMSE Council Workshop on Characterizing Materials Damage in Four Dimensions*
9:10 – 10:00 pm	**Interaction and Discussions**

MONDAY, OCTOBER 4

7:00 – 8:00 am	Breakfast
Session I	**Ferroelectrics and Domain Structures** Chair: Alexei Gruverman, University of Nebraska
8:00 – 8:30 am	Seungbum Hong, Argonne National Laboratory *Emergent Phenomena in Ferroic Nanostructures: Domain Imaging*
8:30 – 9:00 am	Albina Borisevich, Oak Ridge National Laboratory *Probing Phase Transitions, Chemical Reactions, and Energy Transfer at the Atomic Scale: Multifunctional Imaging with Combined Electron and Scanning Probe Microscopy*
9:00 – 9:30 am	Long-Qing Chen, Pennsylvania State University *Structure and Dynamics of Domains in Ferroelectric Nanostructures -- Phase-field Modeling*
9:30 – 10:00 am	Art Baddorf, Oak Ridge National Laboratory *Mapping Ionic Currents and Electrochemical Reactions on the Nanometer Scale*
10:00 – 10:30 am	***** Break *****
Session II	**Materials for Clean Energy** Chair: Nitash Balsara, Lawrence Berkeley National Laboratory
10:30 – 11:00 am	Paul Weiss, UCLA *Atomic-Scale Chemical, Physical and Electronic Properties of the Subsurface Hydride of Palladium*
11:00 – 11.30 am	Shashank Priya, Virginia Polytechnic Institute *Correlation of Bulk Dielectric and Piezoelectric Properties to the Local Scale Phase Transformations, Domain Morphology and Crystal Structure*
11:30 – 12:00 noon	Shirley Meng, University of California, San Diego *New In Situ Analytical Electron Microscopy for Understanding Structure Evolution and Composition Change in High Energy Density Electrode Materials in Lithium Ion Batteries*
12:00 – 12:30 pm	Christian Kisielowski, Lawrence Berkeley National Laboratory *From Resolution to Time Evolution*

12:30 – 1:30 pm	***** Lunch *****
1:30 – 3:30 pm	**Time for Interaction and Discussions**
3:30 – 5:30 pm	**Poster Session I**
5:30 – 6:30 pm	***** Dinner *****
Session III	**Superconductivity and Novel Probes** Chair: Kam Moler, Stanford Institute for Materials & Energy Science/SLAC
6:30 – 7:00 pm	Ali Yazdani, Princeton University *Probing Correlated Superconductors and Their Phase Transitions on the Nanometer Scale*
7:00 – 7:30 pm	Séamus Davis, Brookhaven National Laboratory *Spectroscopic Imaging STM for Complex Electronic Matter*
7:30 – 8:00 pm	Aharon Kapitulnik, SIMES/SLAC *High-Resolution Polar Kerr Effect Studies of Unconventional Superconductors*
8:00 – 8:30 pm	Venkat Chandrasekhar, Northwestern University *Point Contact Measurements on Thin Films of Ferropnictide Superconductors*
8:30 – 9:00 pm	Benjamin Lev, University of Illinois, Urbana-Champaign *Atom Chip Microscopy: A Novel Probe for Strongly Correlated Materials*
9:00 – 10:00 pm	***Interactions in Poster Room***

TUESDAY, OCTOBER 5

7:00 – 8:00 am	Breakfast
Session IV	**Advanced Capabilities** Chair: Yimei Zhu, Brookhaven National Laboratory
8:00 – 8:30 am	Sok Pantelides, Vanderbilt University *Physics of Complex Materials Systems through Theory and Microscopy/EELS*

8:30 – 9:00 am	John Spence, Arizona State University *Quantitative Nanodiffraction for Atomic Processes in Clean Energy Materials*
9:00 – 9:30 am	Andreas Scherz, SIMES/SLAC (invited) *Nanoscale Imaging of Ultrafast Magnetization Dynamics with Resonant Coherent X-rays*
9:30 –10:00 am	Geoff Campbell, Lawrence Livermore National Laboratory *Complex Fundamental Mechanisms of Transient States in Materials Quantified by DTEM*
10:00 –10:30 am	***** Break *****
Session V	**Magnetic Materials and Imaging** Chair: Marc DeGraef, Carnegie Mellon University
10:30 – 11:00 am	Martha McCartney, Arizona State University *Nanoscale Imaging of Electrostatic and Magnetic Fields*
11:00 – 11:30 am	Jing Tao, Brookhaven National Laboratory *Direct Imaging of Nanoscale Phase Separation in Colossal Magnetoresistive* $La_{1-x}Ca_xMnO_3$
11:30 – 12:00 noon	J.M.K. Wiezorek, University of Pittsburgh *Electron Density Determination, Bonding and Properties of Tetragonal Ferromagnetic Intermetallics*
12:00 – 12:30 pm	Chris Hammel, Ohio State University *Nanoscale Understanding of Exchange Bias and Spin Wave Manipulation using Advanced MRFM Imaging Techniques*
12:30 – 1:30 pm	***** Lunch *****
1:30 – 3:30 pm	**Time for Interaction and Discussions**
3:30 – 5:30 pm	**Poster Session II**
5:30 – 6:30 pm	***** Dinner *****

Session VI	**Surfaces and Interfaces** Chair: Peter Flynn, University of Illinois, Urbana-Champaign
6:30 – 7:00 pm	Konrad Thürmer, Sandia National Laboratories *Nanometer-Scale Surface and Interface Phenomena*
7:00 – 7:30 pm	Laurie Marks, Northwestern University *New Methods for Atomic Structure Determination of Nanoscale Materials*
7:30 – 8:00 pm	Ward Plummer, Louisiana State University *Emerging Functionality in Transition-Metal Oxides Driven by Spatial Confinement*
8:00 – 8:30 pm	Nigel Browning, University of California, Davis *Materials Properties at Interfaces in Nanostructured Materials: Fundamental Atomic Scale Issues*
8:30 – 9:00 pm	Martin P. Harmer, Lehigh University *Discovering the Role of Grain Boundary Complexions in Materials*
9:00 – 10:00 pm	***Interactions in Poster Room***

WEDNESDAY, OCTOBER 6

7:00 – 8:00 am	Breakfast
Session VII	**Nanoscale Phenomena** Chair: Bob Westervelt, Harvard University
8:00 – 8:30 am	Saw-Wai Hla, The Ohio University *Single Atom and Molecule Manipulation and Its Application to Nanoscience and Technology*
8:30 – 9:00 am	Hari Manoharan, SIMES/SLAC *Spin Physics and Nanoscale Probes of Quantum Materials*
9:00 – 9:30 am	David Cobden, University of Washington *Intrinsic Properties of Correlated Materials Derived from Combined Nanoscale Transport and Ultrafast Spatio-Temporal Imaging Experiments*
9:30 – 10:00 am	Amir Yacoby, Harvard University *Transport and Imaging of Mesoscopic Phenomena in Single and Bilayer Graphene*

10:00 – 10:30 am	***** Break *****
Session VIII	**Nanomaterials and Defects** Chair: Jim Zuo, University of Illinois
10:30 – 11:00 am	Steve Pennycook, Oak Ridge National Laboratory *Scanning Transmission Electron Microscopy: Atomic Structure and Properties of Materials*
11:00 – 11.30 am	Susanne Stemmer, University of California, Santa Barbara *Phonons and Electrons in Thin Complex Oxides*
11:30 – 12:00 noon	Paul Voyles, University of Wisconsin-Madison *Characterization of Dopant / Point Defect Complexes in Semiconductors by STEM*
12:00 – 12:15 pm	Closing Remarks Kam Moler and John Spence, Meeting Chairs Jane Zhu, Meeting Organizer
12:15 pm	***** Lunch ***** Open Discussions and Adjourn

POSTER SESSION I
Meadow Room

Monday, October 4, 2010
3:30 – 5:30 PM and 9:00 – 10:00 PM

P-I.1 - Local Electronic and Dielectric Properties at Nanosized Interfaces
Dawn A. Bonnell, University of Pennsylvania

P-I.2 - Emergent Phenomena in Multiferroic BiFeO3 Nanostructures
O. Auciello, S. Hong, B. Kabius and G. Bai, Argonne National Laboratory

P-I.3 - Structure and Dynamics of Domains in Ferroelectric Nanostructures -- In-Situ TEM Studies
Xiaoqing Pan, University of Michigan

P-I.4 - Nanoscale Resistive Switching Behavior of Ferroelectric and Multiferroic Tunnel Junctions
A. Gruverman, E. Tsymbal, C.-B. Eom, University of Nebraska-Lincoln and University of Wisconsin-Madison

P-I.5 - Sources and Control of Nucleation and Growth in Ferroelectric and Phase-Change Memory Devices
Bryan D. Huey, University of Connecticut

P-I.6 - Free and Supported Clusters: Interrogated by PES and STM
Kit H. Bowen, Johns Hopkins University

P-I.7 – Hydrogen Generation Using Integrated Photovoltaic and Photoelectrochemical Cells
Jin Z. Zhang and Yiping Zhao, University of California, Santa Cruz and University of Georgia at Athens

P-I.8 - Atomistic Mechanisms of Metal-Assisted Hydrogen Storage in Nanostructured Carbon
Nidia C. Gallego, Cristian I. Contescu, James Morris, Takeshi Egami, and Stephen Pennycook, Oak Ridge National Laboratory

P-I.9 - Soft Matter Electron Microscopy
Nitash Balsara, Kenneth Downing, Christian Kisielowski, Andrew Minor, and Ronald Zuckermann, Lawrence Berkeley National Laboratory

P-I.10 - Quantitative Electron Nanocrystallography
Jian-Min (Jim) Zuo, University of Illinois, Urbana-Champaign

POSTER SESSION II
Meadow Room

Tuesday, October 5, 2010
3:30 – 5:30 PM and 9:00 – 10:00 PM

P-II.1 - Imaging of Buried Nanoscale Optically Active Materials
Ian Appelbaum, University of Maryland

P-II.2 - Discovery of Dielectric Response and Forces in Nanoscale Objects
P.E. Batson, Rutgers University

P-II.3 – In Situ Characterization and Modeling of Formation Reactions under Extreme Heating Rates in Nanostructured Multilayer Foils
Todd C. Hufnagel, Michael L. Falk, Omar M. Knio, and Timothy P. Weihs, Johns Hopkins University

P-II.4 – High-Resolution Photoemission Electron Microscopy
R. Könenkamp, Portland State University

P-II.5 - Dynamical Nanoscale Crystallography with Femtosecond Resolution
Chong-Yu Ruan, Michigan State University

P-II.6 - Experimental Vector Field Electron Tomography of Magnetic Objects
Marc DeGraef, Carnegie Mellon University

P-II.7 - Observing Materials Dynamics on the Fundamental Atomic Scale by Ultrafast In-Situ TEM
N.D. Browning, J.E. Evans, N. Goldman, D.J. Masiel, J.T. McKeown, B. W. Reed, and M. Santala, Lawrence Livermore National Laboratory

P-II.8 - Interfacial Thermal Resistance of Carbon Nanotubes
John Cumings, University of Maryland

P-II.9 - Electronic States and Transport in Semiconductor Nanostructures
Rachel S. Goldman and Harley T. Johnson, University of Michigan and University of Illinois, Urbana-Champaign

P-II.10 - Grain Boundary Complexions and Transitions: A New Thermodynamic Theory and Initial Experimental Observations
Jian Luo, Clemson University

P-II.11 - Visualization and Quantification of Deformation Processes Controlling the Mechanical Response of Alloys in Aggressive Environments
Ian M. Robertson, University of Illinois, Urbana-Champaign

Table of Contents

Table of Contents

University Grant Projects

Invited Talks

LABORATORY PROJECTS

Emergent Phenomena in Multiferroic $BiFeO_3$ Nanostructures (FWP 58931)

O. Auciello, S. Hong, B. Kabius, and G. Bai
Materials Science Division, Argonne National Laboratory, 9700 S Cass Avenue, Argonne, IL 60439.
auciello@anl.gov; hong@anl.gov; kabius@anl.gov, grbai@anl.gov

Program Scope

The research theme discussed in this abstract focuses on the synthesis and emergent ferroelectric phenomena of $BiFeO_3$ (BFO) thin films integrated in nanoscale structures (nanocapacitors). This task is carried out within a broader program that combines advanced materials synthesis, complementary *in situ* and *ex situ* characterization and property measurement techniques combined with computer simulations to elucidate novel and emergent behavior in oxide thin films, heterostructures, and nanostructures with emphasis on systems that exhibit ferroelectric, ferromagnetic and multiferroic properties as well as systems that display novel transport behavior. The program is structured around three interrelated themes: 1) studies to understand how synthesis affects the properties of multiferroic oxide films. 2) studies to understand the mechanisms by which film properties are modified in nanostructures, through effects such as size confinement, charge transfer and band structure modification. 3) studies to understand the dynamic response in multiferroic nanostructures, including the physics underlying ferroelectric domain behavior, and ferromagnetic magnetization reversal mechanisms, in thin films and patterned oxide nanostructures The complementary strengths of simulation and experiment provide fundamental insights into the mechanisms and interfacial driving forces that control composition and microstructure and thus overall film properties and phenomena in nanostructures.

Recent Progress

A variety of film synthesis and nanostructure fabrication techniques and a set of complementary *in situ* and *ex situ* characterization methods have been used to obtain insights into phenomena occurring in BFO thin films induced by the constrains imposed by the nanoscale dimensions of the nanostructures (nanocapacitors).

Synthesis of BFO Thin Films

Currently, we are exploring the synthesis of BFO thin films using two main techniques (magnetron sputter and metal-organic chemical vapor deposition (MOCVD)), as described below.

MOCVD Synthesis of BFO Films: Several techniques have been used to synthesize BFO films, including pulse laser deposition, magnetron sputter deposition, sol-gel synthesis and MOCVD, the latest being the film deposition of choice for integration of BFO films with CMOS devices for fabrication of FeRAMs. However, it has been difficult to produce single-phase BFO films by MOCVD, apparently, due to the multiformity of valences of Fe and Bi elements and the re-evaporation of bismuth oxide during the film processing. Therefore, a delicate balance between the vapor phase partial pressures of precursors and the partial pressure of oxygen in the reactor chamber is essential to get phase-pure BFO film by MOCVD. In this respect, most reports on the synthesis of epitaxial BFO films show growth temperatures equal to, or higher than 650° C, which implies potential problems for fabrication of FeRAMs that require integration with CMOS devices. Thus, we focused our research on investigating the conditions to grow BFO films by MOCVD. Specifically, we investigated the effects of oxygen partial pressure in the MOCVD reactor chamber, growth temperature, and growth rates, on the phase, structure, and morphologies of bismuth oxide, iron oxide, and BFO films. Our data indicate that phase pure BFO films can be synthesized reproducibly by MOCVD. Furthermore, we developed a low temperature (500-550 ˚C) growth process, which is critical for integration of MOCVD BFO films with CMOS devices. The XRD analyses (Fig. 1) show that our low temperature BFO films exhibit epitaxial registry to single crystal $SrTiO_3$ substrates and are phase pure. The rocking curve of (001) oriented BFO film (Fig. 1) shows a 0.1˚ HFWM, which is much lower than all values reported in the literature.

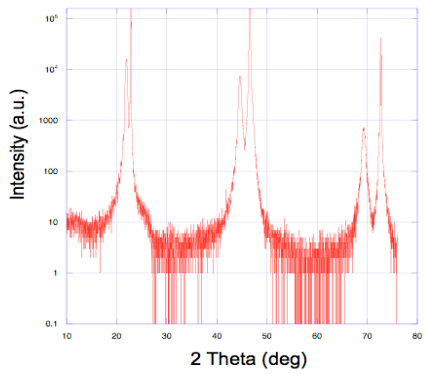

Fig. 1. XRD spectrum for a low temperature $BiFeO_3$ film grown by MOCVD on a single crystal $SrTiO_3$ substrate; the spectrum reveals a phase pure (no impurity peaks), crystalline film.

Magnetron Sputter-Deposition of BFO and SRO Films: For the first studies on the synthesis of $BiFeO_3$ (BFO) films by magnetron sputter-deposition, we used a multi-target magnetron sputter-deposition system to grow 125 nm thick (001) oriented $SrRuO_3$ (SRO) thin films on top of (001) $SrTiO_3$ (STO) single crystal substrate (miscut 0.5° from the (001) plane and 17° from the in-plane [010] directions). This was followed by growth of (001)-oriented 120 nm thick $BiFeO_3$ (BFO) thin films on top of the SRO/STO substrate in an integrated deposition process without exposing the interfaces to air. We characterized the crystallinity and orientation of the films using X-ray diffraction (Huber 4 circle diffractometer) analysis. Both BFO and SRO layers are oriented with the (001) atomic planes in the film plane. We determined the thickness of the SRO electrode layer from the oscillations in the scattered intensity along the 00L crystal truncation rod, and confirmed the thickness of the SRO and BFO layers via cross-section scanning electron microscopy (SEM) measurements. The BFO film thickness is beyond the critical value (36 nm) for a coherently strained film on STO. Accordingly, the BFO (001) Bragg peak (Fig. 2) is broadened due to strain relaxation.

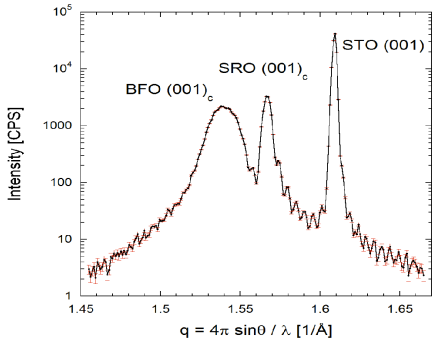

Fig. 2. The X-ray scattered intensity from a specular crystal truncation rod scan through the (001) Bragg diffraction peaks of the BFO and SRO films, and the STO substrate. The data was collected with horizontally and vertically focused Cu Ka_1 radiation from an 18 KW rotating anode source and a 4-circle diffractometer.

Fabrication and Microscopy Characterization of BFO Nanocapacitors

Two-step patterning process was carried out to fabricate BFO nanocapacitors, which for these studies involved 40 nm epitaxial BFO films grown by magnetron sputter-deposition on $SrRuO_3$ (SRO) (70 nm thick) layers as bottom electrodes, grown on single crystal $SrTiO_3$ (001) substrates. Capacitors with sizes ranging from 500 nm to 100 nm, varying shapes (e.g. symmetry, aspect ratio) and orientation (relative to the film in-plane crystallographic axes) were fabricated. Initial fabrication of BFO nanocapacitors using a Pt hard mask layer, for protection of the BFO film from ion bombardment, resulted in partial damage of the BFO layer by the FIB ion bean leading to loss of polarization, as confirmed by no piezoresponse force microscopy (PFM) response (Fig. 3a and 3b-red square). Subsequently, we used a 100 nm thick W hard mask layer, which enabled fabrication of BFO nanocapacitors, using a top-down approach with the combination of electron beam lithography and focused-ion beam (FIB) technique to pattern BFO nanostructures, with negligible or no ion bombardment-induced damage (Fig. 3b-blue square) and good PFM response-polarization (bright rectangles). We produced nanocapacitors as small as 100 nm in diameter for round structures and in length for square capacitors.

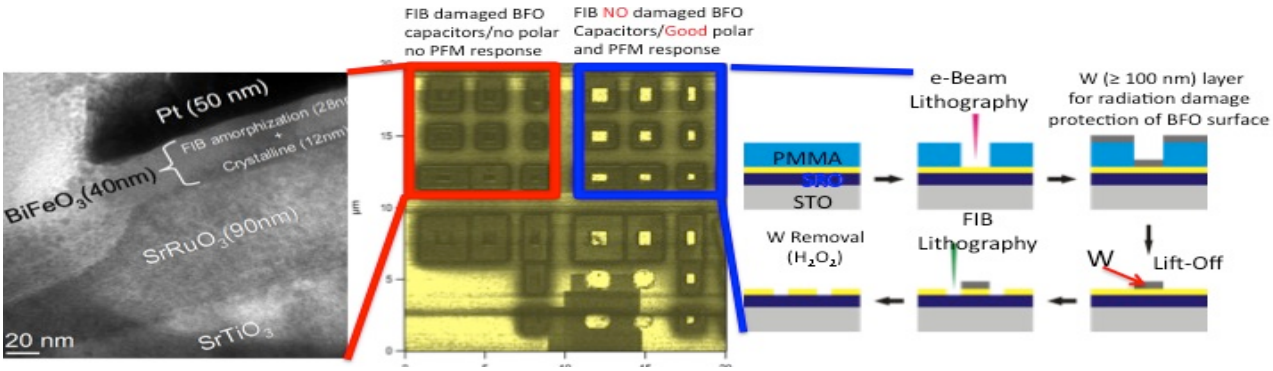

Fig. 3. a) Cross section TEM of BFO nanocapacitor fabricated by FIB with 50 nm Pt protection layer showed partial damage of BFO layer, thus no polarization/PFM response (b-red square); b) PFM images of BFO nanocapacitors (red square-damaged/no polarization; blue square-undamaged/good polarization); c) e-beam lithography+FIB fabrication of BFO nanocapacitor with protective W layer to eliminate FIB damage.

Complementary X-ray Nanoprobe Synchrotron Diffraction Studies and Nanoscale Ferroelectric Domain Imaging of Bismuth Ferrite Nanocapacitors

We used a unique combination of diffraction studies using the APS X-ray nanoprobe beam and PFM to reveal shape effects on the ferroelectric film strain and domain configuration in BFO nanocapacitors, fabricated as described in the *Fabrication and Microscopy Characterization of BFO Nanocapacitors* section above. These nanocapacitors were used to investigate the effect of film strain and nanocapacitor shape (square vs. circular) on ferroelectric domain configuration and dynamics. The X-ray nanoprobe beam revealed high strains in BFO films-based nanocapacitors (Fig. 4), while PFM imaging of ferroelectric domains (Fig. 5) showed that square BFO nanocapacitors have a mono-domain configuration (Figs. 6 a-c), whereas round ones exhibit a seven-domain configuration Figs. 6b-d). We attribute the more symmetric and lower coercive field of round shape to a multi-domain state, which facilitates domain nucleation and growth. These findings have critical implications for the development of nanocapacitors for energy harvesting ferroelectric solar cells and high-density ferroelectric memories.

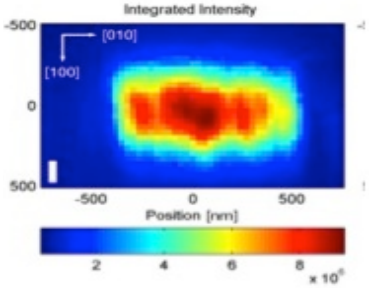

Fig. 4. Diffration image of BFO nanocapacitors obtained with the APS X-ray nanoprobe beam, Showing strain patterns

.

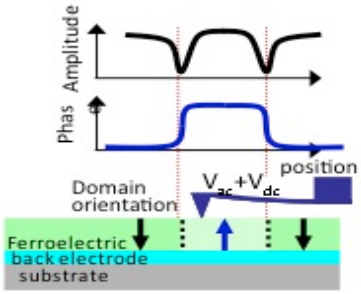

Fig. 5. PFM images FE domains via application of voltage between the top surface of BFO film and back electrode underneath the

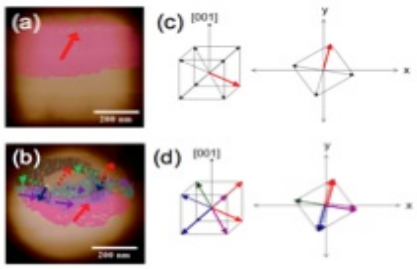

Fig. 6. PFM images of FE domain in square BFO nanocapacitor (a) and corresponding monodomain (c) and in round nanocapacitor (b) and seven domains configuration (d).

Development and Application of a Novel Angle-resolved Piezoresponse Force Microscopy:

We developed angle-resolved PFM (AR-PFM) to circumvent limitations in conventional PFM that limit the capability to construct three-dimensional PFM images, and used our novel approach to identify eight additional in-plane polarization variants in epitaxial $BiFeO_3$ thin films (see companion abstract for details).

Selected Future Directions for the FWP 58931

***Computational design of new ferroic materials and synthesis of these new materials in thin film form*:** Capitalizing on our recent discovery of the new class of polar-phason perovskite-oxide compounds, we plan to utilize a range of predictive first-principles-simulation approaches to (a) elucidate the novel physics that is responsible for the emergence of polar phasons in complex-oxide materials, (b) establish structural and compositional traits for successful "virtual synthesis" of such structures, (c) explore the consequences of adding other functional blocks [e.g., magnetic or superconducting] to polar-phason structures. Synthesis of the new materials, predicted by computational design, will be carried out to achieve a unique integrated computational design/experimental approach to develop novel thin film heterostructures fulfilling the goals of the ANL M2D2 strategic initiative.

Magnetoelectric effects in multiferroic nanostructures: We will explore the behavior of multiferroic nanostructures with adjacent layers (or components in a nanocomposite) exhibiting ferroelectric or magnetic properties.

Resistive change phenomena in oxide thin films and oxide-based nanostructures: Thermoelectric materials (TMs) are emerging candidates for solar energy harvesting devices. A promising TM candidate is a resistance change oxide (RCO) material in which a low-resistance phase is induced by soft electrical breakdown. We propose to study the fundamental physical, chemical, and electrical phenomena involved by using a combination of materials synthesis, compositional and microstructural characterization, and studies of the resistance change processes via in situ TEM and AFM techniques.

The PIs acknowledge extensive collaboration with A. Joshi-Imre (CNM), R. Ramesh (IMRE, Singapore), K. No (KAIST, Korea), J. Klug (ANL, and Northwestern Univ.), M. J. Bedzyk (Northwestern Univ.), R. S. Katiyar (Univ. Puerto-Rico).

Selected publications (2008–2010) related to multiferroic films/nanostructures

"Piezoelectrically Actuated Ultrananocrystalline Diamond Tip Array Integrated With Ferroelectric or Phase Change Media For High-Density Memory", O. Auciello, US Patent # 7,602, 105; Oct 13, 2009.

"Effects of Cantilever Buckling on Vector Piezoresponse Force Microscopy Imaging of Ferroelectric Domains in $BiFeO_3$ Nanostructures", R. Nath, S. Hong, M. J. Bedzyk, R. S. Katiyar, and O. Auciello, APL **96** (2010) 163101.

"Nanoscale Piezoresponse Studies of Ferroelectric Domains in Epitaxial $BiFeO_3$ Nanostructures", S.Hong, J.A. Klug, M. Park, A. Imre, M. J. Bedzyk, K. No, A. Petford-Long, O. Auciello, JAP **105 (**2009) 06 1619

"Magnon sidebands and spin-charge coupling in bismuth ferrite probed by nonlinear optical spectroscopy", M.O. Ramirez, M.J. Bedzyk, O. Auciello, D.G. Schlom, R. Ramesh. et al, *Phys. Rev. B* **79,** (2009) 224106.

"Origin of surface potential change during ferroelectric switching in epitaxial $PbTiO_3$ thin films studied by scanning force microscopy," Y. Kim, S. Hong, H. Shin et al., *APL.* **94** (2009) 032907.

"Piezoelectric force microscopy studies of $PbTiO_3$ thin films grown via layer-by-layer gas phase reaction," M. Park, S. Hong, J. Kim, Y. Kim, S. Bühlmann, Y. K. Kim, K. No, *Appl. Phys. Lett.* **94**, (2009) 092901.

"Coexistence of Weak Ferromagnetism and Ferroelectricity in the High Pressure $LiNbO_3$-type Phase of $FeTiO_3$," T. Varga, A. Kumar, E. Vlahos, S. Denev, M. Park, S. Hong, T. Sanehira, Y. Wang, C.J. Fennie, S.K. Streiffer, X. Ke, P. Schiffer, V. Gopalan, J. F. Mitchell, *Phys. Rev. Lett.* **103**, 047601 (2009).

"Phase diagram in strained $BaTiO_3/SrTiO_3$ superlattices: a UV Raman study," D. A Tenne, J. D. Schmidt, P. Turner, A. Soukiassian , D. G. Schlom, S. Nakhmanson, X. X. Xi, Y. L. Li, L. Q. Chen, R. S. Katiyar, M. Bernhagen, P. Reiche, and R. Uecker, Extended Abstracts of the 2009 Workshop on Fundamental Physics of Ferroelectrics, 133 (2009).

"Materials science and technology for nonvolatile memories," edited by D. Wouters**,** S. Hong**,** S. Soss, O. Auciello, *Mater. Res. Soc. Symp. Proc.* **1071**, (2008).

"Screen charge transfer by grounded tip on ferroelectric surfaces," Y. Kim , J. Kim, S. Bühlmann, S. Hong, Y. K. Kim, S.-H. Kim, and K. No, *Phys. Stat. Sol. (RRL)* **2**(2), 74 (2008)

"Revealing latent structural instabilities in perovskite ferroelectrics by layering and epitaxial strain: A first-principles study of Ruddlesden-Popper superlattices", S.M. Nakhmanson, *Phys. Rev. B* **78**, 064107 (2008).

Program title: Soft Matter Electron Microscopy

Principal Investigators: Nitash Balsara (nbalsara@lbl.gov), Kenneth Downing (khdowning@lbl.gov), Christian Kisielowski (cfkisielowski@lbl.gov), Andrew Minor (aminor@lbl.gov), Ronald Zuckermann (rnzuckermann@lbl.gov)

Program Scope

Our objective is study fundamental aspects of charge transport in nanoscale polymer channels by electron scattering and microscopy. We focus on self-assembled nanostructrues formed by bio-inspired peptoids and synthetic block copolymers within which ion transport is restricted to one of the nanostructures. Our objective is to determine the geometry and chain configurations that lead to the most efficient solid-phase ion-transporting channel. Spatially resolved electron microscopy and energy-loss spectroscopy are crucial for obtaining the relationship between morphology and transport. The proposed microscopy techniques focus on maximizing spatial and energy resolution while minimizing radiation exposure and damage. This will be achieved by using novel techniques to manipulate and detect the incident, transmitted, and scattered electrons. In addition, we will use aberration-correctors, high brightness instruments, and novel 3D image reconstruction algorithms. *In-situ* electron microscopy experiments for investigating the dynamic nature of soft materials on molecular and sub-molecular length scales have been designed.

Recent Progress

We have successfully fabricated, characterized and tested three generations of phase plates. These devices were fabricated in collaboration with the Center for X-Ray optics. The latest generation devices were stable for over a week in the electron microscope. The dimensions of the third generation phase plate allows for imaging of objects as large as 10 nm while maintaining atomic resolution in the Libra microscope. This achievement enables atomic resolution, in-focus imaging of soft/hard interfaces for the first time. Sources of device contamination were identified and removed to enable real space imaging. The measured characteristics of our phase plates are in good agreement with theoretical predictions [1].

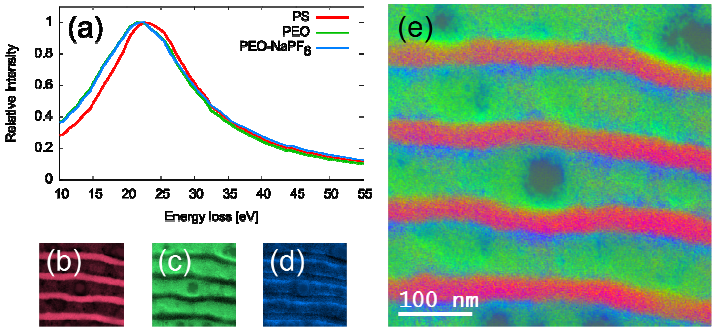

Figure 1. EFTEM SI analysis of SEO/$NaPF_6$ lamellar sample using MSA. Extracted plasmon peaks shown in (a). MLLS fits corresponding to PS (red), PEO (green) and the salt ions (blue) shown in (b), (c) and (d), respectively. Combined RGB image shown in (e).

Solid electrolytes comprising block copolymers with dissolved lithium and sodium salts are being considered for developing the next generation of lithium and

sodium batteries. This is particularly important for the case of lithium batteries due to the flammability of current electrolytes and concomitant issues concerning battery life and safety. Energy-filtered transmission electron microscopy spectrum imaging (EFTEM SI) in the low electron energy-loss range is a valuable technique for probing the chemical structure of a material with high spatial resolution using a relatively low electron dose. By analyzing EFTEM SI datasets using principal component analysis (PCA), the constituent chemical phases of the material can be identified in an efficient manner without prior knowledge of the specimen. We implement low-loss EFTEM SI together with PCA to investigate thin films of the block copolymer electrolyte poly(styrene-block-ethylene oxide) (PS-b-PEO) blended with a sodium salt. PCA identifies three main phases, the first and second phases corresponding to the two blocks of the copolymer and a third phase corresponding to the salt. The low-loss spectra for these phases are then extracted from a noise-reduced EFTEM SI dataset and used to generate a chemical map of the material by multiple linear least-square fitting. The distribution of chemical species in the sample thus obtained is shown in Figure 1. Of particular interest is the fact that the sodium ions are located at the edges of the PEO lamellae. This is in contrast to lithium ions that were located at the center of PEO lamellae [2]. It should be clear that these important differences are not evident in any of the other methods used to characterize block copolymers such as X-ray and neutron scattering.

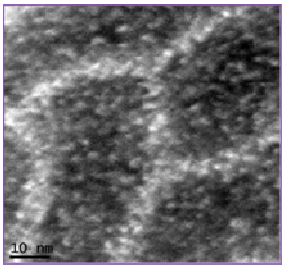

Figure 2. Sulfur clusters (bright spots) in a poly(styrene sulfonate-block-methyl butylene) (PSS-PMB) copolymer imaged by HAADF imaging. The PSS microphase is bright.

Fuel cells, which hold promise for providing energy without pollution, rely on proton transport through a polymer electrolyte membrane (PEM). The PEM is a single-ion conductor with protons attached to sulfonic acid groups that are attached to the polymer backbone. The clustering of these groups has important ramifications on proton transport. In Figure 2 we show a recently acquired High Angle Annular Dark Field electron micrograph of a PEM comprising a poly(styrene sulfonate-block-methyl butylene) (PSS-PMS) copolymer. The bright stripes represent the PSS domains and the remaining relatively dark regions represent the PMB domains. The sample is a thin film (about 50 nm in thickness) and tomographic data indicate that the surface of the thin film is coated with PSS. The brightest spots seen in Figure 2 represent the sulfur clusters. All of the sulfur clusters that play a central role in proton transport are restricted to the PSS domains. Clusters that appear to reside in the PMB domains are actually in the surface PSS domains (established by tomography). These data indicate the importance of 3-D imaging for determining morphology. A simple interpretation of the image in Figure 2 suggests the presence of sulfur clusters in the PMB domains. This result represents a major step forward in our efforts to characterize the relationship between the structure and properties of ion transporting channels [3-7].

Future Plans

In spite of our efforts to model the phase plate, images recorded with phase plates reveal a lack of theoretical understanding of the image formation process on intermediate length scales. We will continue both experimental and modeling efforts to address this limitation. In the range where experiments and theory are in agreement, we can use the phase plate to separate absorption or amplitude contrast from phase contrast. We will investigate the relationship between beam size, phase plate size and contrast enhancement.

It is well known that a certain fraction of electrons is bound to be inelastically scattered as the incident beam passes through a specimen, and that this fraction asymptotically approaches 100% as the thickness increases. Since the presence of inelastically scattered electrons degrades both the contrast and the resolution in an image, the best practice currently is to remove all inelastically scattered electrons with an energy filter. Even so, there is a limit to how thick the specimen can be, due to the fact that the number of zero-loss electrons that remain – i.e. the filtered image intensity – decreases as the specimen thickness increases. The research that we propose here will make quantitative measurements of the extent to which the Cc corrector on TEAM 1.0 is able to "rescue" signal from electrons that are scattered both elastically and inelastically. Occurrence of this type of “plural” scattering is inescapable when the specimen thickness is increased to something in the range of 50 nm or more. By using a Cc corrector, however, it may be possible to retain these electrons, and the additional fraction of the signal that they had acquired in an elastic scattering event. If this idea proves to be effective, then the use of a Cc corrector will provide a significant improvement of the signal-to-noise ratio (SNR) for relatively thick specimens. We will continue to study the systems that were initiated during the first year of the program. This includes studying polymer electrolytes for fuel cells and batteries, development of a robust electrostatic phase plate for electron microscopy, measuring the distortion of vesicles by proteins, and the development of *in situ* probes for studying ion motion by electron microscopy.

While we have developed an understanding of the bulk properties of block copolymer electrolytes, important questions regarding the electrode-electrolyte interface remain. We will focus on the use of EM to study the interface between lithium metal anodes and block copolymer electrolytes. Our objective is to accomplish two goals: Determine the orientation of the block copolymer microphases at the electrolyte/electrode interface, and study changes in this interface as lithium is cycled into and out of the electrode. This effort will provide insight into mechanisms of battery failure and methodologies needed to prevent battery failure.

Our application of EFTEM SI to SEO/salt mixtures demonstrates the development of a robust method for locating salt ions without staining. This is a necessary first step for *in-situ* electrical biasing experiments. We plan to begin *in-situ* biasing in these block copolymer electrolytes is to determine the changes in salt distribution and/or domain orientation in response to the applied fields.

In a brand new project, we seek to mimic the way nature builds precisely defined nanostructures (e.g. proteins and nucleic acids). We accomplish this by arranging *synthetic* monomeric building blocks into a specific linear sequence. Such sequence-specific heteropolymers can spontaneously fold into conformationally-defined 3D structures and have the potential to lead to a new generation of highly robust artificial protein-like materials. We have already completed major steps toward developing materials that combine the exquisite architecture and functionality of proteins with the durability of polymers. The polymers of interest are called "peptoids". Like proteins, they are sequence-specific heteropolymers, capable of folding into specific shapes and exhibiting potent biological activities; and like bulk polymers they are chemically and biologically stable and relatively cheap to make. We will synthesize and characterize peptoid-based block copolymers for transporting the protons, lithium, and sodium ions.

Publications

1." Imaging of soft and hard materials using a Boersch phase plate in a transmission electron microscope", D. Alloyeau, W.K. Hsieh, E.H. Anderson, L. Hilken, G. Benner, X. Meng, F.R. Chen, C, Kisielowski, *Ultramicroscopy*, vol. 110, pg. 563-570, **2010**.

2. "Effect of Ion Distribution of Conductivity of Block Copolymer Electrolytes", E.D. Gomez, A. Panday, E.H. Feng, V. Chen, G.M. Stone, A.M. Minor, C. Kisielowski, K.H. Downing, O. Borodin, G.D. Smith, N.P. Balsara, *Nano Letters*, vol. 9, pg. 1212-1216, **2009**.

3. "On the Origin of Slow Changes in Ionic Conductivity of Model Block Copolymer Electrolyte Membranes in Contact with Humid Air", X. Wang, K.M. Beers, M.J. Park, K. Downing, N.P. Balsara, *Macromolecules*, vol. 43, pg. 5306-5314, **2010**.

4. "Anisotropic Proton Conduction in Block Copolymer Electrolyte Membranes at Equilibrium with Humid Air", M.J. Park, N.P. Balsara, *Macromolecules*, vol. 43, pg. 292-298, **2010**.

5. "Order-Disorder Transitions in Block Copolymer Electrolytes at Equilibrium with Humid Air", M.J. Park, A. Jackson, N.P. Balsara, vol. 42, pg. 6808-6815, *Macromolecules*, **2009**.

6. "Microphase Separation in Sulfonated Block Copolymers Studied by Monte-Carlo Simulations", P. Knychala, M. Banaszak, M.J. Park, N.P. Balsara, *Macromolecules*, vol. 42, pg. 8925-8932, **2009**.

7. "Phase Behavior of Symmetric Sulfonated Block Copolymers", M.J. Park, N.P. Balsara, *Macromolecules*, vol. 41, pg. 3678-3687, **2008**.

8. "Humidity-Induced Phase Transitions in Ion-Containing Block Copolymer Membranes", M.J. Park, A.J. Nedoma, P.L. Geissler, A. Jackson, D. Cookson, *Macromolecules*, vol. 41, pg. 2271-2277, **2008**.

ERKCM67: Probing phase transitions, chemical reactions, and energy transfer at the atomic scale: Multifunctional imaging with combined electron and scanning probe microscopy

PI: Albina Y. Borisevich **Co-PIs***:* Sergei V. Kalinin, Minghu Pan
(albinab, sergei2, mpan1)@ornl.gov

Research Professors: Donovan Leonard. **Postdocs:** Hue Jung Chang, Jun He, Amit Kumar (partial)

Oak Ridge National Laboratory, Oak Ridge, TN 37831

Program scope

This program started in August 2009 as one of the Single-Investigator- Small Group projects. The focus is on local, ideally atomic-level, studies of electrical bias-induced phase transitions and electrochemical reactions in systems with increasing levels of complexity: (A) purely electronic transfer at interfaces and single dopant atoms in oxide grain boundaries, interfaces, and nanowire junctions; (B) electrostatically-driven structural changes and phase transitions in ferroelectrics and antiferroelectrics; (C) electrochemical processes involving mass transfer that occur on charge injection at solid interfaces and at the onset of solid-state reactions. These phenomena underpin a wide range of applications from energy generation, storage and conversion to fundamental science of order parameter-structure couplings. We will accomplish our objectives for the study of energy transformations by developing experimental tools for a seamless combination of high-resolution electron microscopy, imaging by electron-energy loss spectroscopy (EELS), and local scanning probe microscopies, while also formulating new methodologies for data analysis and interpretation using synergistically coupled advanced theoretical methods. The results will enable optimization of a broad range of energy and information technologies from fuel cells, batteries, supercapacitors, data storage and energy transport.

Recent Progress

Ferroic order parameter fields and electronic properties from STEM data: The multifaceted magnetic, electrical, and structural functionalities of perovskite ABO_3 materials are controlled by the subtle distortions of the crystallographic lattice from the prototype cubic phase.[1] These distortions include relative displacements of the cations from the centers of the BO_6 oxygen octahedra, deformations of the oxygen octahedra, and collective tilts of the octahedral network. Correspondingly, the key element of the proposed research is determination of these order parameter fields, associated with only small (10 pm) structural distortions, directly from STEM data.

Direct structural mapping: the initial step towards probing of structural transformations induced by the applied bias is the capability to map the subtle changes in octahedral tilts and deformations, polarization fields, and electronic structure, on a single unit cell level. In the first case study, we utilize direct structural mapping, building on the approach suggested by Jia at al.[2,3] and using high-resolution scanning transmission electron microscopy (STEM) to determine lattice parameters and oxygen octahedral rotations at an epitaxial $BiFeO_3$ - $La_{0.7}Sr_{0.3}MnO_3$ (BFO-LSMO) interface combined with electronic structure imaging by electron energy loss spectroscopy (EELS). This allows us to directly correlate the atomic structure, polarization, strain fields and dielectric behavior on the atomic level. Shown in Fig.1(a) is a STEM bright field image of BFO-LSMO interface, which was analyzed to give the map of octahedral tilts in Fig. 1(b). The map clearly shows the checkerboard order of tilts, as expected from the bulk BFO structure, Fig. 1(c). The checkerboard contrast diminishes toward the interface, indicating the suppression

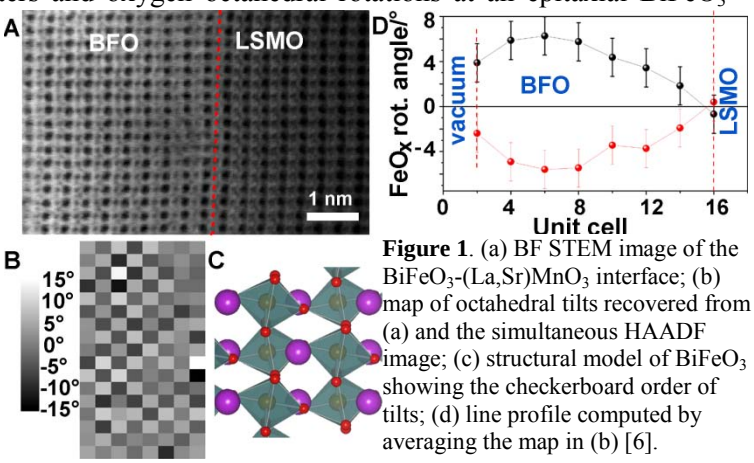

Figure 1. (a) BF STEM image of the $BiFeO_3$-(La,Sr)MnO_3 interface; (b) map of octahedral tilts recovered from (a) and the simultaneous HAADF image; (c) structural model of $BiFeO_3$ showing the checkerboard order of tilts; (d) line profile computed by averaging the map in (b) [6].

of the octahedral tilts, as seen in the profile (Fig. 1(d)) obtained by averaging the map in 1(b). The area of suppressed tilts also coincides with a region of enhanced out-of plane lattice parameter, as well as anomalous dielectric properties detected by EELS. These studies demonstrate the new paradigm of an interface phase transition mediated by the antiferrodistortive coupling across the interface, complementing the established polarization- and charge driven behavior. This also implies that novel ferromagnetic properties can arise in the vicinity of the interface as the result of the deformation of oxygen octahedra surrounding the cations and changes in M-O-M angles.[4] These results illustrate that controlling the octahedral tilts can provide a new, and virtually unexplored, dimension to control the behavior of the ferroelectric and multiferroic films (also see [4]).

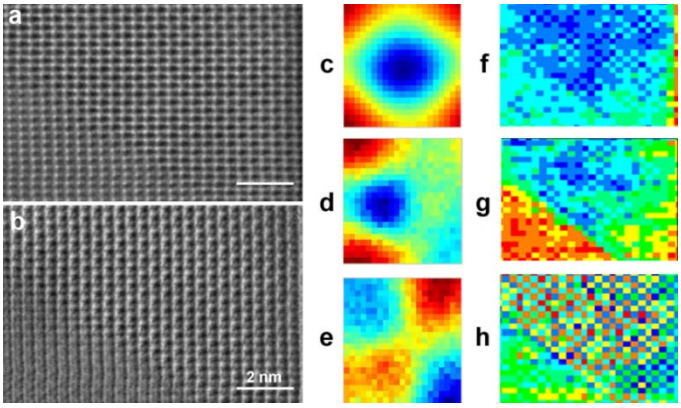

Figure 2. Shape PCA analysis of domain wall image in BFO: (a) HAADF image used for analysis, (b) simultaneously acquired BF image showing domain contrast, (c)-(e) – first 3 eigenshapes and (f)-(h) the corresponding weight factor maps. There are 3 above-noise PCA components with distinct spatial distribution of weight factors [5].

Column shape analysis: In many transition metal oxides in thick (> 10 nm) STEM samples the light atomic columns are not directly visible on the STEM image. We introduce a new technique for robust mapping of order parameters in complex oxides based on a shape analysis of atomic columns. Using advanced Bloch wave simulations,[5] we show that the exact column *shape* contains sufficient information on the positions of the unresolved light atom columns to map octahedral tilt patterns, unit cell by unit cell. We apply the technique to a charged ferroelectric domain wall in a $BiFeO_3$ (BFO) thin film (Fig.2), and compare the results with a classical 109° wall. Coupled with geometric measurements of cation displacements, we demonstrate that while the width of the charged domain wall with respect to cation displacements is of the order of several nanometers, in agreement with existing theoretical models,[6,7] the octahedral tilt-related distortions demonstrate an unexpectedly abrupt transition confined to one unit cell. These observations allow us to separate the polarization and structural contributions to the domain wall energy, and predict the behavior of other topological defects in BFO [5].

Probing bias-induced phase transitions in-situ: As a model system for probing the local bias-induced phase transitions in solids, we have chosen ferroelectric and multiferroic materials, in which the transition is reversible and hence can be readily studied. Furthermore, ferroelastic domain walls that form during switching are readily observed even at the nanometer resolutions due to changes in the strain state of the system. Finally, the breadth of applications in non-volatile memories and continuously growing interest towards multiferroic materials necessitate the spatially resolved studies of domain nucleation and wall pinning on structural defects.

Here, we explored dynamic switching behavior in BFO thin films grown on a $DyScO_3$ (DSO) substrate to induce regular arrays of domain walls. Fig. 3(a) shows the initial state of the material, with the as-grown domain walls visible. In Fig. 3(b) the bias is starting to be applied, and over the frames 3(b)-(d) we can observe the development of a hemispherical domain, which is indicative of in-plane switching. Out-of plane switching is not detectable in this low resolution mode, as 180° degree walls do not produce strain contrast. The kinetics of the switching process can also be studied

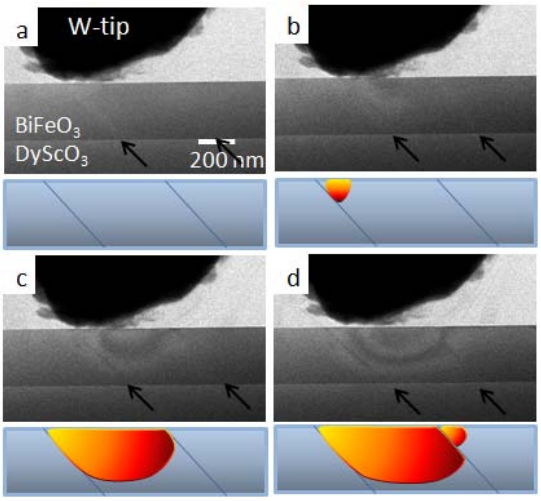

Figure 3(a) BF STEM image showing the 71° domain wall structure of a BFO film on DSO. (b-d) In-situ imaging of bias induced domain nucleation and growth in a BFO thin film by STEM with corresponding schematics representing the domain nucleation and growth. The arrows indicate 71° domain walls [3].

in this setup.

It is noteworthy that this sample has no bottom electrode, and previous observations with scanning probe microscopy have demonstrated that domains in such samples cannot be switched, i.e. the state is unchanged after the bias is removed. While we observe the same effect in the STEM setup, we can for the first time demonstrate that switching still happens dynamically [3]. When the samples with bottom electrodes are studied in this setup, stable switching is observed in agreement with SPM data.

Ex-situ electrochemical studies. As a model system for probing electrochemical functionality, we concentrated the effort on the (La,Sr)CoO_3 family that is being considered for solid oxide fuel cell applications. Recently, additional interest in this system has come from the significant enhancement in the rate of oxygen reduction reaction (ORR) that is achieved when a thin layer of $(La,Sr)_2CoO_4$ is grown on top of the (La,Sr)CoO_3 [1]. This material can support large oxygen vacancy concentrations, and often exhibits oxygen vacancy ordering. In the disordered phase, the lattice parameter strongly depends on oxygen vacancy concentration, as is well studied by macroscopic dilatometric measurements.[8] The ordered phase can be expected to behave as a chemically mediated ferroelastic. This material also possesses exciting electronic properties controlled by the high spin – low spin transition of d^4 Co^{3+} cation, which can be responsive to local lattice strains. Beyond direct structural information on LSCO based fuel cell operation, we now observe the early stages of oxygen vacancy ordering in LSCO that proceed through the formation of ordered domains as small as 3 nm (Fig. 4). Furthermore, we observe gradients in oxygen edge fine structure in EELS through the film that suggest that ordering can be manipulated by electrochemical potential gradients. In the future, we aim to directly correlate the two, and explore the vacancy ordering reaction triggered by the external electric field.

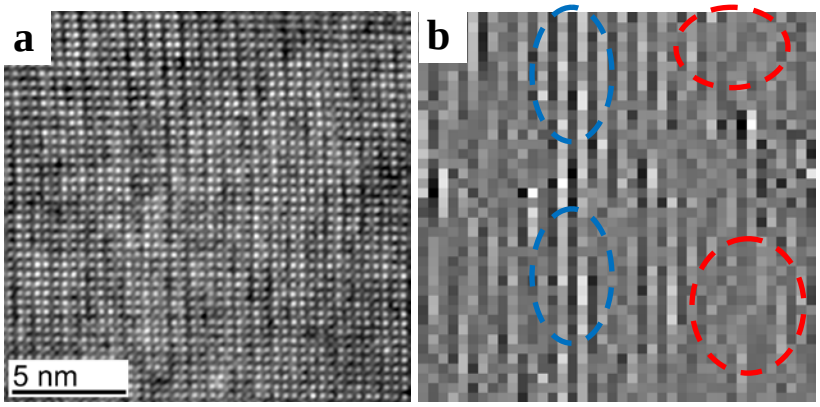

Figure 4. (a) STEM HAADF micrograph of a (100) orientated LSC thin film, showing bright and dark contrast indicative of vacancy ordering. (b) Map of lattice parameters computed from (a) highlighting ordered (blue ovals) and disordered (red ovals) regions. In ordered regions, lattice parameter modulation reaches 15%.

Future plans:

In the first year of the SISGR project, we have explored the individual elements of the proposal, namely the capability to probe the fine structural, chemical, and polarization fields in correlated oxides, perform in-situ experiments in model ferroelectric oxides, and study ex-situ electrochemical transformations through STEM/EELS imaging and multivariate statistical analysis of the data. In the subsequent years, we aim to integrate this knowledge, ultimately in the in-situ EELS and atomic resolution experiments, and in parallel finish the development of the atomic-level in-situ SPM setup. Specifically, we aim to study

- **Atomic-scale ordering near phase transitions:** develop the atomic-level structural analysis of the disordered ferroic systems in the vicinity of morphotropic and ferroelectric-antiferroelectric phase boundaries, and explore evolution of structural order parameters as a function of composition and local electric field.
- **Energy transformation** in multilayers: explore electronic structure and phase transformation in nickelate multilayers, exploring charge transfer behavior as reflected by structure and EELS.
- **Octahedral tilt engineering:** explore octahedral tilt control using films grown on a variety of substrates and determine factors that control relative rigidities and behaviors of octahedral frameworks; study effects of the symmetry mismatch on atomic and electronic structure and emergence of novel interfacial order parameters.
- **In-situ electrochemical transformations:** use the biased STM probe to induce oxygen vacancy transport and ordering in thin films and focused ion beam prepared pillars of the (La, Sr)CoO_3, and correlate the changes in microstructure, atomic structure, and EELS. Expand these studies to oxide nanowires such as V_2O_5.

- Continue developing **instrumentation for in-situ STEM – SPM** measurements with high spatial resolution and advanced spectroscopic modes for SPM component.

This work is sponsored by the Materials Science and Engineering Division, Office of Basic Energy Sciences of the US DOE. The work is done in collaboration with R. Ramesh (UC Berkeley), Y. Shao-Horn (MIT), M. Biegalski (ORNL), and A. Morozovska (Ukrainian Academy of Sciences). Authors also acknowledge instrument access (FEI Titan, Hitachi NB-5000 FIB) via ORNL's ShaRE user facility, which is sponsored by the Scientific User Facilities Division, Office of Basic Energy Sciences, U.S. DOE.

DOE-sponsored publications FY2010 [in total 3 journal papers published – 1 Phys Rev. Lett, 1 ACS Nano (plus 5 submitted), 1 patent disclosure, 14 extended abstracts, 3 invited and 24 contributed talks]

Submitted:

1. E. J. Crumlin, E. Mutoro, S.-J. Ahn, G. J. la O', D. N. Leonard, A. Borisevich, M. D. Biegalski, H. M. Christen, Y. Shao-Horn, *Oxygen Reduction Kinetics Enhancement on a Hetero-Structured Oxide Surface for Solid Oxide Fuel Cells*, submitted to J. Phys. Chem. Lett., 2010
2. H.J. Chang, S.V. Kalinin, A.N. Morozovska, M. Huijben, Y.H. Chu, P. Yu, R. Ramesh, E.A. Eliseev, G.S. Svechnikov, S.J. Pennycook and A. Borisevich, *Atomically-resolved mapping of polarization and electric fields across ferroelectric-oxide interfaces by Z-contrast imaging*, submitted to Adv. Mater., 2010
3. H.J. Chang, S. V. Kalinin, S. Y. Yang, S. Bhattacharya, P. P. Wu, N. Balke, S. Jesse, L. Q. Chen, R. Ramesh, S. J. Pennycook, and Albina Y. Borisevich, Watching Domains Grow: In-situ studies of polarization switching by combined Scanning Probe and Scanning Transmission Electron Microscopy, submitted to Nano Lett. (under review).
4. Jun He, Albina Borisevich, Sergei V. Kalinin, Stephen J. Pennycook, Sokrates T. Pantelides, *Control of the structural and magnetic properties of perovskite oxide ultrathin films through the substrate symmetry effect*, submitted to Phys. Rev. Lett. (under review)
5. A.Y. Borisevich, O. Ovchinnikov, H.J. Chang, M. Oxley, P. Yu, J. Seidel, E.A. Eliseev, A.N. Morozovska, R. Ramesh, S.J. Pennycook, S.V. Kalinin, *Mapping octahedral tilts and polarization across a domain wall in $BiFeO_3$ from Z-contrast STEM image atomic column shape analysis*, submitted to ACS Nano (under review)

Published:

6. A.Y. Borisevich, H. J. Chang, M. Huijben, M. P. Oxley, S. Okamoto, M. K. Niranjan, J. D. Burton, E. Y. Tsymbal, Y. H. Chu, P. Yu, R. Ramesh, S. V. Kalinin, and S. J. Pennycook**,** *Suppression of Octahedral Tilts and Associated Changes in Electronic Properties at Epitaxial Oxide Heterostructure Interfaces*, Phys. Rev. Lett. **105**, 087204 (2010)
7. A.N. Morozovska, E. A. Eliseev, S. V. Svechnikov, A. D. Krutov, V. Y. Shur, A. Y. Borisevich, P. Maksymovych, and S. V. Kalinin, *Finite size and intrinsic field effect on the polar-active properties of ferroelectric-semiconductor heterostructures*, Phys. Rev. **B 81,** 205308 (2010)
8. J. Shin, A.Y. Borisevich, J. Zhou, V. Meunier, E.W. Plummer, S.V. Kalinin, and A.P. Baddorf, *An oxygen-induced surface reconstruction of* $SrRuO_3$ *and its effect on the* $BaTiO_3$ *interface*, ACS Nano **4**, 4190 (2010).

References:

[1] R. G. Mitchell, *Perovskites- Modern and Ancient* (Almaz Press, Thunder Bay, Ontario, 2002).
[2] C.L. Jia, V. Nagarajan, J.Q. He, L. Houben, T. Zhao, R. Ramesh, K. Urban, and R. Waser, Nature Mat. **6**, 64 (2007).
[3] C.L. Jia, S.B. Mi, K. Urban, I. Vrejoiu, M. Alexe, and D. Hesse, Nature Mat. **7**, 57 (2008).
[4] P. Yu, Phys. Rev. Lett. **105**, 027201 (2010)
[5] L.J. Allen, S. D. Findlay, M.P. Oxley, C.J. Rossouw, Ultramicroscopy, **96** 47 (2003).
[6] Lubk, A.; Gemming, S.; Spaldin, N. A. *Physical Review B* **2009,** 80, (10), 104110.
[7] P. Marton, I. Rychetsky, J. Hlinka, Phys. Rev. B 81, 144125 (2010).
[8] S.B. Adler, Chem.Rev., **104** 4791 (2004)

Observing Materials Dynamics on the Fundamental Atomic Scale by Ultrafast In-Situ TEM

N. D. Browning (PI)[1], J. E. Evans[1], N. Goldman[1], D. J. Masiel[2], J. T. McKeown[1], B. W. Reed[1], M. Santala[1]

browning20@llnl.gov, evans80@llnl.gov, goldman14@llnl.gov, djmasiel@ucdavis.edu, mckeown3@llnl.gov, reed12@llnl.gov, santala1@llnl.gov,

[1]Condensed Matter and Materials Division, Physical and Life Sciences Directorate, Lawrence Livermore National Laboratory, PO Box 808, Livermore, Ca 94550

[2]Department of Chemistry, University of California-Davis, One Shields Ave, Davis, Ca 95616

Program Scope

The aim of this project is to develop a fundamental understanding of materials dynamics (from microseconds to nanoseconds) in systems where the required combination of spatial and temporal resolution can only be reached by the dynamic transmission electron microscope (DTEM). Although the DTEM can cover a broad time range, the emphasis of the work in this proposal will be the microsecond timescale. In this regime, the DTEM is expected to have atomic scale resolution, providing an in-situ TEM capable of studying nanoscale dynamic phenomena with several orders of magnitude time resolution advantage over any existing in-situ TEM, i.e. it is an ultra-fast atomic scale in-situ TEM. This capability will be used to develop new insights into long-standing scientific problems related to the identification and control of the active sites on the nanoscale catalysts that are responsible for the selectivity of chemical reactions and the nucleation of nanostructures. The results will be used to study the nucleation and growth of nanowires for solid state lighting applications and the interaction of nanoscale metal clusters used for catalysis. Work will also coordinate with other experiments on structural materials, biological materials and electronic materials to fully develop the DTEM capabilities. Here we present results from our development of annular dark field imaging in pulsed mode on the DTEM, which allows higher contrast levels and better detection of small metal clusters on a support. In combination with in situ gaseous environments with elevated temperatures and increased flexibility in the control of spatial and temporal resolutions, the dark field imaging lays the foundation for our future investigation of catalyst nanoparticles.

Recent Progress

The first 3 years of this project has emphasized the use of the DTEM to establish the basic capabilities for studying nucleation and growth phenomena (aspects of this research have led to the DTEM receiving R&D 100 and Nano 50 awards in 2008, and a Microscopy Today MT-10 Award in 2010). This includes developing an in-situ gas stage to perform dynamic experiments under varying environmental conditions, developing a method to determine accurate nanocluster sizes and most importantly for the current experiments, optimizing the contrast for imaging nanostructures in the DTEM (which will be described in the remainder of this abstract).

Although the DTEM has achieved spatial resolutions of up to 8 nm at 15 ns time resolution using gold and carbon multilayer films, these samples exhibit extremely high mass-thickness contrast when compared to nanoparticle catalysts that are the main aim of this research. To overcome the difficulties associated with time resolved imaging of low contrast samples, one can

employ an annular dark field (ADF) aperture in the back focal plane of the objective lens in a DTEM. The use of an ADF aperture is beneficial for the DTEM in several ways. In typical DTEM imaging experiments, a large convergence angle is required to achieve sufficient signal to noise ratios. The tradeoff for increasing the convergence angle is that the contrast transfer and signal to background ratio are adversely impacted. In annular dark field (ADF) imaging the central disc in the annular objective lens aperture blocks the vast majority of the coherently scattered electrons leaving the incoherent signal as the major contributor to image formation. This produces a dark field image with a vastly higher signal to background ratio allowing even larger beam convergence angles to be used while maintaining high contrast and comparable resolution. ADF-DTEM may also be a significantly better method for imaging on shorter time scales. For a given brightness, there is an inverse relationship between the pulse length and the stochastic blur, due to columbic interactions. Since the contrast of ADF-DTEM is greatly improved, lower fluences can be used to limit the effects of stochastic blurring.

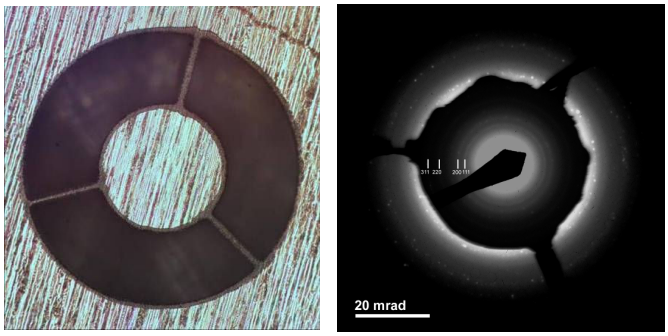

Figure 1: (a) Optical microscope image of a typical ADF aperture after plasma etching and (b) Overlaid selected area diffraction patterns from Au nanoparticles with and without the ADF aperture inserted. The exposure with the ADF aperture inserted was 10 times longer than the exposure without the aperture.

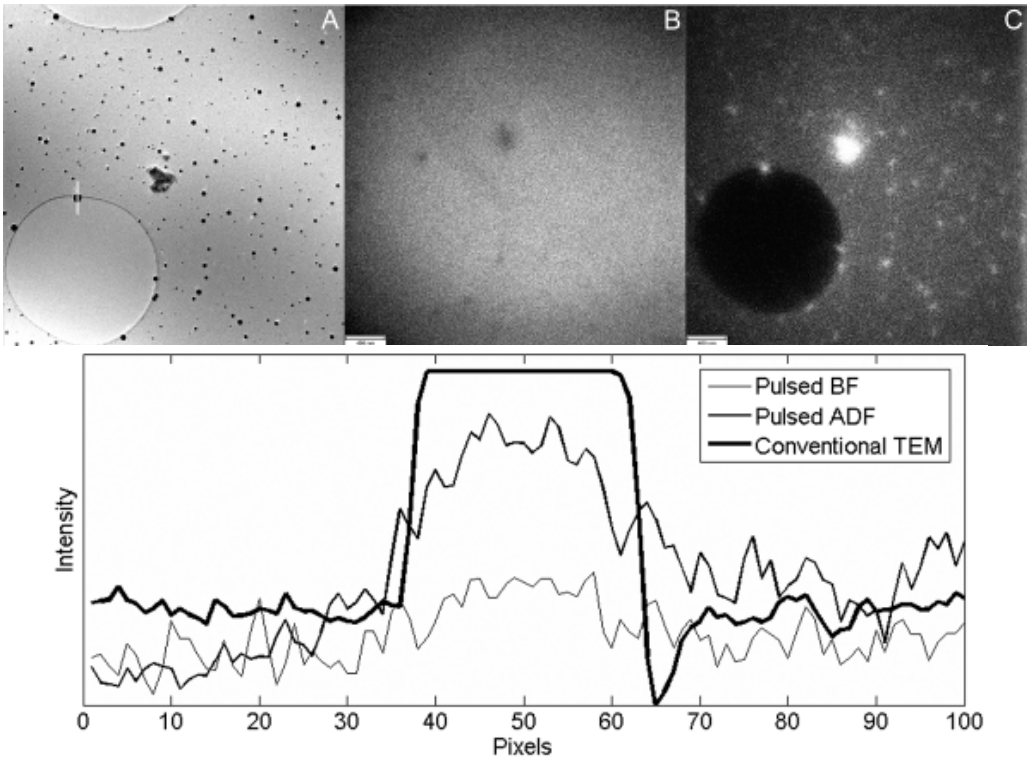

Figure 2: (a) Conventional TEM image, the white line shows where the line scans were taken (b) 15 ns pulsed bright field image (c) 15 ns pulsed ADF image and (d) linescan across the images. The scale bar is 400 nm and is the same for each image.

Figure 1 shows an ADF aperture fabricated using a one mask photolithographic process that blocks the Bragg reflections out to approximately 10 mrad allowing only extremely weak reflections to contribute to the image. Figure 2 shows a conventional TEM image of gold nanoparticles ranging in size from 1 – 100 nm dispersed on a holey carbon film as well as single shot pulsed images at 15 ns time resolution in both bright field and dark field. In the time resolved bright field images most particles below 50 nm are not resolved due to limited signal and low contrast. In the time resolved dark field equivalent, almost every 50 nm particle and many 30 nm particles are clearly visible. The stark difference between these two images clearly demonstrates the efficacy of annular dark field imaging when examining samples with feature sizes near the resolution limit of DTEM. The line scans also shown in figure 2 are integrated over a 5 pixel wide area and are taken across the same feature in each image. They are inverted for the bright field cases and the background levels are matched in intensity for ease of comparison. The signal to background ratios were computed for the pulsed cases and were determined to be 2.21 dB for the pulsed BF image and 11.3 dB for the pulsed ADF image. They clearly show the improved signal to background ratio obtained by pulsed ADF imaging compared to conventional bright field pulsed imaging. While the resolution is not significantly affected, the ability to obtain vastly improved contrast for smaller particles widens the range of catalyst systems that can be usefully studied using DTEM.

Future Plans

The framework to study reactions in-situ in the DTEM has now been established and the following 2 years will see the research program move in the following directions.

1. The in-situ gas stage for the DTEM has been shown to allow atmospheric pressure and temperatures up to 1700^{o}C. This stage will be used to perform oxidation/reduction reactions using cobalt catalysts and also to observe surface diffusion of Au catalysts on TiO_2 supports.
2. The DTEM will be configured to operate on microsecond timescales, greatly increasing the signal levels and the spatial resolution of the images that are acquired. The cobalt and gold experiments will also be performed on these timescales to understand the effects of motion blur, gas pressure and temperature on the resolution of the DTEM.
3. Correlate the DTEM observations of Au nanocluster mobility/sintering under variable gas pressures and temperatures directly with molecular dynamics simulations to elucidate the effects of metal-support interactions on catalytic properties.

This work performed under the auspices of the U.S. Department of Energy, Office of Science, Office of Basic Energy Sciences, Division of Materials Sciences and Engineering by Lawrence Livermore National Laboratory under Contract DE-AC52-07NA27344

DOE Sponsored Publications 2008-2010

N. L. Okamoto, B. W. Reed, S. Mehraeen, A. Kulkarni, D. G. Morgan, B. C. Gates & N. D. Browning, "Determination of Nanocluster Sizes from Dark-Field Scanning Transmission Electron Microscopy Images", J*ournal of Physical Chemistry C* **112**, 1759-1763 (2008)

J. S. Kim, T. B. LaGrange, B. W. Reed, N. D. Browning, M. L. Taheri, M. R. Armstrong, W. E. King & G. H. Campbell, "Imaging of Transient Structures using Nanosecond in situ TEM", *Science* **321**, 1472-1475 (2008)

M. L. Taheri, B. W. Reed, T. B. Lagrange & N. D. Browning, "In-Situ Synthesis of Nanowires in the Dynamic TEM", *Small* **4**, 2187-2190 (2008)

T. LaGrange, G. H. Campbell, B. W. Reed, M. L. Taheri, J. B. Pesavento, J. S. Kim & N. D. Browning, "Nanosecond time resolved investigations using the *in situ* of Dynamic Transmission Electron Microscope (DTEM)", *Ultramicroscopy***108**, 1441-1449 (2008)

M. L. Taheri, T. B. Lagrange, B. W. Reed, M. R. Armstrong, G. H. Campbell, W. J. DeHope, J. S. Kim, W. E. King, D. J. Masiel & N. D. Browning, "Laser Based *In Situ* Techniques: Novel Methods for Generating Extreme Conditions in TEM Samples", *Microscopy Research and Techniques* **72**, 122-130 (2009)

T. LaGrange, D. S. Grummon, N. D. Browning, W. E. King & G. H. Campbell, "Strongly Driven Crystallization Processes in Metallic Glasses" *Applied Physics Letters* **94**, 184101 (2009)

B. W. Reed, M. R. Armstrong, N. D. Browning, G. H. Campbell, J. E. Evans, T. B. LaGrange, and D. J. Masiel, "The Evolution of Ultrafast Electron Microscope Instrumentation", *Microscopy and Microanalysis***15***,* 272-281 (2009)

A. Kulkarni, S. Mehraeen, N. L. Okamoto, B. W. Reed, N. D. Browning & B. C. Gates, "Nearly Uniform Osmium Clusters Supported on MgO: Characterization by X-ray Absorption Spectroscopy and Scanning Transmission Electron Microscopy", *Journal of Physical Chemistry C***113**, 13377-13385 (2009)

B. W. Reed, D. G. Morgan, N. L. Okamoto, A. Kulkarni, B. C. Gates & N. D. Browning, "Validation and Generalization of a Method for Precise Size Measurements of Metal Nanoclusters", *Ultramicroscopy***110**, 48-60 (2009)

"Electron Microscopy and Spectroscopy on the Ultrafast Timescale", N. D. Browning, G. H. Campbell, J. E. Evans, T. B. LaGrange, B. W. Reed, *ChemPhysChem* **11**, 781-782 (2010)

B. W. Reed, T. LaGrange, R. M. Shuttlesworth, D. J. Gibson, G. H. Campbell & N. D. Browning, "Solving the Accelerator-Condenser Coupling Problem in a Nanosecond Dynamic Transmission Electron Microscope", *Review of Scientific Instruments***81**, 053706 (2010)

M. L. Taheri, S. McGowan, L. Nikolova, J. E. Evans, N. Teslich, J. P. Lu, T. LaGrange, F. Rosei, B. J. Siwick & N. D. Browning, "In Situ Laser Crystallization of Amorphous Silicon: Controlled Nanosecond Studies in the DTEM", *Applied Physics Letters* **97**, 032102 (2010)

D. J. Masiel, T. LaGrange, B. W. Reed, T. Guo & N. D. Browning, "Time Resolved Annular Dark Field Imaging of Catalyst Nanoparticles", *ChemPhysChem***11**, 2088-2090 (2010)

Complex Fundamental Mechanisms of Transient States in Materials Quantified by DTEM

Geoffrey H. Campbell, PI
Thomas LaGrange, Nigel D. Browning, Marta Bonds, Co-I
Lawrence Livermore National Laboratory, Condensed Matter and Materials Division
PO Box 808, Mailstop L-356, Livermore, CA 94550
E-mail: ghcampbell@llnl.gov

Project Scope

The thrust of the project is to reveal the fundamental parameters of strongly driven phase transformations and rapid chemical reactions with the novel capabilities offered by the LLNL DTEM instrument (Figure 1). We strive to map the kinetics of martensitic phase transitions and diffusive transformations by developing time-temperature-transformation (TTT) diagrams with nanosecond time resolution. The imaging capabilities of the instrument allow us to quantitatively measure nucleation and growth rates directly. These measurements are used in analytical models of the transformation kinetics. Moreover, the observations allow us to identify changes in the mechanism of transformation as the driving force is changed.

We have studied the crystallization from an initially amorphous structure in two systems that demonstrate markedly differing cases. The first is of a monoatomic, covalently bonded elemental Ge and the second is a two component, intermetallic forming system, NiTi. The rapid annealing of initially amorphous films by a pulsed laser leads to distinctly different microstructures. Time resolved observations with the DTEM have revealed that the C-curve behavior in the TTT diagram leads directly to the observed structures, albeit with a complicating roughening transition in the Ge at lower temperatures that adds a final stage in the grain structure as the annealed material cools.

We can contrast the devitrification processes of the above cases with observations of solidification in pure and alloy metallic systems. We have observed the resolidification of supported thin films of pure Al and Al-Cu alloys. The melt pool formed by laser heating is always in contact with unmelted material and hence solidification initiates by the growth of grains into the melt region, avoiding the nucleation process. We have measured the growth velocities in both systems and compared them to models and we are working to understand the regimes in which the alloy system will experience morphological instability of the growth front.

We also made observations of morphological details of the reaction front in energetic nanolaminates. The DTEM reveals transient structures at the reaction front in these rapid solid-state chemical reactions. In this abstract we focus on the phase transformation results.

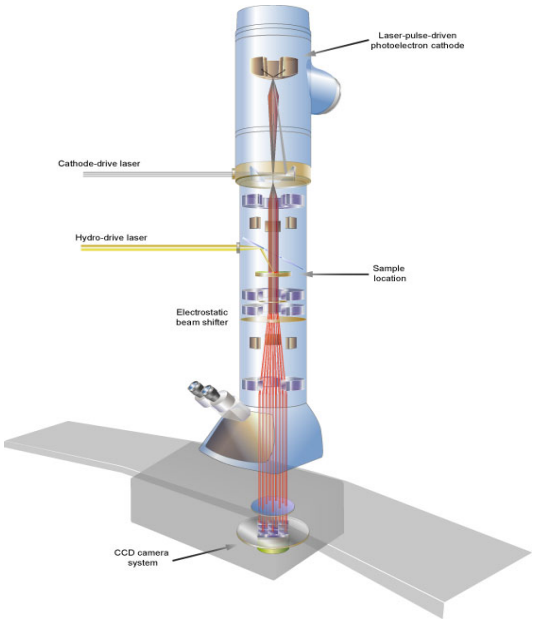

Figure 1 – Schematic drawing of the DTEM showing the TEM combined with two laser systems. The sample laser is used to pump the specimen into a certain state and the cathode laser generates the electron pulse that probes the specimen, forming a diffraction pattern or an image of the transient state of interest.

Recent Results

At the last ESPM contractor's meeting, we reported on strongly driven crystallization of an amorphous NiTi film in the DTEM that revealed striking differences in the devitrification processes as compared to slower, "furnace-based" anneals. The extraordinarily fast crystallization

rates and the observed fine microstructures after crystallization do not correlate with literature reported kinetic data. The measured nucleation rates in the DTEM experiments are six orders of magnitude larger than those predicted by rate theory.

In the last year, we have completely mapped out the nucleation kinetics at the DTEM annealing temperatures and revealed the C-curve behavior, as shown in Figure 2. The C-curve kinetics allows us to explain the microstructure created as a result of the pulsed laser annealing as a function of position within the irradiated spot. In the 15 ns exposure, dynamic images shown in Figure 3, we see a portion of the irradiated spot that shows directly a manifestation of the C-curve behavior. In the center image we see a band of crystallized material at 6 μs after heating. To the left of this band the material is too hot to nucleate (low driving force) at this time and to the right it is too cold (kinetically limited). The rapid growth at high temperatures, however, allows the nucleated crystallites to grow rapidly towards the center, consuming the high temperature materials and leaving a region composed of large grains only. At right, growth is significantly slower and gets even slower as the distance is increased, yet nucleation proceeds forming a nanocrystalline region. This produces a characteristic microstructure that has a radial distribution in grain size from micron-sized grains in the center to nanocrystalline material in the periphery.

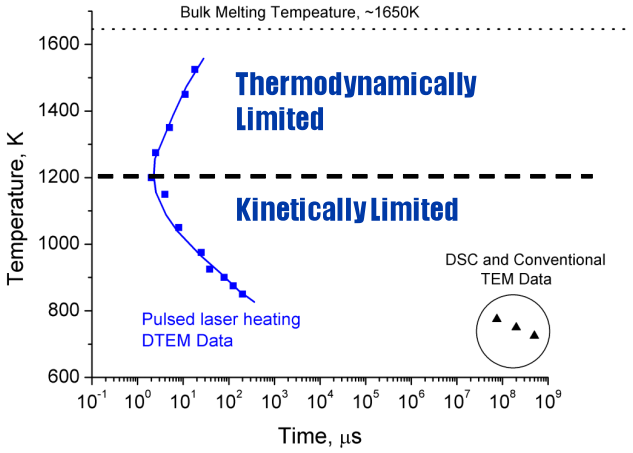

Figure 2. a) plot of the 90% crystallized volume as function of temperature and time. Note the classical C-curve behavior for diffusional phase transformation.

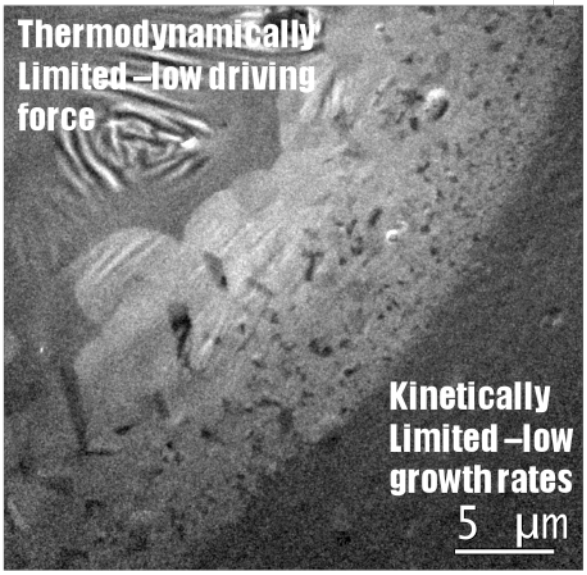

Figure 3. 15ns exposure of the crystallization taken 6 μs after the laser pulse hits the foil. The center of the gaussian laser spot is located in upper left-hand corner.

An interesting contrast to the above picture of devitrification in a metallic alloy is the devitrification of elemental Ge under similar pulsed laser annealing that creates a completely different microstructure. An overview image of the laser-annealed spot is shown in Figure 4, where we see a central region that is nanocrystalline surrounded by large, denditric grains (Zone II), exactly the opposite of the NiTi case. The nanocrystalline central region results from extremely high nucleation rates. Conversely to the

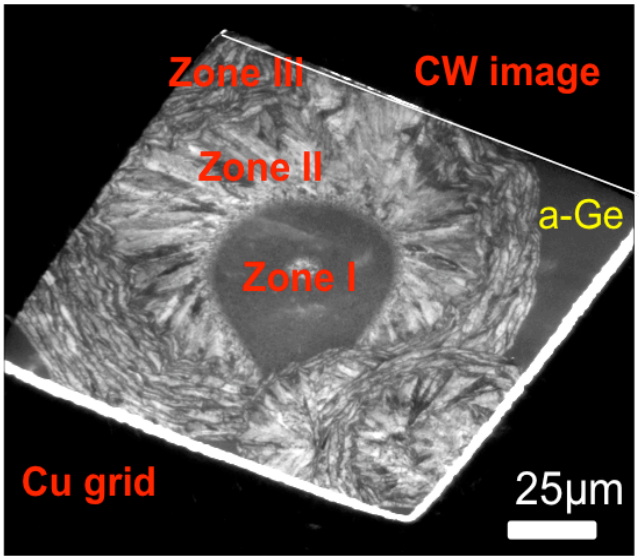

Figure 4. CW low magnification image of the laser crystallized region in an amorphous Ge film display three distinct morphologies, Zone I nanocrystalline, Zone II elongated radial crystals, and Zone III spiraled twined crystals.

devitrification processes in the NiTi system, the nucleation rate increases exponentially with temperature to the melting point. The Ge either does not display a C curve behavior or the nose in the C curve is so close to the melting temperature that it is immeasurable with current temperature and time resolution. The formation of the nanocrystalline central region in Figure 4 is formed within 55 ns. By observing the number of crystals per unit area with time and size of these crystals, nucleation and growth rates were determined (Figure 5). The crystal growth was linear at 50 ns and lower typical for devitrification processes and above 50 ns the growth was much slower, displaying a characteristic parabolic dependency with time for a diffusion controlled process. The intersection of the two fits in the plot shown in Figure 5 estimates the completion for crystallization at 55 ns. Taking the direct derivative of the data in the blue curve in Figure 5, the nucleation rate for each time delay was calculated

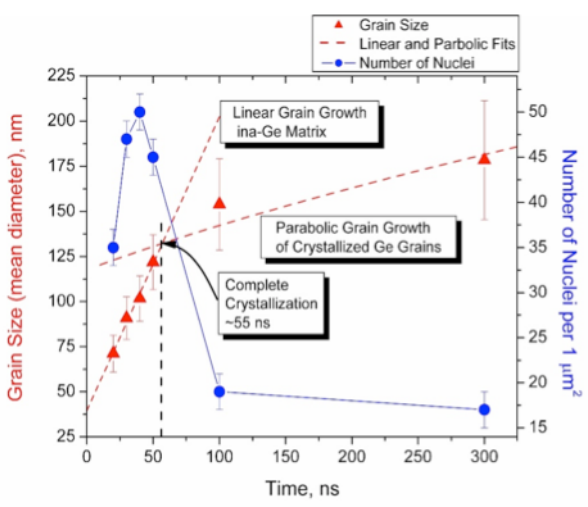

Figure 5. Time-resolved mean size of the crystals (red triangles) with the respective error bars. The red dashed lines represent the fits for the two distinct grain growth regions. Time-resolved number of the crystals per unit area is presented by blue disks.

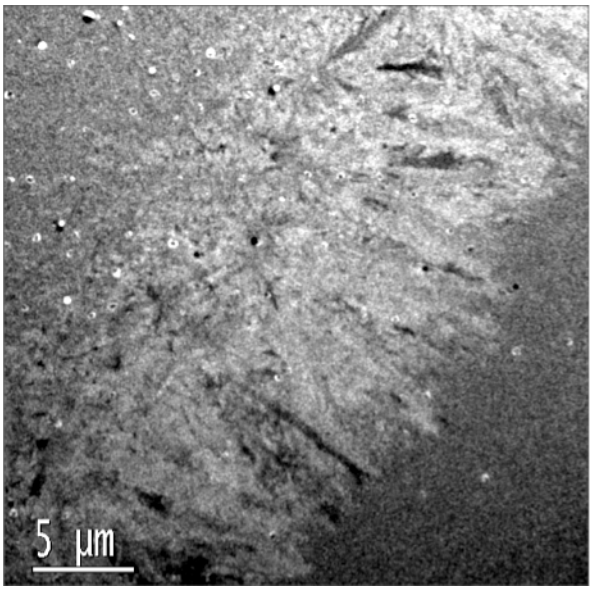

Figure 6. 15ns exposure of the dendritic "spoke" grains growing at 10 m/s into the amorphous Ge film, taken 1 μs after the laser pulse hits the foil

and estimated maximum of $N \approx 1.59 \times 10^{22}$ cm $^{-3}$ ·s $^{-1}$. Although this estimated nucleation was quite high, it was commensurate with the rapid crystallization and fine grain size, indicating that high laser fluence and temperatures near but below the melt temperature are required to produce nanocrystalline Ge films.

The large grained region surrounding the nanocrystalline center is equally interesting. Two distinct regions can be seen in the large grain region. Surrounding the central region are large dendritic grains that have grown radially outwards producing an elongated morphology akin to the spokes of a wheel. Outside this region an abrupt change occurs in the morphology of the grains such that they are now elongated in a direction tangential to the perimeter of the irradiated spot, to continue the wheel analogy these would form the rim of the wheel. While at first mysterious, the origin of these regions becomes clear when their growth modes at the moving crystallization front are observed by dynamic imaging. The growth front is jagged in the wheel spoke region as shown in image of Figure 6, taken shortly after it has transitioned to elongated grain growth. The transition occurs at the point where the temperature is low enough that the growth rate of the grains consumes amorphous material faster than it can generate nuclei. The second transition to wheel rim growth is seen in Figure 7. Here we observe a distinctly different growth front morphology. The growth front is flat (faceted) and it grows laterally to the crystalline/amorphous interface. The transition between the spoke and rim regions is being driven by a faceting transition as the temperature decreases, from an atomically rough interface at the high temperatures that produces a jagged growth front to an atomically flat faceted growth front at lower temperature.

Future Work

We are also performing experiments in the Al-Cu system to explore interface morphology in solidification fronts of alloy systems. We anticipate determining the dependence of morphological instability on growth front velocity via a mechanism of non-equilibrium incorporation of solute atoms that suppresses the tendency for constitutional supercooling that drives dendrite formation.

We will also continue our studies of crystallization from the amorphous phase under strongly driven conditions. We will use double exposures enabled by the soon to be operational arbitrary waveform cathode laser on the DTEM to allow precise measurement of crystallization front velocity for a more accurate separation of nucleation and growth activation energies.

This work performed under the auspices of the Division of Materials Science and Engineering, Office of Basic Energy Sciences, U.S. Department of Energy by Lawrence Livermore National Laboratory under Contract DE-AC52-07NA27344.

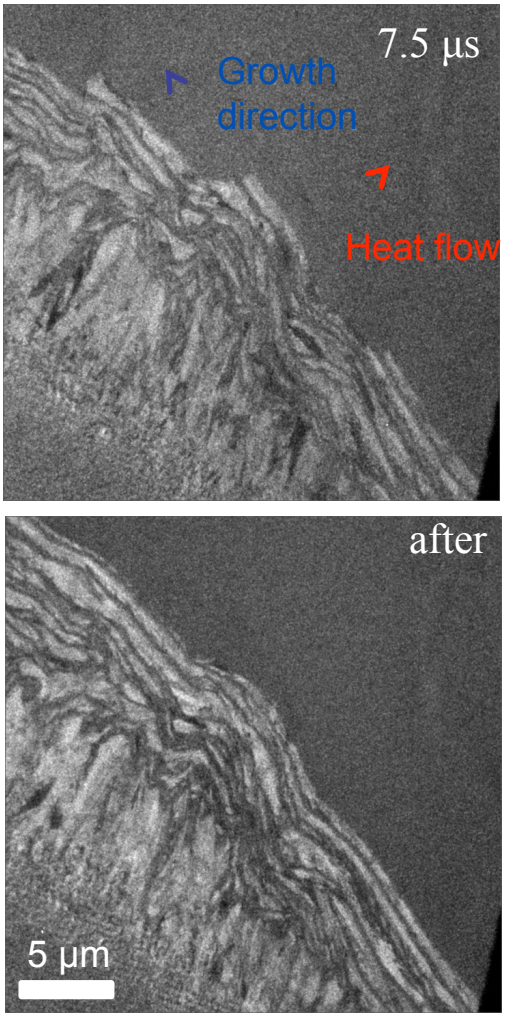

Figure 7. 15ns exposure showing the spiral growth mode which is flat and faceted. Top image taken at 7.5 µs delay, Bottom image taken after film has cooled to room temperature.

2008 – 2010 Publications

[1] Browning ND, Campbell GH, Evans JE, LaGrange TB, Reed BW. Electron Microscopy and Spectroscopy on the Ultrafast Timescale. Chemphyschem 2010;11:781.

[2] Campbell GH, LaGrange T, Kim JS, Reed BW, Browning ND. Quantifying transient states in materials with the dynamic transmission electron microscope. Journal of Electron Microscopy 2010.

[3] Kim JS, LaGrange T, Reed BW, Taheri ML, Armstrong MR, King WE, Browning ND, Campbell GH. Imaging of transient structures using nanosecond in situ TEM. Science 2008;321:1472.

[4] LaGrange T, Campbell GH, Reed B, Taheri M, Pesavento JB, Kim JS, Browning ND. Nanosecond time-resolved investigations using the in situ of dynamic transmission electron microscope (DTEM). Ultramicroscopy 2008;108:1441.

[5] LaGrange T, Grummon DS, Reed BW, Browning ND, King WE, Campbell GH. Strongly driven crystallization processes in a metallic glass. Applied Physics Letters 2009;94.

[6] Masiel DJ, Reed B, LaGrange T, Campbell GH, Guo T, Browning ND. Time-Resolved Annular Dark Field Imaging of Catalyst Nanoparticles. Chemphyschem 2010;11:2088

[7] Reed BW, Armstrong MR, Browning ND, Campbell GH, Evans JE, LaGrange T, Masiel DJ. The Evolution of Ultrafast Electron Microscope Instrumentation. Microscopy and Microanalysis 2009;15:272.

[8] Reed BW, LaGrange T, Shuttlesworth RM, Gibson DJ, Campbell GH, Browning ND. Solving the accelerator-condenser coupling problem in a nanosecond dynamic transmission electron microscope. Review of Scientific Instruments;81.

[9] Taheri ML, Lagrange T, Reed BW, Armstrong MR, Campbell GH, DeHope WJ, Kim JS, King WE, Masiel DJ, Browning ND. Laser-Based In Situ Techniques: Novel Methods for Generating Extreme Conditions in TEM Samples. Microscopy Research and Technique 2009;72:122.

[10] Taheri ML, McGowan S, Nikolova L, Evans JE, Teslich N, Lu JP, LaGrange T, Rosei F, Siwick BJ, Browning ND. In situ laser crystallization of amorphous silicon: Controlled nanosecond studies in the dynamic transmission electron microscope. Applied Physics Letters 2010;97:032102.

[11] Taheri ML, Reed BW, LaGrange TB, Browning ND. In Situ Laser Synthesis of Si Nanowires in the Dynamic TEM. Small 2008;4:2187.

Program Title: **Spectroscopic Imaging STM for Complex Electronic Matter**

Principal Investigator: J. C. Séamus Davis
Email: jcdavis@ccmr.cornell.edu
Center for Emergent Superconductivity
CMPMS, Brookhaven Nat. Lab, NY, USA.
LASSP, Physics, Cornell U., NY, USA.
http://people.ccmr.cornell.edu/~jcdavis/
http://www.bnl.gov/energy/ces/

Program Scope:

Our program covers four major areas of complex electronic matter research. The first is a continuation of our studies of the electronic structure of *cuprates*, and is designed to aid in the identification of the mechanism of high temperature superconductivity therein. The second is a program focused on the newly discovered high temperature superconducting *pnictides*. Here there are a wide variety of open questions which we plan to address including the microscopic cause of the strong electronic anisotropy that we discovered early this year. Our third program focuses on electronic nematic states, especially in the *ruthenates*. Here the key challenge is to image for the first time, a high magnetic field induced transition to a nematic state at sub kelvin temperatures. The fourth new program is the SI-STM study of the mechanism of heavy fermion electronic structure and heavy fermion superconductivity in *intermetallic* metals. To carry out these studies we will use appropriate combination of our four SI-STM instruments: BNL-STM1 (4K→100K, 7.5Tesla), CU-STM1 (300mK/ 9 Tesla), CU-STM2 (1K/20 Tesla), CU-STM3 (10mK/9 Tesla).

Recent Progress:

- **How inter-atomic distance changes impact high-T_c superconductivity within individual crystal unit-cells.**

Many theoretical models of high temperature superconductivity focus only on the doping dependence of the CuO_2 plane electronic structure. Such models are manifestly insufficient to explain the strong variations in superconducting T_c among cuprates which are identically hole-doped but crystallographically different outside the CuO_2 plane. The challenge has been to identify the predominant out-of-plane influence controlling the superconductivity - with attention focusing on the distance d_A between the apical oxygen and the planar copper atom. We determined in the cuprate superconductor ($Bi_2Sr_2CaCu_2O_{8+\delta}$) of how inter-atomic distance variations affect the energy gap Δ within individual unit cells. Over each period within the crystalline 'supermodulation' (~6 unit cells) what variation in Δ occurs in association with the ~12% sinusoidal variation in d_A. We found phenomenological consistency of such effects with the random Δ variations near the dopant atoms under the scenario that the interstitial dopants diminish d_A.

Proc. Nat'l Acad. Sci., 105, 3203 (2008).

- **Evolution of the electronic excitation spectrum with strongly diminishing hole-density in superconducting $Bi_2Sr_2CaCu_2O_{8+\delta}$**

A complete knowledge of its excitation spectrum could greatly benefit efforts to understand the unusual form of superconductivity occurring in the lightly hole-doped copper-oxides. We will use tunnelling spectroscopy to measure the T→0 spectrum of electronic excitations N(E) over a wide range of hole-density *p* in superconducting $Bi_2Sr_2CaCu_2O_{8+\delta}$. We introduce a parameterization for N(E) based upon an anisotropic energy-gap $\Delta(\vec{k}) = \Delta_1(Cos(k_x) - Cos(k_y))/2$ plus an effective scattering rate which varies linearly with energy $\Gamma_2(E) = \alpha E$. We demonstrated that this form of N(E) allows successful fitting of the high energy differential tunnelling conductance spectra throughout much of the $Bi_2Sr_2CaCu_2O_{8+\delta}$ phase diagram. The resulting average Δ_1 values rise with falling *p* along the familiar trajectory of excitations to the 'pseudogap' energy, while the key scattering rate increases from below ~1meV to a value approaching 15 meV as the system is underdoped from *p*~16% to p<10%. We also observe two distinct and diverging energy scales in the system: the energy-gap maximum Δ_1 and a lower energy scale Δ_0 separating the spatially homogeneous and heterogeneous electronic structures.

Nature Physics 4, 319-326 (2008).

- **Discovery of Shrinking Arc of Cooper Pairing in $Bi_2Sr_2CaCu_2O_{8+\delta}$**

The antiferromagnetic ground state of copper oxide Mott insulators is achieved by localizing an electron at each copper atom in real space (r-space). Removing a small fraction of these electrons (hole doping) transforms this system into a superconducting fluid of delocalized Cooper pairs in momentum space (**k**-space). During this transformation, two distinctive classes of electronic excitations appear. At high energies, the enigmatic 'pseudogap' excitations are found, whereas, at lower energies, Bogoliubov quasi-particles—the excitations resulting from the breaking of Cooper pairs—should exist. To explore this transformation, and to identify the two excitation types, we imaged the electronic structure of $Bi_2Sr_2CaCu_2O_{8+\delta}$ in **r**-space and **k**-space simultaneously. We determined that although the low energy excitations are indeed Bogoliubov quasi-particles, they occupy only a restricted arc in **k**-space and that this arc shrinks rapidly with diminishing hole density. Concomitantly, spectral weight is transferred to higher energy **r**-space states that lack the characteristics of excitations from delocalized Cooper pairs. Instead, these states break translational and rotational symmetries locally at the atomic scale in an energy independent fashion. We demonstrate that these unusual **r**-space excitations are, in fact, the pseudogap states. Thus, as the Mott insulating state is approached by decreasing the hole-density, the **k**-space arc of delocalized Cooper pairs vanishes to be replaced by locally translational- and rotational-symmetry-breaking pseudogap states in r-space.

Nature 454, 1072 (2008).

- **Spectroscopic Fingerprint of Phase-Incoherent Superconductivity in the Cuprate Pseudogap State**

A possible explanation for the existence of the cuprate "pseudogap" state is that it is a d-wave superconductor without quantum phase rigidity. Transport and thermodynamic studies provide compelling evidence that supports this proposal, but few spectroscopic explorations of it have been made. One spectroscopic signature of d-wave superconductivity is the particle-hole symmetric "octet" of dispersive Bogoliubov quasiparticle interference modulations. We studied this octet's evolution from low temperatures to well into the underdoped pseudogap regime. No pronounced changes occur in the octet phenomenology at the superconductor's critical temperature Tc, and it survives up to at least temperature T ~ 1.5 Tc. In this pseudogap regime, we observe the detailed phenomenology that was theoretically predicted for quasiparticle interference in a phase-incoherent d-wave superconductor. Thus, our results provide direct spectroscopic evidence confirming the deductions from transport and thermodynamics studies that the cuprate pseudogap phase is a *d*-wave superconductor without long range order.

***Science 325*,** 1099 (2009)

- **Heavy *d*-electron quasiparticle interference and real-space electronic structure of $Sr_3Ru_2O_7$**

Visualization of the many-body quantum states generated by the strong interactions, and of the resulting electronic 'liquid crystal' phases, has been a long term challenge. Soft condensed-matter physics was transformed by microscopies that enabled imaging of real-space structures and patterns. A candidate technique for obtaining equivalent data in the purely electronic systems is spectroscopic imaging scanning tunneling microscopy (SI-STM). With this approach we detect the tenuous but 'heavy' momentum (k)-space components of the many-body electronic state simultaneously with its real space constituents. Sr3Ru2O7 therefore provides a particularly exciting opportunity to address these issues. It possesses a very strongly renormalized 'heavy' *d*-electron Fermi liquid and exhibits a field-induced transition to an electronic liquid crystalline phase.

***Nature Physics 5*,** 800 (2009)

- **Heavy Quasiparticle Interference Imaging of the 'Hidden Order' in URu_2Si_2**

Within a Kondo lattice, the strong hybridization between electrons localized in real space (**r**-space) and those delocalized in momentum-space (**k-**space) generates exotic electronic states called 'heavy fermions'. In URu2Si2 these effects begin at temperatures around 55 K but they are suddenly altered by an unidentified electronic phase transition at To517.5 K. Whether this is conventional ordering of the k-space states, or a change in the hybridization of the r-space states at each U atom, is unknown. Here we use spectroscopic imaging scanning tunneling microscopy (SI-STM) to image the evolution of URu2Si2 electronic structure simultaneously in **r**-space and **k**-space. Above To, the 'Fano lattice'

electronic structure predicted for Kondo screening of a magnetic lattice is revealed. Below To, a partial energy gap without any associated density-wave signatures emerges from this Fano lattice. Heavy-quasiparticle interference imaging within this gap reveals its cause as the rapid splitting below T_o of a light k-space band into two new heavy fermion bands. Thus, the URu2Si2 'hidden order' state emerges directly from the Fano lattice electronic structure and exhibits characteristics, not of a conventional density wave, but of sudden alterations in both the hybridization at each U atom and the associated heavy fermion states.

***Nature 465*,** 570 (2010).

Future Plans

- Studies of the electronic structure of *cuprates* designed to aid in the identification of the mechanism of high temperature superconductivity therein.
- Studies of the electronic structure of *pnictides* including the microscopic cause of the strong electronic anisotropy that we discovered early this year.
- Studies of the electronic structure of *ruthenates* to image the high magnetic field induced transition to a nematic state at sub kelvin temperatures.
- Studies of the electronic structure of heavy fermion electronic structure and heavy fermion superconductivity in *intermetallic* metals.

DOE Award Number: ERKCM43 Oak Ridge National Laboratory

Project Title: Atomistic Mechanisms of Metal-Assisted Hydrogen Storage in Nanostructured Carbon

PI's: Nidia C. Gallego (gallegonc@ornl.gov), Cristian I. Contescu, James Morris, Takeshi Egami, Stephen Pennycook - Oak Ridge National Laboratory, Oak Ridge, TN 37831-6087

Date: August 2010 **Period covered:** 2008 – 2010

Program Scope

The goal of this project is to establish the scientific basis for designing the building blocks of carbon-based adsorbents that enable synergistic metal-carbon interactions, leading to enhanced hydrogen uptake at near-ambient temperatures. Our preliminary results suggest that addition of transition metal catalysts to nanoporous carbons with controlled nanoscale structure and porosity results in enhanced H_2 adsorption. This appears to result from as yet poorly understood atomic-scale interactions between molecular H_2, metal particles, and carbon with proper nanostructures. Theoretical calculations demonstrate that uptake may be significantly increased if sufficient control of the structure can be attained. To optimize the design of such nanostructure, it is essential to develop atomistic models that realistically describe isotropic nanoporous carbons and to gain fundamental understanding, at the atomic and molecular level, of hydrogen interactions within metal-doped carbons. The project is focused on three specific aims: (1) modeling and characterization of medium-range order in partially amorphous – partially graphitic structures of nanoporous carbons; (2) understanding the mechanism of molecular activation of H_2 by metal particles; and (3) elucidation of the energetics and dynamics of hydrogen species confined in the molecular space of pure- and metal-doped nanoporous carbons. State-of-the-art neutron and x-ray (synchrotron) scattering, advanced computation, and high-resolution electron microscopy all contribute to achieving our research goals. Our recent progress and future plans are summarized in the following sections grouped by major programmatic tasks

Understanding and modeling the local structure of nanoporous carbons and their role on hydrogen storage

We have introduced an efficient and direct thermodynamics method to calculate the equilibrium hydrogen adsorption in carbon structures. This method can reproduce previous, more computational intensive calculations in the expanded graphite model,[1] yet is readily applicable to more complex geometries. We show the hydrogen uptake between expanded graphite layers is up to 2 wt% at room temperature and 5 MPa. Nanoporous carbons obtained from molecular dynamics simulations also show appreciable total hydrogen uptake (~ 0.5 wt%) at the same conditions. The results for both the expanded graphite system and the nanoporous carbons indicate that there is a competition between optimizing the volume available to adsorption, and optimizing the heat of adsorption: conditions with the highest uptake balance these two. High isosteric heats of adsorption (14-18 kJ/mol) in the low pressure limit are observed in the expanded graphite model and in nanoporous carbons with different densities (Fig. 1).[2] The generic form of this method makes it applicable to a wide range of solid-gas adsorption problems, and will be used to link more

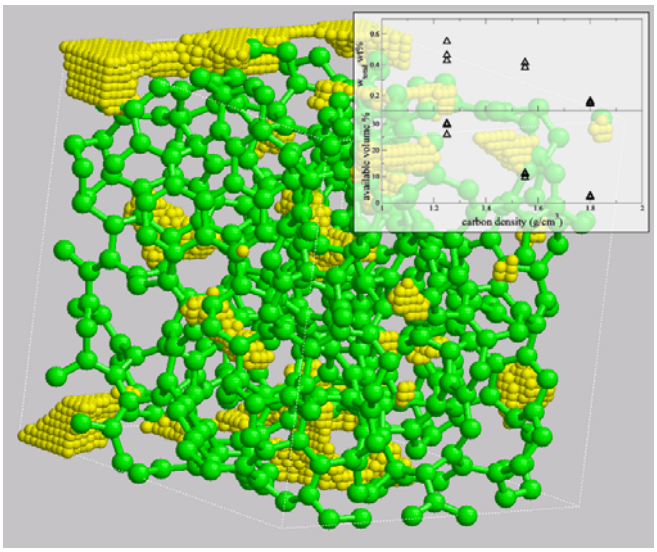

Fig. 1: Structure of the low density carbon, and the H_2 adsorbing regions colored by adsorption energy (cell dimension 2 nm). (Inset) The total H_2 adsorption (top) and available adsorption volume (bottom) in amorphous carbons as a function of carbon density at 298K and 5 MPa.

[1] Aga RS, Fu CL, Krcmar M, Morris JR. (2007): "Theoretical investigation of the effect of graphite interlayer spacing on hydrogen absorption". *Physical Review B* **76** (16): 165404

[2] Peng LJ, Morris JR (2010): "Prediction of Hydrogen Adsorption Properties in Expanded Graphite Model and in Nanoporous Carbon". *Journal of Physical Chemistry C*: in press (jp-2010-04595m)

accurate calculations of physisorption energies using recently developed vdW-DF methods,[3] with actual adsorption as a function of temperature and pressure. In parallel, we have also analyzed the electronic properties of fully hydrogenated graphenes and their isoelectronic analogues.[4,5]

Small angle scattering is a technique to study the structural features at longer length scales than conventional diffraction. Small angle neutron scattering (SANS) of nanoporous carbon with hydrogen gas adsorbed in pores can provide some information regarding pore shape, size distribution, and connectivity. We can directly calculate the intensity of SANS from the simulated amorphous carbons and the adsorbed hydrogen gas. The density profile of hydrogen gas will be evaluated by the above adsorption method. The results will be compared with on-going SANS experiments at the High Flux Isotope Reactor (ORNL).

To accurately model real structures, particularly low density carbons, accurate potentials for carbon must be used. We have developed and tested our own parallel tight binding molecular dynamics simulation programs for this project using DOE's large-scale computational facilities. Large number of simulations will cover different carbon densities and temperatures. The energies, electronic structures, pair distribution functions (PDF), BET surface areas and pore size distributions will be studied and directly compared with experimental measurements.

Understanding the role of metals in the storage capacity of nanostructured carbons

Enhancing hydrogen sorption capacity of nanostructured carbons is a challenge. Physisorption alone is not strong enough to provide high levels of uptake at near-ambient temperatures. Modifying carbons with small amounts of metals is a possible avenue for increasing the amounts adsorbed. However, very different mechanisms may be involved when the promoters are transition metals or alkali metals. We investigated the effect of Pd nanoparticles dispersed in the nanostructured matrix of activated carbon fibers (ACF), and of alkali metal traces (K, Na) remnant in chemically-activated ultramicroporous carbons (UMC).

Pd-modified ACF with 2 wt% Pd was synthesized from a pitch precursor.[6] Characterization by aberration-corrected, high resolution STEM[7] showed that about 82% Pd is present as small particles (~ 5 nm) and about

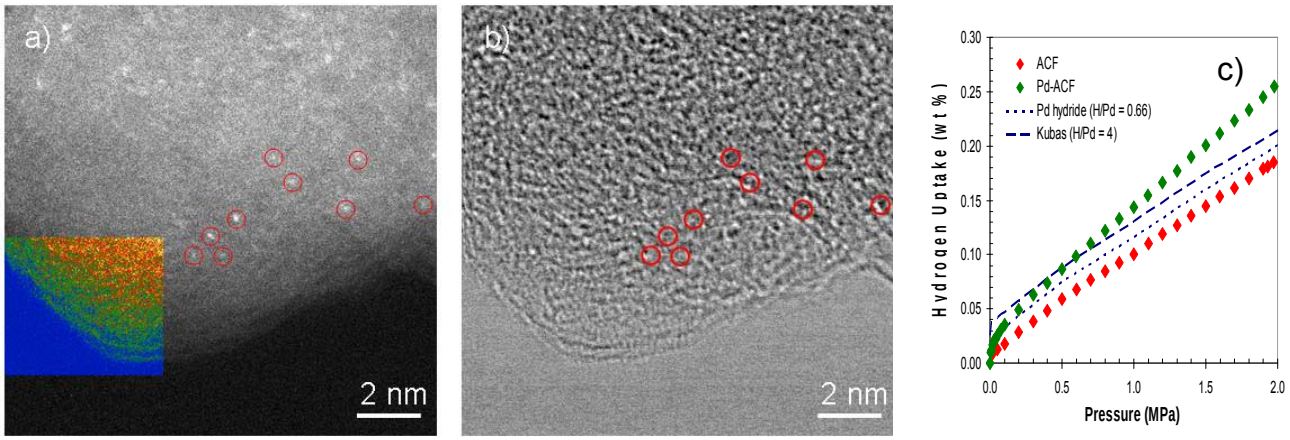

Fig. 2: Single Pd atoms in Pd-ACF embedded in carbon microstructure identified by high-resolution aberration-corrected STEM on simultaneously acquired images: (a) dark field; (b) bright field; (c) hydrogen uptake at 25 °C on Pd-ACF (green symbols) and Pd-free ACF (red symbols), compared with the expected amounts for formation of Pd hydride (H/Pd = 0.66) and of Kubas complexes (H/Pd = 4).

[3] Cooper VR, Peng LJ, Morris JR (2010): "van der Waals density functional calculations of hydrogen uptake in expanded graphite and hexagonal BN" (in preparation).

[4] Averill FW, Morris JR, Cooper VR (2009): "Calculated properties of fully hydrogenated single layers of BN, BC_2N, and graphene: Graphane and its BN-containing analogues". *Physical Review B*, **80**, 195411.

[5] Averill FW, Morris JR (2010): "Computation of the graphene/graphane interface energy and implications for defects" (in preparation).

[6] Wu X, Gallego NC, Contescu CI, Tekinalp H, Bhat VV, Baker FS, Thies MC (2008): "The effect of processing conditions on microstructure of Pd-containing activated carbon fibers". *Carbon* **46** , 54-61.

18% exists as isolated atoms.[8] Hydrogen capacity of Pd-ACF at 25 °C and 2 MPa was 25-35 % higher than that of pure activated carbon fiber (ACF), even after subtracting the contribution from formation of Pd hydride (Fig. 2). In-situ high-pressure XRD showed that Pd nanoparticles in Pd-ACF convert to H-rich β-$PdH_{0.67}$ at ~ 0.003 MPa H_2. The hydride phase is destabilized by multiple contacts with the microporous carbon support, and therefore may act as a source for primary spillover of H atoms.[9] Indeed, new C-H bonds were observed using inelastic neutron scattering on Pd-ACF in prolonged contact with 1.6 MPa H_2 at 20 °C.[10] This demonstrates that atomic H was formed on the surface of Pd-ACF in presence of hydrogen. Together, these results have isolated two elementary steps of the hydrogen spillover mechanism: (1) dissociation of molecular H_2 on metal particles, and (2) chemisorption to unsaturated carbon sites. For Pd-ACF at near-ambient temperatures, strong bonding (irreversible) by chemisorption is secondary to physisorption. In addition, single Pd atoms unambiguously detected by STEM may bind molecular hydrogen in Kubas-type complexes. Molecular simulations currently in progress[11] show that each Pd atom on graphene may bind up to 3 or 4 H_2 molecules at 300 K, and hence reversible Kubas bonding may significantly contribute to enhanced uptake on Pd-ACF compared to Pd-free ACF (Fig. 2).

In contrast, enhanced hydrogen uptake by ultramicroporous carbon (UMC), up to 0.8 wt% at 25 °C and 2 MPa, is hysteretic and much slower. This atypical behavior correlates with higher adsorption enthalpies (17-20 kJ/mol) and suggests a different mechanism, possibly related to the peculiar structure of this material. Another hypothesis, consistent with the presence of alkali metals (1200 ppm K, 550 ppm Na) in UMC, is polarization-induced physisorption caused by local electric fields.[12] Adding Pd nanopowder to UMC did not enhance the capacity, which seems to be controlled by alkali ions, but strongly accelerated adsorption rates; desorption rates were not affected. This suggests that Pd is the source of H spillover during adsorption, but is not effective in desorption and reverse spillover from charge-polarized H_2.[13]

Work continues for structural characterization of ACF and UMC using scattering methods, and for characterization of dynamics and preferential adsorption sites as function of hydrogen pressure using neutrons scattering techniques (QENS and SANS). Also, controlled tests are under way, aiming at understanding the effect of alkali ions as hydrogen uptake enhancer in nanostructured carbon. Since both ACF and UMC were obtained from natural sources with uncontrolled composition, we now use a synthetic polymer, polyfurfuryl alcohol (PFA), as the source of carbon. Initial experiments proved that PFA-derived carbon has similar capacity as ACF, and doping with of K and Pd produced enhanced cumulative effects on adsorption.

Quantitative structural characterization of porous, disordered carbons

We investigated the local atomic structure of ACF (without Pd doping) and UMC using high energy X-ray diffraction, pulsed neutron scattering, and the atomic pair distribution function (PDF) to probe the local atomic structure. The reduced pair distribution function G(*r*) is obtained by the direct Fourier-transformation of the total scattering function including both the Bragg peaks and diffuse scattering intensities. The results (Fig. 3a) show that the local atomic structure of both ACF and UMC up to 6 Å is similar to regular graphite and is essentially defined by a single graphite layer. Above 6-7 Å the peaks are strongly overlapping, but do not follow the pattern of the reference graphite sample. The correlations in the ACF and UMC are clearly lost above 12 Å. This behavior indicates that short range atomic order in nanoporous carbons is similar to the

---

[7] van Benthem K, Pennycook SJ (2009): "Electron microscopy at very high resolution": *in Dekker Encyclopedia of Nanoscience and Nanotechnology*, CRC Press, vol. 2, p. 1217-1229.

[8] van Benthem K, Bonifacio CS, Contescu CI, Pennycook SJ, Gallego NC (2010): "Single Pd atoms in activated carbon fibers for hydrogen storage" (submitted)

[9] Bhat VV, Contescu CI, Gallego NC (2009): "The role of destabilization of palladium hydride on the hydrogen uptake of Pd-containing activated carbons" *Nanotechnology* **20**, 204011 (Special Issue on Nanoscale Phenomena in Hydrogen Storage).

[10] Contescu CI, Brown CM, Liu Y, Bhat VV, Gallego NC (2009): "Detection of hydrogen spillover in palladium-modified activated carbon fibers during hydrogen adsorption" *Journal of. Physical Chemistry C,* **113**, 5886-5890.

[11] Sa L, Morris JR, Contescu CI, Gallego NC, Jena P (2010): "Pd-assisted hydrogen adsorption on graphene and (8.0) carbon nanotubes" (in preparation).

[12] Bhat VV, Contescu CI, Gallego NC, Baker FS (2010): "Atypical hydrogen uptake on chemically-activated, ultramicroporous carbon", *Carbon* **48**, 1331-1340.

[13] Bhat VV, Contescu CI, Gallego NC (2010): "Kinetic effect of Pd additions on the hydrogen uptake of chemically-activated ultramicroporous carbon", *Carbon* **48**, 2361-2364.

graphite but there is limited long-range coherence. The first PDF peak for the UMC carbon is closer to that of the graphite sample, and originates from the atomic coordination entirely in the single plane. Therefore, the extent of the graphene plane must be larger in UMC. On the other hand, ACF has more surface termination (small particle size) and thus a lower average coordination in the first shell.

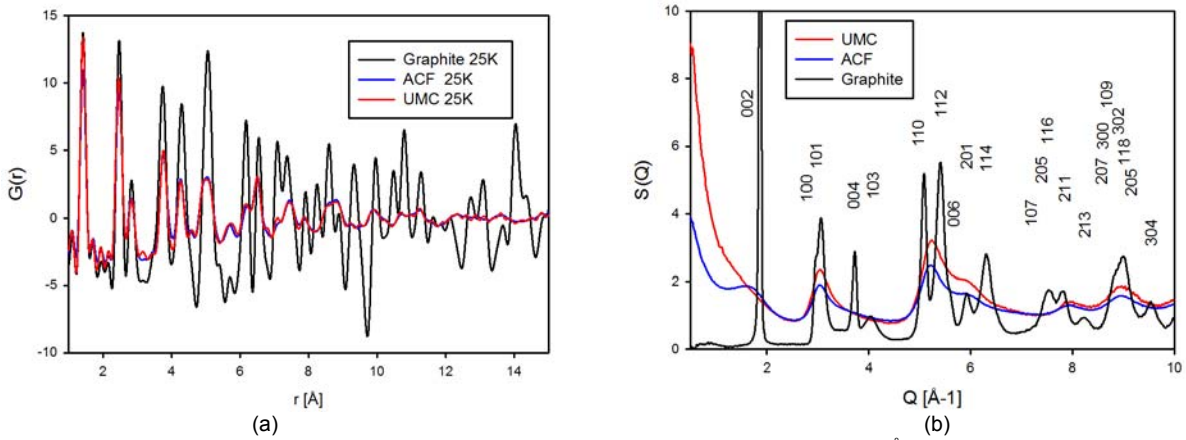

(a) (b)

Fig. 3: (a) Experimental G(r) for the reference graphite sample, ACF, and UMC carbons up to 15 Å; (b) Diffraction patterns for UMC and ACF compared to data for hexagonal graphite. The strong Bragg peaks expected for the alpha-hexagonal P63/mmc, space group #194 (A9), a=2.464 Å, c=6.711 Å, γ=120° are also shown for reference.

The diffraction patterns for ACF and UMC (Fig. 3b) show strong 2D character. The peaks have a saw-tooth shape and are shifted in Q, indicating that they originate from diffraction rods from single graphite layers. Peaks corresponding to (00*l*) are absent or very diffuse. Both UMC and ACF show significant small angle scattering, suggesting very small grain size. However, there is difference in the (002) Bragg peak pattern. The (002) for the ACF carbon is diffuse and broad, for the UMC the (002) peak merges with the small angle scattering. The different pattern of (002) suggests that the stacking order/disorder along the z direction may be dissimilar in these samples.

Summary

This project addresses the BES long-term program targets in the area of design, modeling, fabrication, and characterization, at the nanoscale level and with atomic precision, of novel materials for energy-inspired applications. The objective is to establish the scientific basis for designing building blocks of nanoporous carbons and metal-doped carbons that enable synergistic metal-carbon interactions leading to enhanced hydrogen uptake at near ambient temperatures. To achieve this goal we are first developing a better understanding of the partially amorphous – partially graphitic architecture of high surface area carbon materials. We then study the mechanisms of molecular activation of hydrogen by transition and alkali metals incorporated in the matrix, leading to enhanced hydrogen uptake. We also use in-situ scattering methods to characterize dynamics and the in-pore densification factor of hydrogen confined in the molecular space of nanoporous carbons. Our approach combines synthesis, advanced characterization, simulation and modeling. We are using the state-of-the-art neutron and x-ray scattering facilities at Spallation Neutron Source (ORNL), Lujan Neutron Center (LANL), Advanced Photon Source (ANL), powerful computational facilities at ORNL, and high-resolution electron microscopy facilities at ORNL.

Overall, our research will improve the basic knowledge on the roles of carbon structures and metal catalysts, and will allow designing new structures for hydrogen storage systems. In a more general sense this basic science knowledge will provide new understanding of nanoporous materials tailored for a variety of energy-inspired applications, such as small molecule separation and gas storage systems; high capacity electrochemical energy storage in supercapacitors; and new, more selective catalysts.

Emergent Phenomena in Ferroic Nanostructures: Domain Imaging (FWP 58931)

S. Hong, A. K. Petford-Long, O. Auciello, B. Kabius, S. M. Nakhmanson, D. J. Miller
Materials Science Division, Argonne National Laboratory, 9700 S Cass Avenue, Argonne, IL 60439
hong@anl.gov, petford.long@anl.gov, auciello@anl.gov, kabius@anl.gov, nakhmanson@anl.gov, miller@anl.gov

Program Scope

The goal of our overall research program is to investigate novel and emergent properties of oxide thin films and nanostructures, with a particular emphasis on the development and use of 3D analysis tools such as electron tomography and piezoresponse force microscopy (PFM) and modeling to elucidate chemistry and domain structure at the nanoscale in three dimensions. The term 'emergent' is used to describe the complex and sometimes unanticipated behavior that can be displayed by simple and complex oxide components when combined in nanostructures, and which can be harnessed for a range of energy-related applications. We are combining advanced materials synthesis, complementary *in situ* and *ex situ* microstructural characterization and analysis of physical behavior, and computer simulation and theory to accomplish our research objectives. The program is structured around three interrelated themes: 1) understanding how synthesis affects the properties of multiferroic oxide films. 2) Understanding the mechanisms by which film properties are modified in nanostructures, through effects such as size confinement, charge transfer and band structure modification. 3) Understanding the dynamic response in multiferroic nanostructures, including the physics underlying ferroelectric domain behavior, and ferromagnetic magnetization reversal mechanisms, in thin films and patterned oxide nanostructures. The complementary strengths of simulation and experiment provide fundamental insights into the mechanisms and interfacial driving forces that control composition and microstructure and thus overall film properties and phenomena in nanostructures. This abstract focuses on the third topic, namely domain imaging.

Recent Progress

Development and Application of Novel Vector Piezoresponse Force Microscopy (PFM) Techniques: Together with R. Nath (former post-doc funded by NSF-EPSCOR), Prof. R. S. Katiyar (Univ. Puerto-Rico), M. Park (former guest graduate student funded by Brain Korea), Prof. K. No (KAIST, Korea), A. Joshi-Imre (CNM), J. A. Klug (Northwestern Univ.) and Prof. M. J. Bedzyk (Northwestern Univ.) we discovered and studied in detail the effects of cantilever buckling, induced by the in-plane (IP) motion of the atomic force microscopy (AFM) tip, on the out-of-plane (OP) polarization signal when imaging polarization domains, using PFM. In order to quantitatively understand the contribution of the cantilever buckling to the OP polarization signal, we studied $BaTiO_3$ (BTO) single crystals and $BiFeO_3$ (BFO) thin film based nanostructures to compare weakly and strongly coupled IP-OP PFM signals. For BTO single crystals, which exhibit weakly coupled IP-OP signals, we found no correlation between IP and OP PFM images and no change in OP signal as a function of rotation angle when rotating the sample around an axis perpendicular to the surface. For BFO nanostructures, which exhibit a strong IP-OP signal coupling, we observed a strong correlation between the OP signal for the sample oriented in the plane at 0˚ (defined as the direction of motion of the AFM tip) and the IP signal measured when the samples is rotated 90˚ in the plane with respect to the initial 0˚ direction. In addition, we found that the IP-OP PFM coupling depends strongly on the laser position with respect to the support end of the cantilever. In the case of BTO (weakly coupled IP-OP signals), the IP PFM amplitude signal deviates from the ideal model probably due to the unstable contact condition, which makes conventional vector PFM challenging. Based on our findings, we introduce two novel PFM methods: a) angle-resolved PFM (AR-PFM) and b) in-situ 3D PFM, which can be used to construct 3D PFM images of polarization domains with better efficiency and reliability than current methods that do not distinguish the IP-OP coupling effect. Using angle-resolved piezoresponse force microscopy (AR-PFM), we identified eight additional in-plane polarization variants in epitaxial $BiFeO_3$ thin films, which are formed to mitigate highly unstable charged domain boundaries. This finding elucidates the competing driving forces behind the domain structure, i.e. strain and

electrostatic fields, during the film growth. The AR-PFM technique can provide researchers in the field of integrated ferroelectrics with a new tool to perform nanoscale studies of ferroelectric domains with an unprecedented level of information, to achieve insights critical for the design of the next generation of high-density ferroelectric memory devices (see companion abstract for details of complementary x-ray nanoprobe diffraction studies of geometry and size effects in multiferroic nanostructures.)

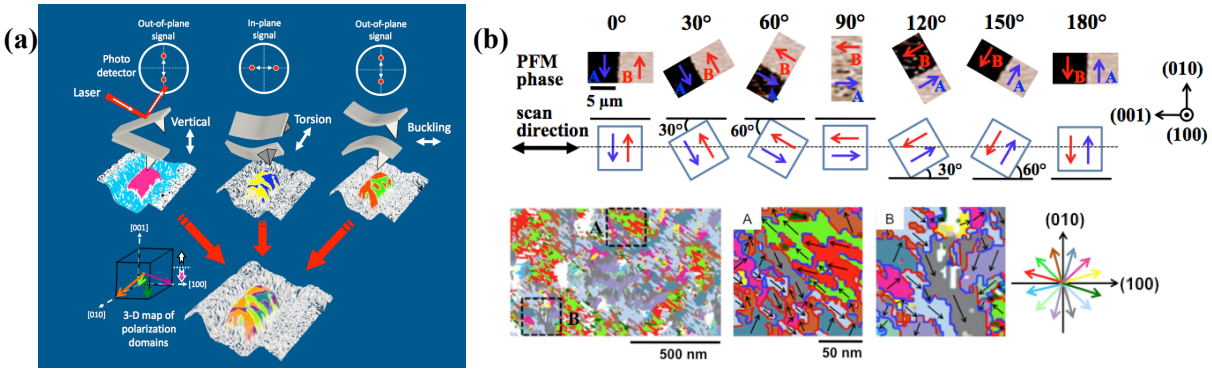

Fig. 1. Schematic of (a) *in-situ* 3D PFM [1] and (b) AR-PFM [2]. AR-PFM images show eight additional in-plane domain variants in epitaxial BFO thin films, deviating from the easy axis, which reveals the competing interactions between electric and strain fields during the film growth.

3-D Visualization of the Magnetic Vector Potential Around Magnetic Structures: Together with Charudatta Phatak (a postdoc funded by FWP 58931) and Prof Marc De Graef (Carnegie Mellon University) we have successfully carried out the first ever 3-D visualization of the magnetic vector potential around a small magnetic structure [3]. This was achieved using vector field electron tomography. The vector potential is central to a number of areas of condensed matter physics, such as superconductivity and magnetism. We have used a combination of electron wave phase reconstruction and electron tomographic reconstruction to experimentally measure and visualize the three-dimensional vector potential in and around a magnetic Permalloy structure. The method can probe the vector potential of the structures with a resolution of about 13 nm. The technique uses Lorentz TEM (LTEM) to record four tomographic tilt series from which the phase shift of the electron wave passing through the sample can be extracted and used to reconstruct the vector potential or magnetic induction. Figure 2 shows the vector potential for a square Permalloy structure with an internal closure domain configuration. This accomplishment was achieved as part of our activity devoted to developing and applying LTEM to the study of magnetic domain behavior in nanostructures. Further activity includes studies of artificial spin ices composed of stadia 200 nm in length and arranged on a square lattice. Imaging the arrays in the as-grown state and after demagnetizing enable the effects of magnetic frustration to be observed directly. The objective lens of our Lorentz transmission electron microscope has recently been fitted with a spherical aberration corrector, and tests are underway to assess the agreement between simulations and experiment for aberration correction of magnetic images.

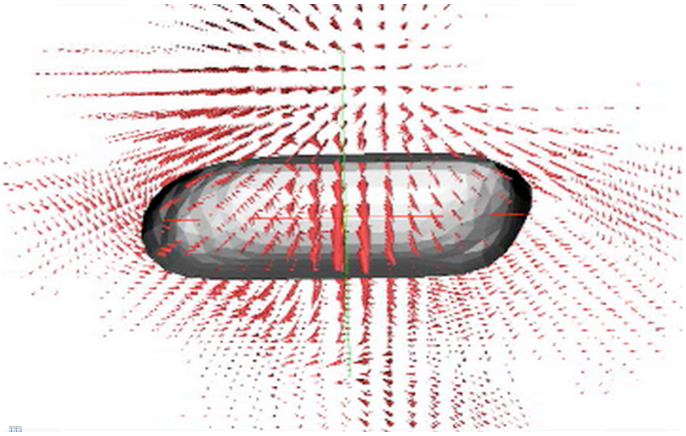

Fig. 2. 3-D reconstruction of the magnetic vector potential surrounding a 1 micron square, 25 nm thick Py element.

Selected Future Directions

***Three-dimensional analysis of interfaces*:** 3-D EFTEM is becoming a very important tool for analysis of interfaces such as in magnetic/ferroelectric multilayers and magnetic tunnel junctions (MTJs). We intend to combine 3-D elemental data with results from other methods such as high-resolution TEM, atom probe tomography, and hollow-cone imaging to model the atomic structure at interfaces. We have already demonstrated how chromatic aberration correction can provide significant improvement in EFTEM. Likewise, combining hollow-cone z-contrast imaging with chromatic aberration (Cc) correction offers significant advantages. Using this approach samples up to 500 nm in thickness may be analyzed with a resolution of 1 nm. This capability would enable us to carry out electron tomography experiments on entire BFO nanocapacitors, for example, or to characterize internal interfaces in 3D with better statistical significance while maintaining high resolution. Oxide systems such as $CoFe_2O_4$ / $PbTiO_3$ have potential for unique magneto-electric properties.

***Domain behavior in ferroic nanostructures*:** Interest in functional nanostructures is created by the strong nanoscale confinement and exchange phenomena shown by these systems. As part of this project, we intend to focus on the domain behavior of nanoscale magnetic, ferroelectric, and multiferroic materials, and in particular on imaging the *local* domain structure. Our efforts will focus on developing a 3-D view of the domain structure and associated fields, using a combination of vector field tomography and three-dimensional PFM. In addition, it is essential to correlate this information with microstructure and microchemistry, on which its ferroic properties are very strongly dependent, and to be able to carry out these studies over a range of temperatures, for example to study materials which are ordered only below room temperature. Our focus will be on the magnetic interactions between the layers in individual elements, interactions between magnetic elements arranged in an array, and on the effect of artificial defects using a focused ion-beam, which can change the energetics of the systems.

Domain wall motion induced by an electric or magnetic field is relatively well known and has been studied in-depth. However, current-driven domain wall motion in ferromagnetic thin films has been less widely studied and provides a suitable platform to study spin torque transfer between spin polarized electrons and magnetic domain walls. Multiferroic materials can offer even richer behavior due to the co-existence of ferroelectricity and ferromagnetism, for example through transport phenomena that can lead to spin torque transfer which induces ferroelectric domain wall motion in a way that has not been possible by electric field application. Finally, domain pinning by electrical trap charges, screening charges, surface states, surface roughness and the contributions of adiabatic and non-adiabatic spin torques plus polarization strain effect complicate the transport of domain wall, and will be investigated.

In collaboration with other staff members at MSD and MCS, we are initiating a program to develop massively-parallel computational tools for simulation of properties and domain behavior of ferroic nanostructures with complex three-dimensional shapes. This simulation approach will be based on the Landau-Ginzburg-Devonshire (LGD) theory of phase transitions in ferroics. However, in our case we will develop methodologies to parametrize the LGD thermodynamic potentials directly from first-principles simulations. This will allow us to understand the observed domain configurations and dynamics for laterally confined multiferroic nanostructures with different size and shape, and predict the properties and the domain configurations in nanostructures that have not yet been synthesized, thus providing guidance for the experimental efforts in this area.

References to selected publications of DOE-sponsored research (2008–2010)

[1] "Effects of Cantilever Buckling on Vector Piezoresponse Force Microscopy Imaging of Ferroelectric Domains in $BiFeO_3$ Nanostructures," R. Nath, S. Hong, J. A. Klug, A. Imre, M. J. Bedzyk, R. S. Katiyar, and O. Auciello, *Appl. Phys. Lett.* **96** (2010) 163101 [Journal Cover] (shared reference with companion abstract).

[2] "Three-dimensional ferroelectric domain imaging of epitaxial $BiFeO_3$ thin films," M. Park, S. Hong, J. A. Klug, M. J. Bedzyk, O. Auciello, K. No, A. K. Petford-Long, accepted for publication in *Appl. Phys. Lett.* (2010).

[3] "Three-dimensional study of the vector potential of magnetic structures", C. Phatak, A. K. Petford-Long and M. De Graef, *Phys. Rev. Lett.* **104**, 253901 (2010).

"Effect of deposition temperature on surface morphology and magnetic properties in epitaxial $CoFe_2O_4$ thin films deposited by MOCVD," M. Pan, G. Bai, S. Hong, V. P. Dravid and A. K. Petford-Long, *J. Appl. Phys.* **107**, 043908 (2010).

"Effect of deposition temperature of TiO_2 on the piezoelectric property of $PbTiO_3$ film grown by PbO gas phase reaction sputtering," J. Kim, S. Hong, S. Bühlmann, Y. Kim, M. Park, Y. K. Kim, K. No, *J. Appl. Phys.* **107**, 104112 (2010)

"Correlating structural and resistive changes in Ti:NiO resistive memory elements," O. Heinonen, M. Siegert, A. Roelofs, A. K. Petford-Long, M. Holt, K. D'Aquila and W. Li, *Appl. Phys. Lett.* **96**, 103103 (2010).

"The role of interfaces in the behavior of magnetic tunnel junction structures," A. K. Petford-Long, *Internat. J. Mat. Res.* **101**, 16–20 (2010).

"Magnetization reversal in circularly exchange-biased ferromagnetic disks," M. Tanase, A. K. Petford-Long, O. Heinonen, K. S. Buchanan, J. Sort and J. Nogues, *Phys. Rev. B* **79,** 014436 (2009).

"Determination of magnetic vortex polarity from a single Lorentz Fresnel image," C. Phatak, M. Tanase, A.K. Petford-Long and M. De Graef, *Ultramicrosc.* **109**, 264–267 (2009).

"In situ TEM observation of magnetic materials," M. Tanase and A. K. Petford-Long, *Microsc. Res, Tech.* **72(3)**, 187–196 (2009).

"Micromagnetic modelling of the magnetization dynamics in a circularly exchange-biased and exchange-coupled ferromagnetic trilayer," D. K. Schreiber, O. G. Heinonen, A. K. Petford-Long, *Phys. Rev B* **80(1)**, 014411 (2009).

"Piezoelectric force microscopy studies of $PbTiO_3$ thin films grown via layer-by-layer gas phase reaction," M. Park, S. Hong, J. Kim, Y. Kim, S. Bühlmann, Y. K. Kim, K. No, *Appl. Phys. Lett.* **94**, 092901 (2009).

"First application of Cc-corrected imaging for high-resolution and energy-filtered TEM," B. Kabius, P. Hartel, M. Haider, H. Müller, S. Uhlemann, U. Loebau, J. Zach, H. Rose, *J. Electron Microsc.* **58**, 147 (2009).

"Quantification of interfacial roughness of In_2O_3/ZrO_2 superlattice films in three dimensions," X. Zhong, B. Kabius, D. Schreiber, Y. Liu, D Fong, J. Eastman and A. K. Petford-Long, *Microsc. And Microanal.* **15(2)**, 600CD (2009).

"Three-dimensional nanoscale structural characterization of magnetic tunnel junctions," Y. Liu, A. K. Petford-Long, D. K Schreiber, Y. -S. Choi, D. Djayaprawira, D. N. Seidman, *Microsc. And Microanal.* **15(2)**, 1248CD (2009).

"Determination of the 3-D magnetic vector potential using Lorentz transmission electron microscopy," C. Phatak, E. Humphrey, M. De Graef and A. K. Petford-Long, *Microsc. And Microanal.* **15(2)**, 134 (2009).

"Improving phase reconstruction for magnetic materials in a low-aberration environment," C. Phatak, M. De Graef and A. K. Petford-Long, *Microsc. And Microanal.* **15(2)**, 1276CD (2009).

"Tuning the structural instabilities in layered-perovskite ferroelectrics by epitaxial strain," S. M. Nakhmanson, Proc. 2009 Workshop on Fundamental Physics of Ferroelectrics, 95 (2009).

"Phase diagram in strained $BaTiO_3/SrTiO_3$ superlattices: a UV Raman study," D. A Tenne, J. D. Schmidt, P. Turner, A. Soukiassian, D. G. Schlom, S. Nakhmanson, X. X. Xi, Y. L. Li, L. Q. Chen, R. S. Katiyar, M. Bernhagen, P. Reiche, and R. Uecker, Proc. 2009 Workshop on Fundamental Physics of Ferroelectrics, 133 (2009).

"Novel aberration corrections concepts," B. Kabius, H. Rose, *Adv. Imaging Electr. Phys.* **153**, 261 (2008).

"Revealing latent structural instabilities in perovskite ferroelectrics by layering and epitaxial strain: A first-principles study of Ruddlesden-Popper superlattices," S. M. Nakhmanson, *Phys. Rev. B* **78**, 064107 (2008).

"Effect of annealing on local composition and electrical transport correlations in MgO-based magnetic tunnel junctions," A. N. Chiaramonti, D. K. Schreiber, W. F. Egelhoff, D. N. Seidman, A. K. Petford-Long, *Appl. Phys. Lett.* **93**, 103113 (2008).

Mapping Ionic Currents and Electrochemical Reactions on the Nanometer Scale

S.V. Kalinin, S. Jesse, P. Maksymovych, N. Balke, A.P. Baddorf
(sergei2, sjesse, maksymovychp, n2b, baddorfap)@ornl.gov

Postdocs and students: A. Tselev, A. Kumar, S. Guo, M. Nikiforov, O. Ovchinnikov (undergraduate)

Oak Ridge National Laboratory, Oak Ridge, TN 37831

Program scope

Properties and functionality of correlated oxides are intrinsically controlled by the oxygen and cation stochiometries that directly couple to the oxidation state of a transition metal, induce structural and metal-insulator transitions, and govern magnetic and transport properties. In this program, we aim to understand the nanoscale behavior of mobile defects, their behavior at structural and topological defects, and their coupling to fundamental physical properties. Furthermore, we aim to extend this knowledge towards fundamental studies of the electronic and ionic transport mechanisms underpinning functionality of energy storage and generation materials. This goal is being accomplished through a synergistic effort involving (a) development of advanced Scanning Probe Microscopies capable of probing ionic transport on the nanometer scale based on dynamic strain measurements, (b) microwave-based capabilities for probing local metal-insulator transitions on the sub-micron level, (c) systems with atomically engineered surface and defect structures, and (d) integration of analytical, atomistic and mesoscopic theories and experimental multidimensional data using artificial intelligence methods. Following the extensive studies of ferroelectric and multiferroic materials, we demonstrate the nanoscale mapping of the Li-ion mobility in intercalation materials and Si and oxygen diffusion on YSZ and related compounds. Extension of these studies towards local stoichiometry-controlled physical behaviors is projected.

Recent Progress

Microscopic and atomistic origins of interfacial functionality in complex oxides. Transition metal oxides exhibit an astonishing variety of intriguing and often useful mesoscopic behaviors that stem from the interplay of electric, magnetic, and transport properties. These behaviors are extremely sensitive to the details of the materials microstructure, ranging from atomic-level cation and oxygen stoichiometries to structural and topological defects. There is therefore an urgent need to develop a comprehensive picture of coupled electronic and structural properties mediated by order parameter and concentration fields. High-resolution electron microscopy yields the capability for probing structure and electronic properties of bulk, interfaces, and extended defects; however, surfaces and ultrathin films have long remained a challenge due to the intrinsic instabilities when in contact even with minute atmospheric contaminates. Furthermore, electrochemical potential of mobile species such as oxygen vacancies long remained outside the realm of classical condensed matter physics.

Addressing the materials properties on the atomic level and mapping electrically-coupled order parameter dynamics requires precise control over surface chemistry, contamination, and electrochemical potentials. The PIs have developed a universal platform (ORNL NanoTransport system) for *in-situ* growth of oxide thin films, and implemented the technique of Piezoresponse Force Microscopy and its spectroscopic variants in an ultra high vacuum (UHV) environment on an in-house modified Omicron UHV AFM-STM platform. The UHV environment allows us to (a) minimize the role of surface polarization screening by atmospheric charges and (b) perform studies in the broad temperature range from 40-400 K. This system has recently been used to establish the structure of the *in-situ* grown $BaTiO_3$ surface using low-energy electron diffraction [Shin PRB 2008], explore the polarization-mediated interactions between $BaTiO_3$ and H_2O uncovering the intricate chemistry-

controlled polarization switching mechanisms [Shin NanoLett 2009], and perform transport experiments [Shin APL 2009] and atomic-level studies of *in-situ* grown oxide surfaces [Shin ACS Nano 2010]. This experimental setup has further enabled probing domain wall conductance in ferroelectrics [Seidel, Nat. Mat 2009], controlling local metal-insulator transitions [Yang, Nat. Mat. 2009], the implementation of polarization-controlled tunneling [Maksymovych, Science 2009], and the determination of intrinsic switching mechanisms [Maksymovych, PRL 2009].

Illustrated in Figure 1 is the direct measurement of polarization-controlled electron transport through thin ferroelectric films. Local polarization switching produces strong hysteresis in the I-V curve, where the conductivity is enhanced by more than two orders of magnitude upon reversal of polarization direction. Building on these results, we will pursue ferroic control of electron transport at topological defects, ultrathin tunnel barriers and new transport and structural phenomena arising from interfacially coupled order parameters.

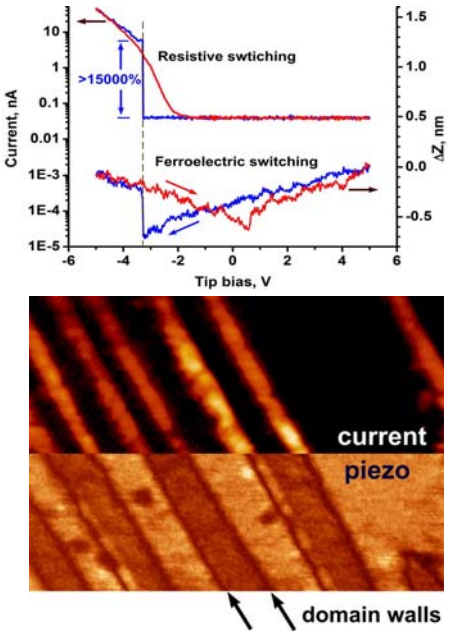

Figure 1. (a) Local I-V curve and strain loop in 50 nm lead zirconate-titanate film [Science **324**, 1421 (2009)]. (b) Local current and piezoresponse at conducting domain 109° domain walls in a 100 nm thick La-doped $BiFeO_3$ film [Nature Mat. **8,** 229 (2009)].

In the future we will apply the comprehensive toolkit of the Nanotransport system to unravel the interplay between electronic transitions, mobile defect-mediated phenomena, and structural and topological defects, with a particular focus on local variations in the emergent behavior. These studies will bridge the studies of the electronic structure by STM and local manipulation of the order parameter and structure of the topological defects to gain direct insight into the interfacial coupling between ferroic and correlated electron materials, where we anticipate the emergence of new electronic behaviors that are confined to the interface and tunable by the strain and electrostatic fields arising from screening of the order parameters. Utilizing the *in-situ* growth capabilities will allow the correlated electron and the ferroic media to be sculpted with unit-cell accuracy, providing access to size-effects on colossal magnetoresistance, metal-insulator transitions and superconductivity in an interfacially-confined geometry.

Probing ionic transport on the nanoscale: Transport of charged species in solids directly underpins the functionality of multiple information and energy materials and devices. These include cation, oxygen vacancy and proton transport in energy storage[1] and conversion systems,[2] as well as in memristive and electroresistive materials.[3,4] For many strongly correlated oxides, the electronic and magnetic properties are controlled by oxygen non-stoichiometry.[5] Notably, many materials classes that are traditional objects of studies in condensed matter physics such as manganites, cobaltites, ferrites,[6] are also broadly used as materials for energy technologies due to high electronic and ionic conductivities,[7] suggesting that oxygen vacancy behavior can be one of the key, but yet poorly understood, parameters affecting physical properties of strongly correlated oxide.

Strong coupling between concentration of mobile species and strain and electrostatic fields produced by structural and topological (e.g. ferroelectric and ferroelastic domain walls) necessitate ionic currents and associated electronic functionality to be studied on the nanometer sale. However, the classical electrochemical strategies[8] for probing ionic transport based on transducer electrodes that link the electrochemical potential of ions in the solid to the electrochemical potential of the electrons. are limited to relatively large (>> 1 μm) electrodes and high temperatures. Consequently the details of ionic transport in solids remain largely unknown.[9]

We note that the characteristic aspect of ionic, as opposed to electronic, transport is that the former strongly affects the molar volume of material (chemical expansivity).[10] Recently, we have demonstrated an approach for mapping ionic dynamics through detection of strain response to applied periodic electric bias, Electrochemical Strain Microscopy (ESM), as well as associated voltage spectroscopy. Shown in Figure 3 is an example of electromechanical hysteresis loops of $LiCoO_2$, illustrating high contrast at the several specific grains and grain boundaries due to higher Li mobility. More generally, a family of time- and voltage spectroscopic imaging methods that allow decoupling of fast- and slow response dynamics have been used to study polarization dynamics in relaxors, ferroelectric polymers, and materials with Li-diffusion and can be extended to systems with other mobile defects provided that defect dynamics couples to local electric or strain field. In the future, these methods will be used to separate intrinsic order parameter driven processes, and much slower diffusion controlled electrochemical phenomena.

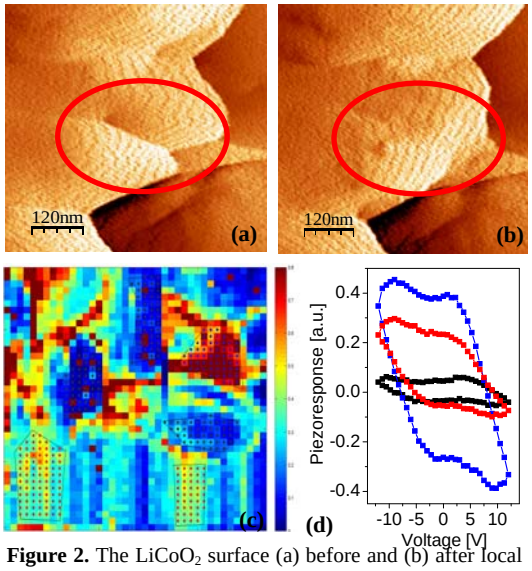

Figure 2. The $LiCoO_2$ surface (a) before and (b) after local voltage pulse, illustrating that Li redistribution can be induced in the material with associated mechanical response (local topography changed, leaving atomic steps invariant). (c) Switchable response map and (d) associated electrochemical strain loops illustrating enhanced response at grain boundaries and selected grains (different scan). [N. Balke, Nature Nano 2010]

Probing local metal-insulator transitions by Scanning Microwave Microscopy. Critical for the understanding the local functionality in correlated oxides is the capability to probe local metal-insulator transition (or, generally, dielectric function) without making direct electrical contacts that can affect strain state of material or create local Schottky regions. The applicability of four and even two-terminal geometry is complicated by percolation and phase-separation phenomena throughout the correlated volume, that become convoluted with the local transport observables. Microwave microscopy can single out local electronic behavior by virtue of measuring AC, rather than DC conductance, and can subsequently probe the frequency dependence of the conductivity, dielectric losses, ionic flow etc. Microwave microscopy offers such capability, as illustrated in Figure 3. Here, the metal-insulator transition temperature is lowered at the ferroelastic domain walls, since the metallic phase is stabilized by the tensile stress.

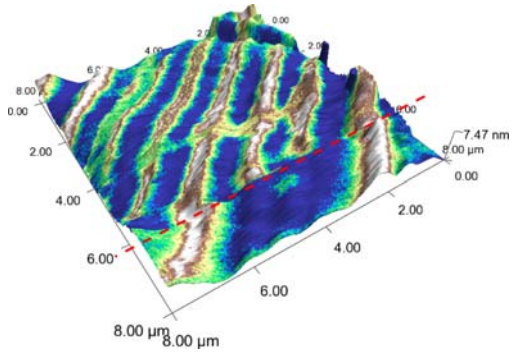

Figure 3. Scanning microwave microscopy of the conductive ferroelastic domain walls in VO_2 [A. Tselev, ACS Nano 2010].

Future plans:

Understanding of the fundamental physics and applied functionality of strongly-correlated oxide materials necessitates a synergistic effort that involves (a) *in-situ* studies of materials in controlled electrochemical environments, (b) development of experimental capabilities for probing local mobile defect dynamics and electrochemical transformations, (c) advanced software and hardware for fast data acquisition and processing beyond conventional force microscopy, and (d) integration with other spatially resolved probes, including STEM-SPM and SPM-focused X-ray methods. Our research effort specifically addresses first three of these directions, aimed at the following fundamental issues:

- **Order parameter and defect dynamics on the nanoscale:** using a combination of environmental and ultra-high vacuum SPM and surface characterization techniques to explore the coupling between mobile defects and ferroic order parameters, structural and topological defects
- **Coupling between the lattice and tunneling transport**, with the focus on the non-linear electron transport in topologically nanostructured ferroic materials and lattice dynamics in multiferroics and improper ferroelectrics.
- **Local ionic mapping** in system with mobile oxygen and cationic vacancies, including development of nanometer-scale resolution imaging tools applicable for solids
- **Energy transformation** pathways, irreversible dynamics, and dissipation on the atomically defined defects and theory-experiment synergy using neural network based models.

This abstract summarizes research reported in the publications below. Papers 1 and 2 are supported by the US Department of Energy, Office of Basic Energy Sciences as part of an FIRST Energy Frontier Research Center. Other papers are supported by the U.S. Department of Energy Office of Basic Energy Sciences Scientific User Facilities Division and by the Laboratory Directed Research and Development program (SVK and SJ). The work is done in collaboration with R. Ramesh (UC Berkeley), R. Garcia (Purdue), N. Dudney and M. Biegalski (ORNL), and A. Morozovska (Ukrainian Academy of Science). The ESM capabilities are available at the CNMS.

Publications 2008-2010 [In total, ~30 peer-reviewed papers (1 Science, 2 Nature Mat, 2 Nature Nano, 1 PNAS, 5 Phys. Rev. Lett., 3 patents and disclosures, 40 invited talks)]

1. N. Balke, S. Jesse, A.N. Morozovska, E. Eliseev, D.W. Chung, Y. Kim, L. Adamczyk, R.E. Garcia, N. Dudney, and S.V. Kalinin, *Nanometer-scale electrochemical intercalation and diffusion mapping of* Li-*ion battery materials*, Nature Nanotechnology, accepted

2. N. Balke, S. Jesse, Y. Kim, L. Adamczyk, A. Tselev, I.N. Ivanov, N. J. Dudney, and S.V. Kalinin, *Real Space Mapping of Li-Ion Transport in Amorphous Si Anodes with Nanometer Resolution*, Nano Lett., in print

3. A. Tselev, V. Meunier, E. Strelkov, W. Shelton, I. Lukyanchuk, K. Jones, R. Proksch, A. Kolmakov, and S.V. Kalinin, *Mesoscopic Metal-Insulator Transition at Ferroelastic Domain Walls in* VO_2, ACS Nano, in print

4. J. Shin, A.Y. Borisevich, J. Zhou, V. Meunier, E.W. Plummer, S.V. Kalinin, and A.P. Baddorf, *An oxygen-induced surface reconstruction of* $SrRuO_3$ *and its effect on the* $BaTiO_3$ *interface*, ACS Nano **4**, 4190 (2010).

5. P. Bintachitt, S. Jesse, D. Damjanovich, S. Trolier-McKinstry, and S.V. Kalinin, *Collective dynamics underpins Rayleigh behavior in disordered polycrystalline ferroelectrics*, PNAS **107**, 7219 (2010).

6. J. Shin, S.V. Kalinin, E.W. Plummer, and A.P. Baddorf, *Electronic transport through in situ grown ultra-thin* $BaTiO_3$ *films*, Appl. Phys. Lett. **95**, 032903 (2009).

7. P. Maksymovych, S. Jesse, P. Yu, R. Ramesh, A.P. Baddorf, and S.V. Kalinin, *Polarization Control of Electron Tunneling into Ferroelectric Surfaces*, Science **324**, 1421 (2009).

References

[1] G. A. Nazri, G. Pistoia, *Lithium Batteries: Science and Technology* (Springer-Verlag, New York, 2009).
[2] V.S. Bagotsky, *Fuel Cells: Problems and Solutions*, Wiley 2009.
[3] A. Sawa, Materials Today **11**, 28 (2008).
[4] D.B. Strukov, G.S. Snider, D.R. Stewart, and R.S. Williams, Nature **453**, 80 (2008).
[5] J.F. Mitchell, D.N. Argyriou, C.D. Potter et al, Phys. Rev. **B 54**, 6172 (1996).
[6] M. Imada, A. Fujimori, and Y. Tokura, Rev. Mod. Phys. **70**, 1039 (1998).
[7] V.V. Kharton, *Solid State Electrochemistry I: Fundamentals, Materials and their Applications*, Wiley 2010.
[8] W. Weppner, R. A. Huggins, Annu. Rev. Mat. Sci. **8**, 269 (1978).
[9] S.B. Adler, Chem. Rev. **104**, 4791 (2004).
[10] X.Y. Chen, J.S. Yu, and S.B. Adler, Chem. Mat. **17**, 4537 (2005).

Correlated Materials: Synthesis and Physical Properties

PIs: I. R. Fisher, T. H. Geballe, A. Kapitulnik, S. A. Kivelson, K. A. Moler,

Geballe Laboratory for Advanced Materials, Stanford University, and Stanford Institute for Materials & Energy Science, SLAC National Laboratory.

Email: aharonk@stanford.edu

Program scope

Work in this FWP addresses the grand challenge of understanding and harnessing emergent phenomena, as well as a number of "Basic Research Needs" areas for energy applications in the realm of quantum materials. In broad terms, we seek to understand how complex interactions in strongly correlated electron systems lead to emergent quantum behavior, including unconventional superconductivity, charge and spin ordered states, and non-Fermi liquid effects. We combine a range of techniques to address these questions, including crystal growth and characterization of novel materials (with a focus on magnetotransport properties - Fisher & Geballe), local electronic (Kapitulnik) and magnetic (Moler) measurements, and theory (Kivelson). In all cases, our focus is on understanding the fundamental factors determining the, often complex, electronic properties of these materials from both from an experimental and theoretical perspective. We work collaboratively on materials and questions of mutual interest.

Kapitulnik's group Report

I. Progress report

In the past year we emphasized three different directions:

a. Magneto-optics studies of strongly correlated systems (Pb-Bi2201, and URu_2Si_2.)

The exotic superconducting states in heavy-fermion systems continue to be a central focus of investigations of unconventional superconductors in strongly correlated electron systems. Among them, URu_2Si_2 has mystified researchers since in this system superconductivity occurs deep inside a mysterious 'hidden order' (HO) state (whose transition temperature is T_H @ 17.5 K). Below T_H, most of the Fermi surface is gapped resulting in a semi-metallic electronic structure, while below ~1.5K the remainder of the Fermi undergo a transition into an exotic superconducting state. With the aim to shed light on the HO state and its relation to the superconducting state we performed polar Kerr effects in a wide temperature range for high quality URu_2Si_2 crystals obtained from the group of Eric Bauer in Los Alamos. A small signal below T_H is consistent with a remnant "ferromagnetic-like" signal that presumably comes from the small portion of antiferromagnetism induced in the otherwise hidden-order state. Superconductivity seems to not be affected by this remnant signal suggesting that it originates from different parts of the sample. Finally, we observe strong signals consistent with TRS breaking in the

superconducting state of URu_2Si_2, with a strong change in slope below ~1K suggesting a different symmetry for the order parameter of this material at low temperatures.

We recently published high resolution Kerr effect measurements on $YBa_2Cu_3O_{6+x}$ crystals with various hole concentrations which revealed a sharp phase transition at a temperature $T_s(p)$ below which there is a non-zero Kerr angle. Both the magnitude and hole concentration dependence of T_s were found to be in close correspondence with those of the pseudo-gap crossover temperature, T* which has been identified in other physical quantities. In particular, T_s is substantially larger than the superconducting T_c in underdoped materials, but drops rapidly with increasing hole concentration, so that it is smaller than T_c in a near optimally doped crystal and extrapolates to zero at a putative quantum critical point under the superconducting dome. The magnitude of the Kerr rotation in $YBa_2Cu_3O_{6+x}$ is smaller by ~ 4 to 5 orders of magnitude than that observed in other itinerant ferromagnetic oxides, suggesting that at most it measures a very small "ferromagnetic-like" component of a magnetic transition. However, the temperature dependence of the Kerr effect near T_s, together with complementary measurements using other probes strongly suggest that the Kerr effect tracks a secondary order parameter which is driven by another transition that is not necessarily magnetic. Corroborating evidence in that direction comes from neutron measurements of Hinkov et al. [Science 319, 597 (2008)] on $YBa_2Cu_3O_{6.45}$ finding evidence for a nematic state in this composition, and from muon-spin-rotation measurements indicating charge ordering transition [J. Sonier et al., PRB 66, 134501 (2002)] near optimal doping. Interpolating between these two ends which find T* that strongly agree with the Kerr measurements, we propose that the Kerr effect tracks an electronic transition that may evolves smoothly from strong charge ordering to a weaker nematic phase.

While the above discussion on YBCO relies on circumstantial evidence, the present results on Pb-Bi2201 may be the first unambiguous set of data that suggests that a pseudogap temperature *T** can be identified, which corresponds to a true symmetry-breaking transition and the primary order parameter that governs that transition correspond to charge ordering. We observed that the evolution of the Kerr effect from high temperatures to ~20K clearly tracks a phase transitionwith a transition temperature of ~125K. ARPES results that tracks the change in character of the temperature evolution of the antinodal states above T_c through T*. The strong correspondence between the two measurements is the first set of results obtained on the same samples.

b. STM studies of the topological insulators Bi_2Te_3 and Bi_2Se_3.

For the surface states of topological insulators, strong spin-orbit coupling causes the electron spin to be intimately tied to its crystal momentum. As a consequence, back scattering from defects should be suppressed, so long as time reversal symmetry is not broken. We were able to reveal this fundamental property of topological insulators by imaging the surface Freidel oscillations associated with a step edge on the surface of a single crystal of Bi_2Te_3 by STM (PRL **104**, 016401 (2010)). Analysis of the energy dependence of the surface wave amplitude and spatial frequency clearly demonstrate the suppression of backscattering for linearly dispersing regions of the surface state. At higher energies, as the surface band becomes concave, oscillations appear which disperse with a particular wave-vector, which results from an unconventional hexagonal warping

term. Furthermore, the data reveal a one-dimensional bound state that runs parallel to the step-edge and is bound to it at some characteristic distance (arXiv:1003.2233). This bound state is clearly observed in the bulk gap region, while it becomes entangled with the oscillations of the warped surface band at high energy and with the valence band states near the Dirac point.

We continued our study with high quality single crystals of Bi_2Se_3 corroborating the results on Bi_2Te_3 that the surface state is indeed "protected," as no scattering from impurities were found to exhibit electronic waves on the surface. In addition, a detailed study of the LDOS near large defects indicated the existence of a bound state that, again similar to the one found in Bi_2Te_3.

The experimental observations of a bound state along macroscopic defects in the two topological insulators that we studied prompted us to investigate its possible theoretical origin. Starting from the three-dimensional 4x4 effective Hamiltonian first introduced by Zhang and Qi we were able to construct a simple model that can treat any step-like defect in a self-consistent way, even if one or more of the surfaces involved are rough. The experimentally observed bound state is then a consequence of interference of the surface state wave function that penetrates a finite distance into the bulk from the adjacent perpendicular surfaces. Our simple model also allowed us to study the spin texture along the step which can be tested experimentally with spin-polarized STM probes.

c. Theoretical investigations of some unconventional superconductors.

Using an asymptotically exact weak coupling analysis of a multi-orbital Hubbard model of the electronic structure of Sr_2RuO_4, we show that the interplay between spin and charge fluctuations leads unequivocally to triplet pairing which originates in the quasi-one dimensional bands (arXiv:1003.2266). The resulting superconducting state spontaneously breaks time-reversal symmetry and is of the form "p_x+ip_y" with sharp gap minima and a d-vector that is only weakly pinned. The superconductor is topologically trivial and hence lacks robust chiral Majorana fermion modes along the boundary. The absence of topologically protected edge modes could explain the surprising absence of experimentally detectable edge currents in this system.

One of the canons of condensed matter physics is the Onsager Reciprocity principle in systems in which the Hamiltonian commutes with the time-reversal operator. Recent results of measurements of the Nernst coefficient in underdoped $YBa_2Cu_3O_{6+x}$, together with the measurements of the anisotropy of conductivity and the inferred anisotropy of the thermopower, imply that this principle is violated. The violation is related directly to the magneto-electric symmetry of phases such as with the Loop-current phase, in which an applied electric field generates an effective magnetic field at right angle to it and to the order parameter vector, and vice-versa (see: arXiv:1007.1215v2).

II. Future Plans

We plan to continue the above studies emphasizing our unique capabilities and broadening our materials selection. In particular we plan to study the magneto-optic properties of $La_{2-x}Ba_xCuO_4$ crystals obtained from BNL.

III. Publications in the past two years

1. Jing Xia, Elizabeth R. Schemm, G. Deutscher, S.A. Kivelson, D.A. Bonn, W.N. Hardy, R. Liang, W. Siemons, G. Koster, M.M. Fejer, and A. Kapitulnik, "Polar Kerr effect measurements of the high temperature $YBa_2Cu_3O_{6+x}$ superconductor: Evidence for broken symmetry near the pseudogap temperature," Phys. Rev. Lett. 100, 127002 (2008).

2. Jing Xia, V. Shelukhin, M. Karpovski, A. Kapitulnik, and A. Palevski, "Inverse proximity effect in superconductor-ferromagnet bilayer structures," Phys. Rev. Lett 102, 087004 (2009).

3. Jing Xia, W. Siemons, G. Koster, M.R. Beasley, and A. Kapitulnik, "Critical thickness for itinerant ferromagnetism in ultrathin films of $SrRuO_3$," Phys. Rev. B 79, 140407 (2009).

4. Aharon Kapitulnik, Jing Xia, and Elizabeth Schemm, "Search for time-reversal symmetry breaking in unconventional superconductors," to appear in Physica B: Physics of Condensed Matter 404, 507 (2009).

5. Aharon Kapitulnik, Jing Xia, Elizabeth Schemm and Alexander Palevski, "Polar Kerr effect as probe for time-reversal symmetry breaking in unconventional superconductors," New J. Phys. 11, 055060 (2009).

6. Zhanybek Alpichshev, J. G. Analytis, J.-H. Chu, I. R. Fisher, Y. L. Chen, Z. X. Shen, A. Fang, and A. Kapitulnik, "STM Imaging of Electronic Waves on the Surface of Bi_2Te_3: Topologically Protected Surface States and Hexagonal Warping Effects," Phys. Rev. Lett. 104, 016401 (2010).

7. S.Raghu, A. Kapitulnik, S.A. Kivelson, "Hidden quasi one-dimensional superconductivity in Sr_2RuO_4," arXiv:1003.2266, accepted for publication in Phys. Rev. Lett.

8. Zhanybek Alpichshev, J. G. Analytis, J.-H. Chu, I.R. Fisher, A. Kapitulnik, "STM imaging of a bound state along a step on the surface of the topological insulator Bi_2Te_3," arXiv:1003.2233, to be published in Phys. Rev. B.

9. R.-H. He, M. Hashimoto, H. Karapetyan, J. D. Koralek, J. P. Testaud, J. Hinton, V. Nathan, H. Yao, K. Tanaka, Y. Yoshida, W. Meevasana, R. G. Moore, D. H. Lu, M. Ishikado, H. Eisaki, T. P. Devereaux, Z. Hussain, S. A. Kivelson, J. Orenstein, A. Kapitulnik, Z.-X. Shen, "From a single-band metal to a superconductor with multicomponent spectra in Bi2201," submitted to Science.

10. C. M. Varma, Victor M. Yakovenko, A. Kapitulnik, "Violation of Onsager Reciprocity in Underdoped Cuprates?," arXiv:1007.1215, submitted.

11. Zhanybek Alpichshev, Weejee Cho, and A. Kapitulnik, "Density of states of a topological insulator in the presence of a step," preprint.

From resolution to time evolution

C. Kisielowski
Helios SERC and National Center for Electron Microscopy, Lawrence Berkeley National Laboratory, One Cylotron Rd., Berkeley CA 94720 / USA,
CFKisielowski@lbl.gov

Nowadays materials design at a nanoscale includes the fabrication of functional composites, which are often made from soft and hard matter components. The development of artificial photosynthetic systems that would produce liquid fuels is an example where the crystalline, hard matter (e.g nanorods) is embedded or attached to soft matter (e.g. polymers) for support, assembly or gas separation [1]. Traditionally, electron microscopy is a primary tool to investigate matter with atomic resolution and it became even possible to detect single atoms across the Periodic Table of Elements in high dose conditions [2,3]. Indeed, after decades of striving for resolution enhancement, electron microscopy has now reached a deep sub-Ångstrom resolution limit that is given at a fundamental level by the Coulomb scattering process itself and by beam-sample interactions for hard and soft materials [4]. Consequently, it seems timely to seek alternatives that differ from the traditional quest for resolution enhancement.

The simultaneous imaging of soft and hard matter with optimized contrast and the time evolution of molecular structures are such new frontiers. In fact, one may even argue that a better understanding of time dependences is at least as important as the achieved understanding of static matter because insight into atom dynamics will help to better understand functionality. Obviously, meaningful time dependences can only be extracted from time series of images if beam-sample interactions can be predicted or even controlled. In our research we pursue the development of phase plate technologies in combination with high performance microscopy to boost the contrast of *high and low* spatial frequencies in electron micrographs in order to minimize the electron dose that is needed for acquiring an atomic resolution image. Recently, the operation of a Boersch phase plate of uncommonly small dimensions was demonstrated [5]. The device allows for the first time an optimized imaging of objects with dimensions smaller than 10 nm (Figure 1, top) while maintaining atomic resolution (Figure 1, bottom). Similarly, it was shown that a Cc corrector in combination with exit wave reconstruction could be used to mimic an obstruction-free phase plate that can be operated across a similar spatial-frequency range [6]. Simultaneously, new materials emerge such as peptoids that can be used as "molecular plywood" because peptoids can be assembled into thin films of large (μm) lateral dimensions and a thickness of only a few nanometer [7]. Unlike many other soft materials, they can exhibit an uncommon resistance to e-beam irradiation that allows for soft matter imaging at atomic resolution. An extreme example is shown in Figure 2 where the electron dose reaches 10^4 e/Å^2 before a beam-induced structural degradation is finalized. For comparison, peptides degrade after exposure to 5 – 10 e/Å^2. The dynamic behaviors of such molecular systems are currently captured in time series of images.

[1] http://www.lbl.gov/LBL-Programs/helios-serc/index.html
[2] Atomic-resolution three-dimensional imaging of germanium self-interstitials near a surface: Aberration-corrected transmission electron microscopy, D. Alloyeau et al., **Phys. Rev. B 80** (2009) 014114
[3] Imaging MoS_2 Nanocatalysts with Single-Atom Sensitivity, C. Kisielowski, et al., **Angewandte Chemie, International Edition 49** (2010) 2708 – 2710

[4] Electron Beam Induced Damage: An Atom-by-atom Investigation with TEAM0.5, C. Kisielowski, R. Erni, J. Meyer, **Imaging & Microscopy 10** (August 2008) 24-25
[5] Imaging of soft and hard materials using a Boersch phase plate in a transmission electron microscope, D. Alloyeau, et al., **Ultramicroscopy 110** (2010) 563-570
[6] Recording low spatial frequencies while maintaining information limit resolution using the TEAM I microscope, S.J Haigh, B. Jiang, D. Alloyeau, C. Kisielowski, A.I.Kirkland, **Microscopy and Microanalysis** 2010, in press
[7] Free-floating ultra-thin two-dimensional crystals from sequence-specific peptoid polymers, Ki Tae Nam, et al., **Nature Materials 9** (2010) 454 – 460

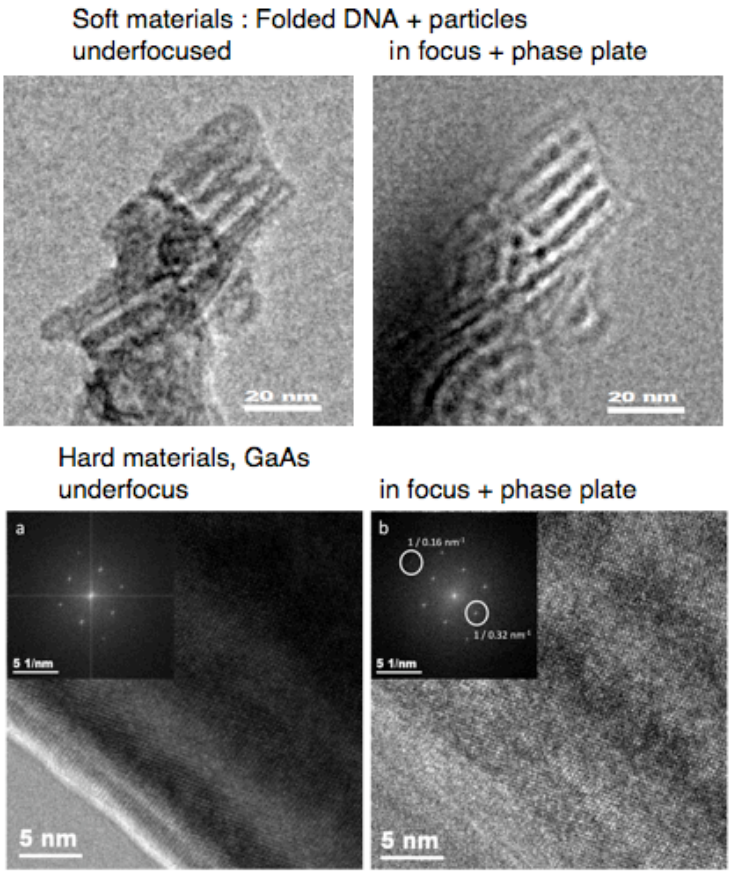

Figure 1:

Top:
Electron micrographs of folded DNA molecules. The contrast of the molecules is enhanced by a factor ~ 4 compared to an underfocused image upon the application of a voltage to a Boersch phase plate [5] that induces a phase shift of the zero-beam by $\pi/2$.

Bottom:
Lattice images of GaAs without (left) and with (right) the phase plate operated to induce a phase shift of the zero-beam by $\pi/2$.

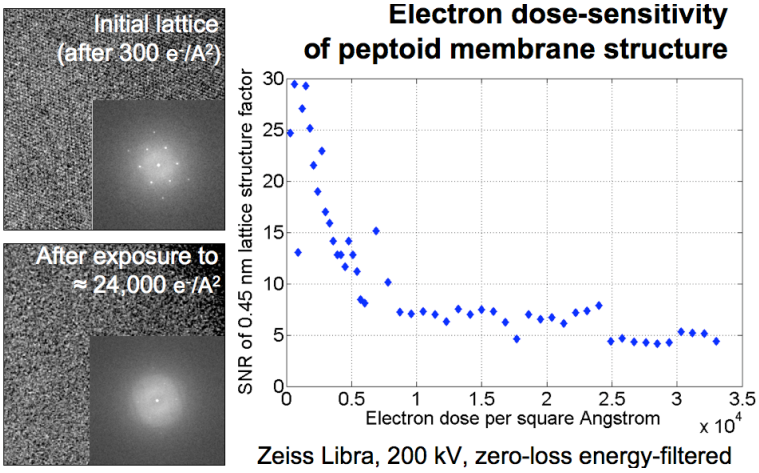

Figure 2:

Atomic resolution images of peptoids [7] and their structural degradation with increasing electron dose. Left: Atomic resolution images after exposure to an electron dose as indicated. Right: Decay of the diffraction spots with dose (Time dependent measurement) .

Spin Physics and Nanoscale Probes of Quantum Materials

Hari C. Manoharan and David Goldhaber-Gordon

Stanford Institute for Materials and Energy Sciences, SLAC National Accelerator Laboratory
Department of Physics, Stanford University, Stanford, CA 94305
manoharan@stanford.edu • goldhaber-gordon@stanford.edu

Program Scope

The goal of this program is to directly measure and manipulate low-dimensional spin, isospin, and electron correlations using scanning probes. The quantum materials and physics targeted in this program span many dimensionalities and are summarized in Figure 1. A diverse array of experimental tools is being applied to these investigations: scanning tunneling microscopy and spectroscopy (STM/STS), atom manipulation STM, Scanning Gate Microscopy (SGM), and a new tool termed a "Virtual STM." A common theme is the precise control of nanoscale geometry through nanofabrication and nanoassembly. The scientific work has been spread over two main thrusts: (A) topological and spin effects in novel quantum materials [1], and (B) mapping low-dimensional electronic structure and manipulating single electronic wavefunctions in nanostructures.

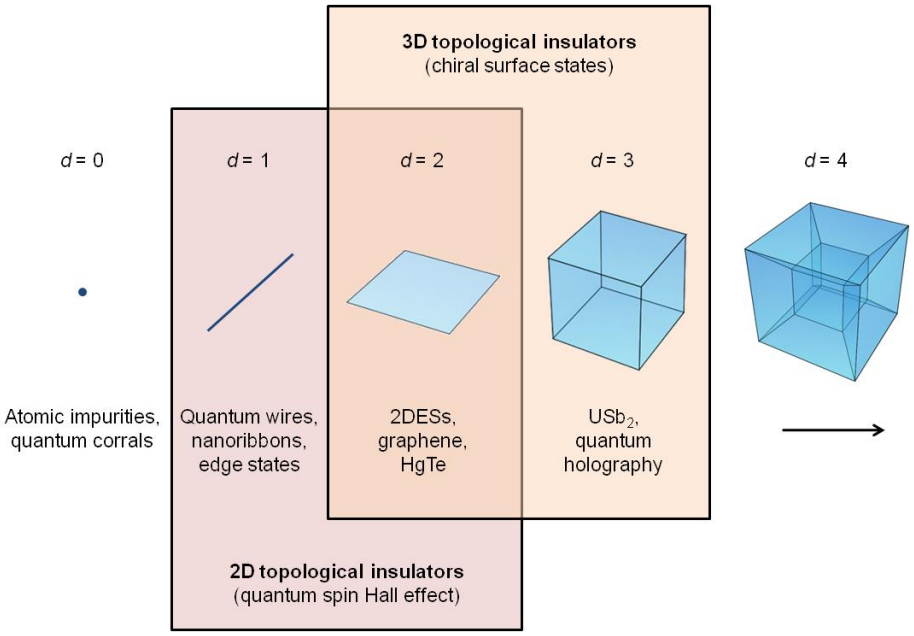

Fig. 1 Summary of materials and physics examined in this program, involving scanning probe interrogation and manipulation across quantum materials of various dimensionality (*d*).

Recent Progress

A. Imaging Dirac Materials and Topological Order

Targeting 2D topological insulator physics, we have studied Quantum Spin Hall (QSH) edge states by SGM. In the QSH state, counter-propagating states exist at the edge of a two-dimensional system, whereas the bulk is insulating. While backscattering between the counter-propagating states in general is prohibited by time-reversal symmetry, several mechanisms have been theoretically proposed where a potential fluctuation can lead to a suppression of the edge state conductance. We applied SGM techniques to study the QSH state in HgTe heterostructures, which is the only material where the QSH effect has been demonstrated experimentally so far. By applying a bias voltage to the scanning gate tip, a potential fluctuation is induced in the device, and the modulation of the conductance is measured as a function of the tip position (Fig. 2, left).

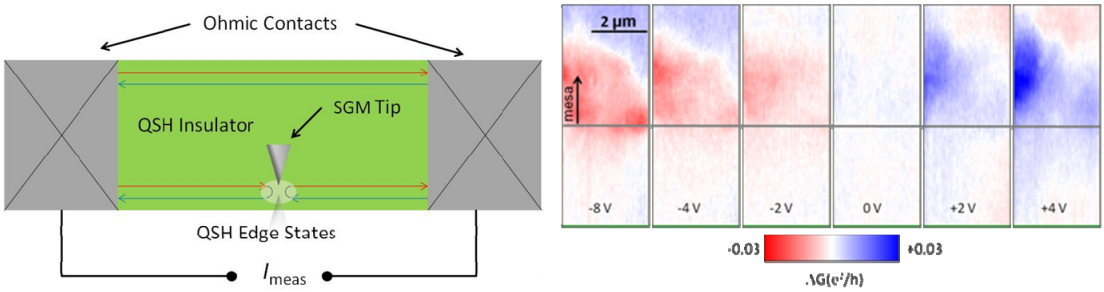

Fig. 2 (Left) Schematic of the SGM setup for study of the 2D topological insulator (not to scale). (Right) In the vicinity of the mesa edge (grey solid line), a clear tip effect on the conductance can be observed.

The length of the studied devices is 5 µm and thus comparable to the mean free path of the QSH edge states (typically a few microns). The large width of 150 µm prevents any interaction between states on the opposite edges, so that the states propagating at opposite edges can be regarded as independent channels. Our first generation of devices all showed a *p*-type bulk carrier density of $n \sim 10^{11}$ cm^{-2}. Nonetheless, we were able to observe signatures of the QSH state. When a negative voltage is applied, the conductance is suppressed when the tip is near the mesa edge (Fig. 2, right). On the other hand, an increase of conductance is observed for positive voltages. This behavior can be understood when the bulk carriers are taken into account. These form a reservoir of states into which the carriers in the QSH edge states can scatter. The amount of backscattering of the edge states due to the bulk carriers increases with the bulk carrier density. When a negative tip voltage is applied, the density of the p-type bulk carriers is increased locally, resulting in the observed decrease of conductance. In contrast, a positive tip voltage will decrease the density or can possibly even tune the system locally into the bulk-insulating regime, which will decrease backscattering and thus increase the edge state conductance. A clear gate effect can be observed approximately 2 µm into the bulk.

Our STM work involves the full-time operation of several custom STM systems including a variable-temperature UHV STM and an ultra-stable high-magnetic-field low-temperature UHV STM. The measurement techniques employed cluster around STM and STS, and include specializations such as atomic manipulation, inelastic electron tunneling spectroscopy (IETS), and simultaneous measurements in a high magnetic field. Figure 3 shows recent results for STM-based work in this program.

Targeting 3D topological insulator physics, using subatomic-precision STM and Fourier-transform STS in collaboration with ARPES measurements (Z. X. Shen group in SIMES), we have mapped the real-space and momentum-space quasiparticle interference of the topological surface states on antimony, the parent matrix of the Bi-Sb class of strong topological insulators. These experiments revealed the non-trivial topological character of the surface Dirac fermions, including suppression of backscattering due to the spin texture, and a transition to a single Dirac cone at high energies characterized but complete suppression of quasiparticle interference due to isotropic Fermi surface and robust spin texture [2]. These experiments have been extended to other recently elaborated families of topological insulators. Topological insulator work was also extended to STM/STS of Bi_2Se_3 and Bi_2Te_3 nanoribbons (synthesized by Yi Cui group at Stanford). These STM experiments revealed atomically precise edges and a variety of geometric structures including ribbons and platelets which can be scaled to quantum dots. STS showed the extinction of quasiparticle scattering in Bi_2Se_3 and has revealed unique electronic structure due to the nanoscale geometry of these materials [3].

Using FT-STS, we have mapped both pseudospin-flipping and chirality-reversing scattering processes on bare graphene, and then extended measurements to the investigation of magnetic adatoms. We observed the Kondo ground state of Dirac fermions around local spin impurities, and we have mapped the spatial and magnetic-field dependence of this highly correlated state. STM/STS work on individual atomic spins on graphene led to a theoretical understanding of observed Fano resonances and a unique polarity switching effect stemming from the underlying Berry phase of graphene pseudospin [4].

Work has now been extended to other forms of graphene including laser-induced monolayer graphene samples and artificial graphene assembled via atomic manipulation. We also performed the first atomic resolution imaging of the heavy-fermion compound USb_2 and STS is underway for a study of correlated spin effects [5].

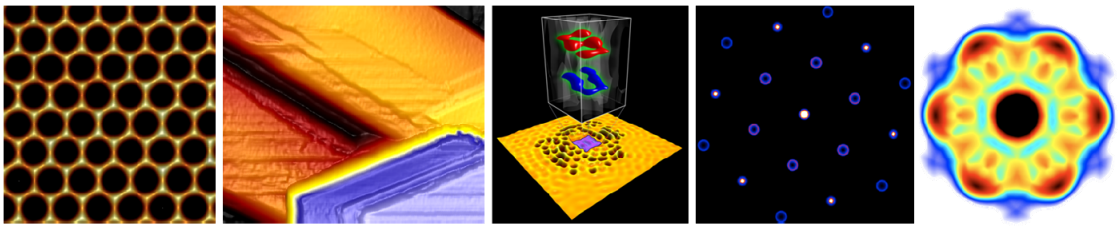

Fig. 3 From left to right: STM topographs of graphene and topological insulator nanoribbons of Bi_2Se_3. 3D quantum holography demonstrated using STM atomic manipulation of a 2DES and readout by STS. Momentum-space FT-STS quasiparticle interference maps of graphene and topological surface states.

B. Imaging and Manipulating Quantum Wavefunctions

The combination of natural or engineered electronic structure creating exact degeneracies due to geometry is a fertile area for robust topological effects in condensed matter. Not surprisingly, quantum mechanical phase often plays a role in the underlying ground states. In nanoassembled materials we have been mapping the effects of quantum mechanical phase in various forms, guided by ideas such as real-space and *k*-space exact degeneracies in band structure. Our atom manipulation and high resolution STS capabilities in magnetic fields up to 11 T were additionally used for sensitivity to Aharonov-Bohm phase, flux effects such as Landau level quantization, and coupling to the spin degree of freedom.

We undertook quantum phase measurements of two kinds in nanoassembled structures. We demonstrated the measurement of the relative phase of two electronic states in a quantum superposition [6], as well as a method to map the internal phase of single quantum states [7], thus operating the STM as a versatile quantum phase meter. Both methods required the precise geometric tuning of topological degeneracies, also describable by supersymmetric quantum mechanics. A highlight of 2009 was the manipulation and mapping of quantum phase and quantum holography [8] which was published and received multiple cover exposure including *Nature Nanotechnology*, the NNI and Presidential FY2010 budget request, and a new review book *Nanoscience and Technology* [9]. Using STM and theoretical modeling, a new method of interrogating and cloaking single molecules in a nanostructure was discovered via inelastic tunneling spectroscopy [10].

In addition to the work done with STM and SGM, we are developing a new kind of scanned probe called the Virtual STM (VSTM) [11]. This probe will also be able to map 2DESs, but instead of relying on backscattering of current flowing in the 2DES, it will use localized tunneling from a nearby parallel electron layer into the 2DES. This offers the benefit of directly mapping the spatial organization and energy states of electrons. Such an instrument is motivated by many predicted, complex electron phases which are expected to occur only in low-disorder heterostructures. In this past, this has limited observation of the phases to indirect bulk transport measurements due the large (near 1 eV) surface potential barrier restricting direct access. Inside a sample, however, barriers can be engineered to be as low as we wish. We take advantage of this with a second "probe" 2DES layer grown above the first, and with a few meV barrier between the two 2DESs. With proper heterostructure design, a scanned metal tip at the surface should be able to induce tunneling locally from the probe into the 2DES phases below, as if STM were being performed on a buried 2DES. Since the induced tunneling follows the scanned tip above, we call this scanning probe system Virtual STM.

The bilayer heterostructure used in VSTM is effectively a vertical quantum transistor, which we have developed as the Wavefunction Extension Transistor (WET) [12]. Current through this transistor is modulated by changing the decay of electrons into the interlayer potential barrier, and we have

empirically shown that this mechanism can increase tunnel current by two to three orders of magnitude at low temperature. Because the cryogenic scanning system we plan to use is under construction (tested at room *T* and 77 K), we have relied on WET structures with large area, non-local measurements to show the feasibility of the VSTM. We can predict a high spatial resolution for VSTM based on the sensitivity of induced tunneling to electric field. We can also show that the probe 2DES excels at screening the sensitive interface below from surface fields, such as from a metal tip. Finally, we have successfully applied the spectroscopic capabilities of the bilayer heterostructure to the quantum Hall regime.

Future Plans

For the next generation of SGM devices and STM studies, we plan to implement a back gate, i.e. a gate electrode at the bottom of the device. In this way, we can control the bulk carrier density and possibly tune the devices into the bulk insulating regime which is required to observe and study the pure topological insulator state in 2D and 3D materials. In the coming year, we will incorporate our functioning scanning systems into a recently received cryogen-free dilution refrigerator. When combined with improved VSTM samples, which should exhibit higher tunnel modulation and mobilities, we expect to be able to probe several exotic electron phases. For example, Wigner crystallization is predicted to appear in low disorder samples as electron-electron interactions overtake electron kinetic energy. Wigner crystallization may arise through a series of "microemulsion" states possible to image. We plan to probe quantum Hall stripes, which are so far only manifested as transport anisotropy in low-disorder quantum Hall systems. Finally, we also plan to probe lithographically-defined structures, such as quantum point contacts and quantum dots in SGM, STM, and VSTM. New forms of graphene and topological insulators will be shared between groups to study in all experimental scanning probe systems in this program.

Literature cited

Publications attributed to work done under BES funding of this task

1. H. C. Manoharan, "Topological insulators: A romance with many dimensions," *Nature Nanotechnology* **5**, 477-479 (2010).
2. K. K. Gomes, W. Ko, W. Mar, Y. Chen, Z.-X. Shen, and H. C. Manoharan, "Quantum imaging of topologically unpaired spin-polarized Dirac fermions," arXiv:0909.0921 (2009).
3. D. Kong, J. C. Randel, H. Peng, J. J. Cha, S. Meister, K. Lai, Y. Chen, Z.-X. Shen, H. C. Manoharan, and Y. Cui, "Topological insulator nanowires and nanoribbons," *Nano Letters* **10**, 329-333 (2009).
4. T. O. Wehling, H. P. Dahal, A. I. Lichtenstein, M. I. Katsnelson, H. C. Manoharan, and A. V. Balatsky, "Theory of Fano resonances in graphene: The influence of orbital and structural symmetries on STM spectra," *Physical Review B* **81**, 085413 (2010).
5. S. P. Chen, M. Hawley, P. B. Van Stockum, H. C. Manoharan, and E. D. Bauer, "Surface structure of cleaved (001) USb_2 single crystal," *Philosophical Magazine* **89**, 1881 - 1891 (2009).
6. C. R. Moon, C. P. Lutz, and H. C. Manoharan, "Single-atom gating of quantum-state superpositions," *Nature Physics* **4**, 454-458 (2008).
7. C. R. Moon, B. K. Foster, L. S. Mattos, G. Zeltzer, W. Ko, and H. C. Manoharan, "Quantum phase extraction in isospectral electronic nanostructures," *Science* **319**, 782-787 (2008).
8. C. R. Moon, L. S. Mattos, B. K. Foster, G. Zeltzer, and H. C. Manoharan, "Quantum holographic encoding in a two-dimensional electron gas," *Nature Nanotechnology* **4**, 167-172 (2009).
9. P. Rodgers (ed.) *Nanoscience and Technology: A Collection of Reviews from Nature Journals* (World Scientific, Singapore, 2009).
10. J. Fransson, H. C. Manoharan, and A. V. Balatsky, "Detection and cloaking of molecular objects in coherent nanostructures using inelastic electron tunneling spectroscopy," *Nano Letters* **10**, 1600-1604 (2010).
11. A. Sciambi, M. Pelliccione, S. R. Bank, A. C. Gossard, and D. Goldhaber-Gordon, "Virtual scanning tunneling microscopy: a local spectroscopic probe of 2D electron systems," arXiv:1008.0670 (2010).
12. A. Sciambi, M. Pelliccione, M. P. Lilly, S. R. Bank, A. C. Gossard, L. N. Pfeiffer, K. W. West, and D. Goldhaber-Gordon, "Vertical field-effect transistor based on wavefunction extension," arXiv:1008.0668 (2010).

Scanning Magnetic Microscopy on Correlated Materials

Part of the "Correlated Materials: Synthesis and Physical Properties" FWP at the Stanford Institute for Materials & Energy Science (SIMES)
PI: Kathryn A Moler ("Kam")
Email: kmoler@stanford.edu

Program Scope and Definition

This abstract addresses the role of scanning magnetic microscopy in understanding superconductivity in the pnictides and cuprates. In broad terms, work in this FWP seeks to understand how complex interactions in strongly correlated electron systems lead to emergent quantum behavior, including unconventional superconductivity, charge and spin ordered states, and non-Fermi liquid effects. We combine a range of techniques to address these questions, including crystal growth and characterization of novel materials (with a focus on magnetotransport properties), local electronic and magnetic measurements, and theory. In all cases, our focus is on understanding the fundamental factors determining the often complex electronic properties of these materials from both from an experimental and theoretical perspective.

Recent Progress

Enhanced superfluid density on twin boundaries in $Ba(Fe_{1-x}Co_x)_2As_2$

Superconducting quantum interference device microscopy shows stripes of increased diamagnetic susceptibility in the superconducting state of twinned, orthorhombic, underdoped crystals of BaFe1−xCox2As2, but not in tetragonal overdoped crystals. These stripes are consistent with enhanced superfluid density on twin boundaries.

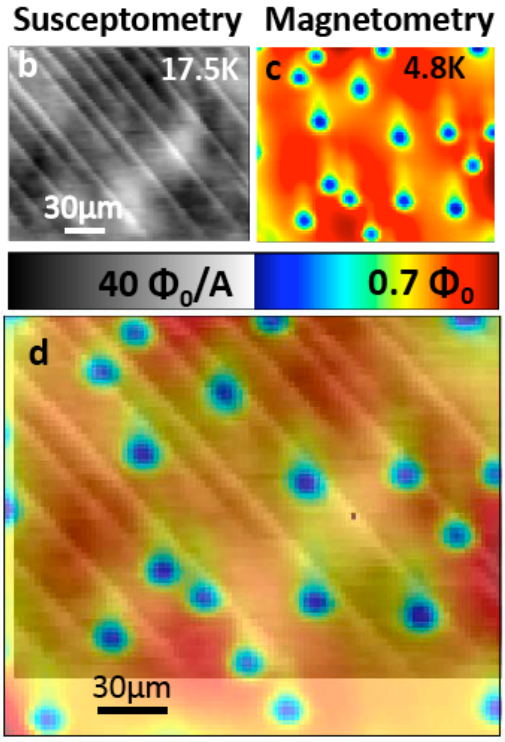

Figure. Enhanced superfluid density on twin boundaries in the pnictide superconductor $Ba(Fe_{1-x}Co_x)_2As_2$
Upper left: Local magnetic susceptibility just below the critical temperature reveals stripes of enhanced diamagnetic susceptibility, indicating that the superfluid density on the twin boundaries is much larger than in the bulk.
Upper right:Local magnetometry reveals trapped magnetic vortices, as expect for the small field in which the sample was cooled.
Bottom: Overlaying the two images shows that the vortices do not pin directly on the twin boundaries. Other data shows that, when deliberately pushed or pulled with a local magnetic force, the vortices avoid crossing the twin boundaries.

Local measurements of the penetration depth in pnictide superconductors
Using scanning SQUID magnetometry, we observed a linear penetration depth in LaFePO (PRL 103, 127003 (2009)). With the ability to make local measurements, we learn that the temperature dependence is uniform throughout the sample and avoid possible variations due to topography or inhomogeneous stoichiometry. These measurements strongly suggest the presence of line nodes in the superconducting gap. General arguments based on the Fermi surface topology favor an s+/- gap symmetry: within this picture, our observation implies the presence of additional factors modulating the gap around individual Fermi surface pockets. As an additional benefit of making local magnetic susceptibility measurements, we map small variations in Tc across the sample. I will also report on our progress in measuring the absolute value of the penetration depth locally.

Limits on superconductivity-related magnetization in Sr_2RuO_4 and $PrOs_4Sb_{12}$ from scanning SQUID microscopy
Sr_2RuO_4 is supposed to be a chiral p-wave superconductor and therefore to have chiral edge currents. Our most recent search for spontaneous magnetism in this material sets stringent upper limits on spontaneous currents at edges or possible domain walls that are 2-3 orders of magnitude less than theoretical predictions for a single-band fully-gapped chiral p-wave superconductor (*Phys. Rev. B* **81** 214501 (1 June 2010).).

Mechanics of Individual, Isolated Vortices in Cuprate Superconductors
Although vortex matter has been studied extensively, the static and dynamic properties of an individual vortex have not. We used magnetic force microscopy (MFM) to image and manipulate individual vortices in a detwinned YBa2Cu3O6.991 single crystal, directly measuring the interaction of a moving vortex with the local disorder potential (*Nature Physics* **5**, 35 - 39 (2009)). We broadly confirmed the picture of a vortex as an elastic string moving through a pinning landscape, but we also found unexpected dynamics that are now under investigation by other theorists. In addition, we found enhanced vortex pinning anisotropy that suggests clustering of oxygen vacancies in our sample and demonstrates the power of MFM to probe vortex structure and microscopic defects that cause pinning. In contrast, in the more anisotropic material YBa2Cu3O6.4, we found that when we pull the top of a pinned vortex, it may not tilt smoothly (*Phys. Rev. B* **79**, 214530 (2009)). Occasionally, we observe a vortex to break into discrete segments that can be described as short stacks of pancake vortices, similar to the "kinked" structure proposed by Benkraouda and Clem. Quantitative analysis gives an estimate of the pinning force and the coupling between the stacks. These measurements highlight the discrete nature of stacks of pancake vortices in layered superconductors.

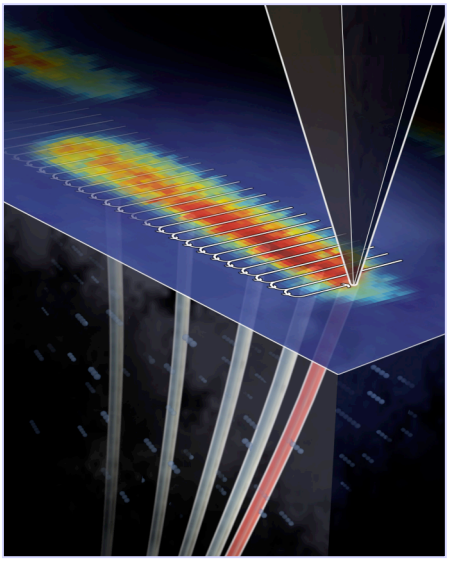

Future Plans

We will continue to use our highly specialized magnetic measurement technology to contribute to the understanding of superconductivity in the pnictides and in Sr_2RuO_4.

DOE sponsored research that has appeared in 2008-2010

E.W.J. Straver, J. E. Hoffman, O. M. Auslaender, D. Rugar, and K. A. Moler, "Controlled manipulation of individual vortices in a superconductor," *Applied Physics Letters* **93**, 172514 (30 October 2008).

Clifford W. Hicks, Thomas M. Lippman, Martin E. Huber, Zhi-An Ren, Jie Yang, Zhong-Xian Zhao, and Kathryn A. Moler, "Limits on the Superconducting Order Parameter in NdFeAsO1-xFy from Scanning SQUID Microscopy," *Journal of the Physical Society of Japan* **78**, 013708 (25 December 2008).

O.M. Auslaender, Lan Luan, E. W. J. Straver, J. E. Hoffman, N. C. Koshnick, E. Zeldov, D. A. Bonn, Ruixing Liang, W. N. Hardy, and K. A. Moler, "Mechanics of Individual, Isolated Vortices in a Cuprate Superconductor," *Nature Physics* **5**, 35 - 39 (2009).
[Accompanied by a News and Views article , "High-temperature superconductors: Vortices wiggled and dragged," by Charles Reichhardt from Los Alamos National Lab]

Lan Luan, O.M. Auslaender, D.A. Bonn, Ruixing Liang, W.N. Hardy, and K.A. Moler, "Magnetic force microscopy study of interlayer kinks in individual vortices in the underdoped cuprate superconductor YBa2Cu3O6+x," *Physical Review B* **79**, 214530 (26 June 2009).

C. W. Hicks, T. M. Lippman, M. E. Huber, J. G. Analytis, J. H. Chu, A. S. Erickson, I. R. Fisher, and K. A. Moler, "Evidence for a Nodal Energy Gap in the Iron-Pnictide Superconductor LaFePO from Penetration Depth Measurements by Scanning SQUID Susceptometry," *Physical Review Letters* **103**, 127003 (2009).

L. Luan, O. M. Auslaender, T. M. Lippman, C. W. Hicks, B. Kalisky, J. H. Chu, J. G. Analytis, I. R. Fisher, J. R. Kirtley, and K. A. Moler, "Local measurement of the penetration depth in the pnictide superconductor Ba(Fe0.95Co0.05)2As2," *Physical Review B*, **81** 100501(R) (2 March 2010). [Accompanied by a Synopsis in *Physics*]

J. C. Keay, P. R. Larson, K. L. Hobbs, M. B. Johnson, J. R. Kirtley, O. M. Auslaender and K. A. Moler, "Sequential vortex hopping in an array of artificial pinning centers," *Physical Review B* **80**, 165421 (22 October 2009).

John R. Kirtley, Beena Kalisky, Lan Luan, and Kathryn A. Moler, "Meissner response of a bulk superconductor with an embedded sheet of reduced penetration depth," *Physical Review B* **81** 184514 (17 May 2010).

Beena Kalisky, John R. Kirtley, James G. Analytis, Jiun-Haw Chu, Arturas Vailionis, Ian R. Fisher, Kathryn A. Moler, "Enhanced superfluid density on twin boundaries in $Ba(Fe_{1-x}Co_x)_2As_2$," *Physical Review B* **81** 184513 (17 May 2010).
[Accompanied by a Viewpoint: John Tranquada, *Physics* **3** 41 (2010).]

Clifford W. Hicks, John R. Kirtley, Thomas M. Lippman, Nicholas C. Koshnick Martin E. Huber, Yoshiteru Maeno, William M. Yuhasz, M. Brian Maple, and Kathryn A. Moler, "Limits on superconductivity-related magnetization in Sr_2RuO_4 and $PrOs_4Sb_{12}$ from scanning SQUID microscopy," *Physical Review B* **81** 214501 (1 June 2010).

Scanning Transmission Electron Microscopy: Atomic Structure and Properties of Materials

Stephen J. Pennycook, Maria Varela, Andrew R. Lupini, Matthew F. Chisholm, Sokrates T. Pantelides
Research Professors: Mark P. Oxley, Weidong Luo, Juan Idrobo
pennycooksj@ornl.gov, mvarela@ornl.gov, 9az@ornl.gov, chisholmmf@ornl.gov, pantelides@vanderbilt.edu
Materials Science and Technology Division, Oak Ridge National Laboratory, Oak Ridge, TN 37831

Program Scope

This program installed its first aberration corrector in 2001 and has contributed actively to both instrumental developments and applications to materials. Current materials studies include energy materials, semiconductor and oxide device structures, advanced metals, alloys and structural ceramics, novel catalysts and nanomaterials. Data from microscopy is combined with first-principles theory to provide new quantitative insights into key issues in these fields. New theoretical methods are being developed for quantitative comparison of microscope data to atomic resolution simulations.

Recent Progress

Just over one year ago this program took delivery of a Nion UltraSTEM 100, a next-generation aberration-corrected scanning transmission electron microscope (STEM). The combination of cold field emission, 5th order aberration correction and flexible column optics allows light elements to be directly imaged. Figure 1a shows a raw image from monolayer BN [Krivanek et al., 2010] imaged at 60 kV, below the 78kV threshold for knock-on damage in the perfect lattice. The individual B and N atoms are clearly distinguishable based on their intensity. In bright field imaging the scattering factors of B and N are very similar and the lattice polarity has so far only been extracted by averaging many B-N pairs. Figure 1b shows a processed image and Fig. 1c shows two line traces in which some peaks are visible with intensity in between that of the B and N atoms, while others are seen with a higher intensity. The intensities are well fitted by a power law dependence on atomic number, and substitutional carbon and oxygen atoms can be identified directly from their image intensity. Carbon atoms only substitute in pairs, replacing a B-N pair, while O atoms substitute only for N atoms. Density functional calculations confirm the stability and coordinates observed, including the distortion of the ring of 6 carbon atoms, see Fig. 1d.

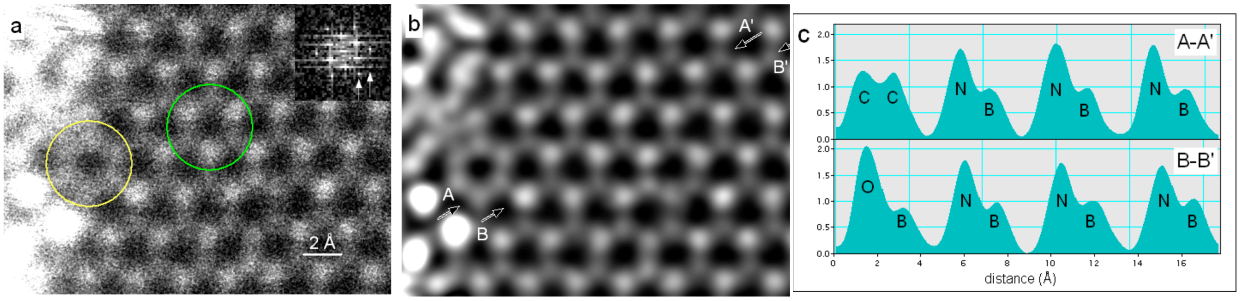

Figure 1. (a) Raw ADF image of monolayer BN taken with a Nion UltraSTEM. Center circle shows a ring of 6 atoms with alternating intensity corresponding to individual B and N atoms, circle on the left shows a ring of 6 equal intensity C atoms. (b) Image corrected for distortion, smoothed, and deconvolved to remove probe tail contributions to nearest neighbors. (c) Line profiles through (b) distinguishing C and O atoms from B and N atoms. (d) Density functional simulation superimposed on part of image (b).

Spectroscopic imaging via electron energy loss spectroscopy (EELS) is also enhanced by the ability to collect 100% of the scattered electrons. Figure 2 show spectroscopic images that not only differentiate the elements in $LaMnO_3$, but also show clearly the octahedral rotations of the O sublattice. Such data allows structural distortions to be correlated with maps of EELS fine structure to explain the surprising interfacial properties in complex oxide heterostructures. For example, charge transfer across $LaMnO_3/SrTiO_3$ interfaces has been shown to reverse direction depending on the state of epitaxial strain.

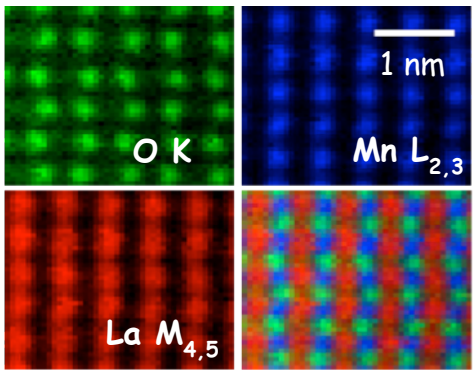

Figure 2. Spectroscopic images of $LaMnO_3$ showing the La (red), Mn (blue) and O (green) signals with a composite of all three. The octahedral rotations are clearly visible in the O image (image recorded by M. Varela).

Future Plans

A 200 kV cold field emission gun will be retrofitted to the Nion UltraSTEM within the next year, providing improved spatial resolution in both Z-contrast and spectroscopic imaging modes. We propose to focus on atomic-resolution mapping of spectral fine structure and theoretical interpretation in terms of materials electronic structure, continuing to address topical issues in complex oxides and low dimensional nanostructures including graphene, BN and semiconductor quantum dots.

DOE-sponsored journal publications 2008-2010

L. F. Allard, A. Borisevich, W. L. Deng, R. Si , M. Flytzani-Stephanopoulos, S. H. Overbury, "Evolution of gold structure during thermal treatment of Au/FeO_x catalysts revealed by aberration-corrected electron microscopy," *J. Electron Microsc.* **58**, 199 (2009).

M. J. Bowers, J. R. McBride, M. D. Garrett, J. A. Sammons, A. D. Dukes, M. A. Schreuder, T. L. Watt, A. R. Lupini, S. J. Pennycook and S. J. Rosenthal, "Structure and Ultrafast Dynamics of White-Light-Emitting CdSe Nanocrystals," *J. Am. Chem. Soc.* **131**, 5730 (2009).

S. Brivio, C. Magen, A. A. Sidorenko, D. Petti, M. Cantoni, M. Finazzi, F. Cicacci, R. De Renzi, M. Varela, S. Picozzi, R. Bertacco, "Effects of Au nanoparticles on the magnetic and transport properties of $La_{0.67}Ca_{0.33}MnO_3$ ultrathin layers, " *Phys Rev B* **81,** 084410 (2010).

H. L. Dang, R. Gudipati, Y. Liu, Y. Li, Y. D. Liu, H. L. Peterson, M. F. Chisholm, T. Biggerstaff, G. Duscher, S. W. Wang, "Carbon Clusters as Possible Defects in the $SiC-SiO_2$ Interface," *J. Comp. Theor. Nanosci.* **6**, 1305 (2009)

R. Das, A. Gupta, D. Kumar, S. Hoh, S. J. Pennycook and A. F. Hebard, "Dipolar interactions and their influence on the critical single domain grain size of Ni in layered Ni/Al_2O_3 composites," *J. Phys. C* **20** 385213 (2008).

N. Galiana, P. P. Martin, C. Munuera, M. Varela, C. Ocal, M. Alonso, A. Ruiz, "Pyramid-like nanostructures created by Si homoepitaxy on Si(001)," *Materials Science in Semiconductor Processing* **12**, 52 (2009).

J. Garcia-Barriocanal, A. Rivera-Calzada, M. Varela, Z. Sefrioui, M. R. Diaz-Guillen, K. J. Moreno, J. A. Diaz-Guillen, E. Lborra, A. F. Fuentes, S. J. Pennycook, C. Leon and J. Santarnaria, "Tailoring Disorder and Dimensionality: Strategies for Improved Solid Oxide Fuel Cell Electrolytes," *Chemphyschem*. **10**, 1003 (2009).

J. Garcia-Barriocanal, A. Rivera-Calzada, M. Varela, Z. Sefrioui, E. Iborra, C. Leon, S. J. Pennycook and J. Santamaria, "Response to Comment on "Colossal Ionic Conductivity at Interfaces of Epitaxial $ZrO_2:Y_2O_3/SrTiO_3$ Heterostructures," *Science* **324**, 465 (2009).

J. Garcia-Barriocanal, F. Y. Bruno, A. Rivera-Calzada, Z. Sefrioui, N. M. Nemes, M. Garcia-Hernandez, J. Rubio-Zuazo, G. R. Castro, M. Varela, S. J. Pennycook, C. Leon and J. Santamaria, ""Charge Leakage" at $LaMnO_3/SrTiO_3$ Interfaces," *Adv. Mater.*, **22**, 627 (2010).

M. Gich, J. Gazquez, A. Roig, A. Crespi, J. Fontcuberta, J. C. Idrobo, S. J. Pennycook, M. Varela and V. Skumryev, "Epitaxial stabilization of epsilon-Fe_2O_3 (00l) thin films on $SrTiO_3$ (111)," *Appl. Phys. Lett.*, **96**, 112508 (2010).

R. A. Gilstrap, C. L. Capozzi, C. G. Carson, R. A. Gerhardt, A.Y. Borisevich, C. J. Summers, "Synthesis of a Nonagglomerated Indium Tin Oxide Nanoparticle Dispersion," *Adv. Mater.* **20**, 4163 (2008)

H. Z. Guo, A. Gupta, M. Varela, S. J. Pennycook, J. Zhang, "Local valence and magnetic characteristics of La_2NiMnO_6," *Phys. Rev. B* **79**, 172402 (2009).

T. Haywood, S. H. Oh, A. Kebede, D. M. Pai, J. Sankar, D. K. Christen, S. J. Pennycook and D. Kumar, "Structural and flux-pinning properties of laser ablated $YBa_2Cu_3O_{7-d}$ thin films: Effects of self-assembled CeO_2 nanodots on $LaAlO_3$ substrates," *Physica C* **468**, 2313 (2008).

J. C. Idrobo, A. Halabica, R. H. Magruder, R. F. Haglund, S. J. Pennycook and S. T. Pantelides, "Universal optical response of Si-Si bonds and its evolution from nanoparticles to bulk crystals," *Phys. Rev. B* **79**, 125322 (2009).

N. De Jonge, R. Sougrat, B. Northan and S. Pennycook, "Three-Dimensional Scanning Transmission Electron Microscopy of Biological Specimens," *Microsc. Microanal.*, **16**, 54 (2010).

S. V. Kalinin, B. J. Rodriguez, A. Y. Borisevich, A. P. Baddorf, N. Balke, H. J. Chang, L. Q. Chen, S. Choudhury, S. Jesse, P. Maksymovych, M. P. Nikiforov and S. J. Pennycook, "Defect-Mediated Polarization Switching in Ferroelectrics and Related Materials: From Mesoscopic Mechanisms to Atomistic Control," *Adv. Mater.*, **22**, 314 (2010).

C. Kisielowski, B. Freitag, M. Bischoff, H. van Lin, S. Lazar, G. Knippels, P. Tiemeijer, M. van der Stam, S. von Harrach, M. Stekelenburg, M. Haider, S. Uhlemann, H. Muller, P. Hartel, B. Kabius, D. Miller, I. Petrov, E. A. Olson, T. Donchev, E. A. Kenik, A. R. Lupini, J. Bentley, S. J. Pennycook, I. M. Anderson, A. M. Minor, A. K. Schmid, T. Duden, V. Radmilovic, Q. M. Ramasse, M. Watanabe, R. Erni, E. A. Stach, P. Denes and U. Dahmen, "Detection of single atoms and buried defects in three dimensions by aberration-corrected electron microscope with 0.5-angstrom information limit," *Microsc. Microanal.* **14**, 469 (2008).

A. L. Kobrinskii, A. M. Goldman, M. Varela and S. J. Pennycook, "Thickness dependence of the exchange bias in epitaxial manganite bilayers," *Phys. Rev. B* **79**, Art. No. 094405 (2009).

O. L. Krivanek, M. F. Chisholm, V. Nicolosi, T. J. Pennycook, G. J. Corbin, N. Dellby, M. F. Murfitt, C. S. Own, Z. S. Szilagyi, M. P. Oxley, S. T. Pantelides and S. J. Pennycook, "Atom-by-atom structural and chemical analysis by annular dark-field electron microscopy," *Nature*, **464**, 571 (2010). Image adapted for the front cover.

R. Kudrawiec, P. Poloczek, J. Misiewicz, M. Shafi, J. Ibanez, R. H. Mari, M. Henini, M. Schmidbauer, S. V. Novikov, L. Turyanska, S. I. Molina, D. L. Sales, M. F. Chisholm, "Photomodulated transmittance of GaBiAs layers grown on (001) and (311)B GaAs substrates," *Microelec J.* **40,** 537 (2009)

D. Kumar, S. H. Oh, S. J. Pennycook and A. K. Majumdar, "Scaling exponent within the side-jump mechanism of Hall effect size-dependence in Ni nanocrystals," *Appl. Phys. Lett.* **93**, 133105 (2008).

W. D. Luo, S. J. Pennycook and S. T. Pantelides, "Magnetic "Dead" Layer at a Complex Oxide Interface," *Phys. Rev. Lett.* **101**, 247204 (2008).

W. Luo, M. Varela, J. Tao, S. J. Pennycook and S. T. Pantelides, "Electronic and crystal-field effects in the fine structure of electron energy-loss spectra of manganites," *Phys. Rev. B* **79**, 052405 (2009).

A. R. Lupini, A. Y. Borisevich, J. C. Idrobo, H. M. Christen, M. Biegalski, and S. J. Pennycook, "Characterizing the Two- and Three-Dimensional Resolution of an Improved Aberration-Corrected STEM," *Microsc. Microanal*. **15**, 441(2009).

A. R. Lupini and S. J. Pennycook, "Rapid autotuning for crystalline specimens from an inline hologram," *J. Electron Microsc.* **57**, 195 (2008).

A. R. Lupini, P. Wang, P. D. Nellist, A. I. Kirkland and S. J. Pennycook, "Aberration measurement using the Ronchigram contrast transfer function," *Ultramicrosc.*, **110**, 891 (2010)

James R. McBride, Andrew R. Lupini, Michael A. Schreuder, Nathanael J. Smith, Stephen J. Pennycook, and Sandra J. Rosenthal, "Few-Layer Graphene as a Support Film for Transmission Electron Microscopy Imaging of Nanoparticles," *ACS Applied Materials and Interfaces,* **1**, 2886 (2009).

S. I. Molina, A. M. Beltran, T. Ben, P. L. Galindo, E. Guerrero, A. G. Taboada, J. M. Ripalda, M. F. Chisholm, "High resolution electron microscopy of GaAs capped GaSb nanostructures," *Appl. Phys. Lett,* **94,** 043114 (2009).

S. I. Molina, D. L. Sales, P. L. Galindo, D. Fuster, Y. Gonzalez, B. Alen, L. Gonzalez, M. Varela and S. J. Pennycook, "Column-by-column compositional mapping by Z-contrast imaging," *Ultramic.* **109**, 172 (2009).

J. Orna, L. Morellon, P. A. Algarabel, J. A. Pardo, C. Magen, M. Varela, S. J. Pennycook, J. M. De Teresa and M. R. Ibarra, "Growth of Sr_2CrReO_6 epitaxial thin films by pulsed laser deposition," *Journal of Magnetism and Magnetic Materials*, **322**, 1217 (2010).

G. S. Painter, F. W. Averill, P. F. Becher, N. Shibata, K. van Benthem and S. J. Pennycook, "First-principles study of rare earth adsorption at ß-Si_3N_4 interfaces," *Phys. Rev. B* **78**, 214206 (2008).

S. J. Pennycook, M. F. Chisholm, A. R. Lupini, M. Varela, A. Y. Borisevich, M. P. Oxley, W. D. Luo, K. van Benthem, S-H. Oh, D. L. Sales, S. I. Molina, J.García-Barriocanal, C. Leon, J. Santamaría, S. N. Rashkeev and S. T. Pantelides, "Solving Energy Problems through Aberration-Corrected STEM," *Philos. Trans. R. Soc. A* **367**, 3709 (2009)

S. J. Pennycook, M. Varela, A. R. Lupini, M. P. Oxley and M. F. Chisholm, "Atomic-resolution spectroscopic imaging: past, present and future," *J. Electron Microsc.* **58**, 87 (2009).

T. J. Pennycook, M. J. Beck, K. Varga, M. Varela, S. J. Pennycook and S. T. Pantelides, "Origin of Colossal Ionic Conductivity in Oxide Multilayers: Interface Induced Sublattice Disorder," *Phys. Rev. Lett.*, **104**, 115901 (2010).

O. Polat, T. Aytug, M. P. Paranthaman, K. J. Leonard, A. R. Lupini, S. J. Pennycook, H. M. Meyer, K. Kim, X. F. Qiu, S. Cook, J. R. Thompson, D. K. Christen, A. Goyal, X. M. Xiong and V. Selvamanickam, "An evaluation of phase separated, self-assembled $LaMnO_3$-MgO nanocomposite films directly on IBAD-MgO as buffer layers for flux pinning enhancements in $YBa_2Cu_3O_{7-d}$ coated conductors," *J. Mater. Res.*, **25**, 437 (2010).

P. Rulis, A. R. Lupini, S.J. Pennycook, and W.Y. Ching, "Spectroscopic imaging of electron energy loss spectra using ab initio data and function field visualization," *Ultramicrosc.*, **109,** 1472 (2009).

V. Serin, S. Andrieu, R. Serra, F. Bonell, C. Tiusan, L. Calmels, M. Varela, S. J. Pennycook, E. Snoeck, M. Walls and C. Colliex, "TEM and EELS measurements of interface roughness in epitaxial Fe/MgO/Fe magnetic tunnel junctions," *Phys. Rev. B* **79**, 144413 (2009).

K. Sohlberg, S. P. Zhuo, P. Nellist, Y. P. Peng and S. Pennycook, "Evidence of high-pressure rhodium sesquioxide in the rhodium/gamma-alumina catalytic system," *J. Phys. Chem. C*, **112**, 11831 (2008).

J Tao, D. Niebieskikwiat, M. Varela, W. Luo, M. Chofield, Y. Zhu, M. B. Salamon, J. M. Zuo, S. T. Pantelides, S. J. Pennycook, "Direct imaging of nanoscale phase separation in $La_{0.55}Ca_{0.45}MnO_3$: Relationship to colossal magnetoresistance," *Phys. Rev. Lett.* **103,** 097202 (2009).

K. van Benthem and S. J. Pennycook, "Imaging and spectroscopy of defects in semiconductors using aberration-corrected STEM," *Appl. Phys. A* **96**, 161 (2009).

M. Varela, M. P. Oxley, W. Luo, J. Tao, M. Watanabe, A. R. Lupini, S. T. Pantelides and S. J. Pennycook, "Atomic-resolution imaging of oxidation states in manganites," *Phys. Rev. B* **79**, 085117 (2009).

M. Varela, J. Gazquez, A. R. Lupini, J. T. Luck, M. A. Torija, M. Sharma, C. Leighton, M. D. Biegalski, H. M. Christen, M. Murfitt, N. Dellby, O. Krivanek and S. J. Pennycook, "Applications of aberration corrected scanning transmission electron microscopy and electron energy loss spectroscopy to thin oxide films and interfaces," *Internat. J. Mat. Res.*, **101**, 21 (2010).

G. M. Veith, A. R. Lupini, N. J. Dudney, "Role of pH in the formation of structurally stable and catalytically active supported gold catalysts," *J. Phys. Chem. C* **113,** 269 (2009).

G. M. Veith, A. R. Lupini, S. Rashkeev, S. J. Pennycook, D. R. Mullins, V. Schwartz, C. A. Bridges and N. J. Dudney, "Thermal stability and catalytic activity of gold nanoparticles supported on silica," *J. Catal.* **262**, 92 (2009).

G. M. Veith, A. R. Lupini, S. J. Pennycook and N. J. Dudney, "Influence of Support Hydroxides on the Catalytic Activity of Oxidized Gold Clusters," *Chemcatchem*, **2**, 281 (2010).

K. Xiao, J. Tao, A. A. Puretzky, I. N. Ivanov, S. T. Retterer, S. J. Pennycook and D. B. Geohegan, "Selective Patterned Growth of Single-Crystal Ag-TCNQ Nanowires for Devices by Vapor-Solid Chemical Reaction," *Adv. Funct. Mater.* **18**, 3043 (2008).

K. Yang, C. Clavero, J. R. Skuza, M. Varela, R. A. Lukaszew "Surface plasmon resonance and magneto-optical enhancement on Au-Co nano-composite thin films," *J Appl. Phys.* **107,** 103924 (2010).

S. J. Zinkle, G. E. Ice, M. K. Miller, S. J. Pennycook and X. L. Wang, "Advances in microstructural characterization," *J. Nucl. Mater.* **8**, 386 (2009).

Nanometer-Scale Surface and Interface Phenomena

Konrad Thürmer, Norman Bartelt, Peter Feibelman, Gary Kellogg, Kevin McCarty,
Nancy Missert, Brian Swartzentruber, and Kevin Zavadil
Sandia National Laboratories, Livermore, CA and Albuquerque, NM

Program Scope

This program focuses on developing an atomic/molecular-scale understanding of processes occurring at solid surfaces, internal interfaces and solid-liquid interfaces. Our ultimate goal is to provide the fundamental information needed to understand and control surface/interface properties for materials applications with emphasis on energy-related technologies. Our approach combines state-of-the-art experimental capabilities with theory and simulation to determine how atomic-scale processes relate to the longer-range interactions that control interfacial behavior. The project has four synergistic tasks:

1) *Atomistic dynamics of surfaces*, whose goal is learning the mechanisms and energetics of atom transport across the surface and into the interior of solids. Experimental tools include scanning tunneling microscopy (STM), *atom-tracking* STM and low-energy electron microscopy (LEEM). Theoretical approaches to interpreting our observations include density functional theory (DFT), molecular dynamics/Monte Carlo simulations and thermodynamic modeling. We focus on diffusion processes underlying the growth and stability of surface alloys, thin-film growth and surface nanostructure formation.

2) *Collective phenomena in surface dynamics* strives to quantify the collective processes that govern the surface structures and morphologies of functional materials. We use STM and LEEM to measure the time-evolution of surface structure on nanometer length scales. We develop equations of motion that account for the observed time dependences precisely, and relate their parameters to the atomic processes studied in Task 1. Our new insights into materials behavior include determining the forces that stabilize self-assembling patterns, identifying the kinetic pathways that promote film instability and revealing that the unexpected processes of cluster diffusion and bulk/surface mass exchange can guide materials growth.

3) *Materials at interfaces: structural and mechanical properties*, where highly sensitive interfacial probes measure adhesion, wetting, and mechanical properties at the nanometer to micron scale, and interpret them with ideas stemming from atomic-level studies. We use the Sandia-developed interfacial force microscope (IFM) to study adhesive interaction between materials by determining the interfacial force as a function of the interfacial separation. We also use STM to probe the structure of the first few layers of atoms or molecules such as water near an interface, and DFT both to interpret images and guide experiments.

4) *Nanoscale electrochemistry*, where the primary focus is developing a quantitative understanding of the mechanisms of localized corrosion initiation in passive metals and to quantify the critical parameters governing nanostructure formation in model systems. Our approach is based on the novel and unique application of nanofabrication techniques to produce tailored surfaces and to simulate specific defect types on controlled substrates in well-defined locations. We shed light on corrosion and nanostructure-formation mechanisms using advanced electrochemical, morphological, chemical and structural analytical tools.

Recent Progress

Atomistic dynamics of surfaces Our recent progress includes: 1) understanding defect-mediated diffusion of embedded Ge atoms in Ge/Si(001), 2) analyzing atom transport during surface alloy formation in the Pd-Cu(001) system, 3) determining the mechanism of Si adatom diffusion on the Au-Si(111) 5x2 surface alloy, 4) understanding labyrinth island growth in Pd/Ru(0001) heteroepitaxy, 5) revealing the competition between bulk and surface diffusion in the chemically

reactive system of Al alloying with NiAl, 6) quantifying the mobility of water moleculces on ice and 7) determining the atomic structure of graphene on metals.

Collective phenomena in surface dynamics Our recent progress includes: 1) understanding how B induces self-assembly of one-dimensional nanostructures on Si(001), 2) determining why patterns form after metal deposition on graphene, 3) identifying the mechanism and energetic driving force for 3D pattern formation, 4) explaining nanoscale periodicity in the high-temperature limit, 5) elucidating how stress relaxes at the nanoscale beyond continuum theories, 6) showing that graphene grows on metals by adding clusters of C atoms, 7) revealing the mechanisms of graphene growth by SiC decomposition and 8) characterizing the growth of ice films on Pt(111).

Materials at interfaces: Structural and mechanical properties Our recent progress includes: 1) explaining epitaxial water nucleation on the surface of salt, 2) first-principles calculations of water-solid interfaces, including water on β-AgI, Pd(111), Ru(0001) and muscovite, 3) understanding NaCl hydration by ice, 4) measuring friction on a self-lubricating surface, 5) evaluating nanoscale adhesion beyond classical descriptions, 6) developing a molecular basis for interfacial deformation, friction, and wear and 7) determining the structure of the water wetting layer on Pt(111) (Fig. 1).

Nanoscale electrochemistry Our recent progress includes: 1) characterizing passive oxide breakdown events on Al microelectrodes, 2) defining the role of oxygen vacancy generation in oxide passivity, 3) creating artificial pit nuclei on aluminum at pre-determined locations to measure local pitting susceptibility, 4) using first-principles calculations of Al and O bonding in the presence of a H-impurity atom to conclude that oxide-metal bonding is weaker at interfacial steps and 5) showing that self-assembly of surface nanostructures can be controlled electrochemically through manipulation of surface stress from specifically adsorbed anion layers.

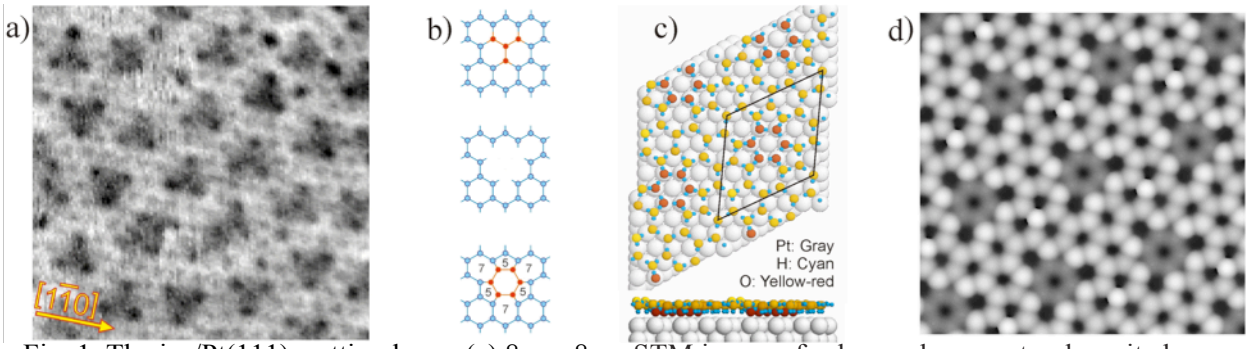

Fig. 1. The ice/Pt(111) wetting layer. (a) 8nm×8nm STM image of submonolayer water deposited on Pt(111) at 140 K. (b) Formation of the structural motif: a ‘‘575757’’ di-interstitial defect. (c) DFT model of the wetting layer incorporating this defect. (d) Simulated STM image based on DFT charge densities.

Future Plans

Atomistic dynamics of surfaces Our future plans include expanding our efforts to include atomic-level studies of transport on oxide and ice surfaces as well between the surface and bulk of oxide materials relevant to energy-storage applications.

Collective phenomena in surface dynamics We plan new studies of: 1) nanoscale-pattern formation, including metal clusters on graphene, stripes on boron-doped Si, and water films on metals, 2) cooperative mechanisms of material growth, including those that cause graphene to grow by cluster addition and 3) the stability of thin films, including the amorphous-to-crystalline ice conversion, and the dewetting of metal films on solid-state electrolytes.

Materials at interfaces: Structural and mechanical properties Our future work includes ongoing efforts in these areas and new applications of the IFM to probe the delamination and mechanical

properties of films only one atom thick (i.e., graphene), and STM investigations of proton order in near-substrate layers of ice films.

Nanoscale electrochemistry We will continue exploring the correlation between nanostructure evolution and pit initiation in pure Al and model Al-Cu alloys, and will expand the scope of our in-situ studies of nanostructure formation to energy storage and conversion materials.

DOE Sponsored Publications 2008-2010

E. Bussmann, S. Bockenhauer, F. J. Himpsel, and B. S. Swartzentruber, "One-Dimensional Defect-Mediated Diffusion of Si Adatoms on the Si(111)-(5 x 2)-Au Surface," *Phys. Rev. Lett*. **101**, 266101 (2008).

A. Davenport, R. Buchheit, N. Missert, B. Shaw and S. Virtanen, Editors, Light Alloys 3, The Electrochemical Society, Pennington, NJ (2008).

F. El Gabaly, K. F. McCarty, A. K. Schmid, J. de la Figuera, M. C. Munoz, L. Szunyogh, P. Weinberger, and S. Gallego, "Noble metal capping effects on the spin-reorientation transitions of Co/Ru(0001)," *New J. Phys*. **10**, 073924 (2008).

P. J. Feibelman, "Pinning of graphene to Ir(111) by flat Ir dots," *Phys. Rev. B* **77**, 165419 (2008).

P. J. Feibelman, "Lattice Match in Density Functional Calculations: Ice Ih vs. beta-AgI," *Phys. Chem. Chem. Physics* **10**, 4688 (2008).

J. de la Figuera, F. Leonard, N. C. Bartelt, R. Stumpf, and K. F. McCarty, "Nanoscale periodicity in stripe-forming systems at high temperature: Au/W(110)," *Phys. Rev. Lett.* **100**, 186102 (2008).

M. P. Goertz, X.Y. Zhu, and J.E. Houston, "Friction, wear, and aging of an alkoxy-monolayer boundary lubricant on silicon," *Trib. Lett.* **30**, 205 (2008).

E. Loginova, N. C. Bartelt, P. J. Feibelman and K. F. McCarty, "Evidence for graphene growth by C cluster attachment," *New J. Phys.,* **10,** 093026 (2008).

N. Missert, R.G. Copeland, "Scanning probe studies of water nucleation on aluminum oxide and gold surfaces," *Appl. Surf. Sci.* **254** 1972 (2008).

J. P. Pierce, N. C. Bartelt, R. Stumpf and K. F. McCarty, "Stability of ultrathin alumina layers on NiAl(110)," *Phys. Rev. B* **77**, 195438 (2008).

B. Santos, J. M. Puerta, J. I. Cerda, R. Stumpf, K. von Bergmann, R. Wiesendanger, M. Bode, K. F. McCarty, and J. de la Figuera, "Structure and magnetism of ultra-thin chromium layers on W(110)," *New J. Phys.* **10**, 013005 (2008).

K. Thürmer and N. C. Bartelt, "Nucleation-limited dewetting of ice films on Pt(111)," *Phys. Rev. Lett*. **100**, 186101 (2008).

K. Thürmer and N. C. Bartelt, "Growth of multilayer ice films and the formation of cubic ice imaged with STM," *Phys. Rev. B* **77**, 195425 (2008).

N. Vasiljevic, L.T. Viyannalage, N. Dimitrov, K. Sieradzki, "High resolution electrochemical STM: new structural results for underpotentially deposited Cu on Au(111) in acid sulfate solution", *J. Electroanalyt. Chem.* **613**, 118 (2008).

K. R. Zavadil "Inducing and Imaging Localized Passivity Breakdown in Aluminum Using an AFM Approach," *ECS Trans.* **11** (22), 13 (2008).

K.R. Zavadil, J.A. Ohlhausen and P.G. Kotula, "Electrolyte Ion Effects on the Formation of Nanoscale Structure in Aluminum's Passive Oxide Prior to Pit Initiation," *ECS Trans.* **11***(15)*, 89 (2008).

E. Bussmann, J. Sun, K. Pohl and G. L. Kellogg, "Palladium Diffusion into Bulk Copper via the Cu(100) Surface," *J. Physics: Condensed Matter* **21**, 314016 (2009).

G. A. Crawford, N. Chawla, and J.E. Houston, "Nanomechanics of biocompatible TiO2 nanotubes by Interfacial Force Microscopy (IFM)". *J. Mech. Behav. Biomed. Mat.* **2**, 580-587 (2009).

F. El Gabaly, N. C. Bartelt and A. K. Schmid, "Preparing arrays of large atomically flat regions on single crystal substrates," *J. Phys.-Condens. Matter* **21**, 314019 (2009).

K.V. Emtsev, A. Bostwick, K. Horn, J. Jobst, G. L. Kellogg, L. Ley, J. L. McChesney, T. Ohta, S. A. Reshanov, J. Rohrl, E. Rotenberg, A. K. Schmid, D. Waldmann, H. N. Weber and T. Seyller, "Towards wafer-size graphene layers by atmospheric pressure graphitization of silicon carbide," *Nat. Mater.* **8**, 203-207 (2009).

P. J. Feibelman, "Concluding Remarks, Water – From Interfaces to the Bulk," *Faraday Disc.* **141**, 467(2009).

P. J. Feibelman, "Onset of three-dimensional Ir islands on a graphene/Ir(111) template," *Phys. Rev. B* **80**, 085412 (2009).

P. J. Feibelman, "Pentagonal ice in chains," *Nature Materials (News and Views)* **8**, 372(2009).

M. P. Goertz, B. L. Stottrup, J. E. Houston, and X. Y. Zhu, "Nanomechanical Contrasts of Gel and Fluid Phase Supported Lipid Bilayers," *J. Phys. Chem. B* **113**, 9335 (2009).

M. P. Goertz, X.-Y. Zhu, and J.E. Houston, "Temperature Dependent Relaxation of a 'Solid–Liquid'," *J. Poly. Sci. B-Poly. Phys.* **47**, 1285 (2009).
J. C. Hamilton and W. G. Wolfer, "Theories of surface elasticity for nanoscale objects," *Surf. Sci.* **603**, 1284-1291 (2009).
E. Loginova, S. Nie, K. Thürmer, N. C. Bartelt and K. F. McCarty, "Defects of graphene on Ir(111): Rotational domains and ridges," *Phys. Rev. B* **80**, 085240 (2009).
E. Loginova, N. C. Bartelt, P. J. Feibelman and K. F. McCarty, "Factors influencing graphene growth on metal surfaces," *New J. Phys.* **11,** 063046 (2009).
A. Mascaraque, L. Aballe, J. F. Marco, T. O. Menteş, F. El Gabaly, C. Klein, A. K. Schmid, K. F. McCarty, A. Locatelli, and J. de la Figuera, "Measuring the magnetization of three monolayer thick Co islands and films by x-ray dichroism," *Phys. Rev. B* **80**, 172401 (2009).
K. F. McCarty, P. J. Feibelman, E. Loginova and N. C. Bartelt, "Kinetics and thermodynamics of carbon segregation and graphene growth on Ru(0001)," *Carbon* **47**, 1806-1813 (2009).
K. F. McCarty, J. C. Hamilton, Y. Sato, A. Saa, R. Stumpf, J. de la Figuera, K. Thürmer, F. Jones, A. K Schmid, A. A. Talin and N. C. Bartelt, "How metal films de-wet substrates-identifying the kinetic pathways and energetic driving forces," *New J. Phys.* **11**, 043001 (2009).
K. F. McCarty, J. C. Hamilton, Y. Sato, A. Saa, R. Stumpf, J. de la Figuera, K. Thürmer, F. Jones, A. K. Schmid, A. A. Talin and N. C. Bartelt, "How metal films de-wet substrates -identifying the kinetic pathways and energetic driving forces*," New J. Phys.* **11**, 043001 (2009).
N. W. Moore, J. H. Luo, J. Y. Huang, S. X. Mao, and J. E. Houston, "Superplastic Nanowires Pulled from the Surface of Common Salt," *Nano Letters* **9**, 2295-2299 (2009).
N. Murer, N. A. Missert, R. G. Buchheit, "Using finite element modeling to determinate the origin of trenching in aluminum alloys", Proceedings, EUROCORR 2009, Nice, France.
N. Murer, N. A. Missert, R. Oltra, R.G. Buchheit, "Towards the modeling of microgalvanic coupling in aluminum alloys : the choice of boundary conditions", *Proceedings*, **COMSOL** Boston 2009.
S. Nie, N. C. Bartelt and K. Thürmer, "Observation of Surface Self-Diffusion on Ice," *Phys. Rev. Lett.***102**, 136101 (2009).
B. Santos, E. Loginova, A. Mascaraque, A. K. Schmid, K. F. McCarty, and J. de la Figuera, "Structure and magnetism in ultrathin iron oxides characterized by low energy electron microscopy," *J. Phys.-Condens. Matter* **21**, 314001 (2009).
A. Seyeux, N. Missert, G.S. Frankel, L.H. Klein, A. Galtayries, P. Marcus, "Combination of ToF-SIMS imaging and AFM to study the early stages of corrosion in Al-Cu thin films", Proceedings, EUROCORR 2009, Nice, France.
D. A. Siegel, S. Y. Zhou, F. El Gabaly, A. K. Schmid, K. F. McCarty and A. Lanzara, "Three-fold diffraction symmetry in epitaxial graphene and the SiC substrate," *Phys. Rev. B* **80**, 241407(R) (2009).
E. Starodub, S. Maier, I. Stass, N. C. Bartelt, P. J. Feibelman, M. Salmeron, and K. F. McCarty, "Graphene growth by metal etching on Ru(0001)," *Phys. Rev. B* **80**, 235422 (2009).
B. Unal, Y. Sato, K. F. McCarty, N. C Bartelt, T. Duden, C. J. Jenks, A. K. Schmid and P. A. Thiel, "Work function of a quasicrystal surface: Icosahedral Al-Pd-Mn." *J. Vac. Sci.Tech.A* **27**, 1249-1250 (2009).
K.R. Zavadil, J.A. Ohlhausen and P.G. Kotula, "Proton Induced Point Defect Generation and Subsequent Interfacial Void Formation in Model Passive Oxides on Aluminum," *J. Electrochem. Soc.*, submitted, 2009.
E. Bussmann and B. S. Swartzentruber, "Ge Diffusion at the Si(100) Surface," *Phys. Rev. Lett.* **104** (2010).
P. J. Feibelman, "DFT Versus the "Real World" (or, Waiting for Godft)," *Top. Catal.* **53**, 417-422 (2010).
P. J. Feibelman, "The first wetting layer on a solid," *Phys. Today* **63**, 34-39 (2010).
T. Herranz, K. F. McCarty, B. Santos, M. Monti and J. de la Figuera, "Real Space Observations of Magnesium Hydride Formation and Decomposition," *Chem. Mat.* **22**, 1291-1293 (2010).
S. Nie, P. J. Feibelman, N. C. Bartelt and K. Thurmer, "Pentagons and Heptagons in the First Water Layer on Pt(111)," *Phys. Rev. Lett.* **105** (2010).
T. Ohta, N. C. Bartelt, S. Nie, K. Thurmer and G. L. Kellogg, "Role of carbon surface diffusion on the growth of epitaxial graphene on SiC," *Phys. Rev. B* **81** (2010).
B. Santos, J. M. Puerta, J. I. Cerda, T. Herranz, K. F. McCarty and J. de la Figuera, "Structure of ultrathin Pd films determined by low-energy electron microscopy and diffraction," *New Journal of Physics* **12** (2010).
Y. Sato, B. Unal, T. A. Lograsso, P. A. Thiel, A. K. Schmid, T. Duden, N. C. Bartelt and K. F. McCarty, "Periodic step arrays on the aperiodic i-Al-Pd-Mn quasicrystal surface at high temperature," *Phys. Rev. B* **81** (2010).
J. Soltis, D. P. Krouse, N. J. Laycock and K. R. Zavadil, "Automated processing of electrochemical current noise in the time domain: I. Simulated signal," *Corrosion Sci.* **52**, 838-847 (2010).
E. Starodub, N. C. Bartelt and K. F. McCarty, "Oxidation of Graphene on Metals," *J. Phys. Chem. C* **114**, 5134-5140 (2010).

Understanding the Electronic and Magnetic Structure of Advanced Materials

Y. Zhu, J. Tao, L. Wu, V.V. Volkov, and M.G. Han
zhu@bnl.gov, jtao@bnl.gov, ljwu@bnl.gov, volkov@bnl.gov, and mghan@bnl.gov
Dept. of Condensed Matter Physics and Materials Science
Brookhaven National Laboratory, Upton, NY 11973

Program Scope

The focus of this program is to research nanoscale phenomena that control the functionality of technologically important materials having significant relevance to the DOE's energy mission. It includes three major areas of research: 1) electronic structure, structural defects and interfaces in strongly correlated electron systems; 2) ferro-electric and -magnetic structure and nanoscale ferroelectricity and magnetism; and 3) energy storage and conversion. Emphasis is on the understanding of structure-property relationships and the underlying mechanisms for the complex physical behavior of various functional materials including high-temperature superconductors, thermoelectric materials and batteries. Advanced quantitative electron microscopy techniques, such as coherent electron diffraction, atomic imaging, electron spectroscopy, and phase retrieval methods are extended to study these materials. Experiments are closely coupled with structural modeling and theory. Although electron scattering and microscopy are the primary tools, complementary methods such as synchrotron x-ray, neutron scattering and scanning tunnel microscopy are also used.

Recent Progress

Electronic inhomogeneities that give rise to unique material properties have been considered as one of the most important discoveries in condensed matter physics in the past decade. In the area of strongly correlated electron systems, we studied manganites with intriguing colossal magnetoresistivity (CMR) and focused on a nanoscale charge-ordered (CO) phase that resulted from the complex charge-orbital-lattice-spin interplay. Earlier work on manganites using diffraction techniques, including neutrons, synchrotron x-rays and electrons found the temperature coincidence of the CO phase and CMR. However, findings in reciprocal space are often difficult to quantify and the role of the CO nanoscale phase in the CMR phenomenon remains elusive. In particular, the density and the volume fraction of the CO phase could not be correctly measured, which became a major obstacle to link the CO nano-structure to the physical properties of the materials. To directly observe the CO nano-phase, we developed a new TEM technique, scanning electron nanodiffraction (SEND), that allows us, for the first time, to map the CO phase in real space [1]. The mapping in $La_{0.55}Ca_{0.45}MnO_3$ clearly revealed the static CO phase in the form of nanoclusters with their density varying with temperature. The volume fraction of the CO nanoclusters at the transition temperature was thus quantitatively determined to be significant enough to contribute to the CMR and the formation of the CO nanoclusters is not due to chemical inhomogeneity, suggesting the nature of the CMR to be spontaneously electronic. Our study opens a door to the exploration of nanoscale electronic phase separation in other complex and exotic functional oxides and to the understanding of physical behavior of these materials. The work was highlighted in Physics Today [2]. Other recent progress under the program includes the study of structure-properties of Fe-based superconductors, magnetic dynamics and switching behavior of lithographically patterned tri-layer elements, and various catalysts with core-shell structures for energy applications.

Future Plans

We will continue our study of the CMR phenomenon by correlating TEM observations with property measurements. In particular, we will explore not only the local structure, but also the magnetic and transport properties of the CO nanoclusters to establish structure-property relationship at nanoscale. Because the properties of manganites are very sensitive to temperature, magnetic field and chemical dopants, we will employ a variety of in-situ TEM techniques on differently doped systems to unveil the role of the inhomogeneity and the diverse phase-separation scenarios in manganite families. In the strongly correlated

electron systems we will also study valence-electron distribution using quantitative electron diffraction in Fe-based superconductors to shed light on the role of orbital symmetry in superconductivity.

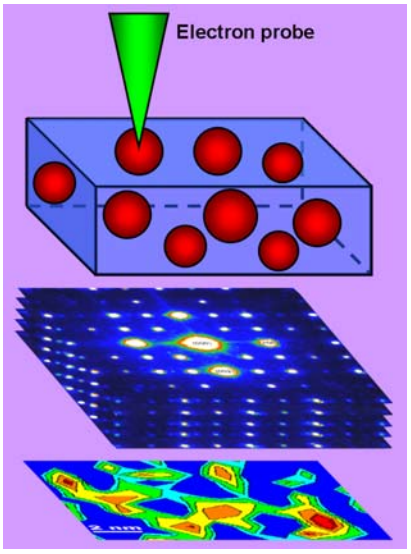

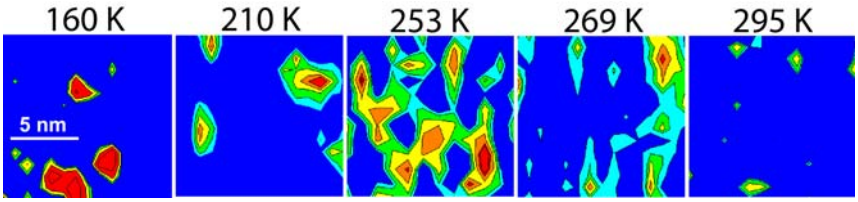

SEND intensity maps of the superlattice reflections upon warming in a single crystal domain in $La_{0.55}Ca_{0.45}MnO_3$. Warm color corresponds to the density of the CO phase. The backgrund blue area has the intensity of the superlattice reflections below the noise level. Although each image is not necessarily in precise registration with any other, the change of the density of the CO nanoclusters is evident through the phase transition. The temperature with maximum density of the CO nanoclusters (~ 253 K) coincides with the CMR peak temperature in $La_{0.55}Ca_{0.45}MnO_3$.

Principle of SEND (left): Using a small electron probe (green) ~ 1.7 nm in size, local structures can be obtained in electron nanodiffraction patterns. A stack of the patterns can be acquired, each corresponds to a point in the scanning area. In a phase separated system, only when the probe is on the CO phase (red) the superlattice reflections appear in the pattern. The recorded intensities of the superlattice reflections allow us to reconstruct real-space distribution of the nanoscale CO phase.

Building upon our expertise on the study of reversal behavior of patterned magnetic elements, we will extend our study to ferroelectrics to understand the switching behavior and dynamics of ferroelectric domains in strongly correlated oxides such as $PbZr_{0.2}Ti_{0.8}O_3$ using in-situ biasing and electron holography including a new resolution enhancement method developed at BNL. We will measure local electrostatic potential distributions and cation-lattice displacement across domain interfaces during electric reversal to address electron-lattice correlation and polarization behavior in ferroelectric materials. In the area of energy conversion and storage, using the new method we developed recently to measure atomic vibration and displacement in thermoelectric material $[Ca_2CoO_3]_{0.62}CoO_2$, we will study Li-ion intercalation and related phase transition and conversion reaction of $LiFePO_4$ cathode battery materials during charge and discharge cycles. Particular emphasis will be placed on the local structural identification, modification and thermal stability to provide insight into how to improve battery charge capacity, cycle ability and safety. Our TEM experiments will be compared with synchrotron x-ray observations as well as theory. Collaborations with prominent groups in these research areas have been established.

The work was supported by the U.S. Department of Energy, Division of Materials Science, Office of Basic Energy Science, under Contracts No. DE-AC02-98CH10886.

References

[1] J. Tao, et al., "Direct imaging of nanoscale phase separation in $La_{0.55}Ca_{0.45}MnO_3$ *Phys. Rev. Lett.*, **103**, 097202 (2009).
[2] C. Day, "Nanoscale phase competition accompanies colossal magnetoresistance" *Physics Today,* Nov., p20-23 (2009).

DOE Sponsored Publications in 2010-2008

2010

Han, M.-G., Zhu, Y., Sasaki, K., Kato, T., Fisher, C.A.J., Hirayama, T., "Direct measurement of electron beam induced currents in p-type silicon", Solid-State Electronics **54** 777–780 (2010).
Han, W., Su, D., Murphy, M., Ward, M., Sham, T.K., Wu, L., Zhu, Y., Hu, Y., and Aoki, T., " Microstructure and electronic behavior of PtPd@Pt core/shell nanowires", Journal of Materials Research **25**, 711 (2010).
He J. Q.; Volkov V. V.; Beleggia M.; Asaka T.; Tao J.; Schofield M. A.; Zhu Y., "Ferromagnetic domain structures and spin configurations measured in doped manganites", Phys. Rev. B **81**, 094427 (2010).

Huang, L., Schofield, M.A., and Zhu, Y., "Control of Double-Vortex Domain Configurations in a Shape-Engineered Trilayer Nanomagnet System", Adv. Mater., **22**, 492–495 (2010).
Jiang, M., Lim, B., Tao, J., Camargo, P. H. C., Ma, C.. Zhu, Y., and Xia, Y., "Controlling the nucleation and growth modes of Pt in seed-mediated syntheses of Pd-Pt bimetallic nanocrystals", Nanoscale, Advance Article DOI:10.1039/C0NR00324G (Paper) (2010).
Morosan E.; Wagner K. E.; Zhao Liang L.; Hor Y.; Williams A. J.; Tao J.; Zhu Y.; and Cava R. J., "Multiple electronic transitions and superconductivity in PdxTiSe2", Phys. Rev. B **81**, 094524 (2010), highlighted as an Editor's suggestion.
Ngai, J. H., Segal, Y., Su, D., Zhu, Y., Walker, F.J., Ismail-Beigi, S., Le Hur, K., and Ahn1, C.H., "Electric field tuned crossover from classical to weakly localized quantum transport in electron doped SrTiO3", Phys. Rev. B **81**, 241307 (R) (2010).
Pan, Z., Tao, J., Zhu, Y., Huang, J.-H., and Paranthaman, M.P., "Spontaneous Growth of ZnCO3 Nanowires on ZnO Nanostructures in Normal Ambient Environment: Unstable ZnO Nanostructures", Chem. Mater., **22**, 149–154 (2010).
Si,W., Jie, Q., Wu, L., Zhou, J., Gu, G., Johnson, P.D., and Li, Q., "Superconductivity in epitaxial thin films of Fe1.08Te:Ox", Physics Review B **81**, 092506 (2010).
Su, D., Yang, B., Jiang, N., Sawicki, M., Broadbridge, C., Couillard, M., Reiner, J.W., Walker, F.J., Ahn, C.H., and Zhu, Y., "Valence electron energy-loss spectroscopy of ultrathin SrTiO3 films grown on silicon (100) single crystal", Appl. Phys., Lett., **96**, 121914 (2010).
Wang, H., Altman, E., Broadbridge, C., Zhu, Y., and Henrich, V., "Determination of electronic structure of oxide-oxide interfaces by photoemission spectroscopy", Materials views article, Adv. Mater., **22**, 2950–2956 (2010).
Wang, J.X., Inada, H., Wu, L., Zhu, Y., Choi, Y.-M., Liu, P., Zhou, W.-P., and Adzic, R.R., "Oxygen Reduction on Well-Defined Core-Shell Nanocatalysts: Particle Size, Facet, and Pt Shell Thickness Effects", J. AM. CHEM. SOC., **131**, 17298–17302 (2009).
Zeng, J., Zheng, Y., Rycenga, M., Tao, J., Li, Z.-Y., Zhang, Q., Zhu, Y., and Xia, Y., "Controlling the Shapes of Silver Nanocrystals with Different Capping Agents", J. AM. CHEM. SOC., **132**, 8552–8553 (2010).
Zhang, Y., Chen, H., Choi, G., Raghothamachar, B., Dudley, M., Edgar, J.,Grasza, K., Tymicki, E., Zhang, L., Su, D., and Zhu, Y., "Nucleation Mechanism of 6H-SiC Polytype Inclusions Inside 15R-SiC Crystals", J. Electronic Materials, **39** 799-804 (2010).
Zheng, J.C., Frenkel, A.I., Wu, L., Hanson, J., Ku, W., Božin, E.S., Billinge, S. J. L., and Zhu, Y., "Nanoscale disorder and local electronic properties of CaCu3Ti4O12: An integrated study of electron, neutron, and x-ray diffraction, x-ray absorption fine structure, and first-principles calculations", Phys. Rev., B **81**, 144203 (2010).

2009

Han, W-Q., Su, D., Wu, L., Aoki, T., and Zhu, Y., "Tri- and quadri-metallic ultrathin nanowires synthesized by one-step phase-transfer approach", Nanotechnology **20**, 495605 (2009).
He, J., Gueguen, A., Sootsman, J.R., Zheng, J.-C., Wu, L., Zhu, Y., Kanatzidis, M.G., and Dravid, V.P., "Role of Self-Organization, Nanostructuring, and Lattice Strain on Phonon Transport in NaPb18-xSnxBiTe20 Thermoelectric Materials", J. AM. CHEM. SOC., **131**, 17828–17835, (2009).
He, J., Volkov, V.V., Beleggia, M., Asaka, T., Tao, J., and Zhu, Y., "Measurement of ferromagnetic domain structures and spin configurations in doped manganite", Phys. Rev. B in press (2009).
Huang, L., Schofield, M.A., and Zhu, Y., "Direct observation of the controlled magnetization reversal processes in Py/Al/Py asymmetric ring stacks", Appl. Phys., Lett., **95**, 042501, (2009).
Huang, H., Schofield, M.A., and Zhu, Y., "Control of double-vortex domain configurations in a shape-engineered trilayer nanomagnet system", Advanced Materials, Adv. Mater. **21** 1–4 (2009).
Huang, L., and Zhu, Y., "Controlled reversal of coupled Néel walls in flux-closure magnetic trilayer elements", Appl. Phys., Lett., **95**, 222502 (2009).
Inada, H.; Wu, L.; Wall, J.; Su, D.; Zhu, Y., "Performance and Image Analysis of the Aberration Corrected Hitachi HD-2700C STEM", J. Electron Microscopy, **58** 111 – 122 (2009).
Ke, X., Chen, C., Yang, J., Wu, L., Zhou, J., Li, Q., Zhu, Y., and Kent., P.R.C., " Microstructure and a Nucleation Mechanism for Nanoprecipitates in PbTe-$AgSbTe_2$", Phys. Rev. Lett., **103**, 145502 (2009).
Lim, B.; Jiang, M.; Camargo, P.H.C.; Cho, E.C.; Tao, J.; Lu, X.; Zhu, Y.; Xia, Y., "Pd-Pt Bimetallic Nanodendrites with High Activity for Oxygen Reduction," Science, **324**, 1302 – 1305, (2009).
Lim, B., Jiang, M., Tao, J., Camargo, P.H.C., Zhu, Y., and Xia, Y., "Shape-controlled synthesis of Pd nanocrystals in aqueous solutions", *Advanced Functional Materials* (feature article) **19**, 189–200 , (2009).
Luo, W.; Varela, M.; Tao, J.; Pennycook, S.J.; Pantelides, S.T., "Electronic and Crystal-field Effects in the Fine Structure of Electron Energy-Loss Spectra of Manganites", Phys. Rev. B, **79**, 052405, (2009).
Meng, Q.P.; Welch, D.O.; Zhu, Y., "Strain-Induced Changes of Oxygen Ordering in YBa2Cu3O6+δ Cuprates", Phys. Rev. B, **79**, 134531 (2009).
McQueen, T. M., Williams, A. J., Stephens, P.W., Tao, J., Zhu, Y., Ksenofontov, V., Casper, F., Felser, C., and Cava, R. J., "Tetragonal-to-Orthorhombic Structural Phase Transition at 90Kin the Superconductor Fe1:01Se", Phys. Rev. Lett. **103**, 057002 (2009).
Tao, J., Niebieskikwiat, D., Varela, V., Luo, W., Schofield, M.A., Zhu, Y., Salamon, M.B., Zuo, J.M., Pantelides, S.T., and Pennycook, S.J., "Direct imaging of nanoscale phase separation in $La_{0.55}Ca_{0.45}MnO_3$: relationship to colossal magnetoresistance", Phys. Rev. Lett., **103** 097202 (2009), highlighted in Physics Today, Nov. issue, p20-23).
Upton, M.H., Klie, R.F., Hill, J.P., Gog, T., Casa, D., Kuc, W., Zhu, Y., Sfeir, M.Y. , Misewich, J., Erese, G., and Lowndes, D., "Effect of number of walls on plasmon behavior in carbon nanotubes", CARBON, **47** 162-168 (2009).
Vaz , C.A.F. , Wanga, H.-Q., Ahn, C.H., Henrich, V.E., Baykara, M.Z., Schwendemann, T.C., Pilet N., Albers, B.J., Schwarz, U.D., Zhang, L.H., Zhu, Y., Wangd, J., Altman, E.I., " Interface and electronic characterization of thin epitaxial Co3O4 films", Surface Science **603** 291–297 (2009).
Wang, J., Inada, H., Wu, L., Zhu, Y., Choi, Y., Liu, P., Zhou, W., and Adzic, R.R., "Oxygen Reduction on Well-Defined Core-Shell Nanocatalysts: Particle Size, Facet, and Pt Shell Thickness Effects", J. AM. CHEM. SOC, **131** 17298-17302 (2009).

Wu, L., Zheng, J.C., Zhou, J., Li, Q., Yang, J.H., and Zhu, Y., "Nanostructures and defects in thermoelectric AgPb18SbTe20 single crystal", J. Appl. Phys. **105**, 094317 (2009).
F. Xu, V.V. Volkov, Y. Zhu, H. Bai, A. Rea, N.V. Valappil, X. Gao, I.L. Kuskovsky, and H. Matsui, "Long Electron-Hole Separation of ZnO-CdS Core-Shell Quantum Dots", J. Phys. Chem. C, **113** 19419-19423, (2009).
Xue, K., Chen, S., Wang,L., Wei, R., Xu,S., Cui, L., Mao, B., Tian, Z., Zen, C., Sun, S., Wu, L., and Zhu,Y., "Fabrication and characterization of oriented carbon atom wires assembled on gold", Chemical Physics Lett., **469**, 284-288 (2009).
Zheng, J.-C. Wu, L., and Zhu, Y., "Aspherical electron scattering factors and their parameterizations for elements from H to Xe", J. of Appl. Crystallography, **42** 1043-1053 (2009).
Zhong, H.; Huang, L.; Wei, D.; Wang, S.; Zhu, Y. and Yuan, J., "Experimental Determination of Ultra-Sharp Stray Field Distribution from a Magnetic Vortex Core Structure, " J. Mag. Mag. Mat., **321** L37 - L40, (2009).
Zhu, Y., Inada, H., Wu, L., Wall, J., and Su, D., "The aberration-corrected Hitachi HD-2700C STEM at Brookhaven National Laboratory", Hitachi E.M. News **3** 2-13 (2009).
Zhu, Y., and Jarausch, K., "Advanced Electron Microscopy in Materials Physics," J. Electron Microscopy, **58**, 73 – 75 (2009).
Zhu, Y., Inada, H., Nakamura, K., and Wall, J., "Imaging single atoms using secondary electrons with an aberration-corrected electron microscope", Nature Materials, **8** 808-812 (2009).

2008

Carrasquilla-Alvarez, J., Castaneda, R., Garcia-Sucerquia, J., Schofield, M.A., Beleggia, M., Zhu, Y., and Matteucci, G., "Retrieving the complex degree of coherence of electron beams", Optik **119** 127–133 (2008).
Chen, H., Wang, G., Dudley, M., Zhang, L., Wu, L., Zhu, Y., Xu, Z., Edgar, J.H., and Kuball, M., "Defect structures in B12As2 epitaxial layers grown on (0001) 6*H*-SiC", J. Appl. Phys. **103**, 123508 (2008).
Chen, H., Wang, G., Dudley, M., Xu, Z., Edgar, J.H., Batten, T., Kuball, M., Zhang, L., and Zhu, Y., "Single-crystalline B12As2 on *m*-plane (1100) 15*R*-SiC", Appl. Phys. Lett. **92**, 231917 (2008).
Cumings, J., Olsson, E., Petford-Long, A.K., and Zhu, Y., "Electric and Magnetic Phenomena Studied by In-Situ Transmission Electron Microscopy", *MRS Bulletin*, **33** 101-106 (2008).
Han, W-Q., Wu, L., Zhu, Y., Watanabe, K., and Taniguchi, T., "Structure of chemically derived mono- and few-atomic-layer boron nitride sheets", Appl. Phys. Lett., **93**, 223103 (2008).
He, J., Zheng, J.C., Chaudhuri, S., Budhani, R.C., and Zhu, Y., "Self-organization of epitaxial $La_{0.35}Pr_{0.275}Ca_{0.375}MnO_3$ manganite nanorods on NdGaO3 substrates", J. Appl. Phys, **103**, 064304 (2008).
Johnson, C.L., Bording, K., and Zhu, Y., "Structural inhomogeneity and twinning in $YBa_2Cu_3O_{7-\delta}$ superconductors: High-resolution transmission electron microscopy measurements", Phys. Rev. B, **71** (2008), highlighted as an Editor's suggestion.
Jooss, Ch., Hoffmann, J., Fladerer, J., Ehrhardt, M., Beetz, T., Wu, L., and Zhu, Y., "Electric pulse induced resistance change effect in manganites due to polaron localization at the metal-oxide interfacial region", Phys. Rev. B **77**, 13 132409 (2008).
Klie, R.F., Johnson, C., and Zhu, Y., "Atomic-resolution STEM in the aberration-corrected JEOL JEM2200FS", invited article, Microscopy & Microanalysis, **14**, 104-112 (2008).
Klie, R.F., Zhao, Y., Yang, G., and Zhu, Y., "High-resolution Z-contrast imaging and EELS study of functional oxide materials", Micron, **39** 723–733 (2008).
Li, Z., Tao, J., Lu, X., Zhu, Y., and Xia, Y., "Facile synthesis of ultrathin Au nanorods by aging the AuCl(oleylamine) complex with amorphous Fe nanoparticles in chloroform", Nano Lett. **8**, 3052- 3059 (2008).
Malac, M., Beleggia, M., Egerton, R.F., and Zhu, Y., "Imaging of radiation-sensitive samples in transmission electron microscopes equipped with Zernike phase plates", Ultramicroscopy, **108**, 126-140 (2008).
Malec, M.; Beleggia, M.; Taniguchi, Y.; Egerton, R.; Zhu, Y., "Low-Dose Performance of Parallel-beam Nanodiffraction", Ultramicroscopy, **109**, 14 – 21, (2008).
Malac, M., Beleggia, M., Taniguchi, Y., Egerton, R.F., and Zhu, Y., "Low-dose performance of parallel-beam nanodiffraction, Ultramicroscopy (2008), **109** 14-21.
Mandal, S., Budhani, R.C., He, J., and Zhu, Y., "Diverging giant magnetoresistance in ferromagnet-superconductor-ferromagnet trilayers", Phys. Rev. B **78**, 094502 (2008).
Phatak, C., Beleggia, M., and De Graef, M., "Vector Field Electron Tomography of Materials: Theoretical Development", Ultramicroscopy **108** 503-513 (2008).
Tan, Z.; Patel, V.; Liu, X.; Lukens, J.E.; Likharev, K.K.; Zhu, Y., "Aluminum-Oxide Tunnel Barriers with High Field Endurance", Appl. Phys. Lett., **93**, 242109, (2008).
Schofield, M.A., Beleggia, M., Zhu, Y., and Pozzi, G., "Characterization of JEOL 2100F Lorentz-TEM for low-magnification electron holography and magnetic imaging", *Ultramicroscopy*, **108** 625–634 (2008).
Solovyov, V.F., Li, Q., Wiesmann, H.,Oleynikov, P., and Zhu, Y., "Strong influence of the YBa2Cu3O7 grain size on critical current densities of thick YBa2Cu3O7 layers made by a metal–organic deposition process", Supercond. Sci. Technol. **21** 125013 (2008).
Villegas, J.E., Smith, K.D., Huang, L., Zhu, Y., Morales, R., and Schuller, I.K., " Switchable collective pinning of flux quanta using magnetic vortex arrays: Experiments on square arrays of Co dots on thin superconducting films", Phys. Rev. B **77**, 134510 (2008)
Volkov, V.V., Wall, J., and Zhu, Y., "Position-sensitive diffractive imaging in STEM by an automated chaining diffraction algorithm", Ultramicroscopy **108** 741–749 (2008).
Wagner, K.E., Morosan, E., Hor, Y.S., Tao, J., Zhu, Y., Sanders, T., McQueen, T.M., Zandbergen, H.W., Williams, A.J., West, D.V., and Cava, R.J., "Tuning the charge density wave and superconductivity in CuxTaS2", Phys. Rev. B **78**, 104520 (2008)
Zhu, Y., and Wall, J., "Aberration-corrected electron microscopes at Brookhaven National Laboratory", Book chapter in *Aberration-corrected Electron Microscopy,* A thematic volume of Advances in Imaging & Electron Physics, Ed., P.W.Hawkes, Elsevier/Academic Press, p.481-523 (2008).

UNIVERSITY GRANT PROJECTS

Imaging of Buried Nanoscale Optically Active Materials

PI: Ian Appelbaum
Department of Physics, University of Maryland, College Park, MD 20742
appelbaum@physics.umd.edu

Program Scope:

Semiconductor heterostructure-based light-emitting diodes (LEDs) and solid-state lasers have benefited enormously from recent developments in materials science and nanotechnology. However, methods to characterize the carrier transport through (and the light emission from) these devices on the nanoscale at which they were designed are limited by the fact that the carrier recombination occurs in layers buried deep below the semiconductor surface. Hence, processes occurring in these layers are hidden from direct observation. The development and introduction of a successful technique to examine the carrier transport and photon emission in deeply buried optically-active layers will provide a means for materials science to unmask the detailed consequences of experimentally controllable growth parameters, such as quantum dot size statistics and orientation, and defect density and charge recombination pathways. This will lead to more efficient, brighter light emitting devices across a broader wavelength spectrum.[1]

Our project goal is to demonstrate and use Ballistic Electron Emission Luminescence microscopy to image the deeply-buried luminescent layer of semiconductor light-emitting devices with local hot electron injection from a Scanning Tunneling Microscope (STM) probe. Briefly, hot electrons are ballistically injected over a rectifying Schottky barrier into a n-i-p LED under bias. Electroluminescence from the optically active region directly below the injection point results from radiative recombination of these injected carriers. Microscopy is possible by raster-scanning the tip position. The electroluminescence mechanism has been demonstrated in solid-state devices using $Al/Al_2O_3/Al$ tunnel-junctions,[2] and in ambient conditions with the STM in spectroscopy mode on QW devices, without imaging.[3]

Recent Progress:

Because the STM tunneling current is only several nA, the ballistically-injected hot-electron current is small (1-100 pA). Therefore, the luminescence intensity is weak, and external collection efficiency is reduced by the large index of refraction mismatch between semiconductors and air. To most effectively use Ballistic Electron Emission Luminescence microscopy, we must efficiently collect as much emitted luminescence as possible with an integrated photodetector.

---

[1] E.F. Schubert and J.K. Kim, "Solid-State Light Sources Getting Smart", Science **308**, 1274, (2005)
[2] Ian Appelbaum et al., "Ballistic Electron Emission Luminescence", Appl. Phys. Lett. **82**, 4498 (2003).
[3] Ian Appelbaum et al., "Room-Temperature Ballistic Electron Emission Luminescence Spectroscopy with a Scanning Tunneling Microscope", Appl. Phys. Lett. **84**, 547 (2004)

Prior work has demonstrated the effectiveness of this approach using an epitaxially-grown structure.[4] However, this method is limited to nearly lattice-matched materials with a tunable bandgap. We have demonstrated this scheme in a **materials-independent** way with a MBE-grown AlGaAs/GaAs quantum well p-n structure and a Si p-n photodetector, joined together using in-situ ultra-high-vacuum metal film wafer bonding.[5] Efficient photon collection was demonstrated by collecting electroluminescence resulting from hot electrons injected by a monolithic solid-state $Al/Al_2O_3/Al$ tunnel junction, as shown in Fig. 1.

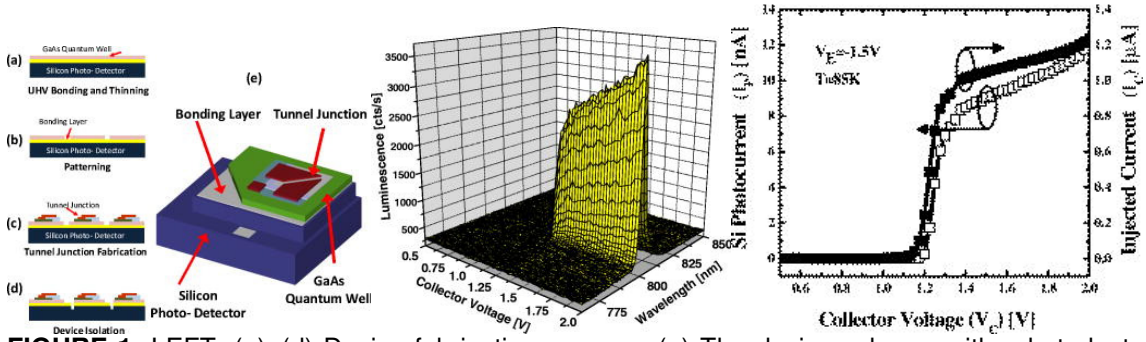

FIGURE 1: LEFT: (a)–(d) Device fabrication process. (e) The device scheme with a hot-electron injector on the top and a silicon *p-n* junction photodiode at the bottom. Hot electrons injected from a tunnel junction into a QW structure induce photon emission, which are then collected by the silicon photodiode, consequently generating photocurrent signal. CENTER: Far-field luminescence measurement by an optical spectrometer with emitter bias V_e V = –1.5 at 85 K for different collector voltage bias on the light emitting structure. No light is generated until the collector voltage exceeds a threshold point corresponding to energy conservation. The emitted light wavelength from the GaAs QW is approximately 815 nm. RIGHT: Collector current and photocurrent measurement at 85 K with V_e V = –1.5 at different collector voltage. The current thresholds are identical to the luminescence measurement, demonstrating that the heterointegrated photodetector can be used for efficient BEEL signal detection.

This technique must now be applied to hot electron injection using the STM scanning probe at high tip bias and large tunneling current. We have assembled an exchange-gas variable temperature STM shown below, and successfully tested its performance as a high voltage, high tunnel current STM and BEEM system for this purpose, as shown in Fig. 2.

[4] Ian Appelbaum et al., "Vertically Integrated Optics for Ballistic Electron Emission Luminescence Microscopy", Appl. Phys. Lett **86**, 063110 (2005)

[5] B.Q. Huang and Ian Appelbaum, "Heterointegrated near-field photodetector for ballistic electron emission luminescence", J. Appl. Phys. **105**, 086105 (2009).

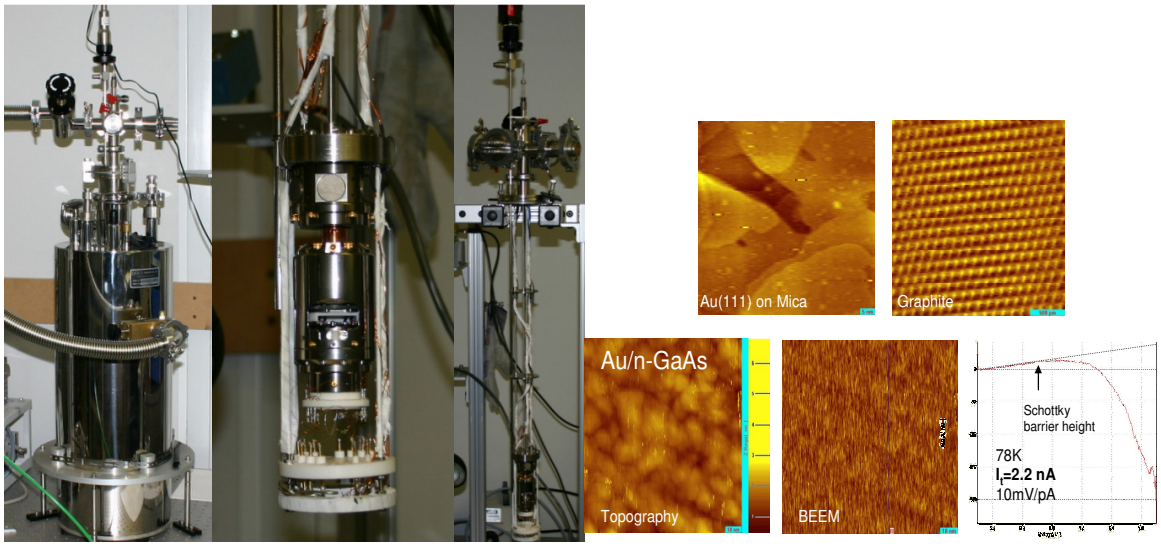

FIGURE 2: LEFT: Photographs of our exchange-gas variable-temperature STM/BEEM/BEEL system. RIGHT: High-resolution STM on Au/mica and graphite (showing atomic resolution at 80K), and simultaneous STM and BEEM/BEES on the canonical Au/n-GaAs system, all acquired with the recently-assembled system.

Future Plans:

The variable-temperature STM is presently being tested in BEEL mode using QW samples with perfect translational symmetry where no image is expected. We plan to begin measurements on LED structures where the luminescent layer has intentional spatial variation; for instance, patterned QDs[6] grown by our collaborator at U. Michigan. After measurements using solid-state hot electron injectors in device mode to establish the presence of the expected transport, luminescence, and photon collection mechanisms, we will use the STM to determine the intrinsic lateral resolution of BEEL microscopy by comparing the obtained image with the pattern used before overgrowth. Beyond that, we will move to other materials systems, for instance to look for In segregation in InGaN LED structures.

Reference to publications of DOE-sponsored research:

B.Q. Huang and Ian Appelbaum, "Heterointegrated near-field photodetector for ballistic electron emission luminescence", J. Appl. Phys. **105**, 086105 (2009).

[6] H. A. McKay, A. Dehne, J. Y. Lee, J. Mirecki Millunchick, "Focused-ion-beam-directed nucleation of InAs quantum dots," Applied Physics Letters **90**, 163109 (2007).

Discovery of Dielectric Response and Forces in Nanoscale Objects

P.E. Batson

Institute for Advanced Materials, Devices, and Nanotechnology,
Department of Physics and Astronomy
Department of Materials Science and Engineering
Rutgers, The State University
136 Frelinghuysen Road
Piscataway, New Jersey 08854
batson@physics.rutgers.edu

As has been recognized for many years in the context of EELS, when a fast electron passes a small object, it induces a dielectric response which produces electron energy loss [1]. Using sub-nanometer electron probes, it was first shown in the 1980's that this mechanism can be used to predict how nanometer-sized systems would couple with light, propagating to and from the far field [2]. Recent work using aberration-corrected electron probes has extended this kind of work to more complicated objects and to smaller energies [3, 4]. It has also been recognized that this dielectric behavior is responsible for many types of attractive forces: VanderWaals dipole-dipole forces, London Dispersion fluctuation forces, Debye induced dipole forces, and Keesom forces between electrostatic charges. Extensive work on these phenomena for estimation of interfacial forces in ceramics from measurements of valence EELS has been discussed by French [5].

This project seeks to discover the optical dielectric response of sub-nanoscale objects, down to single atoms where feasible, singly and in groups, using aloof inelastic scattering of a sub-Angstrom fast electron beam. This information will be useful for better understanding of the coupling of light to these objects. Important systems include reporter-molecule/particle structures designed for Surface Enhanced Raman Scattering, metal/dye composite structures that support surface plasmon amplification and stimulated emission, and semiconductor-organic hybrid structures useful for photon up/down energy conversion. We also wish to understand inter-object forces, the strength of near and far-field photonic coupling, and possible unanticipated optical behavior in molecular and nano-scale objects.

During initial work with aberration corrected STEM imaging, observation of metallic nanoparticles smaller than about 5 nm in size results in movement that often includes coalescence [6], supporting earlier TEM observations of very small nanoparticles [7]. This appears to be a result of two types of behavior: 1) sub-Angstrom STEM imaging injects enough energy into local structures that atomic bonds are destabilized, allowing easier atomic movement among alternative bonding sites; and 2) the resulting motion of sub-5 nm sized metallic clusters on carbon is non-random and apparently directed by forces induced by the passing STEM electron beam.

As summarized in Fig. 1, (on the right, below) Au clusters move while being imaged, often

coalescing with neighboring clusters. Motion is non-random, most often directed towards a neighboring cluster after a latency period that depends on beam current density, and often resulting in violent coalescence with a few Au atoms left bonded to the carbon substrate. Sometimes motion can be directed away from a neighboring cluster. In Fig. 2, (on the left, below) I show an experimental EELS result using oxide-coated Al spheres reproduced from [2]. This experiment showed that in systems having bispherical symmetry, surface plasmon resonances on the two spheres couple, producing a new low frequency mode. This mode couples external photon fields very strongly into the narrow space between the two clusters. In this experiment, the fast electron passes near the end of one of the spheres (position D in the Fig. 2), coupling strongly to surface plasmons having bi-spherical symmetry and an energy of about 4 eV – about half the normal 7 eV energy for an oxide-coated Al sphere. Preliminary theoretical work, in collaboration with others [8], also shown in Fig. 2., confirms this picture. This theoretical work verifies the bispherical coupling behavior for the inelastic scattering case , showing the plasmon field intensity. The important point to realize is that although the surface plasmon field is oscillating rapidly (of order 10^{14} Hz), the field is always anti-symmetric between the two spheres, resulting in an attractive force, for the indicated fast electron impact position. This model geometry was then used to estimate the inter-cluster forces.

Calculations for single spheres at moderate distances show a weakly attractive force directed towards the electron beam, in agreement with earlier work [9]. In the bispherical case, the presence of the second sphere reverses the direction of the force and increases its magnitude by about 10x to 5-10 pico-Newtons. This is a moderate force, but less than a typical force applied using optical tweezers – of order 70 pN for about 5 MW/cm^2 light intensity [10]. Once the particle under the beam becomes loose from the carbon substrate, we expect it to move quite fast, $\simeq$ 1200 nm/sec. If the fast electron does not pass near the end of one of the spheres – for instance if it passes near C in Fig. 2, or even between the two clusters – then coupling to the radiative bi-spherical mode cannot happen, and the attractive force disappears.

This project is intended to explore a range of scattering geometries to map inter-cluster polarization and forces in objects ranging in size from molecular to nanometer scales. For a large metallic cluster, using simple image charge arguments, it is expected that the force exerted by a passing fast electron ought to always be attractive. Theoretical work verified by us shows, however, that the force can reverse in sign at very short distances for very small clusters [9, 8]. We have preliminary confirmation of this behavior, but detailed understanding of it awaits further work. Initially, further work will be carried out at 100-120kV using a VG Microscopes HB501 STEM, aberration corrected to 4th order and using a Wien filter electron spectrometer which obtains about 100 meV energy resolution. We will attempt to obtain energy loss spectra, and detailed inelastic scattering maps, in concert with observation of movement of small clusters of various types on different kinds of substrates. In the

summer/fall of 2012, we expect to have a new 5th order corrected instrument, designed to operate as low as 40 kV, and having a new monochromator-spectrometer system that will deliver <30 meV energy resolution.(Supported under NSF grant #0959905.) With this system we hope to extend these studies to single molecules and groups of molecules, so that the energetics of changes can be obtained using very high resolution EELS while structural changes under the beam are observed.

[1] R. H. Ritchie, *Phys. Rev.*, 106 (1957) 874–881.

[2] P. E. Batson, *Surface Science*, 156 (1985) 720 – 734.

[3] Jaysen Nelayah, Mathieu Kociak, Odile Stephan, F. Javier Garcìa de Abajo, Marcel Tence, Luc Henrard, Dario Taverna, Isabel Pastoriza-Santos, Luis M. Liz-Marzan, and Christian Colliex, *Nat. Phys.*, 3 (2007) 348-353.

[4] Bernhard Schaffer, Ulrich Hohenester, Andreas Trügler, and Ferdinand Hofer, *Phys. Rev. B*, 79 (2009) 041401.

[5] R. H. French, *J. Amer. Ceram. Soc.*, 83 (2000) 2117-2146.

[6] P. E. Batson, *Micros. Microanal.*, 14 (2008) 89 – 97.

[7] L. D. Marks, *Rep. Prog. Phys.*, 57 (1994) 603 – 649.

[8] A. Reyes-Coronado, J. Aizpurua, P. M. Echenique, R. Barrera, and P. E. Batson, *Phys. Rev. B.*, (submitted) .

[9] F. J. García de Abajo, *Phys. Rev. B*, 70 (2004) 115422.

[10] A. J. Hallock, P. L. Redmond, and L. E. Brus, *Proc. Nat. Acad. Sci.*, 102 (2005) 1280-1284.

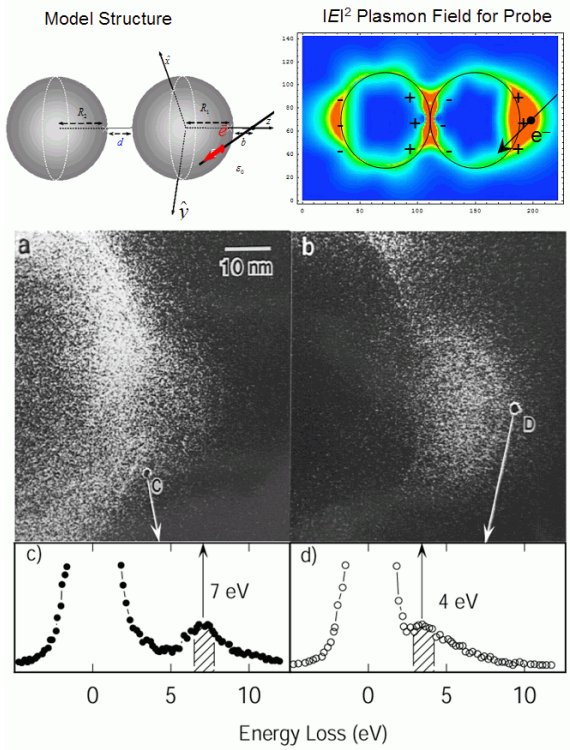

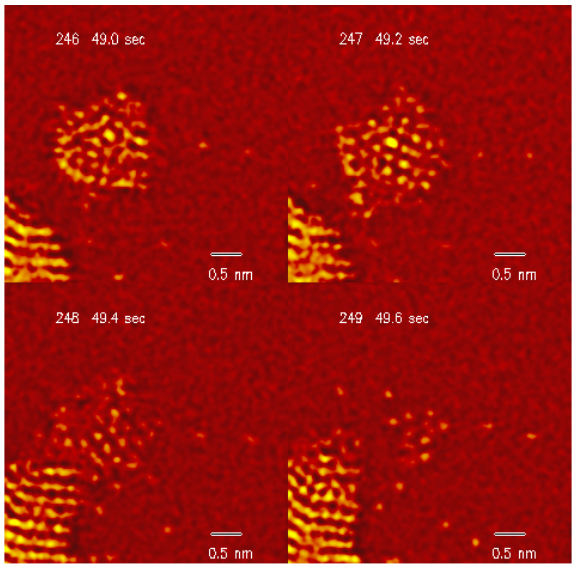

Fig. 1. Coalescence of Au island system under influence of the STEM beam. Reproduced from [6].

FIG. 2. (bottom) Bispherical surface plasmon EELS experiment (reproduced from [2]) showing EELS spectra for two probe positions, and the scattering intensity maps generated using the two observed peaks in the EELS spectra. (Top Left) Model geometry for calculations of electric field and resulting forces for a passing fast electron. (Top Right) The resulting magnitude of the induced electric field between the spheres. The phase of the induced charges is indicated by the signs.

LOCAL ELECTRONIC AND DIELECTRIC PROPERTIES AT NANOSIZED INTERFACES

Dawn A. Bonnell
Department of Materials Science & Engineering
University of Pennsylvania
Philadelphia, PA 19104-6272

Program Scope

This project is aimed at understanding the functional properties of nano-sized interface. This project follows earlier work on SrTiO3 grain boundaries where it was shown that the properties in the vicinity of grain boundaries vary considerably from that of the bulk. We showed that multiple transport mechanisms can operate simultaneously in this class of oxides (PRB 2004), that dielectric constants are suppressed by the local electric field near a grain boundary, and that vacancies in reduced samples are disordered in regions adjacent to grain boundaries (APL 2004), and that grain boundaries in SrTiO3 can induce ferroelectric ordering at low temperatures (PRL 2005). These results suggest that nano-sized interfaces will be influenced by similar phenomena.

In the current project the size dependence of metal-oxide interfaces is being explored. An idealized system of nano particles on SrTiO3 (100) is being used as a model. This requires that methods to quantify properties at specific local sites be developed and approaches to controlling interface structure be developed.

Recent Progress

Local Property Probes

Recently we addressed the issue of spatial resolution in continuum transport related property probes. A number of conductive tip scanning probes have demonstrated spatial resolution on the order of 1nm. This is surprising since the contact diameter in these cases is ~10nm. We developed an analytical model that describes how the load under a scanning probe tip results in a focusing field and greatly increases the spatial resolution. We applied this approach to HfO thin films and characterized nm sized defects. (*Applied Physics Letters* (2008) 182101) We then developed an analysis protocol that that enables the electronic structure of the these defects to be qualitatively compared (*J. Appl Physics* under review). Finally, we have developed the instrumentation and analytical theory to use 2^{nd} harmonic detection in non contact atomic force microscopy to map local variations in dielectric constant. This was applied to two exemplary systems: SrTiO3 thin films and self assembled organic monolayers. (*Applied Physics Letters* under review)

Nano Interface Properties

We recently determined the effect of interface orientation and size on interface potential barriers in Au-SrTiO3 (100) systems (Nano Letters 2010) Single-side epitaxially polished Nb-doped (0.2 atom % Nb) SrTiO3 (100) were annealed in flowing oxygen for 1 h at 1000 °C to remove carbon and point defects. The substrates were removed from the

furnace and placed on a hot plate and heated to 250 °C where 100 nm gold nanoparticles(citrate stabilized in H2O solution,) were boiled onto the surface of the substrate.34 Interparticle distance was controlled by diluting the solutions with water so that aggolermations were limited and so that measurements were between a single nanoparticle and the SrTiO3 and not affected by the depletion region of other nanoparticles. Following the deposition of nanoparticles, the sample was reinserted in the furnace and heated to 900 °C for 1 h. The final annealing step was found to create truncated octahedron gold nanoparticles on the surface. SEM images show the truncated octahedron shape to be the most prevalent shape on both graphite and SrTiO3 using this heat treatment method. The truncated octahedron morphology, the Wulff shape of gold nanoparticles, has been shown both experimentally and theoretically to be the most stable morphology. With this fabrication process that includes multiple annealing steps we are able to fabricate two unique contacts, Type (I) a TiO2 terminated (100) SrTiO3 surface in contact with Au (111) hexagonal facets and Type (II) a TiO2 terminated (100) SrTiO3 in contact with Au (100) square facets

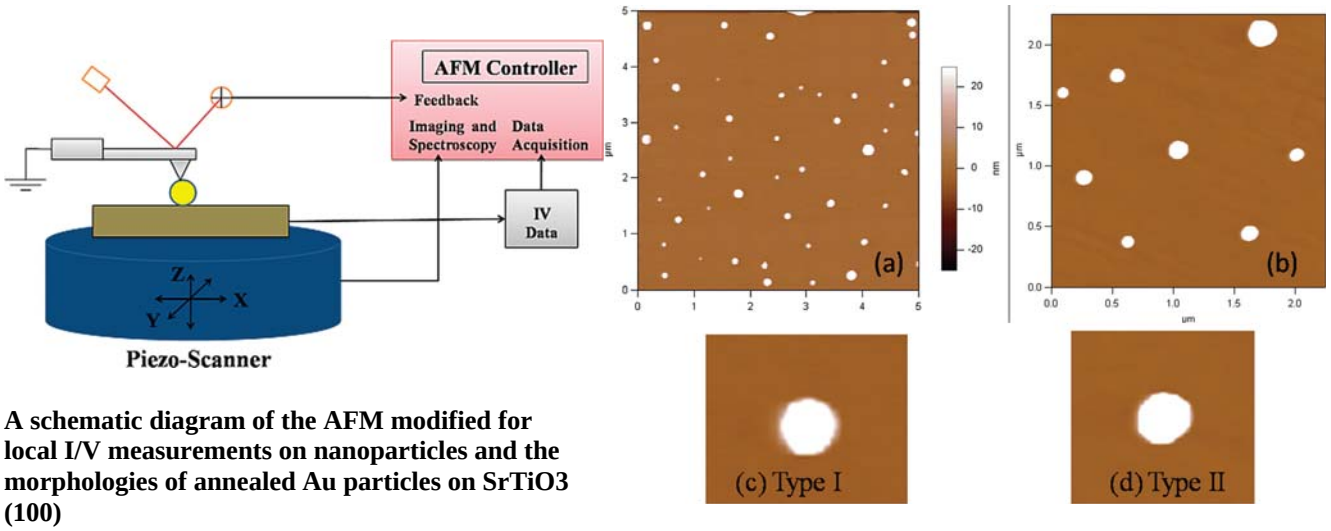

A schematic diagram of the AFM modified for local I/V measurements on nanoparticles and the morphologies of annealed Au particles on SrTiO3 (100)

The type I interface exhibited ideality factors between 1 and 2. The general trend of the data is that as the nanoparticle size decreased we see a decrease in the calculated barrier height and less conformity to pure thermionic emission. The largest nanoparticles, 90 nm heights, exhibited ideality factors closest to 1, and the 70 nm particles began to show greater deviations from these values. For the type II interface, there was much less variation in the barrier heights over the range of sizes with the typical barrier height for type II close to the minimum of type I. The ideality factors are larger than 2 indicating a strong tunneling component to the overall charge transport characteristics. Because of this added transport component, the calculated barrier height would intuitively be calculated as lower using thermionic emission models. The larger the nanoparticle, the

closer to conformity to pure thermionic emission and the higher the measured barrier. For both types of interfaces, as the nanoparticle size decreased the measured SBH decreased. The largest nanoparticles (90 nm) showed the closest conformity to thermionic emission.

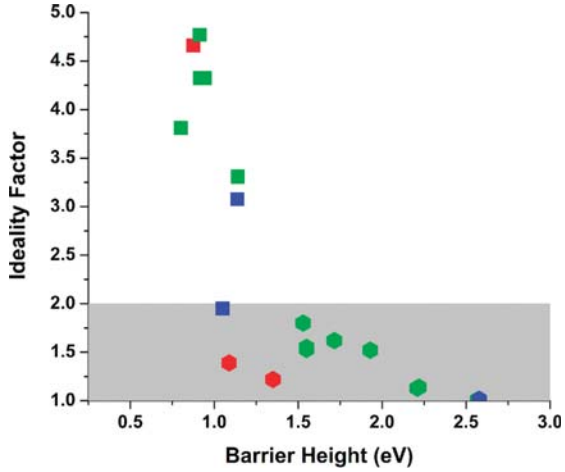

Barrier height and ideality factors for the measured interfaces. Red represents 70 nm particles, green 80 nm, and blue 90 nm. Hexagon-shaped data points are Type I interfaces, and square-shaped data points are Type II interfaces.

Future Plans

The next stage of the project involves characterizing the effect of carrier concentration on barrier height and measurement frequency on properties, and relate these to the atomic structure of the nanoparticle/oxide interface determined by high resolution TEM in collaboration with colleagues at UT Austin.

Recent References

Scanning Probe Microscopy in Materials Science
M. Nikiforov, D. A. Bonnell Science of Microscopy ed P. Hawkes, J. Spence Springer (2007)

Atomic Structures of Oxide Surfaces
J. Garra, D. A Bonnell *Progress in Modern Physics* (2008)

High Resolution Characterization of Defects on Thin Oxide Films
M. Nikifrov, M. Brukman, D. Bonnell APL (2008)

Probing Physical Properties at the Nanoscale
M. Brukman, D. Bonnell *Phyics Today* (June 2008)

Properties at Atomic Resolution
D. Bonnell *ACS Nano* (Sept 2008)

Determining the Size, Position and Energies of Defects in Thin Oxide Films
M. Brukman, D. A. Bonnell *Journal of Applied Physics* under review

Local Capacitance and Dielectric Properties by 2nd Harmonic AFM
M. Brukman, S. Nanayakkara, D. Bonnell *Applied Physic Letters* under review

Orientation Controlled Schottky Barrier Formation at Au Nanoparticle-SrTiO3 Interfaces
R. Kraya, L. Kraya, D. Bonnell *Nano Lett.*, *10*, 1224–1228 (2010)

Free and Supported Clusters: Interrogated by PES and STM

Kit H. Bowen
kbowen@jhu.edu
Departments of Chemistry and Materials Science, Johns Hopkins University, Baltimore, MD 21218

Program Scope

Clusters are aggregates of atoms and/or molecules held together by the same cohesive forces responsible for binding atoms and/or molecules to one another in solids and liquids. Because of their small size, free clusters exhibit a variety of novel properties. For example, clusters tend to have unique geometric structures. In fact, some of them exhibit low dimensionalities, eg., strings and planes of atoms, but when three-dimensional, as most are, they tend to have large surface area-to-volume ratios. They also display other intriguing geometric structures, such as empty shells, cuboids ('baby crystals'), and shells encapsulating atoms or other clusters ('core shells'). In addition, clusters often display extraordinarily novel electronic, magnetic, and reactivity properties. For example, the optical (electronic) properties (band gaps) of clusters can be tailored by controlling their size and composition. Moreover, some clusters enjoy enhanced stability ('magic clusters') due to having achieved closed shell electronic configurations under the 'shell model'. Clusters of non-magnetic elements can also be magnetic, while those of antiferromagnetic elements can become ferromagnetic. Together, their unique size-dependent electronic and magnetic properties provide a unique opportunity for manipulating and controlling electrons in finite size regimes. Furthermore, clusters of noble metals can be reactive, while those consisting of reactive elements can be made chemically inert by suitably changing their size, charge state, and/or composition. Moreover, the valency of some elements can change depending on the number of atoms per cluster. With these novel properties, clusters provide a means of manipulating physical and chemical properties.

While clusters possess many novel properties, in order to harness them for applications in the macroscopic world, most clusters will need to reside on surfaces, where interactions between them and their substrates may alter the clusters' original properties. This is among the most important issues affecting the future of nanocluster technology. Thus, it is important to determine how the intrinsic properties of clusters are changed by surface interactions. To address this issue, experiments are needed that measure both the properties of free (gas phase) clusters and those same properties of the same cluster sizes and compositions deposited on various substrates. This is the motivation for our DOE research program, and it defines our long-range objectives.

The key property to measure is electronic structure, since it sits at the crossroads of optical characteristics, geometric structure, magnetism, and reactivity. Electronic structure can be measured directly in both the free and the supported cluster environments. We have initiated a new research effort which has two, highly complementary parts to do just that. In one part, we conduct photoelectron

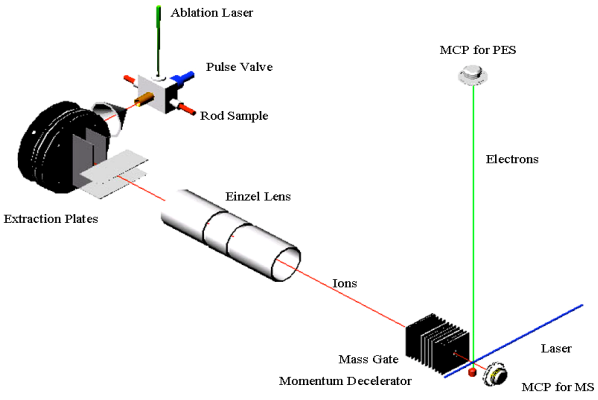

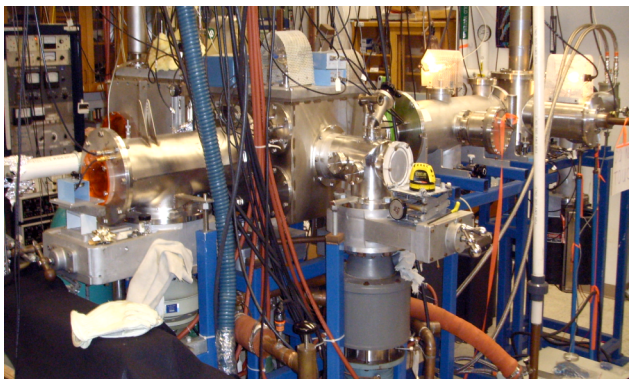

spectroscopic studies of size- and composition-selected cluster anions of materials science interest to map the intrinsic electronic properties of their *neutral* counterparts under conditions which are free from environmental effects. Photoelectron spectroscopy (PES) of anions provides HOMO-LUMO gaps and electronic state splittings (electronic spectra) for their corresponding neutrals (see figure and photo above). In the other part, we are striving to deposit the *same* size and composition, mass-selected cluster anions onto suitable substrates, where we are using *in situ* scanning tunneling microscopy (STM) to examine them (see figure and photo below). In these experiments, mass-selected cluster anions will be

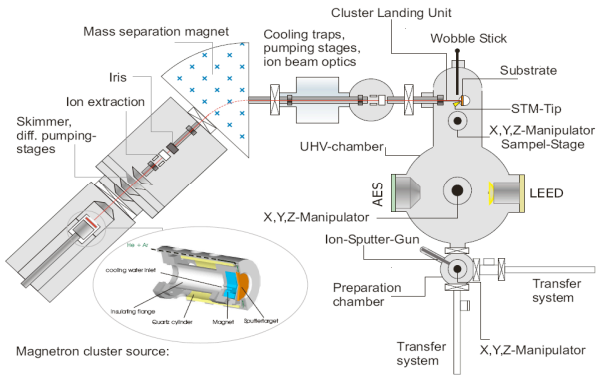

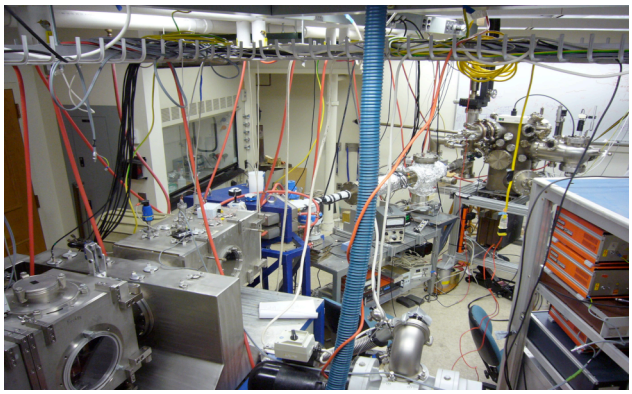

soft-landed, where they will lose their negative charges to the surface and become neutral clusters. Soon, we will also add ultraviolet photoelectron spectroscopy (UPS) to measure the electronic properties of the deposited clusters. STM measurements can measure the HOMO-LUMO gaps of individual clusters, while at higher coverage, UPS can supply information on their densities of states (electronic spectra). In this way, the same electronic properties (HOMO-LUMO gaps and electronic spectra) will be mirrored both in the gas phase and on surfaces for the same size and composition (neutral) clusters, thereby determining how the electronic properties of free clusters are modified by their interactions with substrates. We utilize two sophisticated apparatus in this work, an anion photoelectron spectrometer and a cluster deposition/surface characterization apparatus, and I have two close collaborators, Prof. Howard Fairbrother, a surface chemist and colleague here at Hopkins and Prof. Gerd Gantefoer, a cluster/surface physicist at Konstanz University. In the past our DOE research program was focused exclusively on anion photoelectron spectroscopy of size- and composition-selected cluster anions as a tool for characterizing the electronic structure of free (gas phase) neutral clusters. Our program is currently in the process of transitioning to the combination of photoelectron and surface-deposited cluster studies described above.

Recent Progress

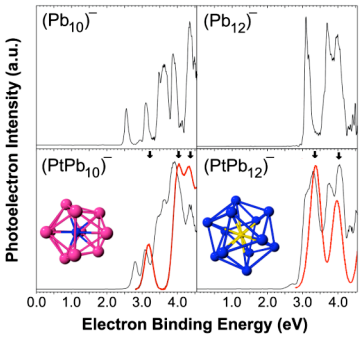

Here, we summarize some of our results both in the free cluster photoelectron arm and in the cluster deposition/surface characterization arm of this work.

On the photoelectron front, we have continued our work with silicon-encapsulated, rare earth (RE) atom cluster anions. Due to the lack of strong bonding interactions between the f-electrons of rare earth atoms and their silicon shells, it may be possible to maintain their high spin states and thus to achieve high magnetic moments in caged, and thus stabilized, silicon-encapsulated, rare earth clusters, $RE(Si)_n$. These clusters may provide a pathway for obtaining magnetic, silicon-based cluster-assembled materials. Such materials may serve as transitional materials between today's silicon-based semiconductor technology and the emerging field of spintronics. See our referenced papers below.

Recently, we have also completed combined synthetic, photoelectron, and computational studies of novel lead-encapsulated, platinum atom clusters. These clusters, with their unusual optical and magnetic properties, were synthesized in macroscopic quantities by Bryan Eichhorn, studied through anion photoelectron spectroscopy by us, and investigated theoretically by Mark Pederson. Above, the photoelectron spectra of $Pt@Pb_{10}^-$ and $Pt@Pb_{12}^-$ are compared to their pure lead counterparts. Computed structures and theoretically-simulated photoelectron spectra (in red) are shown in the accompanying figure.

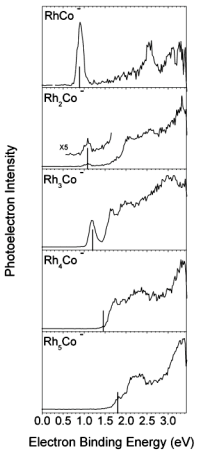

In addition, we have also studied rhodium/cobalt clusters. These clusters are thought to have unusual magnetic as well as catalytic properties. We generated these clusters using two laser vaporization techniques and then characterized the electronic structure of their neutral counterparts using anion photoelectron spectroscopy. The calculations were conducted by Marcela Beltran; predicted origin transitions are shown as stick spectra.

Below, we describe several cluster deposition studies that we have conducted recently. These demonstrate the current state of our combined cluster deposition / STM imaging capabilities. All of these studies were conducted with mass-selected, cluster anion beams, and except for the pinning studies, all were also done with soft-landed cluster ions. In a typical deposition experiment on our apparatus, a beam of metal or metal compound cluster anions is generated in a magnetron sputtering source, accelerated to 1.5 KeV, mass analyzed (the mass-selected) with a sector electromagnet, and then decelerated (soft-landed at a few eV) onto a target substrate in the ultra-high vacuum chamber which contains our surface analytical instruments, i.e., LEED, Auger, and room temperature STM. Several manipulator arms allow us to move the cluster deposited substrate to (and from) the surface characterization instruments.

On HOPG surfaces and at room temperature, we see evidence of highly mobile, deposited clusters, assembling along graphite step edges and forming ordered arrays. The two figures on the left below shows the result of soft-landing large, mass-selected molybdenum cluster anions, Mo_{600}^-, on HOPG. This was accomplished by depositing 50 pAmp of mass-selected Mo_{600}^- for 1.5 hours. Individual clusters with space between them can be seen clearly. We have seen many examples of this behavior. Another example of cluster self assembly along step edges is shown on the far right below. It was a result of depositing $(MoS_2)_{30}^-$ on HOPG (250 pAmp for ¾ hr.) with a landing energy of ~10 eV.

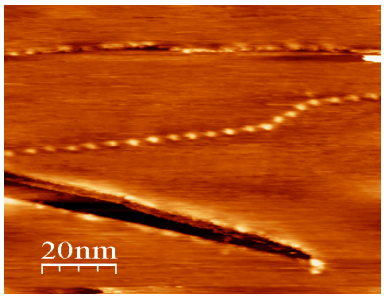

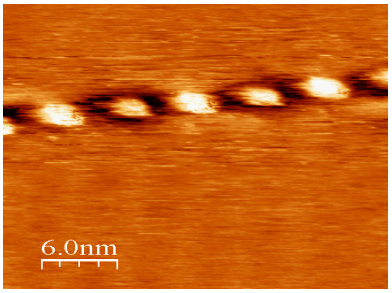

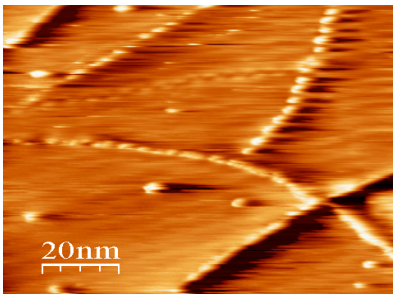

In order to explore additional ways to immobilize the clusters, we also utilized relatively high kinetic energy impacts (landing energies) in order to induce pinning on the surface. The figure at right shows the results of depositing small Mo_7^- clusters onto HOPG with an impact energy of ~30 eV (70 pAmp of mass-selected Mo_7^- for 1 hr.). There, while one can see step edges, the molybdenum clusters have not assembled along them. They appear to have remained intact upon landing with relatively little aggregation (due to residual mobility).

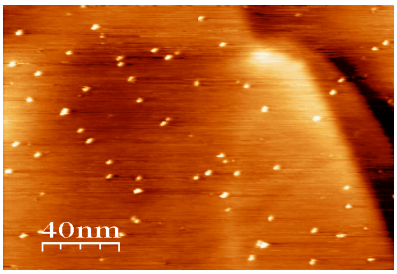

We also investigated high coverage scenarios. The two figures below on the left are due to high coverage depositions, again on HOPG, of Mo_{10}^- (500 pAmp for 4 hr.) and Mo_{100}^- (300 pAmp for 2 hr.), respectively. Slightly aggregated grape-like structures are evident. We also used AFM to examine the Mo_{100}^- sample in air (where the clusters oxidized); AFM is more reliable than STM for measuring heights. There, we saw Mo_{100}^- clusters with heights in the 2-3 nm range, which is about what they should be (see the AFM line-profile below at right). This suggests that we are achieving good soft-landings.

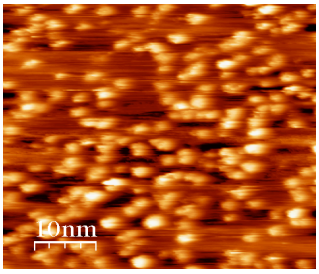

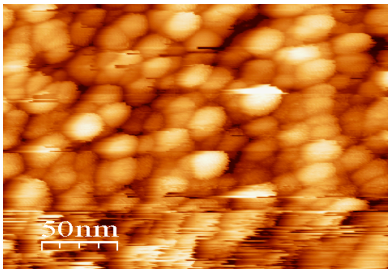

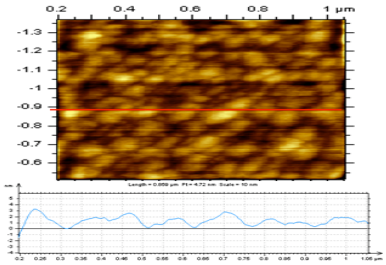

On occasion, we also observed extensive Moire patterns in the vicinity of clusters aligned along step edges. The deposited clusters perturbed the HOPG surface and caused movement of the upper layer, giving rise to these interference-like patterns. Two examples are shown below. The image on the far left resulted from depositing 200 pAmp of Mo_2^- for 1 hr. (these have clearly aggregated), while that in the middle is due to the deposition of 75 pAmp of $(MoO_3)_{100}^-$ for 2 hr., both on HOPG.

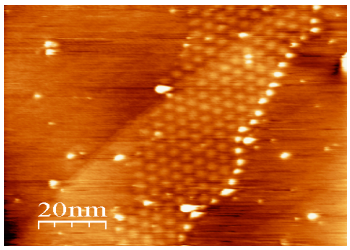

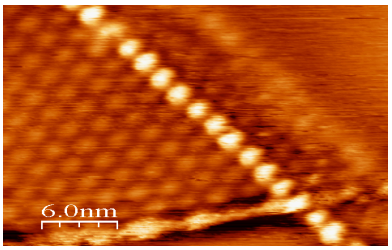

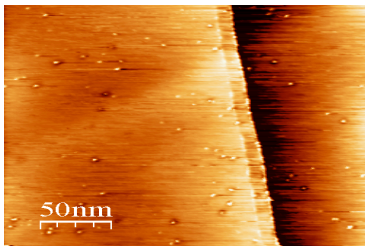

The image on the far right above is due to the deposition of 70 pAmp of $(Al_2O_3)_{100}^-$ for ¾ hr. Unlike pure aluminum clusters, which are mobile and aggregate, these aluminum oxide clusters are relatively immobile and remain largely unaggregated.

Future Plans

Our immediate plan is to emphasize cluster deposition studies in which the outcomes of our experiments are revealed through STM images. We have several such experiments in mind. For example, we hope to induce the formation of extended ionic lattices on surfaces due to the interaction of oven-deposited, alkali metal atoms and soft-landed, mass-selected cluster anions. The lattice pattern of such a two-dimensional, never-seen-before, 'cluster assembled material' should be readily discernible by STM. We also plan to use the tip to initiate electron-induced chemistry (moving beyond HOPG surfaces) in cases where the results can be followed through STM images. Doing STS on clusters at room temperature is difficult. In the short-term, we plan to attempt STS experiments on clusters which have been immobilized at step edges or which have been pinned. Eventually, we hope to acquire a variable temperature (cryogenic) STM/STS instrument as we work toward our long-term goals.

References to Publications from our DOE-Sponsored Research (2008-2010)

1. A. Grubisic,..K, Bowen, J. Am. Chem. Soc, **131**, 10783-10790 (2009).
2. G. Gutsev,…K. Bowen, J. Chem. Phys. **129**, 044310/1-044310/5 (2008).
3. X. Li, … K. Bowen, J. Chem. Phys. **129**, 124312 (2008).
4. W. Zheng,… K. Bowen. Chem. Phys. Lett. **462**, 35-39 (2008).
5. W. Zheng, … K. Bowen, Chem. Phys. Lett. **460**, 68-71 (2008).
6. X. Li,…K. Bowen, J. Chem. Phys. **129**, 074313/1-074313/11 (2008).
7. A. Kandalam,… K. Bowen, J. Chem. Phys. **129**, 134308/1-134308/11 (2008).
8. A. Grubisic, … K. Bowen, J. Chem. Phys. **129**, 054302/1-054302/5 (2008).
9. X. Li, … K. Bowen, J. Chem. Phys. **129**, 134309 (2008).

Materials Properties at Interfaces in Nanostructured Materials: Fundamental Atomic Scale Issues

N. D. Browning, nbrowning@ucdavis.edu.

Department of Chemical Engineering and Materials Science and Department of Molecular and Cellular Biology, University of California-Davis, One Shields Avenue, Davis, CA 95616

Program Scope

The aim of this research program is to develop a robust method to quantify the atomic scale changes in structure, composition and bonding that occur at grain boundaries. Although scanning transmission electron microscopy has long had the ability to deliver atomic resolution Z-contrast images, interpretation of the image contrast and subsequently the properties of the material being studied, has primarily been on an image by image basis – in some cases extrapolating a single image to represent the properties of all grain boundaries in a materials system. However, to truly quantify the properties of grain boundaries, any atomic scale study must give statistical relevance to the analysis. For example, how many grain boundaries, dislocation cores, point defects were analyzed to produce the result? How were the boundaries produced and under what beam conditions were the images acquired? In addition to an increase in spatial resolution, the advent of aberration correctors has provided a stability and robustness of experimental approach that means the experiment can be precisely defined and the statistical variations across many images can be correlated and quantified. This research is using aberration correction to build on statistical crystallography methods developed for structural biology and applied previously in materials science to study doping changes in bulk materials. Research is focusing specifically on [001] tilt grain boundaries in $SrTiO_3$ to act as a prototype system for perovskite materials being developed as superconductors, ferroelectrics, and ionic conductors. Through such a detailed systematic analysis of grain boundaries the most important compositional and structural effects controlling properties can be ascertained, and the mechanism by which grain boundary properties can be manipulated on the atomic scale can be determined.

Recent Progress

The initial analysis was performed on a 6^o low-angle [001] tilt grain boundary in $SrTiO_3$. Here the main aim of the test was not resolution of the FEI Titan used to acquire the images (the important spacing for $SrTiO_3$ is ~0.27nm and probe size in the Titan is ~0.1nm), but rather to see the level of contrast and sensitivity that could be achieved with an aberration corrected instrument. With the advances in specimen preparation technology, the increased signal to noise in the images and the improved stability of the microscope, many images were obtained from the grain boundary plane that highlighted the core structure (167 dislocation core images were obtained). These cores show a high degree of variability, which may be due to the ability to see the structure more clearly with an aberration corrected microscope or may also be due to the method of grain boundary synthesis. Figure 1 shows Z-contrast images of the main three types of dislocation cores that were observed and also a probability density map constructed from all the images of the cores. These three types of dislocation cores are referred to as elongated, composite and transformed. The elongated core appears in both a Sr and Ti rich variety and is marked by the splitting of the column closest to the usual reconstructed columns seen in the structural units - elongating the core. The composite core has the termination of (100) planes in different places on the two sub-lattices making it a composite structural unit of both sub-lattices.

This core structure is reminiscent of partial dislocations but there is no stacking fault separating them. The transformed core is the most surprising, containing closely packed Ti columns closer to a TiO_2 arrangement than a $SrTiO_3$ arrangement of atoms. A clear reason for the differences in structure is the composition variation between the cores. The effect of the composition on the structure is represented by the probability density map which shows probability of finding an atom in the "average" core structure. As can be seen from the core region, the density map is fairly flat indicating that there is a high degree of variability in the core that can be manipulated through doping/processing to form either one of the 3 observed structures or a new structure.

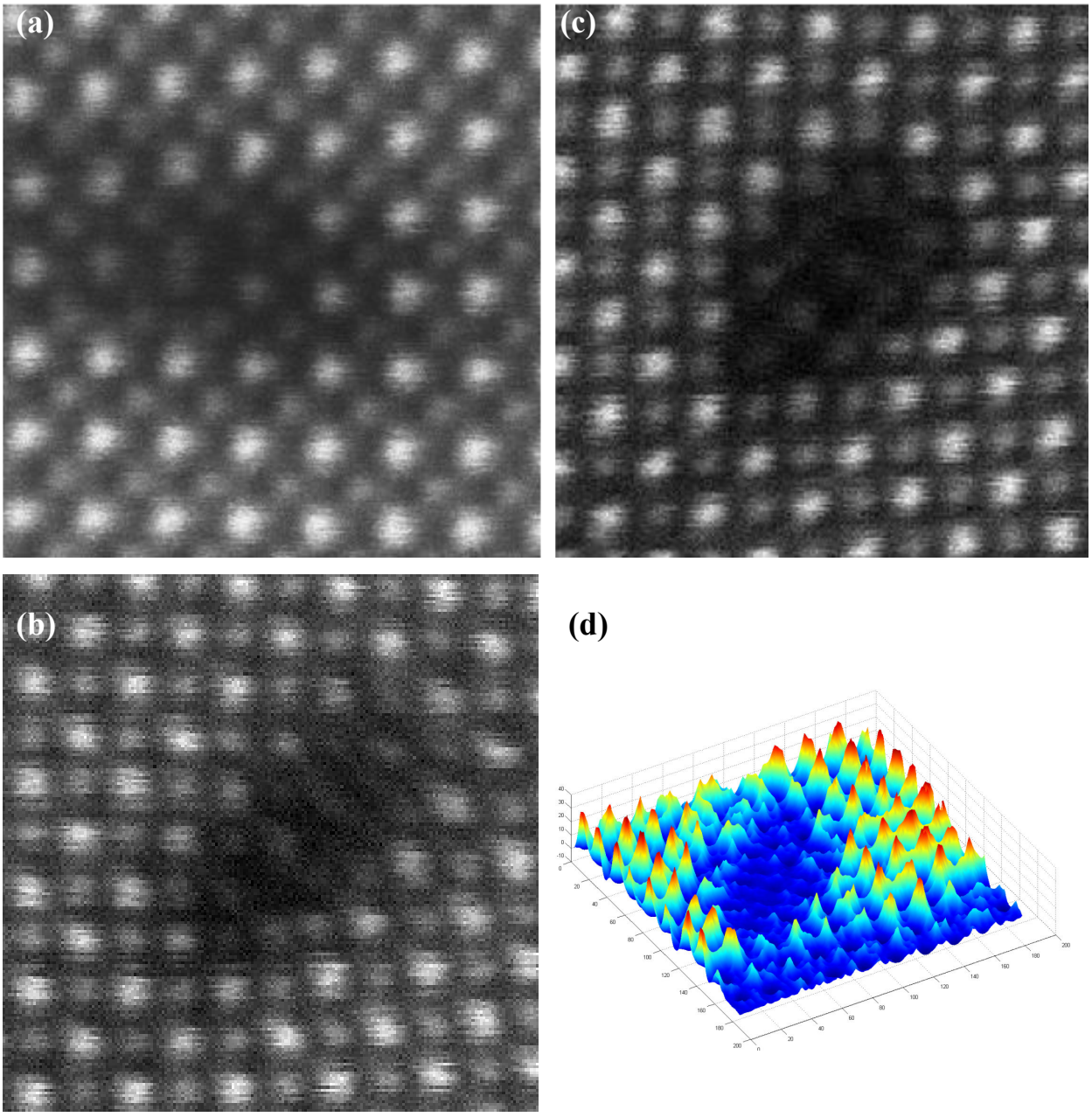

Figure 1: Z-contrast images of (a) the elongated core (b) the composite core and (c) the transformed core (spacing between the brightest spots is the Sr sub-lattice at ~0.4nm). (d) probability density map of the 167 cores showing the potential for variability in the core region.

Future Plans

The results from this years work show that grain boundary variability can be observed and quantified. The aim for the future is to correlate this analysis with deliberate compositional modifications to the grain boundary plane. To achieve this, the following tasks will be addressed:

1. Synthesize a range of grain boundary compositions and perform the statistical analyses of the grain boundary planes for up to 1000 images.
2. Develop in-situ liquid and gas stages to observe the site specific oxidation and reduction of the grain boundary plane as a function of doping level
3. Introduce methods of multivariate statistical analysis to correlate the most relevant structure/composition variations in the dislocation cores.

DOE Sponsored Publications (2008-2010)

A. F. Frame, E. C. Carroll, D. S. Larson, M. Sarahan, N. D. Browning, F. E. Osterloh, "First demonstration of CdSe as a photocatalyst for hydrogen evolution from water under UV and visible light", *Chemical Communications* **19**, 2206-2208 (2008)

M. Herrera, M. Chi, M. Bonds, N. D. Browning**,** J. N. Woolman, R. E. Kvaas, S. F. Harris, D. R. Rhiger**,** C. J. Hill, "Atomic Scale Analysis Of The Effect Of The SiO_2 Passivation Treatment On InAs/GaSb Superlattice Mesa Sidewall" **,** *Applied Physics Letters* **93**, 093106 (2008)

B. B. Nelson-Cheeseman, F. Wong, R. V. Chopdeker, M. Chi, E. Arenholz, N. D. Browning and Y. Suzuki, "Interface Structure and Transport in Complex Oxide Junctions", *J. Vacuum Science and Technology B* **26**, 1521-1525 (2008)

F. Osterloh, M. S. Sarahan, E. C. Carroll, M. Allen, D. S. Larsen, N. D. Browning, "$K_4Nb_6O_{17}$-Derived Photocatalysts for Hydrogen Evolution from Water: Nanoscrolls versus Nanosheets", *J. Solid State Chemistry* **181**, 1678-1683 (2008)

J. E. Evans, C. Hetherington, A. Kirkland, H. Stahlberg, and N. D. Browning, "Low-dose aberration corrected cryo-electron microscopy for organic specimens", *Ultramicroscopy* **108**, 1636-1644 (2008)

D. Gonzalez, J. G. Lozano, M. Herrera, N. D. Browning, S. Ruffenach, O. Briot, R. Garcia, "Structural changes during the natural aging process of InN quantum dots", *J. Applied Physics* **105**, 013527 (2009)

N. Halder, R. Rashmi and S. Chakrabarti, C.R. Stanley, M. Herrera and N. D. Browning, "A comprehensive study of the effect of *in situ* annealing at high growth temperature on the morphological and optical properties of self assembled InAs/GaAs QDs", *Applied Physics A* **95**, 713-720 (2009)

S. Kim, J. S. Lee, C. Mitterbauer, Q. M. Ramasse, M. C. Sarahan, N. D. Browning, H. J. Park, "Anomalous Electrical Conductivity of Nanosheaves of CeO_2", *Chem. Matls.* **21**, 1182-1186 (2009)

D. G. Morgan, Q. M. Ramasse and N. D. Browning, "Application of Two-dimensional Crystallography and Image Processing to Atomic Resolution Z-contrast Images", *J. Electron Microsc.* **58**, 223-244 (2009)

J. P. Buban, M. Chi, , D. J. Masiel, J. P. Bradley, B. Jiang, H. Stahlberg, N. D. Browning, "Structural Variability of Edge Dislocations in a $SrTiO_3$ Low-Angle [001] Tilt Grain Boundary", *Journal of Materials Research* **24**, 2191-2199 (2009)

M. Arredondo, M. Saunders, A. Petraru, H. Kohlstedt, I. Vrejoiu, M. Alexe, N. D. Browning, P. Munroe and V. Nagarajan, "Structural Defects And Local Chemistry Across Ferroelectric-Electrode Interfaces in Epitaxial Heterostructures", *Journal of Materials Science* **44**, 5297-5306 (2009)

M. Herrera, Q. M. Ramasse, D. G. Morgan, D. Gonzalez, J. Pizarro, A. Yáñez, P. Galindo, R. Garcia, M.-H. Du, S.B. Zhang, M. Hopkinson and N. D. Browning, "Atomic scale high-angle annular dark field STEM analysis of the N configuration in dilute nitrides of GaAs", *Phys Rev B* **80**, 125211 (2009)

N. Sengupta, S. Halder, M. Chakrabarti, M. Herrera, M. Bonds, N. D. Browning, "Investigating the effect of varying growth pauses on the structural and optical properties of InAs/GaAs quantum dot heterostructures", *Superlattices and Microstructures* **46**, 611-617 (2009)

R. Vogt, Z. Zhang, Y. Li, M. Bonds, N. D. Browning, E. J. Lavernia, and J. M. Schoenung, "The absence of thermal expansion mismatch strengthening in nanostructured metal-matrix composites", *Scripta Materialia* **61**, 1052-1055 (2009)

Y. Li, Y.H. Zhao, V. Ortalan, W. Liu, Z.H. Zhang, R.G. Vogt, N. D. Browning, E.J. Lavernia, J.M. Schoenung, "Investigation of Aluminum-based Nanocomposites with Ultra-High Strength", *Mater. Sci. Eng. A*. **527**, 305-316 (2009)

S. Adhikary, N. Halder, S. Chakrabarti, S. Majumdar, S. K. Ray, M. Herrera, M. Bonds, N. D. Browning, "Investigation of strain in self-assembled multilayer InAs/GaAs quantum dot heterostructures", *J. Crystal Growth* **312**, 724-729 (2010)

Y. Li, W. Liu, V. Ortalan, W. F. Li, R. Vogt, N. D. Browning, E. J. Lavernia, J. M. Schoenung, "HRTEM and EELS study of aluminum nitride in nanostructured Al 5083/B4C processed via cryomilling", *Acta Materialia* **58**, 1732-1740 (2010)

D. Neiner, N. L. Okamoto, C. L. Condron, M. F. Toney, S. Leonard, Q. M. Ramasse, P. Yu, N. D. Browning & S. M. Kauzlarich, "Synthesis and Characterization of $K_{8-x}(H_2)ySi_{46}$", *Inorganic Chemistry* **49**, 815-822 (2010)

M. R. Allen, A. Thibert, E. M. Sabio, N. D. Browning, D. S. Larson and F. E. Osterloh, "Evolution of Physical and Photocatalytic Properties in layered Titanates A(2)Ti(4)O(9) (A=K,H) and in nanosheets Derived by Chemical Exfoliation", *Chemistry of Materials***22**, 1220-1228 (2010)

E. M. Sabio, M. F. Chi, N. D. Browning, F. E. Osterloh, "Charge Separation in Niobate Nanosheet Photocatalyst Studied with Photochemical Labeling", *Langmuir* **26**, 7254-7261 (2010)

M. A. Arredondo, Q. M. Ramasse, M. Weyland, R. Mahjoub, I. Vrejoiu, D. Hesse, N. D. Browning, M. Alexe, P. Munroe, V. Nagarajan, "Direct evidence for cation non-stoichiometry and Cottrell atmospheres around dislocation cores in functional oxide interfaces", *Advanced Materials***22**, 2430-2432 (2010).

N. Halder, J. Suseendran, S. Chakrabarti, M. Herrera, M. Bonds, N. D. Browning, "Effect of InAlGaAs and GaAs Combination Barrier Thickness on the Duration of Dot Formation in Different Layers of Stacked InAs/GaAs Quantum Dot Heterostructure Grown by MBE", *Journal of Nanoscience and Nanotechnology* **10**, 5202-5206 (2010).

J. P. Buban, Q. M. Ramasse, B. Gipson, N. D. Browning and H. Stahlberg, "Towards Low-dose Imaging in STEM", *Journal of Electron Microscopy***59**, 91-102 (2010)

Point contact measurements on thin films of ferropnictide superconductors

***Venkat Chandrasekhar**, Department of Physics and Astronomy, Northwestern University, 2145 Sheridan Road, Evanston, IL*
***Chang-Beom Eom**, Department of Materials Science and Engineering, 1150 Engineering Drive, University of Wisconsin, Madison, WI*

Recent Progress

Evidence of phase-incoherent superconducting pairs in the normal state of Co-doped Ba122 superconductors by point-contact spectroscopy

The mechanism of superconductivity in the recently discovered ferropnictide compounds is an outstanding issue. As in the cuprates, it is believed that the properties of the superconducting ferropnictides above the superconducting transition temperature might hold the key to revealing this mechanism. We have used our low-temperature scanning probe microscope in the point spectroscopy mode to investigate the normal state and the superconducting properties of high quality epitaxial thin films of the Co-doped Ba122 superconductors synthesized in Chang-Beom Eom's group at the University of Wisconsin-Madison. In these experiments the transport properties of a ballistic point-contact formed by touching the surface of the film by a sharp tip of silver are analyzed for extracting energy resolved spectroscopic information about the charge carriers closed to the Fermi surface. When the film is superconducting, the transport is dominated by a process called Andreev reflection that involves the conversion of quasiparticles in the normal metallic tip into superconducting Cooper pairs in the film.

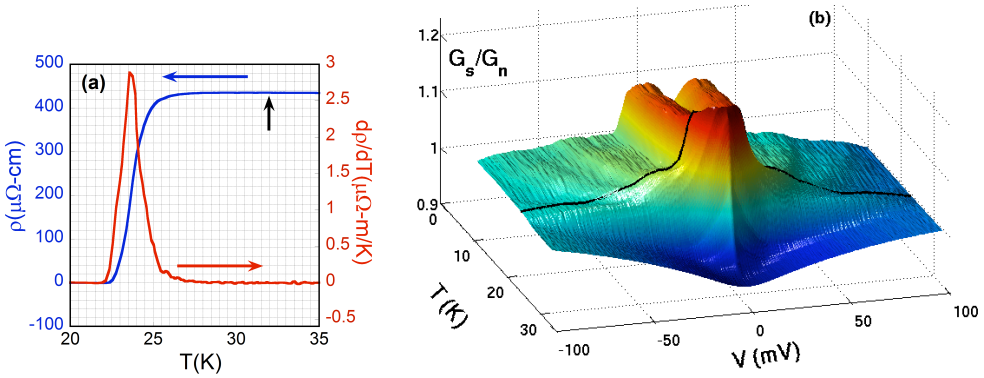

Figure 1: (a) Resistivity of the film as a function of temperature showing the superconducting transition at 23.7 K. The arrow indicates the temperature where the Andreev reflection signal disappears. (b) The temperature evolution of the point-contact spectra. The black line indicates the spectrum obtained at T_c of the film. The Andreev reflection signal survives well above this temperature.

This process gives rise to two peaks in the conductance vs. voltage spectrum. We clearly see the features associated with Andreev reflection in the point-contact spectra between our film and a silver tip at low temperatures. The most striking observation is that, unlike in the point-contacts of most of the other superconductors, the features associated with Andreev reflection do not vanish at the superconducting critical temperature T_c. Rather, such features are sustained up to a temperature of 32 K, 30% more than the superconducting transition temperature T_c (23.7K).

This is demonstrated in Fig. 1b, where the temperature dependence of the symmetric component of the point-contact spectrum is presented while Fig. 1a shows the transition temperature to be 23.7 K as probed by a bulk resistivity measurement. Andreev reflection far above T_c can be understood only if quasiparticle pairs exist in the normal state of the material. In fact, it is possible to have superconducting pairs well above T_c if the pair formation and global phase-coherence among the pairs take place at two different temperatures. Therefore, normal state Andreev reflection in our measurements arises from phase-incoherent pairs that do not superconduct until the sample is cooled down to T_c where global phase-coherence is established.

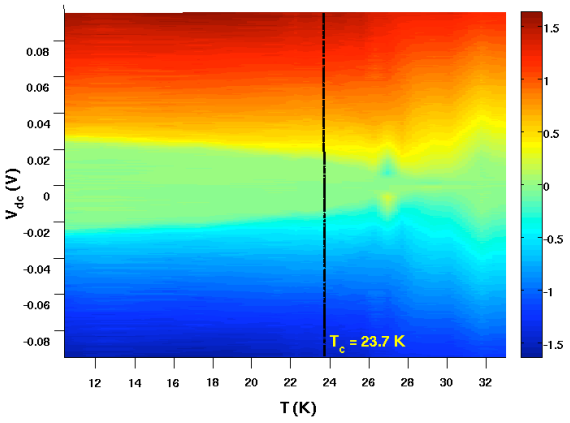

Figure 2: Antisymmetric component of the point contact spectrum dV/dI of an epitaxial Co-doped Ba122 film as a function of voltage bias and temperature. The black line marks the resistive superconducting transition, as shown in Fig. 1(a).

The data shown in Fig. 1(b) is the symmetric part of the point contact spectra. The raw point contact spectra is highly asymmetric. As seen in Fig. 2, the antisymmetric component of the point-contact spectrum also shows the signature of the gap in the quasiparticle density of states. The magnitude of this gap is relatively constant at low temperatures, and the differential resistance does not show any voltage dependence below this gap voltage. The flat region decreases in width as the temperature increases, closes at a temperature slightly higher than T_c, then opens up at higher temperatures, not even closing at T=32 K, where the Andreev contribution to the symmetric spectra disappears. Although the flat region in the antisymmetric data is clearly associated with superconducting correlations in the pnictide film, the exact origin of this behavior is not clear at the moment.

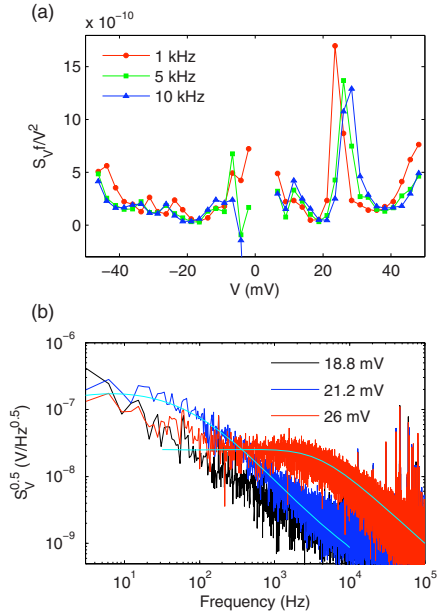

Figure 3: (a) Noise power spectrum of a Ag-Nb point contact normalized by frequency and bias V as a function of V at several different frequencies, at 5.8K. (b) Noise power spectrum corresponding to the peak in (a) at several different values of V. The typical Lorentzian spectrum of a single two-level fluctuator is clearly seen in the data.

Microscopic origin of the large broadening parameter encountered in point-contact spectroscopy by low-frequency noise measurements

The point-contact spectra between a normal metal and a superconductor is usually analyzed within the formalism of Blonder, Tinkham and Klapwijk (BTK). However, in practice, the spectral features are seen to be broadened which is not taken into account in the original BTK formalism. This broadening is typically fitted by adding a complex term ($i\Gamma$) to the energy (E). It is believed that the high value of Γ originates from the finite lifetime of the quasiparticles. A large value of Γ is frequently observed in point-contacts with the cuprates and the heavy fermion superconductors. However, large values of Γ, almost comparable to the gap Δ, are also observed even for point-contacts with conventional BCS superconductors. From low-frequency noise measurements in different types of point-contacts between a silver tip and the conventional superconductor niobium (Nb), we have shown that for spectra with large values of Γ, two level random fluctuators dominate, unlike for the spectra with $\Gamma \sim 0$. Figure 3(a) shows the normalized noise spectrum at several different frequencies for a Ag-Nb point contact. Analysis of the frequency spectrum of the noise

at specific values of the voltage bias V as shown in Fig. 3(b) reveals a Lorentzian frequency response that is characteristic of a two-level fluctuator (TLF). Therefore, our measurements suggest that the origin of large values of Γ may be due to such TLFs for other superconducting systems as well.

Nanostructured $CoFe_2O_4$ arrays fabricated by sol-gel techniques and electron beam lithography

As a first step towards fabrication of novel multiferroic devices in large scale, we have fabricated nano-pillar arrays of ferromagnetic $CoFe_2O_4$ and studied the magnetic properties of individual nano-structures by magnetic force microscopy and ensemble-averaged behavior of the arrays by ferromagnetic resonance spectroscopy. We followed a novel fabrication route involving combined electron beam lithography and sol-gel based chemistry in order to prepare the samples. Two different substrates were tried. On SiO_2, the resulting films are polycrystalline, and the $CoFe_2O_4$ dots form in well-defined elliptical shapes (Figs. 4(a), (c) and (d)). On $BiFeO_3$, however, faceted growth is observed (Fig. 4(b)), indicating that the $CoFe_2O_4$ dots attempt to grow epitaxially on the substrate. From experiments and micromagnetic simulations we have shown that down to the size scale of 200 nm, the $CoFe_2O_4$ dots do not form single-domain structures due to the presence of enhanced pinning sites.

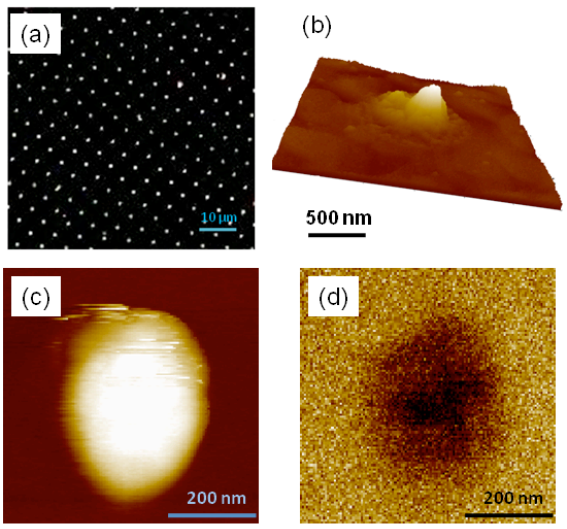

Figure 4: (a) Dark-field optical image of the nano-pillar arrays on SiO_2. (b) 3-D image of a single $CoFe_2O_4$ pillar on epitaxial $BiFeO_3$. (c) Topographic image of a single elliptical pillar on SiO_2. and (d) MFM image on the same pillar as in (c).

Publications (2008-2010)

1. *Pseudogap Formation in the Metallic State of LSMO Thin Films*, Udai Raj Singh, Anjan K. Gupta, Goutam Sheet, Venkat Chandrasekhar, H.W. Jang and C.B. Eom, Appl. Phys. Lett. **93**, 212503 (2008).

2. *Influence of symmetry mismatch on heteroepitaxial growth of perovskite thin films*, D. L. Prot, H. W. Jang, S. Lee, C. T. Nelson, X. Q. Pan, M. S. Rzchowski, and C. B. Eom, Appl. Phys. Lett. **93**, 111912 (2008).

3. *dc and High Frequency Magnetic Properties of Nano-patterned $CoFe_2O_4$ Arrays Fabricated Using Sol-gel Precursors*, Goutam Sheet, Alexandra R. Cunliffe, Erik J. Offerman, Chad M. Folkman, Chang-Beom Eom, and Venkat Chandrasekhar, Journal of Applied Physics, J. Appl. Phys. **107**, 104309 (2010).

4. *Possible origin of the broadening parameter in point Andreev reflection spectroscopy*, J.Wei, G. Sheet and V. Chandrasekhar, Appl. Phys. Lett. **97**, 062507 (2010).

5. *Conductance asymmetry in point-contacts on epitaxial thin films of $Ba(Fe_{0.92}Co_{0.08})_2As_2$*, M. Mehta, G. Sheet, D. A. Dikin, S. Lee, C.W. Bark, J. Jiang, J. D. Weiss, E. E. Hellstrom, M. Rzchowski, C.B. Eom and V. Chandrasekhar, Appl. Phys. Lett. **97**, 012503 (2010).

6. *Phase-incoherent superconducting pairs in the normal state of $Ba(Fe_{1-x}Co_x)_2As_2$*, G. Sheet, M. Mehta, D.A. Dikin, S. Lee, C.W. Bark, J. Jiang, J.D. Weiss, E.E. Hellstrom, M.S. Rzchowski, C.B. Eom, and V. Chandrasekhar, submitted to Physical Review Letters (arXiv:1004.4852).

Future plans

Epitaxial ferropnictide thin films

Our initial experiments on epitaxial ferropnictide thin films have raised a number of interesting issues, and we will continue to work on them in the near future. Our primary goal is to understand the nature of the superconducting state in the ferropnictides using epitaxial thin films grown in Chang-Beom Eom's group. As in the cuprates, understanding the normal state properties is critical to understanding the origin of superconductivity in the ferropnictides. The first point contact experiments on the Ba122 materials discussed above have been on near optimally doped materials. Consequently, we propose to investigate the phase diagram of the $Ba(Fe_{1-x}Co_x)_2As_2$ pnictides from the underdoped to the overdoped regime using point contact spectroscopy in combination with magnetization measurements and temperature dependent magnetoresistance measurements on epitaxial thin films, as well as the point contact noise measurements discussed above. In addition to point contact spectroscopy, we propose to fabricate micron scale devices from the ferropnictide thin films, in particular tunnel junctions with both normal metals and conventional superconductors as counter electrodes. Finally, the ferropnictide films that we have investigated have shown unusual magnetic behavior, specifically a strong paramagnetic response in the presence of small magnetic fields. We propose to investigate this effect at the microscopic level using our low-temperature magnetic force microscope.

Conductivity and superconductivity at the interface between insulating complex oxides

Complex oxides, and in particular the perovskites, form a fascinating range of materials with similar crystal structures but exhibit a wide variety of physical phenomena, including ferromagnetism, ferroelectricity, piezoelectricity and superconductivity, to name but a few. While the bulk properties of the complex oxides are still being investigated, interest recently has focused on the interfaces between two different complex oxides in layered structures. The modification of the electronic structure of either or both complex oxides within a few atomic layers of the interface can lead to completely unexpected results. In particular, it has been discovered that a two-dimensional electron gas (2DEG) can form at the interface between $LaAlO_3$ (LAO) and $SrTiO_3$ (STO), and that this 2DEG demonstrates some very interesting behavior. For example, if the LAO is less than 3 unit cells thick, the system is insulating, but specific conducting pathways can be created by applying a local gate voltage using the conducting tip of an atomic force microscope. The system also makes a transition to the superconducting state at low temperatures. We will investigate the behavior of this system by fabricating devices made from high-quality epitaxial thin films grown in Chang-Beom Eom's group. Figure 5(a) shows an optical image of a device made from a film consisting of 10 unit cells of LAO on STO (Fig. 5(b)). Figure 5(c) shows terraces observed in a non-contact atomic force microscope measurement on the sample, demonstrating the high quality of the epitaxial thin films. We are just starting these experiments: our goal is to investigate the low temperature properties using transport, investigate gating the device using scanning probe microscopes, and create new devices by applying voltages to fabricated top gates.

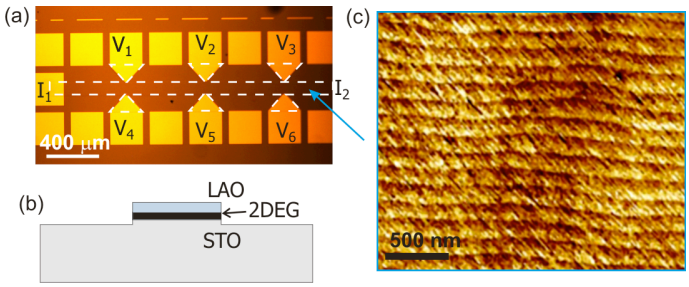

Figure 5: (a) Optical image of a long Hall bar device made by photolithography and Ar-ion milling, with Au covered current and voltage leads (dashed line outlines the actual dimension of the device). (b) Schematic view of a cross section of this device (not to scale). (c) Atomic force microscopy image of $LaAlO_3$ (10 unit cells thick) on $SrTiO_3$ substrate. Long axis of the device is oriented along the atomic terraces of the $LaAlO_3$.

Study of Interfacial Chemistry, Structure, and Properties in Magnetic Tunnel Junctions

Y. Austin Chang (PI) and Paul M. Voyles (Co-PI)
Materials Science and engineering, University of Wisconsin, 1509 University Avenue, Madison, WI 53706, chang@engr.wisc.edu, voyles@engr.wisc.edu

Program Scope

A magnetic tunnel junction (MTJ) consists of two thin-layers of ferromagnetic (FM) electrodes separated by an ultra-thin insulator (I). These junctions exhibit tunneling magnetoresistance (TMR) due to spin-dependent tunneling (SDT) between the pinned and unpinned electrodes and have applications in magnetic read heads and random access memory. The goals of our project are to develop new materials for MTJs and related spintronic devices, especially on silicon substrates, and to understand the fundamental influence of structure and interfaces on spin-dependent tunneling. We have synthesized MTJs with high-quality epitaxial (Co, Fe) bottom electrodes based on novel buffer layers with AlO_x insulators [06Yan1, 06Yan2, 07Ji] and used them to isolate the effects of bottom electrode crystal structure [08Yan] and strain state [09Ji] on the SDT from the potentially confounding effects of composition and interface roughness. We also demonstrated reproducible inverse (negative) TMR in a nominally symmetric $Co_{75}Fe_{25}/AlO_x/Co_{75}Fe_{25}$ junction annealed at 573 K. Recently, we have explored the mechanism of inverse TMR and expanded into Fe_3O_4 and Fe_4N, new materials with negative spin polarization (SP). We also started two new graduate students, who have now mastered the challenging tasks in the synthesis and characterization in this study.

Recent Progress

(1) Effect of the composition of the bcc-(Co, Fe)-FM electrode on spin-dependent tunneling

MTJs with bcc bottom epitaxial CoFe electrode show higher TMR than those with fcc structure, and there is large composition range for bcc $Co_{100-x}Fe_x$, so we further investigated the composition effect of bcc CoFe on TMR. MTJs consisting of Si(001)/TiN (9)/epitaxial $Co_{100-x}Fe_x$ (20)/AlO_x (1.5)/$Co_{100-x}Fe_x$ (6)/IrMn (20)/Ag (50) (nm) were grown by dc and rf magnetron sputtering by a new student, Hua Xiang. The structure for both electrodes is bcc and XRD confirms that the bottom CoFe films are epitaxial and high crystal quality. AFM measurements show the interfaces are smooth, with RMS roughness of 0.27±0.03 to 0.31±0.02 nm. The transport properties of the junctions were measured after 250°C field cooling. With increasing Fe composition, the TMR increases from 52% to 66.7%, reaching the maximum at 28 at.% of Fe, then decreases to 41% with the increasing Fe, as shown in Fig. 1. Using Simmons' relation, the barrier heights and widths of our junctions were calculated to be 2.4±0.2 eV and 1.2±0.1 nm respectively [10Xia]. This research was carried out as Hua Xiang's first project as a graduate student with us. Not only did he obtained important research results but also became an expert in synthesizing some challenging multi-layered structures.

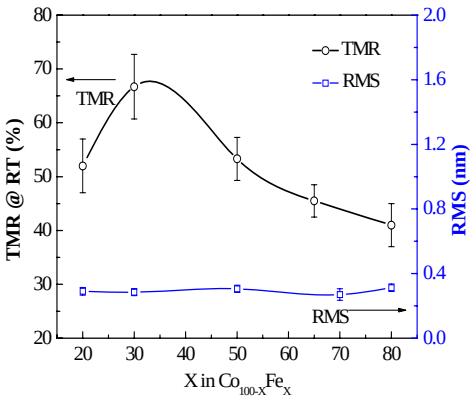

Fig. 1 TMR and RMS values measured at RT with different $Co_{100-x}Fe_x$ compositions.

(2) XPS characterization of the CoFe/AlOx interface of inverse TMR MTJs by delamination

We have observed both normal (positive) and inverse (negative) TMR in CoFe/AlOx/CoFe MTJs. We hypothesize that the inverse TMR is caused by extra oxygen at the bottom CoFe/AlO_x interface forming a

iron oxide with negative spin polarization, like Fe_3O_4. We developed an in-vacuum delamination technique to expose the buried interface for XPS measurements of the Fe oxidation state [09Yan]. CoFe/AlO_x/CoFe MTJs were synthesized by dc and rf magnetron sputtering. For each MTJ an identical CoFe/AlO_x/Au half-MTJ sample was fabricated, where a 50 nm Au metal film replaced the top (Co, Fe) electrode to "seal" the chemical information of the oxide and oxide/metal interface. The in-vacuum delamination method to expose the critical interfaces is shown at the bottom of Fig. 2(a). Ion sputtering was avoided by using mechanical force to "strip" the multilayer at its weakest point.

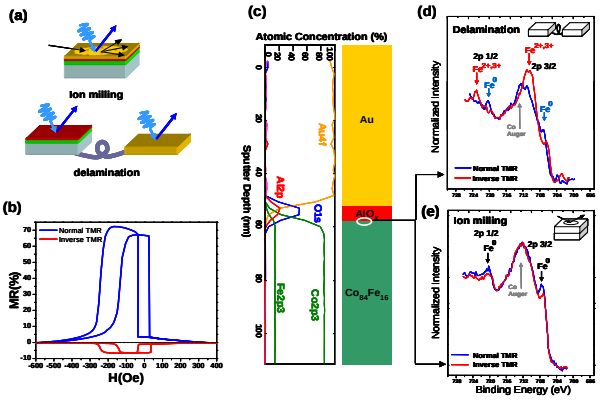

Fig. 2 Delamination and subsequent XPS reveal overoxidation of the AlOx /$Co_{84}Fe_{16}$ interface. (a) Schematic of the ion milling and delamination technique for obtaining X-ray photoelectron spectra of buried interfaces. (b) TMR curves for the two $Co_{84}Fe_{16}$/AlOx/$Co_{84}Fe_{16}$ MTJ samples exhibiting normal TMR and inverse TMR. (c) Depth profile and schematic of a $Co_{84}Fe_{16}$/AlOx half-MTJ with a Au cap layer to enable delamination. (d) Fe 2p photoelectron spectra obtained after delamination. (e) Ion milling destroys this oxidation information and registers no difference between the normal and inverse TMR samples and no oxidation at the $Co_{84}Fe_{16}$/AlOx interface.

We compared two MTJ samples with the same multilayer structure ($Co_{84}Fe_{16}$/AlOx/$Co_{84}Fe_{16}$) but different oxidation times for the Al metal layer. As shown in Fig. 2 (b), the MTJ sample with an optimized oxidation time (130 s) exhibits positive TMR. Strikingly, the other MTJ sample with a longer oxidation time (180 s) exhibits inverse TMR. The XPS Fe 2*p* spectra in Fig. 2(e) from the two samples are ion milling to expose the bottom interface are indistinguishable and both show only the Fe^0 metallic oxidation state. In sharp contrast, the two spectra of Fig. 2 (d) from delaminated samples are different. The Fe $2p_{1/2}$ peak for the normal TMR sample is at about 720 eV, indicated metallic Fe, but the peak from the inverse TMR sample is at 723 eV, which indicates Fe oxide. These data indicate that for the inverse TMR sample an ultrathin layer of Fe oxide, likely Fe_3O_4, formed underneath the AlO_x layer at the bottom interface. O K-edge fine structure in ~1.5 Å spatial resolution STEM EELS spectrum image measurements of the burid interface in similar devices seems to confirm this observation, but only for small areas of some devices. This may explain the relatively weak inverse TMR we observe, but requires additional study.

(3) Epitaxial growth and magnetic properties of Fe_3O_4 thin-films on Si substrates

The high Curie temperature of ~850K of Fe_3O_4 and its perfect negative SP (-100%), predicted theoretically, make it one of the most promising magnetic materials in developing spintronic devices. One of the great challengences in achieving basic research and technological advancement in this field is to grow Fe_3O_4 thin films on semiconductors, especially on Si [09Has, 10Won]. Multilayer structures consisting of substrate/TiN(10)/Fe_3O_4(*t*) (nm) were grown by magnetron reactive sputtering at different substrate temperatures (T_s) on Si(001), Si(110) and Si(111) substrates. XRD indicates epitaxial growth of Fe_3O_4 films on all three Si substrates and that both the in-plane and out-of-plane crystallographic directions of Fe_3O_4, TiN, and the

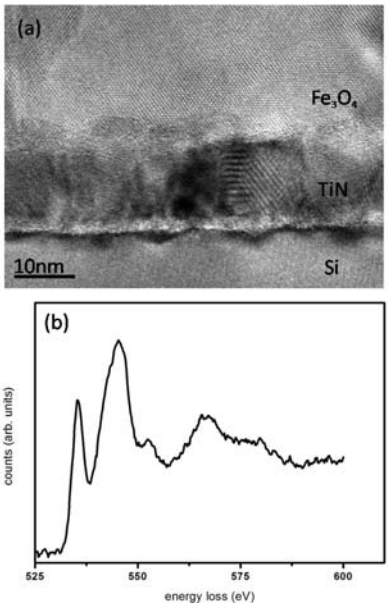

Fig. 3 (a) HRTEM image of Fe_3O_4 film on TiN buffered Si; (b) Oxygen K edge for the deposited Fe_3O_4.

corresponding Si substrates are parallel to one another. Both Fe_3O_4 films and TiN buffer are fully epitaxial when grown at T_s above 150 °C, with textured single phase Fe_3O_4 resulting from room temperature growth. TEM results reveal that the growth mechanism of our Fe_3O_4 films on TiN is coalescence of initial island nuclei followed by epitaxial columnar grain growth which, as shown in Fig. 3. Fig. 3 (a) indicates a good epitaxial relationship between Si, TiN and Fe_3O_4 layers; in Fig. 3 (b) the pre-peak in the oxygen K edge ELNES around 535eV is in a good agreement with the reported O K edge of Fe_3O_4.

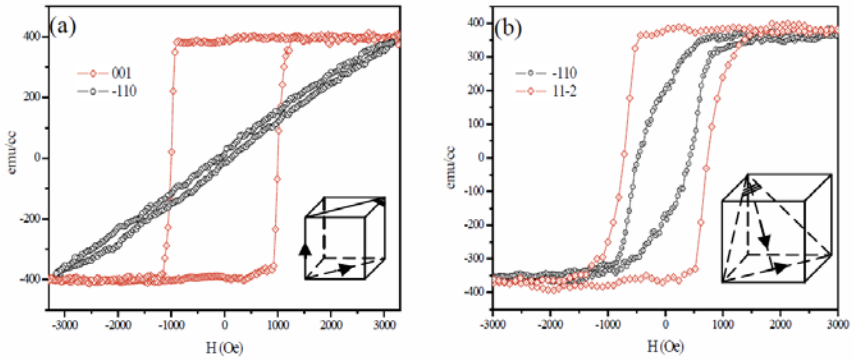

Fig. 4 The room temperature magnetization loops of 90nm Fe_3O_4 films grown at Ts=300°C on (a) Si(110) and (b) Si(111) substrates.

With decreasing film thickness, the magnetization decreases and the coercive field increases. This may be due to the increasing number of antiferromagnetically coupled antiphase domains, the intensive effects of the initial layer, and the relative larger strain for the thinner Fe_3O_4 film. As shown in Fig. 4, both Fe_3O_4 films grown on Si(110) and Si(111) substrates show uniaxial in-plane magnetic anisotropy and the easy axes are determined as [001] and [11-2], respectively. The [001] easy axis of the epitaxial Fe_3O_4(110) film on TiN/Si(110) is opposite to the reported results of Fe_3O_4/MgO(110), which may relate to the relatively larger lattice mismatch between Fe_3O_4 and TiN.

(4). Epitaxial growth of Fe_4N on Si substrates

Fe_4N has been recently predicted theoretically to have nearly perfect negative SP of the conduction current [09Tsu], and a MTJ with Fe_4N/MgO/CoFeB structure yields a much higher room temperature inverse TMR of -75%, than that of Fe_3O_4/MgO/Co (-25%) [08Gre, 09Kom], maybe because of the relatively simpler structure of Fe_4N than Fe_3O_4. We have prepared epitaxial Fe_4N films on TiN buffered Si(001) by reactive sputtering at different substrate temperatures (T_s). The epitaxial relationship is Si(400)[110]//TiN(200)[110]//Fe_4N(200)[110] by XRD. The optimal T_s is 250~350°C. Below 200°C, some other iron nitride phases formed; above 400°C, there is only epitaxial Fe. The HRSTEM image in Fig. 5 (a) shows the good crystal quality of the deposited Fe_4N film. Fig. 5 (b) shows the N K-edge and Fe $L_{2,3}$-edge EELS spectrum. The N/Fe atomic ratio from EELS is 0.20±0.03, which is near stoichiometric. AFM measurements show that the top surface of the epitaxial Fe_4N film exhibits a uniform granular structure. The surface roughness of the Fe_4N film decreases with both T_s and the film thickness, with the rms value of 0.42±0.03 nm for a 20 nm Fe_4N film, which is typically suitable for spintronics applications.

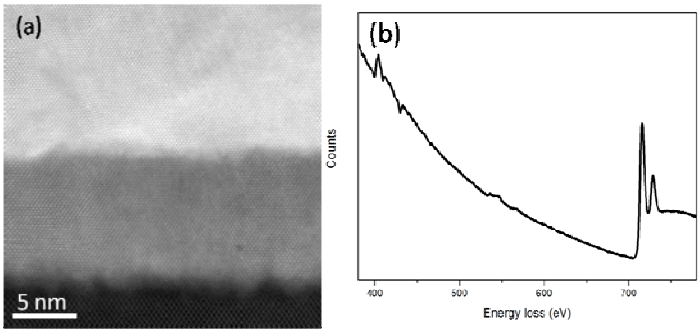

Fig. 5 (a) HRSTEM image of all three layers from bottom to top is Si, TiN and Fe_4N, separately; (b) EELS spectrum on Fe_4N layer.

References of this abstract

[06Yan1] J. J. Yang, PhD Thesis, University of Wisconsin, Madison, WI, 2006.

[06Yan2] J. J. Yang, C.-X. Ji, X. Ke, M. S. Rzchowski, and Y. A. Chang. Appl. Phys. Lett., 2006, 89, 202502.

[07Ji] C.-X. Ji, PhD Thesis, University of Wisconsin, Madison, WI, 2007.

[08Yan] J. J. Yang, A. K. Bengtson, C.-X. Ji, D. Morgan, and Y. A. Chang, Acata Mater., 2008, 56, 1491.

[08Gre] F. Greullet, E. Snoeck, C. Tiusan, M. Hehn, D. Lacour, O. Lenoble, C. Magen, and L. Calmels, Appl. Phys. Lett., 2008, 92, 053508.

[09Kom] Y. Komasaki, M. Tsunoda, S. Isogami, and M. Takahashi, J. Appl. Phys., 2009, 105, 07C928.

[09Has] S. S. A. Hassan, Y. Xu, J. Wu, and S. M. Thompson, IEEE Trans. Mag., 2009, 45, 4357.

[09Tsu] M. Tsunoda, Y. Komasaki, S. Kokado, S. Isogami, C. Chen, and M. Takahashi, Applied Physics Express, 2009, 2, 083001.

[09Yan] J. J. Yang, H. Xiang, C.-X. Ji, W. F. Stickle, D. R. Stewart, D. A. A. Ohlberg, R. S. Williams and Y. A. Chang, Appl. Phys. Lett., 2009, 95, 233117.

[09Ji] C.-X. Ji, A. K. Berta, J. J. Yang, M. S. Rzchowski, H. Xiang, D. Morgan, Y. A. Chang, Appl. Phys. A: Materials Science & Processing, 2009, 97, 73.

[10Xia] H. Xiang, C.-X. Ji, J. Joshua Yang, Y. A. Chang, Appl. Phys. A: Materials Science & Processing, 2010, 98, 707.

[10Won] P. K. J. Wong, W. Zhang, X. G. Cui, Y. B. Xu, J. Wu, Z. K. Tao, X. Li, Z. L. Xie, R. Zhang, and G. van der Laan, Phys. Rev. B, 2010, 81, 035419.

Future Plans

Our future work will be in three areas: (1) We will confirm and extend our tentative STEM EELS observation of Fe_3O_4 at the AlO_x/CoFe interface in inverse TMR junctions. (2) We will optimize the growth of negative spin polarization thin films of Fe_3O_4 and Fe_4N on Si and integrate them into MTJ device structures. (3) We will investigate the atomic structure of the FM/I interface in MTJs based on Huesler alloy intermetallic electrodes. Huesler alloys have, in principle, perfect positive spin polarization, but in practice, MTJs based on Huesler alloys have lower TMR than MTJs based on CoFeB. Our hypothesis is that the interface layers of the Huesler alloy are less well-ordered than the interior of the film. We will develop a layer-by-layer structural order parameter based on quantitative Z-contrast imaging of these films to test this hypothesis.

Publications supported by DOE between 2008 and 2010

(1). Refer to [08Yan] above.

(2). J. J. Yang, C.-X. Ji, Y. Yang, H. Xiang, Y. A. Chang, J. of Electr. Mater., 2008, 37, 355.

(3). J. J. Yang, A. K. Bengtson, C.-X. Ji, D. Morgan, and Y. A. Chang, J. Appl. Phys., 2008, 103, 056102.

(4). C.-X. Ji, J. J. Yang, F. Lu, M. S. Rzchowski, Y. A. Chang, Appl. Phys. Lett., 2008, 92, 022504.

(5). Refer to [09Ji] above.

(6). Refer to [09Yan] above.

(7). Refer to [10Xia] above.

(8). H. Xiang, F.-Y. Shi, M. Rzchowski, P. Voyles and Y. A. Chang, 2010, accepted by Appl. Phys. Lett. for publication.

Structure and Dynamics of Domains in Ferroelectric Nanostructures – Phase-field Modeling

Long-Qing Chen, Department of Materials Science and Engineering, The Pennsylvania State University, University Park, PA 16802; lqc3@psu.edu

Program scope

This program is focused on investigating the domain structures and dynamics in ferroelectric thin films and nanostructures. The main objective is to fundamentally understand the electromechanical effects on ferroelectric domain stability and on mesoscale domain switching mechanisms. The primary material system to be studied is $BiFeO_3$, one of the most promising single-phase candidates for magnetoelectric device applications due to the coexistence of ferroelectricity and antiferromagnetism at room temperature. Specifically, the program is aimed to (1) develop the modeling capability of three-dimensional (3D) ferroelectric domain evolution with spatial distributions and transport of charged defects; (2) study the roles of electric boundary conditions, film thickness, and strain in the formation of ferroelectric and ferroelastic domain structures; and (3) investigate the interactions between domain walls and charged defects as well as their influence on switching mechanisms, remnant polarization, and coercive field. The proposed theoretical research will be carried out in close collaborations with a number of experimental groups who use High Resolution Transmission Electron Microscopy (HRTEM), In Situ TEM with Scanning Probe Microscopy (SPM), or Piezoresponse Force Microscopy (PFM) to characterize the domain structures and dynamics in high-quality ferroelectric $BiFeO_3$ thin films.

Recent Progress

Our recent effort has led to improved capability of our phase-field model for simulating thin films with any crystallographic orientations, for computing local and global polarization, strain, and piezoelectric hysteresis loops under either a local or uniform switching field [2,9,11,12,25], and for modeling domain structure and switching of a ferroelectric island [20,3]. Our phase-field simulations not only played important roles in the interpretation and understanding of observed domain structures by our collaborators but also provided guidance to film growth for improved ferroelectric properties [3,6].

A phase-field model was developed for predicting the 3D domain structures in $BiFeO_3$ films with arbitrary crystallographic orientation, e.g. (001) films on a miscut substrate [21]. As an example, the domain structures of a (001) $BiFeO_3$ film on a (001) STO substrate and a (001) $BiFeO_3$ film on a (001) $SrTiO_3$ with a 4°miscut towards (100) are shown in Fig. 1 for the case of fully compensated boundary conditions on both surfaces. As one can see, the agreement between the phase-field predictions and experimental measured images is quite remarkable.

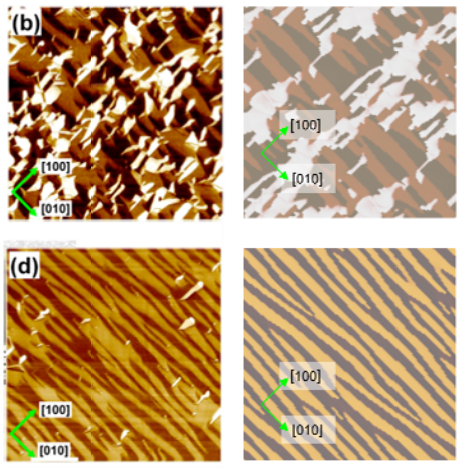

Experiment Simulation

Fig. 1. Comparison between experimentally observed 4-variant and 2-variant domain structures of $BiFeO_3$ films using PFM (left) (Ramesh) and those obtained from phase-field simulations (right).

We studied the ferroelectric domain structures of (001), (101), and (111) oriented epitaxial $BiFeO_3$ thin films and established the correlations between substrate orientation and domain structures, i.e., the number of domain variants present and domain wall orientations [21]. Such information is useful for controlling the domain structures of $BiFeO_3$ thin films. It is shown that the {110} type domain wall orientation in (001) oriented $BiFeO_3$ film also varies with the thickness of a film.

We developed the capability of modeling local switching or domain writing in epitaxial ferroelectric thin films under a piezoresponse force microscopy (PFM) using the phase-field method, in collaboration with Kalinin's group at Oak Ridge [18]. In particular, by combining PFM measurements, analytical theory, and phase-field simulations, we were able to determine basic information with respect to switching such as morphology of a nucleating domain and the activation energy for nucleation. For example, the temperature dependence of ferroelectric domain nucleation in epitaxial films was determined using variable temperature ultrahigh vacuum piezoresponse force spectroscopy and phase-field simulations [12]. It is shown that the weak temperature dependence of nucleation bias indicates an intrinsic nucleation mechanism with minimal contribution of thermal fluctuations. We demonstrated the preference of domain nucleation at a local defect such as a twin boundary [25] or a grain boundary [11]. As an example, we simulated the probing of the spatial distribution of nucleation voltage in a realistic domain structure of PZT epitaxial thin film (Figure 2a) using phase-field simulations. The domain structure was generated under a short-circuit boundary condition starting from an initial paraelectric state with small random perturbations. Each of the colors represents a tetragonal variant. The domain structure consists of a_1 and a_2 domains embedded in a *c*-domain matrix. To understand the correlation between the spatial variation of nucleation voltage and the locations of ferroelectric twin walls and wall junctions, we moved the PFM tip position along the line P-Q-R-S-T-U-V in Fig. 2a. The nucleation voltage as a function of position is recorded in Figure 2(b). It is observed that the nucleation potential is correlated to the number of local twin domain variants.

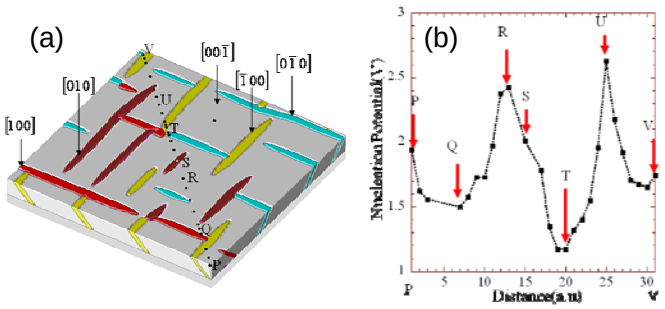

Fig. 2. (a) Domain structure of an (001)-oriented epitaxial $PbZr_{0.2}Ti_{0.8}O_3$ thin film with each color representing a tetragonal variant; (b) Spatial distribution of the nucleation potential along the profile P-Q-R-S-T-U-V obtained from phase-field simulations.

A 3D phase-field model was developed for predicting domain structures in ferroelectric islands attached onto a substrate [20]. It simultaneously takes into account the long-range electric and elastic interactions, substrate constraint, as well as the stress relaxation caused by the surfaces of an island. The simulations demonstrated that the domain structures of ferroelectric islands could be dramatically different from those of continuous thin films due to the change of stress state. The stress distribution inside islands is highly dependent on the aspect ratio of an island. It provides us another degree of freedom to control the domain structures of ferroelectric materials. Indeed, guided by our phase-field simulations, Professor Eom's group at University of Wisconsin developed an approach to stabilizing ferroelastic switching by eliminating the stress-induced instability responsible for back-switching using isolated monodomain $BiFeO_3$ islands on (001) $SrTiO_3$ substrate with 4° miscut [3].

Based on the elastic constants of $BiFeO_3$ from first-principles calculations [7] and existing thermodynamic potential, we calculated the temperature-strain domain stability diagram (Fig. 3)

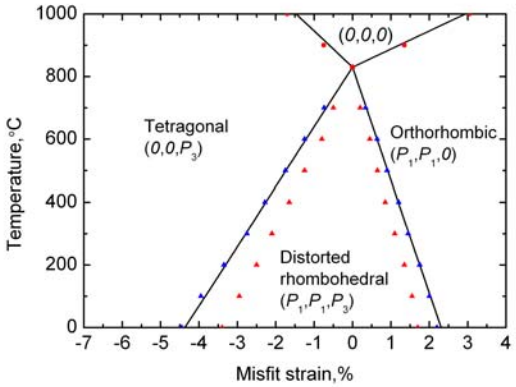

Fig. 3. Phase stability diagram of (001) BFO film as a function of temperature and biaxial strain. Scattered symbols are phase boundaries from phase-field simulations and solid lines are from thermodynamic calculations.

for (001) BFO films using the phase-field method [6]. We discovered a strain-induced morphotropic phase boundary between the strain-distorted rhombohedral phase and a new tetragonal phase. We also show a stable, narrow two-phase region of tetragonal and distorted rhombohedral phase mixture. Both predictions are confirmed by experiments on epitaxially grown (001) $BiFeO_3$ films.

We extended our phase-field model of ferroelectric domain structures by including the stress-field of arbitrary configurations of dislocations [16]. We investigated the influence of dislocations on the ferroelectric hysteresis loops using phase-field simulations. We considered epitaxial ferroelectric $BaTiO_3$ films and found that the hysteresis loops are strongly dependent on the type and density of interfacial dislocations. The dislocations that stabilize multiple ferroelectric variants and domains reduce the coercive field, and consequently, the corresponding remnant polarization also decreases.

In collaboration with Prof. Eom at Wisconsin, we demonstrated that a strain-induced polarization rotation mechanism is responsible for the large change in the out-of-plane polarization of (001) $BiFeO_3$ with biaxial strain while the spontaneous polarization itself remains almost constant [17]. We generalized our results to other epitaxial ferroelectric thin films [10]. For (001)-oriented ferroelectric films with distorted rhombohedral symmetry, strain-induced polarization rotation leads to stronger strain dependences than in films with tetragonal or orthorhombic symmetries while for (111) ferroelectric films with rhombohedral symmetry, the remnant polarization is less sensitive to the strain.

Future Plans

Based on our recent progresses, we will focus on the following tasks in the near future to: (1) understand the relative importance of electrical boundary conditions and strain in determining the domain structures in BFO films at different film thickness (in collaboration with X. Q. Pan at University of Michigan), (2) extend our current phase-field codes of 3D ferroelectric domain structures to study the influence of mobile charged defects on domain stability and switching. In particular, we will design a series of phase-field simulations to understand the relative roles of electrostatic, strain, and domain-wall energies in determining the domain structures in BFO films at different thickness. Our strategy is to first examine some artificial, simple domain structures, e.g. domain structures containing a single domain wall. We will study more realistic 3D inhomogeneous domain structures in BFO by solving the polarization evolution equations starting from the paraelectric phase. We will perform phase-field simulations of transport of oxygen vacancies, electrons and holes in a single BFO domain film on a substrate under a uniform electric field by including interactions between defects with polarization and stress. We will also perform uniform and local switching simulations in the presence of charged defects.

Publications of DOE sponsored research that have appeared in 2008-2010

1. G. Sheng, Y.L. Li, J.X. Zhang, S. Choudhury, Q.X. Jia, V. Gopalan, D.G. Schlom, Z.K. Liu, and L.Q. Chen, *A modified Landau-Devonshire thermodynamic potential for strontium titanate.* Applied Physics Letters, 2010. 96(23).
2. S.V. Kalinin, A.N. Morozovska, L.Q. Chen, and B.J. Rodriguez, *Local polarization dynamics in ferroelectric materials.* Reports on Progress in Physics, 2010. 73(5).
3. S.H. Baek, H.W. Jang, C.M. Folkman, Y.L. Li, B. Winchester, J.X. Zhang, Q. He, Y.H. Chu, C.T. Nelson, M.S. Rzchowski, X.Q. Pan, R. Ramesh, L.Q. Chen, and C.B. Eom, *Ferroelastic switching for nanoscale non-volatile magnetoelectric devices.* Nature Materials, 2010. 9(4): p. 309-314.
4. Y. Wang, J.J. Wang, W.Y. Wang, Z.G. Mei, S.L. Shang, L.Q. Chen, and Z.K. Liu, *A mixed-space approach to first-principles calculations of phonon frequencies for polar materials.* Journal of Physics-Condensed Matter, 2010. 22(20).
5. Y. Wang, S.L. Shang, X.D. Hui, L.Q. Chen, and Z.K. Liu, *Effects of spin structures on phonons in $BaFe_2As_2$.* Applied Physics Letters, 2010. 97(2).
6. R.J. Zeches, M.D. Rossell, J.X. Zhang, A.J. Hatt, Q. He, C.H. Yang, A. Kumar, C.H. Wang, A. Melville, C. Adamo, G. Sheng, Y.H. Chu, J.F. Ihlefeld, R. Erni, C. Ederer, V. Gopalan, L.Q. Chen, D.G. Schlom, N.A.

Spaldin, L.W. Martin, and R. Ramesh, *A Strain-Driven Morphotropic Phase Boundary in $BiFeO_3$.* Science, 2009. 326(5955): p. 977-980.
7. S.L. Shang, G. Sheng, Y. Wang, L.Q. Chen, and Z.K. Liu, *Elastic properties of cubic and rhombohedral $BiFeO_3$ from first-principles calculations.* Physical Review B, 2009. 80(5).
8. E.A. Eliseev, A.N. Morozovska, S.V. Kalinin, Y.L. Li, J. Shen, M.D. Glinchuk, L.Q. Chen, and V. Gopalan, *Surface effect on domain wall width in ferroelectrics.* Journal of Applied Physics, 2009. 106(8).
9. N. Balke, S. Choudhury, S. Jesse, M. Huijben, Y.H. Chu, A.P. Baddorf, L.Q. Chen, R. Ramesh, and S.V. Kalinin, *Deterministic control of ferroelastic switching in multiferroic materials.* Nature Nanotechnology, 2009. 4(12): p. 868-875.
10. Zhang, J.X., D.G. Schlom, L.Q. Chen, and C.B. Eom, Tuning the remanent polarization of epitaxial ferroelectric thin films with strain. Applied Physics Letters, 2009. 95(12).
11. Rodriguez, B.J., S. Choudhury, Y.H. Chu, A. Bhattacharyya, S. Jesse, K. Seal, A.P. Baddorf, R. Ramesh, L.Q. Chen, and S.V. Kalinin, Unraveling Deterministic Mesoscopic Polarization Switching Mechanisms: Spatially Resolved Studies of a Tilt Grain Boundary in Bismuth Ferrite. Advanced Functional Materials, 2009. 19(13): p. 2053-2063.
12. Maksymovych, P., S. Jesse, M. Huijben, R. Ramesh, A. Morozovska, S. Choudhury, L.Q. Chen, A.P. Baddorf, and S.V. Kalinin, Intrinsic Nucleation Mechanism and Disorder Effects in Polarization Switching on Ferroelectric Surfaces. Physical Review Letters, 2009. 102(1).
13. G. Sheng, J.X. Zhang, Y.L. Li, S. Choudhury, Q.X. Jia, Z.K. Liu, and L.Q. Chen, *Domain stability of $PbTiO_3$ thin films under anisotropic misfit strains: Phase-field simulations.* Journal of Applied Physics, 2008. 104(5).
14. G. Sheng, J.X. Zhang, Y.L. Li, S. Choudhury, Q.X. Jia, Z.K. Liu, and L.Q. Chen, *Misfit strain-misfit strain diagram of epitaxial BaTiO3 thin films: Thermodynamic calculations and phase-field simulations.* Applied Physics Letters, 2008. 93(23).
15. P.L. Liu, J. Wang, T.Y. Zhang, Y.L. Li, L.Q. Chen, X.Q. Ma, W.Y. Chu, and L.J. Qiao, *Effects of unequally biaxial misfit strains on polarization phase diagrams in embedded ferroelectric thin layers: Phase field simulations.* Applied Physics Letters, 2008. 93(13).
16. Y.L. Li, S.Y. Hu, S. Choudhury, M.I. Baskes, A. Saxena, T. Lookman, Q.X. Jia, D.G. Schlom, and L.Q. Chen, *Influence of interfacial dislocations on hysteresis loops of ferroelectric films.* Journal of Applied Physics, 2008. 104(10).
17. H.W. Jang, S.H. Baek, D. Ortiz, C.M. Folkman, R.R. Das, Y.H. Chu, P. Shafer, J.X. Zhang, S. Choudhury, V. Vaithyanathan, Y.B. Chen, D.A. Felker, M.D. Biegalski, M.S. Rzchowski, X.Q. Pan, D.G. Schlom, L.Q. Chen, R. Ramesh, and C.B. Eom, *Strain-induced polarization rotation in epitaxial (001) $BiFeO_3$ thin films.* Physical Review Letters, 2008. 101(10).
18. S. Choudhury, J.X. Zhang, Y.L. Li, L.Q. Chen, Q.X. Jia, and S.V. Kalinin, *Effect of ferroelastic twin walls on local polarization switching: Phase-field modeling.* Applied Physics Letters, 2008. 93(16).
19. S. Choudhury, Y.L. Li, N. Odagawa, A. Vasudevarao, L. Tian, P. Capek, V. Dierolf, A.N. Morozovska, E.A. Eliseev, S. Kalinin, Y.S. Cho, L.Q. Chen, and V. Gopalan, *The influence of 180 degrees ferroelectric domain wall width on the threshold field for wall motion.* Journal of Applied Physics, 2008. 104(8).
20. Zhang, J.X., R. Wu, S. Choudhury, Y.L. Li, S.Y. Hu, and L.Q. Chen, Three-dimensional phase-field simulation of domain structures in ferroelectric islands. Applied Physics Letters, 2008. 92(12).
21. Zhang, J.X., Y.L. Li, S. Choudhury, L.Q. Chen, Y.H. Chu, F. Zavaliche, M.P. Cruz, R. Ramesh, and Q.X. Jia, Computer simulation of ferroelectric domain structures in epitaxial $BiFeO_3$ thin films. Journal of Applied Physics, 2008. 103(9).
22. Wang, J., M. Kamlah, T.Y. Zhang, Y. Li, and L.Q. Chen, Size-dependent polarization distribution in ferroelectric nanostructures: Phase field simulations. Applied Physics Letters, 2008. 92(16).
23. Sheng, G., J.X. Zhang, Y.L. Li, S. Choudhury, Q.X. Jia, Z.K. Liu, and L.Q. Chen, Domain stability of $PbTiO_3$ thin films under anisotropic misfit strains: Phase-field simulations. Journal of Applied Physics, 2008. 104(5).
24. Schlom, D.G., L.Q. Chen, X.Q. Pan, A. Schmehl, and M.A. Zurbuchen, A thin film approach to engineering functionality into oxides. Journal of the American Ceramic Society, 2008. 91(8): p. 2429-2454.
25. Jesse, S., B.J. Rodriguez, S. Choudhury, A.P. Baddorf, I. Vrejoiu, D. Hesse, M. Alexe, E.A. Eliseev, A.N. Morozovska, J. Zhang, L.Q. Chen, and S.V. Kalinin, Direct imaging of the spatial and energy distribution of nucleation centres in ferroelectric materials. Nature Materials, 2008. 7(3): p. 209-215.
26. Choudhury, S., Y.L. Li, L.Q. Chen, and Q.X. Jia, Strain effect on coercive field of epitaxial barium titanate thin films. Applied Physics Letters, 2008. 92(14).
27. Chen, L.Q., Phase-field method of phase transitions/domain structures in ferroelectric thin films: A review. Journal of the American Ceramic Society, 2008. 91(6): p. 1835-1844.

SISGR: Intrinsic properties of correlated materials derived from combined nanoscale transport and ultrafast spatio-temporal imaging experiments

PI: David H. Cobden (cobden@uw.edu)
Department of Physics, University of Washington, Box 351560, Seattle, WA 98195
Co-PI: Markus B. Raschke (markus.raschke@colorado.edu)
Department of Physics, and JILA, University of Colorado, Boulder, CO, 80309

Program scope

The complex behavior of many materials relevant for advanced applications is poorly understood, largely because only their macroscopic and long-timescale properties have been extensively studied. These properties can be very different from the intrinsic and often ultrafast dynamic properties of the uniform crystalline material, which in many cases remain largely undetermined. In particular, for transition metal oxides that exhibit non-Fermi-liquid behavior such as magnetism, superconductivity, Mott gaps, and multiferroics, complicated nonuniform strain and domain structure is often present on a submicron scale in the bulk. The aim of this program is therefore to examine such materials under controlled conditions on length scales below those of the characteristic spatial domains and other inhomogeneities, and on time scales comparable with the intrinsic dynamics. Our program combines growth of sub-domain sized crystals with nano-device fabrication, nano-mechanical manipulation, electrical transport, scanning near-field optical microscopy, and ultrafast and nonlinear optical spectroscopy. We are developing approaches for simultaneously measuring transport and optical properties on individual nanocrystals and domains with the necessary control of factors such as strain, magnetic, and electric fields, such as indicated in Fig. 1.

Recent progress

In the first stage we have concentrated on the metal-insulator transition (MIT) in VO_2 as a model system. After intensive study of this relatively simple and stable oxide over five decades using bulk and thin film samples, the combination of domain structure, strain, and the subtlety of strong electron-electron correlation effects has left a controversial picture of the underlying physics and has frustrated technological applications.

We have been investigating individual single-crystal VO_2 nanobeams and platelets, grown in our lab and subjected to varying forms of stress. The MIT is highly sensitive to stress because in its vicinity there are four nearly degenerate phases with different lattice constants, one of which (rutile, R) is metallic. For nanobeams attached to SiO_2 substrates, we studied the formation and spatial evolution of R domains with ~20-nm spatial resolution using infrared scattering-scanning near-field optical microscopy (s-SNOM) [1]. We found that symmetry-selective polarization Raman spectroscopy is effective for distinguishing the monoclinic M1, monoclinic M2, and triclinic T insulating phases at room-temperature, and combining this technique with *s*-SNOM (Fig. 2) we were able to examine the phase composition in detail as a function of temperature. Amongst other things, we showed that the M2 phase always appears during the MIT, and the T phase appears from the M1 phase under tension.

The results illustrate how studying small single crystals presents a new methodical approach in this and similar material systems. The insight provided by the combination of different optical spectroscopies with *s*-SNOM highlights the potential of new nano-optical techniques to isolate and probe the intrinsic optical response of individual nanoscale domains desired for the characterization of the wide range of correlated electron systems.

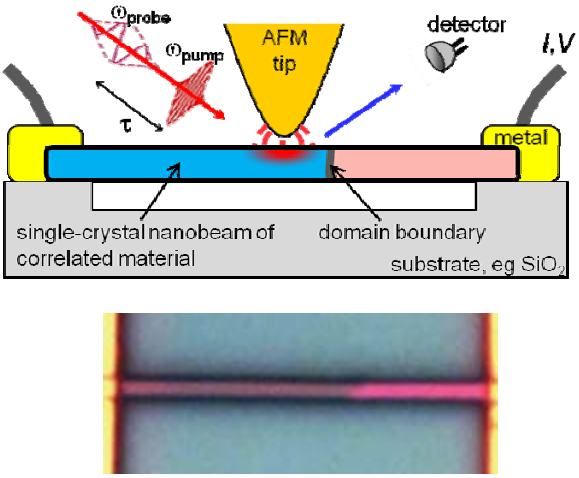

Figure 1. Top: Schematic indicating the combination of dc electrical transport with scattering-scanning near-field optical microscopy (*s*-SNOM) on a single nanobeam sample containing two domains (blue and pink). In *s*-SNOM, the optical antenna properties of an atomic force microscope (AFM) tip allow local probing on the scale of the AFM tip radius, ie, tens of nm. The spatial mapping of the electron and phonon dynamics together with the transport characteristics will provide microscopic insight into the fundamental physics of transition metal oxides and other correlated materials. Bottom: optical image of a suspended VO_2 nanobeam clamped at each end by electrical contacts 20 microns apart. Metallic (gray) and insulating (pink) domains are separated by a single interface. The position of the interface can be controlled by temperature or applying strain along the nanobeam, parallel to the rutile c-axis.

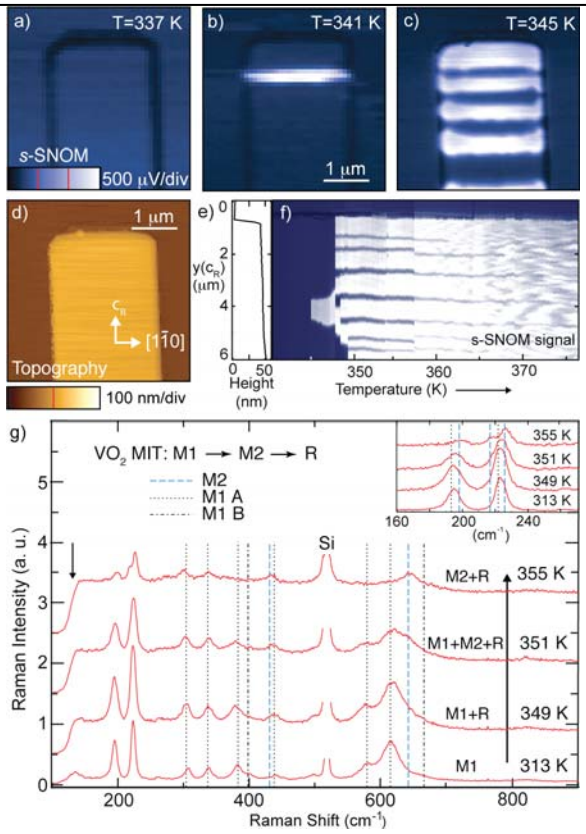

Figure 2. (a-c) s-SNOM images with (d) corresponding topography of a VO_2 crystal (thickness 35 nm) initially in the M1 insulating phase (a) and showing metallic domain formation (b,c) as the crystal is heated. (e,f) Corresponding longitudinal line scan tracing the spatial domain formation on a similar VO_2 crystal with sample heating. The insulating phases are identified by Raman measurements as in (g), finding M1 + M2 + R (351 K) and M2 + R (355 K) intermediate coexistence regimes.

To extend these studies to other materials, we have begun collaborations in chemical synthesis that could allow fabrication of nanocrystalline transition metal oxides, and investigation of effects of shape, stoichiometry and doping, as well as growth of nanocrystals that cannot be produced by physical growth methods. For example, we have synthesized VO_2 rods and formed inverse opals with thermally tunable optical transmissivity with Younan Xia (Washington University) [2]. $LiNbO_3$ is a key material in integrated optics due to its high nonlinear optical coefficient, photostability, and piezoelectric properties. However, few chemical methods have yet succeeded in the large scale synthesis of high quality single crystalline nano-crystals. With Stan Wong (SUNY, Stony Brook) we have chemically synthesized and studied $LiNbO_3$ nanowires [3]. We find rhombohedral-phase $LiNbO_3$ crystals with their long axis corresponding to the crystallographic *c*-axis of high purity and ferroelectric order.

Future plans

- *True phase boundaries and triple point of VO_2.* Further meaurements of the interplay of M1, M2, T and R phases in nanobeams, using a tailor-made nanomechanical stress setup under construction combined with optics, should allow us to establish for the first time the precise location of the M1-M2-R triple point and the slopes of the phase boundaries in the axial-stress-temperature plane. We will also work to disentangle shape and size effects by studying crystals of varying sizes and aspect ratios mounted on substrates in different ways.
- *The metal-insulator interface in VO_2.* We are not aware of previous studies of the properties of an interface between metallic and Mott-insulating states of a single material. We plan to perform the first (combined) transport and photovoltaic measurements on the interface in of VO_2 as realized in our nanobeams (Fig. 1). The photovoltaic properties of such a correlated interface are completely unknown. Questions about the screening length, dielectric function and recombination rate in a homogeneous Mott insulator will be addressed in the absence of strain and grain and domain boundaries for the first time.
- *Other vanadium oxides*. V_2O_3 is also well known for its MIT at ~140 K in the pure stoichiometric form, and is unique in part because its MIT can be tuned to very low temperatures by doping. Studying it presents similar challenges to VO_2, with the addition of low-temperature and magnetic aspects, and we plan to use similar approaches as with VO_2 to investigate it. We have already found that V_2O_3 nanobeams can be produced by reducing our VO_2 nanobeams. We also note that we have observed that the surface of VO_2 can readily be reduced, resulting in a highly conducting layer which we propose to pattern, modify and study using scanning probe techniques including *s*-SNOM.
- *Time-resolved studies.* The phase transitions in transition metal oxides typically involve both electronic correlations and structural changes. Insight into the underlying mechanisms should come from probing real-time dynamics of the transitions in response to ultrafast perturbations. However, as the example of VO_2 demonstrates, despite several time-resolved studies, interpretation of the results has been challenging. Either the experiments had insufficient time resolution, or they were sensitive mainly to only the lattice or the electronic degrees of freedom but not both. In addition, they were carried out on bulk crystals or polycrystalline thin films. We are making preparations to perform femtosecond time- and time-frequency-resolved coherent phonon spectroscopy on individual VO_2 nanocrystals.
- *Coherent phonon studies on $BaTiO_3$.* A variety of potential nanoscale devices are based on the ferroelectric properties of $BaTiO_3$, including piezoelectric actuators and non-volatile memory. Although it has long been considered a prototypical displacive ferroelectric, recent experiments have indicated a more complex mechanism with order-disorder contributions. We plan to perform coherent-phonon spectroscopy probing low-frequency soft-phonon modes phonon associated with the paraelectric-ferroelectric phase transition at T_C=120 °C.
- *$BiFeO_3$*. A polycrystalline film on $LaAlO_3$ substrate will be studied by tip-enhanced phonon Raman spectroscopy to investigate the nano-scale domain formation, extending our corresponding experiments of nanoscale probing of ferroelectric order of $BaTiO_3$. For BFO films on LAO the lattice mismatch stabilizes the otherwise rhombohedral BFO phase in its tetragonal phase. The investigation of the coexistance of both phases at their morphotropic phase boundary and its nanoscale order will provide key insights into the underlying mechanism of this important multiferroic material. The experiments will be extended to pump-probe and coherent-phonon studies to investigate the associated lattice dynamics.
- *Low-temperature s-SNOM:* $YMnO_3$ is a prototypical joint-order multiferroic with an inherent large magnetoelectric effect. The origin of the magnetoelectric interaction is believed to be the interaction of its magnetic and ferroelectric domains. We will extend our previous work,

using the symmetry selectivity of second-harmonic generation in combination with s-SNOM for the simultaneous probing of the topology of both the intrinsic ferroelectric and antiferromagnetic domain order. This allows the investigation of the proposed entanglement of magnetic and ferroelectric domains, providing insights into the origin of the magnetoelectric coupling. Further related low-*T* experiments are planned on the colossal magnetoresistive $La_{1-x}Ba_xMnO_3$ to investigate the domain order associated with the low-*T* metallic to high-*T* insulating transition.

DoE sponsored publications

[1] Andrew C. Jones, Samuel Berweger, Jiang Wei, David Cobden, Markus B. Raschke, "Nano-optical investigations of the metal-insulator phase behavior of individual VO_2 microcrystals", Nano Letters 10, 1574 (2010).

[2] J.-H. Son, J. Wei, D.H. Cobden, and G. Cao, and Y. Xia, "Hydrothermal Synthesis of Monoclinic VO_2 Micro- and Nanocrystals in One Step and Their Use in Fabricating Inverse Opals", Chem. Mater. 22, 3043 (2010).

[3] Alexander C. Santulli, Hongjun Zhou, Samuel Berweger, Markus B. Raschke, Eli Sutter, and Stansilaus S. Wong, "Synthesis of single-crystalline one-dimensional $LiNbO_3$ nanowires", Cryst. Eng. Comm., in press (2010).

Interfacial Thermal Resistance of Carbon Nanotubes

Principal Investigator:
John Cumings
Department of Materials Science and Engineering, University of Maryland, Bldg. 90, Stadium Dr., College Park, MD 20910, email:cumings@umd.edu

Program Scope:
This is a new project, recently funded under the Electron and Scanning Probe Microscopies (ESPM) program with the DoE Office of Basic Energy Sciences. This project seeks to measure the interfacial thermal resistance of carbon nanotubes. Many studies have shown that carbon nanotubes have superlatively high thermal conductivity [1,2], but unfortunately, the scientific understanding about how heat can be transferred into and out of nanotubes is lacking. Some studies have even shown that bulk collections of nanotubes can behave as thermal insulators due to the interface resistance between nanotubes, despite their high intrinsic thermal conductivity [3]. This project will create a comprehensive understanding of the thermal interface conductivity and the mechanisms that drive it by careful measurements of the interfacial resistance in the following three environments: sitting atop an insulating substrate, embedded in a metallic contact and embedded in an insulating contact. More importantly, this project will also produce careful measurements of this interfacial thermal conductivity as a function of temperature. The temperature dependence will allow the thermal conductivity to be cast into a model that includes the inelastic diffuse-mismatch theory of boundary thermal conduction and also the theory of near-field radiation.

Future Plans:
To carry out the measurements, the project will utilize a novel technique for thermal imaging developed in the PI's lab called electron thermal microscopy (EThM), which uses an electron microscope to circumvent the spatial resolution limitations of other thermal imaging techniques [4]. Carbon nanotubes will be dispersed onto substrates and patterned using modern nanofabrication techniques to create measurement samples. These samples will then be imaged using the EThM technique as the nanotubes are heated with nanoscale heating elements. The resulting temperature distributions will be measured and modeled using finite element analysis to extract the interfacial thermal resistance. Analytical theories will be used to understand the results, as described above, and structural characterization of the geometries and interfaces will be performed throughout using transmission electron microscopy. The principles uncovered here for how the interface resistance depends on temperature will produce new models with new understanding. Additionally, the temperature dependence of the interface resistance and the mechanisms that give rise to the temperature dependence will prove invaluable to the future development of the field.

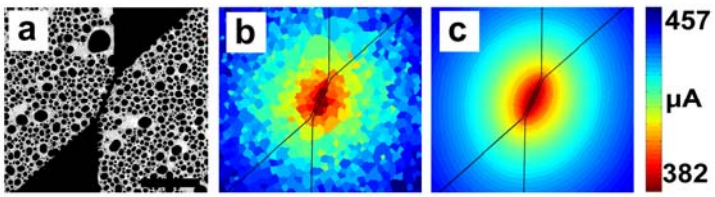

Figure 1. Demonstration of the principle of electron thermal microscopy using a nanoscale heater wire, as described in [4].

Bibliography:
[1] P. Kim et al., Phys. Rev. Lett. 2001, 87, 215502
[2] M. Fujii et al., Phys. Rev. Lett. 2005, 95, 065502
[3] R. S. Prasheret al., Phys. Rev. Lett. 2009, 102, 105901
[4] T. Brintlinger et al., Nano Lett. 2008, 8, 2, 582-585.

Experimental Vector Field Electron Tomography of Magnetic Objects

Marc De Graef (PI), Charudatta Phatak, and Emma Humphrey
degraef@cmu.edu, cd@anl.gov, ehumphre@andrew.cmu.edu
Department of Materials Science and Engineering, Carnegie Mellon University,
Pittsburgh, PA 15213

Program Scope

The increasing complexity of today's materials systems must be accompanied by improvements in the methods used to study those materials. In this project (DOE# DE-FG02-01ER45893), we develop and apply tomographic reconstruction methods to the three-dimensional study of magnetic field distributions around nano-scale magnetic samples. The program consists primarily of an experimental component, supported by a strong modeling component. The modeling component is used to validate experimental observations, by using numerical simulations and analytical evaluation of error propagation. The experimental component makes use of a series of carefully selected samples, used in a series of increasingly more advanced electron microscopes and on a series of length scales.

The resulting 3D magnetic induction maps are to be compared with the results of extensive micromagnetic modeling. The program also further develops methods for the computation of magnetostatic interactions between nano-particles, based on the shape amplitude formalism (developed with prior DOE support).

There are two main program outcomes: an efficient, accurate tomographic reconstruction technique, including an experimental protocol, which can be used in contemporary microscopes to obtain 3D magnetic configurations; and 3D reconstructed magnetic configurations on a number of important magnetic material systems. The experimental and numerical techniques will also be made available to users at the DOE National User Facilities. The main impact of this program is the availability of a novel experimental technique to determine the three-dimensional magnetic induction and the magnetic vector potential in and around nano-scale magnetic objects.

The research is carried out by the P.I., Prof. Marc De Graef, and two graduate students: Charudatta Phatak graduated with a Ph.D. in the Fall of 2009 and is currently working as a post-doctoral researcher at the Argonne National Laboratory (ANL); Emma Humphrey joined the group in 2008, and is currently working towards her Ph.D. degree. The work benefits from a strong collaboration with the group of Dr. Amanda Petford-Long at ANL.

Recent Progress

We have continued our theoretical efforts in the area of magnetostatic properties of and interactions between nanoscale objects. This approach relies on the use of the *shape amplitude*, i.e., the Fourier transform of the object's indicator or shape function (a discontinuous function equal to 1 inside and 0 outside the object). The following list itemizes some of the most important findings of our work (citations are listed at the end of this abstract):

- We have created a new theoretical and numerical approach for the computation of forces and torques between magnetostatically interacting particles of arbitrary shapes. The relevant equations were derived and applied to interacting cubes, octahedra, tetrahedra, and cuboctahedra. The derivation results in both general analytical expressions for forces and torques, as well as expressions that can be implemented in efficient numerical algorithms. This approach allows for the computation of both mechanical and magnetic torques, and may, therefore, become useful in the study of uniformly magnetized interacting particles of arbitrary shape suspended in fluids.

- In collaboration with our colleagues at the Argonne National Laboratory (ANL), we have derived a novel approach to extracting both the chirality and polarity of a magnetization vortex from a single Lorentz Fresnel image obtained with the sample tilted with respect to the optical axis. Nearly all methods in existence today are sensitive to either the chirality or the polarity, but not to both. Our approach is the first one to be sensitive to both vortex characteristics. This method offers direct evidence of the three-dimensional structure of the magnetic vortex and has significant advantages over the more complex methods currently in use.

- In collaboration with Marco Beleggia (Danish Technical University) and David Vokoun (Czech Academy of Science) we have obtained analytical expressions for the demagnetization factors of cylindrical shells and rings with rectangular and square cross-section. These results have enabled us to compute the dipolar coupling integral encoding the magnetostatic interactions between a magnetized cylinder and a thin coating on its lateral surface. This collaboration is currently continuing with a study of magnetostatic interactions in exchange-coupled composite particles.

- We have completed the analytical derivation of the demagnetization factors of the uniformly polarized torus and its derivative self-intersecting (spindle) shapes, the "apple" and the "lemon." Despite the apparent simplicity of the torus shape, these factors have never been derived in closed form before. The derivation consists of both a Fourier space and a real space components and was carried out, for the most part, using the toroidal reference frame. Our results were published in the prestigious Proceedings of the Royal Society, and we contributed a poster on this topic to the *Aharonov Bohm Effect and Berry Phase Anniversary Conference*, held in Bristol in the Fall of 2009.

- We have completed work on a theoretical and numerical technique to compute the mechanical stability and bending energy of a chain of uniformly magnetized particles of arbitrary shape. The approach can deal with chains of arbitrary length and may have applications in a variety of fields, e.g., magnetic colloids, magnetotactic bacteria, etc. Our approach makes use of the shape amplitude formalism when the chain components are close together, and the standard dipolar approach for spacings larger than a threshold distance. This work is currently being written up for publication.

In addition to the theoretical work summarized above, a significant portion of our work has focused on the application of tomographic reconstruction methods to the 3-D analysis of magnetic fields. We apply exit wave reconstruction methods and 3D scalar and vector field electron tomography algorithms developed during the previous portion of the program to determine the magnetic field distribution in and around magnetic materials at the nano-scale. Vector field electron tomography (VFET) extends the concept of conventional tomography to the reconstruction of vector objects (e.g., velocity field, magnetic induction or vector potential).

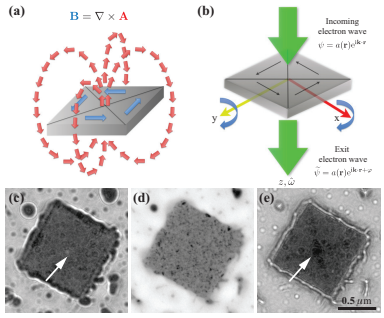

Figure 1: (see text)

The example to the right shows a schematic of a square Permalloy island with a closure domain state (blue magnetization arrows) and four magnetic domain walls (black lines) along with the corresponding magnetic vector potential (red arrows). Note that the vector potential is non-zero outside the particle, despite the fact that the magnetic induction (fringing field) mostly vanishes outside. A typical VFET experimental setup is shown in Fig. 1(b), illustrating the fact that two tilt series around perpendicular axes are needed. The input to the tomographic reconstruction consists of the magnetic phase shift for each sample tilt; this phase shift is obtained from a through-focus series of images, such as the series shown in Fig. 1(c)–(e), acquired for the sample in the conventional orientation, and also a series with the sample flipped upside down (to eliminate the electrostatic phase shift).

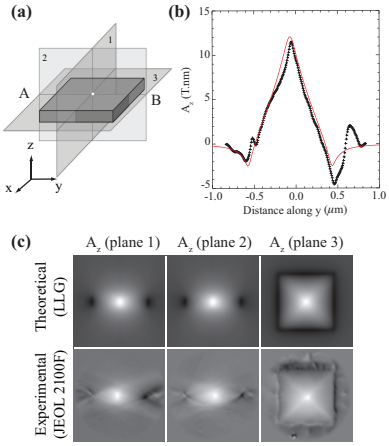

Figure 2: (see text)

Our best result so far is shown in Fig. 2. Fig. 2(a) shows a schematic of the square island; (b) shows a line profile of the theoretical (red) and reconstructed (black) A_z component along the line AB indicated in (a). Fig. 2(c) shows gray scale plots of the theoretical (upper row) A_z component of the vector potential, computed using LLG micromagnetic simulations, and the experimentally reconstructed A_z component (bottom row). It should be noted that both magnitude and shape of the reconstruction are in good agreement with theoretical expectations, except near the edges of the patterned structure. Deviations near the edge of the field of view are due to the limited tilt range leading to a missing wedge of information. The reconstruction was performed on a 256^3 grid with a voxel size of 6.52 nm.

There are two major reasons for these deviations near the island edges: (1) the tomographic tilt series

were recorded only in the tilt range ±70°, which results in an angular wedge of missing information. This introduces reconstruction errors, such as elongations and blurring, which are particularly noticeable in section planes 1 and 2 of Fig. 2(c); (2) since the phase recovery method is an out-of-focus method, there is some loss of spatial resolution due to defocus blurring. In addition, the large defocus values used to acquire the images cause Fresnel interference fringes to appear near the edges of the structures, which, in turn, introduces local errors in the reconstructed phase. When two reconstructed phases are subtracted from each other to recover the magnetic phase shift, slight misalignments introduce errors in the phase separation; these errors then propagate to the 3-D reconstructions. The effects of the missing wedge and the microscope defocus are seen clearly by comparing the two rows of Fig. 2(c). We anticipate that the reconstructions will benefit from the implementation of an iterative reconstruction method, as well as from the use of spherical aberration correction.

Fig. 3(a) shows a 3-D visualization of the magnetic induction near the $x - y$ plane of the square island, clearly revealing the vortex configuration and the 90° domains. Fig. 3(b) shows the 3-D vector potential for the square island; the red arrows indicate the local direction of the vector field. The vector potential has a large z component at the vortex core and gradually decreases towards the edge and reverses direction just outside the edge of the island. The rotational character of the vector potential is clearly observed in this oblique view.

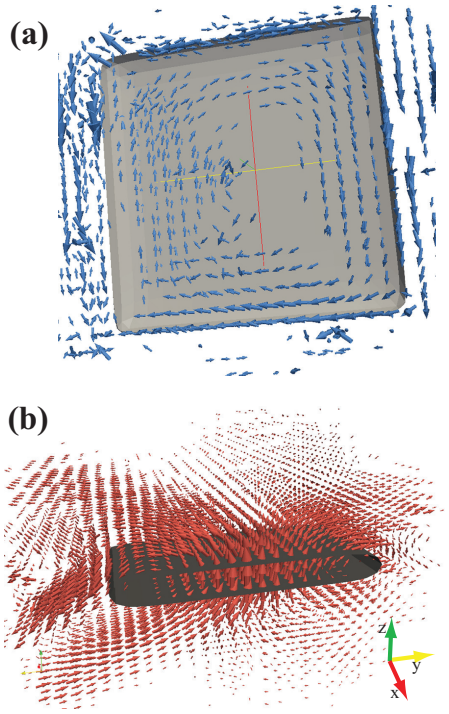

Figure 3: (see text)

Our analysis also shows that C_s correction is absolutely essential for the tomographic reconstructions to be accurate. In a typical Lorentz setup, the spherical aberration of the Lorentz pole piece is in the range of 5 to 10 meters, resulting in a theoretical spatial resolution (at Scherzer defocus) of about 2 nm. In reality, delocalization effects worsen the resolution, since Lorentz images are typically taken far out of focus, so that the actual spatial resolution is closer to 10 or 15 nm. C_s correction will improve the theoretical resolution to well below 1 nm, and will also virtually eliminate delocalization effects, so that the actual resolution becomes nearly an order of magnitude better than what is currently available. We have completed the installation of a new 300 kV FEI Titan microscope, equipped with an image aberration corrector and Lorentz pole piece. Early results confirm that correction of C_s from about 8 meters down to less than 10 mm is possible.

We anticipate that our approach will be used in the near future to gain an understanding of the vector potential and its implications, particularly in areas of magnetism and superconductivity. From the measured vector potential, the magnetic field distributions in and around particles with dimensions in the sub-micron range can be simultaneously derived along with their shape, which will be particularly useful to elucidate magnetostatic interactions between neighboring elements in patterned magnetic arrays.

Future Plans

The PI will spend four weeks (between October 18 and November 12, 2010) working at the Argonne National Laboratory, in the group of Dr. Amanda Petford-Long. During this time, a number of VFET data acquisition experiments will be carried out on the ANL corrected Lorentz microscope (JEOL 2100F). This work will be carried out in collaboration with Charudatta Phatak, a post-doctoral researcher in Dr. Petford-Long's group. To compare the tomographic reconstruction process for different microscopes, we will also carry out VFET observations on the same samples using our own Titan 80-300 corrected microscope; this data will be acquired during the first half of 2011.

We will continue to work on the implementation of a standardized file format for the archival storage of tomographic data. This file format, which has been partially designed with AFOSR support, consists of a series of high level routines (in C++ and IDL) written on top of the public domain Hierarchical Data

Format 5 (HDF5), created at and supported by the University of Illinois. We will work towards making this file format a new standard in the electron microscopy community, in particular for the long-term archival storage of tomographic data.

All 3-D reconstructions thus far have been carried out on a volume of 256^3 voxels; while larger reconstructions can be carried out using the same algorithms, they will need to be optimized for memory use. We will explore an alternative approach using Graphical Processing Units (GPUs), which are designed to deal with large amounts of 3-D data; all reconstruction algorithms will be optimized to run on multiple GPUs. We currently have a 2-GPU system available to us, and the graduate student working on the project will take a training course to learn how to write efficient programs for this hardware. All algorithms created under this program will be made available to the microscopy community and to the DOE user facilities.

Finally, we will continue our exploration of the use of iterative reconstruction methods, since those methods allow for the inclusion of prior knowledge, such as the exact object shape (which can be derived from the scalar reconstruction of the electrostatic potential) and the fact that the magnetization can only be non-zero inside the object. We anticipate that the iterative approach, which starts from the filtered back-projection reconstruction, will allow for a much more accurate reconstruction of the magnetic vector potential and/or the magnetic induction in the presence of a missing wedge.

The personnel currently working on the project consists of the PI, Prof. Marc De Graef, and a graduate student, Emma Humphrey. Emma has the necessary background to be successful at executing the research plan, and is closely monitored by the PI. Dr. Amanda Petford-Long from the Argonne National Laboratory will be a member of the thesis overview committee, thereby guaranteeing a close collaboration and knowledge transfer between the PI's group and ANL.

DOE Sponsored Publications in 2008-2010

- C. Phatak, M. Beleggia, and M. De Graef, "Vector field tomography of magnetic materials: Theoretical development," *Ultramicroscopy*, vol. 108, pp. 503–513, 2008.
- C. Phatak, J.A. Bain, J.G. Zhu, and M. De Graef, "Aberration corrected lorentz microscopy for magnetic recording media," *Microscopy and MicroAnalysis*, vol. 14 (S2), pp. 832–833, 2008.
- C. Phatak, M. De Graef, A.K. Petford-Long, M. Tanase, and A. Imre, "Reconstruction of 3d magnetic induction using Lorentz TEM," *Microscopy and MicroAnalysis*, vol. 14 (S2), pp. 1054–1055, 2008.
- M. Beleggia, D. Vokoun, and M. De Graef, "Demagnetization factors for cylindrical shells and related shapes," *J. Magn. Magn. Mater.*, vol. 321, pp. 1306–1315, 2009.
- M. De Graef and M. Beleggia, "General magnetostatic shape-shape interactions forces and torques," *J. Magn. Magn. Mat.*, vol. 321, pp. L45–51, 2009.
- M. Beleggia, M. De Graef, and Y.T. Millev, "Magnetostatics of the uniformly polarized torus," *Proc. Roy. Soc.*, vol. 465, pp. 3581–3604, 2009.
- C. Phatak, M. De Graef, and A.K. Petford-Long, "Improved phase reconstruction for magnetic materials in a low-aberration environment," *Microscopy and MicroAnalysis*, vol. 15, pp. 1276CD, 2009.
- C. Phatak, E. Humphrey, M. De Graef, and A.K. Petford-Long, "Determination of the 3-d magnetic vector potential using lorentz transmission electron microscopy," *Microscopy and MicroAnalysis*, vol. 15, pp. 134–135, 2009.
- C. Phatak, A.K. Petford-Long, and M. De Graef, "Three-dimensional study of the vector potential of magnetic structures," *Phys. Rev. Lett.*, vol. 104, 253901, 2010.
- N.T. Nuhfer, A. Budruk, and M. De Graef, "Aberration-corrected Lorentz microscopy," *Microscopy and MicroAnalysis*, vol. 16, pp. 142CD, 2010.

LEEM Investigations of Clean Surfaces Driven by Energetic Ion Beams.

C P Flynn and W Sweich, University of Illinois at Urbana, Urbana, IL 61801.

Staff

C P Flynn, Principal Investigator; cpf@mrl.uiuc.edu;
W Swiech, Senior Research Scientist;
E A Sammann, Research Engineer;
Da Wei, Student Programmer.

1 Purpose.

We seek to understand the effects, on clean crystal surfaces, of ion beam irradiation in creating thermal defects (adatoms and advacancies), creating novel steady state configurations, promoting enhanced surface mobility, and in developing new surface nanostructure that evolves with time. To do so we: (1) examine the simplest limiting systems, with extremely clean surfaces; (2) use only self-ions (eg Pt^- on Pt(111)); and (3) work at high temperatures ~ 1000K to create adequate surface mobility. The main probe is a unique low energy electron microscope (LEEM) fitted with a source of negative ions, to permit both spatial and diffraction analysis of structure under the desired conditions.

2 Research Progress.

We pursue three avenues of research, two experimental, and one, theoretical, that permits quantitative interpretation of the experimental discoveries. Important progress has been made in each of these research foci over the course of the past funding year.

1. Surface evolution driven by a self-ion beam. Our work last year revealed: (1) driven *growth* of islands (universal in form, and for both adatom and advacancy islands); and (2) driven *nucleation* of solitary islands near the centers of perfect synthetic pans or mesas, again for both signs of local structure. Both types of observed time evolution arise from the chemical potential μ^* on the terrace created by the ion beam; μ^* itself follows from the theory of linear response in a reacting assembly of driven adatoms and advacancies, as developed on this project (see section 3). Lacking a theory of the nucleation process for these experiments, the interpretation of the observed μ^* for nucleation could go no further. This year we have developed a full theory (see 3) that brings a signficant advance. Specifically, the conditions for nucleation determined earlier now reveal that the excess free energy of the critical island nucleus on Pt(111) is 3.1 ± 0.5 eV.

This is an unusually informative result. In earlier step fluctuation spectroscopy we have determined the free energy per unit length of macroscopic step edges at these high temperatures is 210 ± 10 meV/nm[a]. This small value arises from the proliferation of kinks, whose entropy greatly reduces the line free energy (by a factor ~ 10). But a small island embryo with this perimeter and total energy ~ 3 eV must have a perimeter of 15 nm, which is much too big. We infer that the ragged profiles of macroscopic steps caused by kink proliferation are not relevant to the tight geometry of island embryos or, presumably, to other 2D nanostructures. Researchers elsewhere also have been led to the conclusion that step kinetics are changed for structures of small size[b-d].

2. Ion pulse-LEEM probe studies of kinetics. We are pioneering measurements in which the time evolution of the surface perturbation, created by an ion beam pulse, is examined at delayed times by LEEM. Our tests had shown that the experiments benefit from a high sensitivity per added ion. This is shown in figure 1 where signal strength frozen at low T

from 600 eV irradiation varies rapidly with accumulated dose. Here the signal is a specular peak passed though a 10 μm aperture in the LEEM back focal plane. The signal is reduced with coverage because surface irregularities broaden the specular beam. The response appears at a spot on the channel plate from which it is relayed by an elliptical mirror to a second focus at a semiconductor photomultiplier. For time-dependant processes we have engineered the detection with time resolution < 100 psec (a phosphor with decay time < 60 psec was employed). The system is now stably operational, and is being placed in service to explore a variety of new phenomena sketched in what follows.

Illustrations of attractive new experiments.

(i) Diffusion to step edges of adatoms and advacancies selectively created on terraces by pulses of irradiation (typical time scale msec or less at relevant temperatures);

(ii) Local recombination of adatoms and advacancies (typical time scale μsec or less);

(iii) Regression of island embryos created by irradiation (time scale ~ 10 μsec, see 3);

(iv) Fast recovery of ion beam damage, such as semiconductor surface amorphization, at high T (time scale unknown);

(v) Sublimation of sub-ML adsorbates from beam tuned to the msec time domain;

(vi) Evolution and healing of surface reconstructions following deposition of excess advacancy or adatom populations (time scale unknown); and so on.

Progress in experiments.

Over the summer our initial work has used Pt(111) irradiated with Pt^- in an effort to follow adatom and advacancy relaxation from the beam to sinks at step edges. To date these have failed to detect significant surface-related signals. We infer that much of the signal in Fig 1 is from damage embryos created by the beam, and that the backscatter from adatoms and advacancies must be too small. A constraint is that low beam strength and high temperature are required to avoid island nucleation. The resulting fast kinetics reduce the available coverage per sub-msec cycle to small values, less than 10^{-5} ML.

3. Theory for irradiation of reacting assemblies. Intrinsic to particle irradiation of surfaces is the creation of both advacancies and adatoms so that, given mobility, the surface supports a reacting assembly of mobile antidefects. It is this medium, driven by chemical potential gradients, that provides transport on irradiated surfaces at high temperatures. We have been working through a number of important problems for this regime that include (1) island growth; (2) island nucleation with both energetics and now kinetics; (3) regression of island embryos, both equilibrium and irradiation-induced; (4) sublimation from surfaces including ion beam irradiation; and (5) the analogous problems in 3D of swelling and creep of irradiated reactor materials. We have discovered that these problems can all be solved exactly when the reacting system responds linearly to the driving irradiation. From experiments for Pt^- irradiation of Pt(111) we find that the surface perturbation driven by the ion beam under experimental conditions is indeed small, so that the linear response theory is valid. The mean field variables of the theory are (i) an effective chemical potential μ^* and (ii) an effective defect temperature T^*. These unfamiliar quantities are closely analogous to those that describe the driven electronic steady state in optical semiconductors that undergo photo- or other excitation. Their applications to problems of interest will now be outlined.

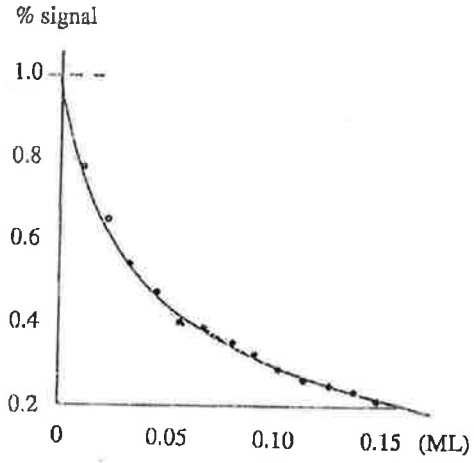

1. Change in signal strength with coverage for 600 eV Pt- irradiation of Pt(111) at 500K.

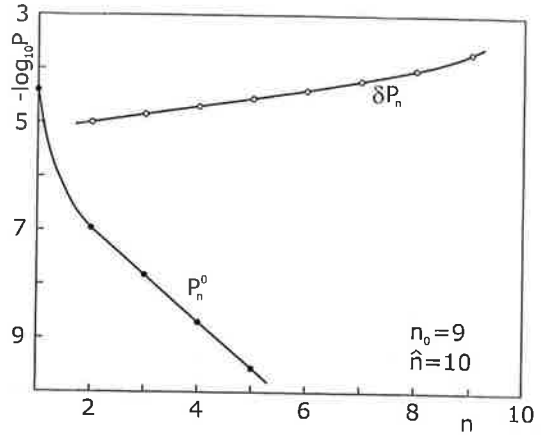

2. Embryo densities in equilibrium, P_n^0 and from the decay chain of an ion impact, δP_n, for a particular case.

.Nucleation. We have devised boundary conditions on μ^* and T^* at step edges, so that the Gibbs Thompson potential at steps can be incorporated. In this way we have been able to solve the problem of nucleation from a 2D reacting assembly with the transport treated within linear response. There is an important 2D signature with a logarithmic dependence on island size that has not previously been evaluated accurately. One can see that a similar signature must determine all synthesis of nanostructures by 2D processes.
Embryo regression. Island embryos, both adatom and advacancy, occur in the reacting assembly both in equilibrium and as entities driven by ion impacts. The latter case sets up a driven decay chain, as beam-induced embryos shrink into the thermal background. We have calculated the populations of embryo sizes n for equilibrium and drive cases to find very different variations, shown in Fig 2, characteristic of logarithmic transport. These differences should become apparent in a future spectroscopy of the fluctuations.
The interaction of irradiation with sublimation. A description of sublimation from linearly responding surfaces at high temperatures has been completed. A paper detailing this work has been written but not yet been submitted for publication. Sublimation is the ultimate high temperature limitation on materials performance A new dimensionless constant that specifies material merit in sublimation has been discovered in this research. As in (ii) above, linear transport from linear response is embedded in a theory that contains the essential nonlinearity of the sublimation process itself. Also of interest is the coupling of these features to the added perturbation of an embedding field of irradiation, so that the effect of irradiation on the high temperature materials limitation is revealed.
(iv) *Swelling from Frenkel pair creation in bulk reactor materials.* Surface irradiation and bulk irradiation are identical problems set respectively in 2 and 3 dimensions. But while many surface problems center on weak perturbations at high temperatures that can be solved using linear response, this is not generally the case for the bulk. The difference is that the equilibrium interstitial concentration is so small that perturbed values may be enhanced by many orders of magnitude. We have developed mean field methods by which inhomogeneous processes like diffusion to sinks can be treated by linear response from the steady state of the uniform mean field response. This brings the response to Frenkel pair creation in reactor metals into the framework of the linear response approach

exemplified above. A radically modified perspective on swelling emerges in which the main idea can be expressed in words. Because, in the creation of Frenkel pairs, the interstitial energy greatly exceeds the vacancy energy, if follows[e] that Frenkel pairs increase the effective chemical potential μ^*. This, in effect, produces an excess effective population of vacancies, that subsequently precipitate out in voids, causing the material to swell.

It remains to be seen whether or not this quantitative perspective can guide materials development that may help to control or eliminate practical problem of reactors.

References

[a] M. Ondrejcek, W. Swiech, M. Rajappan and C.P. Flynn, Phys.Rev B 72, 085422 (2005)

[b] J. Ikonomov, K. Starbova, H. Ibach and M. Giesen Phys. Rev. **B 75**, 245411 (2007).

[c] M. Degawa, T.L. Stasevich, W.G. Cullen, A. Pimpinelli, T.L. Einstein and E. D. Williams, Phys. Rev. Lett. **97**, 080601 (2006).

[d] M. Degawa, T.L. Stasevich, A. Pimpinelli, T.L. Einstein and E. D. Williams, Surf. Sci. **601**, 3979 (2007).

[e] C P Flynn, Phys Rev **B 71**, 085422 (2005).

3 Future plans. As changes of source and crystal are time consuming, we plan first to examine fast sublimation of Ge and Si (see **2** 2(v) above) from the Pt(111) crystal already installed and clean. Proceeding then to a Si substrate we will explore processes **2** 2(iv) and (vi), particularly amorphization, for Si^- on Si(111) and, later, on Si(001). Theory support for the experimental project will be maintained as it selects each new direction.

4 Publications for 2008-2010 on DE-FG02-08ER46549:

Real-time imaging of surface evolution driven by variable energy ion irradiation. W. Swiech, M. Rajappan, M. Ondrejcek, E. Sammann, S. Burdin, I. Petrov and C.P. Flynn Ultramicroscopy, 108, 646 (2008).

Surface islands nucleated by a beam of energetic self-ions. C. P. Flynn, W. Swiech, M. Ondrejcek and M. Rajappan, Phys. Rev. B 77, 045406 1-7 (2008).

Universal growth of islands driven by ion beams. C. P. Flynn, W. Swiech and M. Ondrejcek, Phys Rev B 78, 075420 (2008).

LEEM investigations of surfaces using a beam of energetic self-ions, M. Ondrejcek, W. Swiech, I. Petrov, M. Rajappan and C. P. Flynn, Microscopy Research and Technique **72**, 197 (2009): special issue on 'In situ electron microscopy methods'.

Boundary effects on universal growth of islands driven by ion beam irradiation, C P Flynn, Phys Rev **B 81**, 075426 (2010).

LEEM investigations of ion beam effects on clean metal surfaces: quantitative studies of the driven steady state, W. Swiech, M. Ondrejcek and C. P. Flynn, J Phys: Condensed Matter, **21**, 314021 (2009).

Driven island nucleation in the linear regime, with application to Pt(111), C P Flynn, W Swiech and M Ondrejcek, Phys Rev **B** (submitted).

Island embryo regression driven by a beam of self-ions in the linear regime, C P Flynn, J Phys Condensed Matter (in press).

Electronic States and Transport in Semiconductor Nanostructures

Rachel S. Goldman[1] and Harley T. Johnson[2]
[1]Department of MSE, University of Michigan, Ann Arbor, MI 48109; rsgold@umich.edu
[2]Department of MechSE, University of Illinois, Urbana, IL 61801; htj@uiuc.edu

Program Scope

The understanding of electronic states and transport through dimensionally-confined semiconductor structures is a classic problem in materials physics. Advances in experimental probes and computational methods have led to several important breakthroughs including lattices of quantum dots (QDs) and accurate electronic structure models for nanostructures. Yet, a number of critical fundamental questions regarding the effects of QD size, spacing, and arrangements on the electronic states and transport through semiconductor nanocomposites remain unanswered. For example, how many atoms are needed in a QD for it to cross over from behaving as an impurity state to a band of states? How do point defects and dopants (magnetic and non-magnetic) influence the band structure, the positions of confined states, and transport through ensembles of QDs? How do interface disorder and strain affect the QD electronic states and transport through QD nanocomposites? The program combines leading edge experimental and computational methods to answer these questions and develop a set of design rules for predicting the electronic states and transport in semiconductor nanocomposites.

This program seeks to understand electronic states and transport in dimensionally-confined semiconductor structures. Specifically, the effects of nanostructure size, spacing, and arrangement; strain and interface disorder; and the presence of point defects and dopants on the electronic band structure, confined states, and transport will be investigated using a novel combination of state-of-the-art experiments and theory. Using the probe tip of a scanning tunneling microscope, electronic spectroscopy measurements with nanoscale spatial resolution will be performed on precisely fabricated QD nanocomposites. The imaging and spectroscopy measurements will be performed over a wide temperature range, thereby facilitating measurements of the influence of magnetic dopants on nanostructure confined states and the probing of transport properties over a wide range of electron-phonon scattering conditions. Simultaneously, electronic structure based calculations of confined states and electron transport will be performed using experimentally-determined QD morphologies. Comparisons between experimental and computational studies will reveal both the origins of the electronic states and transport properties in semiconductor nanostructures, as well as the validity of the physical assumptions underlying the experimental and computational techniques.

Recent Progress

In this program, we have generated key results in quantum dot (QD) formation, strain/electronic coupling, measurement and modeling of confined states, and examination of the influence of QDs on thermoelectric and photovoltaic properties of nancomposite structures.

In our initial coupled computational-experimental studies of InAs/GaAs QD confined states, we found that real-space tight-binding calculations could accurately represent the mid-gap states observed using XSTM/STS in small InAs QDs fully embedded in GaAs [Lu, 2006]. The good agreement between calculated and measured densities of states suggested the possibility of using calculations to interpret the origins of fine structure observed in the experimental spectra.

Under the support of the program, advances in our ability to collect experimental spectra have since made it possible to observe spatial dependence of effective electronic properties. For example, we quantified the variation of the effective bandgap with position in InAs/GaAs QDs, demonstrating the key role of composition gradients on the effective bandgaps of both

individual QDs and the surrounding wetting layers, shown in Fig. 1 [Dasika, 2009a]. Our most recent results show that dopant atoms account for additional confined states in InAs QDs. Experimental STS measurements reveal that Mn atoms, particularly near the QD/matrix interface, account for mid-gap states; calculations show that dopant atoms of various kinds lead to screening of the STM tip-induced potential that can also account for confinement [Dasika, 2010].

We have also made several key observations about strain and composition coupling to the electronic structure of individual QDs. Using both first principles atomistic models and effective mass models, we have demonstrated that in the smallest QDs, confined states couple to strain and actually induce localized deformation -- a so-called reverse coupling [Zhang, 2007; Zhang, 2009]. We have also shown that in alloy QDs with highly nonuniform composition, electronic states can be strongly localized with much higher confinement energies than in QDs of uniform composition [Hossain, 2010]. Interestingly, we have shown experimentally that appropriate alloy layers reduce buffer/dot and dot/cap mismatch strain, leading to a high density of large dots [Dasika, 2009b]. Together, these lead to the possibility of producing high densities of large QDs, which are engineered to function as much smaller quantum dots via controlled compositional segregation.

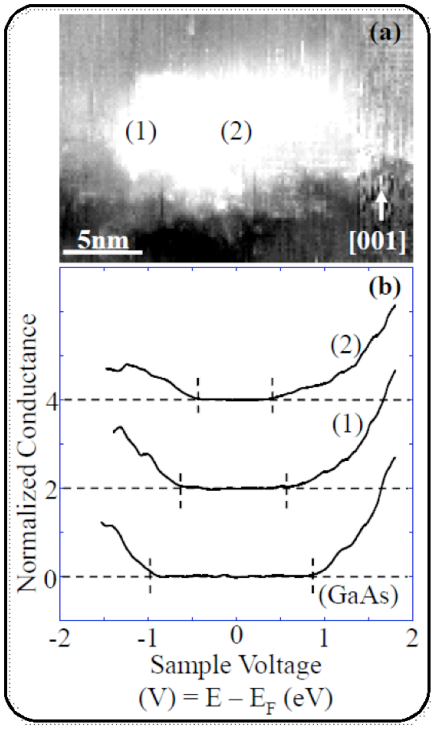

Fig. 1: (a) XSTM image of InAs/GaAs QD. Spatially resolved STS spectra from points (1) and (2) are plotted in (b) in comparison with a region of clean GaAs. The effective valence and conduction band edges are indicated by vertical dashed lines at negative and positive sample voltages, respectively [Dasika, 2009a].

In terms of properties, we have also examined the influence of QDs on the thermoelectric and photovoltaic properties of nanocomposite structures. For example, our calculations of the electrical conductivity, Seebeck coefficient, and thermoelectric power for QD nanocomposites, demonstrating the potential for increasing the power factor by a factor of 3 through the use of QD chains [Yadav, 2009]. Recently, we have established that confined states in InAs QD arrays can lead to enhanced optical absorption and solar cell external quantum efficiency when embedded in the intrinsic region of a standard GaAs p-i-n photovoltaic structure. Experimental measurements and continuum electronic structure calculations are in excellent agreement, and highlight the importance of quantum dot size, shape, and spacing in improving intermediate band solar cell efficiency using quantum dot confined states [Semichaevsky, 2010].

Future Plans

In the renewal program, semiconductor nanocomposites with various QD sizes, spacings, and arrangements will be fabricated using our unique capabilities of focused-ion-beam assisted molecular-beam epitaxy. Using a combination of plan-view and cross-sectional scanning tunneling microscopy (STM), 3D data regarding the structure and electronic states associated with the nanostructures will be obtained. This information will be input into atomistic computational studies of the electronic properties, using a newly developed order(N) real-space tight-binding method to compute local densities of states (LDOS) to be compared directly to scanning tunneling spectroscopy (STS) data. In addition, special structures will be designed for measurements of nanoscale transport through QD nanocomposites using STM-based transport

measurements, namely Ballistic Electron Emission Spectroscopy (BEES). These data will be modeled using a quantum mechanical Monte Carlo calculation of the collector current density including tunneling, scattering, capture, and recombination in the quantum dot heterostructure. The Monte Carlo calculations will be based on accurate 3D representations of the QD heterostructure states determined using k-dot-p Hamiltonian calculations. The close comparison between XSTM/STS and ONTB, and BEES and Monte Carlo transport studies will enable elucidation of the influence of nanostructure sizes, spacings, and arrangements; strain and interface disorder; and the presence of point defects and dopants on the electronic band structure, confined states, and transport. Using the combined expertise of the co-PIs in state-of-the-art nanofabrication, measurements with unprecedented spatial and energy resolution, and multi-scale simulations, a set of design rules for predicting the electronic states and transport in semiconductor nanostructures will be developed.

An important task in this program is Task 3, "Influence of Point Defects and Dopants". In this task, we will consider the effects of defects on spectral and transport properties of neighboring QDs and QD arrays. For this purpose, we will consider both magnetic and non-magnetic dopants. To facilitate these investigations, the Goldman group has expanded the capabilities of its molecular-beam epitaxy (MBE) system by adding a bismuth (Bi) source to the primary MBE. We will soon be interconnecting a dual-MBE Riber system with magnetic dopant cells, including manganese (Mn) and nickel (Ni). The availability of the Bi, Mn, and Ni dopant cells will enable tailoring of dopant concentrations in the direction of film growth, i.e. vertically. To extend this approach to *lateral* tailoring of dopant concentrations, an alternative approach to incorporation of Bi, Mn, and Ni in the plane of QDs is needed. Therefore, we are also searching for funding for the acquisition of an ultra-high vacuum (UHV) mass-filtered focused-ion-beam (FIB) column and a corresponding electron beam column. Both instruments would be attached to an extension chamber of the dual-MBE Riber system, shown in Fig. 2, thereby enabling simultaneous epitaxial growth of QDs; nanoscale spatially-resolved implantation of Bi, Mn, and Ni; and real-time imaging via SEM.

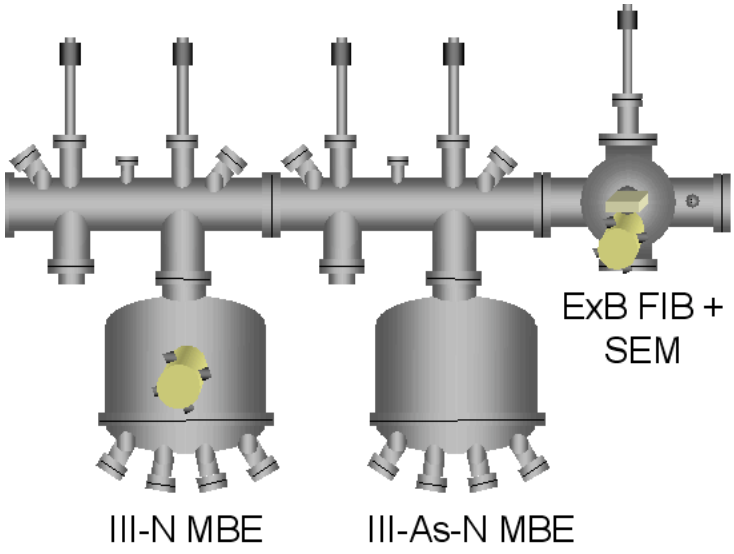

Fig. 2: Diagram of the dual-MBE Riber system, with a proposed FIB/SEM set-up attached to the extension chamber. The left MBE, a RIber 32, is capable of III-N growth and in-situ patterning with a Ga+ FIB. The left MBE is connected via UHV transfer modules to the right MBE, a Riber Compact 21, capable of III-V-N growth. Connected to the transfer modules is an extension chamber housing the proposed UHV mass-selecting FIB for Mn, Ni, and Bi implantation and UHV-SEM for real-time microscopy.

Publications supported by the Grant

[Dasika, 2009a] V. D. Dasika, R. S. Goldman, J. D. Song, W. J. Choi, I. K. Han, J. I. Lee, "Nanometer-scale measurements of electronic states in InAs/GaAs quantum dots" *J. Appl. Phys.* **106**, 014315 (2009).

Support Details: XSTM work (VDD and RSG) supported by the Department of Energy under

grant No. DE-FG02-06ER46339, monitored by J. Zhu. Others are collaborators supported by MEST and KIST in Korea.

[Dasika, 2009b] V. D. Dasika, J. D. Song, W. J. Choi, I. K. Han, J. I. Lee, and R. S. Goldman, "Influence of alloy buffer and capping layers on InAs/GaAs Quantum Dot Formation", Appl. Phys. Lett. **95**, 163114 (2009).
Support Details: XSTM work (VDD and RSG) supported by the Department of Energy under grant No. DE-FG02-06ER46339, monitored by J. Zhu. Others are collaborators supported by MEST and KIST in Korea.

[Dasika, 2010] V. D. Dasika, A. M. Dangelewicz, J.Dibbern, R. S. Goldman, W. A. Morgan, H. T. Johnson, M. Holub, and P. K. Bhattacharya, "Influence of Dopant Atoms on InAs/GaAs Quantum Dot Electronic States," to be submitted (2010).
Support Details: XSTM work (VDD, AMD, RSG) and modeling (WAM, HTJ) supported by the Department of Energy under grant No. DE-FG02-06ER46339, monitored by J. Zhu. Others are collaborators supported by DoD.

[Hossain, 2010] M. Z. Hossain, N. V. Medhekar, V. B. Shenoy, and H. T. Johnson, "Enhanced quantum confinement due to nonuniform composition in alloy quantum dots," *Nanotechnology* **21**, 095401 (2010).
Support Details: MZH and HTJ supported by the Department of Energy under grant No. DE-FG02-06ER46339, monitored by J. Zhu. Others (NVM, VBS) are collaborators supported by NSF.

[Lu, 2006] Jun-Qiang Lu, H. T. Johnson, V. D. Dasika, and R. S. Goldman, "Moments-based tight-binding calculations of local electronic structure in InAs/GaAs quantum dots for comparison to experimental measurements," *Applied Physics Letters*, **88**, 053109 (2006).
Support Details: Published acknowledgement was deficient. This work was supported by the Department of Energy under grant No. DE-FG02-06ER46339, monitored by J. Zhu.

[Semichaevsky, 2010] A. V. Semichaevsky, S. Huang, L. Webster, K. T. Shiu, H. T. Johnson, S. R. Forrest, and R. S. Goldman, "Theoretical and experimental characterization of a p-i-n photovoltaic structure with InAs/GaAs quantum dots," to be submitted, (2010).
Support Details: AVS, SH, LW, HTJ, and RSG supported by the Department of Energy under grant No. DE-FG02-06ER46339, monitored by J. Zhu. Others (KTS, SRF) are collaborators supported by DoD.

[Yadav, 2009] A. Yadav, K. P. Pipe, W. Ye, and R. S. Goldman, "Thermoelectric Properties of Quantum Dot Chains", *J. Appl. Phys.* **105,** 093711 (2009).
Support Details: RSG supported by the Department of Energy under grant No. DEFG02-06ER46339, monitored by J. Zhu. WY supported by NSF. AY and KPP supported by AFOSR.

[Zhang, 2007] X. Zhang, P. Sharma, and H. T. Johnson, "Quantum confinement induced strain in quantum dots," *Physical Review B*, **75**, 155319 (2007).
Support Details: Published acknowledgement was deficient. This work (HTJ) was supported by the Department of Energy under grant No. DE-FG02-06ER46339, monitored by J. Zhu. Others (XZ, PS) are collaborators supported by DoD.

[Zhang, 2009] X. Zhang, M. Gharbi, P. Sharma, and H. T. Johnson, "Quantum field induced strains in nanostructures and prospects for optical actuation," *International Journal of Solids and Structures*, **46**, 3810-3824 (2009).
Support Details: Published acknowledgement was deficient. This work (HTJ) was supported by the Department of Energy under grant No. DE-FG02-06ER46339, monitored by J. Zhu. Others (XZ, MG, PS) are collaborators supported by DoD.

Nanoscale resistive switching behavior of ferroelectric and multiferroic tunnel junctions

A. Gruverman, E. Tsymbal, C.-B. Eom[1]

Department of Physics and Astronomy, University of Nebraska, Lincoln, NE 68588-0111
[1]Department of Materials Science and Engineering, University of Wisconsin, Madison, WI 53706-1595
agruverman2@unl.edu, tsymbal@unl.edu, eom@engr.wisc.edu

Program Scope

The main objective of the proposed research is the experimental implementation and demonstration of polarization-controlled tunneling resistance switching in multiferroic tunnel junctions. This project will employ a set of advanced scanning probe microscopy (SPM) techniques for nanoscale studies of electrical and transport properties. Nearly perfect epitaxial ferroelectric and multiferroic heterostructures containing ferroelectric barriers of only a few unit cells will serve as model systems for the SPM measurements. Experimental studies will be supported by first-principle calculations of perspective material structures. The fundamentally important issues that will be addressed within this research include (a) interplay between the intrinsic and extrinsic switching mechanisms in ultra-thin ferroelectric films; (b) relationship between ferroelectric switching, magnetization state of the electrodes and tunneling electroresistance in FTJs and MFTJs; (c) role of structural defects in the transport behavior; and (d) physical limits to FTJ and MFTJ scaling.

Fabrication of ultrathin ferroelectric heterostructures. Success in achieving this goal critically depends on deployment of model systems with carefully controlled electrical and mechanical boundary conditions and defect structure. We will use atomic layer-by-layer growth controlled *in-situ* monitoring with reflection high energy electron diffraction (RHEED) and atomically smooth and single surface terminated substrates to achieve the necessary atomically abrupt and well-defined interfaces. This provides essential real-time monitoring and feedback to the growth process by pulsed laser deposition, and provides atomic-layer control of epitaxial oxide heterostructures at high oxygen partial pressure (up to 1 Torr).

The electrodes will be chosen to have the best lattice match with the ferroelectric layer and substrate to maintain coherency. As bottom electrodes we will use $SrRuO_3$ [1, 2, 3] for symmetric FTJ and $La_{0.67}Sr_{0.33}MnO_3$ for symmetric MFTJ structures. We will also use $SrRuO_3$ and $La_{0.67}Sr_{0.33}MnO_3$ electrodes in a single FTJ heterostructure for asymmetric electrodes because the asymmetric interface will enhance the difference in tunneling conductance between two different polarization states of ferroelectric layers. Recently, we have successfully grown the $SrRuO_3/BaTiO_3$(10ML) /$La_{0.67}Sr_{0.33}MnO_3$ asymmetric FTJ on TiO_2 single surface-terminated (001) $SrTiO_3$ substrates by atomic-layer-controlled pulsed-laser deposition (PLD). Four-circle XRD reciprocal space mapping shows that the whole heterostructure is fully coherent to the $SrTiO_3$ substrate.

The ferroelectric barrier layer electrically isolates two conducting bottom electrode, and must provide two different polarization states. For the ferroelectric layer we will use $BaTiO_3$ or $PbTiO_3$ along [001] direction among ferroelectrics. Theory predicts a stronger effect for a ferroelectric with higher remnant polarization. Atomically abrupt and well-defined interfaces will alleviate the detrimental effect of interface roughness and local variations in composition on the overall resistance switching behavior of the heterostructures.

Experimental approach. Scanning probe microscopy (SPM) proved to be an indispensable tool for high-resolution characterization of epitaxial ferroic and multiferroics heterostructures and made it a method of choice to address the problems relevant to realization of the FTJ and MFTJ devices [4]. A critically important capability of SPM to be employed in this research is simultaneous direct monitoring of nanoscale polarization along with the electronic behavior of ferroic heterostructures.

The scientific issue that will be addressed in this part of research is examining the feasibility of polarization-controlled resistive switching in the FTJs and determining the scaling effect on transport properties of FTJs. These objectives will be achieved by using a unique combination of state-of-the-art SPM approaches to achieve parallel control of polarization and electrical conductance in atomically smooth epitaxial heterostructures with controlled geometry.

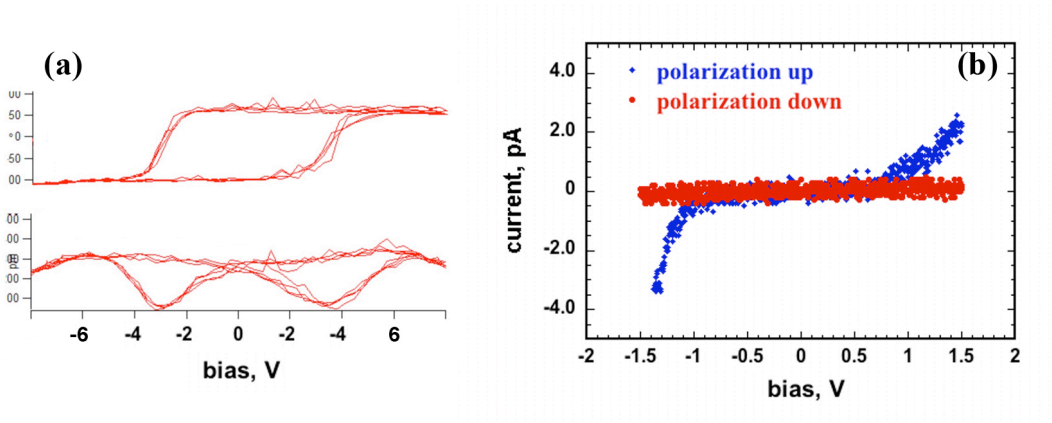

Figure 1. Local hysteresis loops (a) and I-V curves as function of polarization direction (b) measured in the 3-nm thick $BaTiO_3$ film using PFM and C-AFM approaches, respectively.

The inherent property of the FTJ is a drastic change in electric resistance upon polarization reversal under application of a voltage pulse. The most apparent approach to probing the transport behavior is measurements of the current-voltage (I-V) characteristics using conductive AFM (C-AFM), which proved to be instrumental in addressing the transport behavior of complex oxide materials at the nanoscale. Our recent results (Fig. 1) illustrate simultaneous testing of local switching and transport behavior of ultra-thin $BaTiO_3$ films. These results are very exciting as they indicate the predicted behavior of FTJs, namely a strong difference in conductance for two opposite polarizations.

Modeling of Ferroelectric and Transport Properties of FTJs and MFTJs. Finally, modeling of the electronic and transport properties of these heterostructures is a key element in providing a theoretical feedback for experimental results and valuable suggestions for the experimental realization of the FTJs and MFTJs. We will focus on predicting transport properties of FTJs to be fabricated and investigated experimentally. The modeled FTJs will consist of a ferroelectric barrier and two different metal terminals (e.g., an C-AFM tip and a bottom electrode or two different thin-film electrodes) and/or have different interface terminations (such as in the $SrRuO_3/BaTiO_3/SrRuO_3$ FTJs). Our predictive modeling will be aimed at the understanding of the fundamental physical properties of these FTJs, involving the interplay between the conductance and the polarization state in the barrier, and making valuable suggestions for the experimental thrust to realize the proposed FTJs in practice. We will calculate from first principles the conductance of FTJs where perovskite ferroelectrics placed between two different metal electrodes, such as M1/FE/M2, where M1, M2 = $SrRuO_3$, $La_xSr_{1-x}MnO_3$, and Pt, and FE = $BaTiO_3$ and $PbTiO_3$. We will analyze changes in the conductance when the polarization is reversed and will search for combinations of metallic electrodes and ferroelectric barriers and other conditions that provide stronger TER responses. We will extend our first-principles calculations to FTJs with ferromagnetic electrodes, i.e. to multiferroic tunnel junctions, and analyze the interplay between ferroelectricity and magnetism and in support of experimental studies of spin-dependent transport. Our spin-polarized calculations for $SrRuO_3/BaTiO_3/SrRuO_3$ MFTJs with different interface terminations have demonstrated the impact of magnetism of $SrRuO_3$ on electron and spin transport. Figure 8 shows the $\mathbf{k}_{\|}$-resolved transmission across the MFTJs indicating that the transmission varies significantly both with the reversal of the polarization of $BaTiO_3$ (TER) and with the change in the relative magnetization orientation of the electrodes (TMR). This coexistence of TMR and TER effects makes

the MFTJs a four-state resistance device.

Further studies will be aimed at the prediction of transport properties of MFTJs with $SrRuO_3$ and $La_xSr_{1-x}MnO_3$ bottom electrodes and a soft ferromagnetic top electrode, e.g. LSMO. Modeling of LSMO using first-principles calculations is challenging due to substitutional disorder and strong correlation effects. We have recently adopted a method based on virtual crystal approximation [5] and the LDA+U approach [6, 7], which allows predicting properties of a similar compound $La_xBa_{1-x}MnO_3$ (LBMO) reasonably well. We will use these techniques to make predictions regarding MFTJs to be studied experimentally. In particular we will investigate the effect of polarization reversal on tunneling magnetoresistance (TMR) properties in relation with experimental results. We will also explore interface magnetoelectric effects in these systems and correlate them with TMR and TER.

Recent Progress

This is a new program starting after September 1, 2010. There are no technical or scientific results to report at this time.

Future Plans (next 12-18 months)

- Fabrication of $BaTiO_3$-based heterostructures and evaluation of SPM
- SPM studies of polarization retention state in ultra-thin ferroelectric heterostructures
- Investigation of intrinsic switching behavior in ultra-thin ferroelectric films
- SPM studies of switching and transport behavior of ferroelectric tunnel junctions
- Correlation between spatial variations in electric conductance and nucleation sites.
- Modeling of the polarization effect on transport behavior in relevant heterostructures

References

[1] C. B. Eom, R. J. Cava, R. M. Fleming, Julia M. Phillips, R. B. van Dover, J. H. Marshall, J. W. P. Hsu, J. J. Krajewski, and W. F. Peck Jr. "Single-Crystal Epitaxial Thin Films of the Isotropic Metallic Oxides $Sr_{1-x}Ca_xRuO_3$" Science **258,** 1766 (1992).

[2] Q. X. Jia, X. D. Wu, S. R. Foltyn, and P. Tiwari, "Structural and electrical properties of $Ba_{0.5}Sr_{0.5}TiO_3$ thin films with conductive SrRuO3 bottom electrodes", Appl. Phys. Lett. **66**, 2197 (1995).

[3] J.-P. Maria, H. L. McKinstry and S. Trolier-McKinstry, "Origin of preferential orthorhombic twinning in $SrRuO_3$ epitaxial thin films", Appl. Phys. Lett. **76**, 3382 (2000).

[4] Ferroelectrics at Nanoscale: Scanning Probe Microscopy Approach, edited by M. Alexe and A. Gruverman (Springer, 2004).

[5] L. Nordheim, Ann. Phys. Leipzig **9**, 607 (1931).

[6] V. I. Anisimov, J. Zaanen, and O. K. Andersen, "Band theory and Mott insulators: Hubbard U instead of Stoner I", Phys. Rev. B **44**, 943-954 (1991).

[7] A. I. Liechtenstein, V. I. Anisimov, and J. Zaanen, "Density-functional theory and strong interactions: Orbital ordering in Mott-Hubbard insulators", Phys. Rev. B **52**, R5467-R5470 (1995).

Program Title: Nanoscale understanding of exchange bias and spin wave manipulation using advanced MRFM imaging techniques

Principal Investigator: P. Chris Hammel
Address: Department of Physics
191 W Woodruff Ave
Ohio State University
Columbus, OH 43212
email: hammel@mps.ohio-state.edu

Program Scope

Spin waves have been used to transmit information at gigahertz frequencies and for logic operations. These demonstrations of spin wave based logic and communication indicates an attractive approach to information processing and logic that avoids charge transport with its attendant power dissipation.

Exchange bias plays a central role in information storage through its role in giant magnetoresistance magnetic field sensors employed in high density disk drive read heads. However understanding of the detailed mechanisms by which exchange bias couples to and pins the magnetization of an adjacent ferromagnetic layer remain incomplete. This is due in part to the complicating fact that observed behavior represents the spatial average over a nonuniform interfacial layer of the antiferromagnet leading to complex and poorly understood behavior.

There is an intense need for spatially resolved probes of exchange bias fields and magnetic properties in order to unravel the complex phenomena occurring at the buried antiferromagnet/ferromagnet interface at the heart of exchange bias systems. As spin devices become smaller to enable large scale applications, microscopic imaging of spin wave phenomena including interactions with the local fields used to manipulate the spin waves will also be essential.

Below, we describe the demonstration of a novel technique, Ferromagnetic Resonance Imaging (FMRI), that can provide microscopic information regarding static and dynamic properties of buried ferromagnetic structures and interfaces. We have shown that the intense, spatially confined magnetic field of the micromagnetic probe tip mounted on a cantilever can localize the FMR mode immediately under the probe. With this microscope we have demonstrated imaging in ferromagnets with 200 nm spatial resolution and 1 Gauss/$\sqrt{\text{Hz}}$ field resolution in nanoscale volumes.

Recent Progress

The discovery of new phenomena in multicomponent magnetic devices and expanding opportunities for their application is driving rapid growth in nanomagnetics research. There is an intense need for high resolution magnetic imaging tools able to characterize these complex, often buried, nanoscale structures. We have demonstrated a technique, ferromagnetic resonance imaging (FMRI), based on spin wave localization that allows internal fields, interactions and spin wave dynamics in buried ferromagnets to be imaged with nanoscale spatial resolution and spectroscopic precision [1]. Conventional ferromagnetic resonance (FMR) provides quantitative information about ferromagnetic materials and interacting multicomponent magnetic structures with spectroscopic precision and is able to distinguish components of complex bulk samples through their distinctive spectroscopic features, however it lacks the sensitivity to probe nanoscale volumes and has no imaging capabilities. Though the strong interactions in a ferromagnet favor the excitation of extended collective modes, we have shown that the intense, spatially localized magnetic field of the micromagnetic probe tip used in FMRFM can be used to confine the FMR mode immediately beneath the probe. We demonstrate FMR modes confined within volumes with 200 nm lateral dimensions, and straightforward improvements of the approach will allow this dimension to be decreased to tens of nanometers. First images in permalloy films demonstrate that this approach is capable of providing the microscopic images required for the study and characterization of ferromagnets employed in fields ranging from spintronics to biomagnetism. This method is applicable to buried or surface magnets, and, being a resonance technique, measures local internal fields, interactions and spin dynamics with spectroscopic precision.

Scanning probe FMR, or FMRFM, [1–9] is based on Magnetic Resonance Force Microscopy (MRFM) in which magnetic resonance is sensitively detected

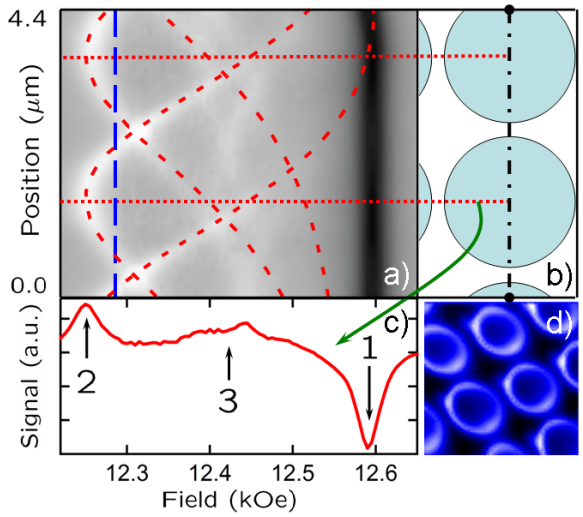

Figure 1: a) FMR spectra recorded by sweeping the external magnetic field and spatially scanning the probe along the one-dimensional trajectory indicated by the dash-dotted line across the diagram of the dots in panel b). The red dashed curves in a) show the analytically calculated dependence of the resonance field on probe position. c) Spectrum from image a) with the tip located over the center of the upper dot [see panel b)]. The first order tip induced resonance (TFR) modes of the dots close to the micromagnetic probe are indicated as peaks 2 and 3, and the first and the second order zero tip field magnetostatic modes are indicated (peak 1 and 4 respectively); these arise from dots far from the probe tip. d) Fixed-field FMRFM image.

through the magnetic dipole force exerted on the cantilever by means of the micromagnetic tip. MRFM has demonstrated the sensitivity necessary to study nanoscale objects. Magnetic resonance imaging requires controllable localization of the excitation that is detected. In a paramagnet MRFM relies on the principles of magnetic resonance imaging (MRI) to define the imaged volume; however the strong interactions amongst spins in a ferromagnet render the principles of MRI inapplicable there. Ferromagnetic resonance imaging requires the localization of spin wave excitations; we will show such probe-induced localized modes as well as their application to scanning probe FMR imaging in ferromagnetic films.

For sufficiently weak probe field $H_p(r,z)$ the magnetostatic mode shape will be negligibly perturbed [2,5] (see Fig. 1). The effect of this or any other spatially varying field on the ferromagnetic resonance will be given by the spatial average $\langle H(r)\rangle$ of the field weighted

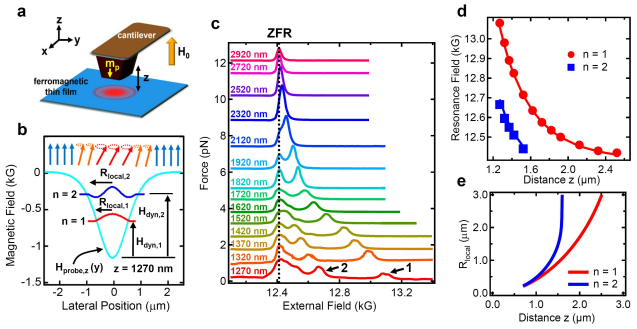

Figure 2: Observation and characterization of localized FMR modes. a) FMRFM geometry. The micromagnetic probe creates a magnetic field "well," shown by the solid light-blue line in b), that localizes spin wave excitations. c) FMRFM spectra of a continuous Py film for different tip-sample separations. The vertical dotted line shows the resonance field for the uniform FMR mode (ZFR). The dependence of the resonance fields on z is shown in Panel d). The solid lines are variational calculations. e) Calculated local mode radius $R_{\mathrm{loc,n}}$ versus z for first two magnetostatic modes obtained using the variational method.

by the mode it is perturbing:

$$\langle H_p(z,r)\rangle_n = \frac{\int_S H_p(r-r',z)m_n^2(r')\,dS'}{\int_S m_n^2(r')\,dS'} \equiv \frac{H_p(r,z)*m_n^2(r)}{\int_S m_n^2(r')\,dS'}$$

where $*$ indicates a convolution and $m_n(r)$ is an unperturbed magnetostatic mode given by a zeroth order Bessel function J_0: $m_n(r) = m_{0,n}J_0(\alpha_n r/R_{\mathrm{dot}})$, where α_n is the n^{th} zero of the Bessel function: $J_0(\alpha_n) = 0$ and R_{dot} is the dot radius. For $z > 2.29\mu$m, the probe field is small and this weak perturbation limit is applicable.

However when the probe field exceeds the transverse dipolar field ($\sim 2\pi M_s[t/R_{\mathrm{dot}}]$ for a ferromagnetic disk of thickness t and saturation magnetization M_s) it will localize spin wave modes. Here we consider a negative probe field that will produce a local field "well." The FMRFM spectra obtained from extended films, shown in Fig. 2c, demonstrate that magnetostatic modes have been confined by the localized magnetic field of the high coercivity (> 2 T) $SmCo_5$ probe tip. These experiments were performed on a $t = 40$ nm thick continuous permalloy (Py) film in an applied field H_0 applied perpendicular to the film plane, anti-parallel to the tip moment m_p, and sufficient to saturate the film. The tip creates a magnetic field "well" in the saturated film as illustrated in Fig. 2b.

We can apply localized mode FMRI as a highly sensitive internal field sensor which can probe not only demagnetizing fields but also internal fields such as

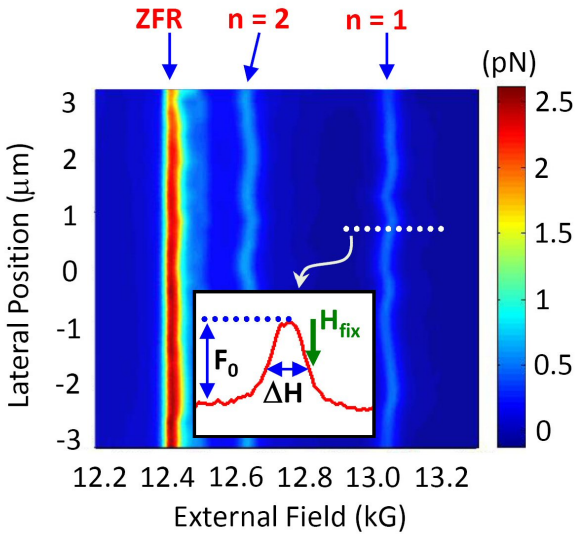

Figure 3: Field-position FMRFM image mapping the variation of the internal field in the Py film through the resonance fields of the n=1 and n=2 localized modes. By setting the external field to $H_{\rm fix}$ as shown spatial variations of the resonance field are detected as variation in the FMRFM force. Images obtained by this method are shown in Fig. 3a.

crystalline/surface anisotropy fields, exchange fields in buried structures and even stray fields from external magnetic sources. Fig. 3a shows a localized-mode field-position FMRI image of the internal fields in our continuous Py film at $z = 1.32\,\mu$m. The lateral variation of the resonance fields of the localized modes (n=1, 2), repeatable from measurement to measurement, reflects variations in the saturation magnetization or crystalline anisotropy, or the film roughness.

A two dimensional internal field image is obtained by setting the external field to $H_{\rm fix}$ where the slope $\partial F/\partial H$ of the FMRFM signal vs. field for the 1$^{\rm st}$ order localized mode is maximum (see the inset to Fig. 3), then monitoring the spatial variation of the force signal. A change of the internal field will shift the position of the resonance peak by δH thus changing the FMRFM force: $\delta F = (\partial F/\partial H)\delta H$.

Fig. 4 schematically illustrates the local mode scheme for ferromagnetic resonance imaging: the well created by the localized magnetic field of the micromagnetic tip confines the ferromagnetic resonance mode. The background image shows the spatial variation of the internal field of the film that is obtained by scanning this confined mode over the sample and monitoring the variation in resonance field of the mode.

Ferromagnetic resonance imaging offers a powerful tool for imaging buried ferromagnetic structures. Because it is based on spectroscopic detection of internal fields, this approach offers high precision measurements of internal fields and interactions as well as spin dynamics with nanoscale resolution.

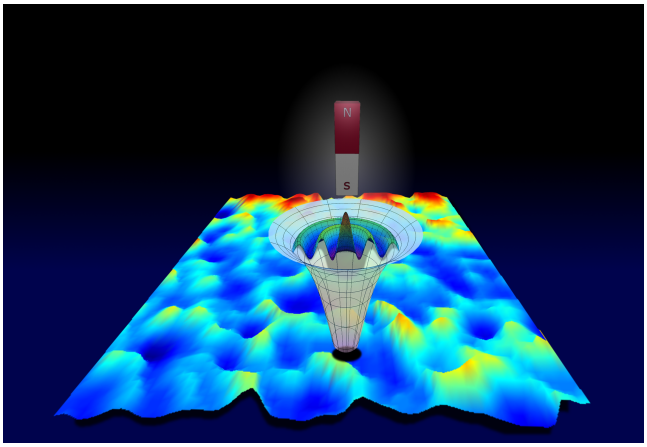

Figure 4: A two dimensional image of the spatial variation of the internal field inside a permalloy film is shown along with a schematic illustration of the ferromagnetic resonance imaging technique. The magnetic field well is indicated in the diagram is created by the localized magnetic field of the micromagnetic tip; this well confines the ferromagnetic resonance mode thus enabling local imaging.

Future Plans

We will apply the microscopic imaging capabilities of FMRI to two systems: exchange bias systems and spin wave logic devices. Improvements in our ferromagnetic resonance imaging technique and hardware will allow resolution to be improved to tens of nanometers. This important milestone provides a mechanism for extracting detailed, quantitative information about magnetic properties of buried ferromagnetic structures and interfaces.

We seek to map the interfacial exchange coupling between an exchange bias antiferromagnet and an adjacent ferromagnet. We will explore intentionally introduced spatial variation of the exchange bias field and map the microscopic naturally occurring variation of exchange bias field in exchange bias systems.

Spin wave device functionality will rely on efficient mechanisms for manipulating spin waves. We will microscopically study spin wave manipulation techniques to understand the interaction mechanisms and improve their ability to control the spin waves.

Publications

[1] I. Lee, Y. Obukhov, G. Xiang, A. Hauser, F. Yang, P. Banerjee, D. V. Pelekhov and P. C. Hammel. "Nanoscale scanning probe ferromagnetic resonance imaging using localized modes." *Nature*, **466**(7308) 845–848 (2010)

[2] Y. Obukhov, D. V. Pelekhov, J. Kim, P. Banerjee, I. Martin, E. Nazaretski, R. Movshovich, S. An, T. J. Gramila, S. Batra and P. C. Hammel. "Local Ferromagnetic Resonance Imaging with Magnetic Resonance Force Microscopy." *Physical Review Letters*, **100**(19) 197601 (2008)

[3] E. Nazaretski, E. A. Akhadov, K. C. Cha, D. V. Pelekhov, I. Martin, K. S. Graham, P. C. Hammel and R. Movshovich. "Ferromagnetic resonance force microscopy studies of a continuous permalloy-cobalt film." *Physica Status Solidi A-Applications And Materials Science*, **205**(8) 1758–1761 (2008)

[4] Y. Obukhov, D. V. Pelekhov, E. Nazaretski, R. Movshovich and P. C. Hammel. "Effect of localized magnetic field on the uniform ferromagnetic resonance mode in a thin film." *Appl. Phys. Lett.*, **94** 172508 (2009)

[5] Y. Obukhov, D. V. Pelekhov, E. Nazaretski, R. Movshovich and P. C. Hammel. "Effect of localized magnetic field on the uniform ferromagnetic resonance mode in a thin film." *Applied Physics Letters*, **94**(17) 172508 (2009)

[6] E. Nazaretski, Y. Obukhov, I. Martin, D. V. Pelekhov, K. C. Cha, E. A. Akhadov, P. C. Hammel and R. Movshovich. "Localized ferromagnetic resonance force microscopy in Permalloy-cobalt films." *Journal of Applied Physics*, **106**(4) 046103 (2009)

[7] E. Nazaretski, D. V. Pelekhov, I. Martin, M. Zalalutdinov, D. Ponarin, A. Smirnov, P. C. Hammel and R. Movshovich. "Detection of localized ferromagnetic resonance in a continuous thin film via magnetic resonance force microscopy." *Physical Review B (Condensed Matter and Materials Physics)*, **79**(13) 132401 (2009)

[8] E. Nazaretski, E. A. Akhadov, I. Martin, D. V. Pelekhov, P. C. Hammel and R. Movshovich. "Spatial characterization of the magnetic field profile of a probe tip used in magnetic resonance force microscopy." *Appl. Phys. Lett.*, **92**(21) 214104 (2008)

[9] E. Nazaretski, K. S. Graham, J. D. Thompson, J. A. Wright, D. V. Pelekhov, P. C. Hammel and R. Movshovich. "Design of a variable temperature scanning force microscope." *Review of Scientific Instruments*, **80**(8) 083704 (2009)

Discovering the Role of Grain Boundary Complexions in Materials

Martin P. Harmer and Christopher J. Kiely
mph2@lehigh.edu chk5@lehigh.edu
Department of Materials Science and Engineering,
Lehigh University, Bethlehem PA 18015

Program Scope

Grain boundaries are inherently an area of disorder in polycrystalline materials which define the transport and various other material properties. The relationship between the interfacial chemistry, structure and the material properties is not well understood. Among the various taxonomies for grain boundaries, *Grain Boundary Complexion* is a relatively new conceptual scheme that relates the structure and kinetic properties of grain boundaries. In this classification scheme, grain boundaries are considered to be distinct three dimensional (the thickness being considerably smaller as compared to the other two dimensions but nonetheless discernable) equilibrium thermodynamic phases abutted between two crystalline phases. The stability and structure of these interfacial phases are dictated by various thermodynamic variables such as temperature, stress (pressure), interfacial chemistry (chemical potential) and most importantly by the energies of the adjoining crystal surfaces. These phases are only stable within the constraint of the adjoining grains. Although these interfacial phases are not stable in bulk form, they can transform from one complexion to another as a function of various thermodynamic variables analogous to the behavior of bulk phases.

A unique trend was observed in an elaborate investigation on the grain growth kinetics in alumina as a function of temperature and interfacial chemistry (figure 1A). All the data points can be grouped in six subsets irrespective of differences in grain morphology, grain boundary chemistry and microstructural evolution. Each of these sets corresponds to a distinct complexion type and has been labeled Type I to VI in order of increasing mobility. It is worth noting that the large variation of the kinetic behavior results from the entropy of the grain boundaries. The enthalpy is relatively constant for each of these complexions. The divergence of the entropic contribution has been illustrated in the microstructures of the various complexions as observed with the aid of HREM and STEM imaging techniques (Figure 1B). A greater degree of the structural disorder can be observed in the boundaries with faster grain growth kinetics (higher entropic contribution).

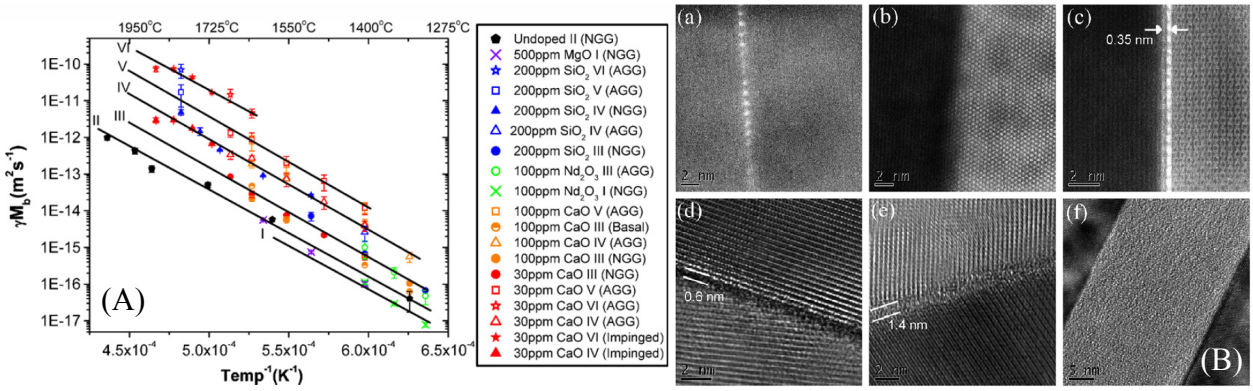

Figure 1: (A) Summary of data for the product of grain boundary mobility and grain boundary energy for normal and abnormal grain growth in a number of doped alumna's. Six different grain growth type (complexions) were identified and marked type I –VI in order of increasing grain boundary mobility; (B) STEM-HAADF and HRTEM images of the 6 different grain boundary complexions. Images (a) through (f) correspond to complexions I through VI respectively.

Examples of different complexions have been reported in various publications. However, a systematic investigation exploring the existence of grain boundary complexions in material systems other than alumina remains to be done. Although the role of interfacial chemistry on grain

boundary complexions in alumina has been addressed, a clear understanding of the underlying thermodynamics governing complexion formation is lacking. Finally, the effects of grain boundary complexions in bulk material properties are widely unknown. Factors above urge a thorough exploration of grain boundary complexions in a range of different materials systems The purpose of the current program is to verify the existence of grain boundary complexion in a range of materials systems, and to characterize their structures, range of stability and selected physical properties.

Recent Progress

1. Grain Boundary Complexions in copper doped titania (TiO_2)

In a preliminary screening experiment a drastic increase in grain growth kinetics was observed in copper oxide doped titania as compared to identically prepared undoped titania samples indicating higher order complexions in the doped material. To identify the complexions in these materials with the aid of electron microscopy copper oxide doped titania bicrystal samples were prepared and annealed in an identical fashion as the screening experiments. The samples were air quenched from the annealing temperatures. HRTEM images revealed a wetting-dewetting transition of copper in the titania grain boundaries (figure 2). The HRETM and STEM-HAADF (high angle annular dark field) images (figure 2 insets) indicated three distinct features in these samples. The thicker films were 5-9 nm thick whereas no film was apparent in the dewetted areas. The transition from the thicker regions was continuous and a thinner film (~ 0.7 nm) was observed in the transition region. It was concluded that the air quenching is not fast enough to preserve the high temperature complexions. These results also indicate that at annealing temperatures a thick wetting copper film might have existed in the titania grain boundaries.

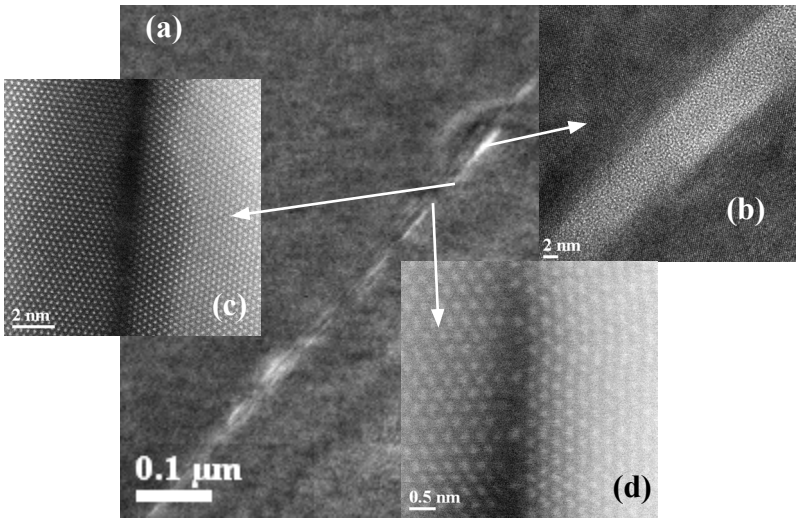

Figure 2: (a) The HRTEM image of a discontinuous Cu-rich intergranular film in titania bicrystal boundary (b) HRTEM image of the thick regions as indicated in (a), (c) STEM-HAADF image of a 0.7 nm thick film in the intermediate region and (d) STEM-HAADF image of the area indicated in (a); no film is observed in this region.

2. Grain Boundary Complexion Transition in Yttria (Y_2O_3)

An enhanced grain growth rate was observed in a 100 ppm calcium oxide doped yttria sample as compared to undoped ytrria fabricated in a similar fashion. Additionally, abnormal grain growth was observed in the doped samples. These results indicate the presence of higher order complexions and possibly multiple complexions in these samples. High resolution microscopy was performed to confirm these postulates. Formation of calcium-rich phases at triple junctions was observed in the samples (figure 3). In areas close to the triple junctions a 0.7 nm thick calcium rich film was observed at an abnormal normal grain boundary interface. EELS analysis was performed to confirm that these films were calcium rich and there is no calcium in the grains. The presence

of a homogeneous 0.7 nm thick film along the abnormal to normal grain boundary indicates that it is a true equilibrium feature. However a better quenching technique (all the samples were furnace quenched, < 1000°C in < 60 seconds) will confirm if this homogeneous film is a high temperature feature or a result of a complexion transition during cooling. Although the normal grains in the doped samples had a higher grain growth rate as compared to undoped samples, no calcium rich layers were apparent in the normal normal grain boundaries of the doped sample (figure 4). Based on the above results, it is considered highly likely that the quenching rate used in current work was not sufficiently rapid to preserve the high temperature equilibrium state. Higher order complexions (type III-VI) existed in both normal normal and abnormal normal grain boundaries. Because of insufficient cooling rates, the grain boundaries most likely underwent complexion transition to a lower order state, resulting in an apparently clean normal normal grain boundary (type I) boundary and a type III or IV complexion for abnormal normal grain boundaries. Bilayer segregation (type III) of calcium oxide in yttria could not be directly imaged by HAADF-STEM imaging because the atomic number of calcium (20) is much lower than yttrium (39).

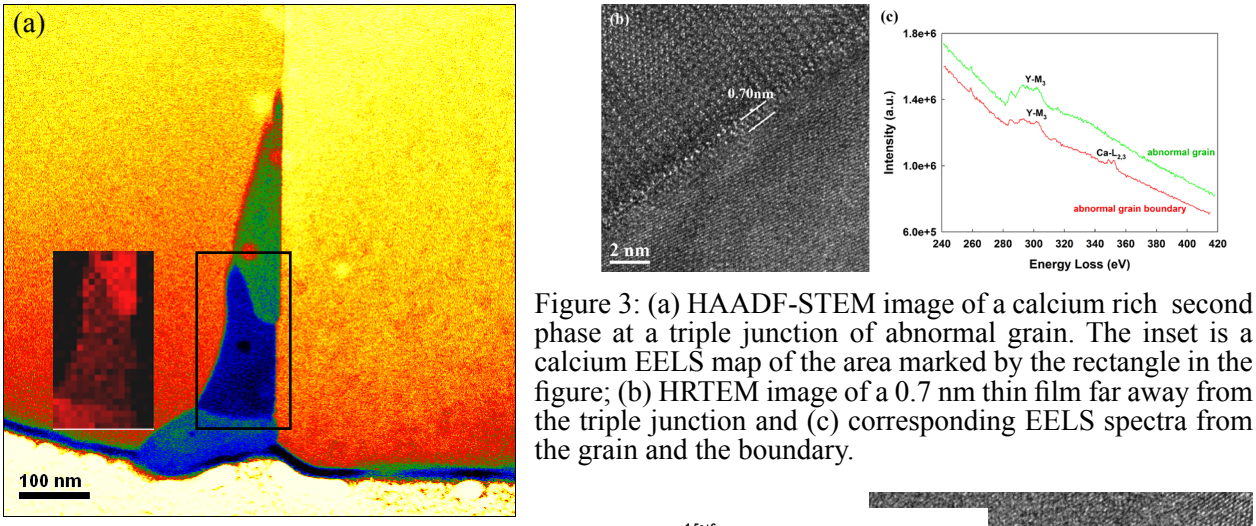

Figure 3: (a) HAADF-STEM image of a calcium rich second phase at a triple junction of abnormal grain. The inset is a calcium EELS map of the area marked by the rectangle in the figure; (b) HRTEM image of a 0.7 nm thin film far away from the triple junction and (c) corresponding EELS spectra from the grain and the boundary.

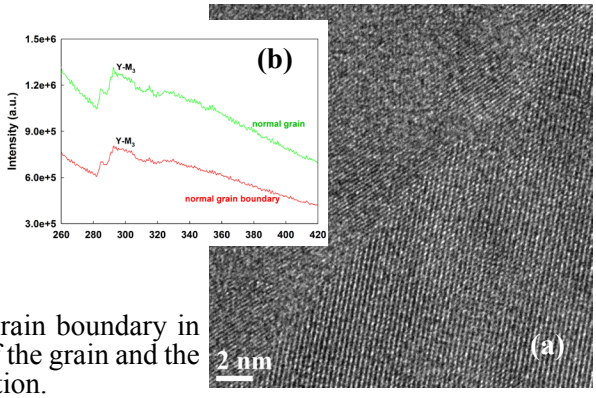

Figure 4: (a) HRTEM image of a normal to normal grain boundary in 100 ppm calcia doped yttria sample, (b) EELS spectra of the grain and the grain boundary, showing no detectable calcium segregation.

3. Grain Boundary Complexions in gold-silicon and aluminum-silicon materials

Grain boundary complexions in Si-Au and Si-Al systems were studied in collaboration with Dr. Jian Luo's group at Clemson University, who is also funded under the DOE-BES-DMSE-ESPM program for their research on GB complexions in silicon. Gold coated silicon bicrystals were annealed at suitable temperatures to facilitate the formation of complexions. Complexion type I has been observed in this material (figure 5). Sub monolayer segregation of gold atoms along the high angle silicon grain boundary was confirmed by STEM- HAADF imaging and STEM EDS (figure 5a and 5b respectively).

Aluminum-silicon samples were prepared by placing an aluminum foil on a diffusion bonded silicon bicrystal and annealing at suitable temperatures. The single crystal surfaces were chosen in

such a fashion that they form a high energy boundary. Although the presence of aluminum in the grain boundaries was not apparent from the STEM-BF images (figure 6a), presence of aluminum atoms in the silicon grain boundaries has been confirmed by STEM EELS (figure 6b). This indicates the presence of a lower order complexion in this material.

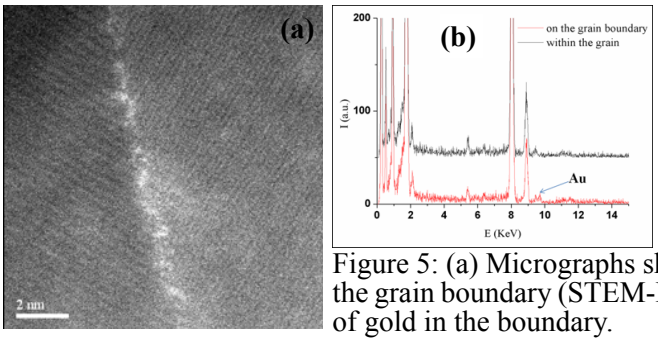

Figure 5: (a) Micrographs showing sub monolayer segregation of Au atoms on the grain boundary (STEM-HAADF); (b) EDS analysis indicating the presence of gold in the boundary.

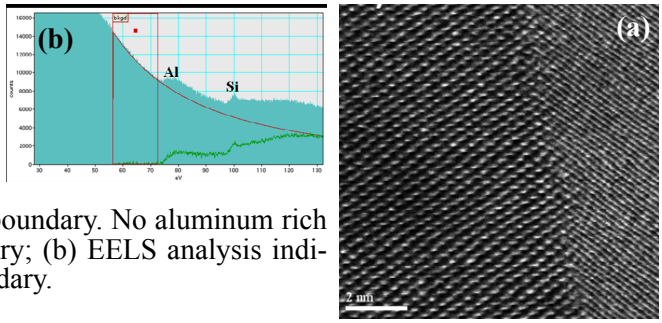

Figure 6: (a) STEM-BF image of a silicon grain boundary. No aluminum rich intergranular film can be observed in the boundary; (b) EELS analysis indicates the existence of aluminum in the grain boundary.

Future Plans

➔We started with the titania bi-crystal experiments since there is not substantial data on the nature of grain boundaries in titania. The bi-crystal experiments are beneficial in orienting the grain boundaries amenable to electron microscopy characterization. Experiments on titania bi-crystals with tungsten oxide doping and copper oxide/tungsten oxide co-doping will be conducted in a similar manner. Another innovative sample preparation method will be adopted involving fabricating samples with a polycrystalline layer sandwiched between two single crystal substrates whose orientation are known. This experiment will provide more realistic sintering conditions as compared to the bi-crystal experiments but the electron microscopy specimen preparation will be more challenging. Additionally, with proper choice of the single crystals we will be able to compare the nucleation and stability of grain boundary complexion transitions directly as a function of boundary energy.

➔We will continue the collaborative work with Dr. Jian Luo's group. Specifically, a detailed high resolution microscopy analysis (both imaging and analytical) will be performed to interpret the grain boundary complexions in the Si – Au and Si – Al material.

Publications

M. Bäurer, S.-J. Shihb, C. Bishop, M. P. Harmer, D. Cockayne and M. J. Hoffmann, "Abnormal Grain Growth in Undoped Strontium and Barium Titanate," Acta Materialia, 58[1] 290-300 (2010).

Shen J. Dillon, Martin P. Harmer and Jian Luo, "Grain Boundary Complexions in Ceramics and Metals: An Overview," JOM, 61[12] 38-44 (2009).

Martin P. Harmer, "Interfacial Kinetic Engineering: How Far Have We Come Since Kingery's Inaugural Sosman Address?," Journal of the American Ceramic Society, 93[2] 301-317 (2010).

Jian Luo, Shen J. Dillon, and Martin P. Harmer, "Interface Stabilized Nanoscale Quasi-Liquid Films", Microscopy Today, 17[4] 22-26 (2009).

Single Atom and Molecule Manipulation and Its Application to Nanoscience and Technology
(DE-FG02-02ER46012)

Saw-Wai Hla
Ohio University
Clippinger 251B, Physics & Astronomy Department, Ohio University, Athens, OH 45701.
Email: hla@ohio.edu

1. Program Scope

We utilize the unique capabilities of scanning tunneling microscope atom/molecule manipulation schemes combined with tunneling spectroscopy methods to investigate nanoscale phenomena in molecular charge transfer complexes on metallic surfaces. When two types of molecules having opposite tendency to donate and accept electrons are put together, the electronic charge can transfer from one molecule to another. The charge transfer process alters the electronic states of materials, and thus it can be used to engineer novel materials having a wide range of properties. In this project, we investigate charge transfer between donor and acceptor type single molecules to develop nanoscale materials having superconducting[1], semiconducting[2] and magnetic[3] properties for nanoelectronics, for charge and energy transfer applications, and for information transport at the nanoscale.

2. Recent Progress

We have achieved a significant progress in the area of charge transfer based nanomaterials. In particular, we have been able to form an ordered $(BETS)_2$-$GaCl_4$ molecular layer on Ag(111) surface, which exhibits a superconducting gap in just one sheet of molecular packing. $(BETS)_2$-$GaCl_4$ is a D_2A type molecular charge transfer system (D = donor, A = acceptor) and each BETS molecule transfers 0.45 electronic charge to $GaCl_4$. The charge transfer results in half-filled molecular orbitals in BETS and thus it becomes metallic. Below a critical temperature, $(BETS)_2$-$GaCl_4$ shows superconductivity. Interestingly, the superconducting gap can still be detected down to just four pairs of molecules in these materials, and thus making it the smallest superconductor ever study to date.

In another work, we show that the spin of Co atom in a TBrPP-Co molecule is delocalized and redistribution of spin density from the Co atom to the organic ligands of the molecule occurs due to an interfacial charge transfer process. As a result, the entire molecule becomes magnetic. This effect is reflected in the Kondo resonance, which is observed over the entire molecule. Brief descriptions of these works are described in the proceeding paragraphs.

2.1 *Superconductivity in Just Four Pairs of $(BETS)_2$-$GaCl_4$ Molecules*

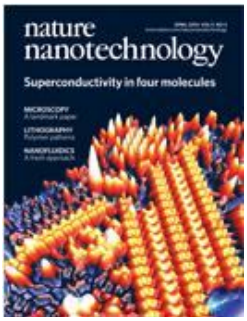

Nature Nanotechnology 5*, 261-265 (2010) by* K. Clark, A. Hassenien, S. Khan, K.-F. Braun, H. Tanaka, & S.-W. Hla [**DOE-ER46012-24**]

Abstract: How small can a sample of superconducting material be and still display superconductivity? This question is relevant to our fundamental understanding of superconductivity, and also to applications in nanoscale electronics because Joule heating of interconnecting wires is a major problem in nanoscale devices. It has been shown that ultrathin layers of metal can display superconductivity[4-6], but any limits on the size of superconducting systems remain a mystery. $(BETS)_2$-$GaCl_4$, where BETS is bis(ethylenedithio)tetraselenafulvalene, is an organic superconductor[7], and in the bulk it has a superconducting transition temperature T_c of approximately 8 K and a two-dimensional layered structure that is reminiscent of the high-T_c cuprate superconductors[8,9]. Here, we use scanning tunneling spectroscopy to show that a single layer of $(BETS)_2$-$GaCl_4$ molecules on an Ag (111) surface displays a superconducting gap that increases exponentially with the length of the molecular chain. Moreover, we show that a superconducting gap can still be detected for just four pairs of $(BETS)_2$-$GaCl_4$ molecules. Real-space spectroscopic images directly visualize the chains of BETS molecules as the origin of the superconductivity.

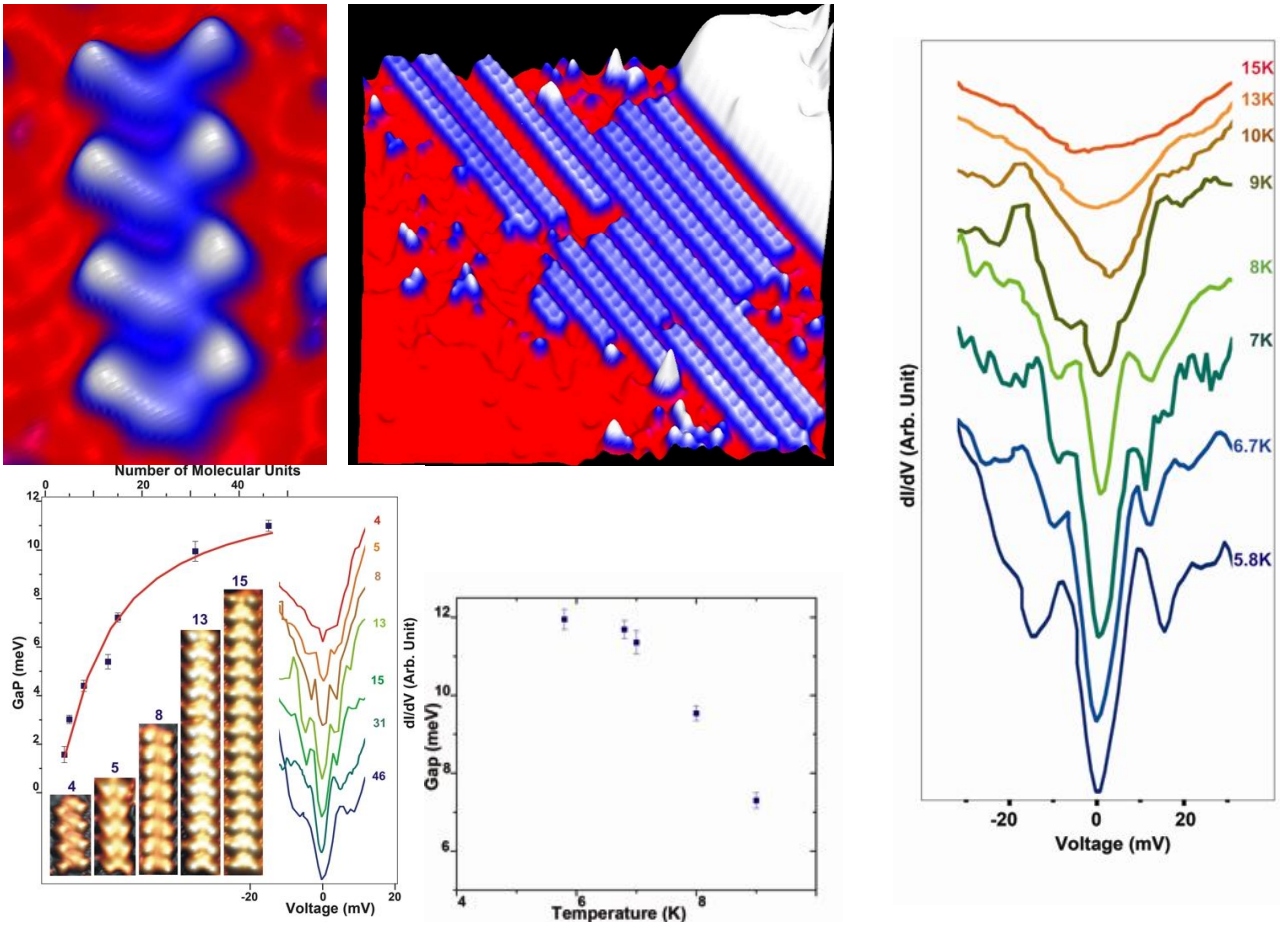

Fig. 1. Clockwise from top-left: An STM image of four pairs of $(BETS)_2$-$CaCl_4$ molecules that still exhibit superconducting gap (0.87 nm wide, 3.5 nm long), superconducting molecular wires grown on a Ag(111) surface, superconductor-metal transition is observed above 10K substrate temperature, superconducting gap versus temperature plot, and the superconducting gap exponentially increases with the length of the molecular wires.

2.2 *Spatially Extended Kondo State in Magnetic Molecules Induced by Interfacial Charge-Transfer*

Physical Review Letters *(in press) by* U.G.E. Perera, H. Kulik, V. Iancu, L. G. G. V. Dias da Silva, S. E. Ulloa, N. Marzari, & S.-W. Hla. [**DOE-ER46012-25**]

Abstract: An extensive redistribution of spin density in TBrPP-Co molecules adsorbed on a Cu(111) surface is investigated by monitoring Kondo resonances at different locations on single molecules. Remarkably, the width of the Kondo resonance is found to be much larger on the organic ligands than on the central cobalt atom --reflecting enhanced spin-electron interactions on molecular orbitals. This unusual effect is explained by means of first-principles and numerical renormalization-group calculations highlighting the possibility to engineer spin polarization by exploiting interfacial charge transfer.

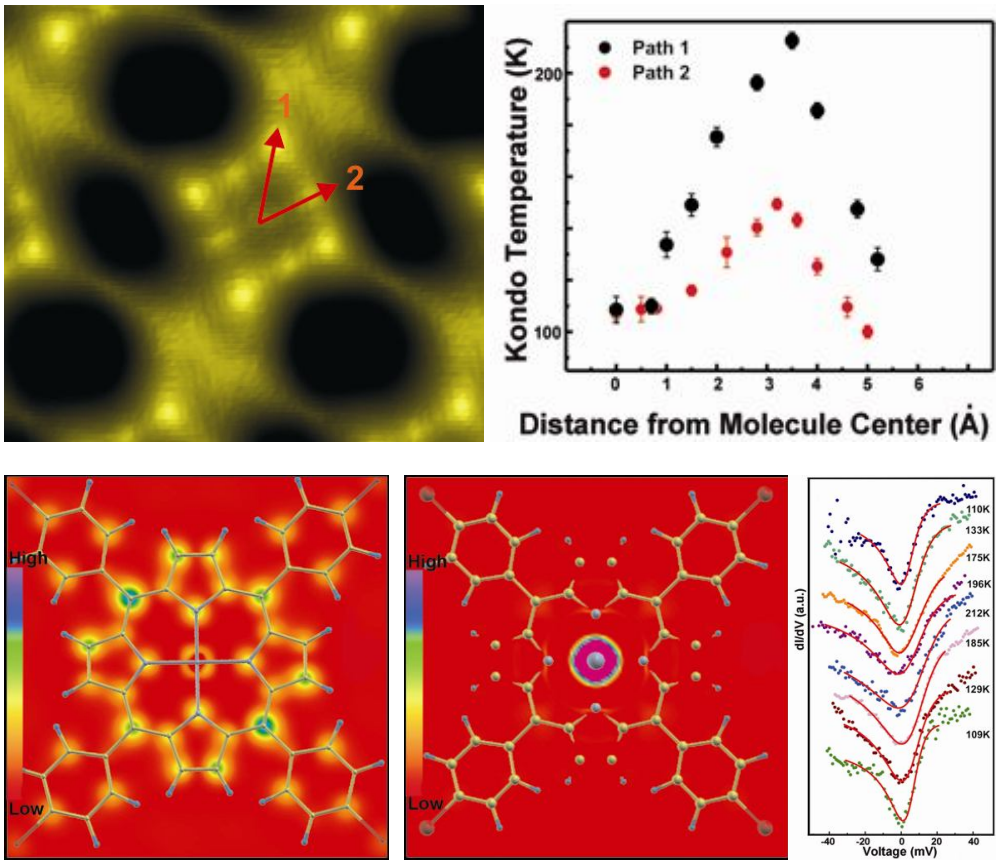

Fig. 2. Clockwise from top-left: An STM image of a TBrPP-Co molecule inside a self-assembled molecular net work on Cu(111), the increase in Kondo temperature is observed on porphyrin ring when measured along the path 1 and 2, a series of dI/dV tunneling spectroscopy curves measured along path 1 showing a Kondo resonance, a DFT calculated image of a gas phase TBrPP-Co reveals that the spin density is concentrated at the Co atom caged at the molecule's center, and when the molecule is adsorbed on Cu(111), the spin density is delocalized and spread throughout the porphyrin ring of the molecule.

3. Future Plan

Following the achievement of molecular superconductivity, we are investigating the proximity effect, and the Cooper pair formation mechanism in this unconventional superconductor. We are also investigating charge transfer processes in other molecular complexes involving various metallo organic molecules such as porphyrin, and manganocene to search for novel nanoscale materials.

4. References

[1]. K. Clark, A. Hassanien, S. Khan, K.-F. Braun, H. Tanaka, and S.-W. Hla. ***Nature Nano*** **5**, 261-265 (2010).
[2]. F. Jäckel, U.G.E. Perera, V. Iancu, K.-F. Braun, N. Koch, J.P. Rabe, & S.-W. Hla, ***Phys. Rev. Lett.*** 100,126102 (2008).
[3]. U.G.E. Perera, H. Kulik, V. Iancu, L.G.G.V. Dias da Silva, S.E. Ulloa, N. Marzari, & S.-W. Hla. ***Phys. Rev. Lett.*** (in press).
[4] S. Qin, J. Kim, Q. Niu & C.-K. Shih. Science 324, 1314-1317 (2009).
[5] M.M. Özer, Y. Jia, Z. Zhang, J.R. Thompson & H.H. Weitering. *Science* **316**, 1594-1597 (2007).
[6] T. Zhang et al. *Nature Phys* (2010).
[7] S. Uji et al. *Nature* **410**, 908-910 (2001).
[8] H. Kobayashi et al. *Synthetic Metals* **70**, 867-870 (1995).
[9] H. Kobayashi et al. *Chem. Letters* **9**, 1559-1562 (1993)

5. DOE Sponsored Publications in 2008 – 2010

1. U.G.E. Perera, H. Kulik, V. Iancu, L.G.G.V. Dias da Silva, S.E. Ulloa, N. Marzari, & S.-W. Hla. *Spatially Extended Kondo State in Magnetic Molecules Induced by Interfacial Charge-Transfer*. ***Phys. Rev. Lett.*** (in press). **[DOE-ER46012-25]**

2.* K. Clark, A. Hassanien, S. Khan, K.-F. Braun, H. Tanaka, & S.-W. Hla. *Superconductivity in Just Four Pairs of (BETS)2-GaCl4 Mo*lecules. ***Nature Nanotechnology*** **5**, (2010) 261-265.
[DOE-ER46012-24]

3. K.-F. Braun, & S.-W. Hla, "Charge Transfer in the TCNQ-Sexithiophene Complex", ***J. Chem. Phys.*** **129** (2008) 064707. [**DOE-ER46012-23**]

4. S.-W. Hla, "Scanning Tunneling Microscope Atom and Molecule Manipulations: Realizing Molecular Switches and Devices", ***Jap. J. Appl. Phys.*** **47** (2008) 6063-6069. [**DOE-ER46012-22**]

5. F. Jäckel, U.G.E. Perera, V. Iancu, K.-F. Braun, N. Koch, J.P. Rabe, & S.-W. Hla. *Investigating Molecular Charge Transfer Complexes with a Low Temperature Scanning Tunneling Microscope*. ***Phys. Rev. Lett.*** **100**, (2008) 126102. [**DOE-ER46012-21**]

Media news: www.phy.ohiou.edu/~hla/HotResearch.html

Sources and Control of Nucleation and Growth in Ferroelectric and Phase-Change Memory Devices

Bryan D. Huey
University of Connecticut
Department of Chemical, Materials, and Biomolecular Engineering
Unit 3136, 97 N. Eagleville Rd, Storrs, CT 06268
860 486 3284, bhuey@ims.uconn.edu

Scope

This effort is aimed at investigating and leveraging the causes and effects of nucleation vs. growth mechanisms during switching in solid state memory devices in order to improve device speeds, reliability, and energy efficiency. The work focuses on two systems, polarization switching in ferroelectric thin films, and phase changes in chalcogenide films. The project leverages high speed scanning probe microscopy methods to obtain movies of switching events during *in situ* biasing and/or pulsing, thereby allowing nucleation and growth to be identified, mapped, quantified, and related to film microstructure along with other engineered defects.

Recent Progress

This is a new effort with DOE. Preliminary research has emphasized the development of a capability to measure and quantify growth during switching with spatial resolution less than 400 nm^2. The growth statistics indicate a strong correlation between nucleation and growth mechanisms, and the switching speed as well as directionality.

For example, Figure 1 sketches a SPM probe biasing a thin film in a data storage device, initiating switching in an area beneath the tip (red) that progressively grows with poling time (green to yellow). Growth rates can vary nonlinearly with position and direction, leading to asymmetric growth patterns. Crucially, these growth patterns are deterministic, establishing essentially the same pattern in repeated switching events presuming the same initial conditions are met (the film is repoled to the original configuration). Such growth patterns are the emphasis of the work presented here.

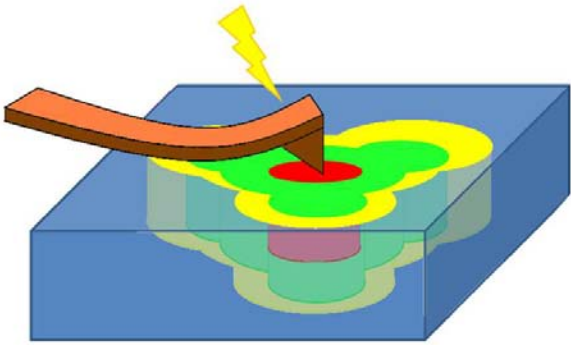

Figure 1: High Speed SPM during *in-situ* poling allows progressive steps during switching to be efficiently monitored, thereby allowing nucleation sites and times to be identified, and especially growth rates and directions to be calculated.

For instance, Figure 2 presents a series of ten 2μm by 2μm images extracted from a movie of more than 50 images. These was acquired with a simultaneous negative bias applied to the scanning probe with respect to a grounded back electrode for a (001) epitaxially grown PZT thin film. A cross-hatched pattern is apparent identifying the positions of in-plane (90º) domains, while dark contrast highlights the development of 180º domain walls between (001) and (00-1) polarizations. Nucleation clearly occurs at the intersection of 90º domains, while the growth that follows is absolutely influenced by the in-plane domain interfaces.

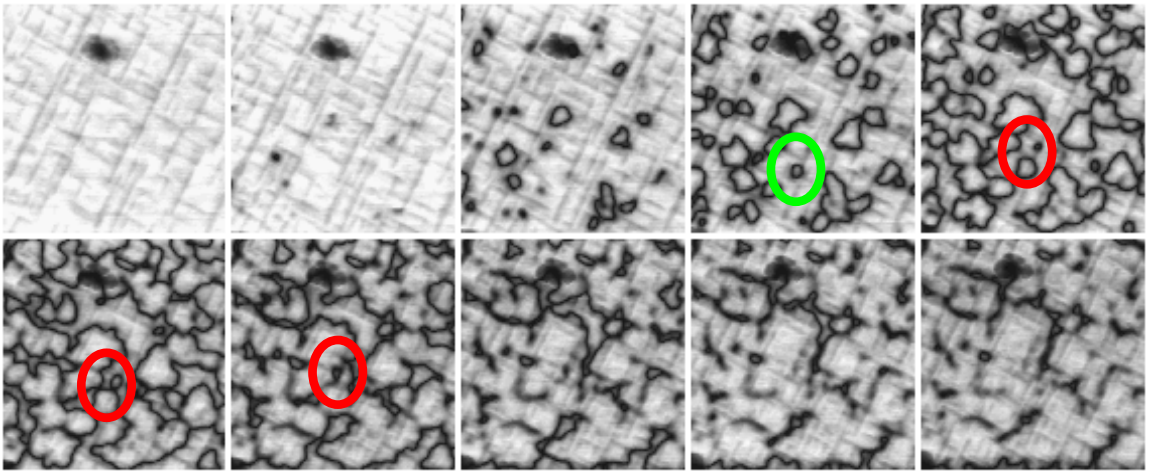

Figure 2: Consecutive HSPFM images revealing domain walls during switching, highlighting certain sample regions where switching occurs quickly (green oval), and another adjacent region where switching is impeded by microstructural local defects (red ovals).

To quantify these effects, a method to determine the local domain wall velocity and direction has been developed. Essentially, the frame for which every single pixel switches is determined computationally by analyzing the entire movie. For any given pixel, the switching time for adjacent pixels (or weighted collection of nearby pixels) is then determined, allowing the magnitude of the velocity to be determined with resolution down to 20 nm on a side. The local growth direction naturally results from calculating velocity vectors in x and in y. Figure 3 presents these results, where color indicates the switching time. Close inspection of the image (see zoomed figure, right, where sketched) reveals embedded arrows that identify the local domain wall velocity based on the magnitude of the arrows, while their orientation signifies the local growth direction.

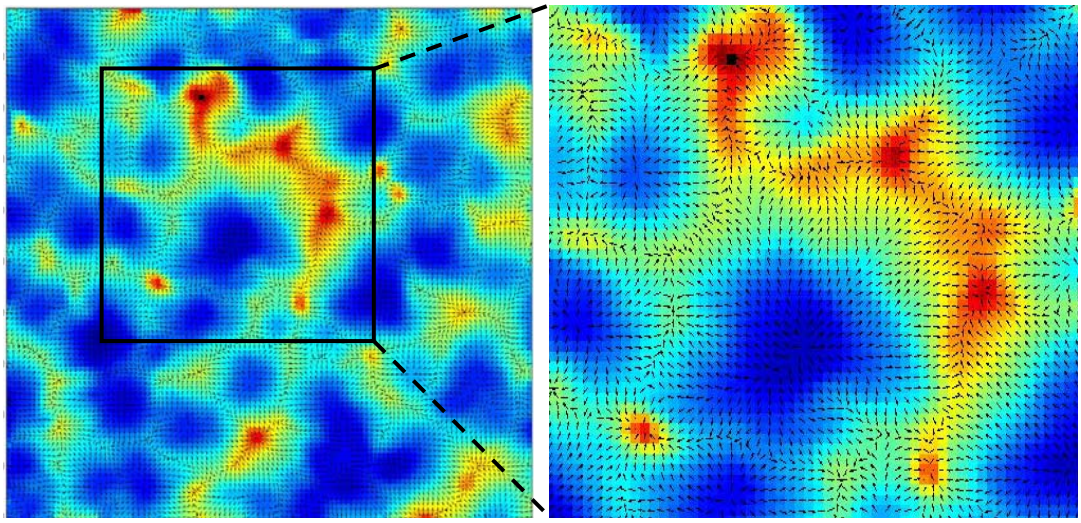

Figure 3: Switching time (color) and growth velocity (arrows) from Figure 2, quantifying influence of in-plane domains on polarization switching.

Beyond analyzing the switching data visually as with Figure 3, a statistical analysis of the local velocities can easily be conducted. Figure 4 presents a histogram of the domain velocities for every region in the area imaged by the movie of Figure 2. The data is normalized to the maximum velocity measured during the movie, limited by the poling time between frames (< 5 usec) and the separation between the analyzed pixels (<50 nm). In this case, that amounts to 1 cm/sec, though lower or higher speeds can be achieved with lower or higher biases applied to the scanning probe while acquiring the switching movie, scanning faster, applying narrow voltage pulses, etc. Domain velocities in this case are primarily near this max speed, though some distribution is apparent. In analyses of results from different specimens, the results strongly depend on the switching mechanism, sample processing presence of defects, etc. as is expected for this defect-mediated process.

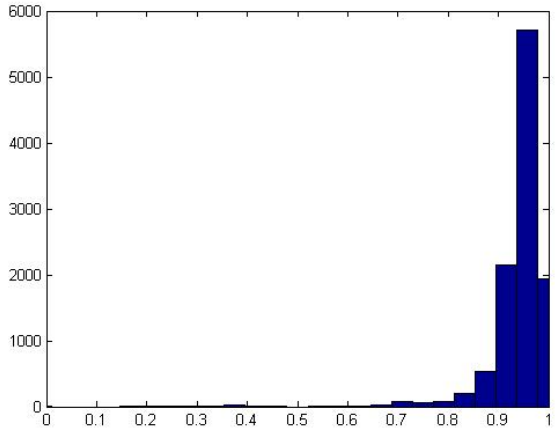

Figure 4: Histogram of normalized domain wall velocities (max speed ~1 cm/sec), identifying a predominant though not perfectly uniform speed for domain growth.

Figure 5 statistically analyzes the data of Figure 3 and Figure 4 still further, plotting a histogram of the number of pixels that switched for any given switching direction. Each

bin represents a 2º directional span. The data is uniform, identifying that switching is relatively homogeneous for this nucleation dominated case. Slight peaks at 0, 90, 180, and 270 degrees are artifacts of the image pixelation and associated direction calculation, confirmed by separate data (real and test) upon rotating the specimen, for completely random growth, and for purely directional growth. Finally, as with Figure 4, the distribution of directions is a strong function of specimen conditions.

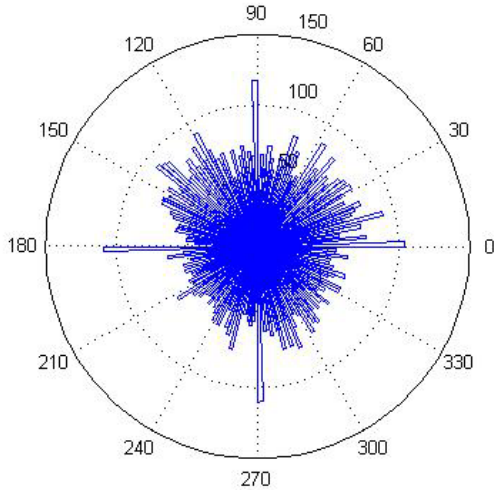

Figure 5: Histogram identifying nearly uniform local switching directions based on statistics of the number of domains growing in any given orientation (peaks at 90 degree intervals are an artifact of the calculation).

Future Plans

The next steps of this research will apply these concepts to ferroelectrics, and also with chalcogenide (phase change) materials. For ferroelectrics, the emphasis is on relating nucleation and growth to various engineered defects. These include substrate steps, surface flaws, and sub-surface effects such as those created by ion implantation. With chalcogenides, where the experimental capabilities are less mature, the research will initially focus on developing the necessary capabilities to investigate the switching energetics. In particular, nucleation site densities, activation energies, and intrinsic (infinite field) nucleation times will be determined. Investigations of growth statistics, as with the more advanced ferroelectric studies, will naturally follow.

Acknowledgements

The specimen described was provided by R. Ramesh, UCBerkeley. The images were acquired by graduate students N. Polomoff and G. Santone, while the image analysis is by undergraduate student A. Rakin.

DOE Supported Publications

None yet as this project has only just begun, though the work discussed here will be submitted for publication shortly.

In situ characterization and modeling of formation reactions under extreme heating rates in nanostructured multilayer foils

Todd C. Hufnagel[1], Michael L. Falk[1], Omar M. Knio[2], and Timothy P. Weihs[1]
1. Department of Materials Science and Engineering
2. Department of Mechanical Engineering
Johns Hopkins University
206 Maryland Hall, 3400 N. Charles St. Baltimore, MD 21218-2681
Email: *hufnagel@jhu.edu*

Program scope

Processing under extreme environments presents unique challenges and opportunities for controlling the microstructure and thus properties of materials. Our research program emphasizes advanced techniques for *in situ* structural characterization tightly coupled with a multiscale modeling effort to explore the effects of heating rate and composition gradients on interdiffusion and phase formation in nanoscale systems.

In the experimental portion of our program we exploit self-propagating exothermic reactions in multilayers to study interdiffusion and phase transformations at heating rates of up to 10^8 K s^{-1}. We use a combination of time-resolved x-ray microdiffraction and dynamic transmission electron microscopy (DTEM) to achieve the necessary spatial and temporal resolution to follow the transformation sequences in detail. These are supplemented with pyrometry, nanocalorimetry, and reaction front velocity measurements, all of which can be directly correlated with the structural observations.

The first goal of our modeling program is to bridge the gap between experiments and atomistic simulations by using continuum models of self-propagating reactions as an intermediary. Atomistic models are used to generate thermodynamic and kinetic parameters as inputs to the continuum models, which in turn allow predictions which can be directly compared with experimental results. The second goal is to obtain direct insight into the atomic-scale processes associated with phase transformations under conditions of extreme heating rates and steep composition gradients.

Scientific issues of particular interest are diffusional asymmetries between the elements, nucleation and growth of transient phases, melting of either the elemental constituents or reaction products, and solid-state amorphization. Although the effect of rapid heating and steep composition gradients on these phenomena are relevant to many systems of technological interest, highly exothermic reactions in multilayers provide a convenient and experimentally tractable setting for exploring them.

Recent progress

In situ x-ray microdiffraction

Figure 1 shows x-ray microdiffraction data from Al/Zr multilayers of nominal overall composition Al_3Zr and average bilayer period 90 nm. We have previously observed in this alloy system an unusual dependence of the reaction velocity on the bilayer period. One proposed explanation of this behavior is that the transformation of the Zr to the high-temperature bcc phase will speed interdiffusion and hence the reaction kinetics and reaction velocities for samples with bilayers greater than ~20nm. The *in situ* x-ray microdiffraction experiments were intended to answer this question definitively. As Figure 1 shows, however, we see no evidence for the formation of bcc Zr at any point in the reaction sequence. Since the experiment has sufficient temporal and spatial resolution to isolate changes occurring in the reaction front, we take this as a compelling indication that the hcp-bcc transformation does not take place, at least not to any significant extent.

We had previously examined phase transformations in Al/Ni multilayers of nominal overall composition Al_3Ni_2 at the Cornell High Energy Synchrotron Source, where our spatial and temporal resolution were not as good as what we can achieve at APS. In that earlier work, evidence for both the first new crystalline phase to form (cubic AlNi) and of an amorphous (probably liquid) phase appeared simultaneously. We believed, however, that it was likely that the liquid phase formed first, followed by nucleation of AlNi from the melt. As Figure 1b shows, however, even at APS we see these two phases form simultaneously.

A common theme in several of the multilayer systems we have studied is the importance of the formation of an amorphous phase as one of the first reaction products. For instance, in earlier *in situ* x-ray studies of both Al/Ni and Zr/Ni multilayers we saw a rise in scattering that we attributed to the formation of an amorphous phase. In the case of Al/Ni this was due to melting of the Al layers, but in

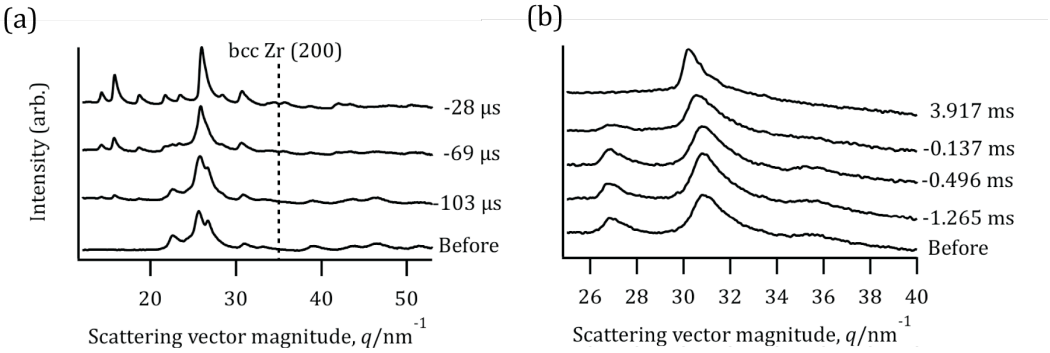

Figure 1: Recent in situ *x-ray microdiffraction results. (a) In Al/Zr multilayers of overall composition Al_3Zr we see no evidence for the formation of bcc Zr, as had been hypothesized. No intermediate phases form between the original microstructure of hcp Zr and fcc Al (bottom) and the final product, Al_3Zr (top). (b) In Al/Ni multilayers of overall composition Al_3Ni_2 there is no point during the sequence when the microstructure is completely liquid; we always see evidence for crystalline phases, either fcc Al and Ni (bottom) or the cubic AlNi intermetallic (top).*

the Zr/Ni multilayers it appears that a solid-state amorphization reaction happens first, followed by a glass transition to form the supercooled liquid. Rapid diffusion in the liquid seems to be important to sustain the self-propagating reaction. Recently, we have seen evidence for a similar mechanism in Al/Zr multilayers. Figure 2 shows a cross-section TEM image of an Al/Zr multilayer heated through the first exotherm in a differential scanning calorimeter, with clear evidence for extensive amorphous phase formation.

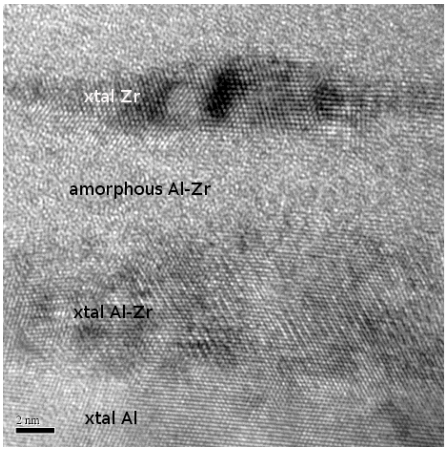

Figure 2: Cross-sectional transmission electron microscopy (TEM) of an Al/Zr multilayer annealed at 265 °C for four hours. There is clear evidence for extensive amorphization at the Al/Zr interfaces (along with the formation of an Al-Zr intermetallic phase). Micrograph by Marta Bonds of UC Davis, through our collaboration with Geoff Campbell (LLNL).

Simulations

One theme of our simulation effort is to link atomic-scale events in our molecular dynamics (MD) simulations to macroscopic observables using continuum simulations (of reaction front velocity, for instance) as an intermediate step. Our recent efforts have focused on using information regarding interdiffusivity in Al/Ni multilayers from MD as input to the continuum simulations. Prior work to infer macroscopic diffusivities from MD simulations (by others) involved either extracting the diffusivity from the slope of the mean-squared displacement *v*. time plot (the Einstein-Smoluchosky equation), or use of the Green-Kubo relation in which the diffusivity is expressed in terms of time integral correlation functions.

We developed a new technique based on analyzing the moments of the cumulative distribution functions of the constituents, using Bayesian inference to determine the diffusion coefficient *D* for Ni diffusing into Al. The results are consistent with experimental correlations for diffusion of Ni into molten Al. Significantly, the estimate for diffusivity obtained in this way is an order of magnitude larger than that based on large-time evolution of the mean-square displacements using more traditional methods. This is because the majority of the mixing occurs in the early stages of the MD computations, where the slope of the mean-square displacements with time fails to provide a reasonable estimate of the mixing rate. Furthermore, semi-empirical correlations using the measured reaction front velocity give an effective interdiffusivity which is some three orders of magnitude smaller than the value we obtain from the MD simulations. This suggests that the reaction velocity may be primarily determined by atomic mixing that occurs at low to intermediate temperatures, rather than at the maximum temperature of the reaction front.

Another goal of the simulation program is to provide direct insight into the atomic-scale mechanisms of interdiffusion and reaction. We have recently performed MD simulations of the reaction process in Al/Ni multilayers, to complement the *in situ* experiments described above. In agreement with the experiments, the simulations show melting of the Al layer, and nucleation and growth of the AlNi (B2) intermetallic phase. In the simulations, the melting event clearly occurs first, followed by interdiffusion of Ni into the molten Al and finally nucleation of AlNi. In the experiments, we cannot resolve these events separately.

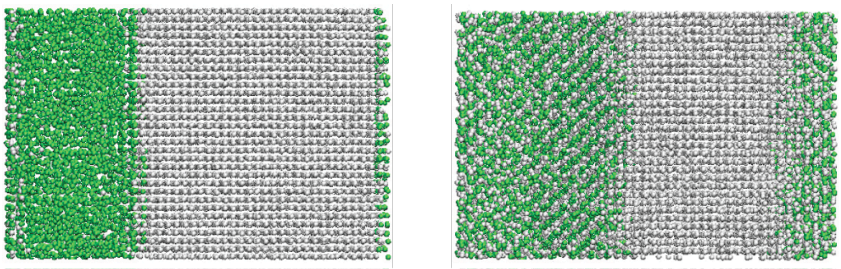

Figure 3: Snapshots from MD simulations of reacting Al (green)/Ni (white) multilayer. (a) The first phase transformation is melting of Al, following by intermixing of Ni into the molten Al. (b) The crystalline intermetallic AlNi nucleates from the intermixed liquid.

Future plans

1. X-ray technique development will focus on continued refinement of the microdiffraction work, as well as implementation of time-resolved x-ray reflectivity to study the earliest stages of interdiffusion and reaction of the multilayers.
2. Low temperature pyrometry will be utilized to identify signs of melting in self-propagating and homogeneous reaction events. High temperature pyrometry will be utilized to identify Ni-Al, Zr-Al and Ni-Zr chemistries that have delayed phase transformations that occur after the maximum reaction temperature has been reached. Results will be combined with in situ studies and nanocalorimetry for comparison with model predictions.
3. Modeling work will focus on extending atomistic-continuum coupling formalism to the study of mixing under adiabatic conditions, specifically aiming at developing diffusivity-temperature correlations that are suitable for describing self-propagating reaction fronts.

References to publications of DOE-sponsored research

Five manuscripts describing the results to date (described above) have either been submitted or are in preparation, but none have yet appeared or been accepted for publication.

Vortex Matter in Confined Superconductors and Mesoscopic Hybrid Herostructures

Maria Iavarone
Physics Department
Temple University
Barton Hall, 1900 N. 13th Street
Philadelphia PA 19122

e-mail: iavarone@temple.edu

Program Scope

This program is aimed at understanding the fundamental features that underlie the behavior of vortices in confined superconductors, hybrid superconductor-normal metal and superconductor-ferromagnet systems. The task is to identify new physical phenomena associated with the competition between *spatial confinement* and *proximity effect*, to investigate vortex matter in these systems and to correlate macroscopic transport properties with local electronic density of states. The goal is to understand how the physics of vortex matter changes in order to be able to predict and control the electronic properties of new hybrid systems. Scanning Probe Microscopy and Spectroscopy is an integral part of this study. The vortex configuration in confined superconductors can be probed with high spatial resolution using Magnetic Force Microscopy or by mapping the spatial variations in the electronic density of states with Scanning Tunneling Microscopy (STM). The understanding of the local changes in the electronic density of states is crucial as it also affects all the thermodynamic properties of the material.

Recent Progress

In our preliminary research, performed at Argonne National Laboratory, on magnetically coupled Permalloy(Py)/$NbSe_2$ (single crystal) bilayers I and my collaborators have shown that magnetic stripe domains induce vortex chain configurations [1] that are quite different from the ones observed in superconductor/normal metal (S/N) hybrids (Figure 1) [2]. First, the vortices form chain structure in domains with same polarity as the applied field and no chains are observed in the superconductor above the domains with opposite polarity. Second, the superposition of applied magnetic field and the stray field of the magnetic domains leads to slow expansion of the confinement potential for the superconducting vortices as the applied magnetic field is increased. Thus we observe formation of multi-chain vortex structure that progressively widens in magnetic field accompanied by the proliferation of vortices in anti-pinning sites (above the domains with opposite polarity) that freely slide along the magnetic domain stripe. These novel effects observed by Scanning Tunneling Microscopy (STM) vortex imaging were supported by the Ginzburg-Landau simulations [1].
There are questions that remain to be answered. In our preliminary STM studies no spontaneous formation of vortex-antivortex pairs were observed in zero applied magnetic

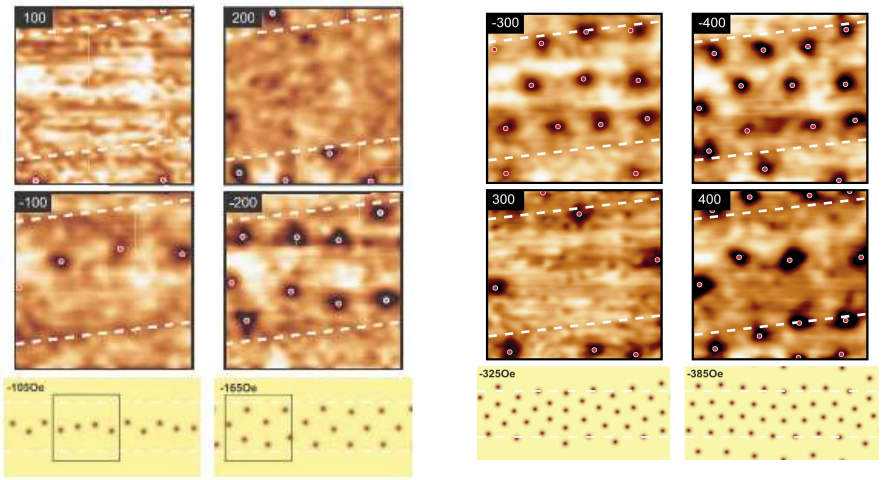

Figure 1. STM images of vortex chain configurations in the Py/$NbSe_2$ bilayer at 4.2K. Applied magnetic field values (in Oe) perpendicular to the surface of the superconductor are shown in the upper right corner. The white dotted lines show the underlying magnetic stripe domain boundaries. The scanning area is 700x700nm. Lower: Cooper-pair density plots calculated at magnetic fields shown, using GL simulations (plot size 1x2μm.) [1].

field. By tuning the strength and geometry of the magnetic domains and choosing the right superconducting material with optimal coherence length and penetration depth it has been predicted theoretically that vortex-antivortex pairs are induced by the ferromagnet's out-of-plane magnetization [3]. When equilibrium vortex-antivortex pairs are subjected to external driving force such as Lorenz force, vortices and anti-vortices are driven in opposite directions causing unbinding of vortex-antivortex pairs and mutual annihilation resulting in excess dissipation. Although the signature of this effect we have observed in transport measurements [4,5], no conclusive evidence of the mechanism causing this dissipation has been obtained yet. It should be outlined that STM and transport measurements were performed on different systems (Py/$NbSe_2$ single crystal bilayers with a $NbSe_2$ thickness of 400nm have been used for STM [1], while Py/MoGe bilayers with a MoGe thickness of 20 nm for transport measurements [4,5]).

More recently we have been carrying out low temperature Magnetic Force Microscopy in collaboration with the Physics Department at University of Salerno. We studied the effect of the periodic stray fields induced by thick Py film on Nb thin films in magnetically coupled bilayers. Permalloy is a ferromagnetic material which at thicknesses above $t_c = 2\pi(A/K_u) \approx 200nm$, has well ordered stripe domain structure (here A is the exchange constant and K_u the anisotropy constant). Spatial variation of the magnetic moment direction in the plane normal to the plane of the film has non-trivial two-dimensional behavior. The width of the stripes at the surface of the Py as well as the stray magnetic depend upon the thickness of the Py film and upon the fabrication parameters such as temperature and changes in composition of the Py. We measured bilayers with different Py as well as Nb thicknesses.

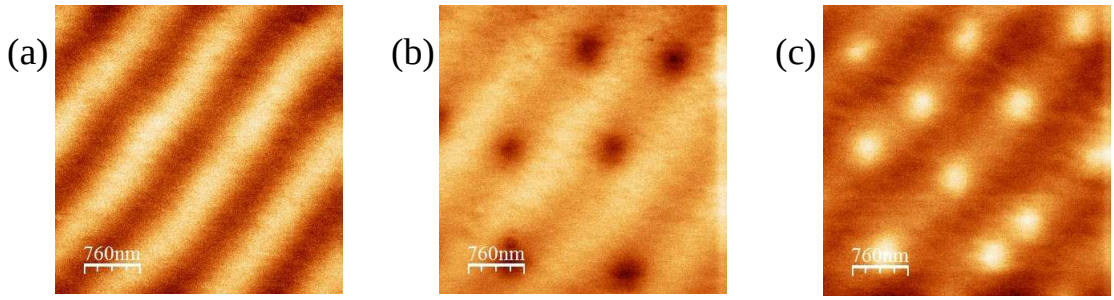

Figure 2 MFM measurements of a Py/Nb bilayer. (a) The image acquired at T=16 K shows the stripe domain of a 1μm film of Py observed on the surface of the 200nm Nb film above the superconducting transition, at T=16 K. (b) Image acquired at T=6K. The sample has been cooled in a magnetic field of H=+12 G. (c) Image acquired at T=6K. The sample has been cooled in a magnetic field of H=-18 G.

We observed a rich variety of phenomena deriving from a combination of pinning and confinement of vortices in channels defined by the underlying Py magnetic stripe domain structure. In Figure 2 the stripe domain of the Py is observed through a 200nm Nb film above and below the superconducting transition temperature of the bilayer T_c=8.5 K. Below the superconducting transition we observe vortices only along the stripes having the same polarity as the magnetic field applied during the cooling process.

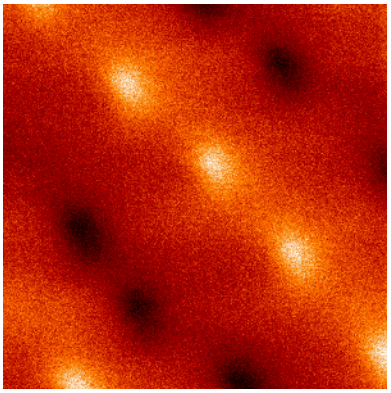

Figure 3 MFM image of spontaneous V-AV pairs acquired at T-6K on a Py/Nb bilayer. Scanning area is 3.7 μm x 3.7 μm.

We were the first to find general equilibrium conditions for which vortex-antivortex pairs are formed during zero-field cooling of the hybrid F/S bilayers. In Figure 3 a MFM image acquired at 6 K on a Py/SiN/Nb is shown. Vortex-Antivortex pairs are spontaneously created in zero applied magnetic field due to the presence of the Py stray field.

In the non-equilibrium state the strong magnetic pinning of the vortex lattice results in avalanches of antivortices when changing the polarity of the applied magnetic field. The threshold of avalanches depends upon the specific history and temperature. As a consequence of strong pinning for applied field less than the avalanche threshold, configuration of vortex and antivortex can also be stabilized.

Future Plans

We will continue to advance on the fundamental understanding of vortex matter and its impact on applications. Indeed, the studies of vortex-antivortex dynamics could have far-reaching impact going beyond the basic understanding and control of vortex dynamics.

Many applications of superconductors in sensors are limited by noise believed to be due to dissipation from vortex-antivortex dynamics.

We propose to correlate STM measurements with MFM, transport and magnetization measurements on the same samples in order to address in a systematic approach fundamental questions related to the formation and annihilation of vortex-antivortex pairs in S/F bilayers. Specific planned activities include:

- STM imaging of vortex-antivortex pairs subjected to Lorenz force by superconducting transport current would elucidate the strength of the vortex-antivortex binding potential as well as non-equilibrium vortex-antivortex states. The basic dynamics of such system remains unknown.
- Ferromagnetic materials with different magnetic properties will be explored.
- The possibility of tuning the ferromagnetic state by changing size and shape of the ferromagnet offers an additional degree of freedom to modify the vortex-antivortex state in the superconductor.
- STM imaging of the spatial modulation of electronic density of states evolution as a function of the magnetic domain width as well as superconducting film thickness. Transport measurements have shown that different regimes of coupling between the superconductor and the ferromagnet are influenced by the periodicity and the magnitude of the out-of-plane magnetization of the magnetic domain structure in the ferromagnet [6].

References

[1] G. Karapetrov, M. V. Milošević, M. Iavarone, J. Fedor, A. Belkin, V. Novosad, and F. M. Peeters, "Transverse instabilities of multiple vortex chains in superconductor-ferromagnet bilayers", *Phys. Rev. B **80**, 180506* (2009)

[2] G. Karapetrov, J. Fedor, M. Iavarone, D. Rosenmann, and W.K. Kwok, "Direct observation of geometrical phase transitions in mesoscopic superconductors by scanning tunneling microscopy", *Phys. Rev. Lett.* **95**, 167002 (2005)

[3] R. Laiho, E. Lähderanta, E.B. Sonin, and K.B. Traito, "Penetration of vortices into the ferromagnet/type-II superconductor bilayer" *Phys. Rev. B* **67**, 144522 (2003)

[4] A. Belkin, V. Novosad, M. Iavarone, J. Pearson, and G. Karapetrov, "Superconductor/ferromagnet bilayers: Influence of magnetic domain structure on vortex dynamics", *Phys. Rev. B* **77**, 180506 (2008)

[5] A. Belkin, V. Novosad, M. Iavarone, J. Fedor, J. E. Pearson, A. Petrean-Troncalli, and G. Karapetrov, "Tunable transport in magnetically coupled MoGe/Permalloy hybrids", *Appl. Phys. Lett*. **93**, 072510 (2008)

[6] A. Belkin, V. Novosad, M. Iavarone, R. Divan, J. Hiller, T. Proslier, J. E. Pearson, and G. Karapetrov, " Giant conductance anisotropy in magnetically coupled Ferromagnet-Superconductor-Ferromagnet structures", *Appl. Phys. Lett.* **96**, 092513 (2010)

Program title: **Electron and Scanning Probe Microscopies**

Office of Basic Energy Sciences, DoE

Project title: **High-resolution photoemission electron microscopy**

R. Könenkamp (PI), R. Word, T. Dornan, J. Fitzgerald

Physics Department, Portland State University, 1719 SW 10th Avenue, Portland, OR 97201, PI e-mail: rkoe@pdx.edu

Photoemission electron microscopy (PEEM) combines in a unique way light-optical probing with electron-optical imaging. The fundamental process underlying this type of microscopy is the photoelectric effect in which electrons are emitted from a solid sample surface after excitation with ultraviolet light. PEEM can utilize light from synchrotrons, lasers and ultraviolet lamps. It allows specific and gentle probing of physical and chemical (1) surface properties, and the observation of fast dynamic processes with temporal resolution down to the sub-femtosecond regime (2). To obtain high resolution and brightness, the photoelectrons are accelerated to energies of a few 10 kV. This acceleration produces strong aberrations which, in combination with the lens aberrations, have until recently limited the resolution in PEEM to approximately 8-10nm. While this resolution is better than in other optical probing techniques (3), it can further be improved with an aberration corrector. In addition to resolution, also brightness, contrast and sensitivity can be enhanced.

We report on bringing the spatial resolution in photoemission electron microscopy towards a level of 5.4nm. This resolution was obtained in an aberration-corrected photoemission electron microscope with a hyperbolic mirror as the correcting element for spherical and chromatic aberration (4). In-situ measurements and numerical simulations confirm the low residual aberration in the instrument and indicate the ultimate resolution in this type of microscopy to be below 2 nm.

With the aberration-corrected instrument we are currently exploring localized surface plasmon distributions in metallic nanostructures. We use femtosecond laser pulses at a wavelength of ~800nm for the plasmon excitation. Photoelectron emission in these structures and their vicinity occurs by a three-photon process. In metallic random structures we observe nanometer-sized areas in which the photoemission rate is enhanced several thousand-fold compared to non-plasmonic structures (5). Our results also show that plasmon-enhanced photoemission can be induced in non-absorbing materials located in the near-field region of a plasmon-active material. This opens new opportunities in photonics and microscopy.

Aberration-correction

For the low electron energies in PEEM, mirror-based correctors are considered suitable and aberration-corrected instruments have recently been built in several labs around the world (6-8). For our instrument we have developed and built a hyperbolical mirror which simultaneously corrects for chromatic and spherical aberration, and a low-angle beam separator (8). 5.4 nm resolution were demonstrated on biological membrane structures. Our experimental and theoretical results indicate that the type of corrector used by us may ultimately bring the resolution to below 2nm. In the on-going project we will work towards this goal by improving the microscope mechanically and enhancing the mirror by adding a second electrode with adjustable voltage. This will eventually allow an independent correction of the two aberrations

at all magnifications, which is currently not yet possible. Fig. 1 shows the overall lay-out of the microscope and some details of the old and new correcting mirrors.

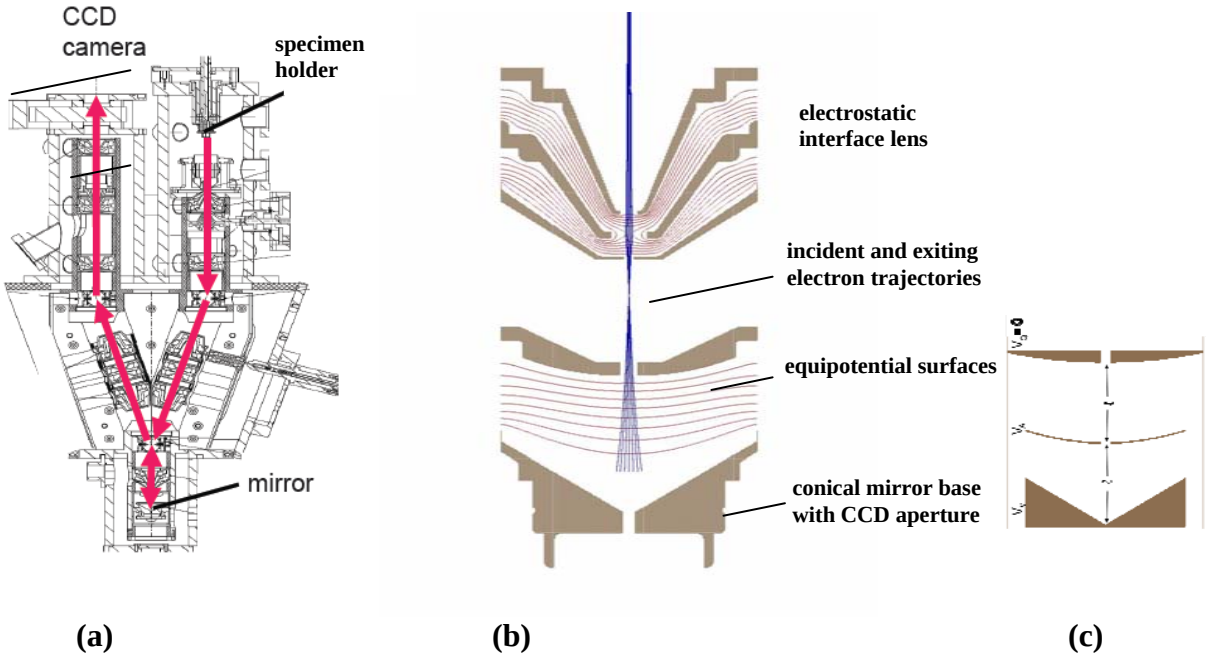

Figure 1: Microscope and corrector design. a: Design lay-out of the aberration-corrected PEEM with specimen holder in the upper right, mirror at the bottom, and image plane in the upper left portion of the Y-shaped beamline. b: Hyperbolic mirror with 3-electrode interface lens. Incident and exiting electron trajectories are plotted to visualize the symmetric operating mode of the mirror. c: Schematic design of the new mirror with mirror electrode at potential V_M, center electrode at potential V_C and grounded entrance electrode.

Plasmon enhanced photoemission and microscopy

Beyond the instrument development our research group has addressed plasmon characterization in metallic nanostructures and time-resolved pump-and probe microscopy. Both activities make use of a femtosecond-laser system which covers the wavelength spectrum of 200-230nm, 260-310nm and 780-920nm.

In our recent work we have used nanostructured metal layers to generate intense localized surface polaritons. The localization can lead to a strong enhancement in the local plasmon intensity: Plasmonic "hot spots" with optical intensities several orders of magnitude higher than the average background intensity have previously been observed (9,10), and are thought to be the source for surface-enhanced Raman scattering, enhanced luminescence, lasing, and other phenomena. Large photon densities can also occur in the near-field region of hot spots, and this can be used to generate photoemission from non-plasmonic materials. The photoemission enhancement can reach (11,12) several orders of magnitude as compared to the case without plasmonic enhancement. We investigated a configuration where localized surface plasmons in gold lead to photoemission in near-by indium-tin-oxide (ITO) which is transparent to the exciting light. We were able to resolve the size of the photoemission area, and provide simple estimates for plasmon transport lengths and plasmon excitation efficiencies in these nanostructures (5).

Fig. 2 shows a close-up of the photoemission environment. In this particular example a gap-type geometry with two separate Au areas is used. The Au areas are separated by a gap of ~60nm. The gap exposes the underlying ITO film. The composite of micrograph, consisting of a combined SEM and PEEM image, shows the photoemission originating from the ITO film. The diameter of the emission area is typically ~50 nm as shown in part c. Comparing the count rates in the bright spots to count rates for unstructured planar areas of ITO films we find that the photoemission is enhanced by a factor ~6000 in this random structure. Accounting for the cube-law in the underlying 3-photon process, the optical intensity enhancement is calculated to be about 18.

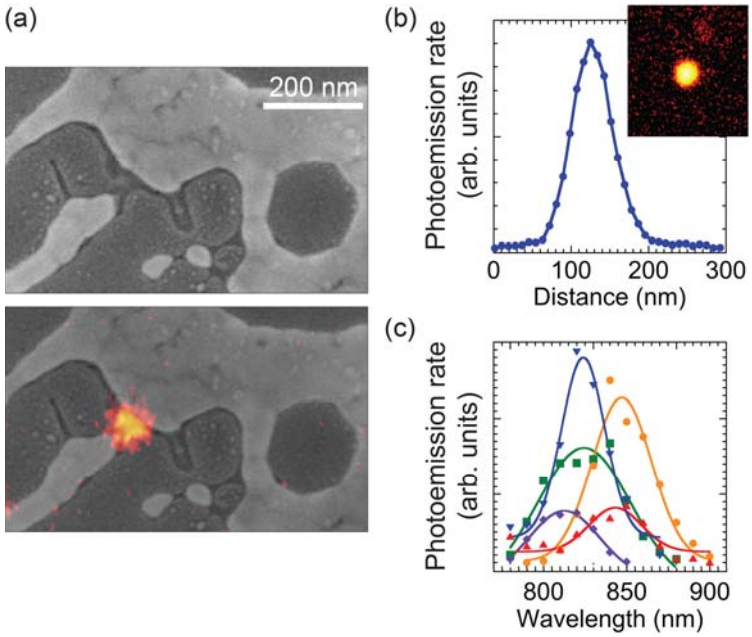

Figure 2: Plasmonic nanostructures. a (top): SEM micrograph of typical hot spot environment, bright areas are Au covered; bottom: composite micrograph of SEM and multi-photon PEEM images of localized photoemission at λ=792nm from the gap between two Au islands; b: Photoemission count rate across a localized photoemission area, insert: PEEM image of localized emission; c: PEEM excitation spectra of various hot spots.

Taking account of all instrument parameters we find that the average hot spot delivers approximately a few hundred electrons per second. The low emission rate can mostly be attributed to the combination of inefficient light-to-plasmon coupling in this random geometry, low probabilities for the 3-photon processes, and the short-range plasmon energy transfer. Clearly, all of these factors could be improved significantly in future work, and powerful electron sources should then become feasible in planar geometry. Such electron sources may be useful in signal routing and processing, nano-electrochemistry and in nanometrology.

To summarize, we have developed an aberration-corrected photoemission microscope and improved the resolution towards 5nm – the best in photoemission microscopy at this time. The next step in the instrument development is a new and improved mirror which will allow independent adjustment of chromatic and spherical aberrations under all experimental conditions. We have carried out first work on plasmonically enhanced photoemission in random metal nano-structures. We find that simple planar structures can emit a few hundred electrons per second from areas of ~50nm diameter. We will next improve the optical and

plasmonic environment in these structures to explore the feasibility of efficient electron sources on the nanoscale. Eventually we will use these electron sources in advanced microscopy applications.

Publications:

- *Image properties in an aberration-corrected photoemission electron microscope,* R. Könenkamp et al., Physics Procedia 1, 505 (2008)
- *Nanostructured semiconductor heterojunctions from quantum dot layers* R. Könenkamp, A. Nadarajah, and Robert C. Word, Appl. Phys. Lett. 95, 053103 (2009)
- *5.4 nm resolution in a photoelectron-microscopy,* R. Könenkamp, Robert C. Word, G. F. Rempfer, et al., Ultramicroscopy 110, 899 (2010)
- *Photoemission from localized surface plasmons in fractal metal nanostructures* R. C. Word and R. Koenenkamp, Appl. Phys. Lett. 96, 251110 (2010) (also in Virtual Journal of UltrafastScience)

Conference contributions:

- *Localized multi-photon photoelectron emission from indium tin oxide in proximity to gold in nanostructured gold-ITO-glass films,* Microscopy and Microanalysis Conference, Portland, OR 2010
- *5.4 nm spatial resolution obtained from an aberration-corrected photoemission electron microscope utilizing an electrostatic mirror,* Microscopy and Microanalysis Conference, Portland, OR 2010
- *Plasmon photoemission electron microscopy using a sub-workfunction infrared fs pulse laser,* APS March Meeting, Portland, OR. (2010)
- *Resolution of 5.4 nm from a photoemission electron microscope corrected with an electrostatic mirror,* APS March Meeting 2010, Portland, OR.

References:

(1) J. Feng J and A. Scholl in "*Science of Microscopy*", P. Hawkes, J. Spence (eds.), Springer, New York (2007)
(2) M. I. Stockman, M. F. Kling, U. Kleineberg, and F. Krausz, *Nature Photonics* 1, 539 (2007)
(3) K.R. Chi, *Nature Methods* 6, 15 (2009)
(4) R. Könenkamp, Robert C. Word, G. F. Rempfer, T. Dixon, L. Almaraz and T. Jones, *Ultramicroscopy* 110, 899 (2010)
(5) R. C. Word, T. Dornan, R. Könenkamp, *Applied Physics Letters* 96, 251110 (2010) (6) J. Feng et al., *J. Phys.: Condens. Matter* 17, S1339 (2005)
(7) R. Wichtendahl et al., *Surf. Rev. and Lett.* 5, 1249 (1998)
(8) R. Könenkamp et al., *Physics Procedia* 1, 505 (2008)
(9) M. Moskovits, *Rev. Mod. Phys.* 57, 783 (1985)
(10) M. I. Stockman, *Phys. Rev. Lett.* 84, 1011 (2000)
(11) H. Chen, J. Boneberg, and P. Leiderer, *Phys. Rev. B* 47, 9956 (1993)
(12) A. Gloskovskii, D. Valdaitsev, S.A. Nepijko, G. Schönhense, B. Rethfeld, *Surface Science* 601, 4706 (2007)

Atom chip microscopy: A novel probe for strongly correlated materials

Benjamin L. Lev
Department of Physics
University of Illinois at Urbana-Champaign, Urbana, IL 61801-3080 USA
benlev@illinois.edu

Program scope

Improved measurements of strongly correlated systems will enable the predicative design of the next generation of supermaterials. In this program, we are harnessing recent advances in the quantum manipulation of ultracold atomic gases to expand our ability to probe these technologically important materials in heretofore unexplored regions of temperature, resolution, and sensitivity parameter space. We are working to demonstrate the use of atom chips to enable single-shot, large area detection of magnetic flux at the 10^{-7} flux quantum (Φ_0) level and below. By harnessing the extreme sensitivity of atomic clocks and Bose-Einstein condensates (BECs) to external perturbations, the cryogenic atom chip technology developed here will provide a magnetic flux detection capability that surpasses other techniques—such as scanning SQUIDs—by a factor of 10^1–10^3. We are testing the utility of this technique by using rubidium BECs to image the magnetic fields emanating from charge transport and magnetic domain percolation in strongly correlated materials as they undergo temperature-tuned metal–to–insulator phase transitions.

Cryogenic atom chip microscopy introduces three very important features to the toolbox of high-resolution, strongly correlated material microscopy: simultaneous detection of magnetic and electric fields (down to the sub-single electron charge level); no invasive large magnetic fields or gradients; simultaneous micro- and macroscopic spatial resolution; freedom from $1/f$ flicker noise at low frequencies; and, perhaps most importantly, the complete decoupling of probe and sample temperatures. The first of these features will play an important role in studying the interplay between magnetic and electric domain structure. The last two are crucial for low frequency magnetic noise detection in, e.g., the cuprate pseudogap region and for precision measurements of transport in the high temperature, technologically relevant regime inaccessible to other techniques based on superconducting scanning probes. Figures 1 and 2 illustrate the atom chip trapping principle [1] and microscopy technique [2], respectively.

In addition to imaging static current and magnetic domain structure, we are working to study spatially resolved variations in magnetic field noise spectra versus temperature using AC atom chip microscopy. In this detection mode, magnetic flux noise can either drive spin flips or reduce spin coherence in a nearby atomic sample. Measuring either trap population loss due to spin flips or T_2 dephasing times using Ramsey interferometry can produce maps of noise power spectra much akin to those obtained from SQUIDs, but with better resolution, better temperature tunability, and without $1/f$ noise. Recent calculations predict a $S_\Phi \geq 10^{-9}\ \Phi_0^2/\mathrm{Hz}$ sensitivity from near-DC to several MHz [3]. Alternatively, Larmor precession of spin waves in the BEC can be used for sensitive AC field detection, as proposed in Reference [4].

Figure 3(a) depicts the capabilities of magnetic probes for resolving magnetic fields emanating above surfaces. State-of-the-art scanning probes lie along or above the $\sim 10^{-6}\ \Phi_0$ line, as shown in cyan in the figure. Toward the high sensitivity (1 fT) end of the spectrum lies the technique of measuring the Larmor precession of spins in an atomic vapor confined inside a cm-sized paraffin coated cell. On the opposite, high resolution (sub-100 μm) end of the spectrum are scanning magnetic force microscopy (MFM) and the

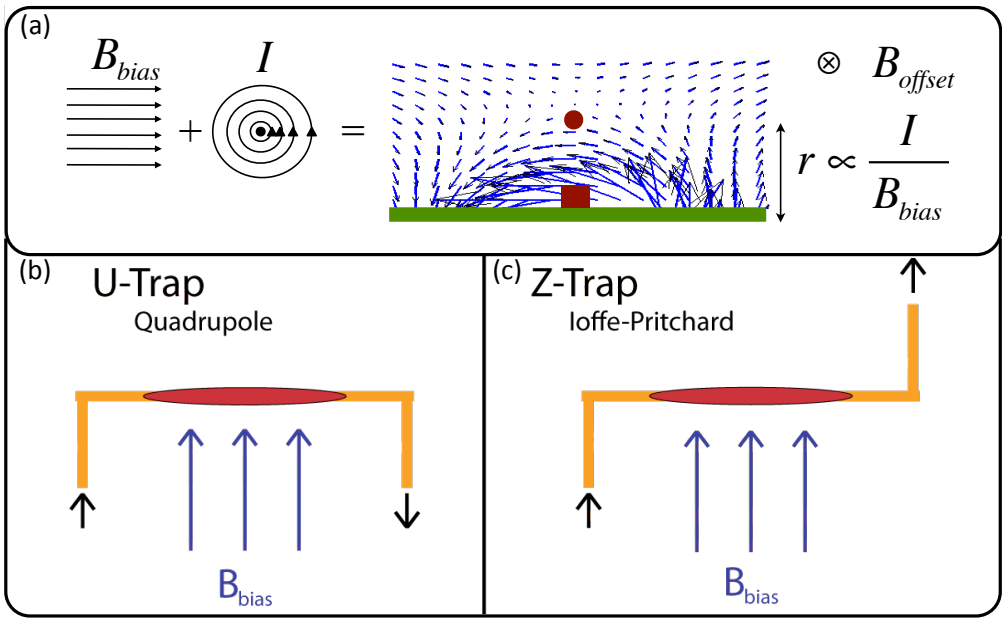

Figure 1: **Atom chip trapping principle.** (a) A cylindrically symmetric quadrupole magnetic field is created by superimposing a weak, homogeneous bias field B_{bias} with that from a wire with current I. Weak-field seeking atoms—i.e., atoms in a Zeeman state whose energy decreases for increasing magnetic field magnitude—are trapped in a small region around the zero of the magnetic quadrupole field. If the microwire is attached to a surface via standard photolithography, then the trap may be brought to an arbitrarily close distance r from the surface by adjusting the ratio of I to B_{bias}. (b–c) A slowly varying offset field B_{offset} confines the atoms along the wire axis. Trapped atoms may be be translated perpendicular to the axis of the wire by rotating the angle that B_{bias} subtends with the substrate surface, thus enabling the precise positioning of atoms above adjacent materials (see Figure 2).

new technique of measuring fields with diamond nitrogen vacancy (NV) centers. Traditionally, scanning superconducting quantum interference devices (SQUIDs) have provided an optimal compromise in sensitivity and resolution and have been employed to great success in imaging condensed matter (CM) materials.

While the BEC is the coldest object realizable (sub-100 nK temperatures are typical), the atom chip can be positioned $\geq$0.5 μm away from the BEC and be as hot as 100 C or as cold as $<$ 4 K without disturbing the atom chip microscopy performance. With this technique it is now possible to image samples with micron resolution and sub-10^{-7} Φ_0 flux sensitivity *above* 77 K, a feat which cannot be done with scanning SQUIDs. Many phenomena associated with strongly correlated systems have never been explored at $>$77 K due to the inability of high temperature superconducting (HTS) scanning SQUIDs to operate with high resolution and sensitivity in this regime [5].

Recent progress and future work

With DOE support, we have built a rubidium laser cooling and trapping apparatus, including a stabilized, high-power laser system and UHV chamber. See Figures 3(b–c). The system is now able to rapidly produce large magneto-optical traps (MOTs) of $\sim$100 μK Rb, as shown in Figure 3(d). We are now working toward cooling the trapped Rb to Bose degeneracy. Simultaneously, we have designed and begun assembling the cryogenic atom chip "science" chamber and have designed the high-resolution atom detection system. The optical dipole trap laser and air-bearing translation stage needed for shuttling the ultracold Rb to the science

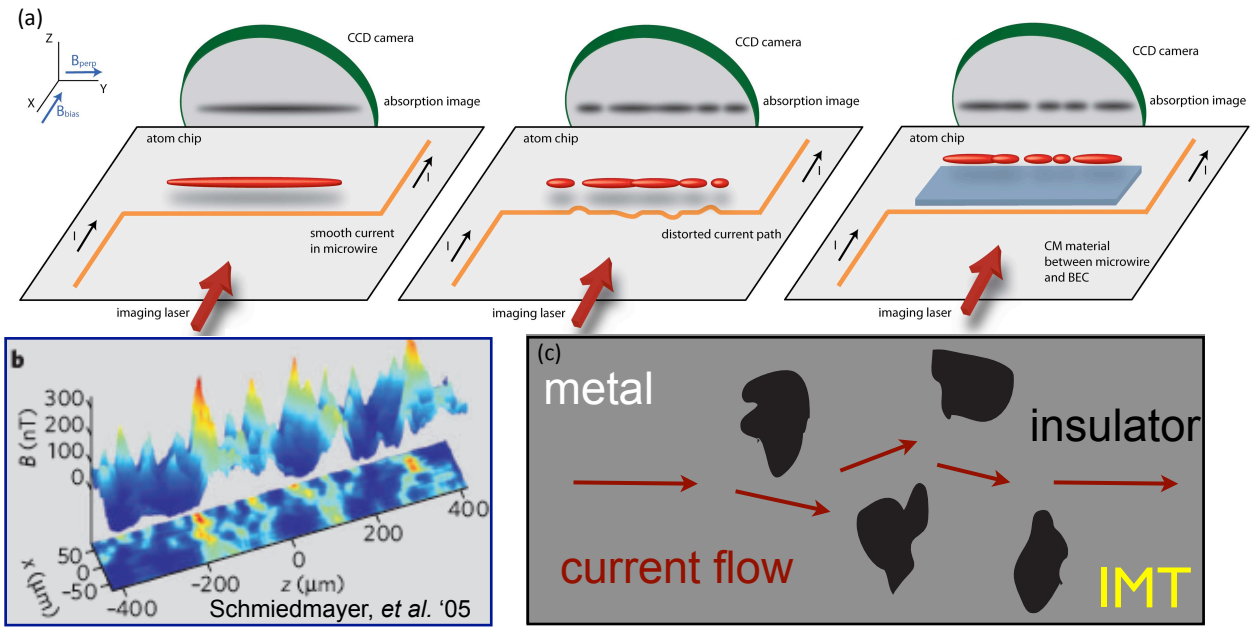

Figure 2: **Atom chip microscopy.** (a, left) A Bose-Einstein condensate (BEC, shown in red) is confined above the atom chip by the Z-trap formed by the fields from the Z-shaped microwire (orange) and B_{bias} produced by an external (not shown) Helmholtz coil pair whose axis is aligned with $\hat{x}$. Adjusting current I in the trapping wire and B_{bias} controls—with sub-micron precision—the position of the BEC above the surface of the substrate with $\leq$0.5 mm distance separation. (a, middle) Current running through the sample wire does not flow parallel to the wire's axis due to scattering centers (exaggerated in figure), which result in 1 ppm variations of the magnetic field above the sample. This inhomogeneous field deforms the trap, imprinting density modulations onto the otherwise smooth, cigar-shaped BEC cloud. The absorption of a near-infrared laser casts a shadow onto a CCD camera, providing μm-scale resolution of density perturbations in the sub-micron wide, 1 mm-long cloud. (b) Such images may be post-processed to create a map of the sample wire's inhomogeneous current pattern [2]. The BEC can be recreated and repositioned every $\leq$20 seconds, thus in a few minutes providing a wide area map of the inhomogeneous current flow. (a, right) To image a condensed matter (CM) sample, the atoms can be cantilevered over the sample—and away from the Z-wire—by rotating B_{bias} in the xz-plane. The thin CM sample (shown in blue) may be mounted on the cryogenically cooled atom chip or on a thermally isolated platform. (c) The BEC suspended above the CM sample fragments due to inhomogeneous fields from either static magnetic domains or meandering currents.

chamber has been tested. The atom chip supports are being machined and the atom chips themselves are beginning to be microfabricated. The LN2/He flow cryostat is on order and we expect to achieve a BEC and a working atom chip by the end of the year. On the theoretical side, we have designed a novel atom chip capable of trapping highly dipolar atoms such as Dy near surfaces. This new type of atom trap will be reported in a forthcoming publication.

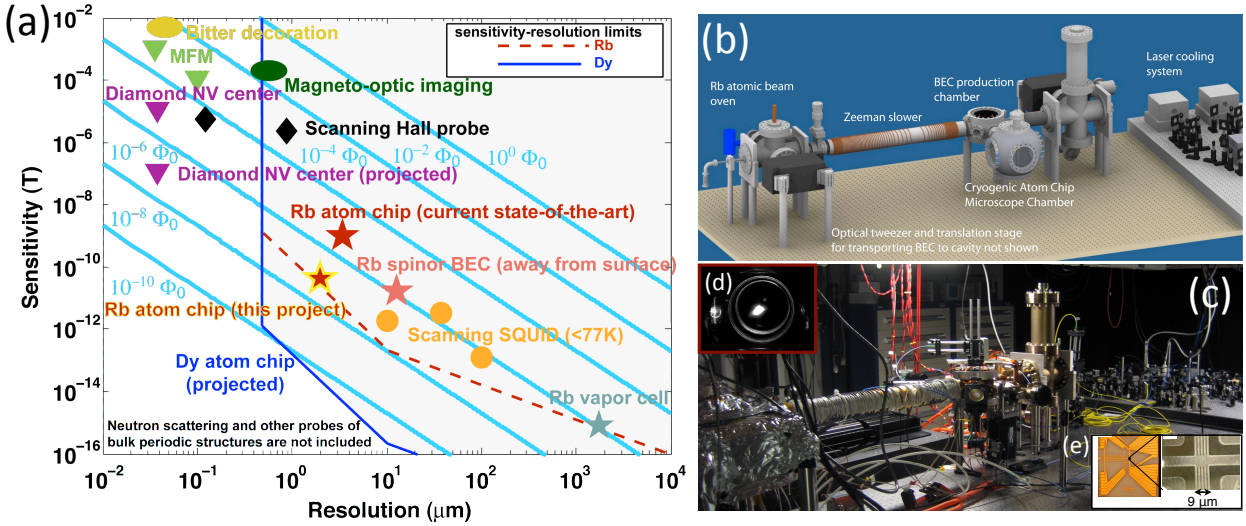

Figure 3: (a) Comparison of techniques [2] for high sensitivity, high resolution magnetic field measurement. The stars indicate atomic physics-based techniques. The red dashed (Rb) and blue solid (Dy) lines denote the sensitivity–resolution limits for atom chip microscopy with either Rb atoms or more exotic, highly magnetic atoms such as Dy that have recently been trapped and laser cooled to the sub-100 μK regime by our group [6]. The leftmost boundary is due to a 500-nm imaging resolution limit and the lower bounds arise from limits on obtainable trap frequencies and depth. (b) Our Rb laser cooling and trapping apparatus design. (c) The assembled Rb MOT apparatus, including UHV chamber and stabilized high-power laser. (d) A sample Rb MOT (white area in center) produced with this apparatus. (e) Examples of atom chips that will be fabricated for suspending the Rb BECs near cryogenic CM samples.

References

[1] J. Fortagh and J. C. Zimmermann. Magnetic microtraps for ultracold atoms. *Rev. Mod. Phys.*, **79** 235, (2007).

[2] S. Wildermuth, S. Hofferberth, I. Lesanovsky, S. Groth, P. Krüger, J. Schmiedmayer, and I. Bar-Joseph. Sensing electric and magnetic fields with Bose-Einstein condensates. *Appl. Phys. Lett.*, **88** 264103[3], (2006).

[3] S. Scheel, R. Fermani, and E. A. Hinds. Feasibility of studying vortex noise in two-dimensional superconductors with cold atoms. *Phys. Rev. A*, **75** 064901[4], (2007).

[4] M. Vengalattore, J. M. Higbie, S. R. Leslie, J. Guzman, L. E. Sadler, and D. M. Stamper-Kurn. High-resolution magnetometry with a spinor bose-einstein condensate. *Phys. Rev. Lett.*, **98** 200801[4], (2007).

[5] R. L Fagaly. Superconducting quantum interference device instruments and applications. *Rev. Sci. Instrum.*, 77(10) 101101[45], 2006.

[6] M. Lu, S.-H. Youn, and B. L. Lev. Trapping ultracold dysprosium: a highly magnetic gas for dipolar physics. *Phys. Rev. Lett.*, 104 063001, 2010.

Project Title: "Tailoring magnetism in epitaxial graphene on SiC"

Principle Investigator: Lian Li

Mailing Address: 1900 E Kenwood Blvd, Milwaukee, WI 53211

Email: lianli@uwm.edu

Program Scope:

Graphene, a one-atom-thick planar sheet of sp^2-bonded carbon atoms in a honeycomb lattice exhibits a linear band dispersion near the K points, leading to exotic physical and electronic properties such as a room temperature (RT) Quantum Hall effect [1], and high carrier mobility. Extensive research is devoted to explore the use of graphene as the 2D channel in conventional field effect transistors [2], and to enable new computational state variables (e.g., pseudo spin) and switching mechanisms (e.g., Veselago lens with a negative optical index) in novel graphene devices [3-5].

Our BES-supported program addresses magnetism in graphene: 1) how are local magnetic moments created; and 2) how do these moments interact with each other and with the graphene host to attain long range ferromagnetic ordering, through an integrated approach using spin-polarized scanning tunneling microscopy/spectroscopy (STM/STS) and first principles calculations. While magnetism is typically associated with the *d*- and *f*-shell materials such as iron, magnetic moments can also be created by localized states of vacancies in graphene [6,7], leading to *magnetism without magnetic ions*, which can be further tailored by substitutional doping or adsorption of molecules.

Recent Progress

Our latest results indicate that because of the very strong in-plane σ bonds that form the backbone of its honeycomb lattice, the substitutional doping of graphene requires the assistance of high-energy ions of insert gases (e.g., nitrogen plasma), which also produces impurity-vacancy complexes (e.g., N-vacancy), whose magnetism can be further engineered by hydrogenation.

In addition, we have resolved the atomic structure at the interface between epitaxial graphene and SiC(0001) substrate; uncovered novel Si diffusion paths during the epitaxial growth of graphene on SiC(0001); observed electric field switching of Ar-vacancy complexes; and investigated vacancy-assisted incorporation of Cu in graphene. Lastly, in preparation for *in situ* transport measurements, two-terminal graphene devices have been fabricated using photolithography and dry etching techniques.

1.1 ***Epitaxial graphene on SiC(0001): More than just honeycombs***

Epitaxial growth through the thermal decomposition of SiC provides a viable method to produce wafer-sized graphene. On the Si-face SiC(0001), although the graphitization has been known (since 1975) to begin with the formation of a $(6\sqrt{3}x6\sqrt{3})$ structure, which also remains at the interface during the growth of the subsequent layers, its exact structure remains controversial to date [8]. Yet, the interfacial layer plays a critical role in the gap opening near the K points as observed by angle-resolved photoemission spectroscopy – a property crucial for its use in electronic devices, but found only for the Si-face, and absent for the C-face and exfoliated graphene.

In this part of research, based on atomic resolution STM imaging (Fig. 1(a)) using functionalized W tips, which selectively probes graphene-related states, we observe a structure that consists of two types of features: up-pointing trimers (blue arrow) and rosettes (green arrow) (Fig. 1(a)). Aided by first principles calculations, we have discovered that the $(6\sqrt{3}x6\sqrt{3})$ structure is a warped graphene layer with the periodic inclusion of hexagon-pentagon-heptagon ($H_{5,6,7}$) defects in the honeycomb to relieve the

mismatch with the SiC substrate. These defects also break the local symmetry of the honeycomb, thereby inducing a gap. Our results provide a consistent explanation of available experimental data for

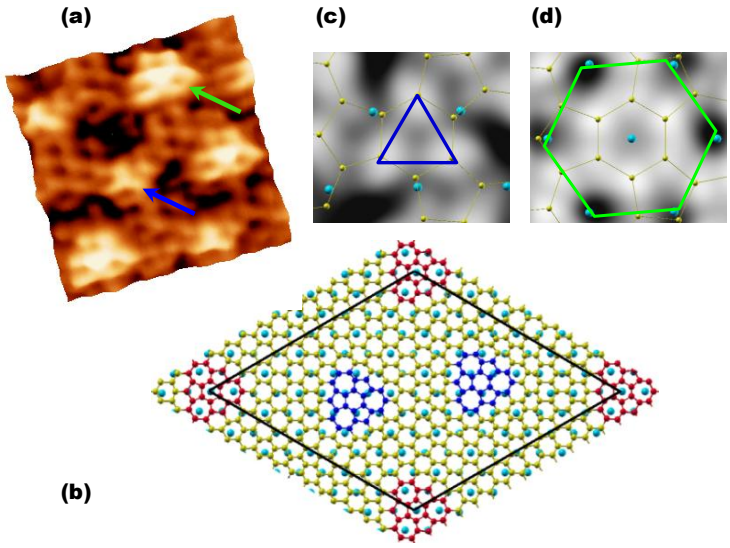

Fig. 1 (a) An STM image taken with an Fe/W tip (V_s: -0.5 V and I_t=0.4 nA, size=4x4 nm^2). (b) Ball-and-stick model for the ($6\sqrt{3}$x$6\sqrt{3}$) structure with "top" (marked blue) and "hollow" (marked red) variants. Calculated DOS isosurfaces for occupied states between -0.1 eV and E_F for the (c) top and (d) hollow variants. C: small balls; Si: larger balls. The main features of the STM images are well reproduced in the calculations.

the defining properties of the ($6\sqrt{3}$x$6\sqrt{3}$) layer – the gap at K points, the presence of two localized states near K, and C core level shifts. These results are published in *Phys. Rev. Lett.* ***105****, 085502 (2010).*

1.2 ***Origin and manipulation of epitaxial graphene ridges on SiC(0001)***

Ridges and wrinkles are often observed on epitaxial graphene on SiC, which have been thought to be domain boundaries and/or the formation of carbon nanotubes on the surface. Here, by imaging them at the atomic scale using STM, the origin of these ridges is revealed: they are bulged regions of the graphene layer (Fig. 2), which is compressively strained due to the mismatch in lattice constant and thermal coefficient with the SiC substrate. While bulk materials typically relieve strain through the formation of dislocations, a truly two-dimensional material such as graphene, which possesses strong in-plane covalent bonding and weak interlayer interaction, is free to buckle and bend away from the surface to relieve the strain. It's also possible to manipulate and create these ridges and wrinkles using the STM during imaging. Using vicinal SiC substrates where terrace sizes are significantly reduced and the compressive strain minimized, the growth of nearly ridge-free graphene films has also been achieved. These results have been published in *Nanotechnology* ***20,*** *355701 (2009).*

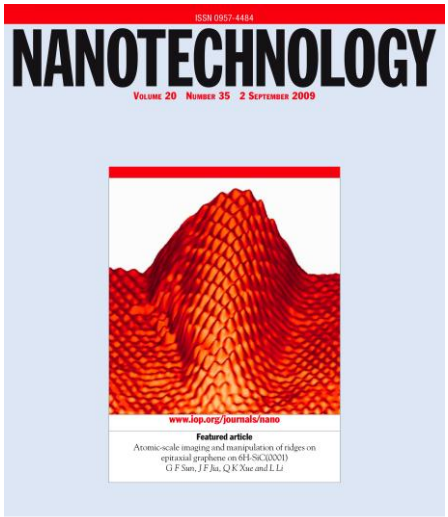

Fig. 2 3D STM image of a ridge in epitaxial graphene on 6H-SiC(0001) on the cover of *Nanotechnology*. Size: 55x55 nm^2, V_s = -20 mV, I_t = 0.02 nA.

1.3 ***Magnetism of nitrogen doped epitaxial graphene on SiC(0001)***

In this part of research, we demonstrate that N doping of epitaxial graphene on SiC(0001) leads to the formation of N-vacancy complexes. Based on the calculated energetics and comparisons with STM observations, we find that the most probable configuration is a nonmagnetic single vacancy with a substitutional N at the nearest neighbor site, a motif that also serves as the building block for various other N-vacancy complexes.

Figure 3(a) is an STM image of bilayer graphene after ~ 1% N doping at RT. The main features observed are: type *I*, resembling a vacancy, type *II*, similar to type *I* but surrounded by bright features, and type *III*, lattices with slightly enhanced contrast. The atomic resolution image of a type *II* defect in Fig. 3(b) shows that it consist of bright spots that roughly form two interlaced triangles, though one spot of the solid triangle appears dimer, giving rise to the appearance of a depression in the STM images. This triangular feature also appears in different variants of type *II* complexes for N doping at different temperatures. Even for RT doping, type *I* and *II* defects are the most dominant feature at ~50%, which further increases to ~80% at 800 ^{o}C, indicating that they are a common building block after N-doping of graphene.

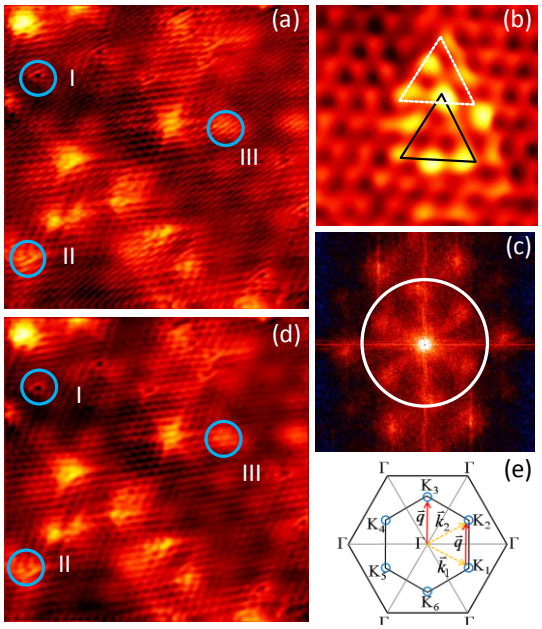

Fig. 3. (a) STM image of N-doped graphene (V_s: -0.15V, I_t: 1.9nA, size: 15x15nm^2). (b) Close-up view of type *II* defect (V_s: -0.19V; I_t: 1.86nA, size: 2.1x2.1nm^2). (c) FT of the image in (a). (d) Inverse FT image of (a) after removing the 1x1 spots. (e) Diagram of the 2D Brillouin zone.

The 2D Fourier transform (FT) of the image Fig. 3(a) is shown in Fig. 3(c). In addition to the graphene 1x1 spots, six additional features (i.e., the √3×√3 spots) are also observed, which can be attributed to inter-valley scattering of quasiparticles between K points ($K_i \rightarrow K_{i+1}$ type) (Fig. 3(e)) [9]. After removing the lattice spots in Fig. 3(c), the resulting image is shown in Fig. 3(d), which highlights the threefold √3×√3 symmetry near the defects.

To elucidate the atomic structures of these defects, we have calculated the electronic structure of several defect configurations: (i) a simple N substitution; (ii) three N-vacancy complexes, α, β, and γ; and (iii) single vacancy and an N adatom. Comparisons of the calculated iso-density local density of states plots with the STM images indicate that the α complex reproduces feature qualitatively similar to the predominant type *I* and *II* seen in the STM images. Given that it is also the most energetically favorable, it's determined to be the building block for the more complicated complexes observed.

We have also found that the hydrogenation of this complex leads to meta-magnetism, as shown in the M-H curve in Fig. 4. As indicated by the small blue circles, there are three zero field solutions: M = 0, 0.3, and 1.6 μ_B. For small fields, the system exhibits paramagnetic behavior, and for M between the two

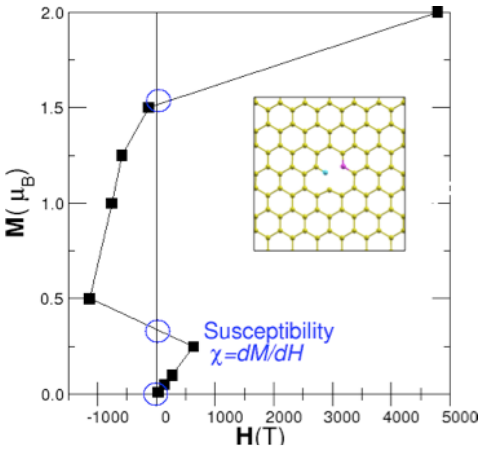

Fig. 4 Calculated M-H curve for the hydrogenated α complex. Inset: ball-and-stick model for the complex, the red and blue balls represent the N and H atoms, respectively.

larger H=0 solutions, there is magnetic instability. The magnetic solution with a moment of 1.6 μ_B is lower than the paramagnetic solution by 0.38 eV/cell. These findings indicate that the engineering of N-vacancy complexes presents a promising avenue for controlling the electronic and magnetic properties of graphene. These results have been submitted to *Nano Letters*.

Future Plans

We will continue the experimental work already in progress on the N(Ar)/graphene systems to determine the magnetic properties of the N(Ar)-vacancy complexes using scanning tunneling spectroscopy, as well as experimental and theoretical investigation of the electronic and magnetic properties of Cu doped graphene. The incorporation of other transition metal dopants such as Mn and Cr in epitaxial graphene, as well as their magnetic properties will also be investigated. Transport measurements on the two-terminal graphene devices will be carried out to determine the effect of doping and defects at the atomic scale on the transport properties of epitaxial graphene on SiC.

Publications of DOE Sponsored Research (2008-2010)

1. "Atomic-scale imaging and manipulation of ridges on epitaxial graphene on 6H-SiC(0001)", G. F. Sun, J. F. Jia, Q. K. Xue, and L Li, (Cover article) *Nanotechnology* **20,** 355701 (2009).
2. "Electronic structures of Mn-induced phases on GaN(0001)", Y. Qi, G. F. Sun, M. Weinert, and L. Li, *Phys. Rev. B* **80**, 235323 (2009).
3. "Epitaxial graphene on SiC(0001): More than just honeycombs", Y. Qi, S. H. Rhim, G. F. Sun, M. Weinert, and L. Li, *Phys. Rev. Lett. **105**, 085502 (2010).*
4. "Epitaxial graphene on SiC(0001): More than just honeycombs", L. Li, chapter in a book entitled "Graphene, Theory, Research and Applications" (to be published in 11/2010).
5. "Electron standing waves on the GaN(0001)-pseudo (1x1) surface: A FT-STM study at room temperature", G. F. Sun,Y. Liu, Y. Qi, J. F. Jia, Q. K. Xue, M. Weinert, and L. Li, *Nanotechnology* (Revised manuscript submitted 8/19/10).
6. "Nitrogen doping of epitaxial graphene on SiC(0001): The formation of nitrogen-vacancy complexes and their magnetism", S. H. Rhim, Y. Qi, Y. Liu, G. F. Sun, M. Weinert, and L. Li, *Nano Lett.* (Submitted 5/22/10).

References:

1. "The electronic properties of graphene", A. H. Castro Neto et al., Rev. Mod. Phys. **81**, 109 (2009).
2. "100-GHz Transistors from Wafer-Scale Epitaxial Graphene", Y. –M. Lin, C. Dimitrakopoulos, K. A. Jenkins, D. B. Farmer, H. –Y. Chiu, A. Grill, and Ph. Avouris, Science **327**, 662 (2010).
3. "Pseudospin valve in bilayer graphene: Towards graphene-based pseudospintronics", P. San-Jose, E. Prada, E. McCann, and H. Schomerus, Phys. Rev. Lett. **102**, 247204 (2009).
4. "Negative refraction for electrons?" J. B. Pendry, Science **315**, 1226 (2007).
5. "The focusing of electron flow and a Veselago lens in graphene p-n junctions", V. V. Cheianov, V. Fal'ko, and B. L. Altshuler, Science **315**, 1252 (2007).
6. "Irradiation-induced magnetism in graphite: A density functional study", P.O. Lehtinen, A. S. Foster, Yuchen Ma, A.V. Krasheninnikov, and R.M. Nieminen, Phys. Rev. Lett. **93**, 187202 (2004).
7. "A defective graphene phase predicted to be a room temperature ferromagnetic semiconductor", L. Pisan, B. Montanari, and N. M. Harrison, New J. Phy. **10**, 033002 (2008).
8. "The growth and morphology of epitaxial multilayer graphene", J. Hass, W. A. de Heer, and E. H. Conrad, J. Phys.: Condens. Matter **20**, 323202 (2008).
9. "Scattering and interference in epitaxial graphene", G. M. Rutter, J. N. Crain, N. P. Guisinger, T. Li, P. N. First, and J. A. Stroscio, Science **317**, 219 (2007).

Grain Boundary Complexions and Transitions: A New Thermodynamic Theory and Initial Experimental Observations

Program Title: Grain Boundary Complexions and Transitions in Doped Silicon
(Award #: DE-FG02-08ER46511; Start Date: 7/15/2008; $95k/11 months)

PI: Jian Luo

Address: 206 Olin Hall, Clemson University, Clemson, SC 29634

E-mail: jianluo@clemson.edu

Program Scope:

In a series of articles published since 2006, Tang, Cannon, Carter, Dillon and Harmer proposed to treat grain boundary (GB) regions as distinct "interfacial phases," and they named these "interfacial phases" as "complexions" [1,2]. While the existence of analogous "surface phases" is well established [3], identification of GB analogues at internal interfaces offers new perspectives to solve a variety of outstanding scientific problems such as the origins of abnormal grain growth [2] and solid-state activated sintering [4], both of which have puzzled the materials community for over half a century.

This DOE project aims to discover the atomic-level and thermodynamic factors that control GB "phase" stability and transitions. Our goals are **1)** to develop the thermodynamic theories for GB transitions and **2)** to verify our theories and models with careful experimentation using well-controlled specimens and advanced electron microscopy. Initially, we proposed to use the doped Si system as the primary model system, and to use Ni-Bi and Cu-Bi as the secondary model systems. Due to interesting initial results that we observed for Ni-Bi, we are conducting more experiments in this system; at the same time, we are still actively investigating the Si based systems, particularly Au-doped Si.

Recent Progress:

In the theoretical thrust, we proposed a thermodynamic model for coupled adsorption and disordering transitions at GBs by combining diffuse-interface and lattice-gas models and incorporating colloidal type interfacial forces. This model produces a systematical spectrum of interfacial phenomena for GBs, including (first-order and continuous) coupled prewetting and premelting transitions, critical points, multilayer adsorption, layering and roughening, and complete wetting and drying. Furthermore, this model produces a series of GB "phases" (complexion types) with character similar to those observed by Dillon and Harmer [2]. We further demonstrated that the presence of dispersion and electrostatic forces in ceramic materials can appreciably change the GB phase behaviors. This work was published in *Applied Physics Letters* [a], and it was further elaborated in an invited overview article [b].

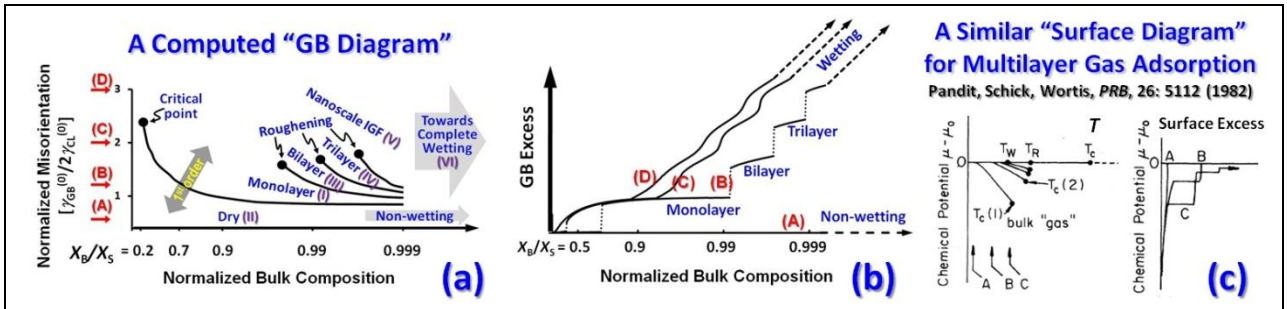

Figure 1: (a) A representative "GB phase diagram". First-order transition lines and critical points are plotted. GB "phases" and the associated Dillon–Harmer Complexion types (I-VI) are labeled. **(b)** Computed GB excess vs. normalized bulk composition for four selected GBs. Panels (a) and (b) are reprinted from our DOE-BES supported publication [*a*]. **(c)** Analogous "surface phase diagrams" are well established [3].

The development of the above thermodynamic model for GB "phase" transitions represents an important step towards realizing our **long-range scientific goal** of developing **GB "phase" diagrams** as new and useful tool for mechanism-informed materials design [d]. Importance and novelty stem from the large changes in properties that accompany GB transitions, and to the fact that high-temperature GB structures can often be retained on cooling. Specifically, such "GB diagrams" can be used in three ways:

- Guided by GB diagrams, fabrication protocols can be designed to utilize the most appropriate GB structures to achieve optimal microstructures;
- Heat treatment protocols can be devised to optimize GB structures for the desired mechanical and physical properties; and
- GB diagrams can provide information for predicting high-temperature properties.

Clear phenomenological similarities exist between the newly developed "GB phase diagrams" [a, b] and the well-known "surface phase diagrams" for multilayer gas adsorption [3] (Fig. 1). While the surface science has led to great technological advancements that have revolutionized our society, the interfacial science of GBs, which can have equal or more significant impacts, has lagged considerably because of the great challenges in studying internal interfaces. Addressing these challenges with the advanced electron microscopy tools is a primary goal of our BES program.

An Exciting New Discovery: In the experimental thrust, we recently made an exciting discovery in Ni-Bi, a model liquid metal embrittlement (LME) system. LME, a phenomenon of practical importance (especially in the scenario of liquid-metal cooled nuclear reactors), refers to the catastrophic intergranular brittle fracture of usually ductile metals in the presence of certain liquid metals. The failure is known to originate at the GBs where the adsorption (segregation) of the liquid metal element occurs, but the exact atomic level failure mechanism has been the subject of scrutiny and debate for over 100 years. In collaboration with Prof. Martin Harmer's group at Lehigh University, we directly observed bi-layer adsorption of Bi atoms at random GBs of Ni (Fig. 2) [9], which may be considered as the Dillon-Harmer Complexion type III. To our knowledge, this is *the first time* that such a GB adsorption structure has been observed in a metallic system. Careful measurements of Bi-Bi bond lengths using aberration corrected (AC), high angle angular dark field (HAADF), scanning transmission electron microscopy (STEM) indicate that these bi-layers may be bonded to each other by weak van der Waals forces. This observation provides an entirely new perspective to understand the atomic-level mechanism of LME, suggesting that the bi-layer adsorption of Bi atoms at random GBs in Ni provides an easy mechanism for the GBs to "unzip" between the layers, thus causing the material to become embrittled. A joint manuscript is under preparation and will be submitted soon.

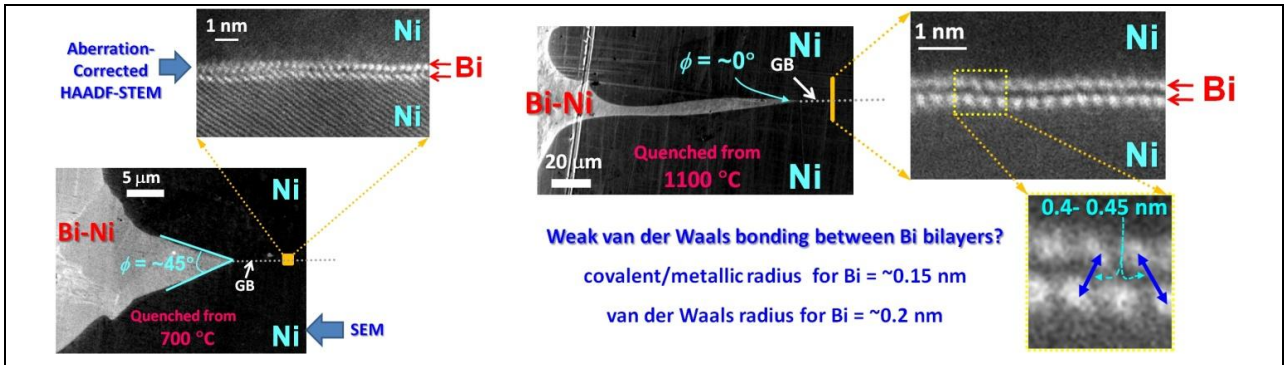

Figure 2: Our recent collaborative study (with Prof. Harmer and Dr. Chen at Lehigh University) observed bi-layer adsorption of Bi atoms at random GBs in Ni. This is the first time that this type of GB structure has been observed in a metallic system, providing a new perspective to understand liquid metal embrittlement (LME).

The observation of bi-layer adsorption in a metallic alloy fills an important gap to prove the generality of the GB complexion theory. We may rationalize the universal existence of the six generic GB complexion types, initially observed in doped Al_2O_3 (Fig. 3(a)) [2], by understanding their physical

origins from surface analogues (which are not restricted to any particular materials) in three steps, as shown in Fig. 3(b). First, the intrinsic GB (type II), Langmuir-McLean type monolayer adsorption (type I) and complete wetting films (type VI) are three well-known GB "phases." Second, below the bulk solidus line, liquid-like films with nanoscale "equilibrium" thicknesses can persist (type V; analogous to surface prewetting and premelting). Third, bi-layer and multilayer (tri-layer) adsorption can emerge as additional distinct GB complexion types III and IV, if the adsorbates have discrete thicknesses (analogous to a case of multilayer surface adsorption). Other GB "phases" (complexions) may exist, but these six types are likely the most "generic" types based on surface analogies. If the above interpretations are true, these generic GB complexion types should also exist in simpler metallic systems. In fact, five of the six types have been found in metals in prior studies (Fig. 3(b)), and this study filled the critical gap.

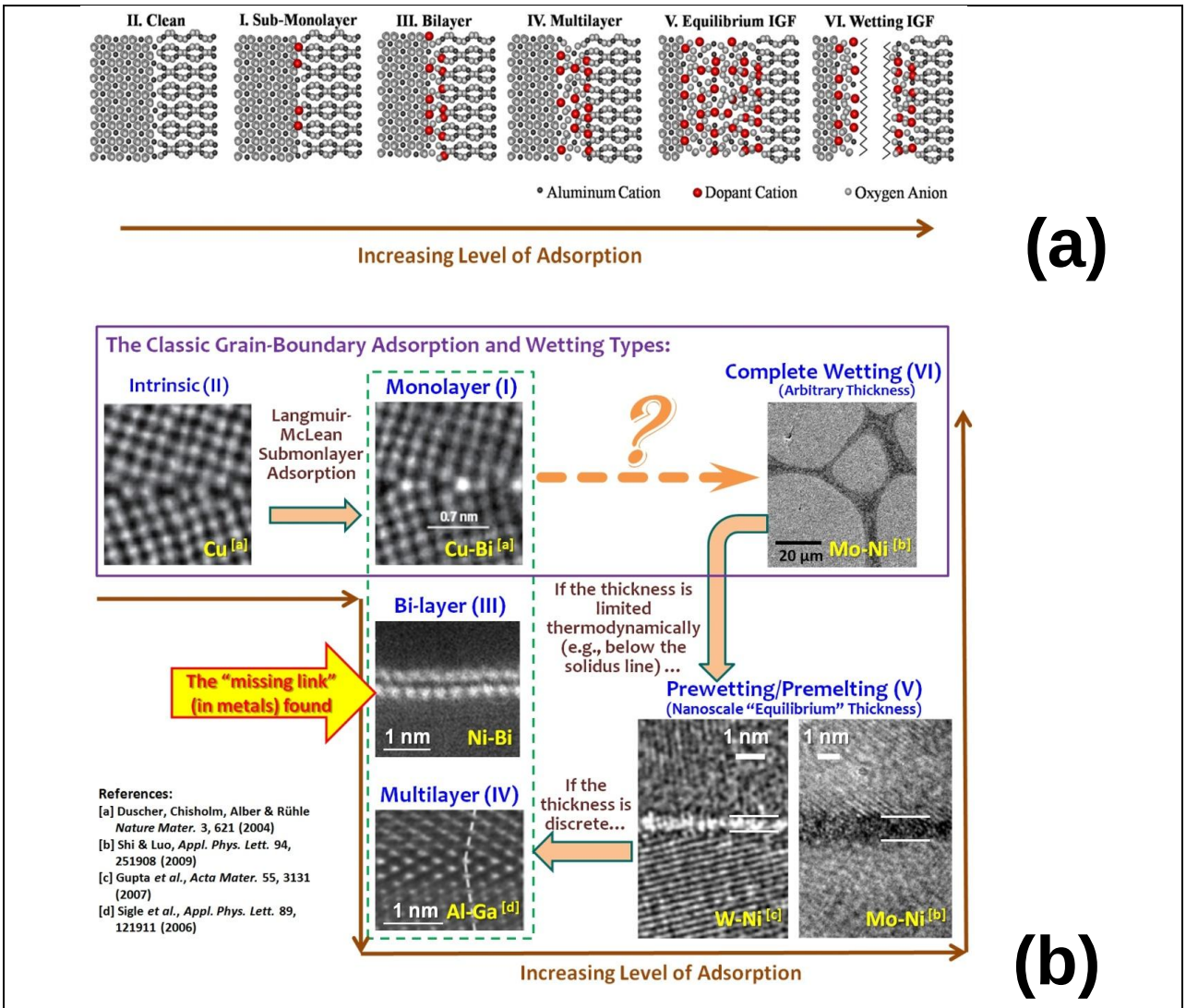

Figure 2 (a) Schematic of six types of GB "phases" (complexion types) found in alumina, which are re-ordered based on the increasing level of adsorption. [2] **(b)** Observations of analogous GB structures in metals.

In another model system, Au-doped Si, we found that the twisted (100) Σ29 GBs remain ordered up to ~ 14 ° below the bulk melting temperature of Si (Fig. 4). This is a somewhat supervising observation since Si-Au is one of the best metallic glass systems (thus we had expected that amorphous intergranular films might be fairly stable in this system). This result also appears to contradict the prior atomistic

modeling results [5]. Interestingly, HAADF-STEM showed that atomic level faceting occurs at Si GBs at this temperature (Fig. 4), which may be induced by Au adsorption.

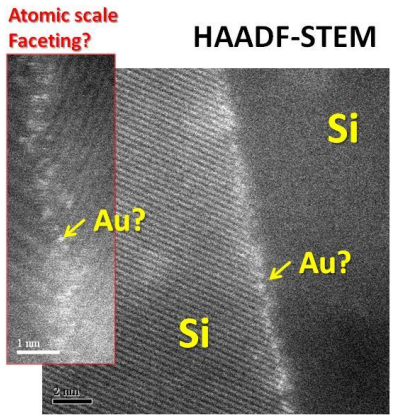

Figure 4 HAADF-STEM image of an Au-doped Si GB in a specimen that was quenched from ~ 14° below the melting temperature of Si. This twisted (100) Σ29 GB remains ordered but exhibits atomic scale faceting (in collaboration with Prof. Harmer and Dr. Chen at Lehigh University)

Future Plans:

We will continue to collaborate with Prof. Harmer's group at Lehigh University to investigate Ni-Bi (and, if it is feasible, Cu-Bi) **1)** to discover the roles of GB bi-layer adsorption in LME, **2)** to understand the formation mechanism and thermodynamic stability of the newly observed bi-layer adsorption in metal alloys, and **3)** to seek other GB complexion types.

We will further investigate the Au-doped Si system, where we will characterize **a)** twisted (100) GBs at even smaller undercoolings and **b)** twisted (111) GBs. The latter may yield particularly interesting results because a recent *Nature* article [6] showed that a nanometer-thick, undercooled, Au-based layer could be stabilized on the Si (111) surface at 350K below the bulk liquidus line. If this is true, we expect nanoscale, liquid-like, Au-based films (complexion type V), as well as their derivative complexion types (bi-layer and tri-layer adsorption), can be fairly stable at the twisted (111) GBs of Au-doped Si.

We will also further develop our thermodynamic theories and models for GB transitions, and we will refine/validate them via critical comparisons with experiments.

DOE Sponsored Publications in the Last Two Years (2008-2010):

[a] J. Luo, "Grain Boundary Complexions: The Interplay of Premetting, Prewetting and Multilayer Adsorption," *Applied Physics Letters*, **95**, 071911 (2009).

[b] S. J. Dillon, M. P. Harmer, and J. Luo, "Grain Boundary Complexions in Ceramics and Metals: An Overview" (**invited**), *JOM*, **61** [12], 38-44 (December 2009).

[c] J. Luo, S. J. Dillon and M.P. Harmer, "Interface-Stabilized Nanoscale Quasi-Liquid Films" (**invited**; an overview for non-specialists), *Microscopy Today*, **17** [4], 22-26, July 2009.

[d] J. Luo, "Liquid-Like Interface Complexion: from Activated Sintering to Grain Boundary Diagrams" **(invited review)**, *Current Opinion in Solid State & Materials Science*, **12**, 81-88 (2008).

[e] R. H. French, V. A. Parsegian, R. Rodgornik, R. F. Rajiter, A. Jagota, J. Luo, D. Asthagiri, M. K. Chaudhury, Y.-M. Chiang, S. Granick, S. Kalinin, M. Kardar, R. Kjellander, D. C. Langreth, J. Lewis, S. Lustig, D. Wesolowski, J. Wettlaufer, W.-Y. Ching, M. Finnis, F. Houlihan, O. A. von Lilienfeld, C. J. van Oss, and T. Zemb, "Long Range Interactions in Nanoscale Science," *Reviews of Modern Physics*, **82**, 1887-1944, (2010).

Other General References:

[1] M. Tang, W. C. Carter, and R. M. Cannon, *Phys. Rev. B* **73**, 024102 (2006); *Phys. Rev. Lett.* **97**, 075502 (2006);

[2] S. J. Dillon, M. Tang, W. C. Carter, and M. P. Harmer, *Acta Mater.* 55, 6208 (2007); S. J. Dillon and M. P. Harmer, *J. European Ceram. Soc.* **28**, 1485 (2008); M. P. Harmer, *J. Am. Ceram. Soc.* **93**, 301 (2010).

[3] R. Pandit, M. Schick, and M. Wortis, *Phys. Rev. B* **26**, 5112 (1982).

[4] J. Luo, *Curr. Opin. Solid State Mater. Sci.* **12**, 81 (2008); V. K. Gupta, et al., *Acta Mater.* **55**, 3131 (2007).

[5] S. von Alfthan, K. Kaski, and A. P. Sutton, *Phys. Rev. B* **74**, 134101 (2006).

[6] T. U. Schuli, *et al.*, *Nature* **464**, 1174 (2010).

New Methods for Atomic Structure Determination of Nanoscale Materials

L. D. Marks
Department of Materials Science and Engineering
Northwestern University
Evanston, IL 60201
L-marks@northwestern.edu

I ask you to look both ways. For the road to a knowledge of the stars leads through the atom; and important knowledge of the atom has been reached through the stars.

Sir Arthur Stanley Eddington, 1882-1944[1]

Oxide Surfaces

For many years the structure of oxide surfaces has been an area of considerable debate and some controversy. One of the major issues, if not the major one has been the question of what determines the structure. Many different models have been proposed ranging from minimization of "dangling bonds" [1] to reduction of Coulomb forces [2], and surface structures have largely been viewed as inherently different from bulk structures .

One feature of all these models is that they have been outward looking, i.e. they focus on trying to reduce the long-range electrostatic terms extending out into vacuum. While such ideas are important and an electrically charged surface will in principle have an infinite energy, this alone is not what determines the structure of bulk oxides. If instead of looking outwards we look inwards, our view changes. Rather than just long-range electrostatic terms being important, we have to consider as well the short-range chemical bonding terms. In bulk oxides this is now a comparatively mature area, with extensions of the original Pauling rules routinely used, what are called bond-valence sums. These are routinely taught in high-schools or to university undergraduates. If a bulk structure is proposed where the bond-valences calculated based upon the distances between atoms do not match what is expected from the formal valences of the compound, this is strong grounds for believing that the structure is at best metastable, at worst incorrect. While initially developed based upon a statistical analysis of known oxide structures there is now ample evidence from ab-initio calculations that the approach is a very good first analysis which can be slightly off in the fine details, but rarely too far.

Beyond the bond-valence approach, there are also many other concepts in bulk inorganic oxide solid-state chemistry which have not been considered as relevant to oxide surfaces. Significant examples are the concepts of homologous series, intergrowths and network disordered structures. In the bulk it is well established that local chemical order is generally preserved,

[1] Sir Arthur Stanley Eddington (1927). In *Stars and Atoms*. New Haven: Yale University Press; London: H. Milford/Oxford University Press

with structural disorder or reorganization superimposed upon this local order driven by stoichiometric changes and/or entropic terms.

One of the initial objectives of this program was to compare the thermodynamics and energetics of oxide surfaces as revealed using advanced electron microscopy with first-principles theoretical calculations, to determine the degree to which they agree. We have made substantial strides with this, demonstrating that local chemical concepts as described above are critical, particularly the bond-valence concept [3, 4] – not what we expected to find when the proposal was written.

The first and clearest example is the $SrTiO_3$ (110) surface which forms a homologous series of nx1 reconstructions; we solved the 3x1 and using STM images from a collaborator were able to solve the 2x1, 4x1, 5x1 and 6x1 members [3]. They are all remarkably similar with tetrahedral TiO_4 units assembled in ring structures, to go from one to another "all" that is required is to change the ring packing and stoichiometry, similar to classic solid-state analogues such as Magnéli or Ruddlesden-Popper phases. Indeed, if the STM images were conventional HREM images of a complex oxide they would not be remarkable; the fact that one has monolayer intergrowths is new and somewhat remarkable.

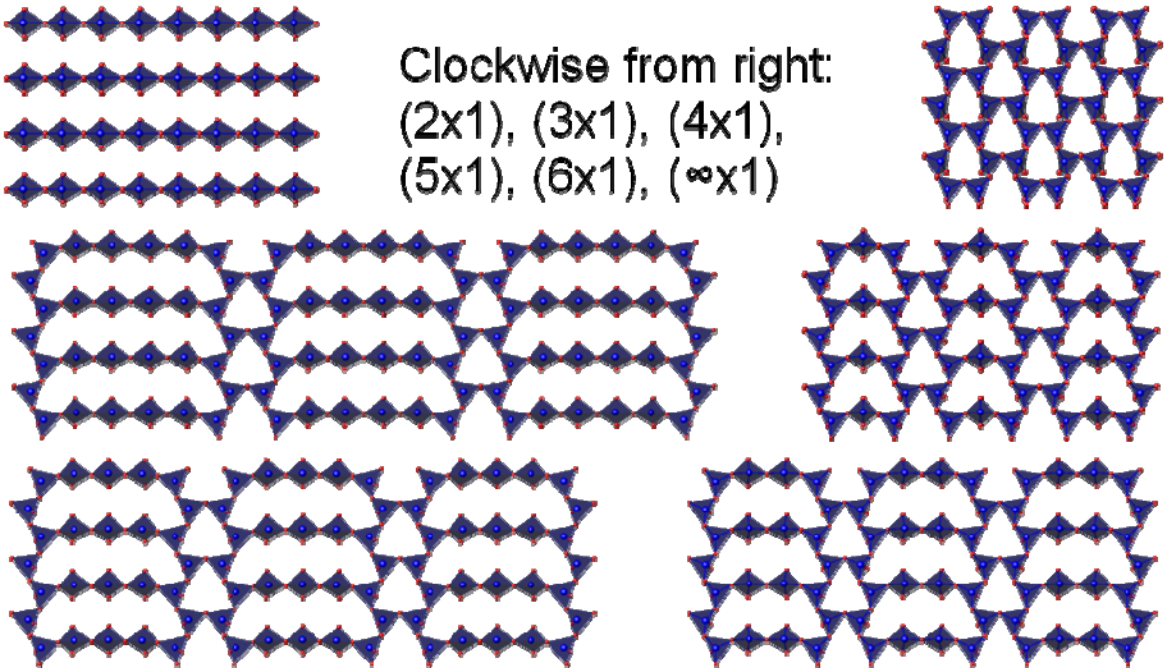

Figure 1: Reconstructions on the $SrTiO_3$ (110) surface. The blue units are TiO_4 tetrahedra, and changing their packing produces a valence neutral homologous series.

The comparison to bulk oxides goes further than this, as demonstrated by the √13x√13 R34° reconstruction on the $SrTiO_3$ (001) surface [5]. Using transmission electron diffraction coupled with direct methods and density functional methods we have been able to solve the structure, as shown in Figure 2. Significant about the structure is that it contains tetrahedral TiO_4 units at the surface with some $TiO_5◊$ octahedra (◊ indicating a vacant site) in the second layer. These

tetrahedral units (very similar to $SrTiO_3$ (110)) are arranged in an ordered fashion of square units with linear linkers. If one changes the number of linear units between the square units this produces a homologous series of valence neutral $\sqrt{(n^2+(n+1)^2)}x\sqrt{(n^2+(n+1)^2)}$ surface reconstructions where *n*=1 results in a $\sqrt{5}x\sqrt{5}$ R27° (experimentally reported by others), n=2 results in a $\sqrt{13}x\sqrt{13}$ R34°, n=3 results in a (5x5)R37°, with a TiO_2 surface excess of $0.5+4n/(2n^2+2n+1)$ monolayers.

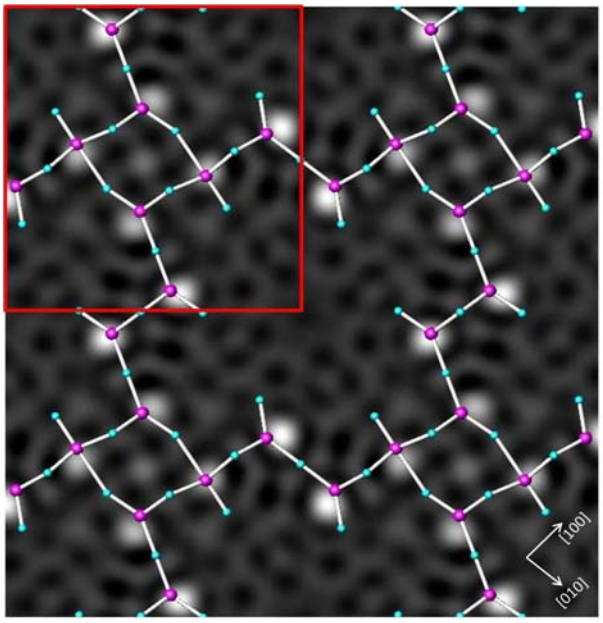

Figure 2. Geometrically relaxed atomic surface layer superimposed on the scattering potential map solution obtained from direct methods showing excellent agreement between direct methods and DFT structural results. Larger atoms (red) are Ti and smaller atoms (blue) are O. Changing the number and packing of square versus linear units produces a sequence of valence neutral reconstructions or a tetrahedral network glass.

Going further, instead of tiling the tetrahedral units in a regular fashion one can tile them in a disorder fashion and produce a glass. (Note that just as SiO_2 can have the rutile structure under pressure, TiO_2 in negative pressure or tensile strain at a surface can in principle have the quartz structure [3] and by induction readily form glasses similar to SiO_2.) This is a highly plausible structure for the disordered 1x1 surface of $SrTiO_3$ which are commonly used for epitaxial thin-film growth, and is consistent with STM data (Castell, private communication, 2010).

The same trend appears for other surfaces, for instance the $LaAlO_3$ (001) 5x2 reconstruction [6] although sometimes more macroscopic effects such as entropy-driven surface segregation can occur as in $SrLaAlO_4$ [7].

Precession Electron Diffraction

A second aim of this project has been to understand the details of precession electron diffraction (PED) and push this technique to its technical limits. When the project started most experts in electron microscopy probably considered PED to be a curiosity which might prove useful. It is now, mainly with x-ray crystallographers and solid-state chemists in Europe (the US is at least a year behind if not more) a mainstream technique that they use routinely. Part of this has been technical developments, again mainly in Europe, another part has been the widespread availability of multislice to simulate PED patterns, a tool which we pioneered.

One original goal, to formulate "Precession Electron Diffraction for Dummies" has not been realized, and may never be. It has become clear that increasing the cone-angle is very important [8, 9] to obtaining quasi-kinematical data, but this does not have a simple explanation. A detailed analysis [10] has indicated that it is not simply tilting off the zone-axis which matters, but a combination of this with integration over directions. This shows up in both a principal component analysis as well as phase-scrambling tests.

The time is ripe for PED to move away from being a technique that needs development to one which should be exploited. We have progressed on this in two directions:

a. Joint with Lukas Palatinus and Wharton Sinkler a 2-beam approximation for PED is being built in to Jana2006 (a widely used, free refinement code) so it can be used for moderately accurate structural refinements. As we have previously demonstrated [11], this is much better than a kinematical approximation.

b. The technique is now being used together with other funding on more applied problems, for instance to identify phases in nanoscale solid-oxide fuel cells or carbide precipitates in metal-on-metal hip-replacements.

References

1. Pashley, M.D., *Electron counting model and its application to island structures on molecular-beam epitaxy grown GaAs(001) and ZnSe(001).* Physical Review B: Condensed Matter, 1989. **40**(15): p. 10481-10487.
2. Wolf, D., *Reconstruction of NaCl surfaces from a dipolar solution to the Madelung problem.* Physical Review Letters, 1992. **68**(22): p. 3315-3318.
3. Enterkin, J.A., A.K. Subramanian, B.C. Russell, M.R. Castell, K.R. Poeppelmeier, and L.D. Marks, *A homologous series of structures on the surface of SrTiO3(110).* Nature Materials, 2010. **9**(3): p. 245-248.
4. Enterkin, J., K.R. Poeppelmeier, and L.D. Marks, *A Chemical Approach to Understanding Oxide Surfaces.* In Preparation, 2010.
5. Kinzle, D., A.E. Becerra-Toledo, and L.D. Marks, *Structure of the R13 Reconstruction on $SrTiO_3$ (001).* Submitted, 2010.
6. Kinzle, D. and L.D. Marks, *Structure of the $LaAlO_4$ (001) 5x2 Reconstruction.* In Preparation, 2010.
7. Becerra-Toledo, A.E. and L.D. Marks, *Strontium oxide segregation at SrLaAlO4 surfaces.* Surface Science, 2010. **604**(17-18): p. 1476-1480.
8. Ciston, J., C.S. Own, and L.D. Marks, *Cone-angle dependence of ab-initio structure solutions using precession electron diffraction.* Electron Microscopy and Multiscale Modeling, Proceedings, 2008. **999**: p. 53-65.
9. Ciston, J., B. Deng, L.D. Marks, C.S. Own, and W. Sinkler, *A quantitative analysis of the cone-angle dependence in precession electron diffraction.* Ultramicroscopy, 2008. **108**(6): p. 514-522.
10. Sinkler, W. and L.D. Marks, *Characteristics of precession electron diffraction intensities from dynamical simulations.* Zeitschrift Fur Kristallographie, 2010. **225**(2-3): p. 47-55.
11. Sinkler, W., C.S. Own, and L.D. Marks, *Application of a 2-beam model for improving the structure factors from precession electron diffraction intensities.* Ultramicroscopy, 2007. **107**(6-7): p. 543-550.

Nanoscale Imaging of Electrostatic and Magnetic Fields

Martha R. McCartney and David J. Smith
molly.mccartney@asu.edu, david.smith@asu.edu
Department of Physics, Arizona State University, Tempe, AZ 85287

Program Scope

This research program involves using the technique of off-axis electron holography to quantify nanoscale electrostatic and magnetic fields. One major focus of this research emphasizes the electrostatic potential profiles developed across undoped and doped heterojunctions and actual semiconductor devices, with recent activity involving doped and core/shell nanowires. Our second focus relates to magnetic thin films and nanostructures, with recent focus on field-induced domain-wall motion, and future focus on exchange-coupled nanostructures and antiferromagnetic oxides. Here, we plan to probe the nature of the coupling between the magnetic material and different ferromagnets. Changes in magnetic properties such as coercivity and reversal mechanisms attributable to reduced particle dimensions, in addition to differences arising from chemical reactions at the oxide/metal interfaces will be investigated.

Recent Progress

Our most recent electron holography investigations of electrostatic potential profiles have mainly involved Group IV-IV semiconductor heterojunctions. Our successful study of hole accumulation in epitaxial germanium quantum dots embedded in B-doped silicon has since been followed up by observations of Ge/Si core/shell nanowires in both plan-view and cross-section geometries. The usefulness of our earlier work in determining the fundamental materials parameters of mean inner potential and inelastic mean free path for AlAs and GaAs was emphasized in the subsequent holographic analysis of compound semiconductor devices comprised of doped heterojunctions, including GaAs/AlGaAs/AlAs heterostructures and AlGaAs/GaAs and InGaAs light-emitting diodes. The second major emphasis of our electron holography investigations has been nanostructured magnetic materials, which continue to be of much fundamental interest as well as topical importance because of their possible utilization in high-density magnetic recording devices. Off-axis electron holography represents a powerful tool for evaluating these basic properties as lateral dimensions are reduced since the technique can be used both to determine remanent states of individual elements *and* to follow hysteresis cycles *in situ* with spatial resolutions on the scale of 5 nm or better.

i) Electrostatic fields

Our electron holography observations of AlAs and GaAs during the previous period had established reliable values for the mean inner potential and mean-free-path for inelastic scattering, which are essential parameters that are needed for future device characterization studies to ensure that electrostatic doping effects can be distinguished from material effects. The electrostatic potential profiles across n-doped (or p-doped) GaAs/AlGaAs/AlAs heterostructures have been measured, and simulations of the expected profiles agreed very closely with the experimental measurements once allowance was made for the presence of unintentional carbon impurities at the buffer/substrate interface. More complex structures involving p-n junctions in

AlGaAs/GaAs and InGaAs light-emitting diodes (LEDs) have since been observed. The introduction of linear graded triangular AlGaAs barriers into these structures, which is preferred in order to enhance transport properties, normally makes it difficult experimentally to establish the dopant distribution *and* activation in such devices. In the case of the AlGaAs/GaAs LED heterostructure, careful comparison of the holography measurements with simulations revealed reduced activation of both the Si (p-type) and Be (n-type) dopants. For the InGaAs/AlGaAs LED, which again had linearly graded triangular barriers, small discrepancies between simulations and the holography measurements were initially apparent. These differences could eventually be resolved by taking into account the low-level presence of oxygen impurities that were causing unintentional carrier traps in the AlGaAs barriers. Overall, these results confirmed that electron holography with nanometer-scale resolution represents a powerful tool for the quantitative analysis of dopant distributions across such graded heterojunctions, and that the electron holography approach should be highly useful for future device development and process optimization.

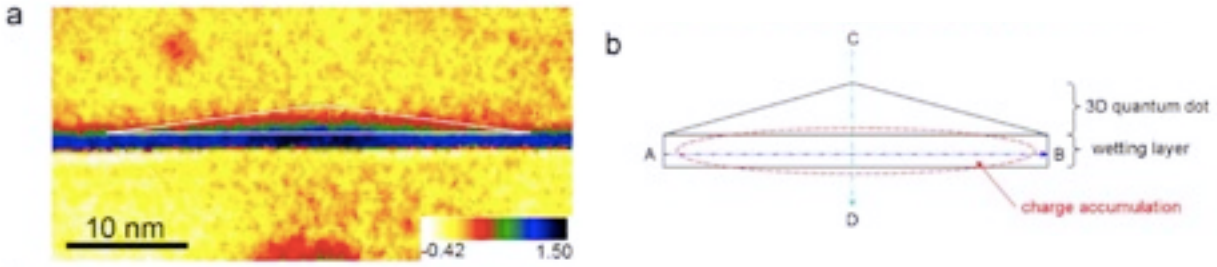

Fig. 1 (a) Reconstructed phase image of Ge QD. Dark region under dot in wetting layer indicates excess positive charge; (b) sketch of QD and wetting layer. (Li, et al., APL. 2009)

In a more recent study, the accumulation of positive charge (i.e., holes) in individual Ge quantum dots (QDs) embedded in Si was investigated (see Fig. 1). This particular geometry causes valence-band offsets that are anticipated to lead to the physical confinement of holes in the Ge QDs Excess positive phase shift was clearly observed across the Ge QDs, especially near the QD base. However, extracting meaningful numbers from the phase image about the amount of accumulated charge involved extensive geometrical analysis taking into account the shape of the dot and the amount of Si above and below the dot when projected in the beam direction. By applying a one- dimensional Poisson equation to the projected electrostatic potential due only to the confined holes, the resulting average number of holes per unit volume which corresponded to ~30±3 holes/dot for one specific 25-nm-wide Ge QD . This calculated number of holes was close to the average number of 40 holes per each Ge QD that was found using a capacitance–voltage measurement with a macroscopic-sized sample. Overall, this study demonstrated the possibility of applying off-axis electron holography to the challenging problem of quantifying electric charge confined to nanoscale regions of a heterogeneous sample.

ii) Magnetic fields

The second major emphasis of our electron holography investigations has been nanostructured magnetic materials, which continue to be of much fundamental interest as well as topical importance because of their possible utilization in high-density magnetic recording

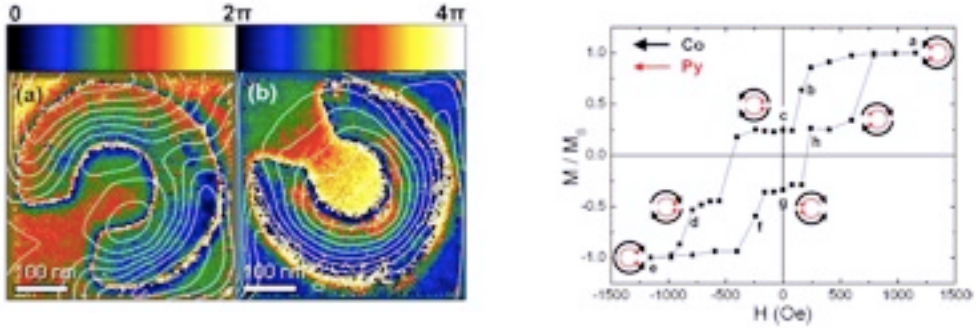

Fig. 2 (a)Holographic phase images of Co/Cu/Py elements showing remanent magnetization; (b) Three-step hysteresis loop for right-had spin-valve slotted nanoring element with applied magnetic field parallel to the slot direction. (K. He, et al. APL, 2009a)

devices. Understanding magnetization states and controlling reversal mechanisms is essential for practical applications of such nanomagnets. Off-axis electron holography represents a powerful tool for evaluating these basic properties as lateral dimensions are reduced since the technique can be used both to determine remanent states of individual elements *and* to follow hysteresis cycles *in situ* with spatial resolutions on the scale of 5 nm or better. Our recent attention has been directed towards slotted rings, which we find can have very stable and well-defined remanent states, and they also display rapid magnetization switching provided that the formation of vortex states can be avoided. Our holography observations suggest, however, that a more complicated, three-step hysteresis behavior associated with vortex formation and removal often occurs for both single Co layers as well as for Co/Cu/Py (where Py = Permalloy) spin-valve elements (see Fig. 2). In addition, we have just completed a comprehensive investigation of the effects of vortex chirality and shape anisotropy on the reversal mechanisms.

More recently, we have initiated *in situ* studies of domain-wall (DW) nucleation and propagation, which is a subject of intense activity due to the proposed development of related memory and logic devices based on ferromagnetic nanowires. Using notched Permalloy nanowires as test objects, we have used electron holography to study various aspects of the field-driven DW motion, including nucleation, injection, pinning and depinning. The relative chirality (i.e., sense of field rotation) of the notch and the nucleation pad was found to have the major influence in determining the characteristics of the DW behavior.

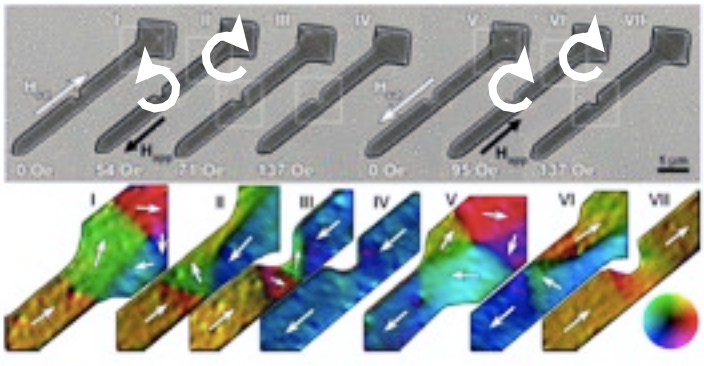

FIG. 3. Fresnel images (top) and corresponding magnetic induction maps (bottom), as extracted from holograms: (I) nucleation, (II) injection, (III) pinning, and (IV) depinning during forward half-cycle. (V) nucleation, (VI) injection, and (VII) pass-through for reverse half-cycle. Initial saturation direction and applied field direction as indicated by white and black arrows. Directions in magnetic induction maps indicated by color wheel or overlaid arrows. (K. He, et al. APL, 2009b)

Future Plans

Our future research will continue to emphasize the electrostatic potential developed across undoped and doped heterojunctions, since direct measurements using electron holography are essential for characterizing nanoscale devices and highly doped materials with steep concentration profiles. We will examine further Si/Ge core/shell nanowires with and without B doping in order to gain a better understanding of band-bending effects and charge accumulation. We will also carry out electron holography observations of GaAs-based nanowires, which are of potential interest for both light-emitting and photovoltaic device applications, in particular to provide insight into the effects of growth and annealing conditions on the potential profiles associated with vertical and lateral *p-n* junctions. The micromagnetic behavior of nanostructured magnetic elements will continue to be investigated, in particular since the nucleation and annihilation of individual magnetic vortices is a topic attracting considerable attention in the scientific literature and electron holography can provide unique insights. We will also continue with our *in situ* observations of field-driven DW pinning/depinning mechanisms in notched magnetic nanowires. Finally, we have started experimenting with different geometrical designs that should permit *in situ* holography studies of DW motion via a spin-torque mechanism induced by current pulsing. Our first trials are still focused on controlling the applied current so as not to melt the nanowire, but we anticipate overcoming this problem and moving towards direct current-pulsing and holography observations in the near future.

References to journal publications of DOE-sponsored research for period 2008-2010:

(invited review) M. R. McCartney, N. Agarwal, S. Chung, D. A. Cullen, M-G. Han, K. He, Luying Li, H. Wang, L. Zhou, D. J. Smith, (2010), "Quantitative phase imaging of nanoscale electrostatic and magnetic fields using off-axis electron holography", Ultramicroscopy, **110**, 375-382.

K. He, D. J. Smith, M. R. McCartney, (2010), "Effects of vortex chirality and shape anisotropy on magnetization reversal of Co nanorings" (invited) Journal of Applied Physics, **107**, 9, Art. # 09D307.

S. Chung, S. R. Johnson, D. Ding, Y. H. Zhang, D. H. Smith, M. R. McCartney, (2010), "Quantitative dopant profiling of p-n junction in InGaAs/AlGaAs light-emitting diode using off-axis electron holography", Journal of Vacuum Science & Technology B, **28**, 1 C1D11–C1D14.

K. He, D. J. Smith, M. R. McCartney, (2009a) "Direct visualization of three-step magnetization reversal of nanopatterned spin-valve elements using off-axis electron holography", Applied Physics Letters, **94**, 17, 172503.

K. He, D. J. Smith, M. R. McCartney, (2009b), "Observation of asymmetrical pinning of domain walls in notched Permalloy nanowires using electron holography", Applied Physics Letters, **95**, 18, 182507.

L. S. Chung, S. R. Johnson, D. Ding, Y. H. Zhang, D. H. Smith, M. R. McCartney, (2009) "Quantitative Analysis of Dopant Distribution and Activation Across p-n Junctions in AlGaAs/GaAs Light-Emitting Diodes Using Off-Axis Electron Holography", IEEE Transactions on Electron Devices, **56**, 9, 1919-1923.

K. He, N. Agarwal, D. J. Smith, M. R. McCartney, (2009) "Vortex Formation During Magnetization Reversal of Co Slotted Nanorings", IEEE Transactions on Magnetics, **45**, 10, 3885-3888.

K. He, D. J. Smith, M. R. McCartney, (2009), "Remanent states and magnetization reversal of nanopatterned spin-valve elements using off-axis electron holography", Journal of Applied Physics, **105**, 7, 07D517.

L. Li, S. Ketharanathan, J. Drucker, M. R. McCartney, (2009), "Study of hole accumulation in individual germanium quantum dots in p-type silicon by off-axis electron holography", Applied Physics Letters, **94**, 23, 232108.

S. Chung, S. R. Johnson, Y. H. Zhang, D. J. Smith, M. R. McCartney, (2009) "Off-axis electron holographic potential mapping across AlGaAs/AlAs/GaAs heterostructures", Journal of Applied Physics, **105**, 1, 014910.

M. G. Han, D. J. Smith and M. R. McCartney (2008) "In situ electron holographic analysis of biased Si n(+)-p junctions", Applied Physics Letters, **92**, 14, 143502.

New *In Situ* Analytical Electron Microscopy for Understanding Structure Evolution and Composition Change in High Energy Density Electrode Materials in Lithium Ion Batteries

Principle Investigator: Dr. Shirley Meng
Student and Postdoc: Ming-Che Yang and Dan Gostovic
Mailing Address: 2703 Atkinson, MC0448, Department of NanoEngineering, University of California San Diego
Email: shirleymeng@ucsd.edu
Collaborators: Feng Wang, Yimei Zhu and Jason Graetz at Brookhaven National Laboratory

Program Scope and Objectives

Our goal for this project is to develop novel analytical transmission electron microscopy (TEM) for understanding the chemistry and structure evolution of the electrode and electrolyte bulk and interfaces during electrochemical process. The main objectives are: I. Use pulsed laser deposition technique to fabricate multi-layer all-solid state batteries. II. Design and build a specialized in situ TEM holder to ensure vacuum transfer (controlled atmosphere), temperature control and electric bias. III. Study the delithiation process during the charging of the lithium ion electrodes in which delithiation proceeds as a two-phase reaction.

Summary of Recent Progress

- **Materials processing and thin film battery fabrication**

A series of spinel oxides have been synthesized and their properties are optimized for higher energy density and/or higher power density (a manuscript is submitted for publication). The optimized oxides are made into the targets for all solid state thin film battery fabrication by pulsed laser deposition.

Significant efforts have been made to fabricate all solid-state lithium ion battery using pulsed laser deposition (PLD) technique. We have made an $Li_{3.4}V_{0.6}Si_{0.4}O_4$(LVSO)/$LNi_{0.5}Mn_{1.5}O_4$/$SiO_2$/Si multi-layer thin film. Fully amorphous LVSO electrolyte layer on spienl-$LiNi_{0.5}Mn_{1.5}O_4$ cathode film were successfully grown by PLD. The microstructure and crystallinity of $LiNi_{0.5}Mn_{1.5}O_4$ thin films are dependent on different substrates and deposition parameters. Figure 1(a) shows the XRD patterns of the NiMn spinel films deposited on SiO_2 substrates at 600°C. All diffraction peaks attributed to the films can be indexed based on a spinel structure with space group $Fd\bar{3}m$. A (111) texture structure developed for NiMn spinel films. The relative intensity of (111)/(311) and (111)/(222) NiMn spinel films are larger than relative intensity of NiMn spinel powders (not shown here). The EDS of the NiMn film shows the atomic ratio of Ni:Mn is 24.58:75.42 that is identical to the theoretical values. NiMn spinel films deposited on stainless steel (SS) have similar results but the film is composed of bigger grains. Figure 1(b) shows the XRD pattern of LVSO/$LiNi_{0.5}Mn_{1.5}O_4$/SiO_2/Si thin film. All diffraction peaks attributed to the films can be indexed based on a spinel structure with space group $Fd\bar{3}m$. The results show that the LVSO electrolyte films are amorphous, which will provide fast lithium ion transport.

Figure 2 shows the SEM micrograph of the LVSO/$LiNi_{0.5}Mn_{1.5}O_4$/SiO_2/Si films. The dense and smooth LVSO thin films were deposited on NiMn spinel film successfully. The top

view picture of the LVSO films show the roughness is similar to NiMn spinel films. The thickness of cathode film deposited is about 200nm. The thickness of LVSO film is ~800nm. Although the electrochemical properties of such battery are not optimized yet, we have shown that a nano-battery half cell could be made with FIB technique using Pt as the anode electrode. For complete all solid state full cell battery we yet need to deposit the proposed spinel titanate anode; meanwhile, we obtain the full cell of microbattery $LiCoO_2$/LVSO/SnO_2 from our collaborator in National University of Singapore for testing the in situ holder and newly custom-designed TEM grid.

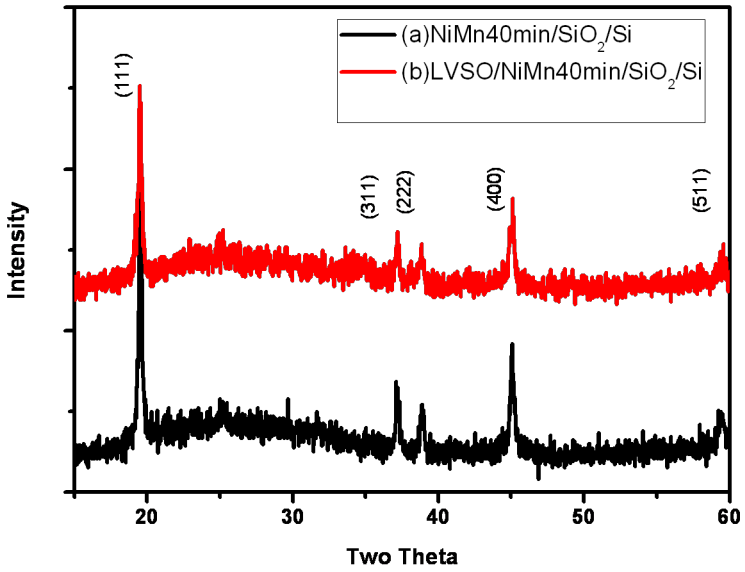

Figure 1. XRD pattern of $LiNi_{0.5}Mn_{1.5}O_4/SiO_2/Si$ and LVSO/$LiNi_{0.5}Mn_{1.5}O_4/SiO_2/Si$

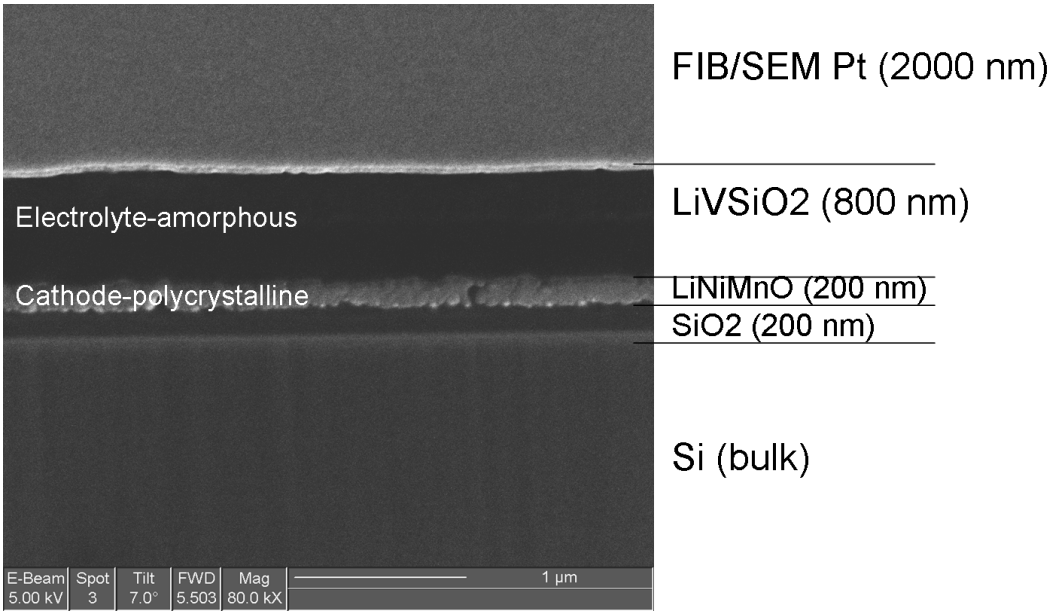

Figure 2. FIB/SEM prepared cross-section of solid-state LIB cathode/electrolyte half cell.

- **In-situ technique development**

The Gatan TEM holder with N_2 cooling, vacuum transfer capability and electric feedthroughs has been modified so that the electric contacts are close to the sample grid. New TEM sample grids with gold pads for electric contacts are built and we have successfully mount the contacts to the holder. We have completed testing of the Gatan TEM holder for N_2 cooling, controlled atmosphere transfer from a glove box and electric feedthroughs for ex situ/in situ biasing.

LVSO/$LiNi_{0.5}Mn_{1.5}O_4$/SiO_2/Si films were initially made into a 150 nm thick TEM foil and with the use of in-situ liftout were placed on a *TEM Windows* purchased SiN, 50 nm thick window. Ion beam sputter deposited platinum contacts were made to touch the top (electrolyte) layer and another platinum contact was made on the cathode side. This sample was analyzed in the TEM and it was observed that there was a platinum gradient on top of the electrolyte. Additionally, the deposition of the contacts using FIB/SEM took around 6 hours to get the contacts to be 2 mm long. This length was required to have the contacts touch gold wires on the edge of the TEM grid, which would be connected to the holder and used externally to apply a bias. The platinum gradient issue has been solved by mounting the sample on half grids and cleaning both faces after the Pt contacts have been made. In order to reduce the FIB/SEM sample preparation time (by 6 hours per sample), a novel TEM grid (UCSD's Triton TEM Grid, an invention disclosure has been filed) was developed and manufactured in collaboration with *TEM Windows Inc*. This Triton TEM grid consists of a Si substrate on top of which lies a 50 nm thick SiN layer machined into an electronically transparent window. SiN was used because of it is an electrical insulator, which is necessary to prevent shorting of the microbattery cross section. On top of this SiN film were deposited 200 nm thick gold pads which come close to the TEM window and greatly reduce the time to machine the contacts between the TEM foil and the external wires.

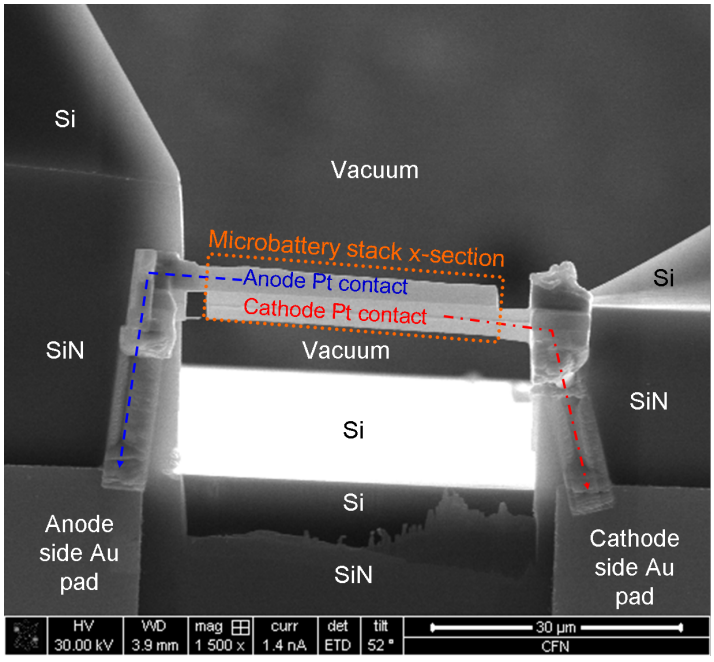

Figure 3. A microbattery stack complete with platinum cathode/anode contacts is mounted on a Triton TEM grid which consists of a 50 nm SiN film sandwiched between Au contacts and Si support grid.

After such a nano-battery half cell sample was fabricated (with foil thickness <50 nm) TEM electron energy loss spectroscopy (EELS) allowed for the atomic mapping of all constituents of the PLD deposited films (Figure 4a-c). In Figure4a the TEM micrograph of an as grown LVSO/$LiNi_{0.5}Mn_{1.5}O_4$/SiO_2/Si films is labeled. Figure 4b depicts the chemical mapping of the Ni, V, and Li constituents. Figure 4c shows the relative Li intensity in the PLD deposited cathode. Although there is some inhomogeneity in Li distribution in the cathode film, this was a successful proof of concept that the various atomic constituents of a LIB half cell could all be mapped relatively quickly (<10 minutes per EELS scan). EELS mapping allowed for visualization of the electrolyte and cathode chemical distributions.

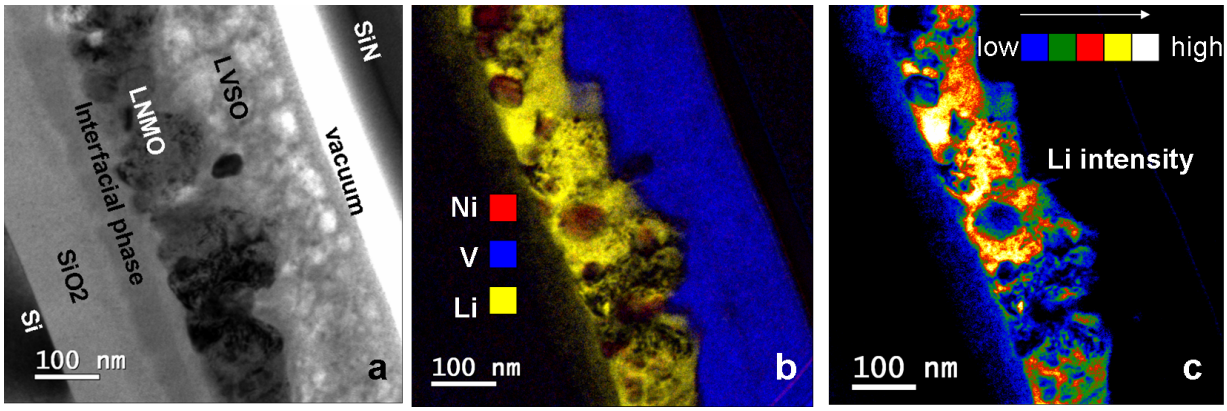

Figure 4. TEM micrograph with associated EELS chemical and elemental intensity maps

Planned Activities

The PLD deposition parameters will be tuned to get better crystalline and more dense films. The ionic conductivity of the LVSO and the electrochemical properties of the NiMn spinel film will be tested in Swagelok Cell. Moreover, in order to get smoother surface of thin film batteries, new substrate Pt/Ti/SiO_2/Si, much further optimization are needed for fabricating the multi-layer oxides nano battery. Our final goal is to make Pt/$Li_4Ti_5O_{12}$ (spinel) /LVSO (amorphous) /$LiNi_{1/2}Mn_{3/2}O_4$(spinel)/Pt/SiO_2/Si to study the two technologically important electrode materials. Both spinel oxides exhibit complex two phase reactions during charge, real time observations of the phase transformation process by in situ TEM will be vital to understand the mechanisms of delithiation and re-lithiation, and to achieve the objectives of proposed project.

All solid state nanobattery half cells are being mounted on custom made TEM Windows grids with gold contacts. This will allow for relatively robust contacts to be made on ~50 nm thick LIB x-section foils. This should increase the stability of the pA galvanostatic measurements. A FIB/SEM in-situ technique is also being developed which would allow for in-situ SEM scale analysis of site specific regions of larger LIB stacks. We are also working on developing a novel cartridge transfer device with *Omniprobe Inc.* which will allow for transfer of air/moisture sensitive materials and samples between glove box ⟷ FIB/SEM ⟷ TEM without any exposure to atmosphere.

Paper submitted

Ming-Che Yang, Bo Xu, Ru Ju-Hsiang Cheng, Hsiang Cheng and Bing-Joe Hwang, Ying Shirley Meng, "Electronic, Structural and Electrochemical Properties of $LiNi_xCu_yMn_{2-x-y}O_4$ ($0<x<0.5$, $0<y<0.5$) High-voltage Cathode Materials in Li-ion Batteries", submitted. 2010.

Program Title: **Structure and Dynamics of Domains in Ferroelectric Nanostructures – In-situ TEM Studies**

Principal Investigator: Xiaoqing Pan
Address: Department of Materials Science and Engineering
University of Michigan
2010 H.H. Dow Building
2300 Hayward Street
Ann Arbor, MI 48109
Tel: 734-647-6822;
E-mail: panx@umich.edu

Program Scope:

The main objective of this research program is to explore the fundamental nature of ferroelectric domains in strained ferroelectric thin films and fabricated nanostructures by advanced transmission electron microscopy (TEM) techniques in close collaboration with phase field modeling. The experimental techniques to be used include high-resolution transmission electron microscopy (HRTEM) and *in-situ* TEM using a novel scanning tunneling microscopy (STM) - TEM holder which allows for the direct observation of the nucleation and dynamic evolution of ferroelectric domains under an applied electric field. Specifically, we plan (1) to study the roles of static electrical boundary conditions in controlling the equilibrium domain structures of $BiFeO_3$ thin films with controlled substrate constraints, (2) to explore the fundamental mechanisms of ferroelectric domain nucleation, growth, and switching under an applied electric field in both uniform thin films and artificially nanofabricated islands, and to understand the roles of crystal defects such as dislocations and interfaces in these processes, and (3) to understand the physics of ferroelectric domain wall structure and properties (transport, band-gap, and dielectric response function), and the influence of defects (charged defects, dislocations, surfaces, and interfaces) on the domain structure and properties. The nucleation and dynamic evolution of ferroelectric domains observed by *in-situ* TEM under applied external electric field will be quantitatively analyzed and directly compared with phase field simulations in collaboration with Professor Long-Qing Chen's group at Penn State University.

Recent Progress

Effect of Mechanical Boundary Conditions: Substrate Miscut and Lattice Misfit

We have performed a systematic investigation of domain structures of epitaxial $BiFeO_3$ (BFO) thin films grown on different single crystal substrates and obtained a fundamental understanding of the effects of lattice misfit and substrate miscut on the ferroelectric domain structure and formation mechanisms of BFO thin films. This finding has guided the successful synthesis of BFO thin films with controlled domain structures and orientations, which provides an excellent model system for the fabrication of nanoscale nonvolatile magnetoelectric devices. TEM showed that the BFO films grown on exact (001) $SrTiO_3$ (STO) and (001) Si substrates consist of randomly distributed, 4-fold degenerate ferroelastic variants with a mixture of 71° and 109° domain walls. In contrast, the BFO films grown on (001) STO with a 2-4° miscut along the [100] direction have only two variants with a one-dimensional array of 71° domain walls perpendicular to the miscut direction. This study suggests a mechanism in which the two of four variants of BFO preferentially nucleate at the substrate surface steps. When the miscut is applied

along the [110] direction of STO, the BFO film consists of a monodomain of the r_1 variant [79]. Guided by these observations, an approach is developed to stabilize ferroelastic switching by eliminating the stress-induced instability responsible for back-switching using isolated monodomain $BiFeO_3$ islands on (001) STO substrate with 4° miscut along the [110] direction. TEM characterization of domain structures for nanofabricated BFO islands before and after electrical switching revealed the ferroelectric switching path in $BiFeO_3$. This work opens a new avenue to designing magnetoelectric coupling routes and device geometry to realize nonvolatile magnetoelectric coupling devices at the nanoscale.

Effect of Electrical Boundary Conditions on Equilibrium (Static) Domain Structures

The depolarization field of a thin film ferroelectric depends on the charge of the surfaces and on the separation between those surfaces (film thickness). If the space charge existing in the ferroelectric films during growth is not enough to compensate the depolarization field, electrically self-compensated domain structures will form. TEM of a 20 nm $BiFeO_3$ film grown on (110) $TbScO_3$ shows a 109° type domain pattern (Fig 1a and b). Analysis of the selected area electron diffraction patterns indicates that the striped array of domains consists of only r_1 and r_4 ferroelastic variants. Domain configuration and polarization orientations were determined by mapping the cation displacement, shown below the cross sectional TEM images. The exclusive presence of alternating r_1 and r_4 ferroelastic variants is the result of the low symmetry of the orthorhombic TSO substrate which reduces the degeneracy of the four ferroelastic variants to favor only these two.

Fig. 1c shows a TEM image of a 20 nm thick BFO film fabricated on a (110) TSO substrate with a coherent conducting $La_{0.7}Sr_{0.3}MnO_3$ (LSMO) buffer layer. The film forms large domains several hundred nanometers in width with little discernable long-range pattern. The domain boundaries typically take the form of paired 109° and 180° domain walls such as the region shown in Fig. 1c. This suggests that free carriers in the LSMO buffer effectively screen the bound surface charges at the BFO/TSO interface negating the depolarizing field.

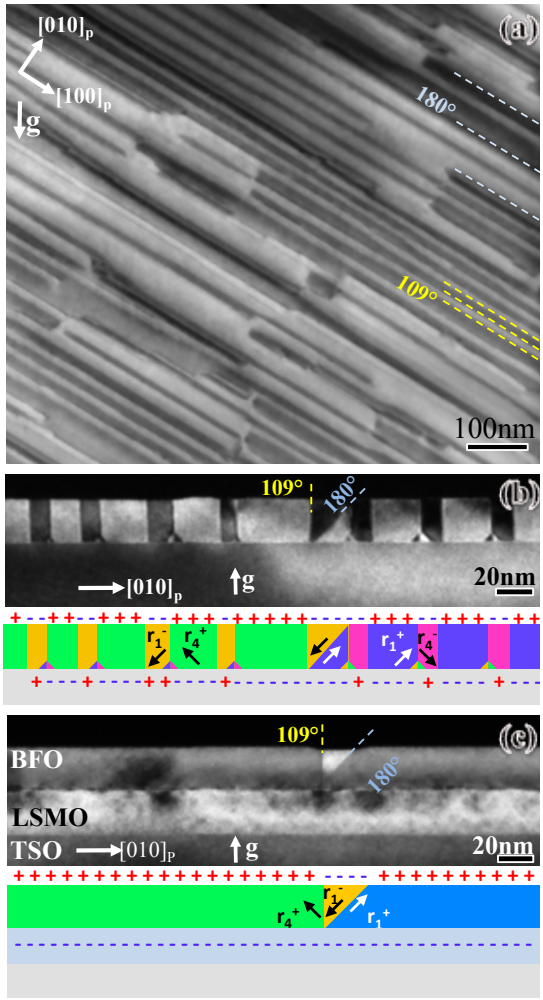

Fig. 1. Planar view (a) and cross sectional (b) images of a 20 nm $BiFeO_3$ film on $TbScO_3$ showing the striped domain pattern. (c) Cross sectional image of a 20 nm $BiFeO_3$ film with a conductive 20 nm $La_{0.7}Sr_{0.3}MnO_3$ buffer layer under the same conditions as for (b).

Effect of the Internal Depolarizing Field on the Stability of Local Polarization

Using sub-Å resolution Z-contrast images we obtained a spatial distribution of the displacement vector $\boldsymbol{D}_{FB}$ (which is the atomic displacement in the image plane of the Fe cation from the calculated center of the unit cell formed by its four Bi neighbors) in the near surface region of the BFO/TSO interface to determine the polarization distribution. The polarization direction is opposite that of $\boldsymbol{D}_{FB}$. A Z-contrast image of two adjacent 109° domain walls is shown in Fig. 2a and the corresponding angle of $\boldsymbol{D}_{FB}$ in Fig. 2b. The 109° domain wall terminations have two flavors: they either terminate directly (Fig. 2a−left) or form a triangular pattern of domain walls (Fig.2a−right). The $\boldsymbol{D}_{FB}$ maps are shown in Fig. 2c (for the directly terminating domain wall) and 2d (for a triangle domain terminating 109° wall). The magnitude and angle of the displacement vectors are shown in color maps at right. It is seen that the triangle domains are formed by mirrored pair of inclined 180° domain walls. Fig. 2e and 2f show the polarization distribution of the corresponding domain walls from a phase field simulation. Analysis of the local depolarizing field due to bound charges at the surface/interface surface of the 109° domain structure revealed that geometries where the surface fields and polarization are

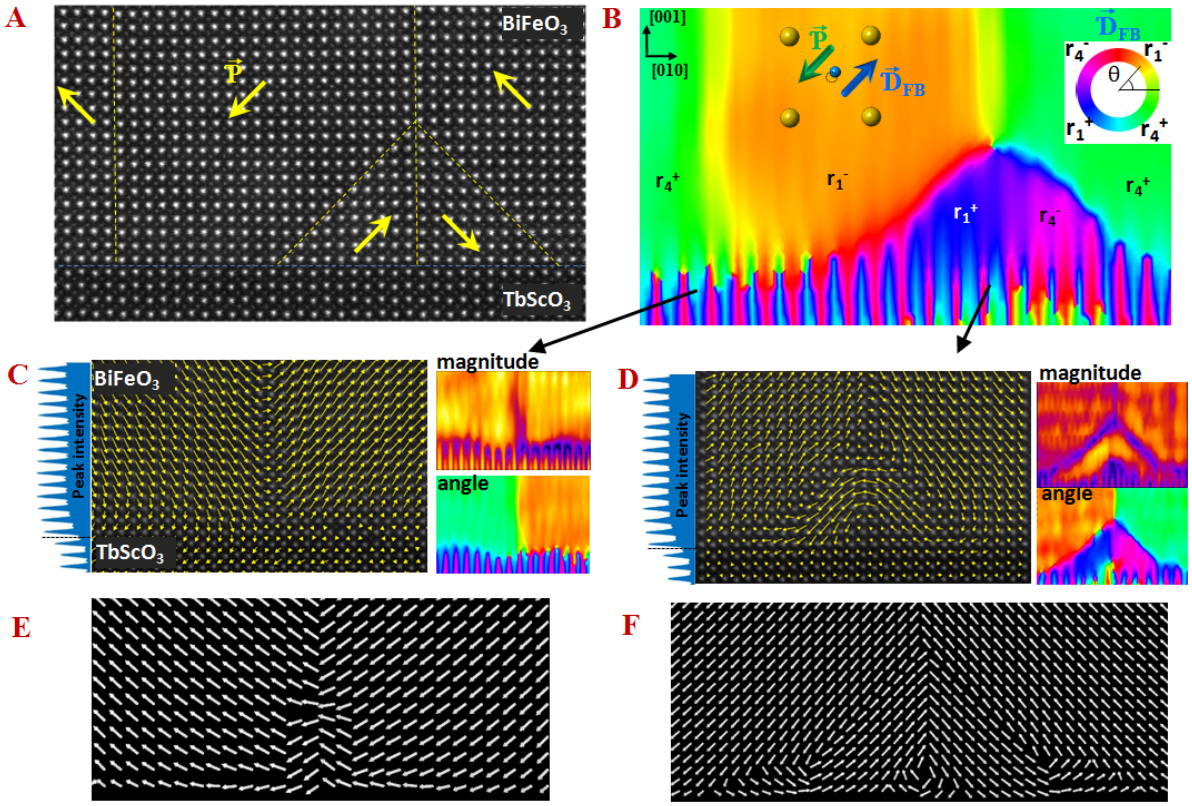

Fig. 2. Polarization distribution of 109° domain walls at the film/substrate interface. (a) Z-contrast STEM image of the intersection of two 109° domain walls with the $TbScO_3$ surface. (b) Color map of the angle of the cation displacement corresponding to (a) shows the domain structure of the $BiFeO_3$ and the oscillating structure of the substrate. (c) Plot of the vectors for a 109° domain wall which terminates directly with the interface. (d) Plot of the vectors for a 109° domain wall which forms a pair of 180° triangle domains at the interface with color maps of the magnitude and angle of at right. (e) and (f) The polarization distribution of a directly terminating and a triangle-domain terminating109° wall from a phase field simulation.

parallel the domain walls (Fig. 2 – left) have low electrostatic energy and that in geometries where the surface electric field opposes the polarization large electrostatic energies drive the formation of compensating 180° triangle domains (Fig. 2 – right). It is also found that within the triangle domains there is a significant (>50%) enhancement of the in-plane polarization vector. The 109° and 180° domain walls associated with these domains therefore have polarization distributions which deviate from their bulk counterparts. These localized effects on the polarization distribution are likely to influence the functionality and switching properties especially for very thin films.

List of publications (2008-2010):

1. M.D. Biegalski, D.D. Fong, J.A. Eastman, P.H. Fuoss, S.K. Streiffer, T. Heeg, J. Schubert, W. Tian, C.T. Nelson, X.Q. Pan, M.E. Hawley, M. Bernhagen, P. Reiche, R. Uecker, S. Trolier-McKinstry, and D.G. Schlom, *Critical thickness of high structural quality SrTiO3 films grown on orthorhombic (101) $DyScO_3$.* Journal of Applied Physics, 2008. **104**(11): p. 114109.
2. H.W. Jang, S.H. Baek, D. Ortiz, C.M. Folkman, R.R. Das, Y.H. Chu, P. Shafer, J.X. Zhang, S. Choudhury, V. Vaithyanathan, Y.B. Chen, D.A. Felker, M.D. Biegalski, M.S. Rzchowski, X.Q. Pan, D.G. Schlom, L.Q. Chen, R. Ramesh, and C.B. Eom, *Strain-induced polarization rotation in epitaxial (001) $BiFeO_3$ thin films.* Physical Review Letters, 2008. **101**(10): p. 107602.
3. H.W. Jang, D. Ortiz, S.H. Baek, C.M. Folkman, R.R. Das, P. Shafer, Y. Chen, C.T. Nelson, X. Pan, R. Ramesh, and C.B. Eom, *Domain Engineering for Enhanced Ferroelectric Properties of Epitaxial (001) $BiFeO_3$ Thin Films.* ADVANCED MATERIALS, 2009. **21**(7): p. 817.
4. C.M. Folkman, S.H. Baek, H.W. Jang, C.B. Eom, C.T. Nelson, X.Q. Pan, Y.L. Li, L.Q. Chen, A. Kumar, V. Gopalan, and S.K. Streiffer, *Stripe domain structure in epitaxial (001) $BiFeO_3$ thin films on orthorhombic $TbScO_3$ substrate.* APPLIED PHYSICS LETTERS, 2009. **94**(25): p. 251911.
5. C.M. Folkman, S.H. Baek, C.T. Nelson, H.W. Jang, T. Tybell, X.Q. Pan, and C.B. Eom, *Study of defect-dipoles in an epitaxial ferroelectric thin film.* Applied Physics Letters, 2010. **96**(5): p. 052903.
6. W. Guo, L. Fu, Y. Zhang, K. Zhang, L.Y. Liang, Z.M. Liu, H.T. Cao, and X.Q. Pan, *Microstructure, optical, and electrical properties of p-type SnO thin films.* Applied Physics Letters, 2010. **96**(4): p. 042113.
7. S.H. Baek, H.W. Jang, C.M. Folkman, Y.L. Li, B. Winchester, J.X. Zhang, Q. He, Y.H. Chu, C.T. Nelson, M.S. Rzchowski, X.Q. Pan, R. Ramesh, L.Q. Chen, and C.B. Eom, *Ferroelastic switching for nanoscale nonvolatile magnetoelectric devices.* Nature Materials ***9,*** 309 - 314 (2010)..
8. S. Lee, J. Jiang, Y. Zhang, C. W. Bark, J.D. Weiss, C. Tarantini, C.T. Nelson, H.W. Jang, C.M. Folkman, S.H. Baek, A. Polyanskii, D. Abraimov, A. Yamamoto, J.W. Park, X.Q. Pan, E.E. Hellstrom, D.C. Larbalestier, and C.B. Eom, *Template engineering of Co-doped $BaFe_2As_2$ single-crystal thin films.* Nature Materials **9**, 397 - 402 (2010).

Future Plans

The future work will focus on the atomic resolution TEM imaging and in-situ measurements of domain structures in $BiFeO_3$ nanostructures with controlled strain and electromechanical boundary conditions aimed at answering the following fundamental questions: (1) how do ferroelectric domains nucleate, grow, and switch under an applied electric field in both uniform thin films and artificially nanofabricated islands, and what roles do crystal defects such as dislocations and interfaces play in these processes? (2) how does the local atomic displacement, and thus electrical polarization, vary across domain walls, interfaces and surfaces, and how do they interact with defects? and (3) what are the electronic properties of domain walls in comparison to the bulk film, and what is the influence, if any, of conducting domain walls on domain formation and domain switching in multiferroic $BiFeO_3$ films?

Physics of complex materials systems through theory and microscopy/EELS

Sokrates T. Pantelides, lead PI; Mark Oxley, Kalman Varga, co-PIs
Department of Physics and Astronomy, Nashville, TN 37235
pantelides@vanderbilt.edu

1. Objectives

The main objectives of this research program are: a) to create an integrated simulation capability of electron-energy loss spectra (EELS), including both diffraction theory that describes the propagation of the electron beam of a scanning transmission electron microscope (STEM) through the thin film to the detector and density functional theory (DFT) for the calculation of the core excitation process, including interference effects (so far, the two objectives have been addressed by different communities with minimal overlap, one community leaving out solid-state effects, the other leaving out diffraction and interference); b) explore the implementation of time-dependent calculations as an alternative to the standard steady-state multislice method for diffraction and related techniques; and c) pursue calculations to interpret available Z-contrast and EELS data for particular materials systems using available and newly-developed theoretical tools. Accomplishments in all three areas are described below.

2. Diffraction + EELS

2.1 Background:

Electron diffraction theory was developed more than 50 years and computer codes for simulating the process in the context of the transmission electron microscope have been written by several groups. Co-PI Mark Oxley is a practitioner of this discipline, having received his training at the group of Les Allen at the University of Melbourne in Australia. The existing diffraction code simulates the propagation of a microscope's electron beam as it travels through the focusing lenses and then traverses the thin film and is diffracted by the periodic crystal potential. EELS simulations for STEM experiments in this context have been limited to atomic approximations for the potential resulting in simulations that lack solid-state effects such as energy-loss near-edge structure (ELNES). When the beam is analyzed in terms of component plane waves, there are plane waves travelling in all directions (different momenta **q**). The transferred momentum determines the scattering angle. Realistic EELS simulations, therefore, require calculations of what is called the mixed dynamical form factor (MDFF), that captures all waves arriving at an atom to be excited, corresponding to the beam position, and tracks the arrival of all scattered waves into the detector, i.e., a sum over **q** and **q**′.

The simulation of ELNES using realistic solid potentials has traditionally been pursued by a different community of researchers that includes the lead PI. This community typically ignores all diffraction effects and essentially assumes that the electron beam travels in vacuum and appears at each atom where it causes an excitation. The contributions of various excitation processes to the experimental signal are calculated from the band structure, which has been the traditional focus of this community. Only the dynamical form factor (DFF), typically calculated at zero momentum transfer (dipole approximation), is needed. The approximation is equivalent to calculating the imaginary part of the dielectric constant as in x-ray or optical absorption.

The goal of this project is to combine theoretical state-of-the-art spectral and diffraction methods to produce realistic simulations of electron microscope experiments involving dynamical electron diffraction *and* core excitation (e.g. STEM-EELS). Such simulations are increasingly becoming essential in the interpretation of data obtained by aberration-corrected STEMS in complex materials systems.

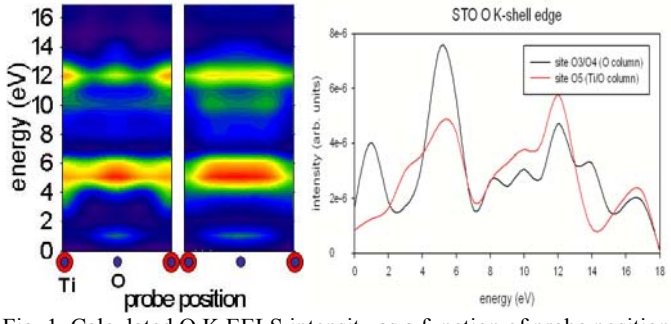

Fig. 1. Calculated O K EELS intensity as a function of probe position in $SrTiO_3$. Left color panel: without diffraction; Right color panel: with diffraction in 30-nm film. Right panel: EELS at two probe positions.

2.2 Work completed so far

The main elements of the mathematical development and computer code have been completed and tested and initial results have been obtained, illustrated in Fig. 1.

There were two main ingredients that led to the construction of the final code. The first is the calculation of the MDFF, of which the DFF is a special case, using bban electronic-structure approach and the second is integration with existing diffractions codes as needed for STEM (or TEM) simulation. Prior ap-

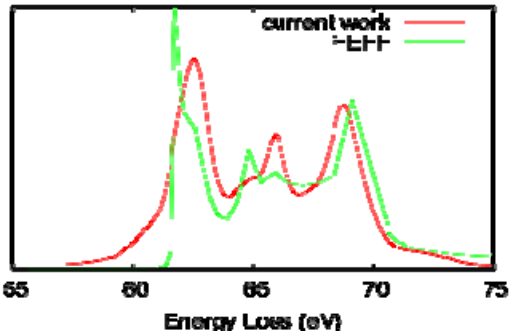

Fig. 2 Calculated K shell EELS spectrum for bulk LiF compared to the FEFF code.

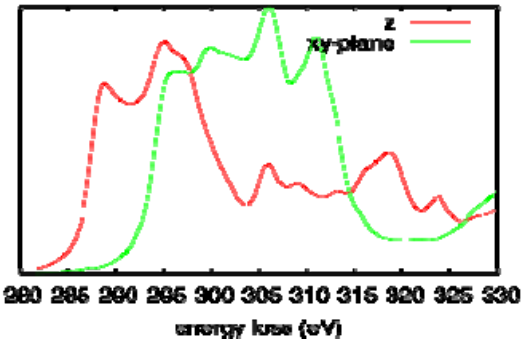

Fig. 3 Calculated K shell EELS for a graphene sheet for two orientations of the momentum transfer.

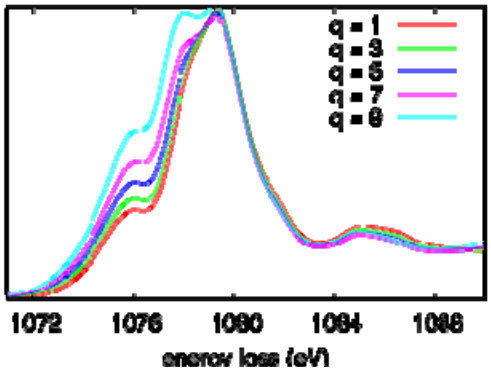

Fig. 4 Calculated Na K EELS in NaCl at several momentum transfers q, in $Å^{-1}$.

proaches for DFF calculations are based on either all-electron calculations carried out in real space or pseudopotential calculations carried out in momentum space. Real-space all-electron calculations, as in the codes WIEN2000 and FEFF, have the advantage of explicit core wave functions, but are time-consuming and do not match well with the diffraction calculations that are typically carried out in momentum-space. Pseudopotential calculations are based on plane waves, that are the most efficient and formally complete basis set, but do not have explicit core states. One is typically forced to adopt the Z+1 approximation (the core hole approximated by an extra proton on the nucleus, i.e., converting it to an impurity atom). On the other hand, plane waves in momentum space are an excellent match to so-called Bloch wave simulations of diffraction and the form of the MDFF. Furthermore, there is a type of pseudopotential scheme known as Projected Augmented Waves (PAW), developed by Peter Bloechl, that contains explicit core states and yet employs plane waves as a basis set. PAW is implemented in the widely used Vienna Ab Initio Simulation Package (VASP), but has not been used for EELS calculations so far. PAW meets all requirements for efficiency and applicability to complex systems, and was adopted for MDFF calculations in the present project.

The intent has been to build the new STEM simulation code on VASP so that it can be easily accessible to the community. The following tasks have been carried out:

1. The (large and complex) VASP code has been extended to allow the reconstruction of the all-electron wavefunctions from the PAW plane waves. To establish confidence in the undertaking, several auxiliary programs were written to compute relevant quantities and run tests and diagnostics.
2. The calculation of transition matrix elements that enter the MDFF for the EELS spectrum, including a core hole and quantum interference, has been implemented in a stand-alone, post-processing modular code with an input file parser that facilitates further development, adaptation, and production runs.
3. The transition matrix elements are tabulated and fed into the STEM Bloch wave simulator that includes detector geometry, thermal motion of the atoms, and other experimental conditions.

The net result is realistic simulations of the STEM-EELS signals and its dependence on both the probe position and energy loss, including band-structure, excitonic and diffraction/interference effects. These extensions to VASP considerably extend the capability of this popular code to simulations of many core loss spectroscopies including EELS, x-ray absorption (XAS), and nonresonant inelastic X-ray scattering (NRIXS) with or without beam diffraction. An example of an EELS calculation without diffraction is shown in Fig. 2.

The new code *does not employ the dipole approximation,* allowing us to explore the dependence of the near-edge signal on both the magnitude and direction of the momentum transfer for both photon and electron scattering experiments. Figures 3 and 4 demonstrate this capability. Figure 4 also demonstrates the usefulness of going beyond the dipole approximation: we show the NaCl K-edge exciton which, due to the smallness of the momentum transfer, is invisible in XAS but can be revealed by high-angle NRIXS. Both dipole and non-dipole behavior are successfully simulated by our approach.

3. Time-domain simulation of electron diffraction in solids

Simulation of the diffraction of a microscope electron beam as it traverses a thin-film sample is traditionally done by the steady-state multislice method. One solves the *time-independent Schrödinger equation* by dividing the sample into

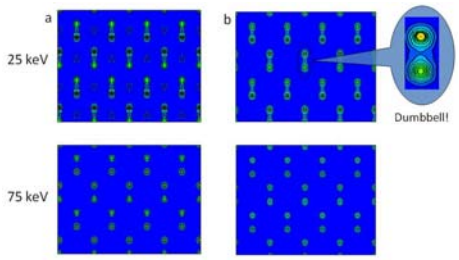

Fig. 5 Comparison of diffraction patterns from a (110) 4.4-nm Si thin film using the multislice (left) and time-dependent (right) approaches.

thin slices and matching the solution from one slice to the next. Back-scattering is usually neglected and other approximations are made, but the method generally provides a satisfactory description of diffraction, especially for high-energy electron beams.

It has long been recognized by several authors that a more desirable method would be to simulate diffraction by calculating directly the time evolution of an incident beam using the *time-dependent Schrödinger equation*. The approach is deemed "prohibitively expensive in both computer memory and computer time"[1]. As promised in the proposal, we have carried out such a simulation (post-doc Jia-An Yan with Professors Varga and Pantelides). Initial work focused on simulating a plane wave incident on a Si crystalline film. For this purpose the incident wave function is written as $\psi(\mathbf{x},t)=e^{ikz}\varphi(\mathbf{x},t)$, where z is the propagation direction. One then derives the time-dependent Schrödinger-like equation for $\varphi(\mathbf{x})$ and adopts a suitable algorithm for direct time-stepping of $\varphi(\mathbf{x},t)$ using discretized time and a real-space grid. The initial form $\varphi(\mathbf{x,0})$ is taken to be a Gaussian in the z-direction with no dependence on x and y, corresponding to plane-wave propagation. Initial results for a 4.4-nm Si thin film in the (110) plane showing the characteristic tilted dumbbells are shown in Fig. 5 and compared with corresponding calculations using the multislice method. A comparison of line scans across dumbbells illustrates the differences in the two methods (Fig. 6). The time-domain simulations are intrinsically more accurate as they do not make the approximations of the multislice method, so that the figures reflect the accuracy of the latter in various regimes.

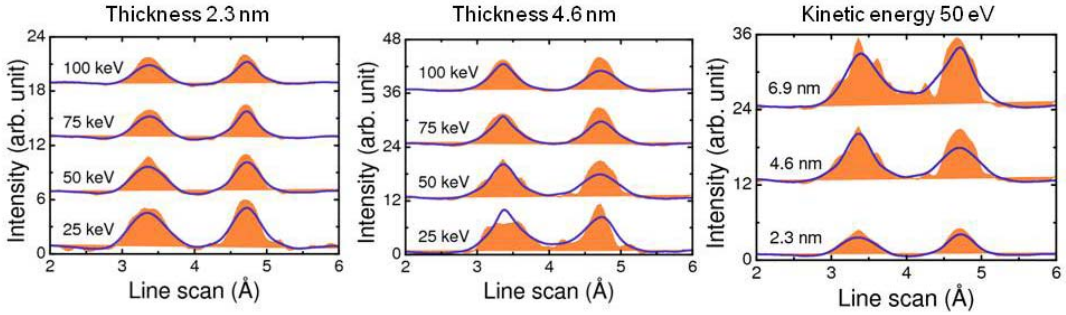

Fig. 6. Comparison of diffraction line scans across a Si dumbbell calculated by the multislice method (brown) and the time-dependent method (black curves) for various film thickness and beam energies.

We have also initiated a study of low-energy electron diffraction (LEED) where the beam is reflected. Initial results for the LEED pattern of an ideal Si (001) surface are shown in Fig. 7.

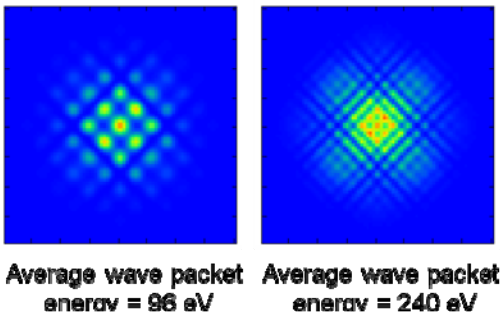

Fig. 7. Calculated LEED pattern for a Si (001) surface at two different energies.

4. Studies of real materials systems (one of four cases – see Publications)

4.1 Colossal ionic conductivity in YSZ/STO heterostructures

Solid-oxide fuel cells depend on oxide electrolytes that conduct O ions from cathode to anode while being electrically insulating. Yttria-stabilized zirconia $(Y_2O_3)_x(ZrO_2)_{1-x}$ (YSZ) is the most commonly used electrolyte, but requires temperatures around 800°C. Maria Varela and Steve Pennycook at ORNL and scientists at the Complutense University of Madrid recently reported in *Science* Z-contrast images, EELS spectra, and ionic conductivity measurements of YSZ-STO superlattices and demonstrated an increase of up to eight orders of magnitude near room-temperature conductivity when the YSZ film is on the order of a few nanometers thick, as compared with bulk ionic conductivity[2].

Tim Pennycook, the graduate student supported by this grant, has been studying this phenomenon as part of his Ph.D. thesis, which combines microscopy and theory. The published STEM images show that sublattices of the YSZ and STO fit together perfectly, implying a 7% expansive lattice-mismatch strain on the YSZ. Tim first used DFT to study 7% strained bulk YSZ and discovered that at 2000 K the O sublattice disorders (Fig. 8). When he did the same simulations for

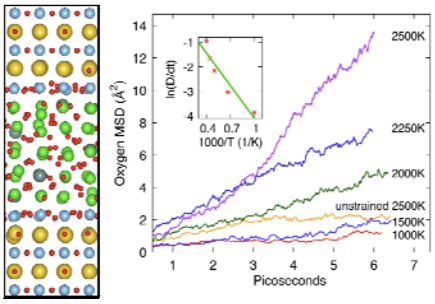

Fig. 8. Left: Structure of the 1 nm YSZ layer sandwiched between layers of STO at 360 K after simulated annealing; Sr atoms are shown in yellow, Ti in blue, Zr in green, Y in gray, and O in red. Right: Mean squared displacements of O ions in strained zirconia at various temperatures compared to that of the unstrained material at 2500 K. Reproduced from [3].

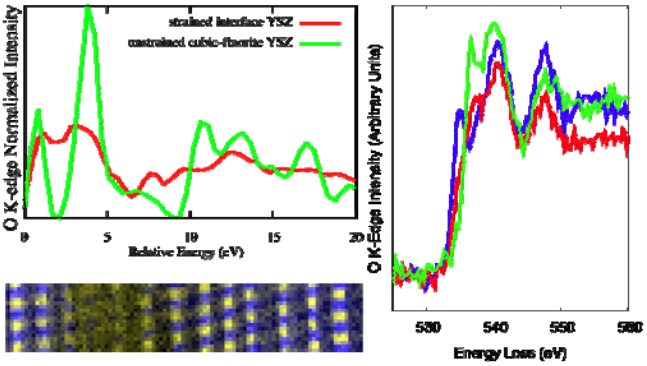

Fig. 9. Top right: O K-edge averaged over sites in the YSZ layer of the superlattice simulated using the Z+1 approximation compared to that for the unstrained bulk structure. Bottom right: O K-edge obtained from STO (blue), strained YSZ (red) and unstrained YSZ (green). Left: O (yellow) and Ti (blue) EELS map showing O disorder in strained YSZ layer and ordered O and Ti columns in the surrounding STO.

a YSZ-STO superlattice, he found that the incompatibility perturbed the YSZ into the disordered O phase *at temperatures even below room temperature*. He determined an energy barrier for O hopping and estimated the ionic conductivity enhancement of the multilayer YSZ over that of bulk YSZ near room temperature to be over six orders of magnitude, close to the 8 orders reported experimentally. These results were published in *Physical Review Letters*[3].

More recently, Tim used microscopy to verify the existence of the disordered O phase. As can be seen from Tim's DFT O K-edge simulation (Fig. 9A), the fine structure from the disordered O-sublattice is washed out compared to that of ordered YSZ. After obtaining samples from the same group that grew the original YSZ-STO superlattices, Tim acquired spectra that show just this sort of washed out O K-edge fine structure (Fig 9B) in strained YSZ. With the elemental mapping capability of the STEM, Tim was also able to image the O disorder with EELS. Figure 9C shows the O and Ti integrated EELS intensities across a YSZ layer sandwiched between STO. The in plane separation of the O columns in ordered YSZ strained 7% is the same as in STO, in which the O columns are clearly resolved. If the O atoms were ordered in the YSZ, they would also be resolved. The fact that we only see some residual STO structure indicates that, with this EELS map, we are truly "seeing" the disorder in the O sublattice, confirming the theoretical results.

5. Future Plans

The new codes for STEM/EELS simulations need further fleshing out to reach their full potential. We will carry out further tests and validations against experimental data and other simulations, where available, and use the new tools to study real complex materials for which data become available. Parallel studies of complex materials for which STEM/EELS data become available will also continue.

6. References

[1] E. Kirkland, "Advanced computing in electron microscopy" (Springer, 1998), p. 102.
[2] J. Garcia-Barriocanal et al., *Science* **321** 676 (2008)
[3] T. J. Pennycook *et al.*, Phys. Rev. Lett. **104,** 115901 (2010)

7. Publications:

1. T. J. Pennycook, M. J. Beck, K. Varga, M. Varela, S. J. Pennycook, and S. T. Pantelides, "Origin of Colossal Ionic Conductivity in Oxide Multilayers: Interface-Induced Sublattice Disorder" Phys. Rev. Lett. 104, 115901 (2010)
2. O.J. Krivanek, M. F.Chisholm, V. Nicolosi, T. J. Pennycook, G. J. Corbin, N. Dellby, M. F.Murfitt, C. S. Own, Z. S. Szilagyi, M. P. Oxley, S. T.Pantelides, and S.J.Pennycook, "Atom-by-atom structural and chemical analysis by annular dark-field microscopy", Nature 464, 571 (2010).
3. W. Walkosz, R. F. Klie, S. Ogut, B. Mikijelj, S. J. Pennycook, S. T. Pantelides, and J. C. Idrobo, "Crystal-induced effects at crystal/amorphous interfaces: the case of Si_3N_4/SiO_2", Physical Review B, in press.
4. J. Gazquez, W. Luo, M.P. Oxley, M. Prange, M. A. Torija, M. Sharma, C. Leighton, S.T. Pantelides, S.J. Pennycook, and M. Varela, "Atomic-resolution imaging of spin-state superlattices in perovskite cobaltite films" submitted to Phys. Rev. Lett.

Electron Diffraction Determination of Nanoscale Structures

Dr. Joel H. Parks
The Rowland Institute at Harvard
100 Edwin H. Land Boulevard
Cambridge, MA 02142
Email: parks@rowland.harvard.edu

Program Scope

The accelerating research into the science and technology of "nanoparticles" has approached a level at which a deeper knowledge of the atomic structure is needed to better understand how the arrangement of composite atoms achieve unique properties at nanoscale sizes. The specific goals of the current research program are to study the size dependence of metal cluster structures and relate this understanding to the structure dependence of catalytic activity, melting dynamics, and bimetallic alloys for metal clusters in the size range of 10-100 atoms. Collaborations with theorists have provided an essential contribution to this program. Comparisons between the measured diffraction patterns and those calculated for theoretically optimized structures is required in order to identify the most probable atomic arrangement.

Current research continues the application of measurements of metal cluster structures to determine how structure plays a role in the dynamical processes of metal cluster nanocatalysis. Diffraction measurements and associated adsorption measurements will be pursued for metal cluster materials of both pure and alloyed compositions which are identified to have interesting interactions with adsorbed molecules. This research program relates to the DOE Electron and Scanning, Probe Microscopies Program in the Materials Science and Engineering Division mission by providing a method for confirming the design of nanosize materials at the atomic level; by providing an experimental tool for characterization of nanoscale reactivity.

Recent Progress: Adsorption on Metal Clusters: Structure Dependence

The following provides a brief summary of the results of the current research program directed to characterize adsorption of small molecules on metal clusters. These results are consistent with a developing understanding in the field that metal clusters composed of <20-30 atoms are optimal for nanoscale reactivity. Comparing these adsorption measurements with cluster structures determined by trapped ion electron diffraction will provide insight into the relationship between cluster reactivity and atomic structure.

- **Structure dependence of CO adsorption on gold clusters (Au_n^+)**
  - 2D↔3D structural changes induced by CO adsorption
  - Enhanced CO adsorption rates with co-adsorbed H_2O
  - Theory of induced structural change for CO adsorption on Au_n^+ for CO
  - Theory of enhanced CO adsorption rates with co-adsorbed H_2O
- **Structure dependence of CO adsorption on gold clusters (Au_n^-)**
  - Theory of single O_2 adsorption on Au_n^-
- **Low Pressure adsorption of O_2, CO and H_2O on palladium clusters (Pd_n^+), (Pd_n^-)**
  - Formation and trapping of Pd_n^+ and Pd_n^- clusters
  - Adsorption of CO and O_2 on Pd_n^+

In particular, two specific research results will be describe below in more detail.

A. CO induced changes in cluster structure

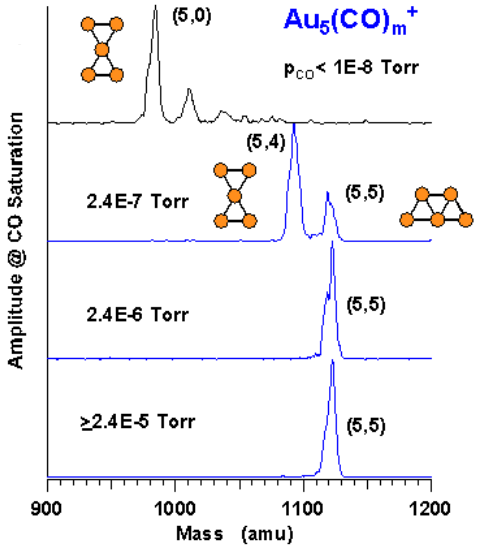

The mass spectra for CO adsorption on Au_5^+ as a function of CO pressure shown in Figure 1 indicates that adsorption begins on the ground state structure of the bare gold cluster which takes up a maximum of 4 CO molecules. Saturation at 5 CO molecules increases abruptly at higher pressures. Independent observations indicate that CO has low binding energy on central atoms of planar structures and also on sites having a coordination >4. In addition, calculations have indicated high binding energies for the edge sites of planar structures. Consequently, the increase in saturation from 4 to 5 CO on Au_5^+ is assumed to be the result of a change in structure which moves the weak binding central atom to a stronger binding edge site. In general, a qualitative understanding of observed CO saturation numbers can be identified by changes in structure within a group of low energy structures. For each cluster size, this will result from energetic tradeoffs of binding energies and energy barriers to a new structure.

Figure 1. Mass spectra of saturated adsorption on Au_5^+ for different CO pressures, p(He)=3.5x10-3 Torr, 150K and 20 s exposure time. The numbers in parentheses (n,msat) indicate the cluster size, n, and CO saturation number, m_{sat}. DFT calculated structures are shown.

Calculations have been performed for Au_6^+ to investigate the changes in structure induced by the adsorption of CO between the ground state triangular structure and a low energy isomer having a chevron structure. Figure 2 illustrates changes in the transition energy barrier between the two isomers as well as the change in relative energy between the initial and final structures.

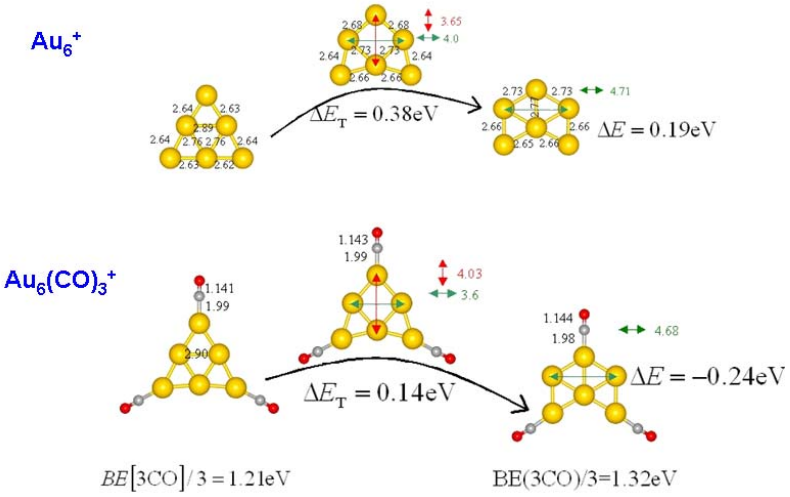

Figure 2. Upper panel shows the energetics for a transition between two structural isomers for bare clusters cations and the lower panel for the cluster with 3 adsorbed CO molecules.

Figure 2 indicates that the adsorption of three CO molecules on the chevron isomer occurs with stronger binding energy than on the triangular isomer. This adsorption decreases the energy

of the chevron structure to 0.24 eV below that of the triangular structure energy. More importantly, the energy barrier for a structural transition is reduced to roughly half the cluster internal energy at 300 K. As a result, a structural transition becomes significantly more probable with the adsorption of 3 covalently bound CO molecules. Similar changes in energetics with CO adsorption are expected to enable structural transitions in these smaller size gold cations, resulting in our previously observed saturation by CO molecules.

B. H_2O enhancement of CO adsorption

During measurements of CO adsorption on Au_n^+, it was observed that for certain sizes the change in saturation number was accompanied by the co-adsorption of H_2O molecules. Measurements were performed to determine if the co-adsorption of H_2O and CO systematically leads to increased CO uptake. In these measurements, the cluster is exposed to the H_2O vapor pressure first followed by exposure to CO. The presence of H_2O strongly influences the adsorption of CO on Au_6^+; however, *adsorbed H_2O is not observed* suggesting that the enhancement does not require H_2O to remain stabilized on the cluster surface. Calculations were performed to understand the dynamics of these observations.

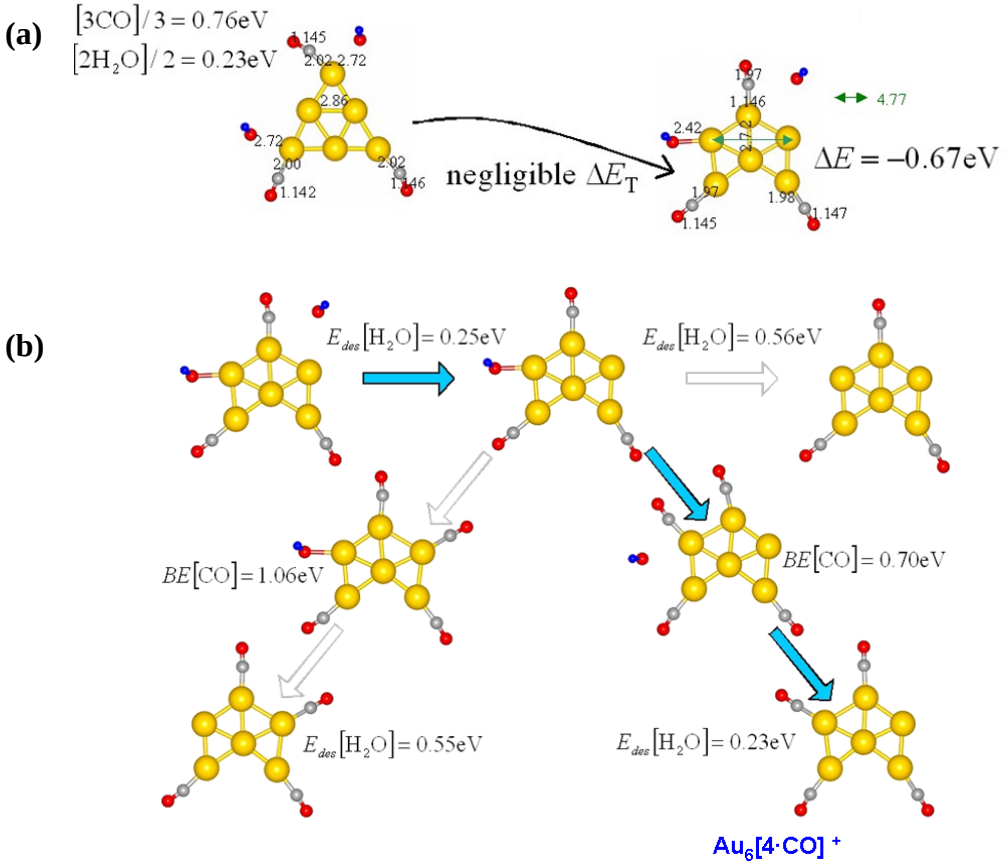

Figure 3. (a) The upper panel shows a configuration of coadsorbed CO/H_2O leading to energetics which exhibit a rapid transition between two structural isomers of Au_6^+, and (b) the lower panel describes the dynamic pathways resulting in the experimentally observed species $Au_6^+(CO)_4$.

Figure 3 depicts a lowest energy kinetic pathway for the coadsorption of CO and H_2O which exhibits the observed saturation of Au_6^+ dominated by 4 CO molecules. In Figure 3(a), the ground state triangular structure is shown with a CO molecule adsorbed at each vertex, a high binding energy site, and 2 weakly bound H_2O molecules. This configuration is unique, resulting in a structure which rapidly transforms to the chevron structure in an endothermic reaction with negligible energy barrier. Figure 3(b) shows the minimum energy pathway to form $Au_6^+(CO)_4$ form the starting structure of Figure 3(a). The dynamics includes the loss of a weakly bound H_2O followed by adsorption of the last CO at the H_2O site. This weakens the H_2O-Au binding energy sufficiently for the last H_2O to desorb leaving only 4 adsorbed CO molecules. It is difficult to show with complete certainty that these kinetics dominate the reactivity of the Au_6^+ ensemble; however, finding a low energy pathway which exhibits the experimental result provides a rationale for the presence of kinetic pathways exhibiting CO adsorption enhanced by H_2O.

Research Plans

1. Experimental: Gold-palladium structures

Efficient gas phase alcohol oxidation has been observed elsewhere on Au-Pd bimetallic particles supported on TiO_2 substrates in the presence of O_2. The structure obtained by x-ray diffraction has an inner Au core with an outer shell of Pd. The perturbation of Pd electronic states by gold cluster surface atoms has been suggested as the dominant factor determining the reaction rate. The gas phase structures of bimetallic Au_nPd_m clusters will be studied as a function of gold cluster size, charge state and Pd impurity level. Isotope enriched Pd (Pd 110 @ 99% pure) can be used to avoid degrading the cluster mass resolution through isotope broadening of the mass spectrum peaks. Pure palladium clusters will be studied initially to provide a quantitative reference for adsorption. A palladium oven has been designed and is being fabricated so that it can be mounted inside the vacuum system to irradiate trapped gold clusters with palladium atoms.

Diffraction measurements of Au_nPd_m clusters can be compared with Au_n to help identify if Pd atoms are interstitial or on the Au_n cluster surface. Since the low number of Pd atoms will weakly contribute to diffractive scattering, the patterns of Au_nPd_m will differ significantly from Au_n only if Pd is interstitial so that the gold structure is distorted. This cluster will be the first bimetallic structure to be studied in cluster form by trapped ion electron diffraction and will serve as the initial investigation of an important class of catalytic species.

2. Theoretical Support

(a) In the coming period we will explore the optimal structures and bonding properties of gold cluster anions with more than a single adsorbed oxygen molecule. These investigations aim at explaining trends observed in the experiments.

(b) Using first-principles calculations we will explore the adsorption of H_2O molecules on gold clusters anions and cations (n=3-11). In particular we will focus on explaining the experimental observation that in this size range only occurs for planar structures $n \leq 7$; and for anions only for the planar structures for n=4-6.

(c) Finally, we will contribute to the experimental measurements on palladium clusters through the calculation of low energy structures and the electronic state characteristics introduced by the adsorbed species

Program Title : ***SISGR- Emerging Functionality in Transition-Metal Oxides Driven by Spatial confinement.*** DOE grant #DE-SC0002136.

Principal Investigator: E. Ward Plummer, Department of Physics and Astronomy, 202 Nicholson Hall, Louisiana State University, Baton Rouge, LA 70803. Phone 225 578 3300: e mail: wplummer@phys.lsu.edu

Co-PI: Jiandi Zhang, Department of Physics and Astronomy, 202 Nicholson Hall, Louisiana State University, Baton Rouge, LA 70803. Phone--225 578 4103. e-mail-- jiandiz@lsu.edu.

Co-PI: Jian Shen, Department of Physics and Astronomy, 312 Nielsen, The University of Tennessee, Knoxville, TN, 37996. Phone 865 974 9811. E-mail—jshen6@utk.edu.

Program Scope and Definition: The exotic properties displayed by correlated electronic materials (CEMs) such as the cuprates, manganites, ruthenates, Fe-based penictides, and heavy-fermion compounds are intimately related to the coexistence of competing nearly degenerate states which couple simultaneously active degrees of freedom—charge, lattice, orbital, and spin states. The striking phenomenon associated with these materials is due in large part to spatial electronic inhomogeneities, or nanoscale phase separation. Complexity in these systems leads to emergent phenomena which have become the focus of several national reports producing grand challenges like *How do complex phenomena emerge from simple ingredients or How do remarkable properties of matter emerge from complex correlations of the atomic or electronic constituents and to control these properties?* "The challenge is to understand how such collective phenomena emerge, discover new ones, and to determine which microscopic details are important and which are essential." *Spatial confinement on the length scale of the inherent phase separation can probe the basic physics and reveal new emergent behavior.*

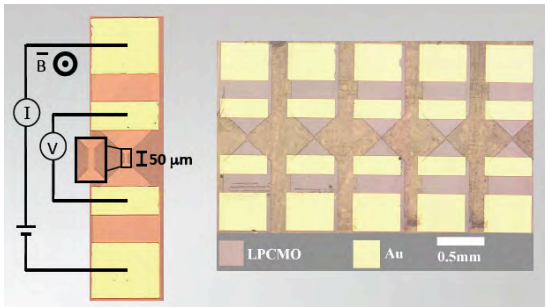

Fig. 1. Left is SEM image of the LPCMO wires fabricated from the thin film with different sizes (largest on left). The gold contacts are in the 200 to 500 μm scale, which is considerably larger than the 20 μm diameter of the wire bonding thread. Right is picture of 4 point contact.

The research conducted in this program will add a new facet to the study of emergent phenomena, the use of spatial confinement. In essence we will combine two of the grand challenges—*Complexity and Nano-structured materials* to explore and exploit emergent behavior. Novel phenomena will emerge when CEMs are fabricated as ultrathin films or wires with dimensions small compared with the inherent length scale in the bulk as shown in Figure 1. This length scale might be the size of the bulk spatial electronic inhomogeneities. In fact, phase separation will occur for any strongly correlated material near a bi-critical or multi-critical point, which is precisely where these studies will be conducted. There will always be a length scale for correlation in these materials. When the spatial confinement has reached that scale, then one would expect a fundamental change of the correlated behavior. What are the appropriate length scales and what new functionality will arise from spatial confinement are the questions addressed by this research project.

Recent Progress

a) Research highlights: Nine invited talks last year related to this research.

Evidence of Coulomb blockade behavior in a quasi-zero dimensional quantum well on TiO_2 surface [1]. This is a collaboration between LSU, Baylor University, Notre-Dame de la Paix (Belgium),the Center for Nanophase Materials Sciences at ORNL and The Computer Science and Mathematics Division at ORNL.

One of the most striking features of quantum mechanics is the distinctive electronic behavior associated with each level of dimensionality. Advances in scanning probe techniques coupled with the ability to prepare low-dimensional systems of unprecedented quality permits the direct observation of a number of manifestations of quantum mechanics in dimensionally confined systems. The electronic behavior of such systems may often be successfully understood within the independent-electron picture. When dimensionality is further reduced from quasi one-dimension (Q1D) to quasi zero-dimension (Q0D), electron-electron correlations are increasingly important and, in some instance, even dominate. In that case, the single-electron picture breaks down.. The failure of the single-electron description is exemplified by Coulomb Blockade behavior. Here, the presence of a net charge in the structure and the associated Coulombic repulsive force hinder the addition of an extra electron. A convenient way to understand this behavior is through the concept of charging energy, similar to the energy stored on the plates of a conventional capacitor. For a typical spherical quantum well with tens of nanometer radius, the equivalent capacitance is on the order of the 10^{-17} F, which corresponds to a charging energy of the order of 10 meV. At sufficiently low temperatures, this energy is not readily available. Consequently, an electron cannot overcome the electrostatic barrier due to net charge present in the system.

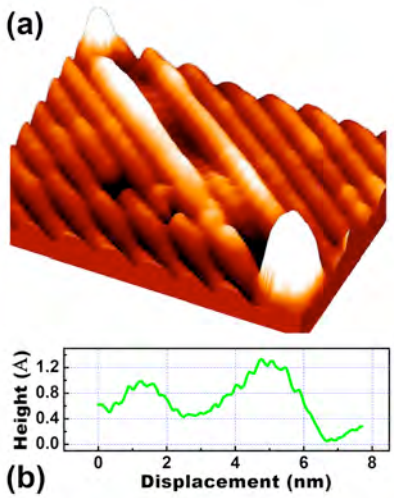

Fig. 2: (a) Constant-current, three-dimensional STM image of a 10-nm long "nanoclip" nanostructure on TiO_2 (110) substrate. A 3.8 nm wavelength oscillation is observed, as shown on the line profile between the two ends of the linear nanoclip reproduced on (b).

We have been able to image (STM) this charging behavior as well as the quantum nature of a Q0D feature using the defects on the surface of TiO_2. Line defects on the surface of TiO_2(110) form in pairs separated by 1.2 nm creating a quantum well, see Figure 2. The well is effectively closed by the presence of two charged structures at both ends separated by a distance in the 10-20-nm range. As expected for quantum confinement a long wavelength oscillatory feature of the LDOS is observed and attributed to the formation of discrete quantum states inside the system. It is at first glance surprising that the lowest energy quantum state of the well can be observed at room temperature. The properties of the quantum state cannot be explained in an independent-electron, band-like theory. Instead, electron-electron correlation must be included to give a satisfactory picture of the spatial distribution of the charge density. Theory predicts charging energies of 1.30 eV and 1.14 eV for quantum well lengths of 14 nm and 16 nm, respectively, in good agreement with a classical calculation and the size dependence of the capacitance. This observation opens up the possibility of experimentally imaging the transition from a Coulomb Blockade localized in a zero-dimensional system to an independent-particle or band-like behavior in an extended one-dimensional system.

An oxygen-induced surface reconstruction of $SrRuO_3$ and its effect on the $BaTiO_3$ interface [2]. This is a collaboration between LSU, the University of Wyoming, the Materials Sciences and Technology Division, the computer Science and Mathematics Division and the Center for Nanophase Materials Sciences at ORNL.

Advances in atomically-controlled oxide growth have generated new classes of materials with unique physical properties highly sensitive to abrupt interfaces. The extreme sensitivity of oxides to electron concentration is coupled to charge transfer, structure, and spin to produce spectacular behavior including interface mediated conduction, superconductivity, magnetism, and phase transitions in parent materials lacking these attributes. The response of oxides to structural instabilities or disorder is greater in two-dimensional systems, seen in examples of Anderson localization, Peierls instability or charge density wave transitions. The central role of oxygen stoichiometry has been repeatedly shown in defining both structure and properties of oxide interfaces, and can be tuned as a means to control static and dynamic distributions of electrons and atoms for a new generation of functional materials with applications ranging from oxide sensors and electronics to energy capture and storage. Nevertheless, few atomic scale studies of interface structures exist for complex oxides, due to a need for multiple tools to probe subsurface features, the need for a highly controlled environment, and the insulating nature of many oxides.

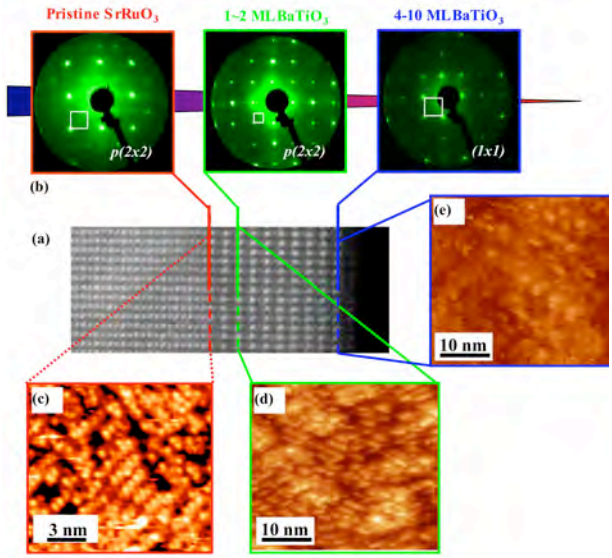

Fig. 3. Tunneling and transmission microscopy images and electron diffraction combined to show the development of the structure of $BaTiO_3$ on $SrRuO_3$ on a $SrTiO_3$ substrate. (a) The center image shows a cross-section acquired with z-contrast STEM. (b) The upper three images are LEED diffraction patterns at the indicated stage of growth taken at 70 eV for the $SrRuO_3$ and at 180 eV for the $BaTiO_3$ surfaces; the first two show a p(2x2) unit cell doubling, while the third is bulk-like (1x1). (c), (d), and (e) STM images of the $SrRuO_3$ surface with atomically resolved rows, and $BaTiO_3$ surfaces from 2 and 10 layer films.

We have followed the growth of ferroelectric $BaTiO_3$ on $SrRuO_3$ electrode with in situ atomic scale analysis of the surface structure at each stage. An oxygen-induced surface reconstruction of $SrRuO_3$ leads to formation of SrO rows spaced at twice the bulk periodicity, (1x2) structure. This reconstruction modifies the structure of the first $BaTiO_3$ layers grown subsequently, including intermixing observed with cross-section spectroscopy. These observations reveal that this common oxide interface is much more interesting than previously reported, and provide a paradigm for oxygen engineering of oxide structure at an interface.

As 1-2 layers of $BaTiO_3$ were grown on $SrRuO_3$, the LEED pattern remained p(2x2) (Figure 3 (b)), however the relative intensities of diffraction spots were altered from those observed from $SrRuO_3$ alone. This change in relative intensities indicates a change of structure, with two important implications. First, this pattern must represent the order of the $BaTiO_3$ film, and cannot arise solely from exposed remnants of $SrRuO_3$. Second, this shows that the $SrRuO_3$ reconstruction influences the structure of the $BaTiO_3$ at the interface, which does not share the symmetry of bulk $BaTiO_3$, but instead has a periodicity two times larger in the plane of the interface.

Growth of thicker $BaTiO_3$ reverts the pattern observed in LEED to the (1x1) symmetry of the bulk. As shown in Figure 3 (b), as few as 4 layers of $BaTiO_3$ produce at a (1x1) periodicity; the additional diffraction spots indicating a doubled unit cell are gone. STM images of Figure 3 (c) no longer reveal rows. The same periodicity and surface topography remain in films of 10 layers of $BaTiO_3$. The LEED technique is highly surface sensitive,

owing to the short mean-free path of low energy electrons in matter. Consequently, while the surfaces of these films show no reconstruction, i.e. no deviation of the in-plane symmetry from the bulk, the p(2x2) structure could persist at the interface. A reconstructed interface would have a profound influence on our understanding and modeling of phenomena such as the recently reported tunneling in ultrathin ferroelectric $BaTiO_3$ into $SrRuO_3$.

b. Collaboration with Fudan University in Shanghai China. Jian Shen with a joint appointment at Fudan University has set up a research group in the department of physics at Fudan, which focuses on nanoscale oxides research with complimentary capabilities (to LSU/UTK). The noticeable advantages for this project are: (1) The group has a high-field, variable temperature magnetic force microscope that can be used for imaging the phase separation in oxides. This is critical for our understanding of emergent phenomena in complex oxides in reduced dimensions. (2) The group will have four laser MBE systems dedicated for growing complex oxides thin films and nanostructures. The strong growth capabilities coupled with a large number talented students (~15) give us possibilities to explore exciting properties in different oxides and map the phase diagram of complex oxides in reduced dimensions.

Future Plans. (next year)

1. The epitaxial growth of $La_{1-x}Sr_xMnO_3$ on $SrTiO_3(001)$ will be the initial project at LSU. Ex-situ lithography for nanostructure studies will be followed to understand the intrinsic nano-phase separation in relative moderate JT-distorted system as to be compared with other more strongly distorted system like $Pr_{1-x}Ca_xMnO_3$.
2. We will use the photo, ion and electron beam lithography capabilities at LSU to form thin wires of the oxides.
3. We will modify the existing PPMS for time-resolved transport measurements.
4. We will investigate the emergent properties in multiferroic LuFe2O4 thin films and wires.
5. We have begun to grow thin films of $FeSe_{1-x}Te0_x$ to explore the thickness dependence of superconductivity. Next we will pattern the films.
6. We will expand our collaboration with the research group in Fudan to give us greater capability to explore new materials and new combinations of films and wires. The new systems and graduate students are shown in fig. 4.

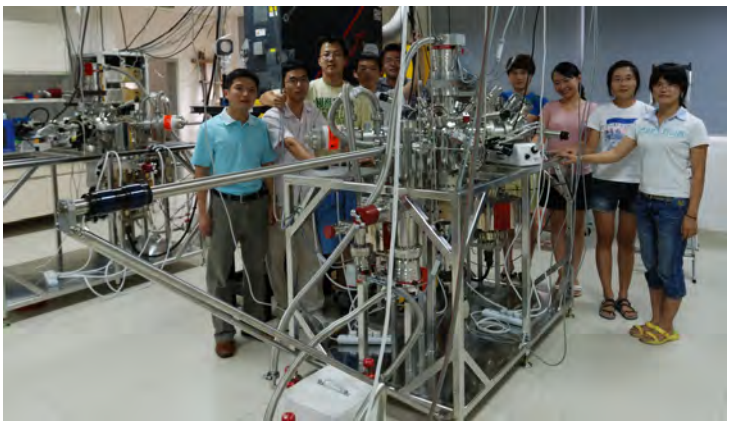

Fig. 4. Students at Fudan University in the laboratory of Jian Shen. Two of the three laser MBE systems are shown.

References to Publications fo DOE Sponsored Research.

1) Evidence of Coulomb blockade behavior in a quasi-zero dimensional quantum well on TiO_2 surface," Vincent Meunier, M.H. Pan, F. Moreau, K.T. Park, and E.W. Plummer, to be published in PNAS.
2) "Oxygen-Induced Surface Reconstruction of $SrRuO_3$ and Its Effect on the $BaTiO_3$ Interface," Junsoo Shin, Albina Y. Borisevich, Vincent Meunier, Jing Zhou, E. W. Plummer, Sergei V. Kalinin, and Arthur P. Baddorf, submitted to ACS Nano, **4**, 4190 (2010).

Correlation of Bulk Dielectric and Piezoelectric Properties to the Local Scale Phase Transformations, Domain Morphology and Crystal Structure (DE-FG02-07ER46480)

Shashank Priya and Dwight Viehland
Materials Science and Engineering, Virginia Tech, Blacksburg, VA 24061.
Phone: (540) 231 – 0745 email: spriya@vt.edu

Abstract: The objective of this research program is to discover the fundamental mechanisms and atomic level phenomenon's that can provide understanding of piezoelectric response in lead-free ferroelectrics. We are systematically studying the polymorphic phase transitions, local domain and crystal structure and their effect on properties. (Na,K)NbO_3 (KNN) polycrystalline ceramics, single crystals, and textured nano-grain ceramic systems close to polymorphic phase boundaries (PPBs) are being used as the representative lead-free system. For comparative studies, we are also investigating $(Na_{1/2}Bi_{1/2})TiO_3$ single crystals with composition close to morphotropic phase boundary (MPB). Nanoscale domain structure and its ferroelectric response are being investigated as a function of electric field, pressure and temperature to identify the volumetric and phase fraction changes in the PPB region and to determine the presence of (any) intermediate phenomenon. Another challenging issue confronted in this research program is to formulate the mechanism of domain engineering in the lead-free materials. The crystal structure in the oriented single crystals is being investigated under varying electric field and temperature conditions to identify the lattice parameters, and domain distributions for various crystallographic directions. In collaboration with our colleagues in national laboratory and Warwick University, the microstructure of the lead-free crystals is being studied using diffraction and spectroscopic techniques to delineate the symmetry relations, nature of the dipole moment, and orientation of polarization. X-ray and neutron diffraction techniques were used to analyze the simultaneous changes in structural parameters. The results from these studies will establish the link between the physical property in question and the way certain parameters change.

Recent Progress:

(i) *Hierarchial domains in $(Na_{1/2}Bi_{1/2})TiO_3$ (NBT) single crystals.*

We have performed polarized light microscopy or PLM and atomic force microscopy or AFM investigations on single crystals of $(Na_{1/2}Bi_{1/2})TiO_3$ (NBT). All crystals were provided by Haosu Luo. First, we show the phase transformational characteristics in Figure 1. Temperature dependent dielectric data are given in Part (a). In this figure, we can see that the dielectric maximum occurs near 330°C, near and just below which the dielectric constant is frequency independent. On further cooling, an inflection was found near 250°C below which notably frequency dispersion was observed. This dispersion was similar to that of relaxors below T_{max}, indicating polar heterogeneities with low frequency fluctuations. In Part (b), temperature dependent lattice parameters are given. These data reveal a splitting of the *c* and *a* parameters in the temperature range between 300 and 530°C: demonstrating that both the polar (near and below T_{max}) and prototypic ($>T_{max}$) phases have tetragonal symmetry. Below 300°C, the structure transformed to rhombohedral (i.e., pseudo-cubic). No other structural changes were found at the Curie temperature, or at the inflection in the dielectric constant near 250°C.

Figure 2 shows PLM images taken at (a) room temperature in the R phase, (b) above the ferroelectric Curie temperature but below the T→C transition at 350°C, and (c) in the C phase at 580°C. The angles (θ) provided in the images is that between the polarizer/analyzer (P/A) pair

and the pseudocubic <110>.The images clearly reveal the presence of tetragonal ferroelastic domains for temperatures below T→C transition, which have a width of about 10~100μm and a length on the order of hundreds of microns, and which are oriented along the <110>. These ferroelastic domains disappeared on heating at the T→C transition near 550°C. We next show how these images were changed by the P/A angle setting. As can be seen in Figure 2(d) at 25°C, the contrast was darkest for θ=28°: complete extinction could not be achieved, as one can clearly still see the ferroelastic domains. However, at 350°C, the domain structures became completely extinct for θ=45° (see Fig.2e): i.e., when one of the P/A axes was oriented along the <100>cub. This is the typical extinction position for a crystal structure with tetragonal symmetry, and is consistent with the XRD results of Fig.1(b). Since the tetragonal ferroelastic domains persist into the R phase field, the ferroelectric R domains must then nucleate on cooling under the geometrical and elastic restrictions of the ferroelastic T domains. We believe that complete extinction could not be achieved in the R phase because the distribution of polar R microdomains within larger ferroelastic T macrodomians could not achieve a completely elastically relaxed condition. When the temperature was increased to the C phase field, complete extinction was obtained with P/A angle changing in the range from 0 to 360° (see Figs.2c and f).

It is important to note that the size, shape, and position of these ferroelastic domains were somewhat unchanged with temperature on cooling between 550°C and room temperature, even though the sample went through (i) two polar phase transformations on cooling, and (ii) that the ferroelastic tetragonal strain (c/a) disappeared at 300°C on cooling into the R phase. These findings clearly demonstrate that the ferroelastic domain structure is inherited into the rhombohedral polar phase at room temperature.

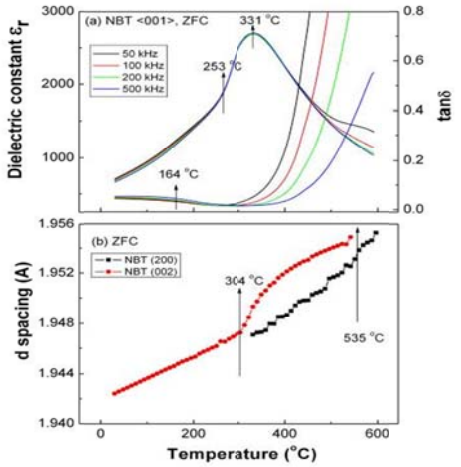

Figure 1. Phase transformation characteristics of <001> oriented NBT single crystal in the zero-field cooled condition, observed by (a) temperature dependent dielectric constant measurements taken at various frequencies; and (b) temperature dependent lattice parameter measurements.

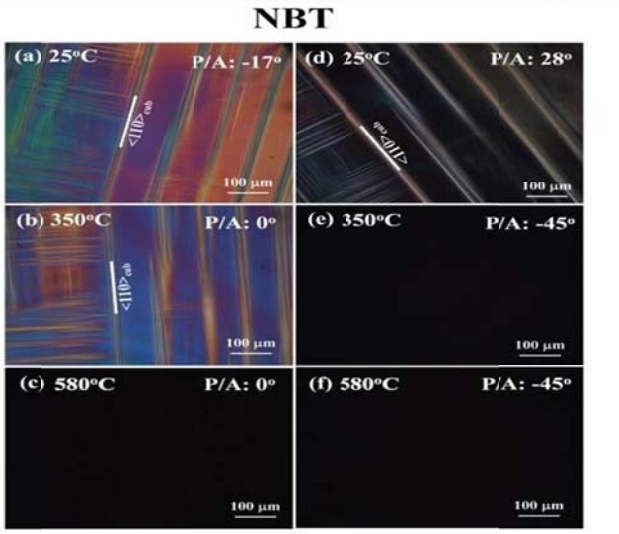

Figure 2. Polarized light microscopy (PLM) images taken at various temperatures of (a, d) 25°C, (b, e) 350°C and (c, f) 580°C

(ii) Phase transition studies under field for Li:$K_{0.5}Na_{0.5}NbO_3$ <100>-textured ceramics

Figures 3 shows temperature dependent $(200)_{cub}$ X-ray line scans for Li:KNN textured ceramics taken under (a) zero-field heating or ZFH, (b) zero-field-cooling or ZFC, and (c) field-cooling or FC conditions. These data revealed that the O and T phases coexisted in the temperature range between 90°C to 125°C in the ZFH condition (see Fig.3a), and between 84°C to 112°C in the ZFC (see Fig.3b). These findings show that the thermal hysteresis in the dielectric constant data near the O→T boundary is due to O and T phase coexistence. In Fig.3b for the ZFC state, it can be seen that the $(022)_O$ diffraction peak appears at 112°C and becomes stronger with decreasing temperature. However, under E=8kV/cm, the $(022)_O$ diffraction peak did not appear on cooling until below 108°C. These structural data demonstrate that E applied along $<100>_{cub}$ favors the T phase, as also revealed by the dielectric results under bias.

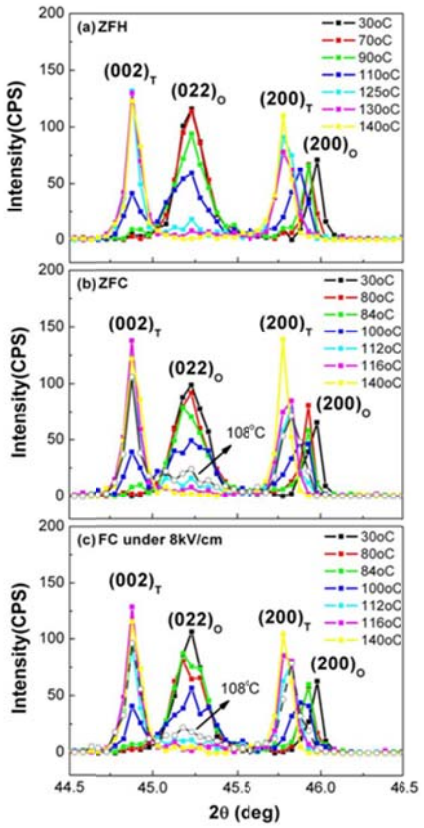

Figure 3. Temperature dependent (200)linear scans for Li:KNN textured ceramics under ZFH (a), ZFC (b) and FC (c)conditions. It was found that the peak corresponding to O→T transition became sharper with increasing electric field for E>2kV/cm. For E>4kV/cm, the O→T boundary was shifted towards lower temperature with increasing E; at the same time, the dielectric constant in the T phase field decreased dramatically with increasing E. Our findings demonstrate that phase coexistence occurs about polymorphic phase boundaries in ferroelectric systems. This phase coexistence results in enhanced piezoelectric constants. We have not yet completed our investigations whether or not low symmetry structurally bridging phases exists between the orthorhombic and tetragonal phases, which would need to be a monoclinic C structure whether the polarization would be free to rotate between the (110) and (001) directions under electric field. To more thoroughly study this possibility, we will study both single crystal and textured-ceramics. Single crystals of KNN are presently been grown at the Shanghai Institute of Ceramics for this purpose.

(iii) *Synthesis and ferroeletric characterization of KNN single crystals for template grain growth* - we found unique approach to synthesize textured ceramics through combination of TGG process with KNN seeds ($K_{0.5}Na_{0.5}O_3$). Molten salt synthesis method was used for the preparation of seed particles. Figure 4 shows the XRD pattern of KNN seed crystals which appear to possess (100) orientation further confirmed by EBSD. The orientation of individual seed particle was analyzed using EBSD mapping. Kikuchi patterns were obtained at eight points on cubical seeds exhibiting identical texture as shown in Fig. 4(a). Inverse pole figure (IPF) – IPF was obtained for the area 150 μm x 300μm to confirm the uniformity of orientation thought the crystal. We confirmed the ferroelectric nature of the seed crystals using sample of the dimension 3.1 mm^2. This crystal was mounted on a Pt / SiO_2 substrate using silver paste for these measurements and remanent polarization of up to 2μC/cm^2 was recorded. These results are very

exciting and open the possibility of realizing high quality textured KNN ceramics which will used for understanding the role of anisotropy towards piezoelectric performance of this system.

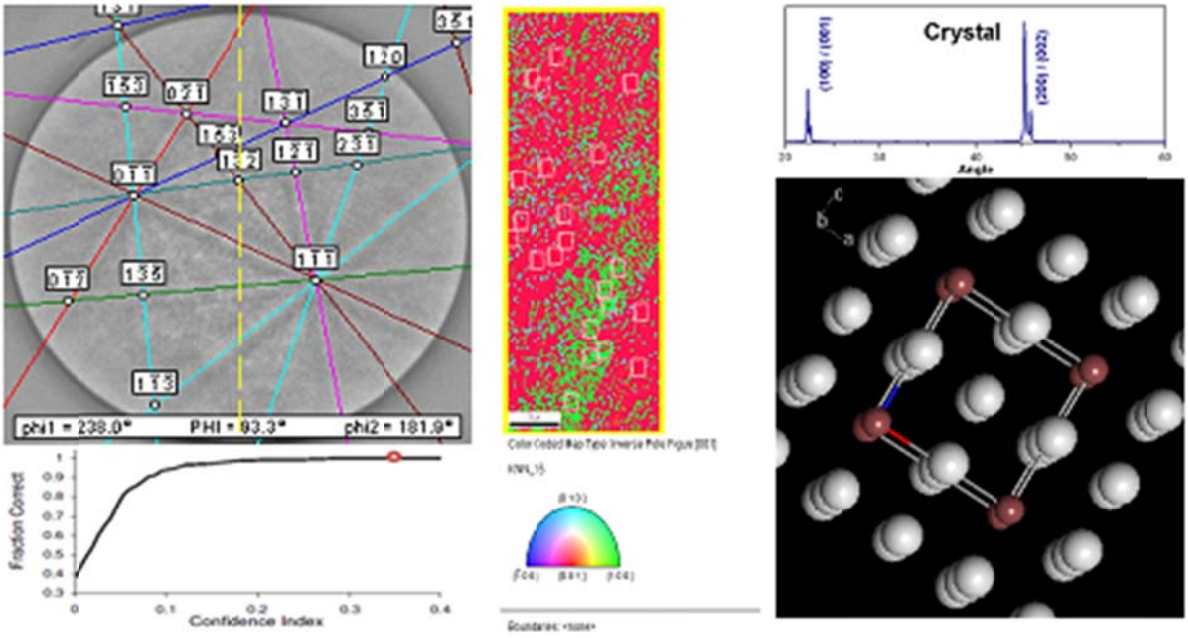

Figure 4: *EBSD and XRD analysis on the KNN cubical seed crystals.*

We have also conducted studies on the KNN composite systems where layers of varying T_{O-T} compositions were utilized to tailor the temperature dependence of piezoelectric constant. We were able to demonstrate a flat piezoelectric response up to 300^{o}C in KNN systems.

List of papers (already published, in press, submitted) in which DOE support is acknowledged.

1. C.W. Ahn, C.S. Park, D. Viehland, and S. Priya, "Correlation between Phase Transitions and Piezoelectric Properties in Lead-Free (K,Na,Li)NbO_3-$BaTiO_3$ Ceramics", Jap. Journal Appl. Phys. 47, 8880-8883 (2008).
2. C. W. Ahn, D. Maurya, C. S. Park, S. Nahm, and S. Priya. "A generalized rule for large piezoelectric response in perovskite oxide ceramics and its application to design lead-free composition," Journal of Applied Physics, 105, 114108 (2009).
3. Cheol-Woo Ahn, Chang-Hak Choi, Hwi-Yeol Park, Sahn Nahm, Shashank Priya, "Dielectric and piezoelectric properties of (1-x)($Na_{0.5}K_{0.5}$)NbO_3–x$BaTiO_3$ ceramics", J. Mater. Sci. 43:6784–6797 (2008).
4. Qinhui Zhang, Yaoyao Zhang, Feifei Wang, Yaojin Wang, Di Lin, Xiangyong Zhao, Haosu Luo,Wenwei Ge, and D. Viehland, "Enhanced piezoelectric and ferroelectric properties in Mn-doped $Na_{0.5}Bi_{0.5}TiO_3$–$BaTiO_3$ single crystals", Appl. Phys. Lett. 95, article # 102904 (2009).
5. Wenwei Ge, Hu Cao, Jiefang Li, D. Viehland, Qinhui Zhang, and Haosu Luo, "Influence of dc-bias on phase stability in Mn-doped $Na_{0.5}Bi_{0.5}TiO_3$-5.6 at. %$BaTiO_3$ single crystals", Appl. Phys. Lett. 95, article # 162903 (2009).
6. Wenwei Ge, Jiefang Li, Dwight Viehland, Haosu Luo, "Influence of Mn Doping on the Structure and Properties of $Na_{0.5}Bi_{0.5}TiO_3$ Single Crystals", Journal of the American Ceramic Society, in press.
7. Jianjun Yao, Wenwei Ge, Liang Luo, Jiefang Li, and D. Viehland, Haosu Luo, "Hierarchial domains in Na1/2Bi1/2TiO3 single crystals: Ferroelectric phase transformations within the geometrical restrictions of a ferroelastic inheritance", Appl. Phys. Lett, submitted.
8. C. W. Ahn, C. S. Park, C. H. Choi, S. Nahm, M. J. Yoo, H. G. Lee, S. Priya, "Sintering behavior of lead-free (K,Na)NbO_3 based piezoelectric ceramics", J. Amer. Ceram. Soc. 92, 2033-2038 (2009).
9. C.-W. Ahn, C.-S. Park, and S. Priya, "Island-Matrix Microstructure for Low Temperature Coefficient of Piezoelectric Property in (K,Na)NbO_3 Ceramics", Functional Mater. Lett., (2009) (accepted).

Program Title: Study of Energy Transport at The Nanoscale

Pramod Sangi Reddy
University of Michigan, Ann Arbor, Michigan 48109
Phone: 734-615-5952
E-mail: *pramodr@umich.edu*

Program Scope: The goal of this program is to experimentally study energy and charge transport in metal-organic molecule-metal junctions (MMMJs). It is well known that the transport properties of MMMJs (figure 1a) are specific to the junction and are unlike that of either the metal electrodes or the organic molecules. In support of this view, recent computational studies of thermoelectric effects in MMMJs have shown that it should be feasible to create extremely efficient thermoelectric devices by engineering the molecular structure of MMMJs(*1, 2*). Large thermoelectric efficiencies are indeed expected on theoretical grounds, as MMMJs can be tuned to have a sharp electronic density of states, which is the key to creating a very efficient thermoelectric material(*3-5*). Further, computational studies have also suggested other interesting possibilities like the creation of organic spin-valves (i.e. devices whose electrical conductance is dependent on the relative magnetization direction of the electrodes) by trapping organic molecules between ferromagnetic electrodes made of Nickel/Cobalt (figure 1b).

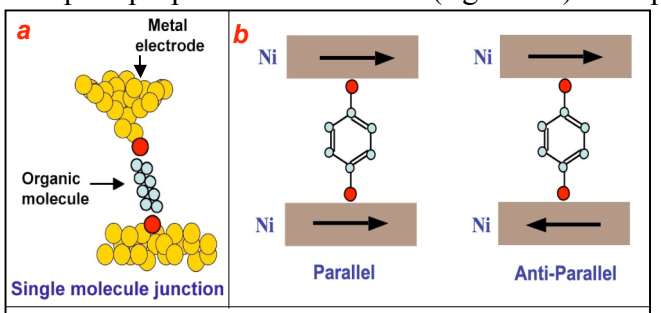

Figure. 1 *a) Single Molecule MMMJ, b) single molecule spin valve in the parallel and anti-parallel configuration (arrows indicate magnetization direction).*

While some initial progress has been made in understanding electrical conductance of MMMJs, the thermal conductance and thermoelectric properties of MMMJs remain largely unexplored. This program seeks to bridge this gap by elucidating the effect of molecular structure, chemical composition of the electrodes, and the relative magnetization direction of the electrodes on 1) the Seebeck coefficient (voltage output per unit temperature differential, also called thermopower), 2) the thermal conductance, and 3) the electrical conductance of MMMJs. This gap in the understanding of heat transport in MMMJs is primarily due to the lack of experimental tools to study these complex phenomena. For example, heat transport in MMMJs has been investigated computationally for over three decades and several unique effects like the length independence of thermal conductance, phonon-filtering, i.e. the suppression of phonon transport in certain frequency ranges and rectification of heat flow have been predicted. However, in spite of this long history, these interesting *energy* transport phenomena, remain experimentally unverified. This absence of experimental data is due to the lack of tools to 1) trap molecules between electrodes to form a MMMJ, 2) apply known temperature differentials of a few Kelvin across electrodes that are separated by about a nanometer, and 3) measure the small heat flux due to the temperature differential across the electrodes of these junctions. The first steps towards such measurements have been taken recently; first, techniques to form MMMJs have been developed by researchers in the field of molecular electronics. Second, the application of temperature differentials across electrodes to study thermoelectric effects has recently been demonstrated by the PI and coworkers(*6*). Finally, ***a novel instrument that combines a picowatt***

calorimeter and a scanning probe microscope, that can overcome the third challenge—measuring extremely small heat flows in MMMJs—is currently being built by the PI and his group as part of this program. Using this technique, investigations will be performed to discover novel phenomena that arise in the transport of MMMJs. In this program we seek to address three major sets of questions:

1) What is the dependence of the Seebeck coefficient of a MMMJ on its molecular structure? Can the Seebeck coefficient and electrical conductance be tuned by adding substituents and side groups to a molecule? Can this approach be used to create molecules with very large Seebeck coefficients(*1*)?
2) Can the electrical conductance of a MMMJ, created by trapping organic molecules between ferromagnetic electrodes, be changed by changing the relative magnetization direction of the electrodes? Is such spin-valve behavior strongly dependent on the structure of the molecule?
3) What are the electronic and phononic contributions to the thermal conductance of MMMJs? Can the Wiedemann-Franz law be used to correctly describe the electronic contribution to thermal conductance at the molecular scale?

Recent Progress and Future Plans: In order to accomplish these challenging goals we have designed and microfabricated a calorimeter (Figure 2) which is expected to have the ability to resolve heat currents of ~1 picowatt. This micro-fabricated device consists of 1) a thermally isolated island that is suspended by thin and long silicon nitride beams and 2) an integrated bimaterial cantilever temperature sensor that is capable of detecting extremely small temperature changes (< 10^{-5} K). This microdevice will be integrated, in a vacuum environment, with an ultra stable scanning probe microscope that is being constructed within our lab. This novel setup will be used to create molecular junctions between the microdevice and a metal coated tip of the scanning probe instrument. Using this instrument, we will perform a variety of transport experiments to determine the charge and heat transport properties of molecular junctions at various temperatures.

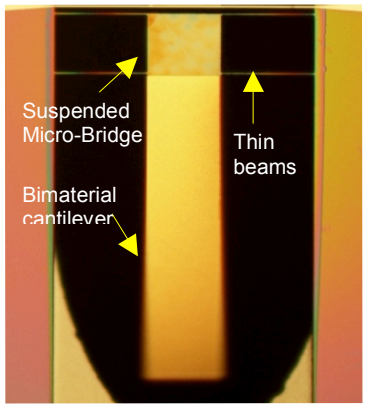

Figure. 2 *A picture of a microfabricated suspended island fabricated by us (work in progress).*

References:

1. C. M. Finch, V. M. Garcia-Suarez, C. J. Lambert, Giant thermopower and figure of merit in single-molecule devices, *Physical Review B* **2009**, 79.
2. P. Murphy, S. Mukerjee, J. Moore, Optimal thermoelectric figure of merit of a molecular junction, *Physical Review B* **2008**, 78.
3. L. D. Hicks, M. S. Dresselhaus, Thermoelectric Figure of Merit of a One-Dimensional Conductor, *Physical Review B* **1993**, 47, 16631-16634.
4. G. D. Mahan, J. O. Sofo, The best thermoelectric, *Proceedings of the National Academy of Sciences of the United States of America* **1996**, 93, 7436-7439.
5. R. Venkatasubramanian, E. Siivola, T. Colpitts, B. O'Quinn, Thin-film thermoelectric devices with high room-temperature figures of merit, *Nature* **2001**, 413, 597-602.
6. P. Reddy, S. Y. Jang, R. A. Segalman, A. Majumdar, Thermoelectricity in molecular junctions, *Science* **2007**, 315, 1568-1571.

Visualization and quantification of deformation processes controlling the mechanical response of alloys in aggressive environments.

Ian M. Robertson
Department of Materials Science and Engineering
University of Illinois, 1304 West Green Street, Urbana IL 61801
ianr@illinois.edu

Program Objective: To understand the fundamental processes governing the mechanical properties of materials exposed to different stimuli. To achieve this understanding, visualization and analysis tools to recover the through thickness information lost in a conventional electron micrographs are being developed and applied to discover the behavior of dislocations.

Electron micrographs display the structure projected on the electron exit surface of the sample and, consequently, are two-dimensional with through thickness information being lost. This information can be recovered through acquiring stereographic images, acquired at say $\pm$ 10° about a major zone axis, and viewing the image pair through a stereo viewer or by forming red /blue anaglyphs and using appropriately colored glasses to reveal the depth information. These approaches provide through thickness information, but extracting and presenting quantitative information is difficult. An alternate approach and one that has been applied extensively and successfully in the life sciences for over sixty years is electron tomography. This method is just emerging as a capability in materials science and is seeing application predominantly in cases in which there is a significant difference in Z, but less so for assessing the spatial distribution of defect structures. To form an electron tomogram with a spatial resolution approaching 1 nm, many images must be acquired over a large angular range, typically $\pm$ 70°, with images acquired every degree. In addition, there must be minimal contrast fluctuation across the range of images. Most applications of electron tomography utilize high-angle annular dark-field imaging conditions to acquire the images as this avoids these issues. However, diffraction contrast imaging conditions have been used with some success.[1,2] Here we demonstrate the applicability of diffraction contrast imaging in forming tomograms of dislocation structures.[3-5]

To investigate dislocation interactions with each other and with obstacles such as grain boundaries and precipitates, diffraction contrast images were acquired every one or two degrees over an angular range of approximately $\pm$ 40^{o} and used to reconstruct a tomogram. This tilt range was enabled by aligning one Kikuchi band with the primary axis of tilt of the holder. The imaging condition used was selected to yield the best images of the structure of interest and had minimum contrast fluctuations over the angular range. Alignment of the series of images and the actual reconstruction was accomplished using software packages that are freely available. As the available angular tilt range, even with acquisition of an image every degree of tilt, is still too small, the reconstructed tomogram has poor resolution in the beam direction. To overcome this issue and to reduce the number of images used in the reconstruction, a 3D model is constructed from the tomogram. In addition, a method to impose the sample coordinate system on the tomogram and on the three-dimensional model has been developed – this is a critical step for dislocation structure analysis. By comparing the placement and orientation of a Thompson tetrahedron with stacking-fault tetrahedra images in Au, it has been demonstrated that the method allows placement to within $\pm$ 3°. This capability allows rapid assessment of the slip

plane of a dislocation, habit plane of a dislocation loop, and quantification of the geometrical relationship between the dislocations and any obstacles. A coupling of this capability with conventional dislocation analysis allows a complete three-dimensional analysis of dislocation structures. The extent of our capability is illustrated by means of two examples: the first is concerned with the interaction of a twist boundary with an Al_3Sc particle in an Al-Mg matrix and the second with the mechanisms of slip transfer across a coherent twin boundary in 304 stainless steel.

A bright-field image of a twist boundary interacting with an Al_3Sc particle in an Al-Mg-Sc alloy, a common feature in this material especially if the deformation is at high temperature, is presented in Figure 1a.[3] A series of such images were used to determine the Burgers vector of each dislocation. To form the tomogram, a weak-beam dark-field series of images was acquired over the angular range from -21.3° to +37.3° with the diffraction condition $\mathbf{g} = 020$ and $\mathbf{s}_g = 6.7 \times 10^{-3}$ Å^{-1} maintained over the entire tilt range. From the tomogram, not shown, a three-dimensional model was constructed. Views from different vantage directions taken from the model, with the dislocations color coded according to the Burgers vector, are presented in Figure 1b and 1c. What is apparent immediately is that there is a striking difference in the actual spatial distribution of the dislocations as seen in the images from the 3D model and that surmised from the electron micrograph. For example, not all dislocations that appear in the bright-field image to reside in the boundary plane actually reside on it – the dislocation marked 1, lies off the plane and the arrowed dislocation has a component extending from the twist boundary – this is more evident in Figure 1c which is a magnified view of the interaction taken from a different viewing direction. This dislocation may be in the process of being ejected from the twist boundary – such a process would account for the formation of dislocations 1 and 2 as debris from the disintegrating twist boundary. In addition, it can be seen that dislocations from the boundary remain attached to the particle and this interaction leaves a loop around the particle, dislocation 3, for example. Three distinct loops around the particle are visible in the model but are less evident in the electron micrograph shown. An unanswered question is the exact position of these loops – on the particle-matrix interface or in the matrix at some characteristic stand-off distance from the interface. Dislocation lines extending from the particle surface to a free surface of the specimen are apparent. Orienting and placing the tetrahedron correctly in the reconstructed space enables identification of the plane on which the loops and line dislocations lie. In other

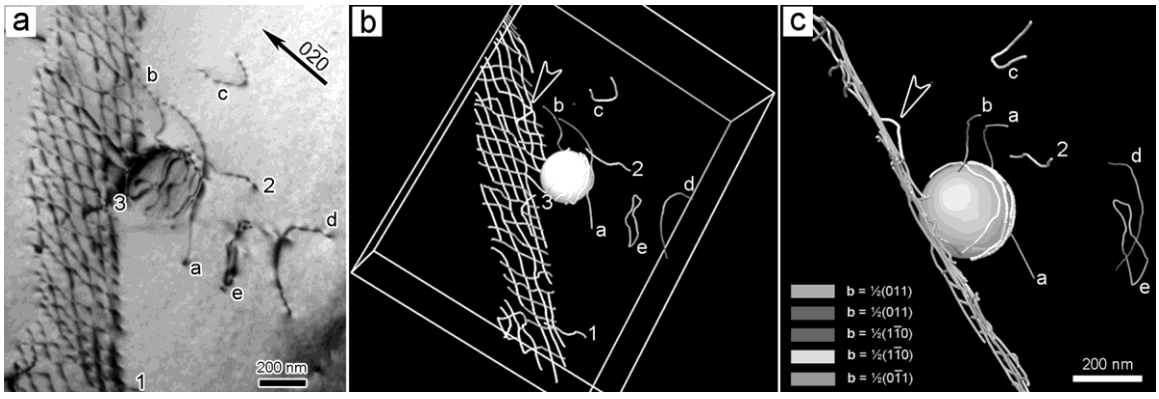

Figure 1. a). Bright-field image showing a twist boundary and the attendant dislocation structure following interaction with a large Al_3Sc particle. b and c) select views from the model constructed from the tomogram. The visual image of the dislocation distribution is certainly very different from the conventional image.

words, the dislocation structure has been characterized completely. Such information is being used to interpret the interaction of dislocations with precipitates, other dislocations and with particles.

The second example illustrates how coupling tomography with conventional analysis procedures provides new insight as well as enhances the interpretation of dislocation interactions with grain boundaries.[6] The grain boundary was identified by electron diffraction as being a Σ3 boundary - this was confirmed by using EBSD. Interestingly, one type of dislocation with a Burgers vector of $b = \pm a/2\,[0\bar{1}1]$ interacts with the grain boundary in multiple locations, three are seen in Figure 2a, but with two different response mechanisms. The first involves emission of just one set of dislocations and the other emission of two sets of dislocations. All three sets of dislocations lie on different slip planes. To interpret the interaction with the grain boundary, the slip system not just the Burgers vector of the dislocations must be identified. The true line direction can be obtained from a series of images taken at different beam directions and diffraction vectors, but as demonstrated this can be done easily from the tomogram and the 3D model.

A series of images were required every two degrees of tilt over an angular range of ± 40° using bright-field imaging conditions. Two views of these interactions, captured from rotations of the 3D-model, are presented in Figures 2b and 2c. The dislocations are color coded according to their Burgers vector in their respective grains and a Thompson tetrahedron is presented in each grain and is oriented with respect to the coordinate system in that grain. The views shown were selected as they provide immediate information about the slip systems. The incoming dislocations, $b = \pm a/2\,[0\bar{1}1]$, can be seen from Figure 2b to reside on the δ-plane and to have a line direction approximately parallel to AB (i.e., $[1\bar{1}0]$), which makes these mixed character dislocations. The outgoing dislocations on system 1 have a Burgers vector $b = \pm a/2\,[0\bar{1}1]$, reside on the β-plane and have a line direction approximately parallel to [211], which would make them edge dislocations. The second interaction, system 2, which results in the emission of two sets of dislocations, has one dislocation, set *a*, with a Burgers vector of $b = \pm a/2\,[1\bar{1}0]$, and these reside on the γ-plane and have a line direction of approximately $[\bar{1}21]$, which makes

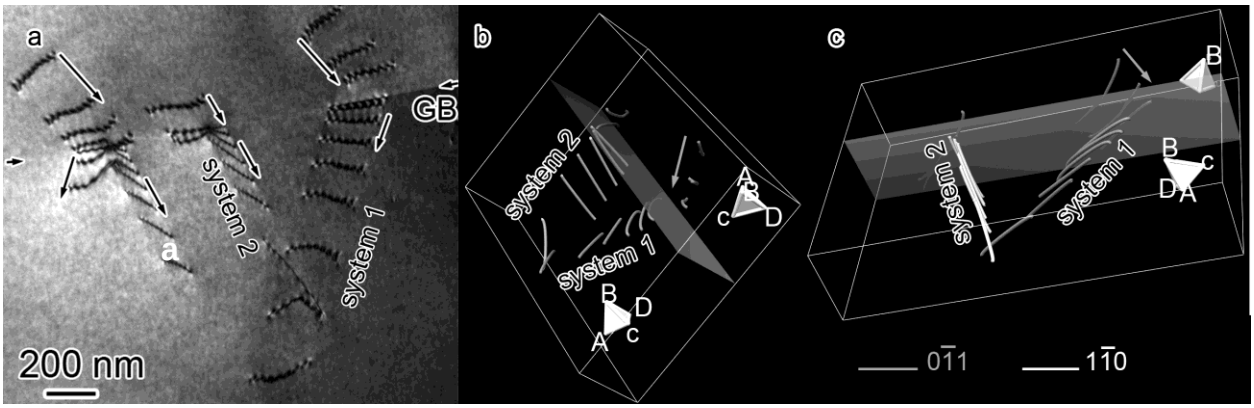

Figure 2. Dislocations interacting with a S3 grain boundary in 304 stainless steel. b and c) snapshots from the three-dimensional model constructed from the electron tomogram. The dislocations are color coded according to the Burgers vector. Note the Burgers vectors as well as the tetrahedron are specific to the coordinate system of the particular grain.

them mixed dislocations. From the **g.b** analysis, the other set of dislocations had a Burgers vector of either $b = \pm a/2\,[1\bar{1}0]\ or\ \pm a/2\,[101]$. From the tilt series it was found these dislocations resided on the δ-plane, which is consistent with them having a Burgers vector of $b = \pm a/2\,[1\bar{1}0]$. The slip transfer involving the $b = \pm a/2\,[0\bar{1}1]$ do not satisfy the slip transfer conditions developed by Lee et al. in that they generate a dislocation in the grain boundary with a significant residual Burgers vector.[7] This does not violate necessarily these criteria as limited dislocation emission can occur on the slip system experiencing the maximum shear stress. Such a system would emit only a limited number of dislocations – this interpretation remains to be verified. The selection of the systems emitting dislocations on the two slip systems satisfies the condition for generating a small residual Burgers vector. Further analysis of this interaction is in progress.

These examples illustrate that these visualization capabilities provide spatial information about the dislocation structures that enhances and enables the interpretation of the interactions.

Future directions include determining the validity of the approach used for generating the 3D model of the dislocation structure, determining the minimum number of images that must be acquired in a tilt series to enable construction of a 3D model that captures the spatial distribution with high reliability, and applying the methods developed and reported herein to reactions and interactions in which the evolution of the microstructure during straining is known. That is, we plan to conduct straining experiments in-situ in the TEM as a function of temperature to gain insight to the evolution of the dislocation microstructure and then to obtain a three-dimensional snapshot of that structure to enhance our ability to discover the interaction processes. This information will be used to determine the rate limiting steps and reaction pathways for dislocation precipitate interaction as well as dislocation-interface interactions. Ultimately, the plan is to develop a capability that enables a material to be stimulated by external forces and to observe the induced microstructural changes with periodic three-dimensional snapshots of the microstructure.

REFERENCES

1 J. S. Barnard, J. Sharp, J. R. Tong, and P. A. Midgley, Science **313,** 319 (2006).

2 J. S. Barnard, J. Sharp, J. R. Tong, and P. A. Midgley, Journal of Physics: Conference Series **26,** 247 (2006).

3 G. S. Liu and I. M. Robertson, Journal of Materials Research **Submitted, August 2010.** (2010).

4 M. Tanaka, G. S. Liu, T. Kishida, K. Higashida, and I. M. Robertson, Journal of Materials Research **submitted for publication** (2010).

5 M. Tanaka, S. Sadamatsu, G. S. Liu, H. Nakamura, K. Higashida, and I. M. Robertson, Journal of Materials Research **Submitted for publication** (2010).

6 J. Kacher, G. Liu, and I. M. Robertson, Scripta Materialia **to be submitted** (2010).

7 T. C. Lee, I. M. Robertson, and H. K. Birnbaum, Philosophical Magazine A Physics of Condensed Matter Defects & Mechanical Properties **62,** 131 (1990).

Project title: Dynamical Nanoscale Crystallography with Femtosecond Resolution

Chong-Yu Ruan
Michigan State University, East Lansing, MI 48824. E-mail: ruan@pa.msu.edu

Program Scope:

The aim of this research program is to understand the photoinduced interfacial processes involving nanostructures and interfaces, where the surface plays an important role in mediating thermal, electrical, and structural processes. We employ a surface sensitive ultrafast electron crystallography (UEC), which has unique sensitivities to simultaneously monitoring the structural, thermal, and charge dynamics on the ultrafast timescale. In addition, ultrafast optical techniques can be performed on the same systems to provide complementary information of the electronic responses. Because of the impulsive nature of the pulse laser excitation and because of the short timescales involved, the nonequilibrium processes under inspection thus allow the elementary couplings between different manifolds (electrons, phonons, and plasmons, etc.) elevated by photo-initiation to be studied directly. Understanding the fundamental energy transduction mechanisms at nanointerfaces is central to the development of novel photovoltaics, nanoelectronics devices, and surface chemistry. Controlled materials synthesis and fabrication by employing lithography and focused ion beam techniques are integrated in the research program to enable systematic studies with controlled sample geometry and lengthscale. Lenthscale control is especially useful in quantifying nanoscale thermal and electric transports. Advancing ultrafast electron diffraction technology, especially in terms of improving sensitivity and temporal resolution, is an important part of on-going research effort. Our long term goal is to be able to employ an ultrabright nanofocused fs electron beam to achieve single-particle/single-site specificity for critical studies in these areas.

Recent Progress

1. *Methodology development of surface probing ultrafast electron crystallography (UEC).* One of our primary efforts in the last several years is to bring the surface probing UEC technology to a more mature stage, which requires us to distill from experimentation a robust data reduction scheme that allows stringent comparisons with different theoretical models. A data reduction and structural refinement procedure has since been coined, as outlined in Fig. 1, which encompasses an array of methods developed to retrieve from time-dependent UEC images robust normalized structural functions, S(s), where s is the momentum transfer wave-vector, from which the structural dynamics can be directly deduced. One interesting phenomenon revealed from this investigation is the ubiquitous presence of photoinduced surface potential change that can cause the diffraction peak to undergo s-dependent shift (refraction effect) [PRB 08]. Since a genuine diffraction pattern is a Fourier transform of the real space distribution of atoms, which follows reciprocity defined by a given parity (odd sine transform for powder, even cosine transform for single crystal), a Fourier Phasing (FP) algorithm is developed to recover the reciprocity distorted by the refraction effect [PRL08, Micros. Microana. 2009], while in the process providing a measure of the transient effective refractive potential. While FP algorithm can almost always recover the reciprocity, the meaning of thus-deduced surface potential can only be quantified when the source of the surface field is known. In almost all cases that involve an interface, we can identify a near-surface dipole field associated with charge redistribution driven by photo-excited hot electrons, while the vacuum field associated with photoemission plays a more significant role in clean surfaces under strong laser fluences. We extended the surface potential retrieval algorithm (ultrafast diffractive voltammetry) to investigate charge transfer at oxide/molecular interfaces, while the effect of photoemission was also evaluated (see discussion in 3).

2. *Probing electronic effects during phase transitions.* A driving force behind the development of ultrafast electron crystallography is the recognition that there are a broad range of phase change materials that respond to photoexcitation nonthermally, thus offering new pathways for controlling and engineering materials compared to those by applying pressure, heat, and chemical doping. The fundamental physics involved is the critical fluctuations near the 'phase transition' diverge when driven

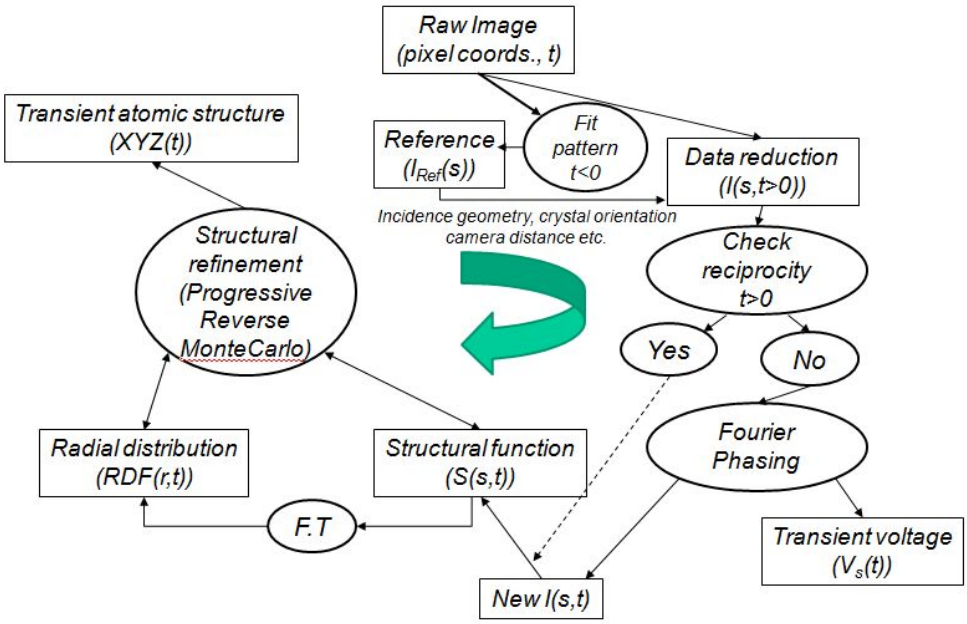

Fig. 1 The data reduction and structure refinement procedure for surface probing ultrafast electron crystallography. First, for diffraction image data reduction, the ground state (t<0) diffraction patter is fitted with geometric parameters (camera distance, beam incidence, sample and camera orientation, lattice parameters, etc.) to obtained the geometric settings of the crystallography for reducing the excited data (t>0) into one-dimension structure function S(s). The normalized and reciprocity-corrected S(s) will then be treated with structural modeling. When high quality excited data are available, a progressive refinement scheme employing Reverse Monte Carlo (RMC) method is used to generate three-dimensional structure models that best match the transient diffraction data through a Metropolis search/minimization algorithm [Micros. Microana. 2009]. The outputs from this data reduction and refinement scheme include the transient voltage, effective temperature -- as represented by rms atomic displacement, and mean atomic structures.

near the critical point. However since the structural transformation studied here is driven through fs laser excitation, the electronic effect (photo-doping) plays an important role, which is yet to be fully clarified. Two systems have recently been investigated by UEC. In the case of photoexcited graphite[PRL 08], we identified transient sp^3 domains formation near the critical point of phase transition, following an initial contraction along the van der Waals c axis. Such hybrid sp^2-sp^3 state along the way towards graphite-diamond transition has been proposed previously [ref.1], and has been identified in a steady-state high-pressure cell study [ref.2]. Our identification of such domains following fs laser excitation, and that of others [ref. 3], suggests that photodoping effect can be useful for driving novel phase transitions. More evidence of cooperative behavior leading to phase transition is revealed in the case of photoinduced fragmentation of silver nanocrystals [PRL10], in which we showed that macroscopic structural transformation is triggered by the creation of local valence instabilities, which leads to bond softening. Such processes can be facilitated in Ag nanoparticles through the strong nonlinear coupling between surface plasmon resonances and interband transition. The valence instabilities grow rapidly when fluence is increased to near critical point, leading to significant reduction of charge screening. Such a dynamical localization feature is central to the creation and growth of topological defects leading to cooperative macroscopic structural changes, and could be common in nonequilibrium photoinduced structural phase transition.

3. Interfacial charge dynamics, including hot-electron driven photoemission. Electron transfer is a primary process responsible for energy transduction at interfaces, especially as the relevant lengthscale approaches 1 nm. Characterizing the microscopic interfacial charge transfer (both forward and backward) beyond the initial steps of photoinduced charge separation is central to the development of

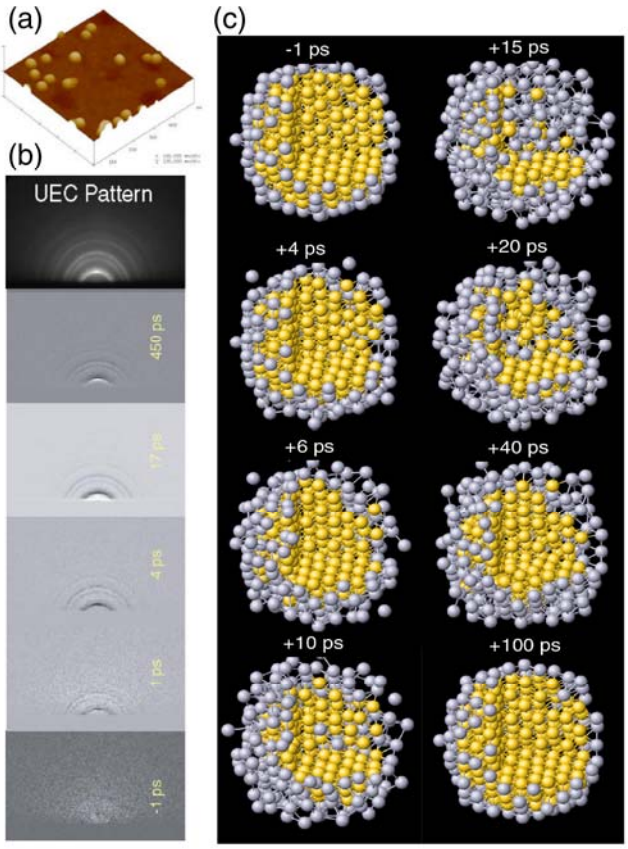

Fig. 2 (a,b) UEC study of surface supported nanoparticles. (c) The 3D rendered excited state transient atomic structures of gold nanocrystals undergoing surface melting are determined through the RMC data refinement procedure[Micros. Microana. 2009].

efficient solar energy transduction devices, sensors, and nanoscale opto-electronics. Utilizing electron diffractive voltammetry approach, we investigated electron transfer near oxide surfaces [PRB 08], and identified different electron transfer channels through excited states via multiphoton process and free-electron absorption at semiconductor and oxide interface, in contrast to the more generic hot-electron tunneling mechanism found under the steady state, or at a lower excitation fluence. Further studies to elucidate the near surface effect and photoemission effect [ref.4] were also conducted. A method was coined to directly image the spatiotemporal evolution of the photoemitted electrons that form a cloud over a femtosecond laser excited surface (Appl. Phys. Lett. 2009). By examining the near surface ballistic expansion of the photoemitted electron cloud, prior to any significant presence of space-charge effects, we can extract the electron temperature associated with the photoemission. Such studies thus open the door for quantitative investigation of hot electron dynamics near the surface, and provide a direct way of charting space-charge effects near a photo-cathode. By using the imaging data of the photoelectron cloud dynamics, we can quantitatively model the refraction and electron beam bending data inherent in the method (Fig. 3) self-consistently without any fitting parameter (once the scaling factor is established for the probing geometry), and such stringent comparison leads to the possibility of tracking the surface image charge dynamics, central for understanding the photoemission process.

4. *Molecular crystals and complex materials.* With gaining maturity in UEC methodology, we are venturing into studying new classes of materials, including complex oxides, chalcogenides, and molecular solids, where interesting properties, such as multiferroics, phase changes, density waves, and superconductivity, emerge due to strong correlations between electronic, magnetic, and lattice degrees of freedom in these materials, and in many cases, creating new macroscopic orders. The emergence of these new macroscopic orders are the low energy excited states with large momentum transfer, which can be best probed by scattering technique such as UEC. We aim to provide the proof-of-principle UEC studies for these materials in transmission geometry. The main challenges in studying these materials are two folds: (1) For molecular film study, one might concern whether or not the molecular film can be fabricated with high enough quality for quantitative UEC study, and even if it can be made, whether or not it can withstand a long-period electron beam radiation from UEC electron pulses. (2) For complex materials, one might concern how to prepare ultrathin regions within the bulk samples to make them amenable to electron diffraction. Our initial successful studies of a 40 nm phthalocyanine molecular film and rare earth chalcogenides suggest such issues can be addressed. A femtosecond coupled dynamics between the charge order and long wavelength lattice distortion was observed.

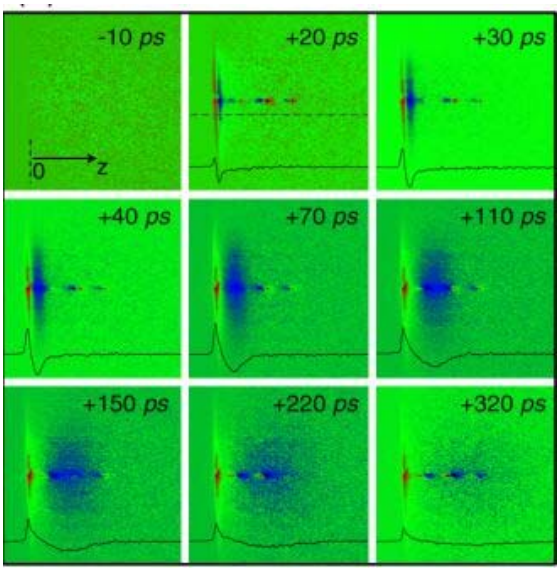

Fig. 3 Shadow imaging results of the ballistic expansion of the photoelectron cloud emitted from a laser heated graphite surface. From these spatiotemporal evolutions, the initial temperature associated with photoelectrons can be extracted to understand the photoemission process[Appl. Phys. Lett. 2009].

Future Plans

The results obtained so far affirms that UEC is a robust tool to track structural, thermal, and charge dynamics. To advance the UEC study of molecular materials, effort is being made to grow large area molecular film for general study – i.e. no need to thin the sample and focus the beam to a small area. We are in the process of installing an optical parametric amplifier, which will allow us to tune the laser excitation wavelength into specific electronic states to explore the complex dynamics near the Fermi surface where the correlation between the macroscopic electronic phase and lattice degree of freedom (phonons) emerges. To advance our understanding of photoemission and control of space-charge effect, *w*e will investigate a series of photocathode materials and geometries under various laser excitation conditions and extraction fields to map out the initial phase space of photoemission. Such studies are coupled with ultrafast voltammetry and photoelectron imaging to investigate the near surface electron dynamics and space charge effects. Such knowledge will be used for a parallel development of a new high-brightness fs photoemission gun to improve the signal-to-noise ratio. To advance our understanding of charge transfer in nanostructures, we will conduct a series of photoinduced thermal and charge transports studies in fabricated interfaces and nanostructures to understand the dynamical responses in these systems. In particular, we would like to differentiate the transport characteristics within the materials versus that at the interfaces.

Reference

1. F. Banhart and P. M. Ajayan. “Carbon onions as nanoscopic pressure cells for diamond formation”. *Nature* 382, 433(1996).
2. W. L. Mao, H.K. Mao, P.J. Eng, T.P. Trainor, M.Newville, C.C. Kao, D.L. Heinz, J. Shu, Y. Meng, and R.J. Hemley. “Bonding changes in compressed superhard graphite”. *Science* 302, 425 (2003).
3. J. Kanasaki, E. Inami, K. Tanimura, H. Ohnishi, and K. Nasu. “Formation of sp3-bonded carbon nanostructures by femtosecond laser excitation of graphite”. *Phys. Rev. Lett.* 102, 087402 (2009).
4. H. Park and J. M. Zuo. “Direct measurement of transient electric fields induced by ultrafast pulsed laser irradiation of silicon”. *Appl. Phys. Lett.* 94, 251103 (2009).

DOE sponsored publications since 2008

1. C.-Y. Ruan, Y. Murooka, R.K.Raman, R.A. Murdick, and R.J. Worhatch, “Transient structural studies of nanoparticles using electron diffraction”. *Microsc. Microanal.* 14 (Suppl 2), 30 (2008).
2. R.A. Murdick, R.K. Raman, Y. Murooka, C-Y. Ruan, “Photovoltage dynamics of the hydroxylated Si(111) surface investigated by ultrafast electron diffraction”. *Phys. Rev. B* 77, 245329 (2008).
3. R.K. Raman, Y. Murooka, C-Y. Ruan, T.Yang, S. Berber, D. Tomanek, “Direct observation of optically induced transient structures in graphite using ultrafast electron crystallography”. *Phys. Rev. Lett.* 101, 077401 (2008).
4. C.-Y. Ruan, Y. Murooka, R.K. Raman, R.A. Murdick, R. Worhatch, A. Pell, “Development and applications of ultrafast electron nanocrystallography”. (Review) *Microsc. Microanal.* 15, 323 (2009).
5. R.K. Raman, Z. Tao, T-R. Han, C-Y. Ruan, “Ultrafast imaging of photoelectron packets generated from graphite surface”. *Appl. Phys. Lett.* 95, 181108 (2009).
6. R.K. Raman, R.A. Murdick, R. Worhatch, Y. Murooka, S.D. Mahanti, T-R. Han, C.-Y. Ruan, “Electronically driven photo-fragmentation of silver nanocrystal revealed by ultrafast electron crystallography”. *Phys. Rev. Lett.* 104, 123401 (2010).
7. Z. Tao, H. Zhang, R.K. Raman, T.-T. Han, K. Chang, M. Berz and C.-Y. Ruan, “Progress of Dynamical Nanomaterial imaging using ultrashort electron pulses”. *Microsc. Microanal.* 16 (Suppl. 2), 498-499 (2010).

Abstract for Electron and Scanning Probe Microscopies Contractors Meeting 2010

1. **DOE Award Number**: DE-FG02-84ER45076

   Recipient Organization: Board of Regents of the University of Wisconsin System, University of Wisconsin-Milwaukee, P.O. Box 340, Milwaukee, WI 53201

2. **Project Title**: "Electron Scattering from Surfaces"

PI: Dilano K. Saldin
Department of Physics
University of Wisconsin-Milwaukee
PO Box 413
Milwaukee, WI 53211
E-mail: dksaldin@uwm.edu

3. **Recent Progress**

Low energy electron diffraction (LEED) [1] is an almost ideal tool for experimentally revealing the atomic-scale structure of the outermost layers of a crystal surface. This is because the strong interaction of such electrons with matter results in a short inelastic scattering length of the depth of only a few surface atomic layers. Thus, the backscattered signal is sensitive only to the structure of these few outermost layers.

We first describe below applications of LEED analyses we have performed in the last two years for a variety of surface structural problems, namely the surface segregation of gold on Au/Pd(111) alloys, the study of a surface alloy model of p(2x2)Sb/Cu(100), the structure of TiO_2 and ZnO metal oxide surfaces, and the structure and reactivity of the organic adsorbate 2-butanol on a Pd(111) surface. We describe each of these pieces of work in turn.

Au/Pd bimetallic alloys have been found to provide both active and selective catalysts for a number of reactions including CO oxidation, cyclotrimerization of acetylene to benzene, vinyl acetate synthesis, selective oxidation of alcohols to aldehydes or ketones, oxidation of hydrogen to hydrogen peroxide, and hydrocarbon hydrogenation. A key issue in understanding the relationship between the composition and surface chemistry of these alloys is a knowledge of the precise proportions of Au and Pd atoms near a surface. We have performed a LEED analysis [2] to determine that Au preferentially aggregates to the surface and can be modeled by a Lagmuir-McLean equation. This is found to be in agreement with a parallel study by low energy ion scattering (LEIS) and with results for Au/Pd(111) alloys grown on Mo(110) substrates.

Since the electrons that form the diffraction probe in LEED are charged particles, the vast majority of LEED studies have been on metal and semiconductor surfaces, which allow the conduction of the charges and thereby prevent a buildup of charge which would interfere with the trajectory of subsequent electrons. Consequently, the determination of the structures of the surfaces of technologically important materials such as metal oxides, which are insulators, have greatly lagged behind those of metal surfaces. An elegant solution to this problem has been employed by my colleague, Prof. Carol Hirschmugl. By using an low-current incident beam and a special delay-line detector (DLD-LEED) [3], it was possible to

measure meaningful LEED patterns even from metal oxide surfaces. We have provided the essential theoretical support analyze such data to deduce structural information about such surfaces.

The surface of titania (TiO_2) has been extensively studied since the discovery in 1972 that its acts as a photocatalyst for the water-splitting reaction [4]. The majority of studies have foucused on the thermodynamically most stable face TiO_2(110). However, other faces are almost as important. For example, the (011) face may have enhanced activity towards water dissociation. A scanning tunneling microscopy (STM) and density functional theory (DFT) investigation of TiO_2(011)-(2x1) has suggested a surface terminated by titanyl (Ti=O) groups, possibly a cause of the enhanced photo-catalytic activity. Another study has suggested a microfaceting missing-row model. Recent surface x-ray diffraction (SXRD) studies have suggested qualitatively similar structures terminated by zigzag rows of twofold coordinated oxygen atoms asymmetrically bonded to five-fold Ti atoms. Since the differences in these structures are larger than the stated error bars, we performed a LEED study with the DLD-LEED apparatus to resolve these differences, particularly exploiting the greater sensitivity of LEED to atomic positions perpendicular to the surface. The results of our analysis [5] were in good agreement with those of the SXRD studies with an agreement between theory and experiment good enough to effectively rule out the other models in the literature. However, we did not find support for a key feature of the bonding in this model that has been proposed to explain the photocatalytic activity of this surface.

Likewise, ZnO is a wide badgap semiconductor with a variety of technological applications. The mechanism by which the electrostatic energy of polar surfaces of such oxides is stabilized has been the subject of much investigation. One of the proposed mechanisms is surface reconstruction. However, clean polar ZnO surfaces are often observed to remain unreconstructed. The explanation of the stability of polar oxide surfaces in this case must involve some other mechanism, such as adsorption of foreign species (e.g. hydroxylation), or metallization, i.e. charge transfer between surface planes, as suggested by Wander et al. [6] However, more recent studies of newly-found reconstructions have called into question such a stabilization mechanism of this surface. A recent SXRD study has found a $(\sqrt{3}x\sqrt{3})R30^o$ reconstruction, which appears to be suppressed in the presence of H. A recent DFT study has suggested that up a ½ monolayer of H coverage may be energetically favorable on O-polar ZnO surfaces. These studies suggest that H may play a crucial role in stabilizing this surface. Although, like x-ray diffraction, LEED is not directly sensitive to H atoms, it should be able to detect their effects on the displacements of other surface atoms. Our LEED analysis [7] found that the outermost O-Zn interlayer spacing of the ZnO(000-1)(1x1) surface was contracted relative to such a spacing in the bulk by about 16%. When compared to the results of DFT calculations of several H coverages, these indirectly suggested a 1/3 monolayer coverage of H.

The ultralow beam current of the DLD-LEED apparatus is also useful for the structure determination of fragile organic adsorbates which are involved in catalysis on transition metal surfaces. It is known that Pd(111) modified by adsorbed chiral 2-butanol leads to the enantioselective chemisorption of propylene oxide. This effect is believed to be due to enantiospecific hydrogen-bonding interactions between 2-butanol and propylene oxide. Measurements of the variation in enantiospecificity with 2-butanol exposure suggest that propylene oxide can interact either with a single adsorbed 2-butanol molecule or, at higher coverages, with two adsorbed 2-butanol species to form enantioselective sites. We have used DLD-LEED to investigate [8] the formation of 2-butoxide on Pd(111) in order to understand the surface chemistry of 2-butanol (and other C4+ alcohols), which have received much less attention in the past than smaller alcohols.

The traditional method of solving surface structures by LEED, which has been employed in the above studies, is that of comparing a large number of simulated LEED spectra for guessed models with experiment. While such a method may be adequate for relatively simple surface structures, and may be sensible for the final stages of refinement, due to the exponential scaling of the required computer time with the number of parameters varied, it is often inadequate for determining a complex unknown structure. In order to overcome this problem, we have developed a method known as the Phase and Amplitude Recovery And Diffraction Image Generation Method (or PARADIGM, for short) [9]. This method combines information about the known part of the structure (the bulk), which serves as a "holographic" reference wave, with a numerical algorithm which iteratively satisfies constraints in real and reciprocal space, as in methods now popular in *diffraction microscopy*. Together with the visiting Japanese student Shohgo Higashi, we have applied this method successfully to recover the structure of the surface alloy p(2x2)Sb/Cu(001) [10] from LEED data from the group of Prof. Hiroshi Toc hihara of Kyushu University.

References

[1] J. B. Pendry, *Low Energy Electron Diffraction*. (London, Academic Press).
[2] J. Li et al., Surf. Sci. **602**, 1084-1091 (2008).
[3] D. Human et al., Rev. Sci. Instrum. **77**, 023302 (2006).
[4] A. Fujishima and K. Honda, Nature **238**, 37 (1972).
[5] S. E. Chamberlin et al., Surf. Sci. **603**, 3367-3373 (2009).
[6] A. Wander et al., Phys. Rev. Lett. **86**, 3811-3814 (2001).
[7] S. E. Chamberlin et al, submitted to Phys. Rev. B.
[8] F. Gao et al. Surf. Sci. **602**, 2264-2270 (2008).
[9] D. K. Saldin and V. L. Shneerson, J. Phys.: Condens. Matter **20**, 304208 (2008).
[10] S. Higashi et al., Surf. Sci. **602**, 2473 (2008).

4. Planned Activities for Next Year

The current grant is due to expire during 2011. However, due to delays in obtaining a visa for the postdoc supported by the project, the following planned projects for the third and final year of this project have been delayed, but will be the subject of our plans for the final year, assuming a no-cost extension is granted.

LEED Studies with a Low Beam Currents

There are two circumstances in which use of an ultra-low beam current is essential for LEED: (1) the study of fragile organic adsorbates on surfaces, and (2) the study of insulating surfaces, such as those of metal oxides where, due to lack of a conduction channel, such samples charge up due to an accumulation of electrons from the incident beam. The apparatus developed in the laboratory of one of the PI's colleagues, Prof. Carol Hirschmugl, which uses a low-current, and a high-count-rate delay-line detector, enables precisely such experiments. During the nest grant period we propose to work on the unsolved structure of MgO(111)-($\sqrt{3}$x$\sqrt{3}$) and on other metal oxide surface structures.

LEED Studies of Chiral Surfaces

It is well known chirally-related molecules cannot be distinguished x-ray crystallography since an x-ray diffraction pattern from a molecule and its enantiomorph are identical. The theoretical argument for this proposition is based on the kinematical (or single-scattering) theory. It is not expected to be valid in a circumstance of strong multiple scattering as in LEED. We have indeed found that LEED is an excellent tool for distinguishing enantiomerically-related structures.

Computing Facilities

The PI has recently purchased a 50-node Beowulf cluster (from other sources) for the performance of large-scale computations that can benefit from parallel calculations. Since LEED intensities for each energy of a spectrum are performed independently, they are ideally suited for parallel computations. Since a typical LEED spectrum consists of approximately 50 different energy points, or cluster is ideally sized to perform such calculations. We have spent the last year gaining experience with parallel programming, and are now poised to use this machine for LEED computations. We would expect to see a 50-fold increase in speed of calculations, thus making tractable many calculations that had previously been beyond reach.

5. Publications Acknowledging DOE Support on this Project in 2006-2008

[1] "Surface Segregation of Gold on Au/Pd(111) Alloys Measured by Low Energy Electron Diffraction"
J. Li, O. Furlong, F. Calaza, L. Burkholder, H. C. Poon, D. K. Saldin, and W. T. Tysoe
Surf. Sci. **602**, 1084-1091 (2008).

[2] "The Structure and Reactivity of 2-Butanol on Pd(111)"
F. Gao, Y. Wang, L. Burkholder, C. Hirschmugl, D. K. Saldin, H. C. Poon, D. Sholl, J. James, and W. T. Tysoe
Surf. Sci. **602**, 2264-2270 (2008).

[3] "Direct Methods for Surface Crystallography"
D. K. Saldin and V. L. Shneerson
Invited Paper in Festschrift to honor the 65th birthday of Prof. Sir John Pendry, F. R. S.
J. Phys.: Condens. Matter **20**, 304208 (2008).

[4] "Surface Alloy Model of p(2x2)Sb/Cu(001) from LEED I/V data"
S. Higashi, H. Tochihara, V. L. Shneerson, and D. K. Saldin
Surf. Sci. **602**, 2473-2477 (2008).

[5] "Geometric structure of TiO_2(011)-(2x1) surface by low energy electron diffraction (LEED)"
S. E. Chamberlin, C. J. Hirschmugl, H. C. Poon, and D. K. Saldin
Surf. Sci. **603**, 3367-3373 (2009).

[6] "Looking for stability: the role of hydrogen on ZnO(000-1) –(1x1) surface"
S. E. Chamberlin, C. J. Hirschmugl, S. T. King, H. C. Poon, and D. K. Saldin
Submitted to Phys. Rev. B.

Atomic and Electronic Structure of Oxides Materials

DE-AC02-06CH11357, DEFG02-91ER45439, and DE-FG03-02ER45996

Amish B. Shah[1,2], Jian-Min Zuo[1] and John Spence[2], and Anand Bhattacharya[3]

[1] Dept. of Materials Science and Engineering and Materials Research Laboratory
University of Illinois at Urbana-Champaign, Urbana, IL 61801, USA. Jianzuo@illinois.edu

[2] Dept. of Physics, Arizona State University, Tempe, AZ, 85287-1504, USA. Spence@asu.edu

3 Center for Nanoscale Materials and Materials Science Division, Argonne National Laboratory, Argonne, IL 60439, USA. Anand@anl.gov

Program Scope:

This research is aimed at understanding the local atomic and electronic structure of oxide materials for energy generation, energy distribution, magnetic devices, and ferroelectric devices. These applications are made possible by synthesizing oxide materials in a highly controlled manner via molecular beam epitaxy (MBE). Our growth collaborators from Illinois and ANL are able to control growth parameters including, cation stoichimetry, oxygen concentration, growth rate, and annealing temperatures. With tightly controlled parameters, one can grow films a single atomic layer at a time, and control termination of each layer. The interface quality and atomic layering sequence strongly influence the behavior of these materials for light absorption, metal-insulator transitions, and ferromagnetic ordering.

To understand the influence of interfaces on the relevant properties of interest, we are investigating the local atomic and electronic structure with atomic resolution transmission electron microscopy. Significant improvement of interfacial studies have been achieved with the recently acquired aberration corrected JEOL 2200FS microscope (2008) at the University of Illinois which is able to directly image the oxide materials at atomic resolution. Collaborations with the National Center for Electron Microscopy at LBNL have extended our ability for collecting electronic structural information via electron energy loss spectroscopy (EELS) in their aberration corrected TEAM microscope and aberration corrected VG501 dedicated STEM.

Recent Progress: Supported by DE-AC02-06CH11357 and DEFG02-91ER45439

1) $LaMnO_3$-$SrMnO_3$ for Ferromagnetic Applications

We have investigated superlattices of $LaMnO_3$ (LMO) and $SrMnO_3$ (SMO). Both materials are each insulating and antiferromagnetic in bulk form. However, superlattices of $(LMO)_{2n}$-$(SMO)_n$ undergo a metal-insulator transition when $n > 3$, where n is the number of unit cell per supercell. For $n < 3$, the samples are metallic[1]. For $n > 3$, the sample is insulating and ferromagnetic. The ferromagnetic moment is enhanced at only one interface[2]. In two papers published in *Physical Review B*[3,4], we investigated the atomic and electronic structure of these superlattices with aberration corrected STEM and EELS. We discovered the interfaces are structurally asymmetric. The LMO on top of SMO interface is atomically sharp while the interface of SMO on top of LMO is slightly intermixed to a few unit cells. The structural asymmetry leads to an enhanced ferromagnetic moment at the sharp interface and a suppressed moment at the rougher interface. With EELS, we found a new electronic state at the sharp interface which contained extra core holes above the Fermi level (Figure 1). These results show

the localization of magnetic moments are highly dependent upon the interfacial structural quality and the presence of new electronic states.

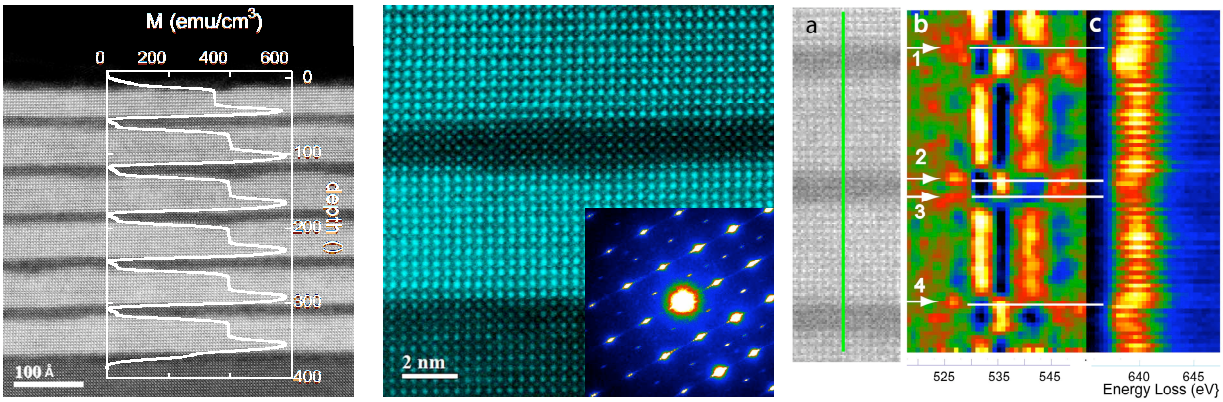

Figure 1: (a) Polarized neutron reflectively shows an asymmetric magnetization confined to LMO in a LMO-SMO superlattice. (b) Aberration corrected STEM imaging shows atomic level structural asymmetries at the interfaces, which result in asymmetries in magnetization. Nanoarea electron diffraction shows additional reflections from a distorted lattice. (c) Atomic scale EELS of the O K and Mn L_3 edges show unique states at the sharp interfaces.

2) $LaMnO_3$-$SrTiO_3$ for Optical Absorption

$(LaMnO_3)_n$-$(SrTiO_3)_n$ (LMO-STO) superlattices are interesting for solar applications. STO in bulk form has no optical absorption below 3.2 eV, making it a poor solar material. LMO in bulk form has one broad optical absorption peak below 3.2 eV. However, superlattices of these two films have additional optical absorption between 1.8 and 3.0 eV, which is ideal for visible light absorption[4]. The magnitude of absorption depends on the thickness of the supercells[4]. In two papers published in *Advanced Materials*[4,5] we used atomic resolution STEM and EELS to investigat the electronic states in the n = 2 superlattice, which is epitaxially strained to a $SrTiO_3$ substrate. (Figure 2). We found direct EELS evidence of interfacial electronic states for band alignment and interfacial electron transfer, or charge leakage, in the n = 2 superlattice. The band alignment, in the form of a 0.22 eV chemical shift of O K and Ti $L_{2,3}$ edges, was observed in ultra-thin STO. The electron transfer from LMO to STO is evidenced by a reduction in the intensity of O K edge prepeak in STO, which is attributed to unoccupied O 2p states from hybridization with the Ti 3d t_{2g} states. Our results show that the oxidation state in the fine structure of the O K edge can be mapped with 4 Å resolution, or better, which had not been experimentally proven previously.

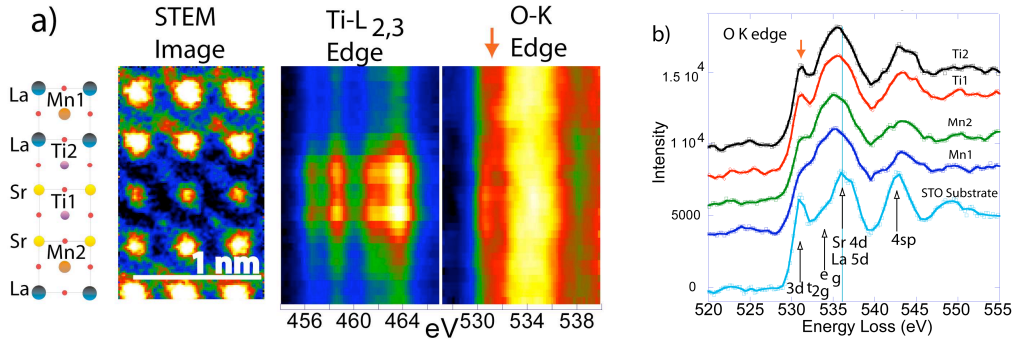

Figure 2: Atomic scale mapping of the Oxygen K edge in the $LaMnO_3$-$SrTiO_3$ superlattice shows the spectra from the $SrTiO_3$ thin films differs from the bulk $SrTiO_3$ substrate due to electron leakage into the films. The O spectra from the Mn sites have a different signature due nearest neighbor termination.

3) $LaAlO_3$-$SrTiO_3$ for Superconductors

We have investigated the interface of $LaAlO_3$ (LAO) grown on $SrTiO_3$ (STO), which is known to be superconducting below 5 K. This system has been studied widely in the literature and reasons for high conductivity at an oxide-oxide interface are believed to be electron leakage from LAO into the STO substrate due to a polar catastrophe and oxygen vacancies during pulsed laser deposition growth. Our investigation with atomic resolution EELS and STEM, in conjunction with several other analytic techniques, revealed an intermixed interface[7]. Both La doping into $SrTiO_3$ and mixtures of $LaTiO_3$ and $SrTiO_3$ are known to be metallic; our characterization of the interface revealed a non-sharp interface due to interdiffusion, which likely contributes to enhanced conductivity at the interface.

Future Plans: Supported by DE-FG03-02ER45996

1) Development of EELS in the STEM

The use of atomic scale EELS in the STEM is increasing, due to ability to map electronic structures high spatial resolution available in aberration corrected electron microscopes and improvements in instrumentation. However, the spatial resolution of EELS has not been measured experimentally to date, and theoretic calculations do not take account of realistic sample thickness or experimental conditions in the electron microscope. We have submitted a manuscript where we have measured the EELS spatial resolution over a range of elements in realistic oxide samples[8]. We show that the Ti L, Mn L, and La M edges EELS spatial resolution measured by the FWHM of the EELS signal is 4.1 Å, 3.4 Å, and 6.8 Å, respectively, in a 200 kV aberration corrected STEM. The resolution of the Ti and Mn L edges matches well with Egerton's empirical model[9], but the La M edge resolution is lower, due to strong elastic scattering from the heavy La columns.

Additionally, we plan to make use of two new aberration corrected STEMs to be received at Arizona State University. The first STEM, a JEOL ARM200F will have an improved column design and a faster EELS detector, which will make use of high speed spectrum acquisition. We plan to make use of two-dimensional (2D) EELS and EDS maps to study interfacial diffusion and defects of areas. The second machine, a Nion UltraSTEM will include a cold field emission gun and a monochromator. This instrument will improve both the energy and spatial resolution of EELS, which will further increase our ability to study interfaces and electronic states such as band gaps on an atomic scale.

2) Ruddleston-Popper Structures

We have begun to synthesize and characterize new oxide superlattices and films, including ($La_{2/3}Sr_{1/3}MnO_4$) on $SrTiO_3$ in a Ruddleston-Popper (RP) structure. The RP structure has an extra layer over a simple perovskite. This layering sequence is expected to enhance electrical and magnetic transport properties over perovskites and random alloy phases. Initial structural characterization with x-ray diffraction and STEM show an ordered layering sequence with defects.

We have also started in investigate (Ba,Sr)TiO_4 for ferroelectric materials. Ba_2TiO_4 typically crystallizes into a silicate structure while Sr_2TiO_4 forms a RP phase. Solid solutions of

$(Ba,Sr)TiO_4$ phase separate into two different structures, due to Ba being two big for the RP phase. We are intending to try to stabilize a layered structure of pure RP phase.

References:

1. A. Bhattacharya et al., Metal-Insulator Transition and Its Relation to Magnetic Structure in $(LaMnO_3)_{2n}$ / $(SrMnO_3)_n$ Superlattices. *Physical Review Letters* **100** (2008).
2. S. Smadici et al., Electronic Reconstruction at SrMnO3-LaMnO3 Superlattice Interfaces, *Physical Review Letters*, **99** (2007).
3. S. J. May et al., Magnetically Asymmetric Interfaces in a $(LaMnO_3)$ / $(SrMnO_3)$ Superlattice Due to Structural Asymmetries. *Physical Review B*, **77** (2008).
4. A. B. Shah et al., Presence and Spatial Distribution of Interfacial Electronic States in $LaMnO_3$-$SrMnO_3$ Superlattices, *Physical Review B*, Accepted 2010.
5. X. Zhai et al., New Optical Absorption Bands in Atomic Layer Superlattices. *Advanced Materials* **22** (2010).
6. A. B. Shah et al., Probing Interfacial Electronic Structures in Atomic Layer $LaMnO_3$ and $SrTiO_3$ Superlattices. *Advanced Materials* **22** (2010).
7. S. A. Chambers, et al., Instability, Intermixing and Electronic Structure at the Epitaxial $LaAlO_3$/$SrTiO_3$ (001) Heterojunction. Submitted to *Surface Science Reports*, 2010, and http://arxiv.org/abs/1006.1378.
8. A. B. Shah et al., Practical Spatial Resolution of Electron Energy Loss Spectroscopy in Aberration Corrected Scanning Transmission Electron Microscopy. Submitted to Ultramicroscopy, 2010.
9. R. F. Egerton, Limits to the spatial, energy and momentum resolution of electron energy-loss spectroscopy *Ultramicroscopy* **107** (2010).

DOE Sponsored Publications on 2008-2010:

1. Instability, Intermixing and Electronic Structure at the Epitaxial $LaAlO_3$/$SrTiO_3$ (001) Heterojunction. S.A. Chambers, M.H. Engelhard, V. Shutthanandan, Z. Zhu, T.C. Droubay, L. Qiao, P.V. Sushko, T. Feng, H. D. Lee, T. Gustafsson, E. Garfunkel, A. B. Shah, J. M. Zuo, and Q. M. Ramasse. Submitted to *Surface Science Reports* (2010) and http://arxiv.org/abs/1006.1378.
2. Presence and Spatial Distribution of Interfacial Electronic States in $LaMnO_3$-$SrMnO_3$ Superlattices. A. B. Shah, Q. M. Ramasse, S. May, J. G. Wen, X. Zhai, J. N. Eckstein, A. Bhattacharya, J. M. Zuo. Accepted, *Physical Review B* (2010).
3. Probing Interfacial Electronic Structures in Atomic Layer $LaMnO_3$ and $SrTiO_3$ Superlattices. A. B. Shah, Q. M. Ramasse, X. Zhai, J. G. Wen, S. J. May, I. Petrov, A. Bhattacharya, P. Abbamonte, J. N. Eckstein, and J. M. Zuo. *Advanced Materials* **22** (2010).
4. New Optical Absorption Bands in Atomic Layer Superlattices. X. Zhai, C. S. Mohapatra, A. B. Shah, J. M. Zuo, and J. M. Eckstein. *Advanced Materials* **22** (2010).
5. DNA Sensing using Nano-crystalline Surface Enhanced Al_2O_3 Nanopore Sensors. B. M. Venkatesan, A. B. Shah, J. M. Zuo, and R. Bashir. *Advanced Functional Materials* **20** (2010).
6. The Formation and Utility of Sub-Angstrom to Nanometer-Sized Electron Probes in the Aberration Corrected Transmission Electron Microscope at the University of Illinois. J. G. Wen, J. Mabon, C. Lei, S. Burdin, E. Sammann, I. Petrov, A. B. Shah, V. Chobpattana, J. Zhang, K. Ran, J. M. Zuo, S. Mishina, and T. Aoki. *Microscopy and Microanalysis* **16** (2010).
7. Magnetically Asymmetric Interfaces in a $(LaMnO_3)$ / $(SrMnO_3)$ Superlattice Due to Structural Asymmetries. S. J. May, A. B. Shah, S. G. E. te Velthuis, M. R. Fitzsimmons, J. M. Zuo, X. Zhai, J. N. Eckstein, S. D. Bader, and A. Bhattacharya. Physical Review B, **77**, 2008.
8. Metal-Insulator Transition and Its Relation to Magnetic Structure in $(LaMnO_3)_{2n}$ / $(SrMnO_3)_n$. A. Bhattacharya, S. J. May, S. G. E. te Velthuis, M. Warusawithana, X. Zhai, B. Jiang, J.-M. Zuo, M. R. Fitzsimmons, S. D. Bader, and J. N. Eckstein. *Physical Review Letters* **100** (2008).
9. Electron Energy-loss Study of the Electronic Structure of Atomic Scale $SrTiO_3$-$SrMnO_3$-$LaMnO_3$ Superlattices. A. B. Shah, X. Zhai, B. Jiang, J. G. Wen, J. N Eckstein, and J. M. Zuo. *Physical Review B* **77** (2008).

1. Program Title: Electron and Scanning Probe Microscopies.

2. P.I. Prof J.C.H.Spence. Period covered: 7/31/08 - 7/31/10.

3. Address: Physics, ASU, Tempe, Az. 85287-1504. Spence@asu.edu

4. **Program scope: Quantitative Nanodiffraction for atomic processes in clean energy materials**. Award: DE-FG03-02ER45996

5. Recent Progress.

This research is aimed at understanding atomic processes in clean energy materials, such as the remarkable metal-organic and covalent-organic framework structures and light-metal hydrides intended for gas storage, Li-Fe-phosphate nanostructures for fast-charge batteries, solid electrolytes such as sodium-β-alumina, solar cell nanostructures, and new nanocrystallites for the photocatalysis of water to hydrogen. We are interested in the atomic-scale characterization of these nanostructures, using new imaging and diffraction techniques in atomic-resolution electron microscopy.

A crucial problem in this field is the determination of the atomic structure of individual nanocrystals *in three dimensions* which are too small to be analysed by X-ray crystallography or precession electron diffraction, and whose functionality may depend on departures from the structure of an ideal large single crystal. This cannot be done using high-resolution electron microscope imaging, because of the large sample-tilts required, and the need to correlate atomic resolution images from widely different projections of the same nanoparticle - an extremely challenging problem which does not arise when using diffraction methods. (In diffraction mode, the two-dimensional diffraction pattern intensities may be merged into three dimensions before the three-dimensional phase problem is solved). Over the past year we have suceeded to determine the atomic structure, in three-dimensions, of a nanocrystal using microdiffraction patterns and a 50nm diameter electron probe in a scanning transmission electron microscope (1). Our method uses a convergent beam of electrons in a modern TEM, an elastic imaging ("Omega") electron filter, an Image Plate detector system, and a new approach to solving the phase problem. This method (Kinematic Convergent Beam Electron Diffraction, or KCBED) can now be applied to range of functional nanocrystalline structures. The method has the advantages of measuring the absolute intensity of the Bragg beams (because the zero-order beam can be recorded within the dynamic range of the detector in CBED mode) , of giving an immediate indication of the severity of any multiple-scattering perturbations (these are absent when the CBED disks are uniformly filled), and of allowing the smallest possible diffraction-limited electron probes to be used. Figure 1 shows the results. The novel instrumentation used included image plates (electronic film) and an Omega type energy filter to elliminate inelastic scattering. A new iterative flipping algorithm (1) has been developed, based on charge-flipping technique, to determine the phases of the Bragg beams. Results from spinel crystals are shown - note identification of oxygen atoms. These 3D maps of atom positions could be obtained while sitting at the electron microscope - with diffraction data collected using a single-axis tilt stage.

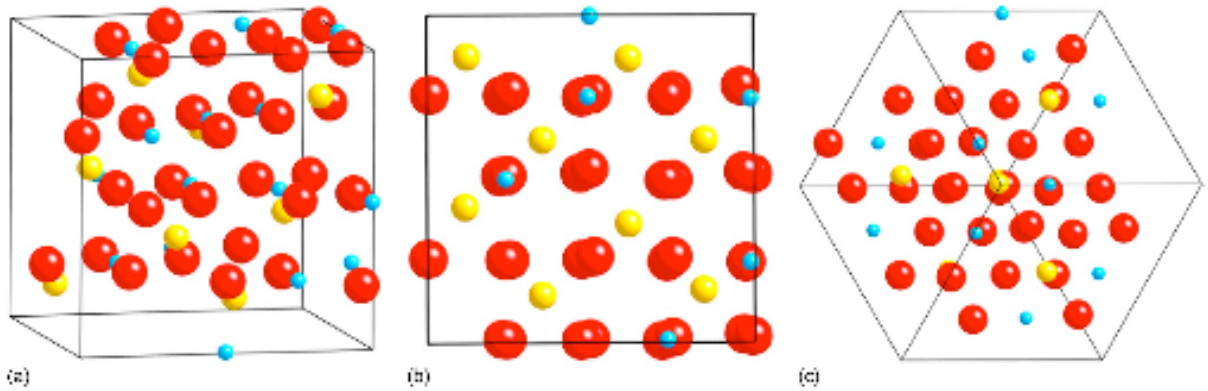

FIG. 5. (Color online) (a) Spinel unit-cell electrostatic potential, obtained after refinement in SHELXL, also shown along the (b) [100] and (c) [111] directions. Mg (medium diameter), Al (smallest diameter), and O (largest diameter) atoms are colored yellow, blue, and red, respectively.

3D atomic nanoxtal structure solved by electron diffraction at the TEM !.

Our work on a different project has demonstrated to us the power of modern X-ray crystallography software for automatically indexing diffraction patterns. This software has been developed primarily for protein crystallography. Given about 20 Bragg spots or more, from different zones, this software (such as MOSFLM in CCP4) is capable of indexing patterns in arbitrary orientations, and providing cell constants. It therefore provides a huge simplication for our KCBED research. It should be possible to collect "tomographic diffraction" data almost continuously as a crystallite is rotated continuously about a single axis. (We use shadow images and autocorrelation methods to "bring back" the nanocrystal onto the optic axis after each tilt). The patterns can then be indexed by MOSFLM, whose source code we now have. Thus, instead of tediously setting up particular orientations in high-symmetry zone axis orientations, the operator can start a singe-axis scan , collect many KCBED patterns, and use automated indexing software to provide cell constants and Miller indices for the spots. Our primary aim for 2010-2011 is therefore to demonstrate online 3D solution of a clean-energy nanocrystal structure *at the electron microscope.* (An atomic charge-density map can be displayed in three-dimensions on a screen beside the electron microscope). Collaborators at the Molecular Foundry at LBNL are providing the nanocrystals.

A second recent highlight has been our paper on mapping out the chemical bonds between atoms in Galium Nitride, an important solid-state lighting material used for energy-saving lighting applications. This has been a large undertaking over several years, in collaboration with the materials department in Cambridge UK. The significance of the work is that the polar bond in this material has now been directly observed for the first time, and that our TEM method of highly accurate structure-factor phase measurement, based on elastic energy-filtered convergent-beam electron diffraction, made this possible (2). The redistribution of valence charge density which occurs when atoms bond to form a solid is extremely small, and has only been seen in non-centrosymmetric crystals using our method of extinction-free structure-factor phase measurement. Fig. 2 shows the *quantitative* maps (contours are given in electrons per cubic Angstrom - a) Experiment - a slice of charge-density normal to [110] through the origin. b). Theory (DFT) c) Experiment minus theory. Atoms are Ga, N, Ga, N, Ga down the page.

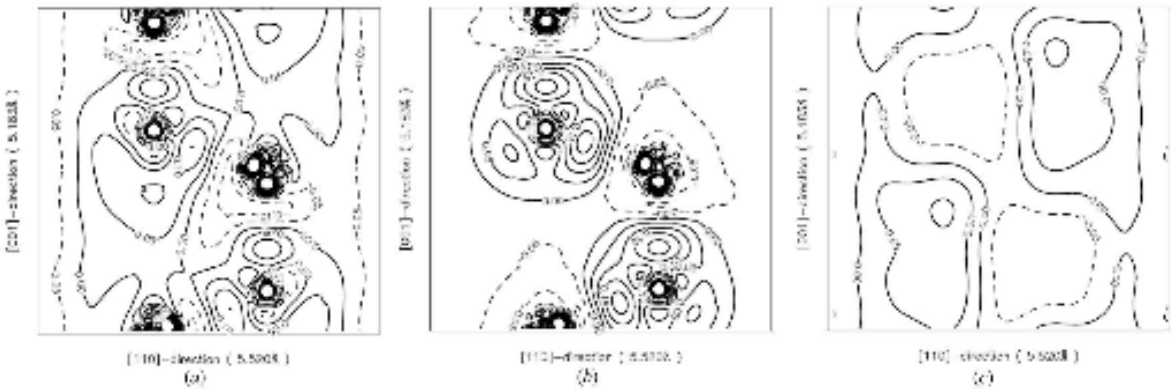

Figure 2
(*a*) Approximation of the experimental deformation charge-density map for GaN. It is obtained from the theoretical charge-density map (Fig. 2*b*) plus the map of Fig. 2(*c*). The result shown uses experiments for the low eight orders and theory for the high orders. (*b*) Theoretical valence electron deformation charge-density map for GaN from DFT (GGA-PBE) calculations. Reading down the figures from the top, the atoms are Ga, N, Ga, N, Ga. The unit of the contour level is e Å^{-3}. (This deformation map is obtained from the theoretical valence charge density minus the valence charge density of the neutral atom model. The *x* axis is along the [110] direction of the GaN crystal with 5.520 Å length, the *y* axis is along the [001] direction of the GaN crystal with 5.183 Å length.) (*c*). Experimental density map minus calculated map, both limited to eight complex structure factors, and using measured phases. Because of the good agreement between theory and experiment, the map is close to zero. Atom positions of Ga and N are also labeled in the map.

Polar bond seen in GaN for the first time - quantitative CBED density map !

A number of smaller projects have been completed as follows: The PI has revised and brought up to date the chapter in the International Tables on Crystallography dealing with electron diffraction and microscopy [3]. A chapter on nanodiffraction was written for a new edition of the widely used text on Electron Microscopy in Materials Science, by Williams and Carter [4]. A new technique for obtaining patterned nanostructures in metals has been developed, based on contolled spinodal decomposition [5].

6. Planned future activities

We now plan to solve clean-fuel zeolite catalyst structures using a combination of this KCBED method and powder X-ray diffraction, together with high-resolution imaging, all applied to the same sample. We find this to be a powerful approach. These new iterative phasing methods have also been applied to X-ray powder diffraction data in our earlier work [6], and that approach has since been taken up by others.

The most significant new project is our new paper on *a competely new method for obtaining phase-contrast in cryo-electron microscopy of organic materials* (7), in collaboration with Prof R. Glaeser and H. Muller at UCB. It can be shown that a laser beam crossing an electron beam will induce a phase shift in the electron beam, and our plan is to use this effect to construct a Zernike Phase Plate for an electron microscope. This will allow images of organic materials and proteins to be obtained when the microscope is adjusted near exact focus, yielding much sharper images with less need for image processing. (At present, the refractive index difference between organics and the ice they are embedded in is so small that images must be recorded greatly out-of-focus). This device is under construction, and has been patented at ASU and LBNL. It will be useful for both the study of organic and biological materials, such as photosynthetic systems.

A second important new project aims to directly observe diffusion at atomic resolution in solid electrolytes under the action of an applied electric field, in-situ, in the TEM (8). By applying a field across a thin slab of sodium beta" alumina in which the sodium atoms are partly replaced by lead, it should be possible to see directly the drift velocity

imparted to the lead atoms at low temperature. We have published preliminary images (8) which show interesting defect structure in the conduction planes, and presented calculations of diffusive motion at various temperatures, with image simulations. Our interest is in the observation of correlated motion among the moving ions, and in the effect of line and planar defects on ionic motion.

All this work will be continued using the two new aberration-corrected electron microscopes which will be delivered (under NSF support) to ASU in January 2011. The university is erecting a new building for these instruments, and new faculty are being appointed to support the new machines. The strong tradition of solid state chemistry at ASU, and our collaboration with Prof W. Petusky, an international leader in the field of solid electrolyte synthesis, is greatly assisting this effort.

In collaboration with Prof D. Saldin, we have also shown how the image of a single molecule can be reconstructed by using the scattering from many identical molecules in random orientations, if these are frozen in time (for example using pulsed diffraction) or space (e.g. molecules in ice). The method is based on ab-inito phasing, not SAXS modelling, and uses fluctuations in the otherwise isotropic scattering [9, 10].

7. References - all these papers cite DOE support. Not all such papers are shown.

1. "The kinematic convergent beam method for solving nanocrystal structures. J. McKeown and J.C.H.Spence. J. Appl Phys. 106, 074309 (2009)
2. "Combined structure factor phase measurement and theoretical calculations for mapping of chemical bonds in GaN". B. Jiang, J.Zuo, D. Holec, C. Humphreys, M. Spackman and J.C.H.Spence. Acta A66, 446 (2010).
3. J. Cowley and J. Spence. "Electron diffraction and electron microscopy," Chapter 2.5, International Tables for Crystallography (2008).
4. Electron Crystallography, Charge-density mapping and Nanodiffraction," Chapter 7 in *Electron Microscopy in Materials Science*, 2nd Edition, Eds. D. Williams and B. Carter (2010).
5 J.T. McKeown, J.D. Sugar, V.R. Radmilovic, A.M. Glaeser, and R. Gronsky. "Nanoscale phase-patterned alloys by constrained spinodal decomposition," *Nature Mater.* Submitted. (2010)
6 "Ab-initio phasing of X-ray powder diffraction patterns by charge flipping". J. Wu, J, Spence et al. Nature Materials 5, 647 (2006).
7. "Design of an electron microscope phase plate using a focussed continuous-wave laser" H. Muller, Jian Jin, R. Danev, J. Spence, R.M. Glaeser. New Journal of Physics. 12, 073011 (2010).
8 " Defects and Ionic diffusivity of Pb in b" alumina". S.D.Kim, Y.W.Kim, J.T. McKeown, M. O'Keeffe, E.E. Hellstrom, W.T. Petuskey, U. Weierstall and J.C.Spence. Proc Int Cong. Micros. Rio (2010) and MSA Proc 2010. In press.
9. "Structure of a single particle from scattering by many particles randomly oriented about an axis " toward structure solution without crystallization". D. Saldin, V. Shneerson, M. Howells, S. Marchesini, H. Chapman M. Bogan, D. Shapiro, R. Kirian, K. Schmidt and J. Spence. New Journal of Physics. 12 p.035014 (2010).
10. "Reconstruction from a single diffraction pattern of azimuthally projected electron density of molecules aligned parallel to a single axis. D.K.Saldin, V.L. Shneerson, D. Starodub, J.C.H.Spence. Acta Cryst. A66, 32-37 (2010)

PHONONS AND ELECTRONS IN THIN COMPLEX OXIDES

Susanne Stemmer
stemmer@mrl.ucsb.edu
Materials Department, University of California, Santa Barbara, CA 93106-5050

Program Scope

The objective of this program is to develop new approaches to understand and control phase transformations in complex oxide thin films as their dimensions approach the nanoscale; in particular, to provide a fundamental understanding of how these transitions are controlled by film strain, the atomic structure of interfaces and dimensionality. Perovskite titanates are grown with high structural perfection, high purity and low intrinsic defect concentrations by oxide molecular beam epitaxy. The project also builds on the unique capabilities of scanning transmission electron microscopy techniques, in particular, *quantitative* high-angle annular dark-field imaging. The combination of macroscopic and microscopic techniques will provide a wealth of information about transport, vibrational modes and defects in ultrathin oxide films.

Recent Progress

Below we summarize several key results from this program obtained in 2009/2010.

Development of stoichiometric oxide films using molecular beam epitaxy (MBE)

A main feature of the program is the investigation of perovskite films with high structural perfection, high purity and low intrinsic defect concentrations. Towards this goal, we have developed a new hybrid MBE for insulating complex oxide films that uses a combination of solid and metal-organic sources to supply the metals. Films grow in layer-by-layer mode, with atomically smooth surfaces and a structural quality that is only limited by those of the substrates (Fig. 1). The metal organic Ti source, titanium tetra isopropoxide [$Ti(OC_3H_7)_4$ or TTIP], has several advantages over metal Ti sources. We have shown that these include (*i*) orders of magnitude of higher vapor pressure than solid Ti, allowing for orders of magnitude higher growth rates, (*ii*) ease of flux control (no flux instabilities in the presence of oxygen) and (*iii*) supplying additional oxygen that already comes bonded to Ti, thereby reducing the problem of oxygen deficiency. A major aspect of this MBE technique is that it provides a route to stoichiometric films. This is achieved by growing films within a "MBE growth window", in which the stoichiometry is self-regulating, independent of the precise metal flux ratios (Fig. 2).

Record electron mobilities in MBE-grown $SrTiO_3$

We have demonstrated that $SrTiO_3$ films grown by the new MBE approach have very high electron mobilities, exceeding those of single crystals (Fig. 3). This opens the way to oxide heterostructures with excellent transport properties and for studying quantum phenomena in oxides.

Absence of a Stobbs Factor in high-resolution transmission electron microscopy

We have carried out quantitative, atomic resolution *bright-field* scanning transmission electron microscopy (STEM) experiments. The image intensities are placed on an

absolute scale relative to the incident beam intensity. Features in the experimental images were compared with image simulations that account for elastic scattering and the effect of phonon scattering. For a $SrTiO_3$ sample with thicknesses between 4 and 25 nm, we demonstrate excellent agreement between the simulated and the experimentally observed image contrast (Fig. 4). The excellent agreement in this and in prior studies of Z-contrast images shows that current models of image formation adequately model both low and high-angle scattering, including thermal diffuse scattering. Other inelastic scattering processes do not play a significant role in contrast formation for samples that are sufficiently thin. The results open the way for extracting quantitative structural and chemical information from STEM images.

Future Plans

We are currently working on developing MBE growth of other titanates, such as ferroelectric $BaTiO_3$, and on developing quantitative characterization of strain and phonons in thin films, using HAADF-STEM.

DOE Sponsored Publications in 2008 – 2010

[1] B. Jalan, S. Stemmer, *Large Seebeck coefficients and thermoelectric power factor of La-doped $SrTiO_3$ thin films*, Appl. Phys. Lett. **97**, 042106 (2010).

[2] J. Son, P. Moetakef, B. Jalan, O. Bierwagen, N. J. Wright, R. Engel-Herbert, S. Stemmer, *Epitaxial $SrTiO_3$ films with electron mobilities exceeding 30,000 $cm^2V^{-1}s^{-1}$*, Nature Mater. **9**, 482 (2010).

[3] B. Jalan, R. Engel-Herbert, N. J. Wright, S. Stemmer, *Growth of high-quality $SrTiO_3$ films using a hybrid molecular beam epitaxy approach*, J. Vac. Sci. Technol. A **27**, 461 (2009).

[4] J. M. LeBeau, R. Engel-Herbert, B. Jalan, J. Cagnon, P. Moetakef, S. Stemmer, G. B. Stephenson, *Stoichiometry optimization of homoepitaxial oxide thin films using x-ray diffraction*, Appl. Phys. Lett. **95**, 142905 (2009).

[5] B. Jalan, P. Moetakef, S. Stemmer, *Molecular beam epitaxy of $SrTiO_3$ with a growth window*, Appl. Phys. Lett. **95**, 032906 (2009).

[6] J. Son, S. Stemmer, *Resistive switching and resonant tunneling in epitaxial perovskite tunnel barriers*, Phys. Rev. B **80**, 035105 (2009).

[7] J. M. LeBeau, A. J. D'Alfonso, S. D. Findlay, S. Stemmer, L. J. Allen, *Quantitative comparisons of contrast in experimental and simulated bright-field scanning transmission electron microscopy images*, Phys. Rev. B **80**, 174106 (2009).

[8] J. M. LeBeau, S. D. Findlay, L. J. Allen, S. Stemmer, *Quantitative atomic resolution scanning transmission electron microscopy*, Phys. Rev. Lett. **100**, 206101 (2008).

[9] J. M. LeBeau, S. Stemmer, *Experimental quantification of annular dark-field images in scanning transmission electron microscopy*, Ultramicroscopy **108**, 1653 (2008).

[10] S. D. Findlay, D. O. Klenov, S. Stemmer, L. J. Allen, *Atomic number contrast in high-angle annular dark field imaging of crystals*, Mater. Sci. & Technol. **24**, 660 (2008). [Invited Review Paper]

[11] D. S. Boesch, J. Son, J. M. LeBeau, J. Cagnon, S. Stemmer, *Thickness Dependence of the Dielectric Properties of Epitaxial $SrTiO_3$ Films on (001)Pt/$SrTiO_3$*, Appl. Phys. Expr. **1**, 091602 (2008).

[12] J. Son, J. Cagnon, D. S. Boesch, S. Stemmer, *Epitaxial $SrTiO_3$ tunnel barriers on Pt/MgO substrates*, Appl. Phys. Expr. **1**, 061603 (2008).

Figures

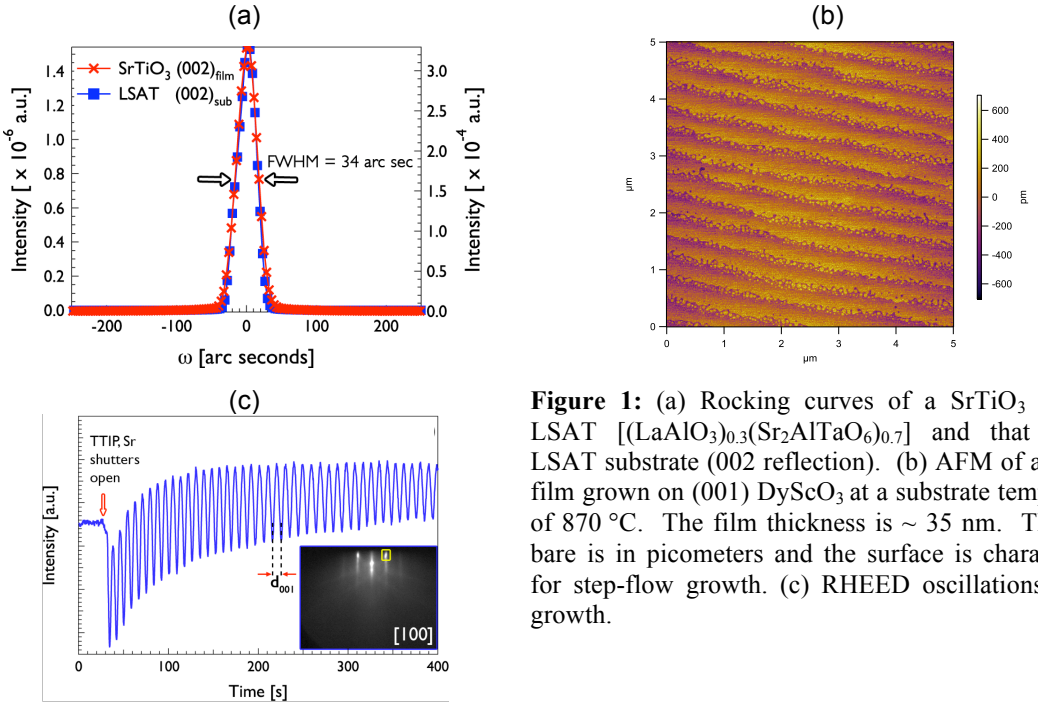

Figure 1: (a) Rocking curves of a $SrTiO_3$ film on LSAT $[(LaAlO_3)_{0.3}(Sr_2AlTaO_6)_{0.7}]$ and that of the LSAT substrate (002 reflection). (b) AFM of a $SrTiO_3$ film grown on (001) $DyScO_3$ at a substrate temperature of 870 °C. The film thickness is ~ 35 nm. The scale bare is in picometers and the surface is characteristic for step-flow growth. (c) RHEED oscillations during growth.

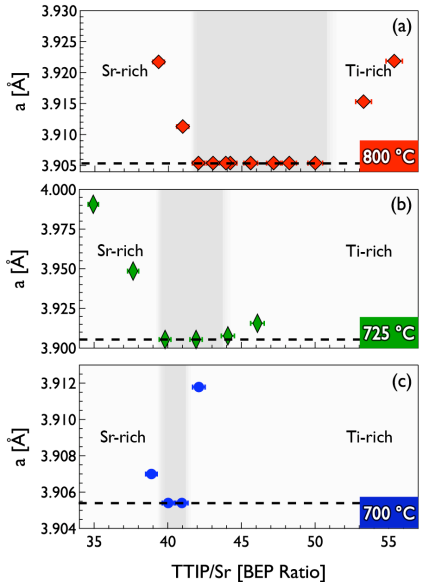

Figure 2: Out-of-plane lattice parameter as a function of TTIP/Sr BEP ratio for epitaxial $SrTiO_3$ films grown on (001)$SrTiO_3$ at (a) 800 °C, (b) 725 °C and (c) 700 °C. All films were grown using an oxygen BEP of 8×10^{-6} torr. The grey-shaded region shows the growth window for stoichiometric films with a lattice parameter that is equivalent to that of the substrate at each temperature.

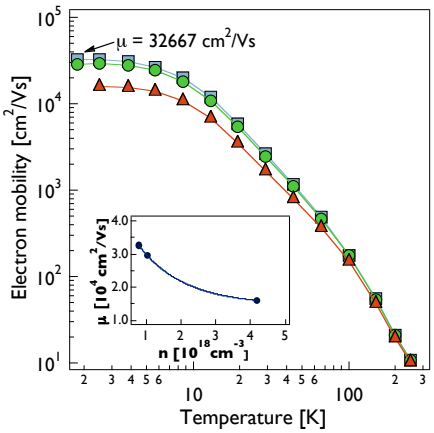

Figure 3: Hall electron mobility (μ) as a function of temperature for three $SrTiO_3$ films grown by MBE with different amounts of La-doping. The inset shows the mobility as a function of carrier concentration at 2.5 K. The lines are guides to the eye.

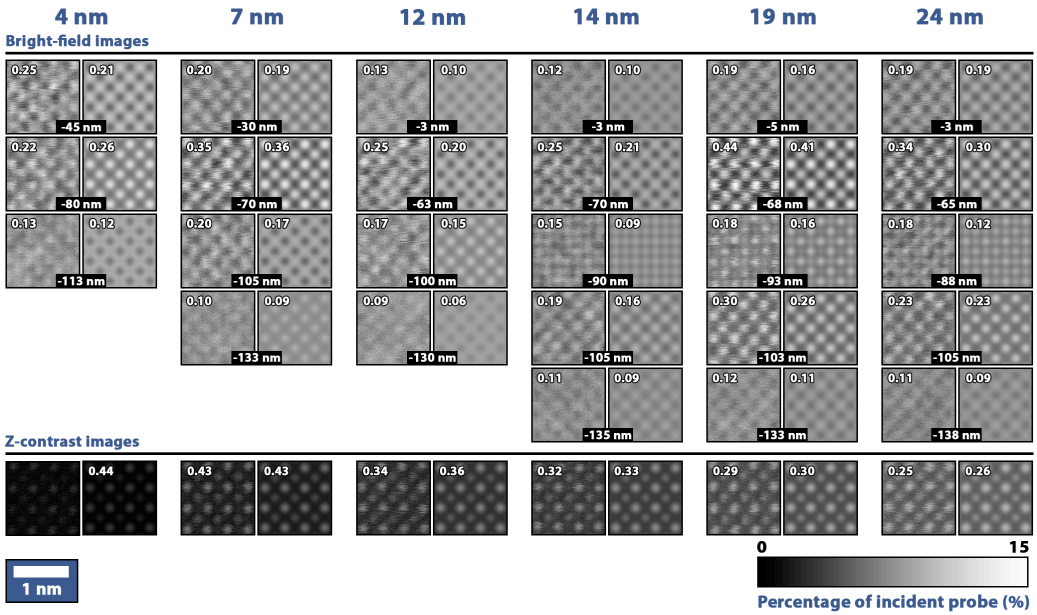

Figure 4: Top rows: experimental bright-field STEM images of $SrTiO_3$ (left panel in each column, unfiltered) compared to multislice absorptive model calculations (right panel in each column). The upper labels in each image show their contrast values. The lower (black background) labels state the defocus, with underfocus being negative. Bottom row: experimental and simulated Z-contrast images (54 nm underfocus). Note that all images are on an absolute intensity scale relative to the incident probe and reported as a fraction of the incident probe intensity. For the Z-contrast images, the experimental contrast value at a thickness of 4 nm suffers from the image intensities being in the level of the noise and is not provided. The simulations have been convolved with a Gaussian of 0.11 nm FWHM to account for the effects of a finite source size.

Characterization of Dopant / Point Defect Complexes in Semiconductors by STEM

Paul Voyles and Dane Morgan
Materials Science and Engineering, University of Wisconsin, Madison
1509 University Avenue, Madison, WI 53706, voyles@engr.wisc.edu, ddmorgan@wisc.edu

Hadis Morkoç
Electrical Engineering, Virginia Commonwealth University
601 W. Main Street Richmond, VA 23284-3072, hmorkoc@vcu.edu

Program Scope

This program combines efforts in high-resolution STEM imaging, thin-film growth, and multiscale first-principles modeling to understand the behavior of dopants in compound semiconductors. ZnO is one focus, due to its potential for optoelectronics and its wide variety of nanostructures. We are working on heavily *n*-type ZnO for transparent conducting oxides in LED lighting applications and on developing *p*-type ZnO by doping with high-*Z* Group V elements. Our overall goal is the characterization of point defects and point-defect complexes which control electrical and optical behavior.

Recent Progress

Ga-doped ZnO Transparent Conducting Oxide

ZnO heavily doped with group-III elements appears poised to replace indium-tin oxide as a transparent conducting oxide (TCO) material for Ohmic contacts in light emitters (light-emitting diodes, or LEDs) and laser diodes), light absorbers (solar cells), and transparent thin-film transistors. We have studied the microstructure, defects, optical, and electrical properties of ZnO thin films heavily doped with Ga (GZO) relevant to TCO applications. TCO thin films should have sheet resistance below 10 Ω/□, (*e.g.* resistivity $< 4\times10^{-4}$ Ω-cm for a 400-nm-thick film), and optical transparency > 90%. We deposited GZO films by molecular beam epitaxy (MBE) which surpass these requirements on sapphire substrates and InGaN/GaN quantum well LED structures.

We found that the metal-to-oxygen ratio during plasma-assisted MBE is crucial to the structure and properties of GZO thin films. Figure 1 shows that as-grown films grown under metal-rich conditions have resistivities $<3\times10^{-4}$ Ω-cm, while films grown under oxygen-rich conditions have lower carrier concentration and mobility and required thermal activation. Electrical measurements as a function of film thickness point to a non-uniform depth distribution of free carriers in the films grown under oxygen-rich conditions. Films grown under metal-rich conditions have optical transparency >90% in the visible spectral range.

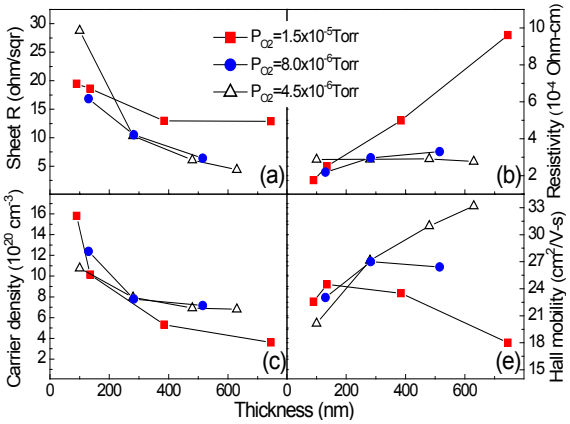

Figure 1: Electrical properties for GZO layers grown at different P_{O2}. Open symbols are as-grown films, and filled symbols are annealed films. P_{O2} of 4.5×10^{-6}, 8.0×10^{-6}, and 4.5×10^{-5} Torr correspond to metal-rich, near-stoichiometric, and oxygen-rich conditions, respectively.

The films grown under metal-rich conditions are high crystal quality but porous, as shown in Figure 2. The pores occur at high density and diameters ranging from a few nanometers to >100 nm. Despite this, the density of dislocations, low-angle grain boundaries, and other defects is lower in the layers grown under metal-rich than the oxygen-rich conditions. For the large pores, the surface near the substrate is misoriented with respect to the substrate and the rest of the film. The pores must reduce the conductivity of the film because they reduce the current-carrying cross-sectional area, but that effect may be more than compensated by the decrease in

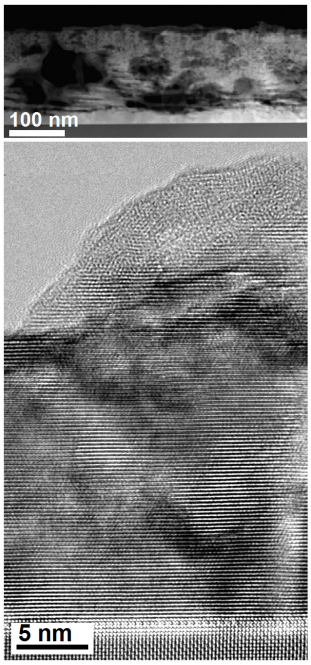

Figure 2: (top) Z-contrast and (bottom) HRTEM images of the a GZO film grown under metal-rich conditions, showing the porous structure and the misoriented grains on the pore surface.

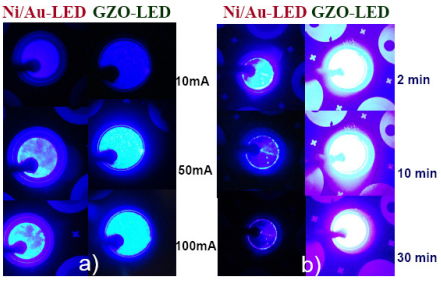

Figure 3: Light emission images of GZO-LEDs and Ni/Au-LEDs under different DC currents (a) and under injection current of 100 mA for different times.

defect density. The pores also increase the transparency.

Optimized GZO films with a resistivity of ~1.9 × 10^{-4} Ω cm were used as top contacts to InGaN-based LEDs. LEDs with Ni/Au (5 nm / 5 nm) contacts were fabricated on the same wafer for comparison. The GZO-LEDs have virtually the same vertical series resistance as the Ni/Au-LEDs. The forward voltage at 20 mA is 3.5 V for GZO-LEDs and 3.7 V for Ni/Au-LEDs. The forward voltage at 20 mA for GZO-LEDs is comparable to or lower than the values of 3.42 to 4.28 V reported for ITO-LEDs.[1]

Unlike the Ni/Au-LEDs, however, the GZO-LEDs showed no filamentation and uniform light emission at high current density due to their small lateral resistance. As shown in Figure 3, unpackaged 200 μm diameter GZO-LEDs showed negligible light output degradation after 30 min under 100 mA CW current (318 A/cm^2 current density), while the light output for Ni/Au-LEDs was reduced by 85% after only 5 min due to severe current crowding. Pulsed electroluminescence (EL) measurements revealed that the GZO-LEDs exhibit 50% higher EL intensity for the same current levels. Under pulsed excitation, GZO-LEDs withstood current densities up to 5000 A/cm^2.

The primary crystallographic defects in the GZO on GaN films are low-angle grain boundaries, dislocations within the GZO layers and misfit dislocations at the GZO / GaN boundary, as shown in Figure 4. Figure 4(c) shows electron mobilities as a function of FWHM of the (002) XRD rocking curves for a variety of GZO films, as a proxy for grain boundary and dislocation density. High mobility is highly desirable for many TCO applications, and the mobilities >70 cm^2/(Vs) in Figure 4 are the highest reported for a ZnO-based TCO with the carrier concentration in the mid-to-high 10^{20} cm^{-3} range.

While working with the GZO LED samples, we noticed an anomaly in the InGaN active layers shown in Figure 5. Although the active layers are nominally 6 nm thick $In_{0.2}Ga_{0.8}N$, the sample in Figure 5(a) shows a narrow band above the active layer with significantly enhanced In. The sample in Figure 5(b)

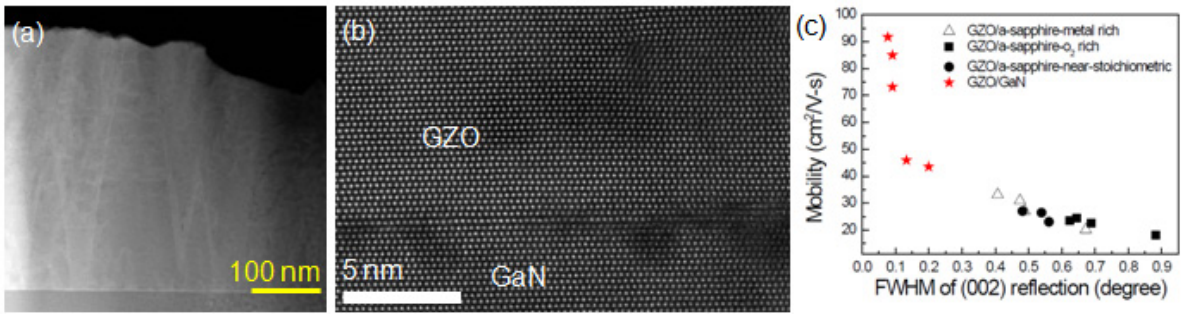

Figure 4: GZO-LED microstructure: (a) DF STEM image of low-angle grain boundaries; (b) Z-contrast STEM of dislocations at the GZO/GaN interface; (c) electron mobility vs (002) XRD peak width for GZO layers on GaN and sapphire.

[1] Y. Yao *et al.*, Displays **28**, 129 (2007); C.S. Chang *et al.*, Semicond. Sci. Technol. **18**, L21 (2003)

shows a much smaller concentration enhancement at the top of the active layer, and a sharper top interface. This is intriguing, because the internal quantum efficiency of (a) is 65% and (b) is 90%, from power-dependent photoluminescence measurements with a resonant excitation. In the high efficiency device, there are surface steps that may support the idea that interface roughness is essential to the high efficiency of InGaN LEDs.[2] We see no evidence for strong lateral In composition fluctuations at the nanometer scale.

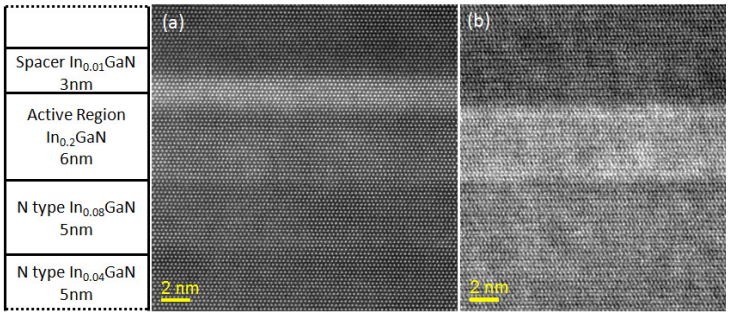

Figure 5 Z-contrast STEM images of InGaN active layers for two GZO-LEDs with (a) 65% and (b) 90% internal quantum efficiency.

Group-V Acceptor Defect Complexes in ZnO

Complexes in ZnO consisting of P, As, or Sb on a Zn site (P_{Zn}, As_{Zn} or Sb_{Zn}), surrounded by two Zn vacancies (V_{Zn}), denoted M_{Zn}-$2V_{Zn}$, are possible electron acceptors in ZnO. Such defects may occur but are not thermodynamically stable, and very little is known about their degradation mechanisms. To model the long-term stability of such defects requires increased knowledge of defect kinetics in ZnO, so we have begun DFT-based modeling of the kinetics of ZnO defects, starting with the kinetic processes associated with diffusion and annealing out or disassociation of the M_{Zn}-$2V_{Zn}$ defect clusters. Initial work has focused on the structure, energetics, and charge states of the M_{Zn}-$2V_{Zn}$ defects.

We have found a new, more stable configuration for the M_{Zn}-$2V_{Zn}$ defect by considering different arrangements of the two vacancies around the metal atom in the M_{Zn}-$2V_{Zn}$ cluster. For As_{Zn}-$2V_{Zn}$ we find it is about 0.3 eV more energetically favorable for the V_{Zn} to be separated from each other, as in Figure 6(a), rather than in neighboring positions as in Figure 6(b), which is consistent with simple electrostatics. However, bringing the V_{Zn} together provides space for the As dopant to shift into a tetrahedral interstitial position and form a significantly more stable defect. In this "popped" configuration, shown in Figure 6(c), the dopant has tetrahedral coordination with O atoms, and three of the Zn atoms which normally surround the position are missing. "Popping" lowers the formation energy of the As_{Zn}-$2V_{Zn}$ complex 0.3 eV below the formation energy of even the As_{Zn}-$2V_{Zn}$ complex with V_{Zn} maximally separated. For P, the popped configuration is 0.1 eV more stable than the configuration with V_{Zn} separated, and Sb is 0.7 eV more stable. We find a similar popped configuration with the metal ion in the octahedral interstitial position, which for P is 2.4 eV less stable than the configuration with V_{Zn} separated. As is 0.3 eV less stable, and Sb is 1.8 eV more stable. Therefore, popped configurations may be especially important for Sb.

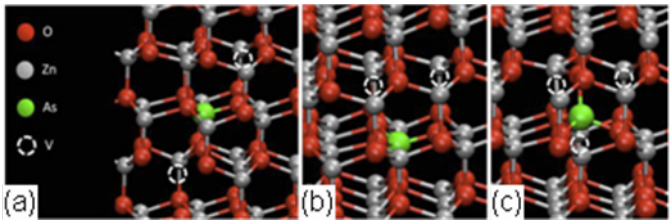

Figure 6 Three configurations of the As_{Zn}-$2V_{Zn}$ complex: (a) with V_{Zn} separated, (b) with V_{Zn} in neighboring positions, and (c) with As "popped" into a tetrahedral interstitial position.

We have grown ZnO doped with As (ZnO:As) films on *a*-plane sapphire substrates by plasma-assisted MBE. Although the ZnO:As films have not yet shown net p-type conductivity, films grown under P_{O2} of

[2] D. M. Graham et al. J. Appl. Phys. **97**, 103508 s2005d

~8-10×10^{-6} Torr and relatively high As flux show very weak n-type conductivity compared with undoped ZnO layers. Undoped ZnO typically show electron concentration n_e of ≥5×10^{17} cm^{-3} and mobility >20 cm^2/V-s, but for the as-grown ZnO:As films, n_e varies from 0.7 to 4×10^{17} cm^{-3} and the mobility varies from 0.05 to 2.2 cm^2/V-s. Reduced n_e and electron mobility are both consistent with As-related acceptor defects compensating native donors. Post-growth anneals in oxygen environment reduce the n_e of films grown at low As flux and P_{O2} from ~10^{19} cm^{-3} to the mid-10^{17} cm^{-3} range.

Future Plans

In film growth and analysis, we plan to further explore the In inhomogeneties in InGaN active layers and the correlation with device efficiency. Figure 7 shows a Z-contrast image of a very thin part of an $In_{0.2}Ga_{0.8}N$ active layer, from which it may be possible to quantify the In concentration column-by-column with single-atom sensitivity by careful reference to simulation. We will develop a model of the transport in our GZO thin films based on the observed defects and temperature-dependent Hall effect data. We will continue to work towards synthesis of *p*-type As-doped ZnO thin films, and we will begin characterization of *p*-type Sb-doped ZnO nanowires synthesized by Prof. X. Wang at Wisconsin.

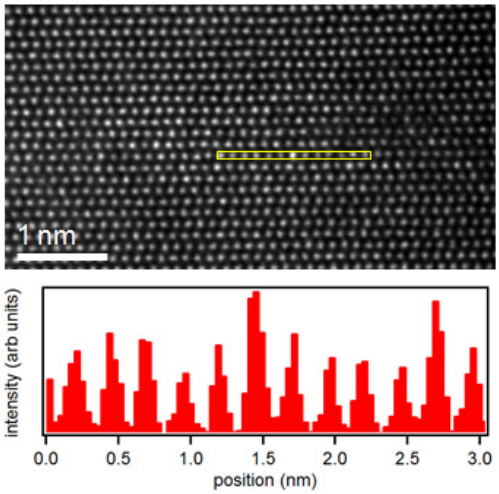

Figure 7: Z-contrast STEM image and line profile of the $In_{0.2}Ga_{0.8}N$ active layer showing column-by-column intensity fluctuations. The image has been smoothed and resampled, but the profile is taken from the raw data.

In modeling, we will calculate kinetic barriers for mechanisms which may annihilate the M_{Zn}-$2V_{Zn}$ complex. This data will allow us to model the competition between diffusion to sinks, dissociation by V_{Zn} unbinding from the complex, and annihilation by diffusion of Zn interstitials or possibly impurity atoms to the complex. Overall, this model will provide an estimate for the lifetime of an M_{Zn}-$2V_{Zn}$ complex under different gaseous environments and thermal schedules. We will simulate STEM images of the defects for comparison to experiments.

References

1. H.Y. Liu, X. Li, S. Liu, X. Ni, M. Wu, V. Avrutin, N. Izyumskaya, Ü. Özgür, A.B. Yankovich, A.V. Kvit, P.M. Voyles, and H. Morkoç, InGaN based Light emitting diodes utilizing Ga doped ZnO as a highly transparent contact to p-GaN, submitted to Physica Status Solidi (c).
2. X. Li, H.Y. Liu, S. Liu, X. Ni, M. Wu, V. Avrutin, N. Izyumskaya, Ü. Özgür, and H. Morkoç, InGaN based Light emitting diodes with Ga doped ZnO as transparent conducting oxide, s Physica Status Solidi (a), **207**, 1993–1996 (2010).
3. H. Liu, V. Avrutin, N. Izyumskaya, M.A. Reshchikov, Ü. Özgür, and H. Morkoç, Highly conductive and optically transparent GZO films grown under metal-rich conditions by plasma-assisted molecular beam epitaxy, Physica Status Solidi: Rapid Research Letters **4**, 70–72 (2010).
4. H. Liu, X. Li, X. Ni, V. Avrutin, N. Izyumskaya, Ü. Özgür, and H. Morkoç, InGaN light-emitting diodes with highly transparent ZnO:Ga electrodes, Proceedings of the SPIE **7602**, 76020I (2010).
5. H.Y. Liu, V. Avrutin, N. Izyumskaya, M.A. Reshchikov, Ü. Özgür, A.V. Kvit, P.M. Voyles, H. Morkoç, Effect of growth conditions on structural and electrical properties of Ga-doped ZnO films grown by plasma-assisted MBE, MRS Proc. **1201**, 115 (2010)
6. X. Ni, X. Li, J. Lee, H. Y. Liu, V. Avrutin, Ü. Özgür, H. Morkoç, T. Paskova, G. Mulholland, K.R. Evans, On the light emission in GaN based heterostructures at high injection, MRS Proc. **1202**, 159 (2010)

Atomic-Scale Chemical, Physical and Electronic Properties of the Subsurface Hydride of Palladium

Paul S. Weiss
California NanoSystems Institute, Departments of Chemistry & Biochemistry and Materials Science & Engineering, UCLA, Los Angeles, CA | http://www.nano.ucla.edu/

Program Scope

We use low-temperature (4 K) extreme high vacuum scanning tunneling microscopy (STM) and spectroscopy (STM) to make direct spectroscopic measurements of hydrogen (H) and deuterium (D) both on *and* beneath the surface of single crystal Pd substrates. We are systematically developing an understanding of the enhanced reactivity towards heterocyclic molecules in hydrodesulfurization (HDS) and hydrogenation (HYD), and of metal embrittlement and hydrogen storage. The scope of this work encompasses the interactions of D as a surface and subsurface species in both Pd{111} and Pd{110} substrates to elucidate isotopic exchange via reaction with surface-bound thiophene. Our studies ultimately rely on the ultrastability and extreme precision of our unique instrumentation to make electronic and vibrational measurements at the single-molecule scale, to determine reaction pathways and energies.

Progress Summary

We have characterized the effect of D deposition on both Pd{111} and Pd{110} at 4 K. We note two distinct behaviors for the respective surfaces. Figure 1 shows the resulting surfaces after depositing D from room temperature onto the Pd{111} sample held at 4 K. In Figure 1A, we note that while D is known to segregate into the bulk and subsurface regions, some D remains on the surface. We can compile subsequent scans with acquisition energies higher than that of a threshold energy and observe diffusion of D on the surface. The underlying hexagonal substrate structure characteristic of Pd{111} remains intact. In contrast to the behavior seen in Figure 1A, deposition of D from the gas phase onto Pd{110} held at 4 K results in a dramatic reconstruction of the surface to accommodate interpolation of D into the (1 × 1) lattice. The resulting surface distortion is a (1 × 2) reconstruction, where Pd atoms pair into rows with a unit cell twice that of the (1 × 1) surface. This effect will prove essential to the reactivity of molecular thiophene with subsurface D on Pd{110}, as its directionality strongly influences the creation of subsurface D by tunneling electrons.

A recent publication has highlighted our efforts to elucidate the role of subsurface D in the desulfurization of molecular thiophene.[1] Figure 2 shows the local bonding orientation of thiophene on Pd{110} at 4 K. In Panel A, thiophene is imaged with two distinct apparent heights, which we attribute to two separate bonding orientations, as in our previous work on thiophene on Ni{110}.[2] We observe both thiophene preferring to adsorb between rows (green

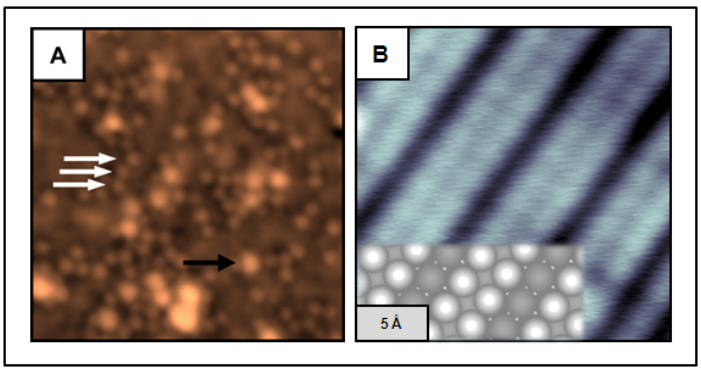

Figure 1. Surface morphology of (A) Pd{111} and (B) Pd{110} upon deposition of D. A) STM topographic images (90 Å × 90 Å, V_s = 100 mV, I_t = 50 pA) acquired over a region of D (white arrows) on Pd{111} at 4 K. The protrusions (black arrow) are impurities on the Pd substrate. D-induced Pd{110}-(1 × 2) surface reconstruction. (B) Atomically resolved STM image (V_s = 0.01 V; I_t = 1.4 nA; 22 Å × 22 Å) with model structure (inset) of the (1 × 2) phase.

arrow in Figure 2A) and a small amount of sulfur impurities (white arrow in Figure 2A). Furthermore, differential conductance imaging enabled us to deconvolve the physical and electronic structure of individual thiophene molecules. The molecule in Figure 2B (topography) is the same as that of Figure 2C (differential conductance), as these images were acquired simultaneously. Because we image in constant-current mode with positive sample bias, the lobes apparent in Figure 2C are attributed to the π^* orbitals of thiophene.

The adsorption geometry of thiophene molecules akin to those in Figure 1A have led us to posit that we can extract information regarding the influence of the surface electronic state based on whether the surface maintains its native (1 × 1) structure, or reconstructs upon addition of D to the subsurface region (*vide infra*). The anisotropy of the surface's directionality should give us a good indicator of the strength of the surface electronic landscape through substrate-mediated interactions (SMI).

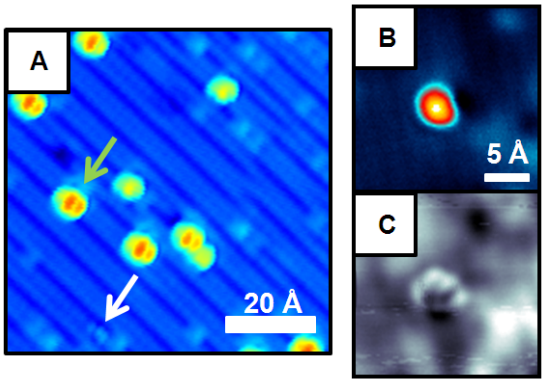

Figure 2. Thiophene adsorption on D/Pd{110}-(1 × 2) and on clean Pd{110}-(1 × 1). (A) Topographic STM image (V_s = -0.015 V; I_t = 0.2 nA; 73 Å × 73 Å) of thiophene on a D-reconstructed Pd{110} surface. Thiophene molecules appear as protrusions with two distinct apparent heights. (B and C) Topographic and differential conductance, respectively, STM images (V_s = 0.1 V; I_t = 0.9 nA; 22 Å × 22 Å) acquired simultaneously. At positive sample bias, we observe lobes attributed to empty states.

However, adding energy to the system by injecting tunneling electrons into the D/Pd{110}-(1 × 2) surface in Figure 2A results in a subsurface effect profoundly different than that which we had previously reported for the subsurface H of Pd{111}.[3] On the (1 × 2) reconstruction, at larger V_s, molecular detail is lost, but higher conductance features increasingly appear along the <1$\bar{1}$0> in the area over which the STM probe rests between images. This phenomenon is observed in Figure 3, acquired after hovering over the center of the scan frame for 2 min at 1 V. The subsurface D is manifested in the diffuse, higher-contrast feature in the center of the frame on the right (dotted white circle in the right image of Figure 3). Subsequent hovering and scanning produces more prominent perturbations. Since other subsurface impurities are minimized by careful preparation, we attribute this effect to the population of subsurface sites by D atoms drawn up from the bulk Pd. In the absence of preadsorbed D, deposition of thiophene and subsequent imaging resulted in no apparent local structural perturbation. Similarly, imaging the D-reconstructed surface shown in Figure 1A at larger V_s (3 eV) in the absence of thiophene also produced no faceting. Thus, we posit that adsorption of thiophene onto the D-reconstructed surface lowers the overall barrier to near-surface D diffusion, and may be coverage dependent, as implied in recent work on a "self-activating" catalyst surface.[4]

We used scanning tunneling spectroscopy to determine the onset of bulk D diffusion to the subsurface region. We first demonstrated that the faceting is localized to the scanning region and selected a subsequent area that encompassed both a faceted region and a non-faceted region. This surface is observed in Figure 4A. Subsequent imaging at small V_s insured that further subsurface site population would be trivial. We denote the non-faceted region α and the faceted region β. The image in Figure 4A is displayed in derivative mode to highlight the angularity of the facets with respect to the flat underlying substrate. Height profiles acquired and averaged

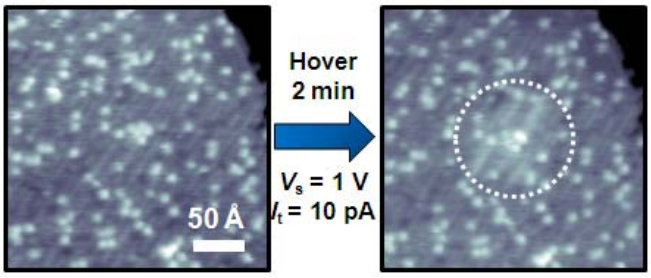

Figure 3. Drawing D to the subsurface sites of Pd{110}. The STM topographic image (V_s = 0.5 V; I_t = 0.010 nA; 260 Å × 260 Å) on the left was acquired before setting V_s = 1 V. After setting V_s = 1 V and having the STM tip hover in its rest position over the center of the frame for 2 min, the image on the right was acquired. A diffuse protruding region (dashed white circle) was observed at the center of the image.

over topographic images in this area reveal that the faceted plane is tilted 3.2 ± 0.8° off the substrate plane. This small value can account for both the presence of the facets and the (1 × 1) structure over the *β* region.

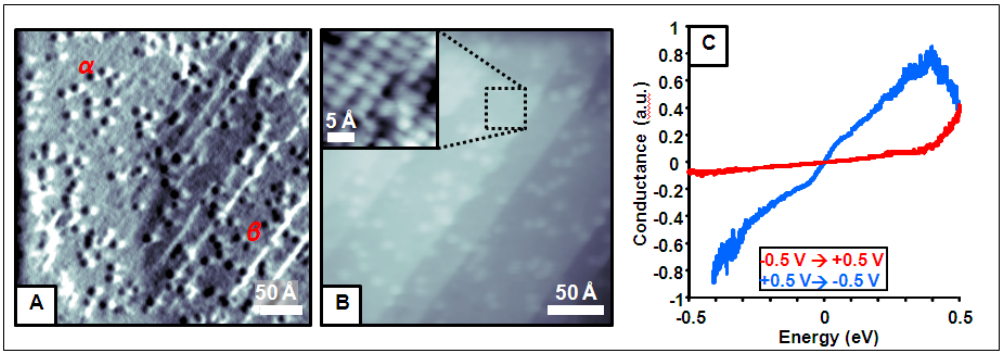

Figure 4. Determining the onset of the population of subsurface D in the presence of thiophene. (A) STM topographic (derivative) image (V_s = 0.05 V; I_t = 0.05 nA; 348 Å × 348 Å) highlighting the deviation of the facet planes (β) from the underlying substrate plane (α). (B) Topographic STM image (V_s = 0.05 V; I_t = 0.05 nA; 260 Å × 260 Å) of region β in panel A, plane subtracted (flattened by tilting the image). The inset is a high-resolution STM topographic image (V_s = 0.01 V; I_t = 1.4 nA; 22 Å × 22 Å) acquired over the region denoted by the black dotted box. Here, the Pd{110}-(1 × 1) structure has returned. The protrusions in both panels A and B are thiophene molecules. (C) Representative I(V) spectrum taken over Pd in area α of panel A (V_{gap} = 0.05 V; I_{gap} = 0.05 nA). The red curve represents the forward bias sweep direction, and the blue curve represents the reverse sweep. The onset value (0.38 ± 0.02 V) is from an average of 45 forward spectra at fresh locations on the surface.

Conductance spectroscopy has enabled us to extract an onset energy of 0.38 ± 0.02 V for drawing D up to the subsurface region. Our ultimate goal within the scope of this and related experiments is to design systems in which we can manipulate, control, and observe single-molecule catalytic processes with the scanning tunneling microscope. We already have evidence of this ability in the surface transition highlighted in Figure 4B. From single-molecule vibrational spectroscopy measurements, the adsorbates remaining over the (1 × 1) surface of the facets are indeed structurally different than those over the (1 × 2) region. These structural differences are highlighted by inelastic electron tunneling spectroscopy (IETS) in Figure 5.

We attribute the different spectroscopic fingerprints observed in Figure 5C to different species that we are able to probe as a result of the HDS mechanism that has been presented previously in the literature.[5] The two structures of note are the 2,5-dihydrothiophene (the initial structure upon thiophene adsorption on Pd) and the 1,3-*cis*-butadiene intermediate at 4 K. At elevated temperatures, the intermediate is expected to desorb as 1,3-butadiene. Currently, we are using molecular dynamics simulations to calculate bond vibrations for both cases and anticipate that our results will demonstrate that we can induce and monitor single-molecule chemical reactions with tunneling electrons and novel subsurface reactants.

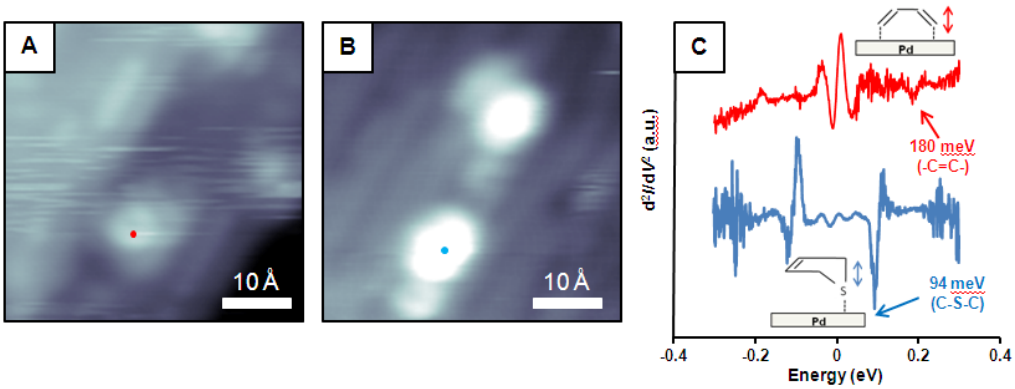

Figure 5. Single molecule vibrational spectroscopy (IETS) of thiopheene adsorbates (A) after and (B) before drawing D up to the subsurface region. The STM image in (A) (V_s = -0.120 V; I_t = 1.4 nA; 43 Å × 43 Å) was acquired after taking spectroscopic measurements (30 sweeps, averaged, red trace in (C)) at the position indicated by the red dot. The STM image in (B) (V_s = -0.120 V; I_t = 1.2 nA; 43 Å × 43 Å) was acquired after spectroscopic measurements (1 sweep, blue trace in (C)) at the position indicated by the blue dot. The vibrational spectra of the two species in (A) and (B) are markedly different, and are attributed to the variences in bond structure described by the mechanism of HDS.

Future Plans

We continue our investigations of the H and D subsurface Pd systems to understand chemical and materials processes. We will use STM and STS to observe the reactants, intermediates, and products of thiophene desulfurization by subsurface D on Pd{110}. We are assessing the electronic effects and roles of perturbed electronic structures on adsorbate location and reactivity.

References Cited

1. A. R. Kurland, P. Han, J. C. Thomas, A. N. Giordano, P. S. Weiss, *J. Phys. Chem. Lett.* **1**, 2288 (2010).
2. J. H. Ferris, J. G. Kushmerick, J. A. Johnson, M. G. Y. Youngquist, R. B. Kessinger, H. F. Kingsbury, P. S. Weiss, *Rev. Sci. Inst*. **69**, 2691 (1998).
3. E. C. H. Sykes, L. C. Fernandez-Torres, S. U. Nanayakkara, B. A. Mantooth, R. M. Nevin, P. S. Weiss, *Proc. Natl. Acad. Sci*. **102**, 17907 (2005).
4. S. Katano, H. S. Kato, M. Kawai, K. Domen, *J. Phys. Chem. C* **113**, 14872 (2009).
5. N. N. Sauer, E. J. Markel, G. L. Schrader, R. J. Angelici, *J. Catal.* **117**, 295 (1989).

Recent Publications

"Identifying Reactive Intermediates in the Ullmann Coupling Reaction by Scanning Tunneling Microscopy and Spectroscopy," M. M. Blake, S. U. Nanayakkara, S. A. Claridge, L. C. Fernández-Torres, E. C. H. Sykes, and P. S. Weiss, *Journal of Physical Chemistry A* **113**, 13167-13172 (2009).

"Heads *and* Tails: Simultaneous Exposed and Buried Interface Imaging of Monolayers," P. Han, A. R. Kurland, A. N. Giordano, S. U. Nanayakkara, M. M. Blake, C. M. Pochas, and P. S. Weiss, *ACS Nano* **3**, 3115-3121 (2009).

"Adsorbate-Promoted Tunneling-Electron-Induced Local Faceting of D/Pd{110}-(1x2)," A. R. Kurland, P. Han, J. C. Thomas, A. N. Giordano, and P. S. Weiss, *Journal of Physical Chemistry Letters* **1**, 2288 (2010).

"Artificial Assembly of Precise Functional Nanostructures," A. N. Giordano, M.S. Thesis, Department of Chemistry, The Pennsylvania State University, University Park, PA, USA (2010).

Electron Imaging in Graphene

PI: R.M. Westervelt
School of Engineering and Applied Sciences
Harvard University
29 Oxford Street, Cambridge, MA 02138
email: westervelt@seas.harvard.edu

Program Scope - Graphene is an exciting new material composed of a single atomic layer of carbon atoms in a hexagonal lattice. Its properties are radically different than traditional semiconductors, and they open the way for new science and new applications (Geim and Novoselov, Nat. Mater. **6** 183 (2007)).

The ***goal*** of our research is to address two important questions:

How do these new kinds of carriers move through a graphene structure - how do they pass through barriers and bounce off edges - what are the effects of disorder?

How can one make and study atomic-scale graphene structures - how stable are different atomic configurations - what are the electronic states?

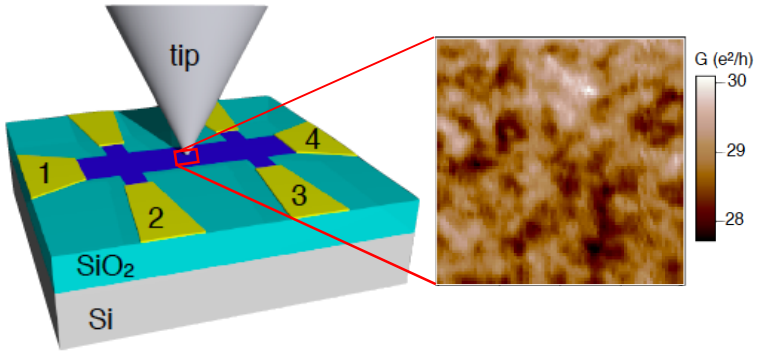

Fig. 1 (left) SPM tip above a graphene Hall bar; the conducting tip creates a movable scatterer in the 2DEG below. (right) SPM image of universal conductance fluctuations at 4K over a 400x400 nm^2 area

Our ***approach*** will be to combine the expertise of PI Westervelt in imaging electron flow using custom-made cooled scanning probe microscopes (SPMs) with the skill of David Bell in characterizing materials with transmission electron microscopes (TEMs). Bell is the Manager of the Imaging and Analysis Facility in Harvard's Center for Nanoscale Systems (CNS), which houses an outstanding pair of instruments; a Zeiss Libra Scanning Transmission Electron Microscope (STEM) and Transmission Electron Microscope (TEM). Both have atomic spatial resolution - this will allow us to sculpt and image graphene structures at atomic size scales.

Recent Progress - To understand the coherent flow of electrons through a graphene device, we employ a nanoscale probe that can perturb the system on the same size scale as the disorder potential and the electron wavelength. As shown in Fig. 1, the tip of a liquid-He-cooled scanning probe microscope (SPM) capacitively couples to a graphene device below, creating a

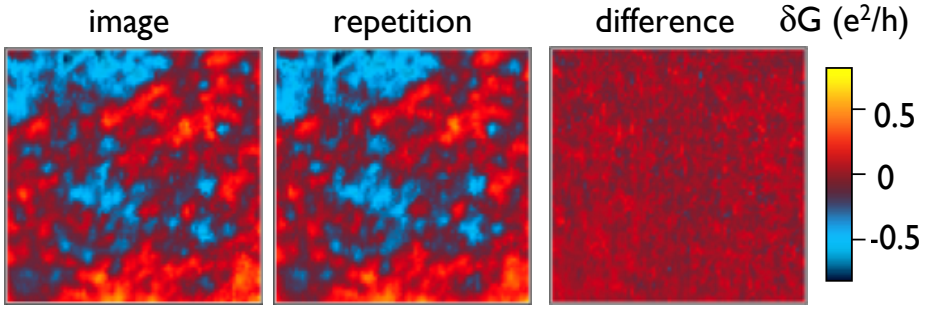

Fig. 2 Conductance image of a graphene device showing UCF with $\delta G \sim e^2/h$ and size scale ~ $\lambda_F/2$. The image repeats over times ~ 1 hr.

movable scatterer for electron waves. At sufficiently low temperatures and small size scales, the diffusive transport of electrons through graphene becomes coherent, leading to universal conductance fluctuations (UCF) and weak localization (WL). By scanning the tip over a device, we map these conductance fluctuations *vs.* scatterer position, producing a conductance image. We find that the conductance G is highly sensitive to the tip position, producing $\delta G \sim e^2/h$ fluctuations when the tip is displaced by $\lambda_F/2$, half the Fermi wavelength, as shown in Figs. 1 and 2 [1].

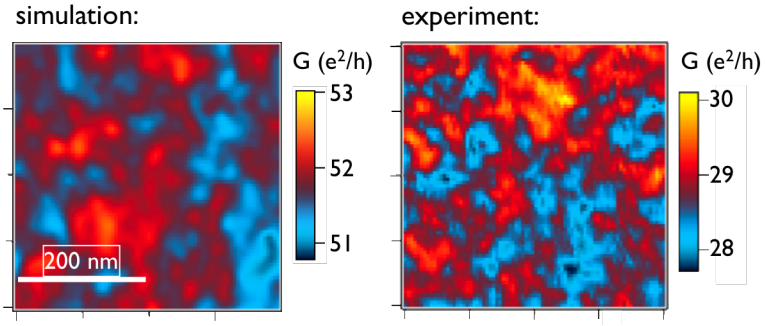

Fig. 3 Simulation of a graphene UCF conductance image *vs.* experimental data.

Universal conductance fluctuations (UCF) occur when a coherent electron wave scatters repeatedly while it travels through a disordered conductor, following all possible paths through the sample (Lee and Stone PRL **55** 1622 (1985); Altshuler and Khmelnitskii JETP Lett. 42 359 (1985); Washburn et al. Adv. Phys. **35**, 375 (1986)). The different paths interfere with each other, creating a change in the conductance known as UCF that depends sensitively on the scatterer positions. When the size of the sample is less than the diffusive phase coherence length $L\varphi$, interference between paths yields a universal magnitude $\delta G \sim e^2/h$ for UCF, independent of the sample size and the degree of disorder. Theory has predicted that the full UCF effect is obtained by moving a single scatterer a distance comparable to λ_F.

The following properties show that our conductance images arise from UCF: a) Repeatability - The conductance images are repeatable over ~1 hr, ruling out temporal fluctuations, shown in Fig. 2; b) Amplitude - The observed amplitude of the conductance fluctuations agrees with UCF theory, shown in Figs. 1 to 4; c) Energy correlation - The change in Fermi energy needed to decorrelate the conductance images matches the theoretical prediction for UCF; d) Simulations - Full quantum simulations of coherent transport and scattering in graphene by Eric Heller's group reproduce the experimental results, as shown in Fig. 3; and e) Correlation length -- The correlation length obtained from the autocorrelation function of the experimental images is $\cong \lambda_F/2$, as predicted for UCF, as shown in Fig. 4.

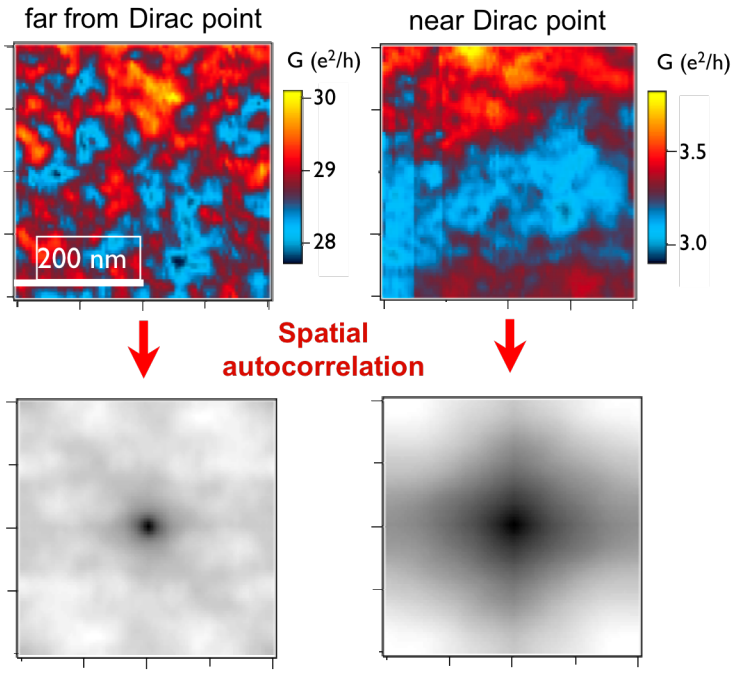

Fig. 4 Spatial autocorrelation of conductance images shows the correlation length $L\varphi \sim \lambda_F/2$.

Our measured conductance images also change with magnetic field [2], and become uncorrelated when ΔB is larger than a characteristic

correlation field ΔB_c. Figure 5 shows the gradual change in the conductance images as the field is descreased. The correlation field ΔB_c is found from the correlation between images taken at two different fields B1 and B2, as shown on the bottom of Fig 5. Weak localization is observed as a dip in the magnetoconductance G at B = 0, with a characteristic width ΔB_{WL}. The width ΔB_{WL} of the dip yields an estimate of the electron coherence length Lφ at fixed charge density. We find the predicted agreement between the values of ΔB_{WL} for weak localization and ΔB_c for UCF. Both ΔB_c and ΔB_{WL} increase as the carrier density n is reduced, and display a maximum at the Dirac point.

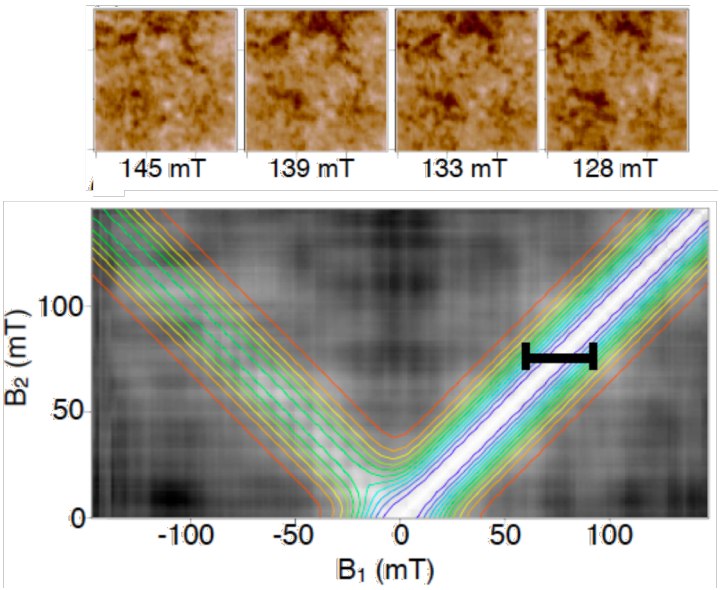

Fig. 5 (top) Gradual change in graphene conductance images with magnetic field B. (bottom) Cross correlation between images at fields B_1 and B_2, the bar shows the correlation field ΔB_c.

This "scanning scatterer" imaging technique provides a new way of investigating coherent transport in graphene by directly perturbing the disorder configuration that creates these interferometric effects.

Future Plans

We plan to develop suspended graphene samples to image the motion of electron waves. Because sources of scattering associated with the substrate are removed, the electron mean free path can increase substantially to values approaching the sample size ~1 μm, undoing the short range scattering that creates UCF and weak localization. In this way we plan to image the free motion of electrons and holes. The development of these structures will be done using the electron microscope facilities of Harvard's Center for Nanoscale Systems.

Figure 6 illustrates a method we plan to use for imaging the motion of electrons in a graphene sheet, based on their deflection by the SPM tip. In our original work imaging flow from a quantum point contact (QPC) in a 2DEG in GaAs (Topinka et al. Science **289**, 2323 (2000)), the conducting tip depleted a 'divot' in the electron gas that backscattered electrons, changing the conductance of the device. For graphene this approach does not work, because electrons and holes are chiral particles and an additional π phase shift occurs for particles that are scattered directly backwards, so the backscattering rate goes to zero. Instead we plan to scatter the particles sideways as shown in Fig. 6. Image contrast will be created by the interference of electron waves bounding off the tip, with those traveling directly between the two QPCs, creating a series of interference fringes that can be used to image the flow. Using this sample geometry we plan to study the Klein

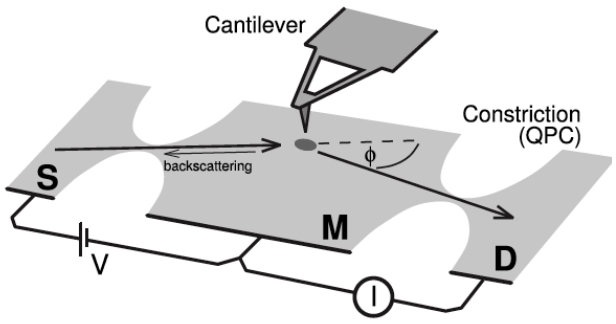

Fig. 6 Imaging electron wave flow between two QPCs in a graphene sheet (M. Braun *et al.* PRB **77** 115433 (2008)).

paradox, in which an electron can pass through a potential barrier by temporarily turning into a hole, and then returning to being an electron.

Using a magnetic focusing geometry with two QPCs facing the same direction, we recently imaged cyclotron orbits in a 2DEG for a GaAs/AlGaAs heterostructure (Aidala *et al.* Nature Physics **3**, 464 (2007)). The SPM tip defects electrons out of their original cyclotron orbit, changing the transmission between QPCs. We plan similar experiments to image cyclotron orbits in graphene, for a magnetic focusing geometry sample. This should be particularly interesting, because the bandstructure of graphene changes the Landau level energies, and the pseudospin adds an additional degeneracy.

*Supported by Dept of Energy grant DE-FG02-07ER46422

References

1. J. Berezovsky, M.F. Borunda, E.J. Heller and R.M. Westervelt, "Imaging Coherent Transport in Graphene (Part I): Mapping Universal Conductance Fluctuations," Nanotechnology special issue - *Quantum Science and Technology at the Nanoscale*, **21**, 274013 (2010).

2. J. Berezovsky and R.M. Westervelt, " Imaging Coherent Transport in Graphene (Part II): Probing Weak Localization," Nanotechnology special issue - *Quantum Science and Technology at the Nanoscale* **21**, 274014 (2010).

Electron Density Determination, Bonding and Properties of Tetragonal Ferromagnetic Intermetallics

J.M.K. Wiezorek, X. Sang and A.K. Kulovits,
(wiezorek@pitt.dedu, xis20@pitt.edu, akk8@pitt.edu)
Department of Mechanical Engineering and Materials Science,
John A. Swanson School of Engineering, University of Pittsburgh, 648 Benedum Hall,
3700 O'Hara Street, Pittsburgh, PA 15261.

Program Period of Performance: August 15, 2008 to August 14, 2011;

Program Scope

Many of the unique properties of intermetallics are directly related to their chemically ordered crystal structures and can be understood most fundamentally in terms of electron interactions and interatomic bonding[1]. Computational materials science approaches have been applied successfully to develop understanding of intermetallic phases and intrinsic properties[2-8]. However, computer modeling, especially electronic structure based calculations, typically require some critical approximations, which often are empirically justified by comparison of theory predicted properties, e.g. bulk modulus, phase stability, unit cell dimensions, to experimental data for a given material. Validation and verification of modeling predictions frequently suffers from the absence of suitable experimental data. Determination of the electron density distribution by experiment offers a direct way to evaluate theoretical electronic structure calculations. Energy-filtered transmission electron microscopy (EF-TEM) in combination with X-ray diffraction (XRD) offers methods for the experimental determination of the electron density distribution in crystals with sufficient accuracy to study the details of the interatomic bonding[9-11]. Unlike XRD, for which accuracy suffers from the presence of defects in the sample, in QCBED experiments defects can be avoided because the electron beam interacts with nanometer scale sample volumes and imaging in the TEM permits selections of perfect crystal volumes for data acquisition, eliminating difficulties with treating 'extinction'[9]. *We combine quantitative experimentation with materials theory for a systematic study of the electron density, bonding, and multifunctional properties in uniaxially ferromagnetic tetragonal ordered intermetallics, using the binary $L1_0$-ordered phases γ_1-FePd and γ_2-FePt as model materials for 3d-4d and 3d-5d electron systems*.

Key experiments use high-quality binary crystals to measure structure (F_{hkl}) and temperature (Debye Waller B_i) factors by quantitative convergent-beam electron diffraction (QCBED) using EF-TEM. Simultaneously with the F_{hkl} we obtain the anisotropic Debye-Waller factors (DWF's) for Fe, Pd and Pt in the chemically ordered $L1_0$-phases, which differ significantly from those of the respective elemental crystals. This facilitates experimental determination of the electron density distribution and bonding studies in these model d-electron systems.

The research team comprises the P.I., Prof. Jörg Wiezorek, a graduate student, Xiahan Sang, and a research associate, Dr. Andreas Kulovits. The project benefits from collaboration with Prof. Oleg Mryasov (Univ. Alabama) for first-principles calculations of electron density, properties, DWF's and F_{hkl} for direct comparison with our experiments.

This effort advances the state of the art in quantitative electron beam experimentation, provides new experimental data uniquely suited for the critically needed evaluation of competing computational models and enables development of improved, robust materials research tools for reliable and ideally predictive studies of $L1_0$-*FePt and* $L1_0$-*FePd and other intermetallics.*

Recent Progress

Using Si single crystals we have calibrated (e.g. CCD characterization, determination of point-spread function) the EF-TEM instrument at Pitt (Jeol JEM2100F, 2kx2k GIF Tridiem) for QCBED and performed initial performance comparison to an in-column energy-filter equipped JEM2200FS available at the Frederick-Seitz Materials Research Laboratory (FSMRL) of the

University of Illinois at Urbana-Champaign (UIUC). We confirmed that both instruments are compatible with our newly acquired LN_2-cooling holder and offer comparable performance for QCBED. Using the JEM2100F and cooling holder at Pitt we have performed QCBED and successfully determined simultaneously highly accurate and precise Debye-Waller (DW) and structure (F_{hkl}) factors for Si and also for the chemically ordered intermetallic phases of simple cubic NiAl and simple tetragonal FePd at temperatures ranging from about 100K to 300K.

Typically, two different sample-to-beam orientations have been used in QCBED F_{hkl} measurements, namely, either the systematic row (SR)[12,13] or the zone axis pattern (ZAP) method [14-16]. In most prior QCBED electron density studies, either F_{hkl} were obtained from QCBED while using DW factors determined by XRD[12,13] or DW factors were obtained from QCBED while using structure factors from first principle calculations[17]. Although simultaneous determination of DW and F_{hkl} factors from one pattern was reported[18,19] for Ni and Cu, application to unknown structures has been rare [20, 21] and requires further development of more robust methods.

We have developed and established a new experimental QCBED method, which enables the robust simultaneous refinements of multiple F_{hkl} and multiple DW factors[22-24]. The new method uses four to eight beams, inclusive of the transmitted beam, for crystal orientations relative to the incident electron beam in the TEM that are tilted away from a low-order, high-symmetry zone-axis orientation by a few Bragg-angles (Fig. 1). This off-zone axis multi-beam QCBED method exploits the similarly strong excitation of three to seven diffracted beams and their mutual dynamical interaction with each other and the transmitted zero-beam. Using Si as a well-known and well characterized test crystal, a comparison of the new multi-beam near zone axis method to the SR- and ZAP-CBED methods showed improved sensitivity regarding Debye-Waller and structure factor refinements[22,23]. The new off-axis CBED method combines advantages of the SR-method, e.g. relative ease of computation and strong dynamical effects and contrast features for robust F_{hkl} and DW factor refinement, and the ZAP-method, e.g. simultaneous refinement of multiple F_{hkl} and robust determination of crystal orientation from a single QCBED experiment. Furthermore, it can be used with widely available TEM instruments equipped with a post-column energy-filter.

For Si we performed simultaneous DW and F_{hkl} refinements from QCBED experiments at 96K, 173K and 298K. Prior reports on Debye-Waller factors for Si exist for comparison at 96K and 298K but not at 173K and agree well with our new higher precision measurements [23].

We also applied off-zone axis QCBED to investigate DW and F_{hkl} factors of chemically ordered β-NiAl with the B2 (CsCl type) structure in Strukturbericht notation. β-NiAl is a simple cubic structure (space group Pm3m) with a unit cell occupied by one Ni atom at 0,0,0 and one Al atom at 0.5,0.5,0.5 and has a lattice constant a_0 = 2.8863Å. In chemically ordered structures of metal species DW factors have to be determined for each atom species in crystallographically non-equivalent sites and will differ from the values reported for the respective elements due to effects from bonding. For instance, the Al and Ni in the respective elemental crystals of face-centered cubic structure are known to have room temperature DW factors of B(Al)=0.86(1) $Å^2$ and B(Ni)=0.37(1) $Å^2$, respectively [25], while in the B2-ordered NiAl the respective atoms have different DW factors of B(Al)=0.47(1) $Å^2$ and B(Ni)=0.51(1) $Å^2$ [26]. Prior experimental and theoretical work on DW and F_{hkl} factors exists for NiAl [17, 26-29]. It represents a suitable test case to evaluate the off-zone axis CBED method for the robust simultaneous refinements of multiple structure factors and the two Debye-Waller factors for the two different atom species that is required for the experimental CBED study of electron density in binary intermetallics, such as FePt and FePd. Previous studies of the temperature dependence of DW factors of β-NiAl reported that a cross-over temperature exists between 90K to 140K, below which the amplitudes of thermal vibrations of Al exceed those of Ni, and above which the converse holds[17, 26-28]. We determined DW factors for Ni and Al and three F_{hkl} for NiAl with unprecedented high precision from full two-dimensional data sets acquired at 103K, 133K, 173K and 298K[24]. Using a Debye model to explain the temperature dependence of the DW factors from our CBED measurements we determine a crossover temperature at which Al and Ni would have the same DW factors of ~91 K (Fig. 2).

Fig. 1

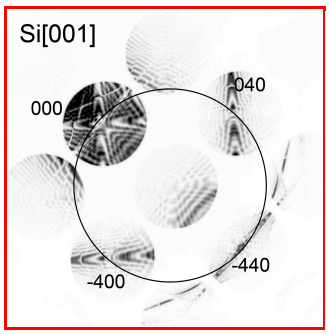

Fig. 2

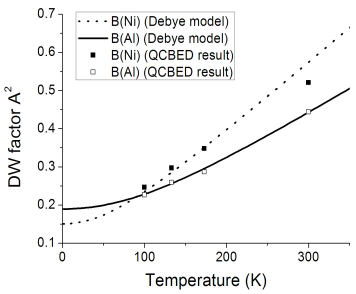

Fig. 3

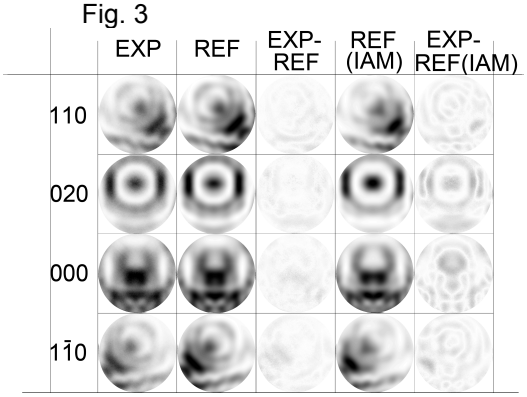

Fig. 1- Example of off-zone axis multi-beam CBED pattern for SI near [001];
Fig. 2- Debye-Waller factors for Ni and Al in NiAl as function of temperature.
Fig.3- Comparison of experimental (EXP), refined (REF) CBED disks, hkl, from 2-D data refined according to the independent atom model (REF(IAM)) for FePd near a [001] orientation, T=120 K;

We also used the off-zone axis QCBED method to collect high quality data sets for single crystals of the chemically ordered equiatomic composition $\gamma 1$-phase FePd for orientations near the [110], [101], [100] and [001] zone axes. These experimental QCBED data sets are suitable to determine the anisotropic DW factors of Fe and Pd and the first 15 F_{hkl} (up to hkl = 400) for the $L1_0$-ordered $\gamma 1$-phase FePd. Similar, to the case of the chemically ordered intermetallic phase β-NiAl, the DW factors for Fe and Pd atoms in the chemically ordered tetragonal intermetallic γ_1-phase FePd are reasonably expected to differ from those of the pure elements, e.g. B(Fe) = 0.35(1) Å^2, where Fe has base-centered cubic structure, and B(Pd) = 0.45(1) Å^2 [25]. Hence, it is necessary to determine the respective DW factors for the chemically ordered FePd crystal structures experimentally. This requires simultaneous robust refinements of multiple structure factors and of anisotropic DW factors with two distinguished amplitudes, e.g. Bz≠Bx=By, for each atom site, from the QCBED data sets, a situation significantly more complex for computational refinements than the case of NiAl. Initial refinements (Fig. 3) performed with a limited number of beams included in the dynamical electron diffraction theory based routines exhibit still large errors but clearly indicated excellent convergence for determination of both DW factors and F_{hkl} and revealed significant differences to predictions from the independent atom model, implying that we probed bonding in FePd. The first sets of DW factors with components, Bx, By and Bz, for the Fe and Pd atoms in $L1_0$-ordered $\gamma 1$-phase FePd obtained from off-zone axis QCBED patterns acquired at 120K near the [100] and [001] zone axes, respectively, are Bx(Fe)=By(Fe) = 0.29(2) Å^2, Bz(Fe) = 0.26(3) Å^2 and Bx(Pd)=By(Pd) = 0.19(1) Å^2, Bz(Pd) = 0.26 (5) Å^2 . Refinements including more realistic larger number of beams are in progress and expected to dramatically improve the precision of these original measurements of DW factor and complete set of low-order F_{hkl} up to hkl=400 for the $L1_0$-FePd intermetallic phase. Based on such a complete set of low order structure factors detailed electron density distributions and bonding charge or charge difference maps can be obtained for comparison with prediction from first-principles calculations.

Future Plans

We plan to perform additional QCBED experiments for the equiatomic and Pd-rich compositions of FePd in the chemically disordered and the chemically ordered state. We will perform a comparative study of the chemical ordering in this binary intermatallic systems using the new CBED method we have developed. We will expand towards application on the fully ordered Fe-Pt system for comparison between Fe-Pd and Fe-Pt. CBED measurements will be performed at or near 100K using the LN_2-cooling TEM holder with the JEM2100F GIF at Pitt. For the chemically ordered $L1_0$-phases we intend to determine quantitatively structure factors, F_{hkl}, with hkl of 001, 110, 111, 200, 002, 201, 112, 220, 202, 221, 003, 130, 131, 113, 222, 400, 004. We plan to perform ab-initio electronic structure based calculations of the electron density

distribution, structure factors and Debye-Waller factors and compare them with the sets of experimentally measurements. Using combinations of the high quality experimental data and theoretical predictions we will obtain electronic charge difference maps to elucidate details of the interatomic bonding in the FePd and FePt based tetragonal ordered ferromagnetic intermetallics.

DOE-sponsored publications

1. X. Sang, A. Kulovits, J.M.K. Wiezorek, Microscopy and Microanalysis (2010) Vol. 16 (Suppl. 2) 938-939; ***First Prize, Best Poster Award***;
2. A. Kulovits, J.M.K. Wiezorek, T. LaGrange, B.W. Reed and G.H. Campbell, Microscopy and Microanalysis (2010) Vol. 16 (Suppl. 2) 490-491;
3. X.H. Sang, A. Kulovits and J.M.K. Wiezorek, Acta Crystallographica A, (submitted 5/2010);
4. X.H. Sang, A. Kulovits and J.M.K. Wiezorek, Acta Crystallographica A, (submitted 6/2010);
5. O.N. Mryasov and J.M.K. Wiezorek, Intermetallics (submitted 8/2010);

References

1 J.H. Westbrook, "Intermetallic Compounds", Robert E. Krieger Publishing Company, Huntington, New York, 1977.
2 Johannesson, G.H., Bligaard, T., Ruban, A.V., Skriver, H.L., Jacobsen, K.W., Norskov, J.K., Physical Review LettersVolume 88, Issue 25 I, 24 June 2002, Pages 2555061-2555065.
3 Song, Y., Guo, Z.X., Yang, R., Li, D., Acta Materialia 49 (2001) 1647-1654
4 Massen, C., Mortimer-Jones, T.V., Johnston, R.L., Journal of the Chemical Society, Dalton Transactions (2002) Pages 4375-4388.
5 Fu, C.L., Wang, X., Ye, Y.Y., Ho, K.M., Intermetallics 7 (1999) 179-184.
6 Fu, C.L., Zou, J., Yoo, M.H., Scripta metallurgica et materialia Volume 33, Issue 6, 1 January 1995, Pages 885-889.
7 Das, G.P., Rao, B.K., Jena, P., Deevi, S.C., Physical Review B Volume 66, Article number 184203, Pages 1842031.
8 Fu, CL, Liu, CT, Wang, XL, Krcmar, M, Fernandez-Baca, JA, Intermetallics (2004), 911-919.
9 J.M. Zuo, Reports on Progress in Physics 67 (2004) 2053-2103;
10 B. Jiang, J. Friis, R. Holmestad, J.M. Zuo, M. O'Keeffe, J.C.H. Spence, Physical Review B69 (2004) Art.No. 245110;
11 M. Saunders, Microscopy and Microanalysis 9 (2003) 411-418;
12 Zuo, J. M., Kim, M., O'Keeffe, M. & Spence, J. C. H. (1999). Nature 401, 49-52
13 Jiang, B., Zuo, J. M., Jiang, N., O'Keeffe, M. & Spence, J. C. H. (2003). *Acta Cryst.* **A59**, 341-350.
14 Saunders, M., Bird, D. M., Zaluzec, N. J., Burgess, W. G., Preston, A. R. & Humphreys, C. J. (1995). *Ultramicroscopy* **60**, 311-323.
15 Mueller, K., Schowalter, M., Jansen, J., Tsuda, K., Titantah, J., Lamoen, D. & Rosenauer, A. (2009). *Ultramicroscopy* **109**, 802-814.
16 Tsuda, K., Ogata, Y., Takagi, K., Hashimoto, T. & Tanaka, M. (2002). Acta Cryst. A58, 514-525.
17 Nüchter, W., Weickenmeier, A. L. & Mayer, J. (1998). *Acta Cryst.* **A54**, 147-157.
18 Saunders, M., Fox, A. G. & Midgley, P. A. (1999a). *Acta Cryst.* **A55**, 471-479.
19 Saunders, M., Fox, A. G. & Midgley, P. A. (1999b). *Acta Cryst.* **A55**, 480-488.
20 Ogata, Y., Tsuda, K., Akishige, Y. & Tanaka, M. (2004). *Acta Cryst.* A60, 525-531.
21 Ogata, Y., Tsuda, K. & Tanaka, M. (2008). *Acta Cryst.* A64, 587-597.
22 X. Sang, A. Kulovits, J.M.K. Wiezorek, Microscopy and Microanalysis (2010) Vol. 16 (Suppl. 2) 938-939
23 X.H. Sang, A. Kulovits and J.M.K. Wiezorek, Acta Crystallographica A, (submitted 5/2010);
24 X.H. Sang, A. Kulovits and J.M.K. Wiezorek, Acta Crystallographica A, (submitted 6/2010);
25 Butt and Bashir, Acta Cryst A44 (1988) 396-398.
26 Georgopoulos and Cohen, Scripta metal. 11 (1977) 147.
27 Gumbsch, P. & Finnis, M. W. (1996). *Philosophical Magazine Letters* **73**, 137 - 144.
28 Mostoller, M., Nicklow, R. M., Zehner, D. M., Lui, S. C., Mundenar, J. M. & Plummer, E. W. (1989). *Phys. Rev. B* **40**, 2856
29 Fox, A. G. (1995). Scripta Metall Mater 32, 343-347.

SISGR - TRANSPORT AND IMAGING OF MESOSCOPIC PHENOMENA IN SINGLE AND BILAYER GRAPHENE

Amir Yacoby, Harvard University, yacoby@physics.harvard.edu

Pablo Jarillo-Herrero, MIT, pjarillo@mit.edu

Project Scope –

The research objective of this proposal is to investigate novel quantum correlated phenomena in single and bilayer graphene. Our research focuses both on isotropic phases as well as spatially varying phenomena where geometry and boundary conditions play an important role. Our investigation explores both naturally occurring inhomogeneities due to intrinsic disorder as well as spatially dependent phenomena arising from patterning graphene into nanostructures, introducing non uniform charge densities using local electrostatic gating, and through contacting graphene with novel materials. Our experimental approach consists of both conventional transport methods as well as sophisticated local probe techniques capable of imaging the local thermodynamic and transport properties of these quantum phenomena

Recent Progress –

The unique energy spectrum of single and bilayer graphene are expected to lead to novel collective phenomena when interactions among charge carriers become important. In this talk we will address two types of interaction driven phenomena: Spontaneously broken symmetries in bilayer graphene in the quantum Hall regime and Andreev reflection and the Josephson effect in a hybrid graphene - superconducting devices.

Broken Symmetries in Bilayer Graphene in the Quantum Hall Regime - The non-interacting energy spectrum of graphene and its bilayer counterpart consists of multiple degeneracies owing to the inherent spin, valley and layer symmetries. Interactions among charge carriers are expected to spontaneously break these symmetries, leading to gapped ordered states. In the quantum Hall regime these states are predicted to be ferromagnetic in nature whereby the system

becomes spin polarized, layer polarized or both. In bilayer graphene, due to its parabolic dispersion, interaction-induced symmetry breaking is already expected at zero magnetic field. In this work, the underlying order of the various broken-symmetry states is investigated in bilayer graphene that is suspended between top and bottom gate electrodes. By controllably breaking the spin and sublattice symmetries we are able to deduce the order parameter of the various quantum Hall ferromagnetic states. At small carrier densities, we identify for the first time three distinct broken symmetry states, one of which is consistent with either spontaneously broken time-reversal symmetry or spontaneously broken rotational symmetry. These conclusions are further supported by local inverse compressibility measurements of suspended bilayer graphene using a scanning single electron transistor.

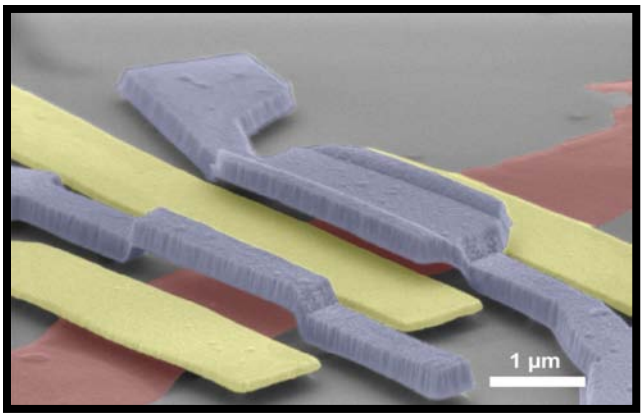

Doubly suspended bilayer graphene device

Graphene Superconducting Devices - The coupling between superconductors and normal metals gives rise to many interesting solid state quantum phenomena. Two such examples are Andreev reflection (AR), where an electron is *retroreflected* as a hole at an S-N interface, and the Josephson effect, where a dissipationless *supercurrent* can flow through an S-N-S structure. It has been predicted that the coupling of superconductors to graphene devices should result in novel types of AR and Josephson phenomena. This is due both to the gapless nature of the graphene band structure, and to its relativistic-like conical dispersion. However the requirements to observe these phenomena are stringent: graphene devices with extremely small disorder and superconductors with as high-gap as possible. Here we will present our efforts to reach these goals. In particular we have demonstrated Josephson coupling and AR in NbN-graphene-NbN devices, reaching a gap value for graphene Josephson devices near an order of magnitude larger

than before. We will also briefly describe our efforts to create Josephson junctions with minimum disorder, where several routes are being explored.

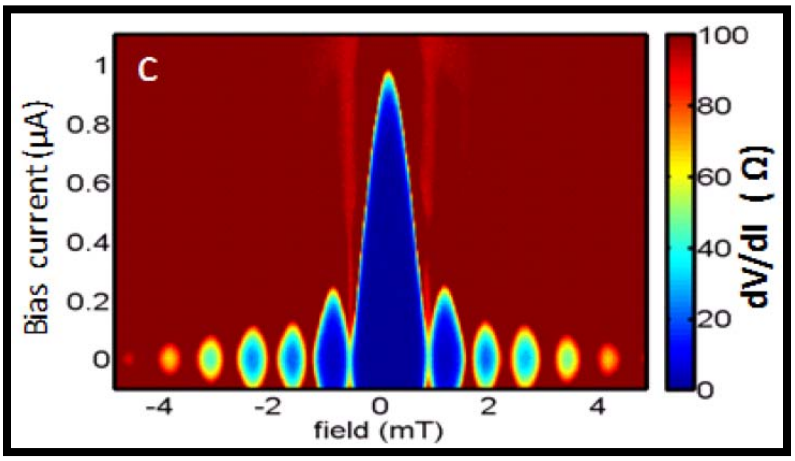

Differential resistance versus magnetic field exhibits a Fraunhofer pattern characteristic of a uniform supercurrent density throught the junction.

Future Plans –

Our focus for next year is twofold. First we would like to gain better control and understanding of the various broken symmetry states in suspended bilayer devices. In addition some of these phases are expected to have unique conduction along the edge of the sample that we would like to explore through transport and imaging techniques. Second we will work to improve the quality of our superconducting- graphene devices. The main objective is to reduce the disorder due to potential fluctuations. For this we will pursue the fabrication and characterization of suspended and graphene on boron nitride superconducting devices. This will enable the exploration of interesting superconducting phenomena in the regime of relativistic-like electron dynamics.

DE-FG02-07ER46446: MULTISCALE ATOMISTIC SIMULATION OF METAL-OXYGEN SURFACE INTERACTIONS: METHODOLOGICAL DEVELOPMENT, THEORETICAL INVESTIGATION, AND CORRELATION WITH EXPERIMENT

PI: Judith Yang, Department of Chemical and Petroleum Engineering, University of Pittsburgh (UPitt), Pittsburgh PA, judyyang@pitt.edu

Co-PIs: Alan McGaughey, Department of Mechanical Engineering, Carnegie Mellon University (CMU), Pittsburgh PA, mcgaughey@cmu.edu

Simon Phillpot, Department of Materials Science and Engineering, University of Florida, Gainesville FL, sphil@mse.ufl.edu.

Susan Sinnott, Department of Materials Science and Engineering, University of Florida (UF), Gainesville FL, ssinn@mse.ufl.edu

PROGRAM SCOPE

Our long-term vision is the comprehensive and fundamental understanding of a critical gas-surface reaction, nano-oxidation— from the adsorption of oxygen atoms on the metal surface to the coalescence of the bulk oxide—via coordinated multi-scale theoretical and *in situ* experimental efforts. Reaching this goal necessitates close collaborations between theorists and experimentalists. The purpose of this specific DOE program is the development of new theoretical and computational tools that can be used to model the early stages of oxidation and the correlation of these predictions with our abundant experimental observations acquired by a unique *in situ* ultra-high vacuum transmission electron microscope (UHV-TEM).

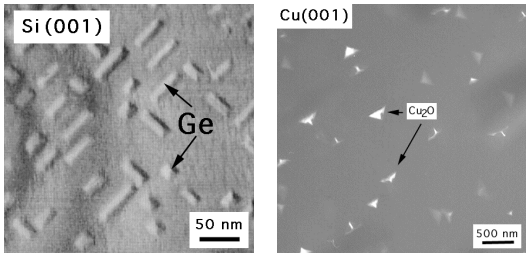

Figure 1: Comparison of Ge on Si heteroepitaxy and Cu_2O nucleation on Cu(001).

The PI previously showed that heteroepitaxial concepts describe the nucleation and growth to coalescence of Cu_2O islands on Cu(001) surprisingly well (Fig. 1). Models of heteroepitaxial growth, where nucleation rate theory is a standard model used to describe the atomistic processes, have been developed and used successfully to describe metal-on-metal heteroepitaxy. However, these models have not yet been developed to include gas-surface reactions. ***The objective of this program is to further develop heteroepitaxial theories for application to oxidation using a multiscale theoretical approach and thus allow the direct quantification of the associated experimental observations and lead to a fundamental understanding of nanoscale oxygen gas – metal surface reactions.***

To achieve this goal, we are (i) developing a kinetic Monte Carlo (KMC) approach, called Thin Film oxidation (TFOx), to simulate the atomistics of transport, nucleation and growth of metal oxides during the oxidation process, and (ii) determining realistic input parameters for TFOx through coordinated electronic structure calculations and molecular dynamics simulations. The TFOx development is the primary responsibility of the PI. The electronic structure calculations and atomic-level simulations are the prime responsibilities of the CMU and UF co-PIs. Our specific goals include gaining fundamental and quantitative insights into the nucleation behavior, morphological evolution of oxide islands during nano-oxidation and coalescence, and providing the surface and interface energies required to augment the available theoretical treatment of island stability. Each of these aspects has not been demonstrated before for gas-surface reactions and, hence, each represents a potential ground-breaking fundamental science in surfaces and interfaces.

RECENT PROGRESS

Development of KMC code: TFOx has been developed to simulate the nucleation and growth of oxide islands on 2D and 3D metal surfaces.[1,2] TFOx is parallelized, can be used with all standard C compilers, and features an easy-to-use graphical user interface. Via movement of atoms with appropriate input parameters (hopping and sticking rates), TFOx considers deposition, surface diffusion, embedment into the subsurface, aggregation, and desorption, as well as homogeneous or heterogeneous nucleation. The effect of temperature can be considered and the surface geometry can include the missing row reconstruction. Using hopping and sticking rates based on a pseudo potential adjusted to reproduce experimental morphologies, we have described oxide island growth in 3D. The resulting rod-like shapes show qualitative agreement with the experimental TEM image, as shown in Fig. 2. The capability of TFOx to describe 3D growth suggests that we can examine heteroepitaxial growth mechanism accurately once theoretically determined physical input parameters are available.

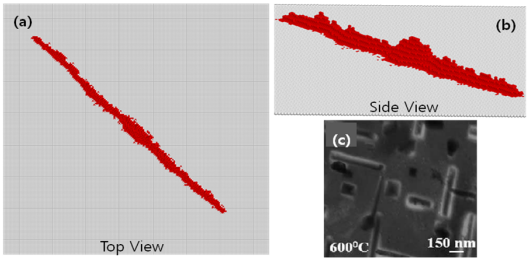

Figure 2: (a).(b): TFOx predictions. (c) TEM image

***Ab initio* KMC:** We are now using transition state theory (TST) and energy barriers predicted from density functional theory (DFT) calculations to predict the required hopping and sticking rates for input to TFOx. Because it is not possible to calculate energy barriers for all possible surface configurations, we are developing a technique by which a small set of energy barriers can be used to predict the barrier for any event. We first investigated oxygen diffusion on the Cu(100) surface. The energy barriers were fitted using the method by Mehl et al.[3] and barriers from Alatalo et al.[4] As the oxygen coverage increases, the mobility of oxygen atoms decreases steeply at 0.3~0.5 monolayers (MLs), indicating the importance of O-O repulsion. The distribution of oxygen atoms is consistent with the experimentally observed c(2×2) structure. We next used KMC to study oxygen embedment on the clean and missing row reconstructed Cu (100) surfaces. The energy barriers were obtained from Lee and McGaughey.[5] Embedment was only found to occur on the reconstructed surface, suggesting that oxygen embedment and sub-surface diffusion are important steps in the early stages of oxidation.

Identifying the Mechanisms of the Initial Stages of Cu(100) Oxidation We studied atomic oxygen embedment into a Cu(100) surface using DFT calculations and the nudged elastic band method.[5] As the oxygen coverage increases on the unreconstructed surface from 0.25 ML to 0.75 ML, the energy barrier for oxygen embedment decreases and an energetically favorable sub-surface site is found at 0.75 ML coverage. At a fixed oxygen coverage of 0.5 ML, the oxygen embedment energetics vary with the surface morphology and the embedment is found to be more probable for reconstructed structures compared to the bare surface. On the missing-row reconstructed surface, we find that the energy barrier for atomic oxygen embedment is smaller through

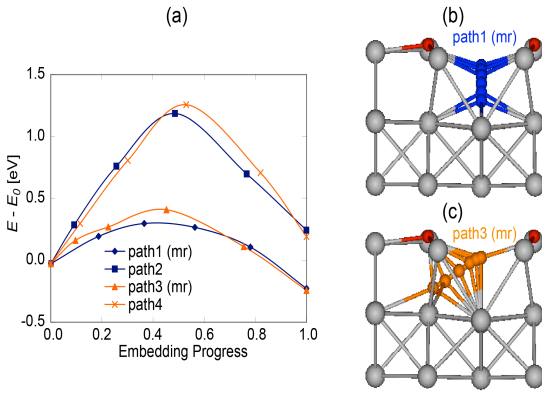

Figure 3: Prediction of energy barriers for oxygen embedment into Cu(100) surfaces.

the missing row compared to other paths (see Fig. 3), suggesting a mechanism for the formation of sub-surface oxygen structures. The energy barrier for sub-surface oxygen diffusion is predicted to be less than that for on-surface diffusion. We then investigated the role of sub-surface oxygen in Cu(100) oxidation using DFT calculations.[6] We found that the presence of sub-surface oxygen atoms causes the top copper layer of the missing-row reconstructed surface to rise by 1.7 Å compared to the bare surface. This prediction compares well to an earlier scanning tunneling microscopy measurement of 1.8 Å.[7] When the missing-row reconstructed surface is exposed to an additional oxygen molecule, surface restructuring that leads to oxide-like structures is only observed when sub-surface oxygen is present. The oxide-like nature of these structures is confirmed through structural, Bader, and electron density of states analysis. These findings demonstrate the key role played by sub-surface oxygen in Cu(100) oxidation.

Development of an Empirical Potential for Copper, Oxygen and Copper Oxides We have developed a variable charge potential for Cu and O based on the charge optimized many body bond (COMB) framework. [8,9] A previous COMB potential was developed for metallic Cu.[10] Oxygen parameters were fit to the dissociation of molecular oxygen and several anions. We determined the parameters governing Cu-O interactions starting with these existing parameters. Several properties of Cu_2O as predicted with the new potential are listed in Table 1. The potential also captures the relative formation enthalpies of the low energy oxide phases. The potential replicates the interaction of oxygen with the metal surface as seen both experimentally and through calculations. Most importantly, the potential predicts several of the same low energy reconstructions of the partially oxidized copper surfaces. For example, the (100) surface is predicted by the potential to reconstruct into the experimentally observed $(\sqrt{2}X2\sqrt{2})R45^\circ$ configuration at up to 0.5 ML coverage. Fig. 4 shows a study where the early stage of the oxidation on Cu(100) surface was examined with the COMB potential. The charges on the copper and oxygen atoms vary based on the surrounding environment.

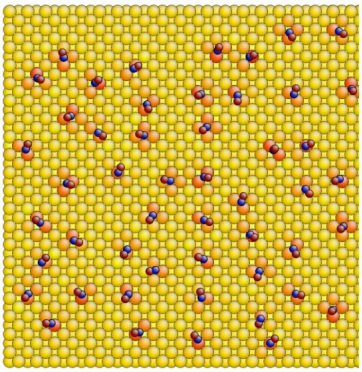

Figure 4: Early stage of Cu(100) oxidation. Cu atoms are yellow and O atoms are red-purple, depending on their charge.

Table 1. Properties of Cu_2O	Experiment	First Principles	COMB
Lattice constant (Å)	4.27	4.31	4.27
E_{coh} (eV/Cu_2O)	11.3	11.4	11.4
Bulk Mod. (GPa)	112	112	111
Shear Mod.(GPa)		8.15	8.27
C_{11} (GPa)	123	123	122
C_{12} (GPa)	108	107	105
C_{44} (GPa)	12	12.1	57.3
V_{Cu} point defect, eV	0.45	0.28-1.17	2.49
V_O		1.55	0.95
O_{i_tet}		1.36-1.47	0.71
Cu_{i_tet}/Cu_{i_Oct}		1.47[e]/1.9	0.95/0.97
Surface Energies ($mJ \cdot m^{-2}$)			
Cu_2O(100):Cu		1570	1510
Cu_2O(110):Cu		1790	2380

REFERENCES

1. X. Han et al. *Multidisciplinary Modeling in Materials and Structures* **3**, 43 (2007).
2. X. Han et al., *J. Computational and Theoretical Nanoscience* **4**, 1 (2008).
3. H. Mehl et al., *Physical Review B* **60**, 2106 (1999).
4. M. Alatalo et al., *Physical Review B* **70**, 245417 (2004).
5. M. Lee and A. J. H. McGaughey, *Surface Science* **603**, 3404 (2009).
6. M. Lee and A. J. H. McGaughey, *Surface Science* **604**, 1425 (2009).
7. M. Lampimaki et al., *Journal of Chemical Physics* **126**, 034703 (2007).
8. J. Yu et al., *Physical Review B* **75**, 085311 (2007).
9. J. Yu et al., *Physical Review B* **75**, 233203 (2007).
10. J. Yu et al., *Philosophical Magazine Letters* **89**, 136 (2007).

FUTURE PLANS

- Increase TFOx functionality to include copper diffusion, pressure, off-lattice diffusion sites.
- Continue developing the procedure for predicting energy barriers for a wide range of surface configurations using a small set of DFT-predicted barriers as well as correlate temperature between experiment and simulation.
- Use TFOx to study oxide island growth on the Cu (100) surface and compare to experiments to estimate the energy barriers and sticking coefficients.
- Use DFT calculations to investigating copper releasing and diffusion pathways during transition from $c(2\times2)$ to $(2\sqrt{2}\times\sqrt{2})R45^{\circ}$ on the Cu(100) surface.
- Apply *ab initio* atomistic thermodynamics to determine the most stable surface structures at finite temperatures and pressures.
- Complete the refinement the Cu-Cu_2O COMB potential to better reproduce properties such as elastic constants, surface energies, stacking fault energies, defect formation energies and thermal expansion coefficients. A portion of the fitting/testing input will be provided from the DFT calculations.
- Use the COMB potential to carry out MD simulations of copper oxidation to provide input for TFOx and to assess the stability of different oxide islans shapes on the Cu(100) surface at different temperatures.

PUBLICATIONS

- X. Han, R. McAfee, J. C. Yang, "Kinetic Monte Carlo Simulations of the Dramatic Effects of Attachment Probability and Potential Gradients on Island Morphology Variations under Heteroepitaxial Growth Conditions", *J. Computational and Theoretical Nanoscience*, 5, 117–128 (2008)
- J. Yu, S.B. Sinnott, and S.R. Phillpot, "Optimized Many Body Potential for fcc Metals." *Philosophical Magazine Letters* **89**, 136-144 (2009)
- M. Lee and A. J. H. McGaughey, "Energetics of oxygen embedment into unreconstructed and reconstructed Cu(100) surfaces: Density functional theory calculations." *Surface Science* **603**, 3404-3409 (2010).
- M. Lee and A. J. H. McGaughey, "Role of sub-surface oxygen in Cu(100) oxidation."*Surface Science* **604**, 1425-1431 (2010).

Probing Correlated Superconductors and their Phase Transitions on the Nanometer Scale

Ali Yazdani
Department of Physics
Princeton University, Princeton, NJ 08540
yazdani@princeton.edu

Program Scope:

This program is focused on understanding how correlated electronic states in materials with *d* and *f* electrons undergo phase transitions to form an unconventional metallic phase and the mechanisms by which these states become superconducting with lowering temperature. Such phenomena are at the heart of some of the most debated issues in condensed matter physics, and their understanding is an intellectual driver for many of the DOE-BES projects for the development of novel materials and the search for higher temperature superconductivity. Our aim is to provide a microscopic view of these exotic materials and their phase transition into the superconducting state using some of the most sophisticated scanning tunneling microscopy (STM) and spectroscopy techniques. The results of the experiments proposed here will provide important evidence that will help constrain theoretical models of unusual normal states in these complex materials and their potential mechanisms for superconductivity. This DOE-BES program is divided into two parts. The first part focuses on examining the properties of high-T_c cuprate superconductors and specifically the high temperature pseudogap phase of these materials. Many believe that understanding this phase is critical to determining how a Mott insulator is transformed into a high-T_c *d*-wave superconductor. Despite many efforts over the last two decades, there is currently no consensus as to what underlies this unusual electronic phase. The second component of our program is to utilize for the first time the power of STM techniques to study the exotic superconducting and normal phases in heavy fermion compounds. The parallels between the puzzles in heavy fermions and cuprates suggest that heavy fermions might provide important general clues into understanding correlated electrons and their superconductivity. Similar to the high temperature superconducting cuprates, understanding the mechanism behind the unconventional superconductivity requires understanding the "normal state" prior to formation of superconductivity. The heavy fermions offer clean materials systems to examine issues that might be very difficult to examine in the cuprates and new Fe-based superconductors due to doping disorder in those systems. The two components of the proposed program provide a broad attack on some of the most important problems in the physics of correlated materials and the emergence of superconductivity in these systems.

Recent Progress:

Electronic Origin of the Inhomogeneous Pairing Interaction in High-T_c Superconductors (*Science* 2008) [1]

One of the most critical questions concerning the underlying mechanism of pairing in high-T_c cuprates is whether there is a low-energy bosonic excitation in these materials that can effectively glue electrons together to make Cooper pairs. Lattice vibrations (phonons), which mediate pairing in conventional superconductors, leave characteristic fingerprints on the excitation spectrum of these superconductors. The detection of electron-photon coupling in the 1960s led to unambiguous proof of the BCS theory of superconductivity. There is, however, an alternative view that cuprates are fundamentally different from BCS superconductors because they arise from doping a Mott insulator, and their superconductivity does not involve low-energy bosonic excitations. In the last 20 years, the search for this bosonic glue has been hampered by a number of experimental and theoretical difficulties, including the inhomogeneous nature of these materials. The development of lattice tracking spectroscopy provided a breakthrough for examining the question of bosonic exchange without averaging over the disorder in the

material. The key advance was the ability to measure both the normal and the superconducting density of states at the exact same atomic location. Although, as mentioned in the previous section, pairing gaps can persist to temperatures above T_c in overdoped $Bi_2Sr_2CaCu_2O_{8+d}$ samples, we were able to make these measurements to temperatures well above the local $T_P > T_c$, where the pairing gaps first appear. Dividing the superconducting spectra by the normal spectra measured at the same location, we were able to follow much of the same analysis that was done in the 1960s to isolate features arising from electron-boson coupling on overdoped samples. Indeed, we found these couplings to be very strong (as ARPES and tunneling studies by others had established before [24-28]); however, our experiments show a lack of correlation between the strength of electron-boson coupling and the local variation of the pairing strength in the samples. Unexpectedly, our experiments showed that the usual electron-hole asymmetric excitation detected in the normal state controls the pairing interaction in these compounds in the superconducting state. (Figure 1) A measurement of the normal state was shown to directly predict the spatially varying strength of superconductivity on the nanoscale at low temperatures. The electron-hole asymmetry of these excitations suggests a connection to the physics of the Mott state, while it disfavors an electron-boson scenario for the underlying mechanism in these compounds. These experiments, together with the effort in visualizing pair formation in the cuprates with the STM, demonstrate the local nature of pairing mechanism in the cuprates.

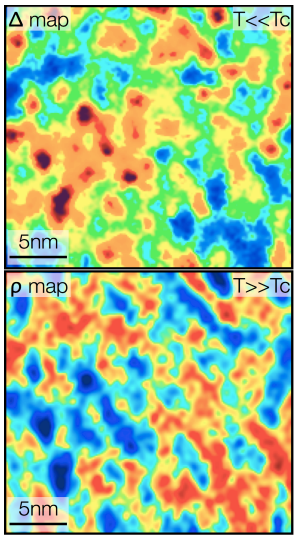

Figure 1. Superconducting state imitates the normal state. The top superconducting gap map is strongly (80%) anticorrelated with the density of state at the Fermi energy well above when the gaps first form in this material well above T_C.

Extending Universal Nodal Excitation Optimizing Superconductivity in High-T_c Cuprate Superconductors (Published & covered in a Perspective in *Science* 2009) [2]

Two of the most hotly debated issues in cuprate superconductors are the question of the origin of the pseudogap behavior and the underlying mechanism for suppression of T_c in underdoped samples. Over the last few years, there has been a great deal of evidence that the spectroscopic properties of underdoped cuprate samples can be perhaps best described by two energy scales, one that has been claimed to diminish as T_c is reduced, and the other to increase with underdoping. We have focused on a systematic investigation of the evolution of tunneling spectra with doping and temperature in $Bi_2Sr_2CaCu_2O_{8+d}$ samples. Unlike the overdoped samples, where a BCS *d*-wave gap having a single energy scale can capture the behavior of the spectra, our experiments demonstrate the systematic breakdown of this behavior with underdoping (Figure 3). The breakdown, however, does not include the behavior of spectra at low energy that probes the excitation spectrum near the nodes of the *d*-wave order parameter. Our experiments show that this region of the spectra has a universal characteristic in underdoped samples, indicating that the strength of the pairing gap near the node is not substantially suppressed with underdoping. Furthermore, our experiments show that smaller regions of the spectra (in energy) were governed by this universal behavior as we reduced the doping. We have developed a method to extract the angular dependence of the gap from the tunneling spectra to illustrate that the nodal and anti-nodal regions are govern by gaps that have different doping dependencies. The analysis of the data, based on a model that allows for the gap to deviate from a pure cos2Θ to capture the shape of the tunneling

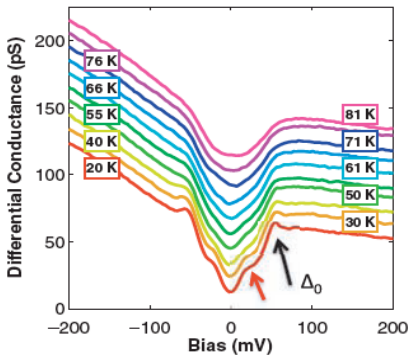

Figure 2. Spectroscopic measurements on a underdoped in $Bi_2Sr_2CaCu_2O_{8+d}$ sample as function of temperature. At the lowest temperature the spectra clear do not exhbit the behaviour of a simple d-wave gap and show two energy scale.

spectra, suggests that different regions of the Fermi surface contribute differently to the pairing interaction. (see schematic in Figure 3) Our observations, together with angle-resolved photoemission, Raman, and other spectroscopies, suggest that pseuodgap behavior (in underdoped samples) competes for the portion of the Fermi surface that causes superconductivity in the cuprates.

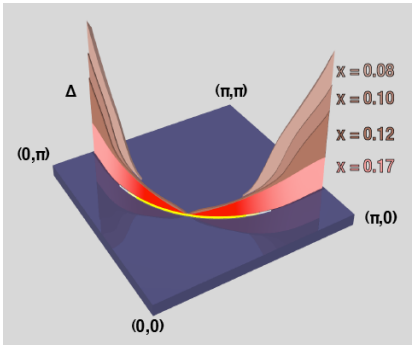

Figure 3. Schematic of the pairing gap as function of momentum or angle in the Cu-O plane. The direction from (0,0) to (π,π) is 45° to Cu-O) bond direction. Near this angle the pairing gap follows a universal doping independent cos(2Θ) function (the red shaded function). Beyond this region, different samples are distinguished by the range over which their gap follows this function. Optimal doping comes close to the ideal cos(2Θ) over the entire angle range.

Nanoscale Proximity Effect in High-T_c Cuprate Superductors (Published in Physical Review Letters & covered in *Viewpoint* in *Physics* 2010) [3]

Many properties of high-temperature cuprate superconductors, such as the transition temperature Tc and the presence of pseudogap, have a strong doping dependence. What happens when two regions with different doping are put into contact? Since pairing in cuprate superconductors has a very local character, one expects the coherence length to be short, and any proximity effects to occur only on microscopic length scales. Nonetheless, some experiments have demonstrated that high-Tc Josephson junctions can be made with thicknesses many times the coherence length. Other experiments on bilayers have shown transition temperatures higher than that of either layer in isolation. Microscopic theories to explain these phenomena include Josephson coupling between superconducting islands and enhancement of the phase stiffness in underdoped regions by proximity to overdoped regions. Such scenarios are inherently interesting due to the possibility that interface superconductivity can occur at temperatures above the maximum possible in bulk samples. Prior to ur work, no experiments have been performed to investigate proximity effects locally at microscopic length scales. We provided the first report of a proximity effect in the cuprate superconductor $Bi_2Sr_2CaCu_2O_{8+d}$ using STM and the intrinsic nanoscale spatial variation of the sample. We show that indeed patches of the sample with weaker superconductivity can be enhanced if surrounded by patches with stronger superconductivity, demonstrating that the collapse of superconductivity is caused by more than local thermal pair breaking.

Visualizing the Formation of the Kondo Lattice and the Hidden Order in URu_2Si_2 (Published in PNAS, 2010)[4]

The local *f* electrons interact both with the itinerant *spd* electrons as well as with each other, resulting in a rich variety of electronic phases in heavy fermion compounds. In many of these materials, screening of the local moments by the Kondo effect begins at relatively high temperatures resulting in heavy fermion state at low temperatures. Exchange interactions between the local moments become more important at lower temperatures and can result in the formation of magnetic phases as well as superconductivity at even lower temperatures. Among the heavy fermion compounds perhaps the most enigmatic is the URu_2Si_2 system, which undergoes a 2^{nd} order phase transition with a rather large change in entropy at 17.5 K from a paramagnetic phase with Kondo screening to a phase with an unknown order parameter(9). This material possesses low-energy commensurate and incommensurate spin excitations, which are gapped below the hidden order (HO) transition temperature. These features are believed to be signatures of a more complex order parameter, the identification of which has so far not been possible despite numerous investigations. Moreover, analogous to other correlated systems, this unusual conducting phase is transformed into an unconventional superconducting state at 1.5 K, the understanding of which hinges on formulating the correct model of the hidden order state. Recently, we have report scanning tunneling microscopy (STM) measurements on URu_2Si_2 single crystals that allow atomic scale examination of this system in the paramagnetic Kondo phase and its phase transition into the hidden order

(HO) state. We isolate electronic signatures of the Kondo lattice state and their transformation at the HO transition. Although there have long been reports on modification of the electronic structure of URu_2Si_2 at the onset of the HO transition, our experiments provide an unprecedented determination of these changes with high energy and spatial resolutions. We find a particle-hole asymmetric energy gap that turns on with a mean-field temperature dependence near the bulk HO transition. More importantly, spectroscopic mapping as a function of temperature further reveals that the hidden order gap is spatially correlated on the atomic scale with the electronic signatures of the Kondo lattice state.

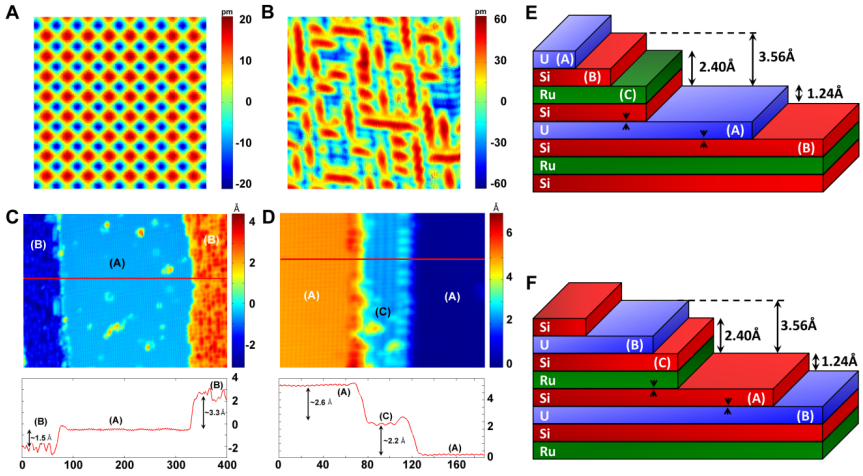

Figure 4. STM imaging and identification of different layers of cleaved URu_2Si_2 system. Figure A-D show different surfaces and figures E and F shows the schematic structural diagram that can help explain the data in C and D panel. The panel E shows the most likely scenario in which breaking of a single U-Si bound exposes a U terminated surface that is unreconstructed. The Si surface appears to reconstruct as shown in panel B.

Future Plans:

Advancing our understanding of cuprate superconductors, we are currently working on obtaining the first spatially resolved measurements through the onset temperature of the pseudogap phase. We also plan to complement these temperature-dependent studies with application of a spin-polarized STM technique to determine whether there are static spin textures in the cuprates as has been suggested by other experiments. We are currently developing the capability to apply spin-polarized techniques to correlated electron systems in general. In addition to these efforts on cuprates, we are expanding our efforts on heacy fermion systems. Addressing the impact of defects on Kondo lattice behavior or hidden order phase in U-based compound will be a priority. Expanding the application of STM to a large class of heavy fermions, such as the 1-1-5 will greatly expand our understanding of unusual normal state of heavy fermion systems.

Publication Supported by DOE-BES:

1. A. N. Pasupathy, A. Pushp, K. K. Gomes, C. V. Parker, J. Wen, Z. Xu, G. Gu, S. Ono, Y. Ando, and A. Yazdani "Electronic Origin of the Inhomogeneous Pairing Interaction in the High-T_c Superconductor $Bi_2Sr_2CaCu_2O_{8+d}$" *Science* **320** 196 (2008).
2. A. Pushp, C. V. Parker, A. N. Pasupathy, K. K. Gomes, S. Ono, J. Wen, Z. Xu, G.Gu, and A. Yazdani "Extending Universal Nodal Excitations Optimizes Superconductivity in $Bi_2Sr_2CaCu_2O_{8+d}$" *Science* **324** 1689 (2009).
3. Colin V. Parker, Aakash Pushp, Abhay N. Pasupathy, Kenjiro K. Gomes, Jinsheng Wen, Zhijun Zu, Shimpei Ono, Genda Gu, and Ali Yazdani, "Nanoscale Proximity Effect in the High-Temperature Superconductor $Bi_2Sr_2Ca_2CuO_{8+\delta}$ Using a Scanning Tunneling Microscope" Physical Review Lett. **104,** 117001 (2010).
4. Pegor Aynajian, Eduado H. da Silva Neto, Colin V. Parker, Yingkai Huang, Abhay Pasupathy, John Mydosh, and Ali Yazdani, "Visualizing the formation of the Kondo lattice and the hidden order in URu_2Si_2" Proc. Nat'l. Acad. Sci USA **107,** 10383 (2010)

Hydrogen Generation Using Integrated Photovoltaic and Photoelectrochemical Cells

Grant Number: DE-FG02-06ER46232

Jin Z. Zhang[a] and Yiping Zhao[b]

a) Department of Chemistry and Biochemistry, University of California Santa Cruz

a) email: zhang@ucsc.edu

b) Department of Physics and Astronomy, The University of Georgia at Athens

b) email: zhaoy@physast.uga.edu

Program Scope

In the pursuit of efficient solar hydrogen generation, the use of tandem cells of photoelectrochemical (PEC) and photovoltaic (PV) cells is a promising route. While PEC cells of a single photoanode have been constructed and characterized from various materials, the efficiency have been low due to the lack of electromotive force (EMF) generated in comparison to the conduction band of the metal oxides and the reduction couple H^+/H_2O. External application of a voltage generated by a PV cell coupled to a PEC cell to properly generate the EMF of 1.23 eV necessary for water splitting. Further improvement of oxide catalysts is to engineer them in such a way that they absorb visible light efficiently. This leads to research into oxide nanomaterials that are doped with nitrogen and/or sensitized with quantum dots (QDs) of small bandgap semiconductors, such as CdSe and CdS. Our specific aims are: 1) to create a PEC device which is much more efficient at absorbing visible light than typical oxides by combing various methods of bandgap engineering such as combining nitrogen doping and sensitizing with CdSe QDs, combining Au/TiO_2 hybrid structures with CdSe sensitization, and graded bandgap structures such as CdSe and CdS cosensitization [1-9], and 2) to study PEC devices based on 1-D nanostructures that strongly absorb visible light, such as nitrogen doped ZnO, QD-senstized TiO_2, or core/shell WO_3 and TiO_2 that exhibit unique and beneficial PEC properties [10-16].

Recent Progress

1. Hydrogen Generation by PEC with QD-sensitized and N-doped TiO_2

We have previously discovered that combined QD sensitization and N-doping have synergistic effect on improving the performance of TiO_2 solar cells. The effect was tentatively attributed to enhanced hole transfer/transport by N-doping. Our more recent studies have found that the enhanced hole transport is more likely related to oxygen vacancies mediated by nitrogen doping. We have shown the effect to be reproducible in both nanoparticulate films and ordered nanowire arrays. The TiO_2 was synthesized by a typical sol-gel method, with polyethylene glycol (PEG) added to increase porosity in the films. Nitrogen doping the films was done by heating the sample in an ammonia atmosphere for various amounts of time. CdSe QDs were synthesized by chemical bath deposition making strong adhering films with high photocurrent.

TEM images show web-like features indicating the formation and cross linking of smallTiO_2 NPs. High resolution TEM study suggests that the NPs are amorphous before calcination. AFM studies show that there was no difference in the morphology between the TiO_2 and the N-doped TiO_2. TiO_2 NPs are continuously linked with a high amount of uniformity and porosity. SEM was done on a TiO_2 film to determine the thickness of the film. **Fig. 1** shows representative AFM and SEM images of the CdSe QD-sensitized TiO_2 films.

UV-visible measurements reveal a slight increase in absorption from 340 nm to 500 nm for the N-doped sample compared to TiO_2. The CdSe sensitized films show increased absorption over the entire visible region with an exciton peak at 525 nm corresponding to 2.6 nm particle size. There is

also increase in the baseline indicating an increase in scattering due to the formation of aggregates. Both the CdSe films are of similar absorption so their thickness and morphology are comparable.

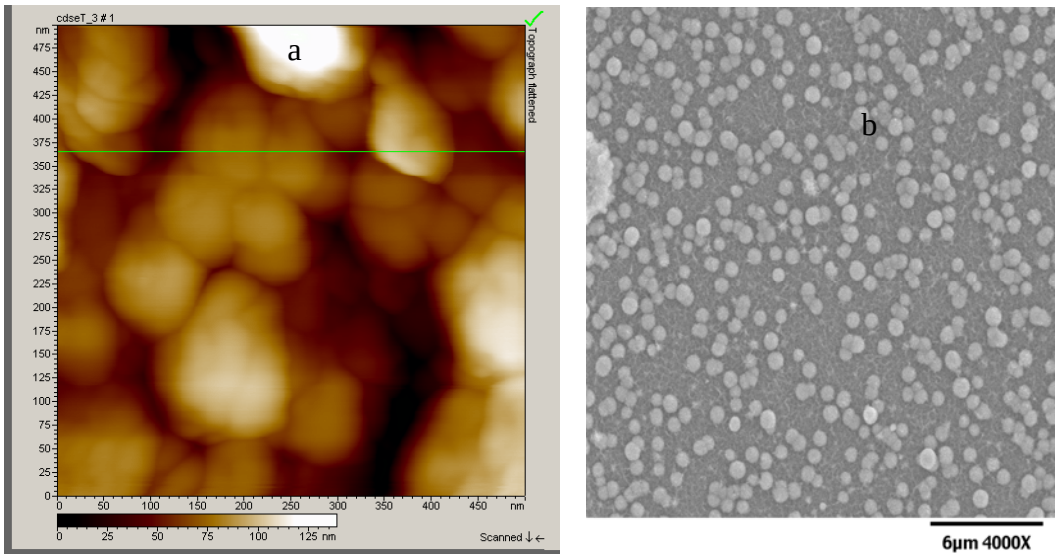

Fig. 1. AFM of CdSe sensitized film shows aggregation of CdSe (a). SEM of CdSe films shows aggregation of small CdSe QDs into large spheres about 700-800 nm in diameter (b).

PEC measurements on both TiO_2 and modified TiO_2 films show that photocurrent is significantly increased for the QD sensitized and N-doped TiO_2 film compared to QD sensitized TiO_2 alone. Incident photon to current efficiency (IPCE) measured show enhancement in the entire visible region. Nanowire arrays of TiO_2, N-doped TiO_2 and CdSe sensitized TiO_2 and N-doped TiO_2 were also characterized and investigated. The nanowire arrays showed enhanced photocurrent as compared to the nanoparticle films due to better charge transport. The QD-sensitized and N-doped TiO_2 nanowires showed the highest photocurrent and IPCE. There is a clear synergistic effect between QD sensitization and N-doping, and this is attributed to enhanced hole transport from CdSe to the oxygen vacancies in N-doped TiO_2. Preliminary ultrafast dynamics studies support the model proposed.

2. PEC Properties of CdSe/TiO_2 Mesoporous Hybrid Structures

In sensitization of TiO_2 using QDs, small molecules, such as TGA or MPA, are often used to link the QDs to TiO_2. Since these small molecules are mainly dielectric materials, they will block the transfer of the photoelectrons from the quantum dots to the TiO_2 film. Here we are trying another connection mode between QDs and TiO_2 that without the small linking molecules by assembly the quantum dots and TiO_2 NPs together into colloid spheres. The CdSe/TiO_2 hybrid mesoporous spheres and films were characterized using SEM and TEM techniques (**Fig. 2**). Relatively uniform sizes and shapes are found for both CdSe QDs and TiO_2 NPs as well as colloidal spheres.

UV-vis spectroscopy and time-resolved fluorescence have been utilized to study the optical properties and electron injection dynamics. The dynamics data confirm fast charge injection from CdSe QDs into TiO_2. The CdSe/TiO_2 hybrid spheres shows an increase in the photocurrent when compared to TiO_2 alone and CdSe sensitized to TiO_2 using a linking molecule. The overall increase in photocurrent from the CdSe/TiO_2 hybrid mesoporous structure is believed to be due to better or stronger coupling between the CdSe and the TiO_2 when compared to the CdSe sensitized TiO_2 linked by organic linkers that an act as a dielectric layer providing poor electron transport and injection.

3. Enhanced PEC Performance of CdSe QD-Sensitized Au/TiO_2 Hybrid Mesoporous Films

To increase the visible light absorption of wide band gap semiconductors such as TiO_2 and ZnO for PEC applications, many methods have come about in the literature such as doping and sensitizing. One approach that groups have focused on recently has been the idea of enhancing metal oxide materials with metals. Here we developed the first ever Au/TiO_2 hybrid structure (0-5%) that has also been sensitized with CdSe QDs made by chemical bath deposition for PEC water splitting.

For the TiO_2 film sample, the absorption onset is around 360 nm. In contrast, the Au/TiO_2 film showed strong absorption in the visible region due to the SPR of Au NPs, and the absorption increases with increasing Au NPs loading. TEM showed uniform size and shape distribution. The strong enhancement for the photocurrent with Au NPs can be explained by an increase in scattering that allows CdSe to absorb more light and inject more electrons into TiO_2. IPCE shows more enhancement at shorter wavelength, supporting the explanation.

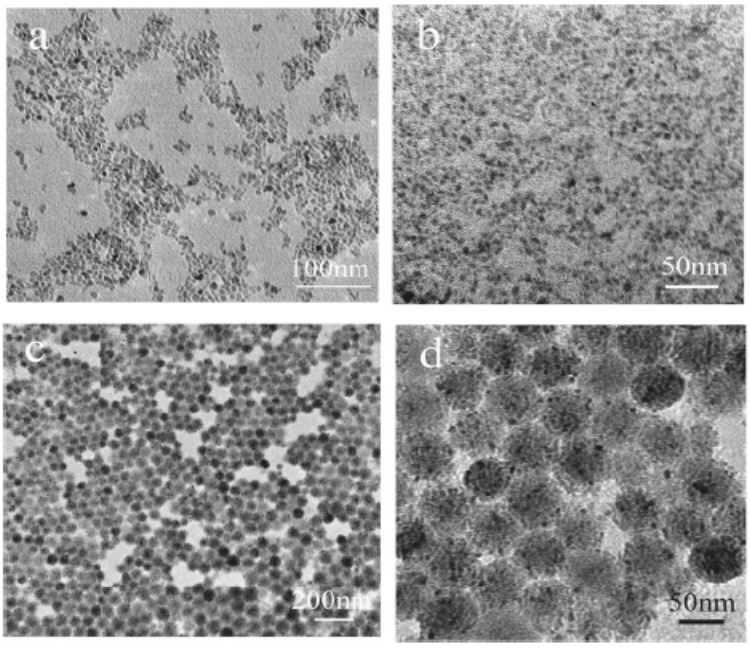

Fig. 2. TEM images of TiO_2 (a) and CdSe (b) alone and CdSe/TiO_2 hybrid spheres (c,d).

4. N-Doped ZnO Nanowire Arrays for PEC Water Splitting

N-doped ZnO (ZnO:N) nanowire arrays have also been studied as photoanodes in PEC hydrogen generation from water splitting. Dense and vertically aligned ZnO nanowires were first prepared from a hydrothermal method, followed by annealing in ammonia to incorporate N as a dopant. Nanowires with N concentration up to 4% were prepared by varying the annealing time. XPS studies confirm N substitution at O sites in ZnO nanowires up to about 4%. IPCE measurements carried out on PEC cell with ZnO:N nanowire arrays as photoanodes demonstrate a significant increase of photoresponse in the visible region compared to undoped ZnO nanowires prepared at similar conditions. Mott-Schottky measurements were conducted to determine the flat-band potential, charge carrier density, and thickness of space-charge layer. In comparison to ZnO nanowires without N-doping, ZnO:N nanowires show an order of magnitude increase in photocurrent density.

5. Photocatalytic Performance Improved in Nanorod Arrays

A systematic study confirms that the surface area of TiO_2 is directly proportional to the decay rate of methylene blue (MB) using the oblique angle deposited TiO_2 nanorod arrays with different lengths. Ag NPs are explored to increase the photocatalytic performance of TiO_2 to create an effective charge-separation between the photogenerated electron-hole pairs. Ag NPs with different loadings were systematically coated onto uniformly aligned TiO_2 nanorod arrays, and their photocatalytic performance was measured. The photocatalytic decay rates are enhanced compared to bare TiO_2. A simple model based on the Ag NP coverage and charge trapping is proposed, and the predicted results

agree very well with the experimental results quantitatively. The effective lifetime of photogenerated holes due to the trapping of the Ag NPs on the surface of TiO_2 nanorods was estimated to be about three times that of pure TiO_2 nanorods. The structural and photocatalytic properties of multi-layered WO_3/TiO_2 nanostructures were also investigated. The results show that the GLAD multi-layered samples have the best photocatalytic performance.

Using two consecutive GLAD at different deposition angles and with different material, a WO_3-core TiO_2-shell nanostructure has been fabricated. Compared with control samples, the photocatalytic performance of the 300^{o}C annealed core-shell sample is significantly better. This can be directly correlated to the relatively large amount of interfacial area between TiO_2 and WO_3, which is optimized in this core-shell morphology and allows for more effective charge separation.

Both WO_3/TiO_2 and TiO_2/WO_3 core/shell nanorod films were used to make electrodes for PEC water splitting. IPCE analysis showed that the WO_3/TiO_2 samples were more efficient at water splitting. The maximum efficiency for the TiO_2/WO_3 sample was under 5% at about 340 nm. The WO_3/TiO_2 achieved near 12% IPCE at 350 nm but the efficiency decreased sharply around 390 nm. These preliminary data show that the WO_3 is the better core material for these core/shell structures but improved efficiency in the visible region through sensitization or doping may allow these structures to achieve greater efficiency. Additional characterization will be needed to determine why the two structures showed such a marked difference in water splitting efficiency.

Planned Activities for Future

Our plan for future research include optimization of composite structures in terms of ratio and morphology of constituent components, design new nanorod catalyst through quantum confinement effect and plasmonic effect through GLAD, validation of the enhanced hole transport model proposed using ultrafast laser techniques using the new fs laser system acquired recently, and improvement of overall PEC performance by carefully considering, determining and controlling the key factors involved, including electrode, interfacial interaction, and optical absorption. A combination of microscopy, spectroscopy, dynamics, and electrochemistry techniques will be employed. Collaboration will be sought to conduct theoretical modeling in relation to the experimental work.

Selected Publications

1. L. Liu, G. Wang, Y. Li, Y. Li and J, Z. Zhang, submitted to Nano Research, 2010.
2. A. Wolcott, R. C. Fitzmorris, O. Muzaffery, and J. Z. Zhang, Chem. Mater., 22, 2814-2821, 2010.
3. G. Wang, X. Yang, F. Qian, J. Z. Zhang and Y. Li, Nano Letters, 10, 1088--1092, 2010.
4. J. Hensel, G. Wang, Y. Li, and J. Z. Zhang, Nano Letters, 10, 478-483, 2010.
5. L. Liu, J. Hensel, R. C. Fitzmorris, Y. Li, and J. Z. Zhang, J. Phys. Chem. Lett., 1, 155-160, 2010.
6. X.J. Lv, J.H. Li, Jennifer Hensel, Jin Z. Zhang, Electrochemistry, 15, 432-440, 2009.
7. J. Li and J. Z. Zhang, Coord. Chem. Rev., 253, 3015-3041, 2009 (invited review).
8. Y. Li and J. Z. Zhang, Lasers and Photonics Review, 4, 517-528, 2009 (invited review).
9. X. Yang, A. Wolcott, G. Wang, A. Sobo, B. Fitzmorris, F. Qian, J. Z. Zhang, and Y. Li, Nano Letters, 9, 2331-2336, 2009.
10. W. Smith, S. Mao, G. Lu, A. Catlett, J. Chen, and Y. Zhao, Chem. Phys. Lett. 485, 171–175, 2010.
11. W. Smith, W. Ingram, and Y.-P. Zhao, Chem. Phys. Lett. 479, 270–273, 2009.
12. W. Smith and Y.-P. Zhao, Catalysis Communications, 10, 1117-1121, 2009.
13. R. Sharma, J.P. Mondia, J. Schäfer, W. Smith, S.-H. Li, Y.-P. Zhao, Z.H. Lu, and L.J. Wang, Microelectronics Journal, 40, 520-522, 2009.
14. W. Smith and Y.-P. Zhao, J. Phys. Chem. C, 112, 19635–19641, 2008.
15. Y. P. He and Y.-P. Zhao, J. Phys. Chem. C, 112, 61-68, 2008.
16. Y. P. He, Y.-P. Zhao, and J.-S. Wu, Appl. Phys. Lett. 92, 063107, 2008.

Quantitative Electron Nanocrystallography
DE-FG02-06ER45923

Jian-Min Zuo
jianzuo@illinois.edu
Dept. of Materials Science and Engineering and Materials Research Laboratory,
University of Illinois, Urbana-Champaign, IL 61801

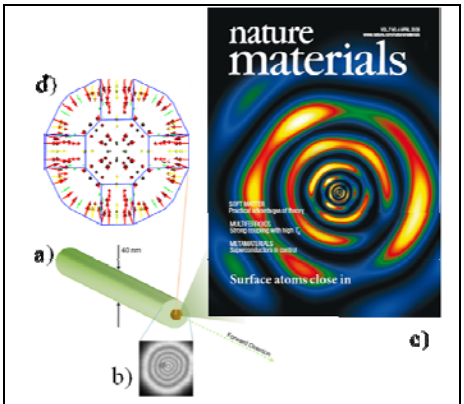

a) and b) The 40 nm diameter coherent electron beam used to illuminating a single Au nanocrystal, c) the journal cover and the diffraction patterns and d) the confirmed model of surface contraction .

Program Scope: The properties of materials ultimately depend on their local atomic structure. While there are well-established diffraction techniques for structure determination of crystals with 2-D or 3-D periodicities, there are no such techniques for nonperiodic structures including many nanostructured materials. Understanding structure-property relationships in these materials thus depends critically on further progress in our ability of characterizing non-periodic structures. This proposal aims to develop quantitative and robust atomic structure determination techniques for nanoparticles, small crystals and one-dimensional materials whose structure cannot be addressed by conventional crystal diffraction techniques. The tool we use to address this problem is based on the nanoarea electron diffraction (NED) technique developed under prior DOE support. Significant improvement to this technique is expected from the new field emission gun transmission electron microscope with an electron probe aberration corrector and an in-column energy filter at University of Illinois. The improvement in resolution (with a smaller probe) and diffraction pattern quality (with energy filtering) will be coupled with new developments in electron diffraction modeling and inversion algorithms. Broad impact is expected from the structural knowledge obtained with the new high-resolution electron diffraction technique, especially in areas of surface and interfacial structures characterization of nanomaterials.

Recent Progress (2008-2010): The progress we made during this period include: 1) complete structural analysis of carbon nanotube bundle and multiwall carbon nanotubes, 2) the achievement of sub-Å resolution diffractive imaging, 3) elucidation of the physics of graphene folding, and 4) imaging of charge ordering cluster and elucidation of phase competition in CMR manganites. These progresses are described below.

1) Carbon-Carbon Bond Length Analysis of Multiwalled Carbon Nanotubes: Carbon, which is the most abundant element in the universe after hydrogen and helium, is of considerable importance for energy science, from petroleum to nuclear energy. The structure of carbon materials, in general, is characterized by the *C*-*C* bond length. However, the *C*−*C* bond length is only known for well defined structures like graphite

and diamond. The carbon-carbon length, in general, is difficult to measure for carbon nanostructures like carbon nanotubes. There are significant disagreements among theory about the *C-C* bond distance in SWCNTs. For example, the predicted *C-C* bond length around the tube ranges from 1.382 to 1.466 Å for CNTs when the tube diameter is smaller than 10 Å in diameter. In a paper published in Carbon[1], we present an accurate structure analysis of a small diameter Multi-walled carbon nanotube (MWCNT) of five walls with diameter ranging from ~17 to 46 Å. The structure was determined based on quantitative analysis of electron diffraction patterns recorded from the MWCNT. We show that the measurement is sufficiently accurate to reveal significant differences between the measured and the calculated wall diameters based on the ideal hexagonal structure of graphene and the *C-C* bond length of 1.421 Å. The diameter difference increases as the tube diameter decreases and is up to ~3.8% for the innermost wall of ~17 Å in diameter. However, the axial periodicities along the tube direction are almost the same as the ideal carbon nanotubes (CNTs) for all five walls. We fitted our experimental results by deforming the graphene unit cell. The results indicate that on average there are three different bond lengths in chiral walls and two different bond lengths in achiral walls.

2) Sub-Å Resolution Diffractive Imaging of Quantum Dots: Diffractive imaging is a promising imaging technique for structure determination of individual nanoparicles and macromolecules that does not require an imaging lens. We have developed a new diffractive imaging technique to combine information from low resolution image and high resolution diffraction pattern. The resolution of diffractive imaging before at best is about several nanometers. This is far away from the Å resolution that is required to determine 3-D atomic structure. Thus, development of high resolution diffractive imaging technique reported in our work and experimental demonstration of resolution at sub-Å here represent a critical breakthrough in the development of diffractive imaging. The major difficulty in atomic resolution diffractive imaging is due to the loss of weak coherent scattering signals in recorded diffraction patterns. The incorporation of additional image information (at lower resolution) provided the object constraint and the starting phase. We demonstrated our new diffractive imaging techniques using CdS quantum dots. The results have been published in a paper in the February issue of Nature Physics, 2009[2].

3) The Physics of Graphene Folding: In a paper published in *Physical Review Letters*[3], we reported a combined experimental, theoretical and simulation study of the physics of graphene folding. Folding is unique to graphene and 2D structures in general. Folding of 2D crystals like graphene, however, is expected to depend on the lattice registry, which affects the adhesion between of the folded flat region. This leads to several interesting discovery in our paper, one is the preferred folding along the armchair and zigzag directions of graphene, and another is stabilization of folded graphene by a small twist of the 2D sheet in the case of folded armchair edges. Our experimental work was enabled by the development of two novel techniques; one is the folding of suspended graphene using high power ultrasound and the other is the electron nanodiffraction method for the structure determination of closed graphene edges. The use of ultrasound provides a random force which allows us to explore free folding in all directions. The electron

diffraction technique allows us to distinguish between closed and open edges and a determination of the folding direction with an accuracy of 0.1^{o}.

4) Imaging of Charge Ordering Cluster (Collaboration with J. Tao, Brookhaven National Laboratory and others):

In a paper that was published in *Physical Review Letters*[4] and highlighted in the November issue of Physics Today, 2009, we reported the imaging of charge ordering clusters in $La_{1-x}Ca_xMnO_3$, $x = 0.45$. The imaging was achieved using scanning-electron-nanodiffraction, a technique developed under the support of this grant. The extra intensity of the charge ordering reflection was used to form images of nanoclusters as they form and evolve with temperature. Our experimental images show that they are not doping inhomogeneities and their structure is that of the bulk compound at $x = 0.60$, which at low temperatures is insulating. Their volume fraction peaks at the CMR critical temperature and is estimated to be 22 % at finite magnetic fields. In view of the known dependence of the nanoscale phase on magnetic fields, such a volume fraction can account for the CMR peak. This finding shed considerable light to the enhancement of the CMR effect, which has been a long standing issue in since it is discovered in the 1990s. The work started here at University of Illinois when the first author, Jing Tao, was a graduate student and supported by this DOE grant. After she graduated and moved to Oak Ridge National Laboratory, she continued this work.

Future Plans: We plan to address the following issues in next one to two years. The first is to improve the iterative transformation algorithm for inversion of electron diffraction patterns and to push the resolution of diffractive imaging and use this technique to overcome the information limit of the microscope. The intended applications are to image nanoparticles and carbon nanostructures. The second is to test the limit of electron diffraction for the study of carbon nanotube peapods. We intend to carry out a systematic study of electron diffraction of peapods to examine the information limit placed by atomic scattering and electron beam damage. This will be coupled with a simulation study. The third is to image nanoparticles in multiple projections to examine their 3-D structure. We are especially interested in imaging at high index zone axes from diffraction patterns, which can be used to supplement or complement information obtained by electron direct imaging.

References:

1) Zhang, J. & Zuo, J. M. Structure and diameter-dependent bond lengths of a multi-walled carbon nanotube revealed by electron diffraction. *Carbon* **47**, 3515-3528 (2009).
2) Huang, W. J., Zuo, J. M., Jiang, B., Kwon, K. W. & Shim, M. Sub-angstrom-resolution diffractive imaging of single nanocrystals. *Nature Physics* **5**, 129-133 (2009).
3) Zhang, J. *et al.* Free Folding of Suspended Graphene Sheets by Random Mechanical Stimulation. *Physical Review Letters* **104**, 166805, (2010).
4) Tao, J. *et al.* Direct Imaging of Nanoscale Phase Separation in La0.55Ca0.45MnO3: Relationship to Colossal Magnetoresistance. *Physical Review Letters* **103**, 097202 (2009).

DOE Sponsored Publications in 2008-2010:

1) W. J. Huang, R. Sun, J. Tao, L. D. Menard, R. G. Nuzzo and J. M. Zuo, “Coordination-dependent surface atomic contraction in nanocrystals revealed by coherent diffraction” Nature Materials, 7, 308-313 (2008)
2) S.W. Kim, J.M. Zuo, N.T. Nguyen, D.C. Johnson, and D.G. Cahill, “Structure of layered WSe_2 thin films with ultralow thermal conductivity”, J. Materials Research, 23, 1064-1067, (2008)
3) T Kim, S Kim, E Olson, and J. M. Zuo, "In situ measurements and transmission electron microscopy of carbon nanotube field-effect transistors," Ultramicroscopy, 108 (7), 613-618 (2008).
4) Y. Y. Jiang, W. Zhou, T. Kim, Y. Huang, and J. M. Zuo, "Measurement of radial deformation of single-wall carbon nanotubes induced by intertube van der Waals forces," Physical Review B 77 (15), 153405 (2008).
5) D. Niebieskikwiat, J. Tao, J. M. Zuo, and M. B. Salamon, "Time-dependent phenomena in phase-separated electron-doped manganites," Physical Review B **78** (1), 014434 (2008).
6) W.J. Huang, J.M. Zuo, B. Jiang, K.W. Kwon and Moonsub Shim, “Sub-Å resolution diffractive imaging of single nanocrystals”, *Nature Physics* 5, 129-133 (2009).
7) J. Tao, D. Niebieskikwiat, M. Varela, W. Luo, M. A. Schofield, Y. Zhu, M. B. Salamon, J. M. Zuo, S. T. Pantelides, and S. J. Pennycook, "Direct Imaging of Nanoscale Phase Separation in La0.55Ca0.45MnO3: Relationship to Colossal Magnetoresistance", *Physical Review Letters* 103 (9), 097202 (2009).
8) J. Zhang and J.M. Zuo, “Structure and diameter dependent bond lengths of a multiwalled carbon nanotube revealed by electron diffraction”, Carbon 47, 3515 –3528 (2009)
9) J. Zhang and J. M. Zuo, "Structure and diameter-dependent bond lengths of a multi-walled carbon nanotube revealed by electron diffraction", *Carbon* 47 (15), 3515-3528 (2009).
10) T. Kim, G. Kim, W. I. Choi, Y. K. Kwon, and J. M. Zuo, Electrical transport in small bundles of single-walled carbon nanotubes: Intertube interaction and effects of tube deformation Applied Physics Letters 96 (17), 173107 (2010).
11) S. I. Sanchez, M. W. Small, S. Sivaramakrishnan, J. G. Wen, J. M. Zuo, and R. G. Nuzzo,Visualizing Materials Chemistry at Atomic Resolution Analytical Chemistry 82 (7), 2599-2607 (2010).
12) H. Park and J. M. Zuo, "Comment on "Structural Preablation Dynamics of Graphite Observed by Ultrafast Electron Crystallography"", *Physical Review Letters* 105 (5), 059603 (2010).
13) B. Jiang, J. M. Zuo, D. Holec, C. J. Humphreys, M. Spackman, and J. C. H. Spence, "Combined structure-factor phase measurement and theoretical calculations for mapping of chemical bonds in GaN", *Acta Crystallographica Section A* 66, 446-450 (2010).
14) T. Kim, G. Kim, W. I. Choi, Y. K. Kwon, and J. M. Zuo, "Electrical transport in small bundles of single-walled carbon nanotubes: Intertube interaction and effects of tube deformation", *Applied Physics Letters* 96 (17), 173107 (2010).
15) W. Chern, K. Hsu, I. S. Chun, B. P. de Azeredo, N. Ahmed, K. H. Kim, J. M. Zuo, N. Fang, P. Ferreira, and X. L. Li, "Nonlithographic Patterning and Metal-Assisted Chemical Etching for Manufacturing of Tunable Light-Emitting Silicon Nanowire Arrays", *Nano Letters* 10 (5), 1582-1588 (2010).
16) Y. K. Che, X. M. Yang, Z. X. Zhang, J. M. Zuo, J. S. Moore, and L. Zang, "Ambient photodoping of p-type organic nanofibers: highly efficient photoswitching and electrical vapor sensing of amines", *Chemical Communications* 46 (23), 4127-4129 (2010).
17) J. Zhang, J. L. Xiao, X. H. Meng, C. Monroe, Y. G. Huang, and J. M. Zuo, "Free Folding of Suspended Graphene Sheets by Random Mechanical Stimulation", *Physical Review Letters* 104 (16), 166805 (2010).

INVITED TALKS

Nanostructures for Energy Storage: What Can We Learn from Imaging and Spectroscopy?

Gary W. Rubloff

Director, Nanostructures for Electrical Energy Storage (NEES), a DOE Energy Frontier Research Center
Minta Martin Professor of Engineering and Director, Maryland NanoCenter, University of Maryland

Nanostructures hold great promise as the basis for next-generation energy technologies. A diverse set of synthesis approaches enables fabrication of individual nanostructures, and massive arrays of them, in geometries and with materials that optimize multifunctional requirements such as surface/volume configuration, length scales between interfaces, and mechanical stability during chemical reactions. However, to provide adequate scientific underpinnings for a nanostructure-based energy technology, improved techniques are needed (1) to characterize the nanostructures in 3-D and (2) to relate synthesis and characterization results to performance metrics for energy applications, a coupled grand challenge for the scientific community.

The DOE-EFRC on Nanostructures for Electrical Energy Storage (NEES) is addressing these issues within its focus on heterogeneous, multifunctional nanostructures and particularly their electrochemistry at the nanoscale. The research scope encompasses bottom-up and top-down fabrication strategies, electrochemical behavior from single defects in individual nanowires to massive ordered arrays of nanostructures, and novel characterization techniques that emphasize real-space imaging and analysis. Indeed, our ability to discern properties of nanostructure systems in 3-D and during charge transport and chemical reaction may well determine how far and fast the science can proceed to underwrite the technology. Accordingly the NEES research program includes several major efforts in novel characterization: (1) in-situ transmission electron microscopy (TEM) involving liquid electrolytes; (2) several advanced microsystem (MEMS) platforms for in-situ TEM and other purposes; (3) in-situ scanning probe microscopy coupled to electrochemistry and chemical analysis; and (4) relation of model nanostructures studied by UHV surface analysis and SPM imaging to nanoscale electrochemistry.

Nanoscale Imaging of Ultrafast Magnetization Dynamics with Resonant Coherent X-rays

Andreas Scherz
SIMES, SLAC National Accelerator Center, 2575 Sand Hill Rd, M/S 69, Menlo Park, CA 94025

Understanding the microscopic mechanisms driving the magnetization dynamics on the femtosecond time scale is of essential importance for manipulating and controlling the macroscopic state in magnetic storage devices. The demagnetization in ferromagnetic films by an ultrashort laser excitation on a time scale of a few hundred femtoseconds raised controversies about the effective path to dissipate angular momentum to the lattice, see e.g. [1]. Even more intriguing is the demonstration of all-optical magnetization reversal in ferrimagnetic compounds using circularly polarized, femtosecond laser pulses [2]. This type of opto-magnetic switching can occur as fast as 30ps and is thus shorter than the fastest reported precessional magnetization reversal (~200ps) with shaped magnetic field pulses. Utilizing a fast optical microscope, recent experiments suggests that the new magnetization direction emerges from a highly quenched, nonequilibrium state and reforms macroscopically on tens of picoseconds that is a long time after the ultrafast laser pulse passed the sample [3]. The origin of this "memory" for the photon helicity remains, however, elusive.

Until only recently, the field of "Femto-magnetism" has naturally been driven by all-optical pump-probe techniques. Femtosecond time-resolved X-ray magnetic circular dichroism spectroscopy has been utilized to unambiguously determine the ultrafast quenching of spin and orbital moments after ultrashort laser excitation [4]. While all-optical pump-probe techniques allow ultrafast excitations (pump) and the study of their evolution (probe) on the macroscopic scale by use of the magneto-optical Kerr or Faraday effect, little is known about the microscopic processes on nano- and sub-nanometer length scales because of the lack of real or momentum space resolution of optical techniques. By combining resonant coherent resonant magnetic scattering with the unique high peak-brightness, short pulse structure, and fully transverse coherence of the new x-ray free-electron lasers, the dynamics of magnetic fluctuations and magnetization relaxation processes can be studied on the nanometer scale with sub-picosecond time resolution. There are, however, also challenges such as radiation and electronic damage limits caused by the intense x-ray pulses that potentially alter the sample while being probed.

A brief overview is given to the current state of x-ray microscopy techniques providing elemental, chemical and magnetic sensitivity. The emphasis will be placed on the coherent imaging techniques based on iterative or holographic phase retrieval that have been developed over the last decade into a mature x-ray microscopy alternative. In particular, the concepts of Fourier transform holography [5], MAD holography [6] and X-ray HERALDO [7] will be elucidated. While the image resolution is in principle set by the wavelength only, the current resolution limits will be discussed. First results on ultrafast magnetization studies with coherent x-ray pulses carried out at the Stanford Synchrotron Radiation Lightsource (SSRL) and the first x-ray laser LCLS will be presented.
The research is supported by the U.S. Department of Energy, Office of Basic Energy Sciences.

[1] Koopmans, B, Malinowski, G, Dalla Longa, F, Steiauf, D, Fähnle, M, Roth, T, Cinchetti, M, Aeschlimann, M, Nature materials 9, 259 (2010).
[2] Stanciu, C.D., Hansteen, F., Kimel, A.V., Kirilyuk, A., Tsukamoto, Itoh, A., Rasing, Th., Phys. Rev. Lett. 99, 047601 (2007).
[3] Vahaplar, K., Kalashnikova, A.M., Kimel, A.V., Hinzke, D., Novak, U., Chantrell, R., Tsukamoto, A., Itoh, A., Kirilyuk, Rasing, Th., Phys. Rev. Lett. 103, 117201 (2009).

[4] Stamm, C., Kachel, T., Pontius, N., Mitzner, R., Quast, T., Holldack, K., Khan, S., Lupulescu, C., Aziz, E.F., Wietstruk, M., Dürr, H.A., Eberhardt, W., Nature materials 6, 740 (2007).
[5] S. Eisebitt, J. Lüning, W. F. Schlotter, M. Lörgen, O. Hellwig, W. Eberhardt & J. Stöhr, Nature **432**, 885-888 (2004).
[6] A. Scherz, D. Zhu, R. Rick, W.F. Schlotter, S. Roy, J. Lüning, and J. Stöhr, Phys. Rev. Lett. 101, 076101 (2008).
[7] D. Zhu, M. Guizar-Sicairos, B. Wu, A. Scherz, Y. Acremann, T. Tyliszczak, P. Fischer, N. Friedenberger, K. Ollefs, M. Farle, J. R. Fienup, and J. Stöhr, Phys. Rev. Lett. 105, 043901 (2010).

AUTHOR INDEX

AND

PARTICIPANT LIST

Author Index

EPSM Contractors' Meeting 2010
Participants

Last Name	First Name	Organization	E-mail Address
Alper	Mark	Lawrence Berkeley National Laboratory	MDAlper@lbl.gov
Auciello	Orlando	Argonne National Laboratory	auciello@anl.gov
Baddorf	Arthur	Oak Ridge National Laboratory	baddorfap@ornl.gov
Balsara	Nitash	Lawrence Berkeley National Laboratory	nbalsara@berkeley.edu
Bartelt	Norm	Sandia National Laboratories, California	bartelt@sandia.gov
Batson	Philip	Rutgers University	batson@physics.rutgers.edu
Bonnell	Dawn	University of Pennsylvania	bonnell@lrsm.upenn.edu
Borisevich	Albina	Oak Ridge National Laboratory	albinab@ornl.gov
Bowen	Kit	Johns Hopkins University	kbowen@jhu.edu
Browning	Nigel	University of California, Davis/LLNL	nbrowning@ucdavis.edu
Campbell	Geoffrey	Lawrence Livermore National Laboratory	ghcampbell@llnl.gov
Chandrasekhar	Venkat	Northwestern University	v-chandrasekhar@northwestern.edu
Chang	Y. Austin	University of Wisconsin-Madison	chang@engr.wisc.edu
Chen	Long-Qing	Pennsylvania State University	lqc3@psu.edu
Chisholm	Matthew	Oak Ridge National Laboratory	chisholmmf@ornl.gov
Cobden	David	University of Washington	cobden@uw.edu
Contescu	Cristian	Oak Ridge National Laboratory	contescuci@ornl.gov
Crockett	Teresa	DOE Basic Energy Sciences	teresa.crockett@science.doe.gov
Cumings	John	University of Maryland	cumings@umd.edu
Davis	JC Seamus	BNL/Cornell University	jcdavis@ccmr.cornell.edu
DeGraef	Marc	Carnegie Mellon University	degraef@cmu.edu
Fiechtner	Gregory	DOE Basic Energy Sciences	Gregory.Fiechtner@science.doe.gov
Flynn	Peter	University of Illinois, Urbana-Champaign	cpf@mrl.uiuc.edu
Gallego	Nidia	Oak Ridge National Laboratory	gallegonc@ornl.gov
Garcia	Andrei	Stanford University	ag254@stanford.edu
Goldman	Rachel	University of Michigan	rsgold@umich.edu
Gruverman	Alexei	University of Nebraska, Lincoln	agruverman2@unl.edu
Hammel	Chris	Ohio State University	hammel@mps.ohio-state.edu
Harmer	Martin	Lehigh University	sls4@lehigh.edu
Heinonen	Olle	Argonne National Laboratory	heinonen@anl.gov
Hla	Saw-Wai	Ohio University	hla@ohio.edu
Hong	Seungbum	Argonne National Laboratory	hong@anl.gov
Horton	Linda	DOE Basic Energy Sciences	linda.horton@science.doe.gov
Huey	Bryan	University of Connecticut	bhuey@ims.uconn.edu
Hufnagel	Todd	Johns Hopkins University	hufnagel@jhu.edu
Iavarone	Maria	Temple University	iavarone@temple.edu
Kapitulnik	Aharon	SLAC/Stanford University	aharonk@stanford.edu

Kisielowski	Christian	Lawrence Berkeley National Laboratory	CFKisielowski@lbl.gov
Könenkamp	Rolf	Portland State University	rkoe@pdx.edu
Kortan	Refik	DOE Basic Energy Sciences	refik.kortan@science.doe.gov
Lev	Benjamin	University of Illinois, Urbana-Champaign	benlev@illinois.edu
Li	Lian	University of Wisconsin-Milwaukee	lianli@uwm.edu
Luo	Jian	Clemson University	jianluo@clemson.edu
Lupini	Andrew	Oak Ridge National Laboratory	9az@ornl.gov
Manoharan	Hari	Stanford University	manoharan@stanford.edu
Marks	Laurence	Northwestern University	L-marks@northwestern.edu
McCartney	Martha	Arizona State University	molly.mccartney@asu.edu
McCarty	Kevin	Sandia National Laboratories, California	mccarty@sandia.gov
McGaughey	Alan	Carnegie Mellon University	mcgaughey@cmu.edu
McKeown	Joseph	Lawrence Livermore National Laboratory	mckeon3@llnl.gov
Meng	Shirley	University of California, San Diego	shirleyment@ucsd.edu
Moler	Kathryn	SIMES/Stanford University	kmoler@stanford.edu
Morris	James	Oak Ridge National Laboratory	morrisj@ornl.gov
Pan	Xiaoqing	University of Michigan	panx@umich.edu
Pantelides	Sok	Vanderbilt University	pantelides@vanderbilt.edu
Parks	Joel	Rowland Institute at Harvard	parks@rowland.harvard.edu
Pellin	Michael	Argonne National Laboratory	pellin@anl.gov
Pennycook	Stephen	Oak Ridge National Laboratory	pennycooksj@ornl.gov
Petford-Long	Amanda	Argonne National Laboratory	petford.long@anl.gov
Plummer	Ward	Louisiana State University	wplummer@phys.lsu.edu
Prange	Micah	Vanderbilt University	micah.prange@gmail.com
Priya	Shashank	Virginia Technological Institute	spriya@vt.edu
Raschke	Markus	University of Colorado	markus.raschke@colorado.edu
Reddy	Pramod	University of Michigan	pramodr@umich.edu
Robertson	Ian	University of Illinois, Urbana-Champaign	ianr@illinois.edu
Ruan	Chong-Yu	Michigan State University	ruan@pa.msu.edu
Rubloff	Gary	University of Maryland	rubloff@umd.edu
Saldin	Dilano	University of Wisconsin-Milwaukee	dksaldin@uwm.edu
Santala	Melissa	Lawrence Livermore National Laboratory	santala1@llnl.gov
Sciambi	Adam	Stanford University	sciambi@stanford.edu
Scherz	Andreas	SLAC/Stanford University	scherz@slac.stanford.edu
Shah	Amish	Arizona State University	Amish.Shah@asu.edu
Spence	John	Arizona State University/LBNL	spence@asu.edu
Stemmer	Susanne	University of California, Santa Barbara	stemmer@mrl.ucsb.edu
Talley	Lee-Ann	Oak Ridge Institute for Science and Education	Lee-Ann.Talley@orise.orau.gov
Tao	Jing	Brookhaven National Laboratory	jtao@bnl.gov
Thiyagarajan	Thiyaga	DOE Basic Energy Sciences	P.Thiyagarajan@science.doe.gov
Thürmer	Konrad	Sandia National Laboratories, California	kthurme@sandia.gov

Viehland	Dwight	Virginia Technological Institute	viehland@mse.vt.edu
Voyles	Paul	University of Wisconsin-Madison	voyles@engr.wisc.edu
Weiss	Paul	University of California, Los Angeles	psw@cnsi.ucla.edu
Westervelt	Robert	Harvard University	westervelt@seas.harvard.edu
Wiezorek	Jorg	University of Pittsburgh	wiezorek@pitt.edu
Wu	Lijun	Brookhaven National Laboratory	ljwu@bnl.gov
Xiang	Hua	University of Wisconsin-Madison	xiang2@wisc.edu
Yacoby	Amir	Harvard University	yacoby@physics.harvard.edu
Yang	Judith	University of Pittsburgh	judyyang@pitt.edu
Yazdani	Ali	Princeton University	yazdani@princeton.edu
Zhang	Jin	University of California, Santa Cruz	zhang@ucsc.edu
Zhao	Yiping	University of Georgia	zhaoy@physast.uga.edu
Zhu	Jane	DOE Basic Energy Sciences	jane.zhu@science.doe.gov
Zhu	Yimei	Brookhaven National Laboratory	zhu@bnl.gov